BNL-102424-2013-CP

A Compilation of Internship Reports

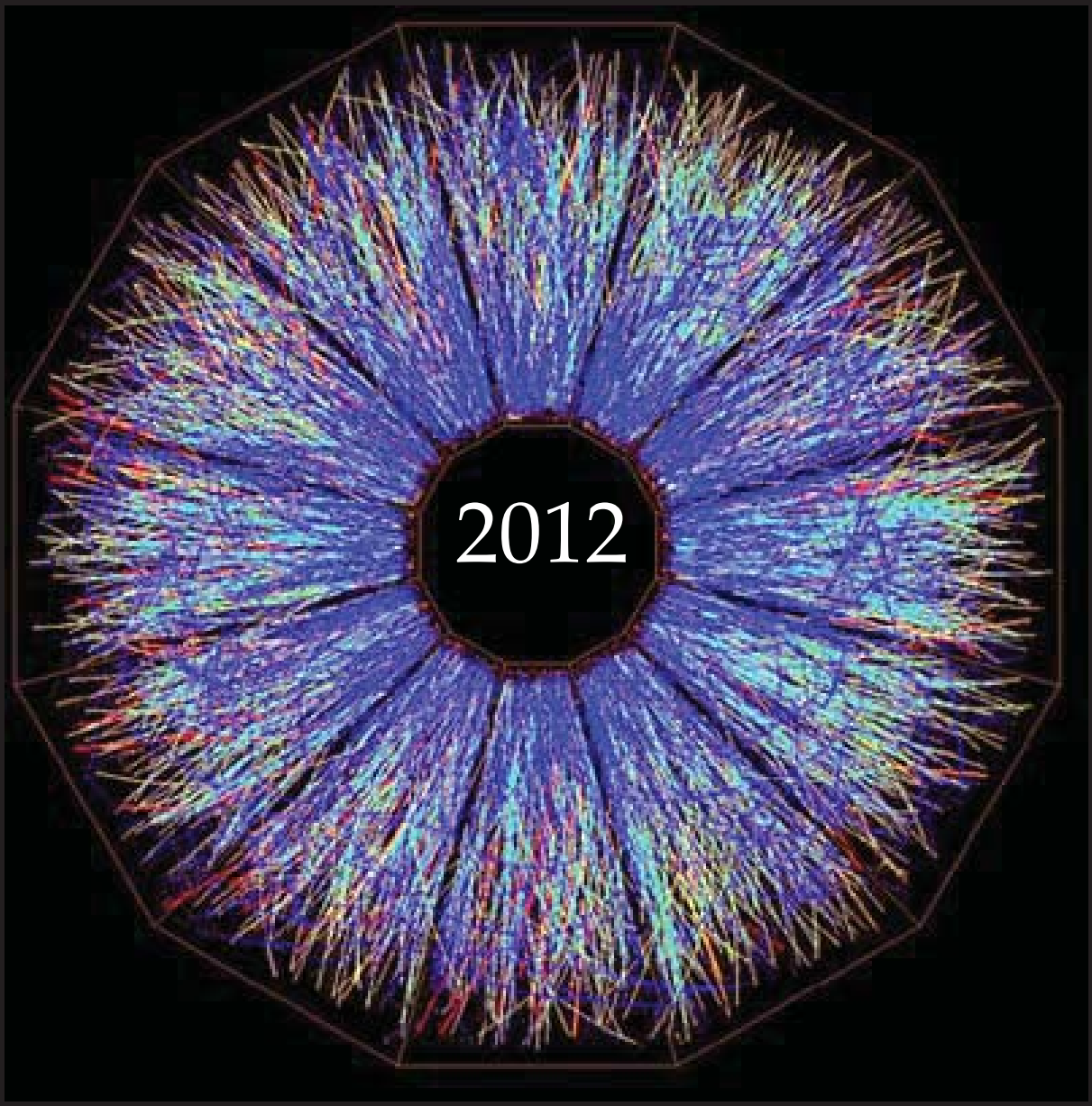

Prepared for The Office of Educational Programs
Brookhaven National Laboratory
Office of Educational Programs

Notice: This manuscript has been authored by employees of Brookhaven Science Associates, LLC under Contract No. DE-AC02-98CH10886 with the U.S. Department of Energy. The publisher by accepting the manuscript for publication acknowledges that the United States Government retains a non-exclusive, paid-up, irrevocable, world-wide license to publish or reproduce the published form of this manuscript, or allow others to do so, for United States Government purposes.

DISCLAIMER

This work was prepared as an account of work sponsored by an agency of the United States Government. Neither the United States Government nor any agency thereof, nor any of their employees, nor any of their contractors, subcontractors or their employees, makes any warranty, express or implied, or assumes any legal liability or responsibility for the accuracy, completeness, or any third party's use or the results of such use of any information, apparatus, product, or process disclosed, or represents that its use would not infringe privately owned rights. Reference herein to any specific commercial product, process, or service by trade name, trademark, manufacturer, or otherwise, does not necessarily constitute or imply its endorsement, recommendation, or favoring by the United States Government or any agency thereof or its contractors or subcontractors. The views and opinions of authors expressed herein do not necessarily state or reflect those of the United States Government or any agency thereof.

BROOKHAVEN
NATIONAL LABORATORY

Table of Contents

Optimization of geometry for hybrid proton-beam target for the long-baseline neutrino experiment . . . 9
Paige Abrunzo

Determining the effects of ionizing radiation using a cell model with mitochondrial dysfunction . . . 14
S. Ackerman

Study of charge mobility in pulse irradiated conducting polymers by simultaneous measurement of optical and microwave absorption . . . 18
Stephen D. Albright

Assessment of clinical and neuropsychological function in comorbid cocaine and alcohol addiction . . . 24
Christine Anerella

Heat island effect of the Long Island Solar Farm . . . 26
Helen Bagnato

Characterization by solution small angle X-ray scattering of the oligomeric state of structural genomics protein targets . . . 32
Kimberly Basil

Synthesis of [^{18}F]fluorosucrose based on enzymatic deacetylation of sucrose octaacetate . . . 37
Caitlin Bennett

Facilities and operations: utilities layout . . . 41
Brian Bergh

Development of an electronic system for managing the change process for Brookhaven National Laboratory Policies and Procedures . . . 44
Kiersten Blauer

Isolation of *Chlamydomonas reinhardtii* mutants with low oil . . . 48
Taryn Boucher

Creating remote access capability for the LINAC Timing System and investigating electromagnetic noise conditions for the LINAC H- source . . . 51
Adeel T. Butt

Characterization of cadmium zinc telluride radiation detectors grown by vapor phase method . . . 55
Trevor Chan

Investigation and confirmation of protein candidates interacting with *Arabidopsis* 4CL1 . . . 57
Morgan Campbell

Electric field distribution nonlinearities in cylindrical and spherical plates in an electrostatic storage ring . . . 60
Richie Chen

Designing the electron Relativistic Heavy Ion Collider and Coherent electron Cooling Proof of Principle's 500 MHz systems . . . 64
Shushanna Cherian

Analysis and Characterization of Viscous Biofuel Sprays
Using Flash Atomization Techniques 71
Thomas Chiesa
Development of the ion rapid cycling synchrotron. 75
William Christie
Formal post-doctoral mentoring program proposal 77
Daniel Comas
Evaluation of the United States Support Program's Internship
and Junior Professional Officer Programs 79
Jessica Cruz
Evaluating the effectiveness of the current Tier 1 process 84
Clara S. Cuervo
Design of beam line setup for high-charge state ions after radio-frequency quadrupole 86
Eric Cushing
Searching for the quantum chromodynamic critical point
in relativistic heavy ion collisions 89
Mike Dai
Fabrication and testing of sub-micron x-ray waveguides using anisotropic etch methods . . . 106
Bianca Datta
Novel characterization techniques of scintillator detectors 112
Remy R. Devoe
Usage and usability analysis of the Atmospheric Radiation Measurement
program's web presence 115
Dan Ferguson
Pefluorocarbon tracers: building industry potential and automated data management 117
Nathan Gubser
Investigation of charge-coupled devices for the Large Synoptic Survey Telescope
using Silvaco simulation software 119
Skyler Hagen
Weather instrumentation calibrations provide base-line data in the
Long Island Solar Farm 123
Jonathan Haimoff
Study of electric field non-uniformity in Cadmium Zinc Telluride
room-temperature, radiation detectors 126
Terance Harper
Sustainment of Meteorological Sensors on a Photovoltaic Solar Farm
(Long Island Solar Farm) 131
Lauren Herrera
Investigating the carbon monoxide effect on the platinum catalyst
in a proton exchange membrane fuel cell 134
Andrew Hubert

Generation and acceleration of a high charge state iron ion beam using a laser ion source and direct plasma injection into a radiofrequency quadropole (RFQ) linear accelerator 137
Peter Jandovitz
Using plant oils as an alternative fuel source 140
Trevor Johnson
Optimizing the Geometry of the Focusing Horn Magnets in the Long-Baseline Neutrino Experiment Beamline 142
Jacob Kiefer
Structural design of a high-temperature, superconductor, cosine theta coil 148
Christopher Kolz
An in-depth analysis of the RF Wien-Filter spin-phase correlation of the Proton and the Deuteron for the Electric Dipole Moment using an electrically and magnetically focused precision storage ring. 152
Benjamin Kramer
Protein crystallization with Lysozyme-NAG binding 157
Benjamin Le
Determination of distribution coefficients for the Zion Solutions nuclear power plant decommissioning project 161
Emily Leonard
Extended defects in Cadmium Zinc Telluride crystals grown by the High Pressure Bridgeman method and the Traveling Heater Method 165
Matthew Marshall, Jamie Butcher
Temperature and vibration isolation system design for the multilayer Laue lens deposition system 168
Jesse A. Miller
Programming a low voltage distribution controller board 173
Louie-John Mistretta
Comparison of the linearity of an energy dispersive detector with fluorescent ion chamber for x-ray spectroscopy 179
Ahmad Mohammad
Brookhaven Atmospheric Tracer Sampler: Fabrication and Revision. 184
Juan Mojica, Adam Batley, Lezou Dali, April McCray
Manual calibration system simulations for the Daya Bay neutrino experiment 186
Alyssa Montalbano
Designing the hadron calorimeter 192
Patrick Montalto
Development of a parametric model for the Super Pioneering High Energy Nuclear Interaction Experiment hadronic calorimeter scintillator design and fabrication 194
Ammar Morgan
Characterization of indium iodide (InI) crystals for room-temperature radiation detector applications 197
J. Mwathi

Modulation enhanced diffraction 200
Max Osmulski
Mechanistic investigation of novel ruthenium π-arene water oxidation catalysts 202
Nicholas Patterson
Optimization of the Copper Zinc Alumina catalyst for the low-temperature water gas shift reaction 205
Alexandre Pereira
Increased prefrontal gray matter volume in structural MRI of cocaine abstainers at 6-month follow-up 210
Amanda Pflumm
Mechanistic investigation of novel Ruthenium π-Arene water oxidation catalysts 213
Long Dinh Phan
Post-growth thermal annealing and characterization of Cadmium Zinc Telluride radiation detector material 216
Asja Radja
Large grain electron gun testing 221
Denzel Pressey
Hot-pressing and physical properties characterizations of polycrystalline specimens of boron carbide (B4C) for elasticity studies at extreme conditions 223
Brandon Rhymer
The science spectrum: Reporting on different disciplines at Brookhaven National Laboratory 225
Aviva Rutkin
Fabrication of a sample holder for air-sensitive samples to be used on X-18B and X-19A beam lines at the National Synchrotron Light Source 231
Wahaj Saleem
A dislocation study of CZT crystals 235
Valissa Sams
Radiosynthesis of [^{18}F] fluorosucrose and purification of sucrose synthase 238
Alexandra Scavelli, Caitlin Bennett
Exploration of the epigenetic state of the Monoamine oxidase A gene 240
Alice Shanklin, Taylor Stiegler
Engineering in the Superconducting Magnet Division 244
Ryan E. Sheedy
Analyzing perfluorocarbon tracer compound stock solutions and gaseous mixtures with a thermal conductivity detector using gas chromatography 246
Mackenzie Shipley
Software development for integrated spectroscopy and X-ray diffraction experiments at the PXRR NSLS beamlines 253
Michael Skinner
In silico knockout analysis of developing ***Brassica napus*** embryos for the overproduction of α-tocopherol 257
Griffin St. Clair

Developing an inventory web application for network switches 260
Isaac Stein
Does cocaine use affect the epigenetic state of DNA? A study of brain candidate genes . . . 263
Taylor Stiegler
Simulating a Training, Research, Isotopes, General Atomics Reactor core through modeling with the Purdue Advanced Reactor Core Simulator 267
Jared Stier
Search for critical behavior in relativistic heavy ion collisions 270
Mingxiu Sun
Manipulating geo-spatial data for managing air quality control 276
Greg Swirson
A graphical user interface for cloud data discovery 278
Josh Tiffany
Comparison and optimization of mechanical designs for enhanced performance of the Long-Baseline Neutrino Experiment 280
Nikita Timofeev
Examining the hydrogen purification performance of an electrochemical separation system 288
Daniel Weinman
South Complex worker efficiency 293
Tarletta Williams
Saving energy in the Brookhaven National Laboratory Computing Center: Cold aisle containment implementation and computational fluid dynamics modeling 295
Rebecca Winter

Appendix 301
List of interns, their colleges or univerisities, and location in this compendium 304

Optimization of geometry for hybrid proton-beam target for the long-baseline neutrino experiment

Paige Abrunzo
Rensselaer Polytechnic Institute, Troy, New York, 12180
Mary Bishai
Brookhaven National Laboratory, Upton, New York, 11973

ABSTRACT

Many simulations were run for increasing the energies of a 250,000 proton beam hitting hybrid targets composed of tantalum and graphite of varying dimensions. A study of the energy deposition through the different targets has been accomplished and the data has been analyzed. With the intent to optimize the geometry of the target, it has been concluded that increasing the width of the beam to 0.70650 cm and the width of the target to 0.9 cm lowers the energy deposition substantially. Increasing the length of the graphite portion of the target to 68.57 cm results in a peak energy deposition in the graphite comparable to the peak energy deposition in the tantalum. Overall, the study can conclude that more geometries must be simulated in order to further optimize the target design.

I. INTRODUCTION

Although neutrinos are present everywhere in abundance as the second most prevalent particle in the universe, our understanding of these particles is severely lacking. The Long-Baseline Neutrino Experiment (LBNE) attempts to gain insight into the fundamental properties of neutrinos. The two principle pieces of information that the LBNE hopes to attain are determining the mass hierarchy of the three different flavors of neutrinos (muon, electron, and tau) and determining the CP angle. With this information, physicists hope to gain a better understanding of how the universe works. This experiment has the potential to provide answers to previously unanswered questions that have arisen in modern physics. One such question is why there is such a discrepancy between antimatter and matter.

Physicists studying neutrinos face the problem of trying to answer fundamental questions about a particle that travels through most materials undetected. The LBNE provides the ability to acquire large sets of data using highly sensitive detectors with the hope that with a large number of neutrinos and a massive enough detector over a period of ten to twenty years, scientists will gather a reasonable amount of detectable interactions. The basic setup for the LBNE's neutrino production and detection consists of a high energy and high intensity proton-beam hitting a cylindrical hybrid target. The proton-beam interacts with the target material and produces pions and kaons through inelastic nuclear collisions. The pions and kaons that come out of the target are focused into a beam by two focusing magnets and ultimately decay into neutrinos.

A. The Target

The target is essential to the LBNE in that it is essentially the source of the neutrinos. Of the several engineering challenges for the design for a target, the greatest hurdle to overcome is melting. The target must be able to withstand a high-energy proton beam accelerated to high intensity. Due to the extreme nature of high radiation areas, choosing chemically appropriate materials for targets faced with the corrosive effects of the high density of charged particles becomes challenging. As stated earlier, the pions are created through inelastic nuclear collisions with the atomic electrons of the material. These interactions are almost solely responsible for energy loss in a target and are highly statistical in nature. Due to the fact that they occur with a quantum mechanical probability, one could calculate the average energy loss per unit path length. In simpler terms, given that the interactions occur statistically, we could map the energy deposition.

B. The Bethe-Bloch Formula

The Bethe-Bloch formula provides us with -dE/dx, or energy transfer, and is commonly used for energy loss calculation. In this equation, the energy transfer is parameterized in terms of momentum transfer, a measurable quantity as opposed to the impact parameter which is not a measurable quantity.

$$-\frac{dE}{dx} = 2\pi N_a r_e^2 m_e c^2 \rho \frac{Z}{A}\frac{z^2}{\beta^2}\left[ln\left(\frac{2m_e\gamma^2\nu^2 W_{max}}{I^2}\right) - 2\beta^2\right] \quad (1)$$

Where:

r_e : classical electron radius $= 2.817 \times 10^{-13} cm$
m_e : electron mass
N_a : Avogadro's number $= 6.022 \times 10^{23} mol^{-1}$
I : mean excitation potential
Z : atomic number of absorbing material
A : atomic weight of absorbing material
ρ : density of absorbing material
z : charge of incident particle in units of e
β : $\frac{\nu}{c}$ of the incident particle
γ : $\frac{1}{\sqrt{1-\beta^2}}$
W_{max} : maximum energy transfer in a single collision

With two commonly made corrections added, the density effect correction and the shell correction:

$$-\frac{dE}{dx} = 2\pi N_a r_e^2 m_e c^2 \rho \frac{Z}{A}\frac{z^2}{\beta^2}\left[ln\left(\frac{2m_e\gamma^2\nu^2 W_{max}}{I^2}\right) - 2\beta^2 - \delta - 2\frac{C}{Z}\right] \quad (2)$$

Where:

δ : density correction
C : shell correction

The density effect correction stems from the fact that the electric field of the particles polarizes the atoms along its path causing electrons that are farther from the path to be shielded from the field's intensity. This results in less energy loss through collisions and, therefore, must be accounted for in the Bethe-Bloch formula. This correction becomes important at high energies. On the other hand, the shell correction is important for low energies since it accounts for situations in which the velocity of the incident particle is approximately equal to or smaller than the orbital velocity of the bound electrons.

II. METHODS

This Bethe-Bloch formula which becomes essential when trying to map the energy deposition in a target was used in simulations that analyzed the output files in order to optimize the geometry of the target. The target was a cylindrical hybrid proton-beam target composed of graphite and tantalum. Graphite, commonly used in heavy radiation areas due to the fact that it is radiation hard, also has thermomechanical properties that enable it to withstand the increased temperature that it will incur when hit by the proton beam. The graphite will also be able to be cooled between proton beam pulses without falling apart. Tantalum was chosen due to the fact that it is a high Z material. We are using a high Z material because of their tendency to have short interaction lengths. In turn, this enables us to have a shorter target length. A shorter target makes it easier to focus the pions and kaons into a parallel beam. As earlier stated, the pions and kaons decay into neutrinos; a more focused beam means more neutrinos. Like graphite, tantalum is also radiation hard, enabling it to stand up to the corrosive nature of a radiation environment.

All simulations are run with the same basic setup. The target was placed in an aluminum casing that was filled with helium. The aluminum casing was surrounded by an encompassing vacuum in an external black hole. The set up can be seen in Figure 1.

There are a number of factors that must be taken into consideration when designing a target including the size, shape, composition and energy of the beam. The variables that I explored were the length of the graphite, the energy of the beam, the width of the beam as well as the width of the target. Using a Monte Carlo simulation program, FLUKA 2011.2.3, I manipulated the input files and ran the simulation for 250,000 protons hitting the target. Every alteration to the target was followed by running the simulation for a 30 GeV, 60 GeV and 90 GeV proton beam. I feel that is important to note that all simulations that had been run had the transport of electrons, positrons, photons and pizero particles enabled. This is important to note due to the fact that they are charged particles and without them being enabled, the results would be slightly different.

The data from the simulations was written into output files. In order to analyze the data effectively, I merged the files using the hadd command in ROOT. The hadd command simply adds together the data into one file without scaling it. Using emacs, I wrote a macro that would scale the file and plot various histograms. The desired plots were 2-dimensional histograms in the xz plane, a summation over the energy deposition through the center of the target for increasing beam energy and a summation over the energy deposition through the center of the target for increasing graphite length. This was done in order to visualize how the energy was being deposited in the different materials and how the length and radius of the materials and energy of the beam effect energy deposition.

III. RESULTS

The default parameters that I began running simulations on were a graphite cylinder with the dimensions: 48.57 cm long and a radius of 0.65 cm. This graphite cylinder is adjacent to a tantalum cylinder with the dimensions: 11.47 cm long and a radius of 0.55 cm. The beam radius is 0.35325 cm. The following histo-

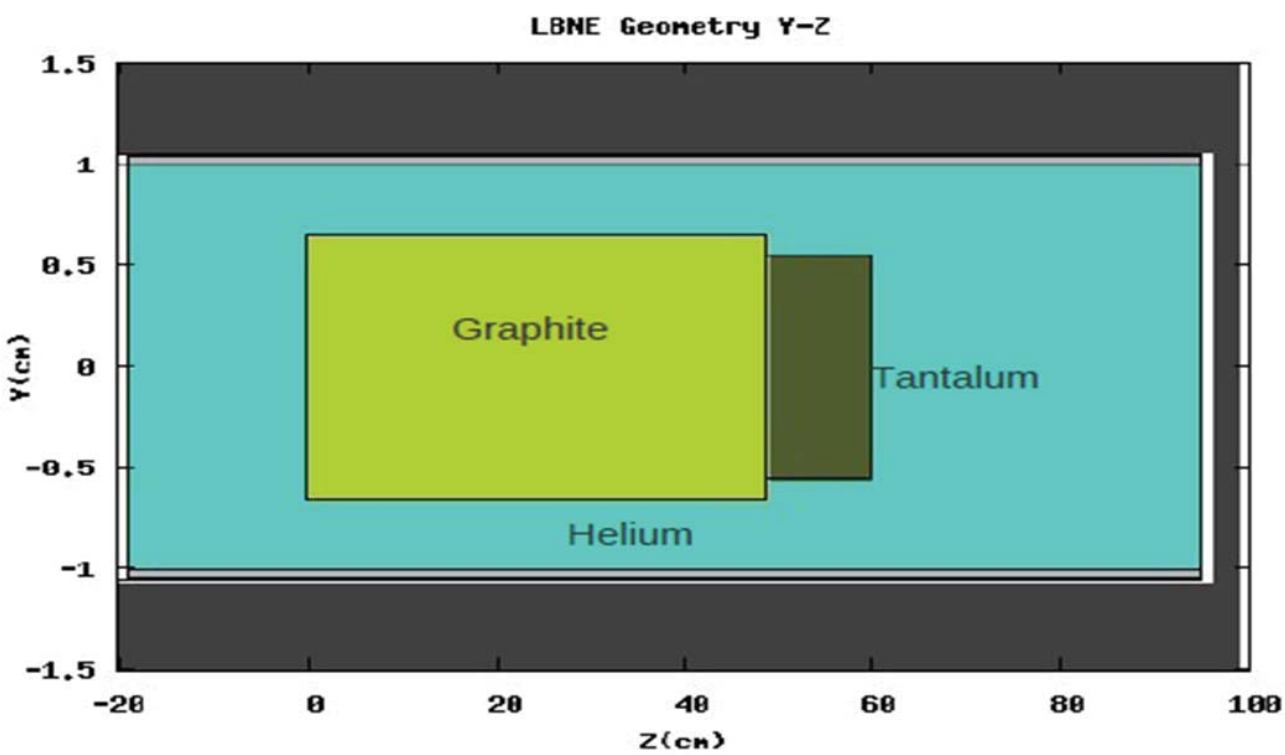

Figure 1: Initial geometry of the target. The target is made up of 48.57 cm of graphite and 11.47 cm of tantalum. It is surrounded by helium in an aluminum casing. The encased target is in an encompassing vacuum within a black hole.

gram (Figure 2) shows the energy deposition through the center of the target for 120 GeV, 60 GeV, and 30 GeV proton-beams. Something to note while viewing this histogram is that the energy deposition for 30 GeV is not half of the deposition for 60 GeV, this is slightly more evident when looking at 120 GeV to 60 GeV. This is contrary to what one would think considering that the energy was halved yet the deposition wasn't half.

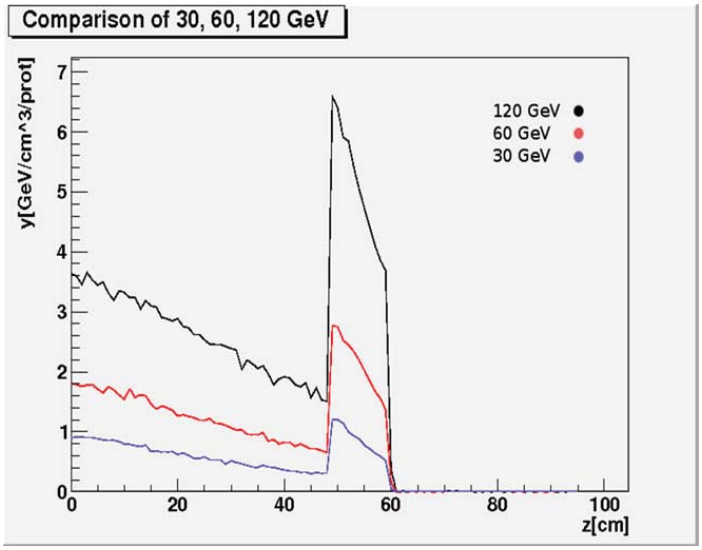

Figure 2: Energy deposition through the center of the target for a 30 GeV, 60 GeV and 120 GeV proton beam with a width of 0.35325 cm hitting a target with 48.57 cm of graphite with a radius of 0.65 cm adjacent to 11.47cm of tantalum with a radius of 0.55 cm.

In order to better visualize the energy deposition through the whole target, 2-dimensional histograms were plotted. The 2-dimensional histograms for a 120 GeV and 30 GeV proton beam are shown in Figure 3 and 4. It is very important to note the difference in scale. The histogram for the 120 GeV proton beam has a scale of 0 GeV per cm squared per proton on target to 30 GeV per cm squared per proton on target while the histogram for the 30 GeV proton beam has a scale of 0 GeV per cm squared per proton on target to 5 GeV per cm squared per proton on target. One can clearly distinguish between the tantalum and the graphite. The graphite appears to be longer with less of a deposition of energy while the tantalum obviously has a higher deposition of energy and is much shorter.

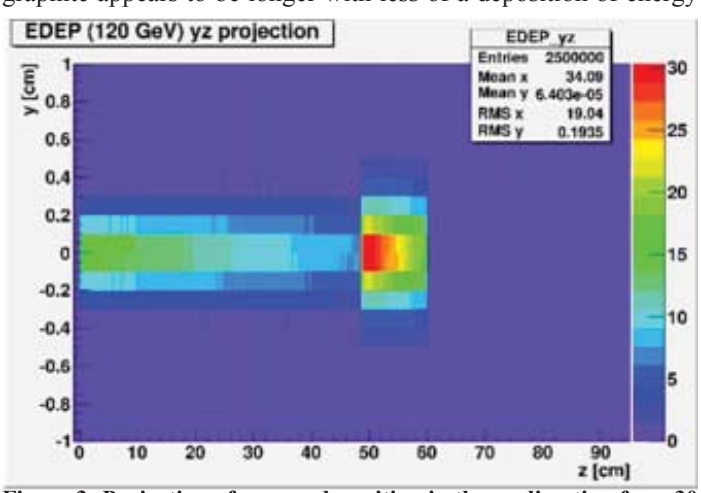

Figure 3: Projection of energy deposition in the yz direction for a 30 GeV proton beam with a width of 0.35325 cm hitting a target with 48.57 cm of graphite with a radius of 0.65 cm adjacent to 11.47cm of tantalum with a radius of 0.55 cm. The color scale is in GeV/cm²/ proton on target.

The next graph is a representation of the energy through the center of the target for an increasing length of graphite and a 120 GeV proton beam. The graphite length was increased from 48.57 cm to 58.57 cm and again to 68.57 cm. The importance of this graph is to see how the length of the graphite relates to the peek energy deposition in the tantalum. The goal is to have the highest energy deposition in the graphite to be comparable to the highest energy deposition in the tantalum.

Along with that comes the 2-dimensional histograms illustrating the energy deposition for a 120 GeV proton beam on a 48.57 cm target adjacent to the energy deposition for a 120 GeV proton beam on a 68.57 cm target. Once again it is very important to note the change in scaling, although it is not as drastic a difference. It can also be noted that the increased length of the graphite leads to a slightly more even deposition of energy between the tantalum and the graphite.

The final variable that was explored was how increasing the radius of the target and the beam would affect the energy deposition. The radius for both the tantalum and graphite was increased to .9 cm as opposed to the 0.65 cm for the graphite and 0.55 cm for the tantalum as was previously the case. The beam radius was also increased from 0.35325 cm to 0.70650 cm. The histogram below (Figure 8) displays the energy deposition through the center of a target being hit by a 120 GeV proton beam for graphite lengths of 48.57 cm and 68.57 cm. I feel that it is important to note that the energy deposition for the increased radius is substantially lower than the default radius, see Figure 5.

The energy deposition mapping for the increased radius of the proton beam is shown below in Figures 9 and 10. Noting the scale of these 2-dimensional histograms in reference to those in Figures 6 and 7 illustrates how increasing the radius decreases the energy per cm squared per proton on target. The scales between the two histograms below are also different and should be noted, but there isn't a drastic difference.

IV. CONCLUSION

Although many simulations have been run, the geometry of the target can still be further optimized. When viewing the plots

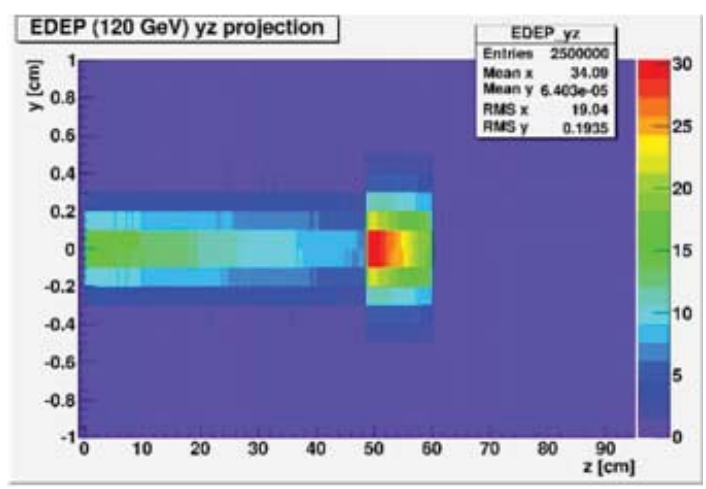

Figure 4: Projection of energy deposition in the yz direction for a 120 GeV proton beam with a width of 0.35325 cm hitting a target with 48.57 cm of graphite with a radius of 0.65 cm adjacent to 11.47cm of tantalum with a radius of 0.55 cm. The color scale is in GeV/cm²/ proton on target.

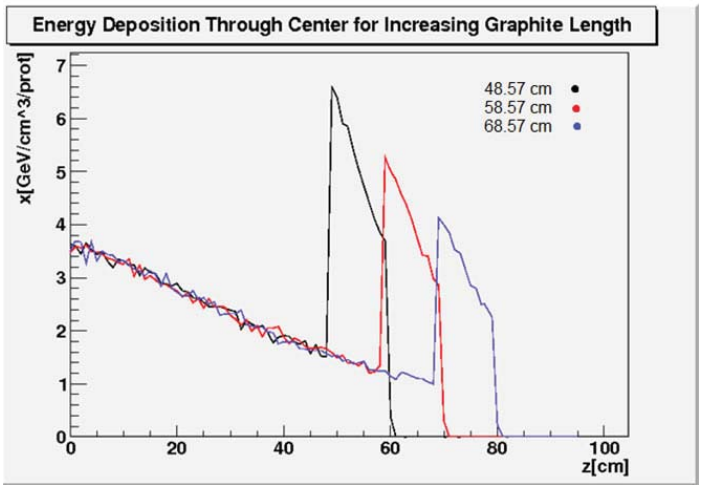

Figure 5: Energy deposition through the center of the target for a 120 GeV proton beam with a width of 0.35325 cm hitting a target with 48.57 cm, 58.57 cm and 68.57 of graphite, with a radius of 0.65 cm adjacent to 11.47cm of tantalum with a radius of 0.55 cm.

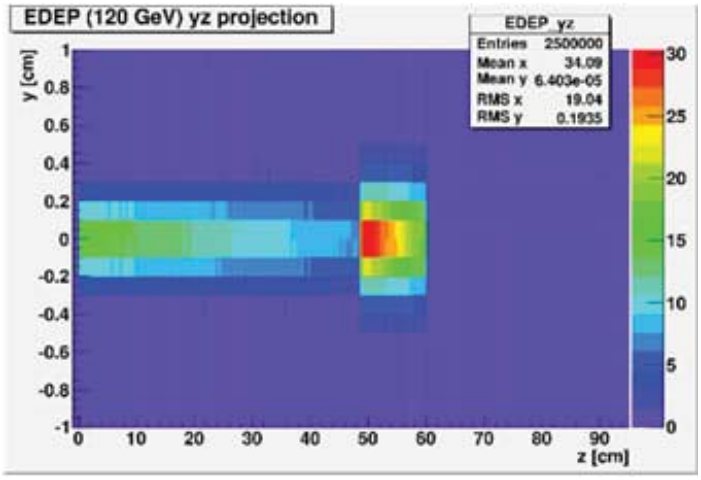

Figure 6: Same as Figure 4. This figure was placed here to more easily see the difference in energy deposition as the length of graphite in-creases. This figure had 48.57 cm of graphite.

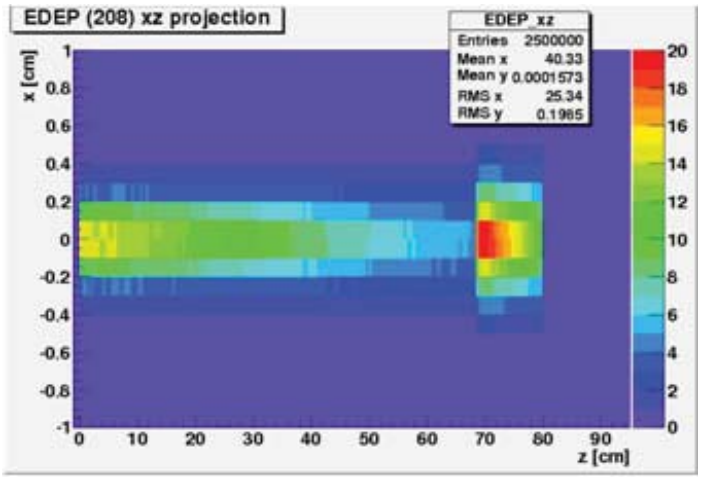

Figure 7: Projection of energy deposition in the xz direction for a 120 GeV proton beam with a width of 0.35325 cm hitting a target with 68.57 cm of graphite with a radius of 0.65 cm adjacent to 11.47cm of tantalum with a radius of 0.55 cm. The color scale is in GeV/cm²/ proton on target.

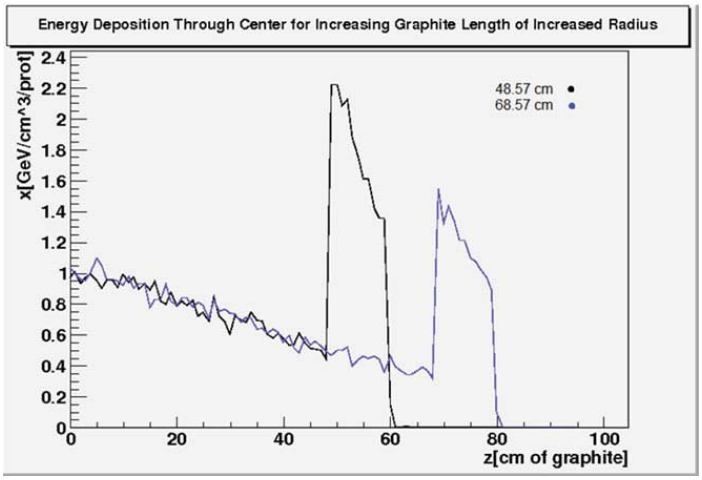

Figure 8: Energy deposition through the center of the target for a 120 GeV proton beam with a width of 0.70650 cm hitting a target with 48.57 cm and 68.57 of graphite, with a radius of 0.9 cm adjacent to 11.47cm of tantalum with a radius of 0.9 cm.

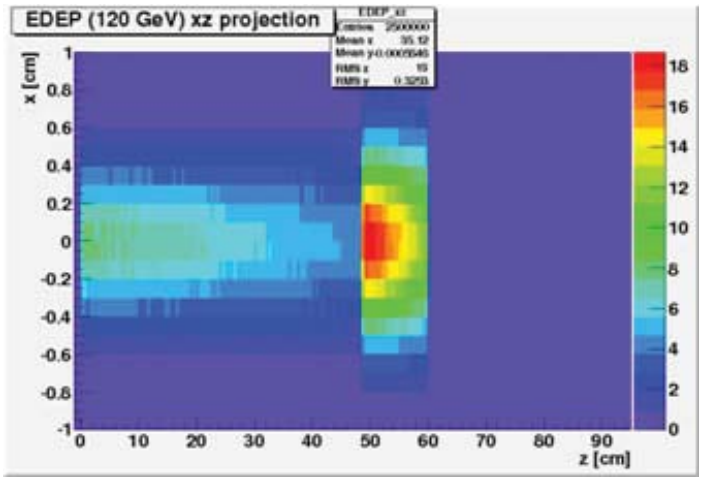

Figure 9: Projection of energy deposition in the xz direction for a 120 GeV proton beam with a width of 0.70650 cm hitting a target with 48.57 cm of graphite with a radius of 0.9 cm adjacent to 11.47cm of tantalum with a radius of 0.9 cm. The color scale is in GeV/cm²/ proton on target.

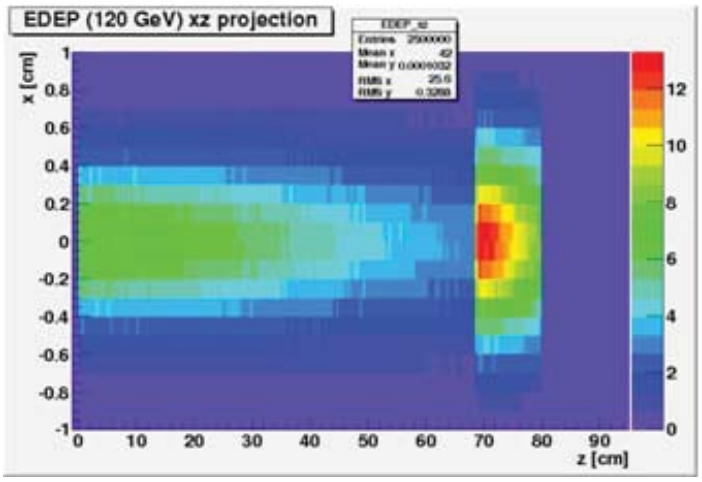

Figure 10: Projection of energy deposition in the xz direction for a 120 GeV proton beam with a width of 0.70650 cm hitting a target with 68.57 cm of graphite with a radius of 0.9 cm adjacent to 11.47cm of tantalum with a radius of 0.9 cm. The color scale is in GeV/cm²/ proton on target.

of the energy deposition through the center of the target, it is important to note that there is still room for improvement. The peak energy in the graphite and the tantalum should be comparable to the peak energy in the tantalum. There are still a number of varying geometries that can be simulated in order to find the most optimal. Increasing the beam radius and target radius has lowered the energy deposition in both materials substantially but as shown in Figure 8, there is a great difference in the peek energy deposition of the tantalum and the graphite. There are several engineering restraints that need to be taken into account such as the fact that the target still needs to fit within the parabolic cone of the horn. Another option to consider would be running simulations with platinum instead of tantalum. This is desirable because both graphite and platinum have similar coefficients of thermal expansion which is useful when a target is exposed to extreme temperatures; the target is less likely to fall apart and can be cooled more easily. The simulations that I have been running have shown how the energy is deposited in the target and have essentially paved the path for a better target design for the Long-Baseline Neutrino Experiment.

V. ACKNOWLDGEMENTS

I wish to thank my mentor, Dr. Mary Bishai, for her kindness and support throughout my experience with the SULI program. I would also like to thank Dr. Zeynip Isvan for her willingness to assist me and the other interns. My time here at Brookhaven National Laboratory would not have been made possible without the sponsorship of the SULI program through the United States Department of Energy. To them, I would like to express my utmost gratitude for this experience. Finally, I would like express my sincerest appreciation for the hospitality and kindness that was shown to me by the employees of Brookhaven National Laboratory.

Determining the effects of ionizing radiation using a cell model with mitochondrial dysfunction

S. Ackerman
Biochemistry Department, SUNY Geneseo, Geneseo, NY 14454

D. J. Keszenman, P. V. Bennett, A. M. Johnson, and P. F. Wilson
Biology Department, Brookhaven National Laboratory, Upton, NY 11973

ABSTRACT

One of the goals of the Radiobiology group at Brookhaven National Laboratory (BNL) is to estimate the risk of exposure of humans to different qualities of ionizing radiation (IR). In space, the exposure to sparsely and densely ionizing radiations such as protons and heavy ions (HZE) constitutes one of the fundamental hazards for humans. On Earth, in addition to photon radiotherapy, proton and carbon ion-based hadrontherapy are increasingly used. The NASA Space Radiation Laboratory (NSRL) at BNL is currently focused on the effects of outer space IR on humans and technology over extended periods of time, such as the three-year journey to Mars. Since IR is a known cause of mutagenesis, cancer, and premature aging, it is important to understand how humans will be affected in space for extended periods of time away from our protective atmosphere. Dr. Keszenman's research focuses on the modulation of DNA damage caused by IR in a mitochondrial dysfunctional cell model (rho-zero cells). A mitochondrial deficient cell cannot complete the electron transport chain, which means that these cells produce less energy and modifications in the levels of endogenous reactive oxygen species (ROS). Therefore these cells have less energy with variable levels of harmful ROS, which may damage DNA. Based on the hypothesis that decreased energy production and lower endogenous ROS levels will modify DNA damage response, we aim to determine the cellular and molecular effects of IR on cells with mitochondrial dysfunction. The results may determine the role of the mitochondria when a cell is damaged by IR. My job this summer was to characterize mitochondrial functionality in rho-zero cell lines and begin to determine their cellular response to IR through survival and growth kinetic studies. Thus far the results have shown rho-zero cells derived from Mouse Lung Carcinoma cells (LL2) to be more sensitive to lower doses of γ-rays as compared with the parental LL2 cells. Also, we have obtained results characterizing the mitochondrial functionality of possible rho-zero clones derived from Chinese Hamster Ovary (CHO) cells previously isolated by Dr. Keszenman. In the future we wish to study the cellular radiation response of a mitochondrial deficient CHO clone and, at the molecular level, the induction of DNA damage response through the determination of DNA double strand breaks using pulsed field electrophoresis.

I. INTRODUCTION

One of the goals of the Radiobiology group at Brookhaven National Laboratory (BNL) is to estimate the risk of exposure of humans to different qualities of ionizing radiation (IR). In space, the exposure to sparsely and densely ionizing radiations such as protons and heavy ions (HZE) constitutes one of the fundamental hazards for humans. On Earth, in addition to photon radiotherapy, proton and carbon ion-based hadrontherapy are increasingly used. The NASA Space Radiation Laboratory (NSRL) at BNL is currently focused on the effects of outer space IR on humans and technology over extended periods of time, such as the three-year journey to Mars. Since IR is a known cause of mutagenesis, cancer, and premature aging, it is important to understand how humans will be affected in space for extended periods of time away from our protective atmosphere. Dr. Keszenman's research focuses on the effect of IR on cells with mitochondrial dysfunction (rho-zero cells).4 Mitochondria are the powerhouses of the cell.1 When these organelles function properly they produce a net value of 38 ATP to be used for cellular processes. Rho-zero cells are only able to undergo glycolysis; therefore, they only produce a net value of 2 ATP. These cells do not proceed to the Krebs cycle or the Electron Transport Chain (ETC) which means that they may produce less reactive oxygen species (ROS), chemical reactants known to induce DNA damage. A rho-zero cell line can still have mitochondria as long as they are defective and cannot complete the electron transport chain and produce ROS. Based on the hypothesis that rho-zero cells' decreased energy production and lower endogenous ROS levels will modify DNA damage response, we aim to determine the cellular and molecular effects of IR on cells with mitochondrial dysfunction. Using a rho-zero cell model for ionizing radiation studies aims to eliminate the background of endogenous DNA damage produced by ROS and to potentially determine the role of the mitochondria in IR nuclear DNA damage.

II. MATERIALS AND METHODS

A. Cell Lines and Culture

Two parental cell lines were used as biological models, Mouse Lung Carcinoma LL2 and Chinese Hamster Ovary AA8. Each cell line had two variations, one with functional mitochondria and one without functional mitochondria (the CHO rho-zero line is still being determined). The cells with mitochondrial function were grown in DMEM high glucose medium with 10% fetal bovine serum. The cells without mitochondria function were grown in DMEM high glucose medium with 10% fetal bovine serum and 50 μg/ml Uridine.4,6

B. Survival to γ-rays

This procedure was used for both AA8 and LL2 cell lines. Information and technique were used from Wilson's previous CHO survival studies.6 Confluent G0/G1-phase cultures were irradiated with 0-5 Gy of cesium-137 662 keV gamma rays delivered at ~160 cGy/min by a J.L. Shepherd Mark I Model 68A cabinet irradiator. The survival value was determined by plating cells at a known number and then counting the visible colonies after 7-10 days in a 37°C and 10% CO2 incubator. The colonies were stained and fixed with ethanol and Kopycake blue. The cell numbers plated in the AA8 survival experiment can be seen in

Table 1.

Ionizing Radiation Dose (Gy)	Cells Plated (cells/dish)
Tester, 0	200
0	200
0.5	200
1	200
2.5	300
5	400

Table 1. *Plating of AA8 Survival:* **This table shows the number of cells plated per dose of ionizing radiation. A 30ml stock was created and then 10ml was added to three plates per dose**

C. DNA damage determination

From the survival curves, some of the cells were frozen immediately after irradiation. These were then used to create InCert Agarose plugs using a method designed by Keszenman and Sutherland.2,3 These plugs contained the entire cell, meaning that the membrane had to be broken in order for the DNA to move on a gel. Thus the plugs were repeatedly treated with Proteinase K and Sarkosyl for three days. Then the plugs were washed continuously with TE buffer until finally ready for the restriction enzyme digest. The enzyme used was NotI. This enzyme cleaves double stranded DNA at known intervals and allows it to pass through pulse field gel electrophoresis. The gel was run for 10 hours with a hexagonal electrode at 240V. The gel was then stained with ethidium bromide and imaged with UV light.

D. Mitochondrial assays

A rho-zero CHO cell line could not be grown well enough to conduct an experiment. Thus six clones of the parent cell line were isolated by prolonged exposure to ethidium bromide to eliminate the functional mitochondria. This process was developed from King and Attardi's method of creating rho-zero human cells.4 The cells were grown to confluency in 12 and 6 well Falcon plates. Then the cells were stained with MitoTracker Green (MTTG) to look for mitochondria5 and MitoSOX Red (MTSOX) to look for superoxides7 which are a sign of functional mitochondria (Invitrogen) and DAPI to look for nuclear DNA. The concentrations of the dyes, listed in Table 2, were as follows: one milliliter of dye was used for 12 well plates and 2 milliliters was used for 6 well plates. 50 µl of ProlongGold with DAPI was used for the slide staining. The MTTG stained cells were fixed after staining with Methanol while the DAPI was fixed before. The MTSOX was imaged live unless combined with another dye. The fluorescence levels were read using a Perkin Elmer Victor3 plate reader.

Stain	Concentration	Location of Stain
DAPI	2µg/ml	DNA
MitoTracker Green	100 nM	Mitochondria
MitoSOX Red	5 µM	Superoxides

Table 2. *DNA and Mitochondrial Stains:* **This table shows the concentrations of the dyes used to analyze all of the cells. One milliliter of stain was used for 12 well plates while 2 milliliters was used for 6 well plates (Falcon). Prolong Gold was used as the DAPI stain for the slides.**

III. RESULTS

A. Survival of LL2 and LL2 rho-zero cells

The survival curve for Mouse Lung Carcinoma LL2 cells shows a decreasing linear quadratic relationship with increasing ionizing radiation dose. The number was then normalized based on the number of cells plated and then divided by the plating efficiency which is determined from the control. The resulting values are all fractions of the control value and the graph shows the expected downward trend at high doses of ionizing radiation, 0 to 5 Gy. Interestingly, at low levels of ionizing radiation, 0 to 0.5 Gy, LL2 cells actually appear to increase in survival. This is not true for rho-zero cells. They appear to make a general downward trend until 0.5 Gy where the rho-zero survival showed no difference with LL2 cells (Figure 1). This suggests that ionizing radiation may affect rho-zero cells differently then regular LL2 cells. It is possible that the low levels of energy cause the initial low survival and then the lack of ROS allows the rho-zero survival to increase before generally decreasing like the parental cell line

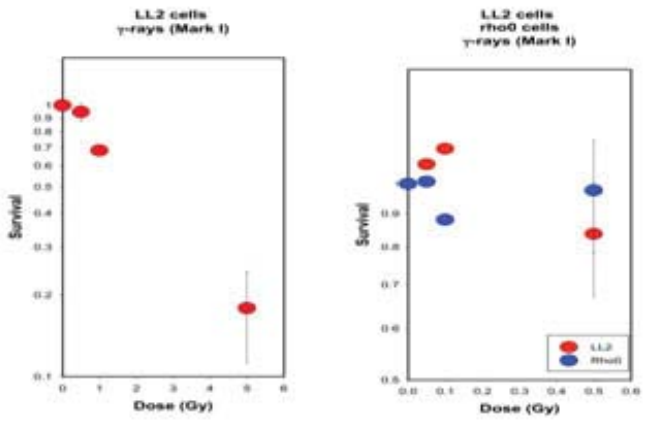

Figure 1. ***Survival of LL2 cells and LL2 rho-zero cells:*** **The graph to the left (above) shows LL2 cells survival declining with increasing ionizing radiation dose. The data will be fit with a quadratic linear curve. The graph to the right (above) shows LL2 and rho-zero LL2 cells survival to lower doses of ionizing radiation. It shows the initial increase in LL2 survival and the initial decrease in LL2 rho-zero cells. It is possible that the low levels of energy cause the initial low survival but the lack of ROS allows the rho-zero survival to be comparable to LL2 at higher doses.**

B. Pulse field Gel Electrophoresis on InCert Agarose Plugs

The agarose plugs in the gel showed clear bands about ¾ down field. Figure 2 shows the regular LL2 cells response to ionizing radiation ranging from 0 to 5 Gy. As the dose increased the DNA fragments became smaller and moved farther along the gel. Figure 3 shows the comparison of normal LL2 and rho-zero LL2 cells under lower doses of ionizing radiation, 0 to 50 cGy. In this figure the bottom bands, which represent the regular LL2 cells, show very little variation in size. However the top bands, which represent the rho-zero cells appear to decrease in size as the dose increases. This furthers the trend seen in the survival curve from Figure 1. It seems that rho-zero cells may be less resistant

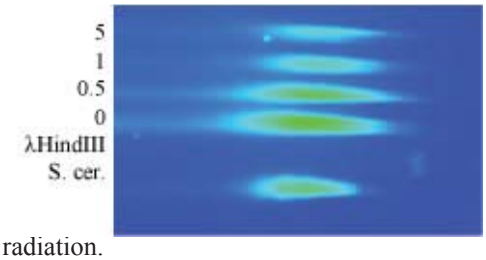

to ionizing radiation.

Figure 2. ***Double Strand Breaks in Parent LL2 cells from 0 to 5 Gy:*** **This shows the Not1 digestion of cells from the survival in Figure 1. The standards are Saccharomyces cerevisiae (S. cer.) and λHind III. The gel ran for 10 hrs at 240 V. It shows smaller DNA fragments at higher doses.**

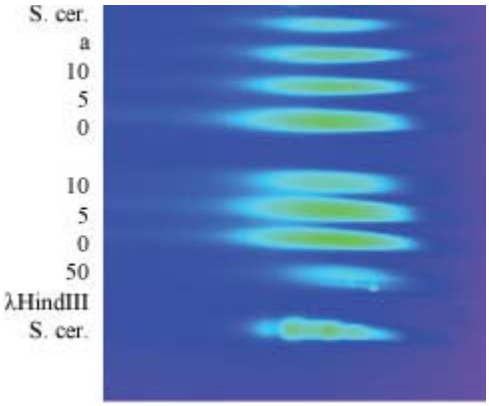

Figure 3. ***Double Strand Breaks in rho-zero and parent LL2 cells from 0-50cGy:*** **This shows the Not1 digestion of cells from the survival in Figure 1. The molecular weight standards are Saccharomyces cerevisiae (S. cer.). and λHind III. The gel ran for 10 hrs at 240V. It shows the rho-zero cells on the top and the regular cells on the bottom. The rho-zero appears to have smaller fragments with increased dose.**

C. Characterizing CHO clones for mitochondrial functionality

After analyzing the survival curves of the LL2 cells, it was decided that a similar experiment using noncancerous cells, Chinese hamster ovary cells (CHO), should be performed. Figure 4 shows the results of some of the stained clones. All of the data was normalized to 1x105 cells and MTTG was divided by a factor of 1000 and DAPI was divided by a factor of 100 for comparison. The LL2 cell line was used for comparison with AA8 control. DAPI stains for DNA, so it seems that during the staining most of the LL2 cells were lost. Clone 2, 5 and 6 showed high levels of MTTG and MTSOX. Figure 5 shows images taken of AA8, LL2 and Clone 2. The images show the presence of nuclear DNA (blue), the presence of mitochondria (green), and the presence of superoxides (red). None of the cells show substantially more or less of the stains. This may mean that the clones are not a rho-zero cell line, but it is not certain. All of the clones need to be further analyzed with the current stains but also possibly with a method to track ATP production. If one of the clones had substantially less production of ATP, then that would be an important sign of dysfunctional mitochondria. When a rho-zero CHO cell line is determined, then proliferation and survival curve experiments will be conducted to compare to the curves seen in the LL2 cells.

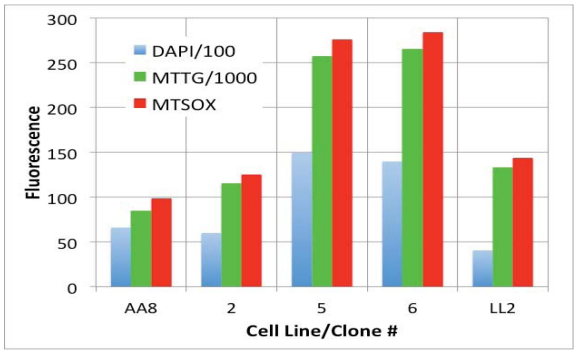

Figure 4. Characterization of CHO clones mitochondrial functionality: This graph shows that clones 5 and 6 are unlikely to be rho-zero cell line due to the high levels of MTTG and MTSOX. LL2 has very low levels of DAPI and therefore it seems that the cells were lost during the staining process. Clone 2 response is still higher than the AA8 control. All of the data was normalized to 1x105 cells and the DAPI was divided by 100 and the MTTG was divided by 1000 for comparison.

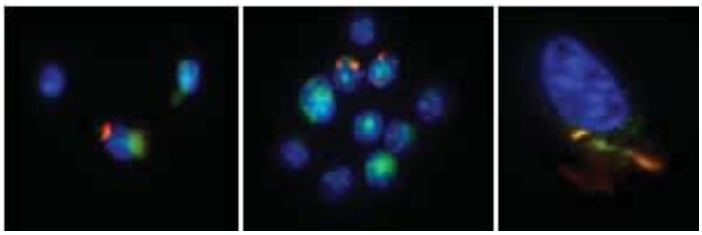

Figure 5. ***DAPI, MTTG, and MTSOX Staining of AA8, LL2, and Clone 2:*** **From left to right, AA8, LL2, Clone 2. Stained with the same concentrations seen in Table 1 except for DAPI which was applied using 50 µl of Prolong Gold. All images show presence of nuclear DNA, mitochondria, and superoxides.** ***Photos taken by A. Johnson.***

D. Survival of AA8 parent strain

While attempting to characterize a rho-zero CHO strain, a survival experiment was conducted on the parental AA8 strain. Figure 6, a graph of the survival of the AA8 parent strain, shows another downward quadratic linear trend with increasing doses, similar to the LL2 parent strain. Since LL2 cells are cancerous and AA8 cells are not, this similarity might suggest that both types of cells react similarly to ionizing radiation. It is also important to note the slight increase in survival at 0.5 Gy. This suggests that at lower doses, AA8 cells may be more resistant to ionizing radiation similar to LL2 cells. When a CHO rho-zero cell line is developed, the same survival experiment will be performed to determine if it reacts similarly to the LL2 rho-zero cells. If both rho-zero cell lines show a decrease in survival at lower doses of ionizing radiation, then that would further the idea that lacking mitochondria affects the cells response to ionizing radiation.

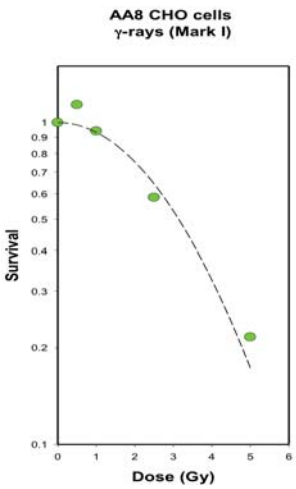

Figure 6, *Survival of AA8 parent strain:* This graph shows the expected downward quadratic linear curve that was seen in the LL2 cells. This suggests that the parent strains of both cancerous and non-cancerous cells may respond similarly to ionizing radiation.

IV. DISCUSSION

These experiments are just the beginning of this research. Once a rho-zero CHO clone is determined, it will be tested for its response to ionizing radiation. If this CHO rho zero clone shows a similar response to LL2/LL2 rho-zero at lower doses of ionizing radiation, then it is possible that other mammalian cells including human will do the same. This might mean that the presence of mitochondria in the cell make it slightly more resistant to radiation at very low doses. This may be due to possible differences between "normal" and mitochondrial defective cells in the mitochondrial–nucleus signaling. If this can be proven, then it is possible to move on to why mitochondria might make a cell more resistant. Further experiments must be conducted and perhaps eventually on human cells to fully decide if the rho-zero model modulates DNA damage due to ionizing radiation.

V. ACKNOWLEDGEMENTS

Supported by the Department of Energy and the Office of Education Programs at Brookhaven National Laboratory, this work was performed under the auspices of the U.S. Department of Energy by Brookhaven National Laboratory under contract DE-AC02-98CH10886 and supported by BNL labwide LDRD grant 12-LW-041 to P.F. Wilson. I would like to thank the following: my mentor Dr. Deborah Keszenman for all of her guidance and patience; Paul Wilson for instructing me in his lab; Paula Bennett and Alisha Johnson for their assistance on this project; and Jim Jardine, John Trunk, and Denise Monteleone for laboratory support; Ann Emrick for all of her help; and Anthony Hoang and Danielle Monteleone for their assistance.

VI. REFERENCES

1. B. Alberts, D. Bray, K. Hopkin, A. Johnson, J. Lewis, M. Raff, K. Roberts, P. Walter (2009) *Essential Cell Biology* Ed. 3
2. D. Keszenman, E.C. Candreva, E. Nunes (2000) *Mutation Research/DNA Repair* 459: 29-41
3. D. Keszenman, B. Sutherland (2010) *Radiation Research* 174: 238-250
4. M. King, G. Attardi (2003) *Methods of Enzymology* 264: 304-313
5. A. Presley, K. Fuller, E. Arriaga (2003) *Journal of Chromotography* 793: 141-150
6. P. Wilson, J. Hinz, S. Urbin, P. Nham, L. Thompson (2010) *DNA Repair* 9: 737-744
7. T. Xia, M. Kovochich, J. Brant, M. Hotze, J. Sempf, T. Oberley, C. Sioutas, J. Yeh, M. Wiesner, A. Nel (2006) *Nano Letters* 6: 1794-1807

Study of charge mobility in pulse irradiated conducting polymers by simultaneous measurement of optical and microwave absorption

Stephen D. Albright, Department of Physics, Brown University, Providence, Rhode Island 02912
Matthew Bird and John R. Miller, Department of Chemistry, Brookhaven National Laboratory, Upton, New York 11973

ABSTRACT We report on the development of new and improved methods for analyzing the charge mobility in conducting polymers (CP), particularly poly(3-hexylthiophene) (P3HT) and poly(fluorene) (PF). We conducted pulse-radiolysis experiments on improved CP samples – solutions and thin, solid state films. To identify charges and excited states in pulse irradiated solid state CPs, we propose adding small molecules that readily accept particular charges and states to CP thin films. By comparing their irradiated absorption spectra with those of neat-CP samples, we can identify which species pulse-radiolysis generated. We've successfully identified an absorption peak in P3HT as negative polarons by adding maleic anhydride, and we believe tetracyanoethylene can also identify negative polarons in PF. We also designed a sample cell in which optical and microwave absorptions can be measured simultaneously which should increase the accuracy of charge mobility determination in CPs. The cell consists of a segment of waveguide that can be irradiated by an electron pulse, and through which a laser is shone. Using this cell (though not yet prepared for a laser), we have successfully reproduced conductivity absorption for pulse-irradiated benzene-PF solution.

I. INTRODUCTION

Conducting polymers (CP) are one of the leading candidates to create the next generation of low-cost electronics and photovoltaics (PV). CPs behave much like inorganic semiconductors (e. g., silicon), and can, therefore, replace them in typical semiconductor applications, including our interest, solar cells. Polymer solar cells are in many ways superior to their inorganic equivalents; they are lighter, more flexible, and should be cheaper and easier to fabricate.[1] They do, however, lack in efficiency. Current polymer PV technology is only around 10% efficient versus 40% for multijunction inorganic cells.[2]

It is generally recognized that the mobility of charges along a polymer chain corresponds to the efficiency a PV cell made of that polymer. Our goal was to gain a better understanding of that mobility, and more generally charge transport, so we can begin work to improve the efficiency of polymer PVs. To calculate the mobility of charges on a polymer, the number of charges and the total conductivity of the sample must be measured. Previously, this was done by irradiating a sample with an electron beam while measuring the absorption of microwaves, a process known as pulse-radiolysis time-resolved microwave conductivity (PR-TRMC). The conductivity of the sample could be calculated from the microwave absorption and the number of charges estimated by the dose of electrons from the beam.[3]

We ventured to improve these measurements. Firstly, we wanted to investigate more reliable samples. Samples in the past were powdered polymer pressed into a waveguide with only an estimated packing density.3 We wanted to analyze the mobility in two better defined samples: solutions and heat pressed films. Secondly, we wanted to eliminate the guesswork involved in calculating the number of charges generated in a sample by combining the microwave absorption with an optical absorption to calculate the number of charges present.

II. THEORY

The conjugation of π-bonds along conducting polymers gives them their semiconducting behavior. In σ-bonded molecules, electrons are found in molecular orbitals between particular atoms. A π-conjugation, however, leads to parallel p-orbitals along the polymer chain which coalesce into one large delocalized molecular orbital. In this situation, the highest-occupied molecular orbital (HOMO) and the lowest-unoccupied molecular orbital (LUMO) are equivalent to the valence and conduction bands, respectively, of a semiconductor.[4,5]

CPs, unlike inorganic semiconductors, have the ability to deform. Therefore, with doping, CPs can distort to stabilize a charge. This process, known as relaxation, gives new energy levels within the band gap (between the valence and conduction bands), as seen in Figure 1. This stabilized charge on a polymer is known as a polaron.4 Since these energy levels correspond to radiation in the visible/near-infrared (Vis-NIR) range, the existence of polarons can be determined by taking absorption spectra in that range. Transitions from singlet and triplet excited states to higher excited states also fall within this range.

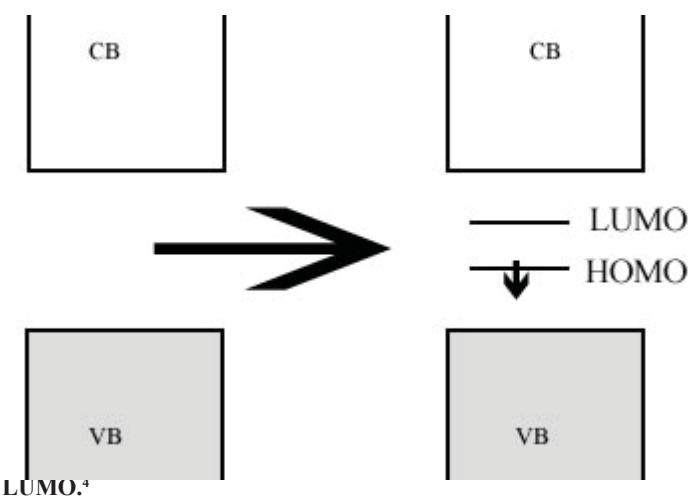

LUMO.[4]

At an absorption peak (where many charges are absorbing), the concentration of charges, and therefore the number, can be calculated from the level of absorbance following the Beer-Lambert Law,[6]

(1) $A = l\,c\,\varepsilon$,

where A is the absorbance, c is the concentration of charges, l is the path length of light through the sample and ε is the extinction coefficient of charges on that polymer.

As defined by Maxwell's equations, conductive materials absorb microwaves very strongly. For this reason, the conductivity of a sample can be determined by measuring the level of microwave absorption. In our experiments, we supplied microwaves to a sample via waveguide and measured the fractional change in reflected power after an increase in conductivity. For small power changes, we can take the fractional change in power to be proportional to the change in conductivity[7,8]

(2) $$\frac{\Delta P}{P} = -a\Delta\sigma$$

where $\Delta P/P$ is the fractional power change, $\Delta\sigma$ is the change in conductivity and a is the sensitivity factor. The sensitivity factor is determined by the geometry of the sample cell, and is calculated for some simple cases in de Haas (1977).

With the number of each charge type (electrons or holes) and total conductivity, we can calculate the mobility of each charge on a polymer:9

(3) $$\sigma = e\sum_i \mu_i N_i$$,

where e is the electron charge, μ_i is the mobility of charge species i and N_i is the number of species i.

III. METHODS & MATERIALS

We investigated the mobilities of two CPs – poly(3-hexylthiophene) (P3HT, see Figure 2.a) and poly(flourene) (PF, Figure 2.b). P3HT was purchased from Reike and PF was synthesized for our experiments by Dr. Sadayuki Asaoka of Kyoto Institute of Technology. We also used two small electron acceptors as additives to samples, tetracyanoethylene (TCNE, Figure 2.c) and maleic anhydride (Figure 2.d). Both were purchased from Sigma-Aldrich. THF and benzene were used as solvents and were also purchased from Sigma-Aldrich. All chemicals were used as received.

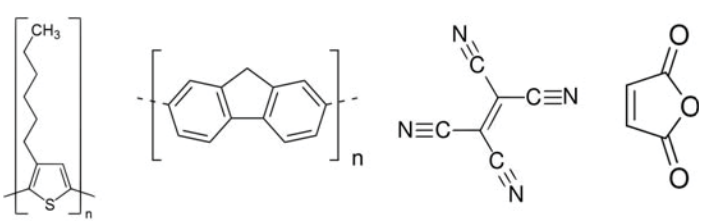

Figure 2: a.(left) poly(3-hexylthiophene) (P3HT) b.(left middle) poly(fluorene) (PF) c.(right middle) tetracyanoethylene (TCNE) d.(right) maleic anhydride

To put charges on our samples, we used pulse-radiolysis to fire electrons from an accelerator at the sample. We used two accelerators: the Laser Electron Accelerator Facility (LEAF) in which photoelectrons are generated by a laser striking a cathode and are accelerated by an RF field; and second, the Van de Graaff accelerator in which electrons are generated on a rotating belt, deposited on a metal hemisphere, and fired through a potential drop. (See Figure 3 for schematic representations of each accelerator.)

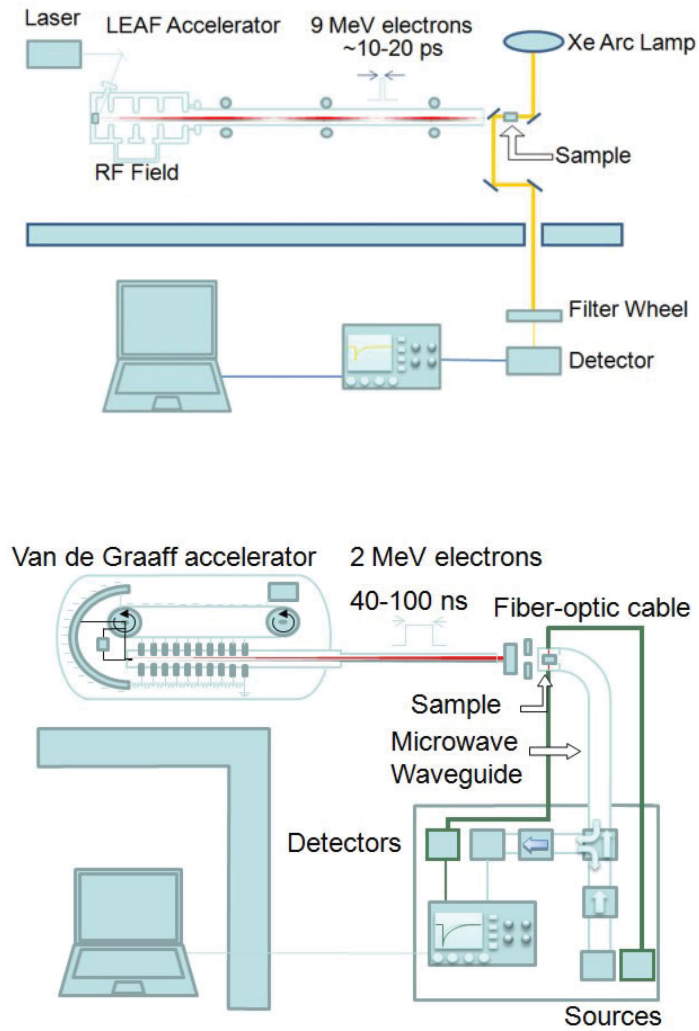

Figure 3: a. (top) The Laser Electron Accelerator Facility (LEAF) b. (bottom) The Van de Graaff accelerator (fiber-optics in green, microwave waveguides in blue). The electronics are in a faraday cage.

When a solution is irradiated by a pulse of electrons, some of the solvent molecules are ionized, and then the charges are transferred to the polymers where they are more stable. From there, the charges can move along the polymer chains and recombine.[9] The mechanics of the pulse irradiation of solid state films is less well known. It is theorized that the pulse ionizes the polymers directly in films. In addition to gaining knowledge of the mobility of charges in polymer films, we hope our experiments will also shed some light onto the mechanics of pulse radiolysis on solid state films.

Vis-NIR absorption spectra (500-1700 nm) were taken using LEAF. As seen in Figure 3.a, a xenon arc lamp shines light on the sample, directed counter-colinearly to the electron beam, and detected in the next room to eliminate RF noise from the pulse. Single wavelengths are selected using a filter wheel.

PR-TRMC was conducted using the Van de Graaff accelerator. Microwaves of 8.5-10.5 GHz were generated by an adjustable source and directed to the sample with X-band waveguide (inner

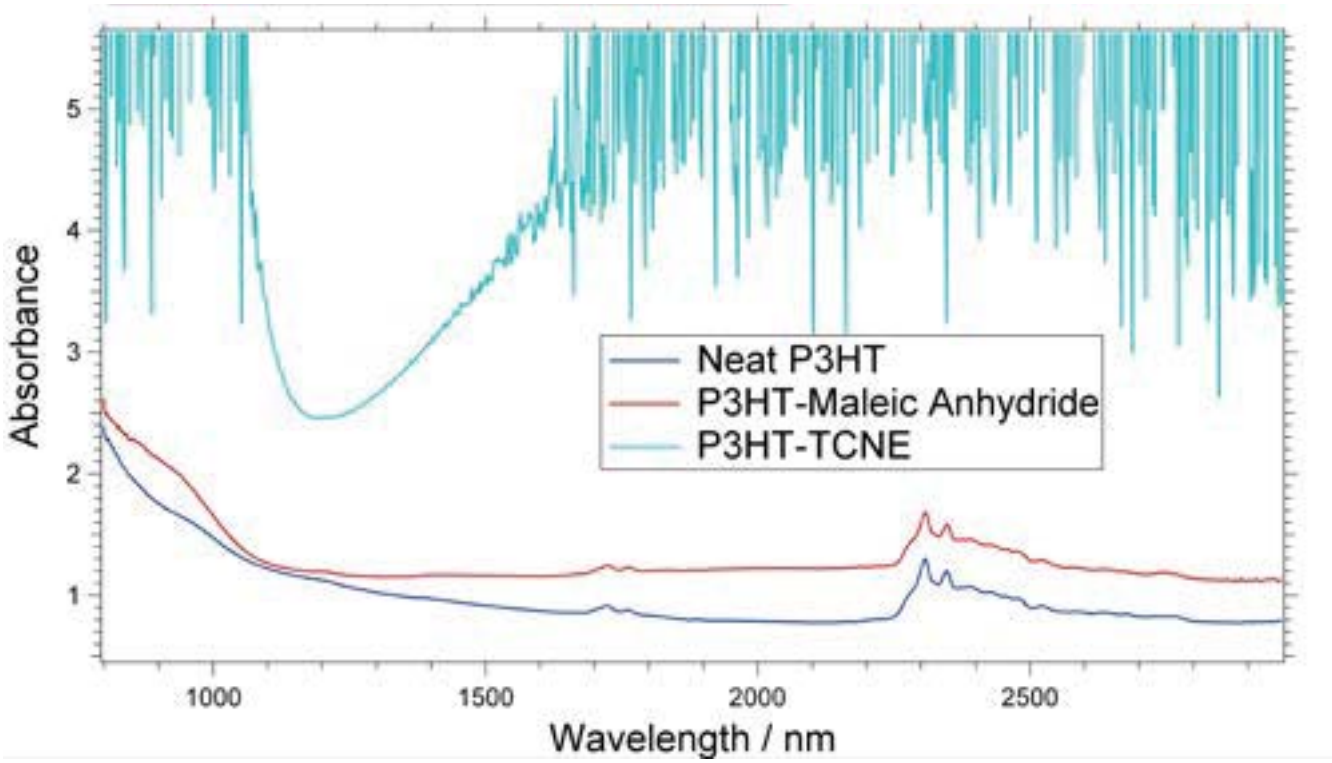

Figure 4: Neutral absorption spectra of 300 µm P3HT films with and without additives.

dimensions 2.29 cm by 1.02 cm). The microwaves passed through the sample and were reflected back to a detector via a circulator as seen in Figure 3.b. We used the Van de Graaff accelerator instead of LEAF because the pulse-width of LEAF (~10-20 ps) is so short that it creates large amounts of microwave noise – so much, in fact, that it saturates the detector. The pulse width on the Van de Graaff is sufficiently large (40-100 ns) that microwave noise is not an issue.

A. Improvement of samples

Although CPs have been extensively studied in powder3 and solution[9,10,11] form, not much work has been done on pressed films – perhaps the most relevant to PV applications. Solid state films present more difficulties than the others, particularly for optical experiments, since films must be thin enough to allow light to pass through, but also thick enough to generate enough absorption upon irradiation. We found that P3HT films of 150-300 µm and

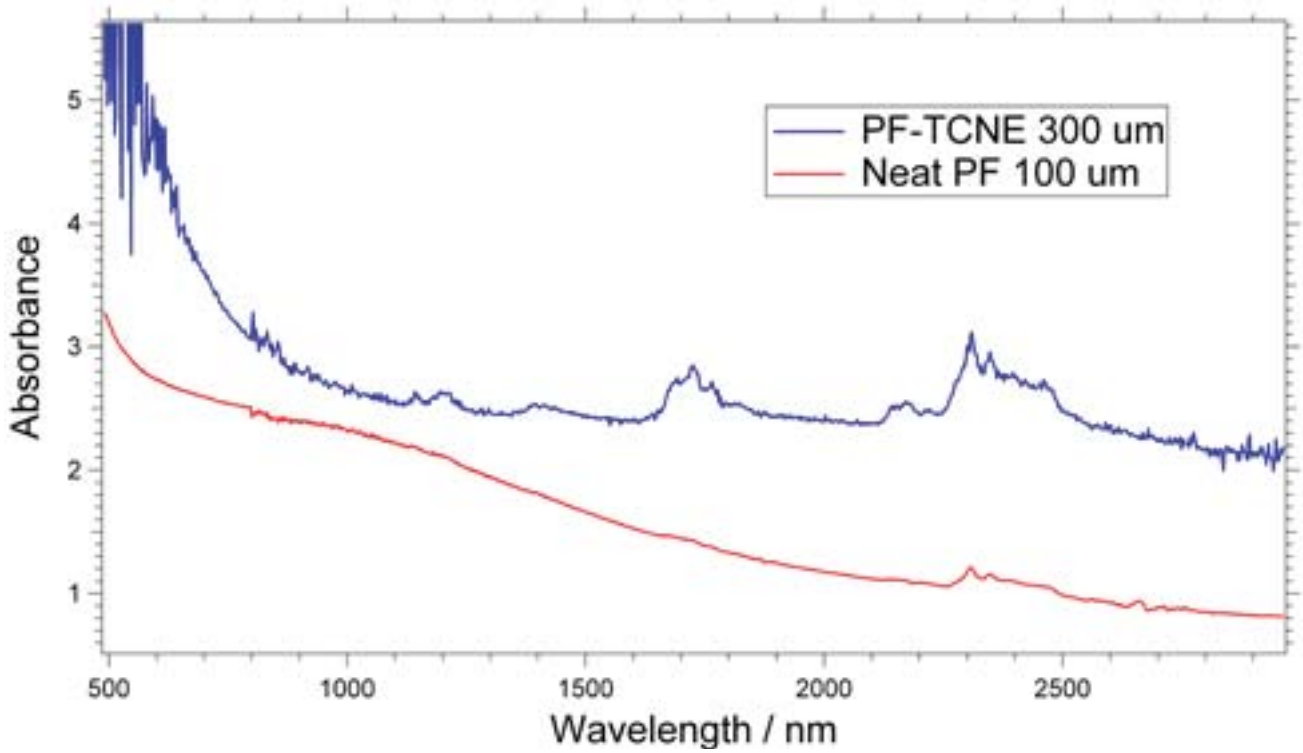

Figure 5: Neutral absorption spectra of PF films with and without TCNE

PF films of 100 µm were able to satisfy both conditions in our experiments.

Our films were pressed using a heat press. Powdered polymer was placed between two dies, heated to 150°C and pressed with a pressure of ca. 1 ton/cm2 for 10 minutes. Films were 10 mm in diameter, and the volume of powdered polymer measured out varied for different thickness of film (we assumed a density of 1 g/cm3 for both polymers). Film thicknesses were measured after pressing using a micrometer.

In addition to the development of more reliable samples, we sought a method to identify Vis-NIR absorption peaks of samples. The energy landscape of these polymers, particular solid films, is not well understood. We therefore have difficulty prescribing particular excited states (e.g. triplets and singlets) or charges to absorption peaks. We proposed that by adding a small molecule that accepts a particular state or charge and having observed the removal of absorption peaks, we can attribute that state or charge to that peak.

We first investigated the use of electron acceptors to remove negative polarons from our samples. We used maleic anhydride in P3HT and TCNE in PF. We wanted to choose acceptors that would only remove electrons from irradiated samples, not dope neutral samples. To make films with these additives, we made solutions of the additives in THF and soaked the polymer powder in solution prior to pressing.

Figure 4 shows neutral absorption spectra taken with a Cary 5 UV-Vis-NIR spectrophotometer of P3HT films with maleic anhydride, TCNE and without any additive. Additive concentrations were 7.8 mM (7.8 µmol/cm3). We can clearly see large new absorptions from the addition of TCNE. These two peaks, at about 975 and 2500 nm, are generally considered to be polaron peaks. These peaks are not evident in the maleic anhydride film, so it appears that TCNE dopes neutral P3HT while maleic anhydride does not. Figure 5 shows neutral spectra of PF films with and without TCNE (again with additive concentration 7.8 mM). There do not appear to be any new absorption peaks. Therefore, TCNE should serve the same role in PF as maleic anhydride in P3HT (the larger absorptions in the TCNE film can be attributed to greater thickness rather than doping).

We took Vis-NIR spectra using LEAF of neat-P3HT and maleic anhydride-P3HT films, seen in Figure 6, to test our proposition. There is a clear reduction of roughly 50% in the absorption peak at 1050 nm, indicating that at least 50% of this peak can be attributed to negative polarons. The remaining 50% could be positive polarons or more negative polarons that would be removed with the addition of more maleic anhydride.

More investigation of this method will continue in the future – we hope to complete a similar analysis with TCNE in PF, as well as find acceptors for holes and excited states.

B. Simultaneous optical and microwave absorption

Our goal of simultaneous measurement of optical and microwave absorption required the creation of a new sample cell to be used on the microwave-Van de Graaff setup. To accommodate the use of either solutions or films, we designed a cell, seen in Figure 7, made of a segment of waveguide, shorted at one end, with a removable window built into a waveguide flange. The cell contains a hole in its flange to allow filling of solution. The window, made of PTFE and glass, can hold a thin copper iris – a partial short, with a hole in the middle. The iris makes the cell a resonant cavity, which increases the sensitivity to absorption, but decreases the time resolution. Vis-NIR radiation will be generated by a laser diode and supplied via fiber-optic cable, connected to the cell using collimators screwed into holes in the side of the wave-

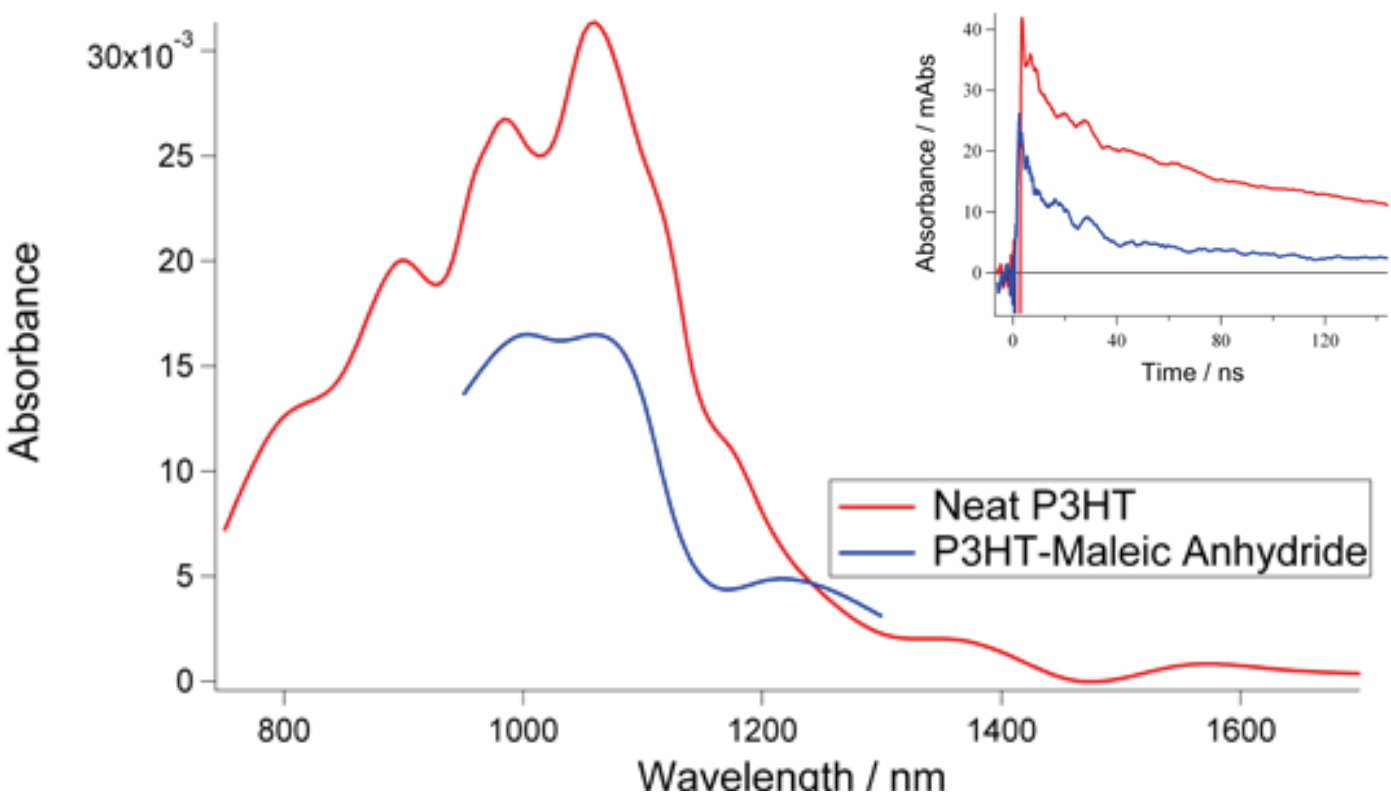

Figure 6: Irradiated absorption spectra of 300 µm P3HT films with additives, taken 10 ns after pulse. Inset shows decay after pulse at 1050 nm.

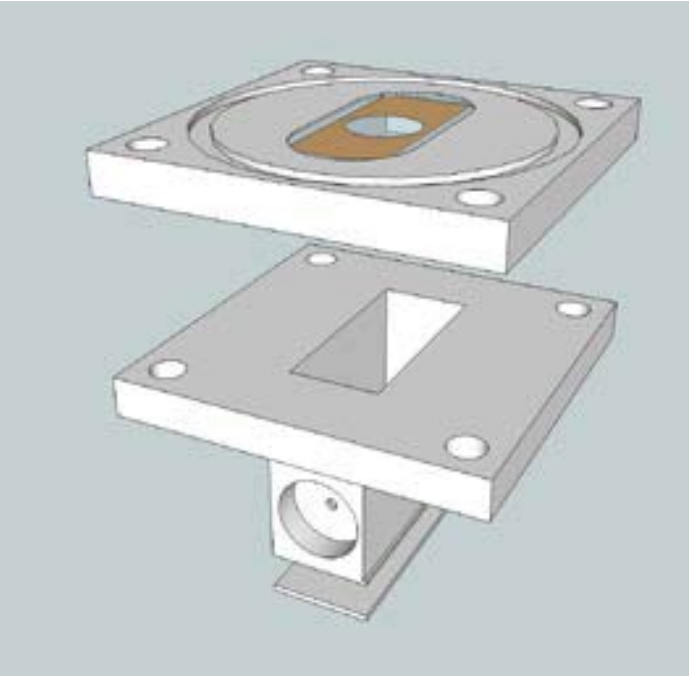

Figure 7: New sample cell. Window contains iris to make the cell a resonant cavity. Collimators will screw into holes in side of cell to supply laser.

guide. The wavelength of the laser will be selected to correspond to a wavelength of high absorption (as determined by the LEAF experiment).

To test the cavity construction, without the holes for the fiber-optics, we attempted to recreate a PR-TRMC study on PF in benzene bubbled with oxygen first published by Prins, et al. (2007). We performed PR-TRMC on 1 mM repeat unit PF in benzene solution with the cavity (with iris). The results appear in Figure 8.a, while the results published by Prins appear in Figure 8.b. The results are strikingly similar, so we can conclude that our new cavity performs very well.

We have yet to fabricate the fiber-optic system to reach our goal of simultaneous optical and microwave absorption, but we have clearly made significant progress towards that goal. Our next step will be to drill the holes in the cavity and perform this experiment again, to ensure the holes do not change the properties of the cavity. Should that prove successful, we can then begin mobility measurements of CPs.

IV. MOVING FORWARD

Although we have been able to perform a great deal of important work towards our eventual goal of an improved methodology for the calculation of charge mobility on CPs, a great deal remains to be done. As mentioned before, we need to continue pursuing peak identification by additives, complete irradiated spectra of PF-TCNE films, as well as find other additives to capture holes and excited states. We also still need to complete the fiber-optic system described above, but even after completion, we need to complete other calibrations before we are able to measure mobilities. Firstly, we need to calibrate our microwave detector. As evident in Figure 8.a, we have only been able to get a $\Delta V/V$ signal, so we need to know how to convert that to $\Delta P/P$. We also need to find a, the microwave sensitivity factor of our cavity. It is calculated theoretically for some simple cases in de Haas (1977), but we have yet to complete analysis for our cell. After we complete these calibrations and the fiber-optic system, we can finally perform simultaneous optical and microwave absorption measurements and get, for the first time, a precise time-resolved measurement of charge mobility without relying on estimates of packing or charge densities.

V. CONCLUSIONS

Although photovoltaic cells made of conducting polymers have great potential to become superb alternatives to inorganic cells, much work still must be done to improve their efficiency. Scientists have yet to develop a thorough method for determining the charge mobility of CPs, an indicator of efficiency, so we ventured to develop one. To improve the calculation of the number of charges on a CP, we've developed a method to identify which excited state or charge creates optical absorption by mixing CP samples with additives that capture charges and observe which absorptions disappear. Even more importantly, we've begun work on an experiment that would find optical and microwave absorp-

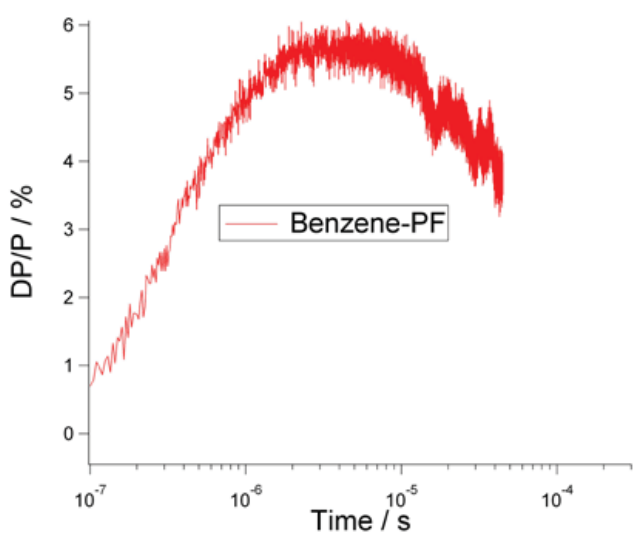

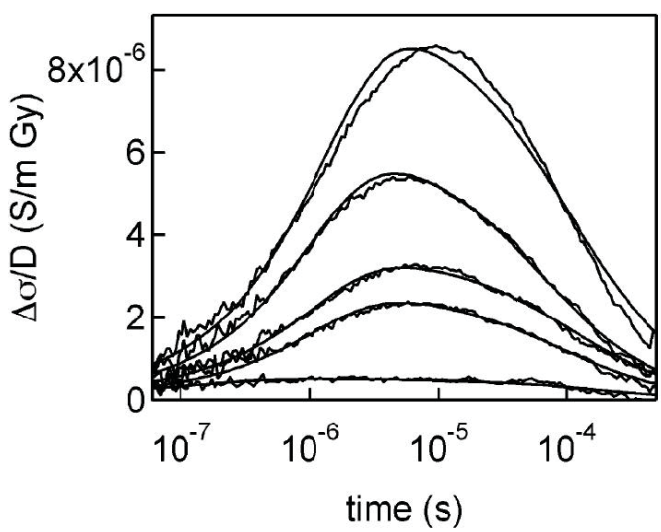

Figure 8: a. (left) Fractional reflected power change for pulse irradiated 7.8 mM PF-benzene solution.The microwave frequency used was 9.1 GHz b. (right) Change in conductivity of 0.315 mM PF-benzene solution published in Prinn (2007) for varying fraction binaphthyl units on the polymer, from top to bottom (top curve has no binaphthyl). The microwave frequency used was 34 GHz.[11]

tions of a sample simultaneously, enabling the direct calculation of charge mobility. With these tools, charge mobility can be calculated precisely. Although a great amount of work remains to be done in reaching these goals, we expect that with these methods we can not only vastly improve the determination of charge mobility of CPs, but gain a better understanding of the mechanisms and interactions of charged and excited CPs.

VI. REFERENCES

1. Alex C. Mayer, Shawn R. Scully, Brian E. Hardin, Michael W. Rowell and Michael D. McGehee, "Polymer-based solar cells," *Materials Today* 10 (11), 28-33 (2007).
2. "Best Research-Cell Efficiencies," NREL. NREL (2012). Web. 6 Aug. 2012.
3. John M. Warman, Gerwin H. Gelinck and Matthijs P. de Haas, "The mobility and relaxation kinetics of charge carriers in molecular materials studied by means of pulse-radiolysis time-resolved microwave conductivity: dialkoxy-substituted phenylene-vinylene polymers," J. Phys.: *Condens. Matter* 14, 9935-3354 (2002).
4. Prasanna Chandrasekhar, *Conducting Polymers: Fundamentals and Applications,* Norwell MA: Kluwer Academic Publishers (1999).
5. "Basic Semiconductor Physics," *Britney Spears' Guide to Semiconductor Physics,* britneyspears.ac. Web. 6 Aug. 2012.
6. Dean Calloway, "Beer-Lambert Law," *J. Chem. Education* 74 (7), 744 (1997).
7. Pierre P. Infelta, Matthijs P. de Haas and John M. Warman, "The study of the transient conductivity of pulse irradiated dielectric liquids on a nanosecond timescale using microwaves," *Radiat. Phys. Chem.* 10, 353-365 (1977).
8. Matthijs P. de Haas, *The measurement of electrical conductance in irradiated dielectric liquids with nanosecond time resolution,* Delft: Delft University Press (1977).
9. Romano J.O.M. Hoofman, Matthijs P. de Haas, Laurens D.A. Siebbeles and John M. Warman, "Highly mobile electrons and holes on isolated chains of the semiconducting polymer poly(phenylene vinylene)," *Nature* 392, 54-56 (1998).
10. Ferdinand C. Grozema, Piet Th. Van Duijnen, Yuri A. Berlin, Mark A. Ratner and Laurens D.A. Siebbeles, "Intramolecular charge transport along isolated chains of conjugated polymers: effect of torsional disorder and polymerization defects," *J. Phys. Chem.* B 106, 7791-7795 (2002).
11. Paulette Prins, Ferdinand C. Grozema, Frank Galbrecht, Ullrich Scherf and Laurens D.A. Siebbeles, "Charge transport along coiled conjugated polymer chains," *J. Phys. Chem.* C 111, 11104-11112 (2007).

Assessment of clinical and neuropsychological function in comorbid cocaine and alcohol addiction

Christine Anerella, Scott J. Moeller, Patricia A. Woicik, Rita Z. Goldstein.

ABSTRACT

Drug addiction costs the United States billions of dollars every year. This summer I worked with Brookhaven National Laboratory's (BNL) Neuropsychoimaging Group whose research aims to reduce this burden on society. My goals of the SULI experience were to receive hands-on training in clinical interviewing and to apply this newly acquired clinical experience to a highly pertinent research question in drug addiction. For the clinical portion of my SULI experience, I received training to administer the Addiction Severity Index (ASI) and the Structured Clinical Interview for the DSM-IV (SCID). Interview questions probe drug abuse history, criminal drug charges, periods of voluntary and involuntary abstinence, and the amount of time and money spent obtaining drugs, among other variables. Specific questions evaluate the detrimental effects of drug use on an individual's quality of life. For example "How many times in your life have you been charged with driving while intoxicated?" For the research portion of my SULI experience, I analyzed neuropsychological performance data using the Wisconsin Card Sorting Task (WCST), a standard measure of executive function, and functional magnetic resonance imaging (fMRI) data as individuals performed the drug and color-word Stroop tasks' measures of ability to inhibit a predominant response. I hypothesized that comorbid alcohol use disorder in cocaine addiction would impair neuropsychological functioning on the WCST, and that such behavioral impairment would be associated with impaired neural response as measured with fMRI during a classical cognitive control task (the color-word Stroop). After my SULI appointment has concluded, I will function as the liaison between BNL and Samaritan Village, the treatment facility where I will administer targeted neuropsychological tasks and collect pertinent clinical information that will be used to predict treatment outcomes in drug addiction.

I. INTRODUCTION

The neuropsychoimaging method is a multi-pronged approach to collecting and analyzing data utilized by the Neuropsychoimaging group at Brookhaven National Laboratory (BNL) to provide insights into the psychological and neurological factors of addiction. Control and cocaine-addicted subjects travel to BNL and undergo a number of procedures over a span of two to three days. A subject's schedule will consist of diagnostic interviews, self-reported measures, and imaging techniques in order to assess neuropsychology and brain activity. During my SULI appointment, I was able to receive training on some of these measures, and was fortunate to become involved with the clinical aspect of the research.

Drug addiction is associated with impaired cognitive function and decision-making. Prior studies indicate that comorbid alcohol use disorders exacerbate such impairments. For example, Fernandez-Serrano, et al. (2010) reported that the severity of alcohol use was associated with poorer fluency and decision-making skills as well as a trend for poorer working memory in subjects with comorbid marijuana, cocaine, or heroin use disorder. The more clinical portion of my SULI experience, which included observation of the ASI, SCID, and neuropsychological testing, suggested similar conclusions. I, therefore, hypothesized that comorbid alcohol use disorder in cocaine addiction would impair neuropsychological functioning on the WCST, and that such behavioral impairment would be associated with impaired neural response as measured with fMRI during a classical cognitive control task (the color word Stroop).

II. METHODS

A. Behavioral

A neuropsychological exam measures test subjects' reading, attention, executive function, motor function, memory, and reasoning abilities. Scores on these exams are used to match controls with substance dependent individuals to avoid confounding variables in results. Scores on cognitive measures can be used to correlate brain activations with specific cognitive tasks; for example, the Wisconsin Card Sort Task, a classic example of a neuropsychological test (WCST). Subjects sort cards based on a specific rule, unknown to the subject, which can include color, shape, or number. Subject is given only feedback on correctness of their current sorting strategy and must either maintain or adjust strategy accordingly. After a number of trials, the rule changes and subjects must again adjust. When subjects adhere to a strategy that is no longer appropriate (i. e., using a previously correct rule), this is referred to as perseverative error. Repeated perseverative errors reflect diminished executive function. Behavioral data is analyzed using Statistical Package for the Social Sciences (SPSS) software.

B. Brain

Functional Magnetic Resonance Imaging (fMRI) noninvasively measures brain function in vivo. Analyses compare brain activations during a baseline condition (e. g., fixation, during which a "+" is displayed on the screen) and during an active task condition. In the Neuropsychoimaging Laboratory, fMRI is collected as subjects perform threat and color word Stroop tasks, among others. Brain data was analyzed using Statistical Parametric Mapping 2 (SPM2) software.

III. RESULTS

A. SPSS

A one-way analysis of variance (ANOVA), followed by a subsequent planned comparison, compared subjects with comorbid cocaine and alcohol use disorder against healthy controls and individuals with only a history of cocaine use disorder. A significant omnibus ANOVA [$F(2,127)=3.93$, $p<0.05$] and subsequent significant planned comparison [$t(127)=2.4$ $p<0.05$] revealed that the individuals with comorbid cocaine and alcohol use disorder performed worse (more perseverative errors / total cards) on the WCST than did healthy controls and individuals with only a history of cocaine use disorder.

B. SPM

In addition to behavior, correlations with this same WCST measure were investigated using whole-brain analyses with Statistical Parametric Mapping (SPM2) software. No correlations emerged between brain activity during fMRI color word Stroop task and performance on the WCST.

IV. DISCUSSION

This summer I trained to administer select clinical (e. g., ASI) and neuropsychological instruments (e. g., California Verbal Learning Test). I also conducted neuropsychological analyses which indicated that individuals with comorbid alcohol and cocaine use disorder have poorer executive function (specifically, reversal learning) than healthy controls or individuals with cocaine use disorder alone. Finally, I conducted preliminary correlations of this WCST measure with MRI data, although such correlations were not significant. A more appropriate correlation to investigate would be with performance on WCST during fMRI. In the future, further investigation of this data should use covariate analyses to account for the possible confounding effects of demographics (e. g., age, education, etc.) that differed between the study groups.

All results in this paper are extremely preliminary and must be rigorously followed up with subsequent analyses both for possible confounding variables and the demographic matching of study groups. Furthermore, the methods section does not identify the way in which subjects were selected for each study group. Specifically the definition of an "alcohol and cocaine" subject must be clarified. This project was designed to supplement a more clinically focused summer experience and the research portion is preliminary to a more developed project.

V. FUTURE WORK

A new offsite protocol will begin shortly after my SULI appointment ends. I will function as the liaison between BNL and Samaritan Village, a treatment facility. I will administer targeted neuropsychological tasks and collect pertinent clinical information that will be used to predict treatment outcome in drug addiction.

VI. ACKNOWLEDGMENTS

This project was supported by grants from the National Institute on Drug Abuse (to RZG: 1R01DA023579 and to SJM: 1F32DA030017-01). I also gratefully acknowledge the contributions of Tom Maloney, Anna Konova, Dan Carrero, Farrah Hruska, Julia Arena, and Nelly Alia-Klein.

VII. REFERENCES

Fernandez-Serrano, M. J., Perez-Garcia, M., Rio-Valle, J.S. and Verdejo-Garcia, A. (2010) Neuropsychological consequences of alcohol and drug abuse on different components of executive functions. *Journal of Psychopharmacology* 24(9) 1317 – 1332.

VIII. APPENDIX

Time	Procedure	Specific Tasks
Day 1		
9:15 AM	Clinical Research Center (CRC)	Provide breakfast after blood draws.
9:30 AM	Consent for IRB 328	Informed consent of protocol.
10:00 AM	Medical Screen	Vitals, Questionnaires, Urinalysis, Blood draw for genetics and CBC panel.
10:45 AM	Pointed Scale Aggression Paradigm	Computerized task measuring aggression.
11:45 AM	Psychological Interview	Measures from the SCID, ASI, CSSA, etc.
1:30 PM	Neuropsychological Exam	Measures include CVLT, WRAT, Matrix Reasoning, Handedness Inventory, etc.
Day 2		
10:00 AM	Medical clearance	Heplock insert. Check blood results for eligibility for MPH protocol.
10:30 AM	328 MRI	MPH ALC Procedures: Structure and baseline connectivity, checkerboard, threat stroop task, colorword stroop task, and post task word ratings.

Table 1: Sample schedule for a new subject.

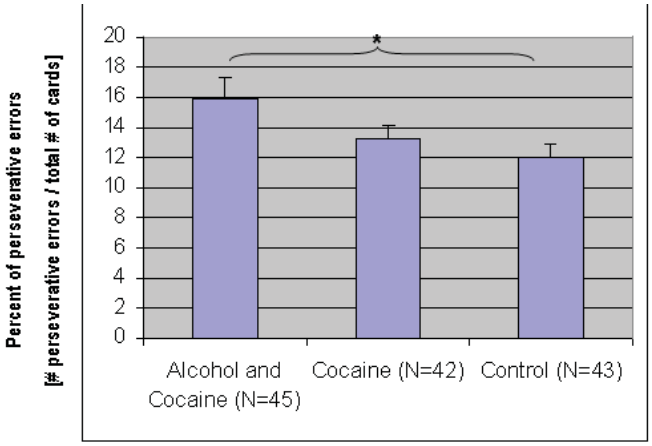

Figure 1: Percent of perseverative errors on the WCST in Alcohol and Cocaine, Cocaine, and Control subjects.

Figure 2: An example of an fMRI task: the Colorword Stroop. The congruent trial is circled (says red

Heat island effect of the Long Island Solar Farm

Helen Bagnato
Environmental Science Department, Suffolk County Community College, Selden, NY 11784
John Heiser
Environmental Science Department, Brookhaven National Laboratory, Upton, NY 11973

ABSTRACT

The Long Island Solar Farm at Brookhaven National Laboratory was built to bring an essential source of renewable energy to homes and businesses throughout Long Island. Field sensors were installed throughout the solar farm to monitor the meteorological and environmental conditions that are relevant to the solar panels and/or local ecology. Of particular interest is the heat island affect the panels have on the microclimate. By comparing the air temperature from the solar fields with the meteorology field we can see how the temperature is affected by the solar panels. On partly cloudy days the air temperature between solar farm and met field is fairly close to each other in the early morning and late evening but during the day light hours it varies considerably. On mostly sunny days the same trend holds true, but the temperature difference is less.

I. INTRODUCTION

The Long Island Solar Farm (LISF) is owned by BP Solar and Met Life and it is one of the largest solar projects in the nation on a government property. LISF, which has 164,312 solar panels within six fields, provides renewable energy to homes and business throughout the Long Island area. Twenty-five power blocks/inverter boxes were installed throughout the six fields in the solar farm to record the air and panel temperature. Each of the twenty-five power blocks has a data logger that records the air temperature and the array temperature. All twenty-five locations have pairs of SP-lite2 pyranometers, Omega model PRCU-10-2-100-1/4-6-e Fast Response Copper Tip RTD's to measure panel temperature and Omega Model SA1-TH-44006-120-T thermistors to measure panel temperature. Ten locations have soil temperature (under array and in the middle of an aisle) and shaded air temperature and relative humidity. The soil temperature probes are Campbell model 109-SS and the air temperature/relative humidity probes are Campbell model HMP-45C. Each power block has a humidity sensor, temperature sensor, and soil temperature sensor installed to record the air, panel, and soil temperature for meteorological and environmental conditions which are very important to solar arrays and local ecology. The solar farm serves as a disturbed field due to the solar panels and results heat from the panels. A met field was also installed at Brookhaven National Laboratory for maintenance, calibration, data collection such as wind speed, wind direction, temperature, and relative humidity. Unlike the solar farm the met field serves as an open, undisturbed field.

The goal of my project was to calibrate temperature sensors, humidity sensors, and soil temperature sensors and compare that data to the met field data. I wanted to see the difference in air temperature on hot days versus cold days between met field and solar farm. Determining the temperature difference due to the solar panels will help scientists to better understand micro-ecology differences (e. g., plant growth rates, plant species differences, small animal preferences) that may occur within the LISF. It will also help to see how much the temperature is affected by the solar panels. I also compared the air temperature and panel temperature between each of the six fields. By comparing the air and panel temperature within the solar farm we can see how temperature varies between each of the six fields.

II. METHODS

There are several methods that I used to record air and panel temperature. I calibrated the temperature sensor, humidity sensor, and soil temperature sensor at each of the 25 power blocks. To calibrate each temperature sensor, I went out to the field and took down the temperature sensor and brought it back to the Meteorology Lab to be calibrated. In the Meteorology Lab, I connected the sensor to the appropriate data logger (CR3000 or CR1000 to match the field unit) and placed the sensor into the Ethylene Glycol water bath along with the reference thermometer. I then set the Ethylene Glycol water bath to -10°C and waited until the temperature bath was stabilized and documented both the reference reading and test unit reading on the calibration form.

I took three measurements one minute apart and found the average and standard deviation for the reference and test unit. I then did the same thing for 5°C, 20°C, and 35°C. If temperature sensor failed to meet the required precision (for stability class measurements; corrected +/- 0.1°C or uncorrected +/- 0.5°C) I calibrated again until it passed the required precision. On the calibration form I put the BNL bar code that belonged to that temperature sensor, signed it, and placed it in the Instrument Calibration Log Book.

In order to check if the temperature sensor passed or failed I put all the information in an Excel sheet, graphed it, found an equation for it, and plugged in the test sensor averages at -10°C, 5°C, 20°C, and 35°C. I did this for all 25 temperature sensors and scanned each bar code after calibrating. Afterwards, I transferred all the bar code information into Met Services inventory file and returned the temperature sensor back to the solar farm.

The humidity probe has two types of sensors: humidity sensor and temperature sensor. To calibrate the humidity sensor, I removed it from the field and brought it to the Meteorology Lab where I connected the sensor to the appropriate data logger (CR3000 or CR1000) to match the field unit. Using three saturated solutions--NaCl (75.5% RH at 20°C), NaBr (59.1% RH at 20°C), and MgCl (32.8% RH at 20°C)--that were already made prior to the calibration procedure, I started calibrating the humidity probe by gently inserting the RH probe through the hole of saturated MgCl solution (32.8% RH at 20°C) until the probe stopped. I allowed the system to equilibrate for one hour. Once it reached the equilibration, I took three consecutive readings five minutes apart and recorded the results in the calibration form.

Then I placed the RH probe through the hole of saturated NaBr solution (59.1% RH at 20°C) until the probe stopped and I allowed the system to equilibrate for one hour. Once it reached the equilibration I took three consecutive readings five minutes apart

and recorded the results in the calibration form.

To finish calibrating this humidity probe I placed the RH probe through the hole of saturated NaCl solution (75.5% RH at 20°C) until the probe stopped and I allowed the system to equilibrate for one hour. Once it reached equilibration, I took three consecutive readings five minutes apart and recorded the results in the calibration form.

After I took all the readings, I took the average and standard deviation for Measured RH and Temperature for MgCl, NaBr, and NaCl solutions. Then I compared the measured RH values to the equilibrium RH values. The equilibrium RH values are: NaCl (75.5% RH at 20°C), NaBr (59.1% RH at 20°C), and MgCl (32.8% RH at 20°C). If the values agreed within +/- 4% then the humidity sensor passed. If the values didn't agree, I calibrated it again until it passed. On the calibration form, I put the BNL bar code that belonged to that humidity sensor, signed it, and placed it in the Instrument Calibration Log Book. I did this for all 25 humidity sensors and scanned each bar code after calibrating. Afterwards, I transferred all the bar code information into Met Services inventory file and returned the humidity sensor back to the solar farm.

To calibrate the temperature sensor from the humidity probe, I went out to the field and took down the humidity probe and brought it back to the Meteorology Lab. In the Meteorology Lab I connected the sensor to the appropriate data logger (CR3000 or CR1000 to match the field unit) and placed the sensor into the Ethylene Glycol water bath along with the reference thermometer. I then set the Ethylene Glycol water bath to -10°C and waited until the temperature bath was stabilized and documented both the reference reading and test unit reading on the calibration form. I took three measurements one minute apart and found the average and standard deviation for the reference and test unit. I then did the same thing for 5°C, 20°C, and 35°C. If the temperature sensor failed to meet the required precision (for stability class measurements; corrected +/- 0.1°C or uncorrected +/- 0.5°C), I calibrated again until it passed with the required precision. On the calibration form, I put the BNL bar code that belonged to that temperature sensor, signed it, and placed it in the Instrument Calibration Log Book. In order to check if the temperature sensor passed or failed I put all the information in an Excel sheet, graphed it, found an equation for it, and plugged in the test sensor averages at -10°C, 5°C, 20°C, and 35°C. I did this for all 25 temperature sensors and scanned each bar code after calibrating. Afterwards I transferred all the bar code information into Met Services inventory file and returned the humidity probe back to the solar farm.

To calibrate soil temperature sensors, I took the reference probe from the Meteorology Lab and placed it in the soil 18 inches in under the arrays. I then recorded the array temperature from the data logger and compared it to the temperature the reference probe recorded. I also placed the reference probe in the soil in the middle of an aisle between the arrays and recorded that temperature and compared it to the temperature that data logger read for the aisle.

III. CONCLUSION

After I placed all the calibrated humidity and temperature sensors out in the field, I recorded the air and panel temperature from the computer that was monitoring them in order to see how the air and panel temperature varies between each of the six fields. I also recorded the air temperature from the met field in order to see how the air temperature is affected by the solar panels. In order to see those results I did a comparison of those temperatures on mostly sunny days and partly cloudy days. On mostly sunny days, the air and panel temperature in the solar farm was fairly close to each other. On partly cloudy days, the air and panel temperature in the solar farm were fairly close to each other except for the panel temperature in the late morning. On partly cloudy days, the difference in air temperatures between the solar farm and the met field were fairly close to each other in the early morning and late evening, but during the daylight hours it varied considerably. On mostly sunny days the same trend held true but, the temperature difference was less.

Recording the air and panel temperature and comparing them to each other will help scientists in future studies on the solar farm such as: understanding micro-ecology differences such as plant growth rates, plant species differences, small animal preferences, and cloud movement/tracking. In the long run, the Long Island Solar Farm will strengthen Long Island as a national leader in renewable and clean energy and create new, high quality jobs that will protect our environment.

IV. ACKNOWLEDGEMENTS

I wish to thank the U.S. Department of Energy and the Office of Educational Programs at Brookhaven National Laboratory for allowing me to participate in the Science Undergraduate Laboratory Institute Program to further my studies and understanding within my field of studies. I would also like to thank NSF-STEM Program for funding me and the Department of Environmental Sciences at Brookhaven National Laboratory for supporting me. I would also like to thank my mentor, John Heiser, for his guidance and support.

V. APPENDIX

Heiser, J; (2011). Brookhaven National Laboratory Meteorological Services: Instrument Calibration Plan and Procedures.

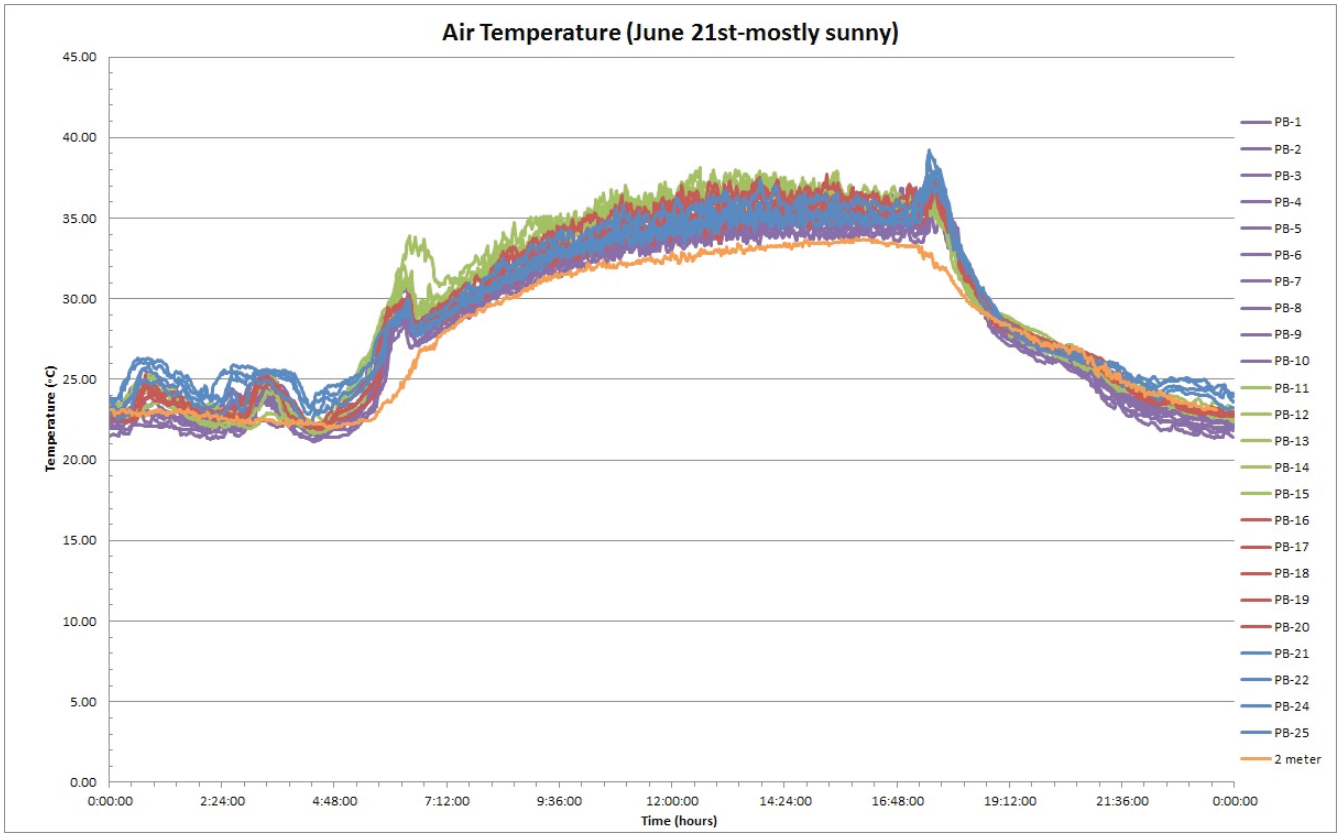
Air Temperature (June 21st-mostly sunny)
Temperature (-C)
Time (hours)
45.00
40.00
35.00
30.00
25.00
20.00
15.00
10.00
5.00
0.00
0:00:00
2:24:00
4:48:00
7:12:00
9:36:00
12:00:00
14:24:00
16:48:00
19:12:00
21:36:00
0:00:00
PB-1
PB-2
PB-3
PB-4
PB-5
PB-6
PB-7
PB-8
PB-9
PB-10
PB-11
PB-12
PB-13
PB-14
PB-15
PB-16
PB-17
PB-18
PB-19
PB-20
PB-21
PB-22
PB-24
PB-25
2 meter

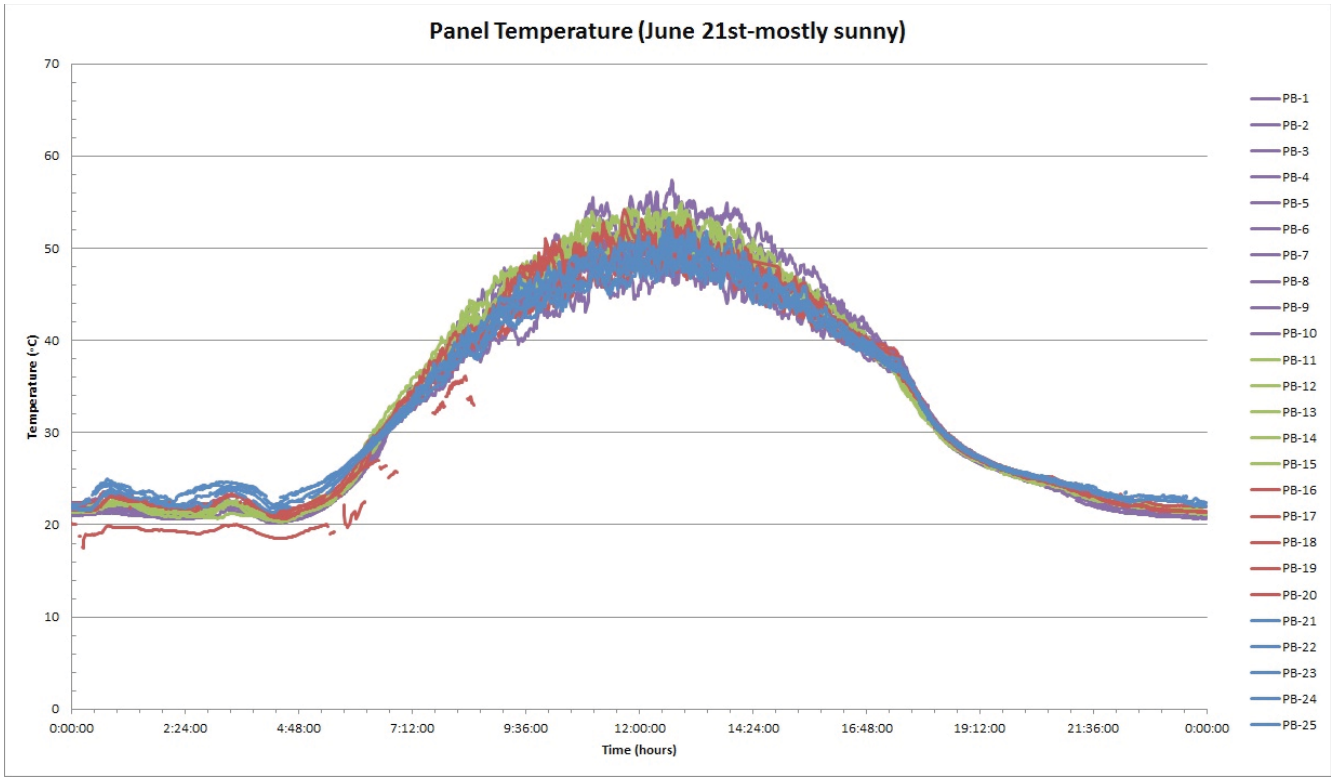
Panel Temperature (June 21st-mostly sunny)
Temperature (-C)
Time (hours)
70
60
50
40
30
20
10
0
0:00:00
2:24:00
4:48:00
7:12:00
9:36:00
12:00:00
14:24:00
16:48:00
19:12:00
21:36:00
0:00:00
PB-1
PB-2
PB-3
PB-4
PB-5
PB-6
PB-7
PB-8
PB-9
PB-10
PB-11
PB-12
PB-13
PB-14
PB-15
PB-16
PB-17
PB-18
PB-19
PB-20
PB-21
PB-22
PB-23
PB-24
PB-25

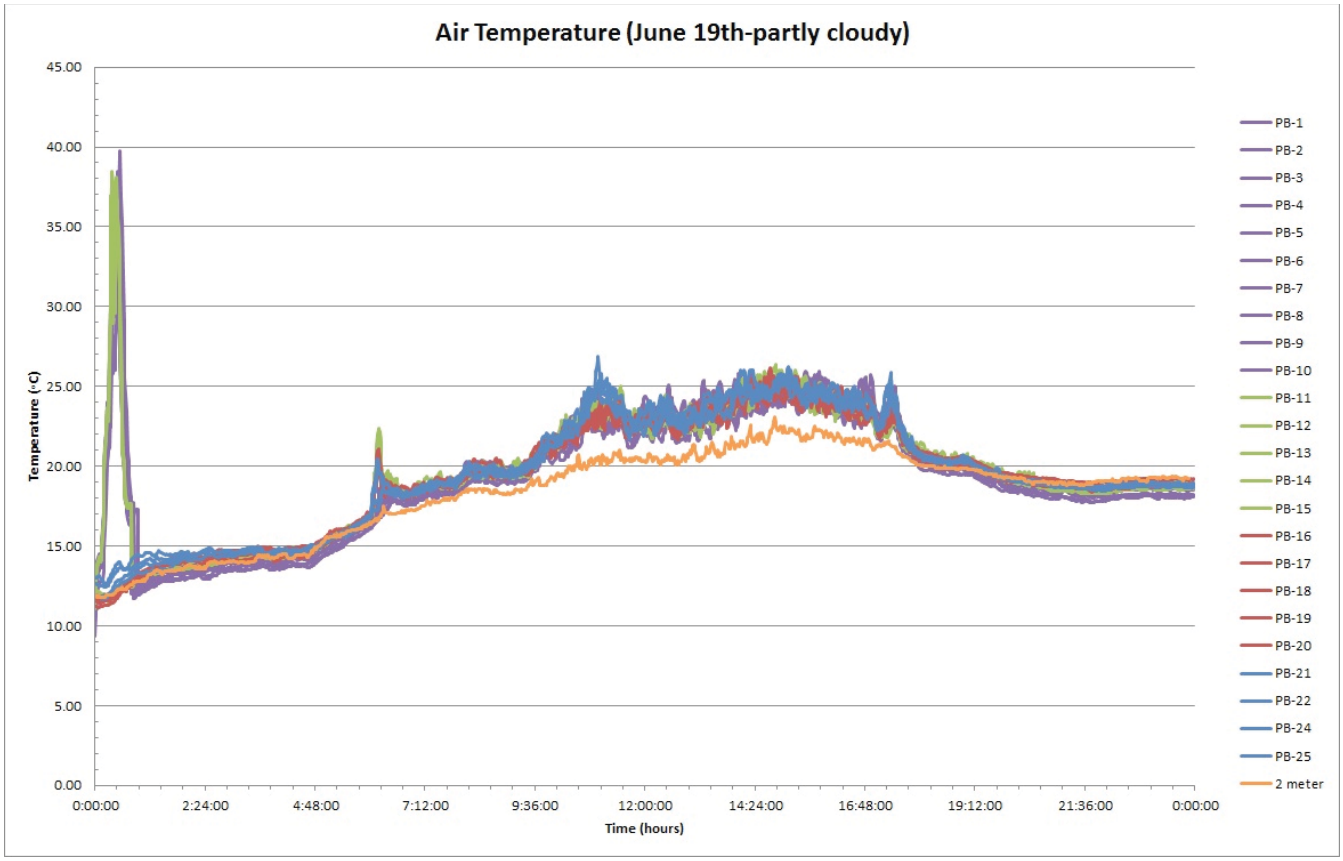
Air Temperature (June 19th-partly cloudy)
Temperature (°C)
Time (hours)
45.00
40.00
35.00
30.00
25.00
20.00
15.00
10.00
5.00
0.00
0:00:00
2:24:00
4:48:00
7:12:00
9:36:00
12:00:00
14:24:00
16:48:00
19:12:00
21:36:00
0:00:00
PB-1
PB-2
PB-3
PB-4
PB-5
PB-6
PB-7
PB-8
PB-9
PB-10
PB-11
PB-12
PB-13
PB-14
PB-15
PB-16
PB-17
PB-18
PB-19
PB-20
PB-21
PB-22
PB-24
PB-25
2 meter

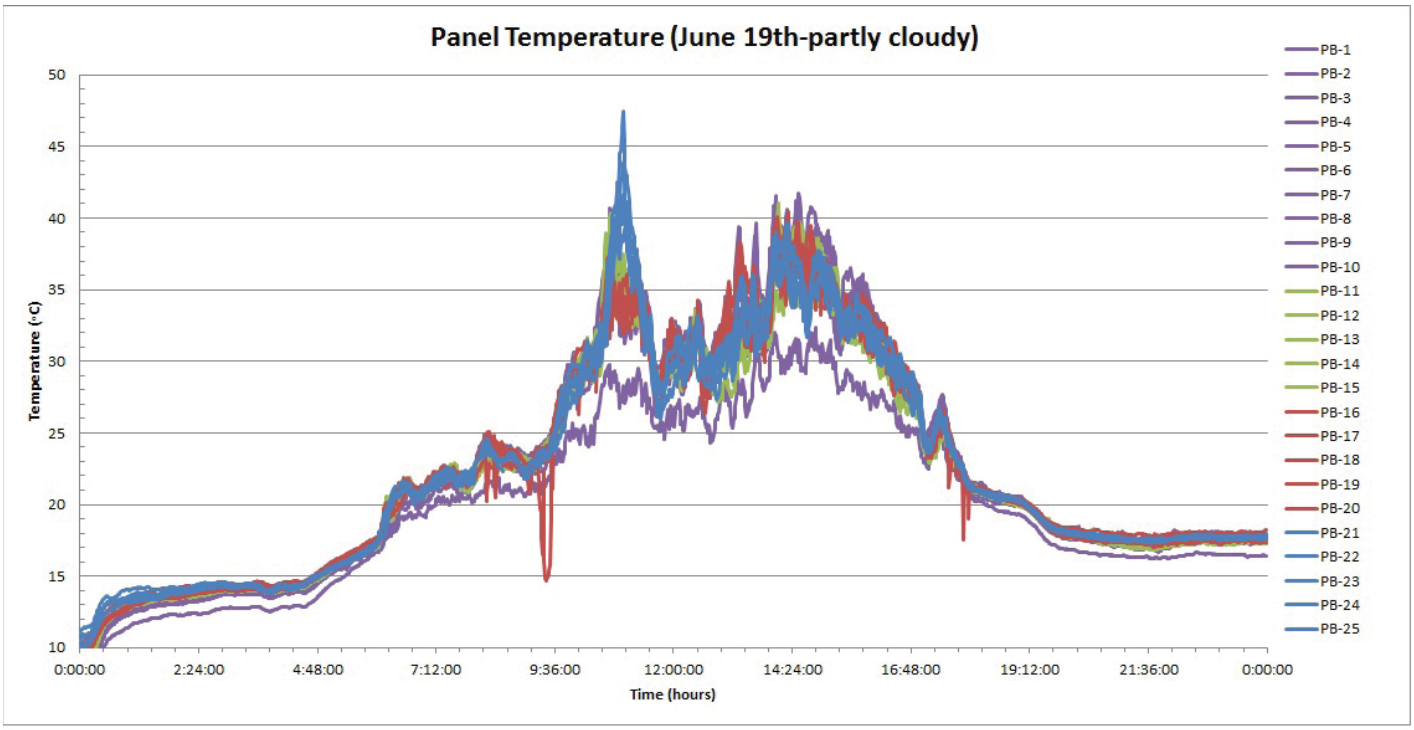
Panel Temperature (June 19th-partly cloudy)
Temperature (°C)
Time (hours)
50
45
40
35
30
25
20
15
10
0:00:00
2:24:00
4:48:00
7:12:00
9:36:00
12:00:00
14:24:00
16:48:00
19:12:00
21:36:00
0:00:00
PB-1
PB-2
PB-3
PB-4
PB-5
PB-6
PB-7
PB-8
PB-9
PB-10
PB-11
PB-12
PB-13
PB-14
PB-15
PB-16
PB-17
PB-18
PB-19
PB-20
PB-21
PB-22
PB-23
PB-24
PB-25

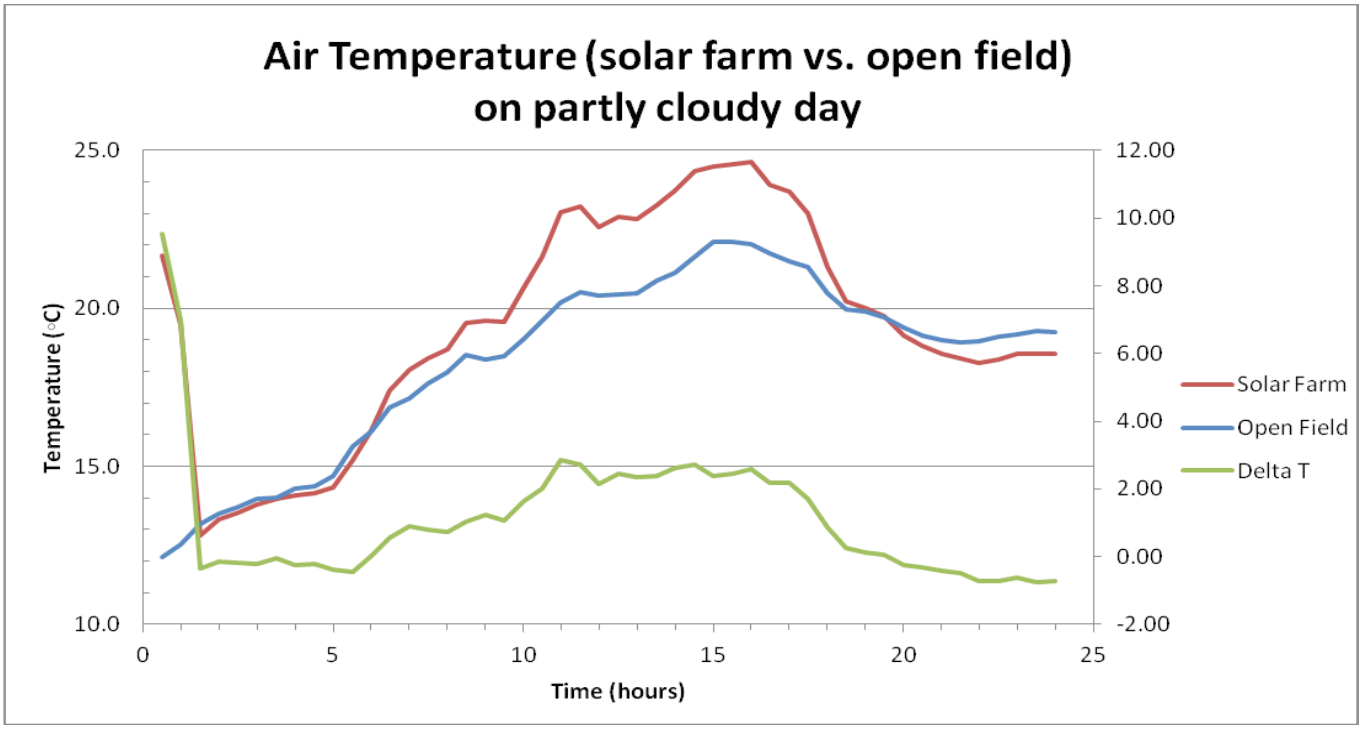
Air Temperature (solar farm vs. open field)
on partly cloudy day
Temperature (°C)
25.0
20.0
15.0
10.0
12.00
10.00
8.00
6.00
4.00
2.00
0.00
-2.00
0
5
10
15
20
25
Time (hours)
Solar Farm
Open Field
Delta T

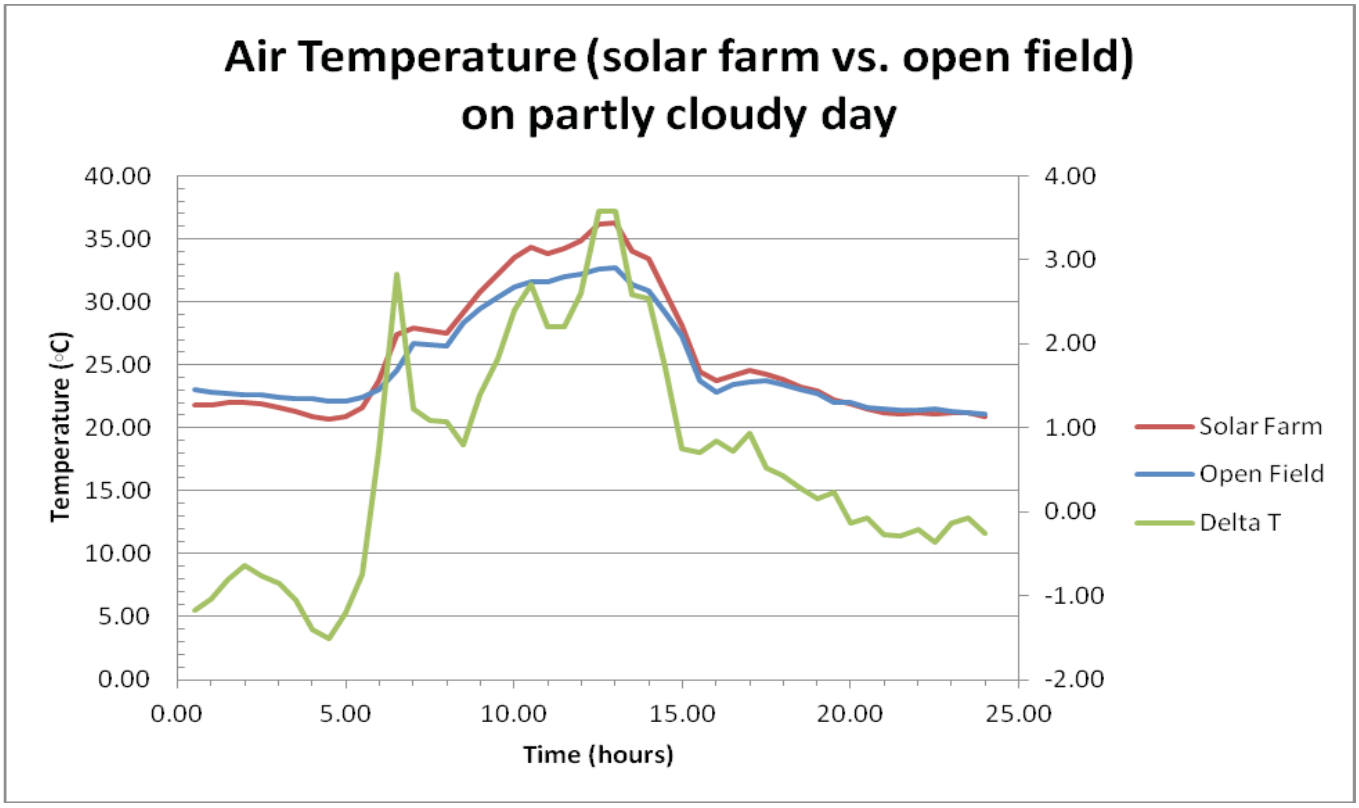
Air Temperature (solar farm vs. open field)
on partly cloudy day
Temperature (°C)
40.00
35.00
30.00
25.00
20.00
15.00
10.00
5.00
0.00
4.00
3.00
2.00
1.00
0.00
-1.00
-2.00
0.00
5.00
10.00
15.00
20.00
25.00
Time (hours)
Solar Farm
Open Field
Delta T

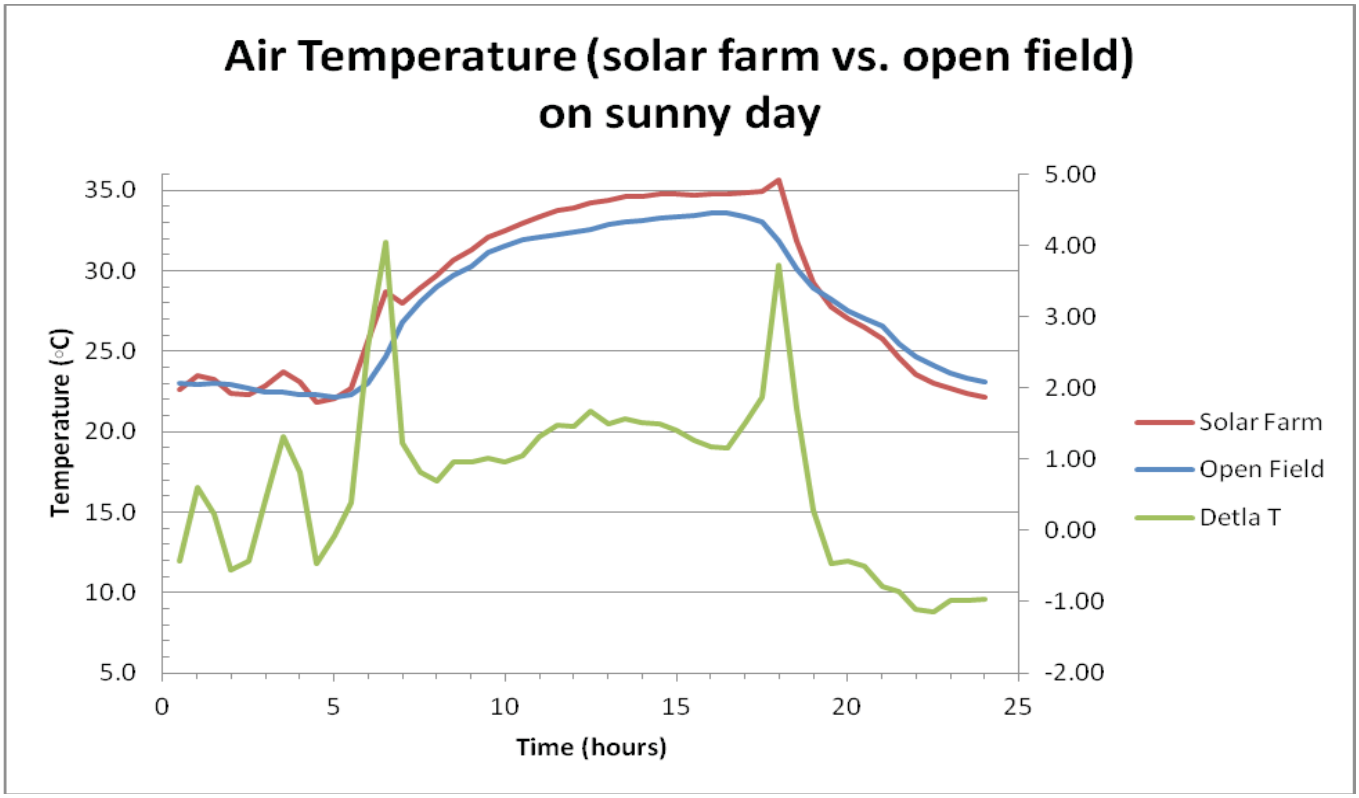
Air Temperature (solar farm vs. open field) on sunny day
Temperature (°C)
35.0
30.0
25.0
20.0
15.0
10.0
5.0
5.00
4.00
3.00
2.00
1.00
0.00
-1.00
-2.00
0
5
10
15
20
25
Time (hours)
Solar Farm
Open Field
Detla T

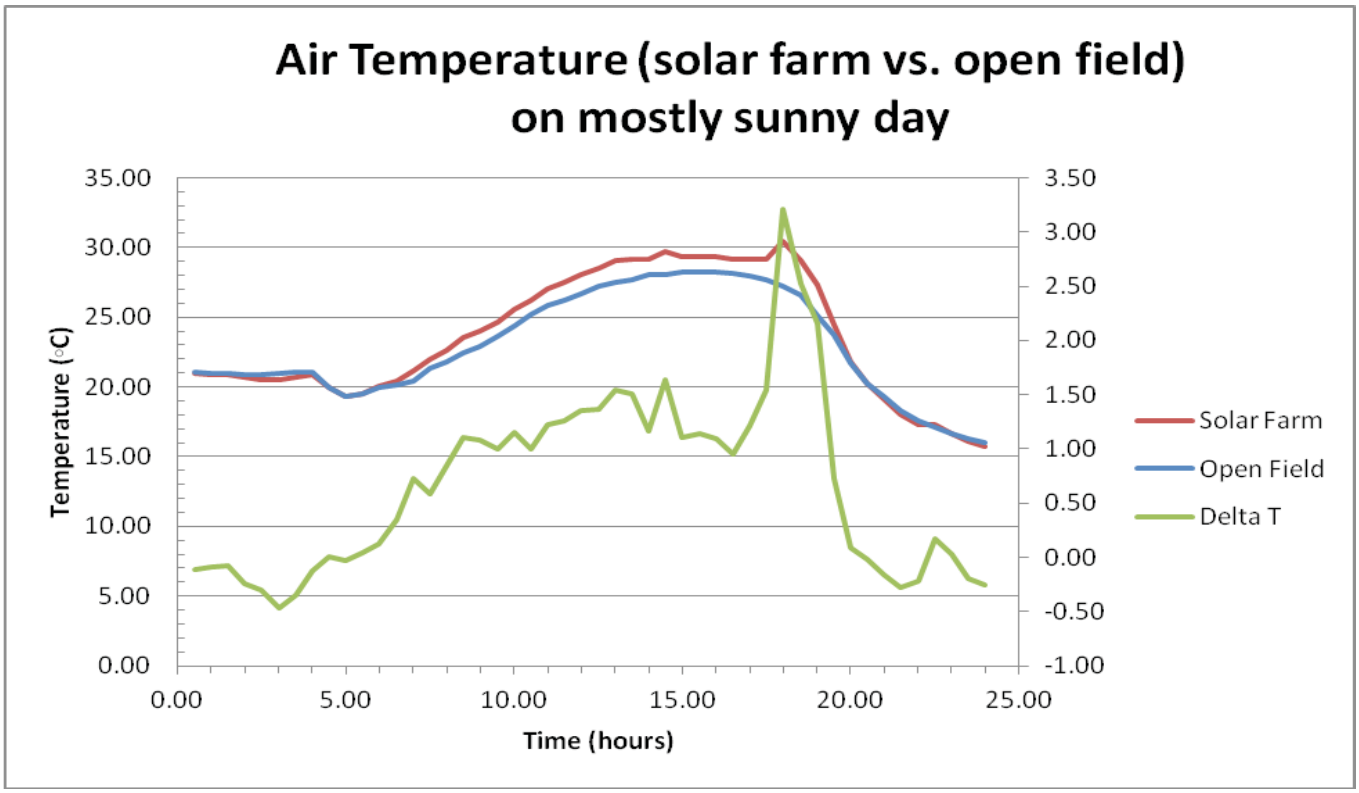
Air Temperature (solar farm vs. open field) on mostly sunny day
Temperature (°C)
35.00
30.00
25.00
20.00
15.00
10.00
5.00
0.00
3.50
3.00
2.50
2.00
1.50
1.00
0.50
0.00
-0.50
-1.00
0.00
5.00
10.00
15.00
20.00
25.00
Time (hours)
Solar Farm
Open Field
Delta T

Characterization by solution small angle X-ray scattering of the oligomeric state of structural genomics protein targets

Kimberly Basil
Department of Environmental Forest Biology,
State University of New York College of Environmental Science and Forestry, Syracuse NY 13210

Marc Allaire
Department of Photon Sciences, Brookhaven National Laboratory, Upton NY 11973

ABSTRACT

Solution small angle X-ray scattering (SAXS) was used to confirm the oligomeric state of several structural genomics protein targets from the New York Structural GenomiX Research Consortium (NYSGXRC). The oligomeric state is representative of the natively active form of the protein and it was determined to corroborate the Protein Data Bank (PDB) structure of a clone or related protein. PDBs are usually modeled from X-ray crystallography (XRC) and the results of crystalline structures are not often representative of the correct biological assembly. Therefore, the analysis done here was essential to find the natural form. Using solution SAXS allowed us to look at each protein in its native state dissolved in a solution, rather than placed into a crystal array where it is unknown if interactions between each molecule are forced or natural. After obtaining a scattering pattern, several software programs from the ATSAS program suite for small-angle scattering data analysis were utilized to distinguish the quaternary structures of the proteins from monomers to tetramers. The final products were low-resolution three-dimensional structures accurate to the biological unit of the proteins.

I. INTRODUCTION

It is largely assumed in structural studies of biological macromolecules that finding the three-dimensional (3D) structure is necessary to an understanding of how the macromolecules function. This paradigm has led to a growth in structural analysis studies and projects, especially in determining the high-resolution structure of individual proteins using XRC, a technique that has been widely used since the amount of available genome sequences has increased rapidly from the start of the Genomics Era.[1] However, XRC relies on the protein's crystalline structure, which can be a tedious and timely process to make, and often displays molecules not accurate to their oligomeric state. During this technique, a protein crystal—a 3D array of ordered and highly packed protein molecules held together by noncovalent interactions—is created and modeled. Then, the smallest asymmetrical unit (ASU) of the crystal is deposited in the PDB.[2] Though correct as the structure for one of the chains for the protein, the ASU may not represent the whole biological unit. Many biological macromolecules, for example, function as a dimer where it takes two ASU structures to complete its task in the biological system.

Some structural genomics projects are aiming to enhance PDB data with information about the protein's quaternary structure in order to best understand its function. Solution SAXS is a quick and relatively simple technique to ascertain the overall shape of a protein without the limits of a crystal array. Four structural genomics protein targets by NYSGXRC were examined for this experiment at the National Synchrotron Light Source (NSLS) on beamline X9 at Brookhaven National Laboratory (BNL.) These proteins, called by the PDB codes 3NF4, 3LKE, 3KFO, and 3NF2, were associated with an already known crystal structure listed in the Protein Data Base archive. 3NF4 refers to the clone of acyl-CoA dehydrogenase from Mycobacterium thermoresistibile, while 3LKE is related to enoyl-CoA hydratase of Bacillus halodurans. 3KFO is a relative of the C-terminal domain from the nuclear pore complex component NUP133 of Saccharomyces cerevisiae, and 3NF2 is related to the polyprenyl synthetase from Streptomyces coelicolor.

II. EXPERIMENTAL METHODS AND MATERIALS

Each protein was dissolved in the buffer, 10mM 4-(2-hydroxyethyl)-1-piperazineethanesulfonic acid at the pH of 7.5, 150mM sodium chloride, 10mM Methionine, and 10% glycerol. The concentrations of protein to buffer were the following: 3N4F at 11.5 mg/ml, 3LKE at 13.74 mg/ml, 3KFO at 10.5 mg/ml, and 3NF2 at 10.3 mg/ml. These solutions were sent directly from NYSGXRC to BNL. One solution at a time was sent through the X9 beam at the NSLS.

Using a synchrotron source for X-rays is useful to study weak scattering systems, typical of biological molecules, in very a short time.[3] The X-ray beam interacts with the sample and secondary waves scatter off of the molecules. These waves are detected as intensities (I) over a range of angles (Θ) and converted to the scattering curve (I(q)) with use of the scattering vector amplitude (q) the wavelength of the radiation (λ) and the equation $q = 4\pi(\sin \Theta)/\lambda$. The scattering data from the proteins was picked up by both a wide angle X-ray scattering detector and a SAXS detector providing a combined q range from 0.005 $Å^{-1}$ to 2.0 $Å^{-1}$. Only the SAXS q range was looked at, up to 0.25 $Å^{-1}$ because this range contains data of the quaternary structure.

Software pyXS, developed at beamline X9, was used for data processing, including azimuthal averaging, of a 2D image provided from the detector into a 1D intensity function, I(q), and background subtraction.[4] From here, components of the ATSAS software program were utilized for data analysis. Analysis began with PRIMUS to manipulate the raw data.[5] In this program, the pure buffer signal was subtracted from the solution signal. Then, the radius of gyration (Rg) was found using AutoRg by using the Guinier approximation

$\ln I(q) = \ln I(0) - (Rg^{2/3})(q^{2})$ in PRIMUS.[6] Subsequently, a Guinier plot was created to see if there was any aggregation in

the sample. GNOM was then run to calculate the particle distance distribution function (P(r)), which indicates what conformation the protein is in, using the Fourier transform and from estimating the D_{max}, the maximum dimension of the molecule, from the Rg.[7,8] It also created the output file necessary to run the modeling programs DAMMIN and GASBOR. After the proper output from GNOM was made, *ab initio* protein shape determination using a dummy atom model was performed by DAMMIN ten times. A similar modeling program, GASBOR, was also used three times for 3NF2 to validate the results. DAMMIN used stimulated annealing, where the D_{max} set in GNOM places the constraints on the size of the protein and the program fills the properly sized sphere with densely packed smaller beads whose positions change places until a best fit model is found.[9] GASBOR also followed the parameters set by GNOM, but employed an ensemble of dummy residues the form a chain-compatible model.[10] Both these programs built slightly different models each time they ran because multiple structures can fit a single scattering curve. DAMAVER aligned all of the models, selected the most common one and constructed an averaged model.[11] The experimental scattering data was then fit to the known PDB data using CRYSOL.[12] CRYSOL compared the two curves in a single plot and was the main tool that was utilized to see the oligomeric state of the proteins. If the two curves overlapped in the SAXS region, then the known PDB information contained the correct quaternary structure. On the other hand, if they did not line up, the XRC data was modified by removing duplicated data from the PDB until the curves fit. The final step was to use SASREF, which modeled the quaternary structure of the proteins with use of both the solution scattering data and the known and possibly modified PDB data.[13]

III. RESULTS AND DISCUSSION

The first protein, 3N4F, was found to have an Rg of 19.97 and minimal aggregation, which was avoided in data analysis by omitting the first 20 points of the scattering data. The Dmax was set to 60 and DAMAVER provided a model as seen in Figure 1.

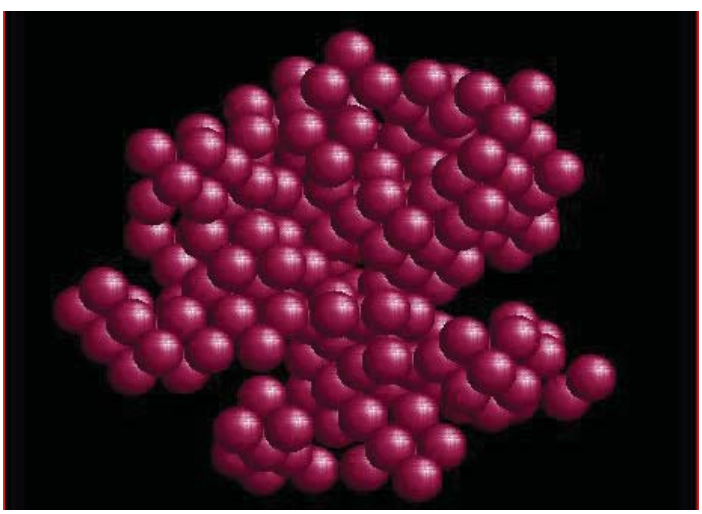

Figure 1. Above displays an image of the DAMAVER result of 3N4F after ten runs of DAMMIN modeling.

CRYSOL was used to compare the scattering data and the PDB data. The PDB data of the experimental protein's clone contained coordinates for four chains in the protein, but the experimental data implied a monomer. This was shown in Figure 2 where there is a poor fit between the two curves.

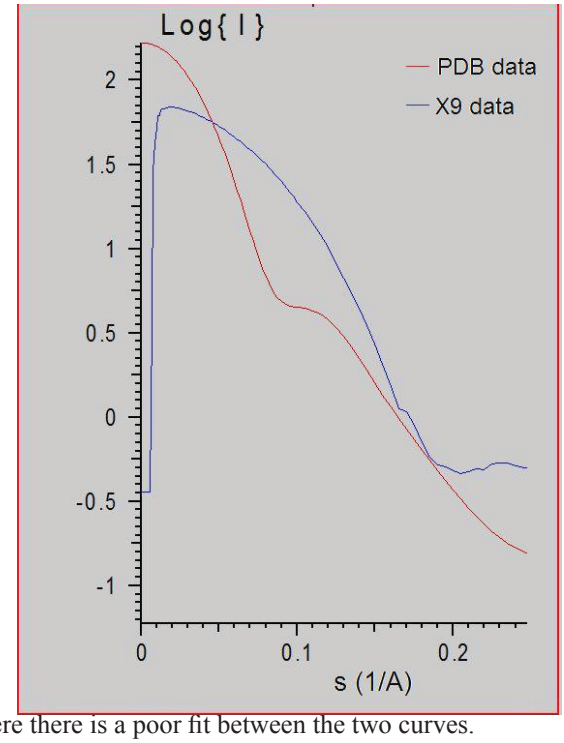

Figure 2. This graph is the CRYSOL output cut to 0.25 (1/Å), labeled as s. In this case s is comparative to q. The blue experimental data does not line up with the red given data.

After three chains were removed from the PDB data, CRYSOL was run again and the error between the two curves was decreased. This can be seen in Figure 3.

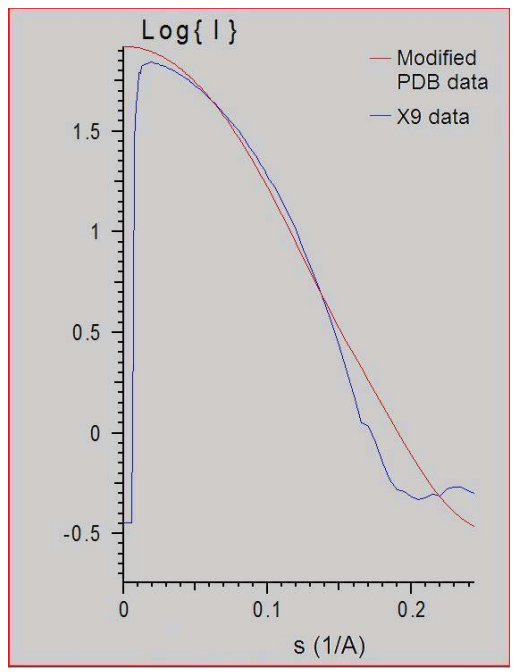

Figure 3. One chain from the crystalline PDB data compared to the scattering data of 3N4F.

The SASREF image, Figure 4, produced for 3N4F with the modified PDB and experimental data also corroborated the mono-

meric result for the quaternary structure of the protein.

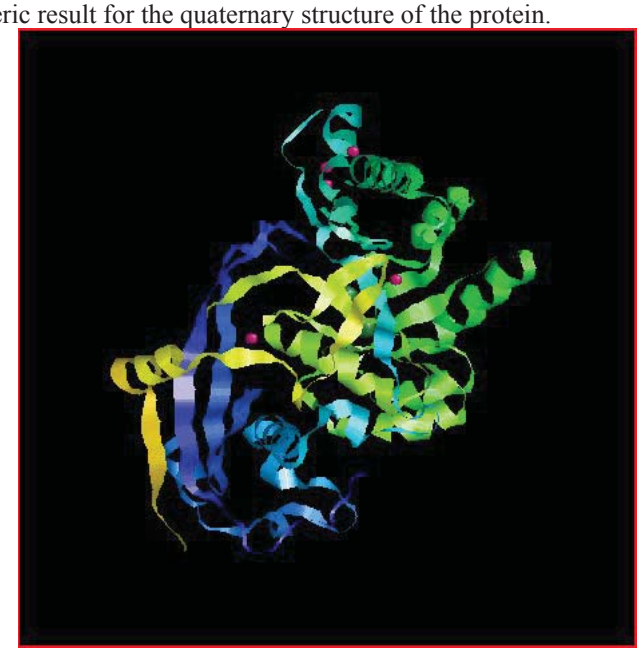

Figure 4. SASREF result of the monomer 3N4F.

The next protein, 3LKE, had an Rg of 27.94 and a D_{max} set to 84. The first 18 points were omitted in GNOM. This protein had a trimer for its oliomgeric state. The model created for 3LKE is shown in Figure 5.

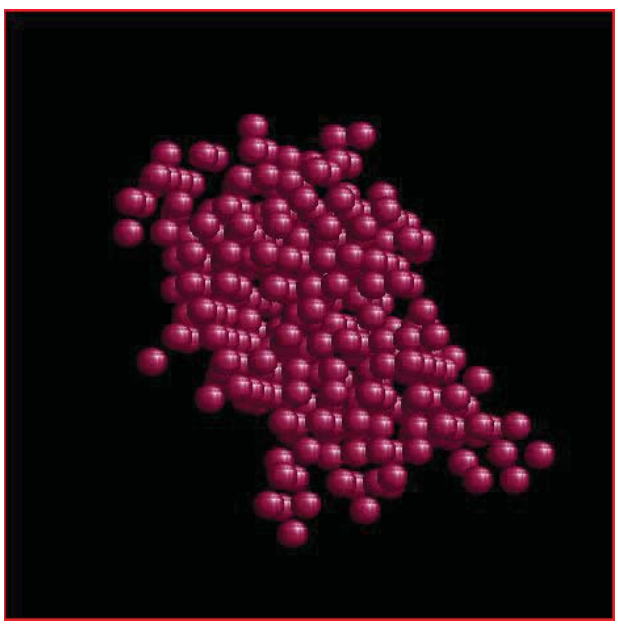

Figure 5. DAMAVER result of 3LKE after ten runs in DAMMIN.

Unlike the CRYSOL results from 3N4F, the first run showed a good fit between the experimental and known data, figure 6.

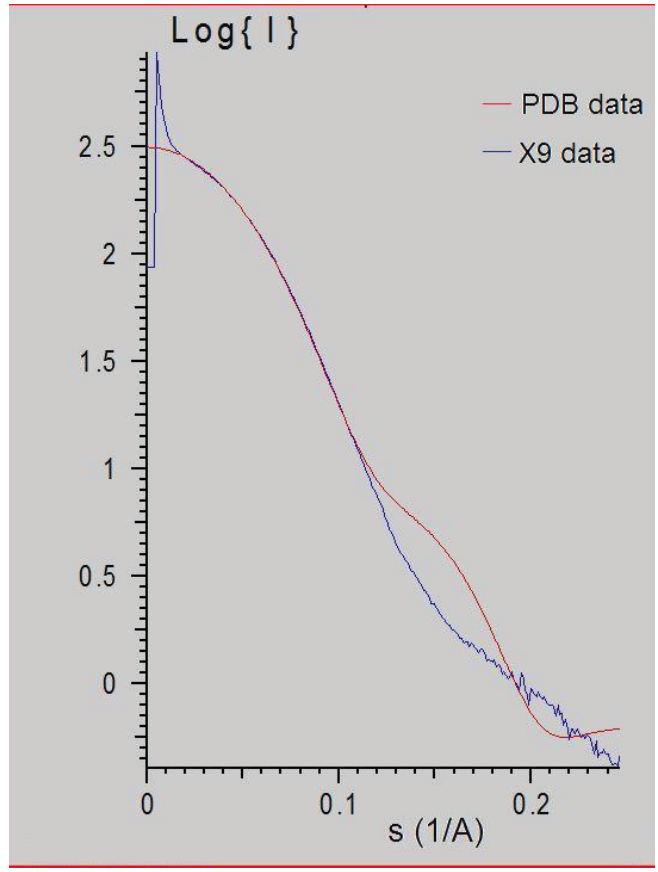

Figure 6. The graph shows 3LKE XCR data compared to SAXS data in CRYSOL. This confirms the PDB information is representative of the biological unit with three chains.

To further support this, two chains were removed from the PDB data and the program was run again. This produced a poor fit between the two data sets seen in Figure 7.

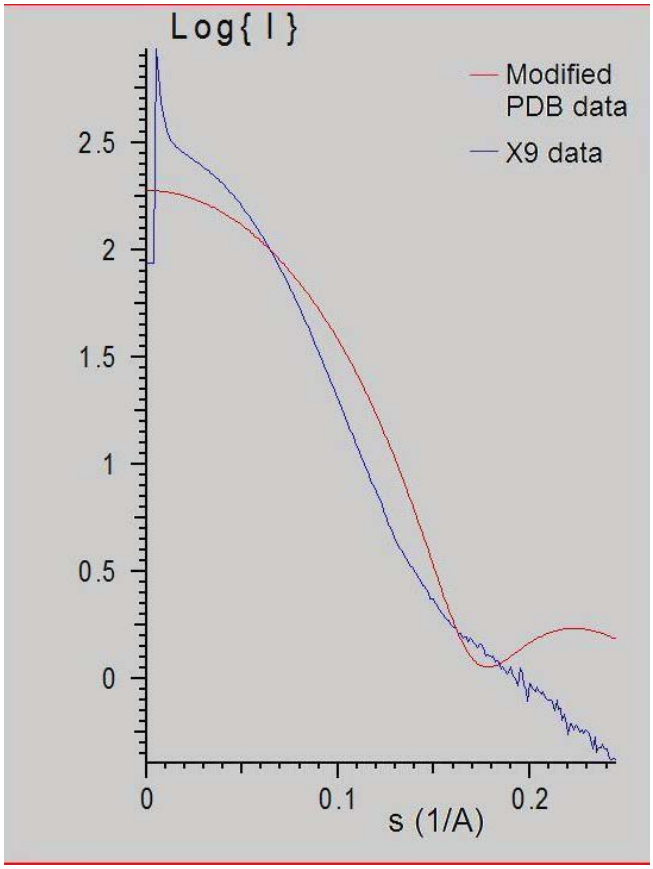

Figure 7. The above is modified 3LKE XCR data to one chain compared to the SAXS trimer data. The fit is worse than with the original XCR data.

The SASREF result for 3LKE is a trimer that is nearly identical to the PDB that can be downloaded from the PBD database

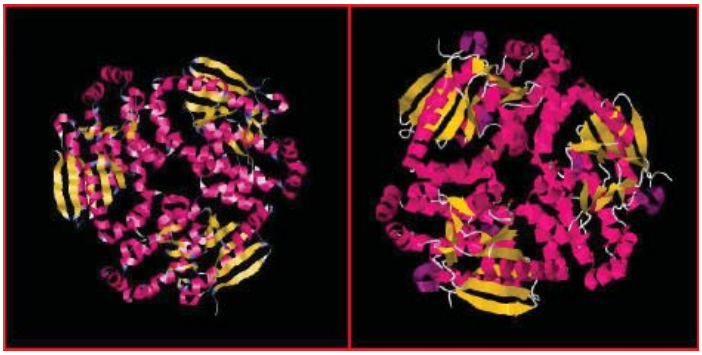

(Figure 8).

Figure 8. Image of SASREF result of 3LKE on the right next to the downloaded XCR PDB image. Both images are very similar.

The third protein, 3KFO, had an Rg of 19.65 and the first 13 points from the experimental data was removed in GNOM. The D_{max} was set to 60. These results were similar to 3LKE such that the XCR PDB data was a match to the SAXS data for its quaternary structure; both produced results demonstrated a monomer. The DAMAVER result can be seen in Figure 9, while the SASREF image is Figure 10.

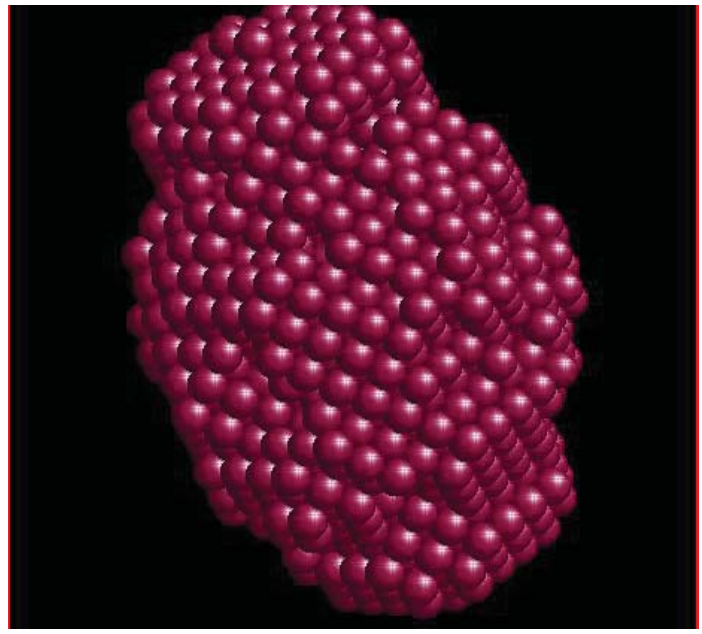

Figure 9. DAMAVER image produced from ten DAMMIN runs of 3KFO. The protein is a monomer.

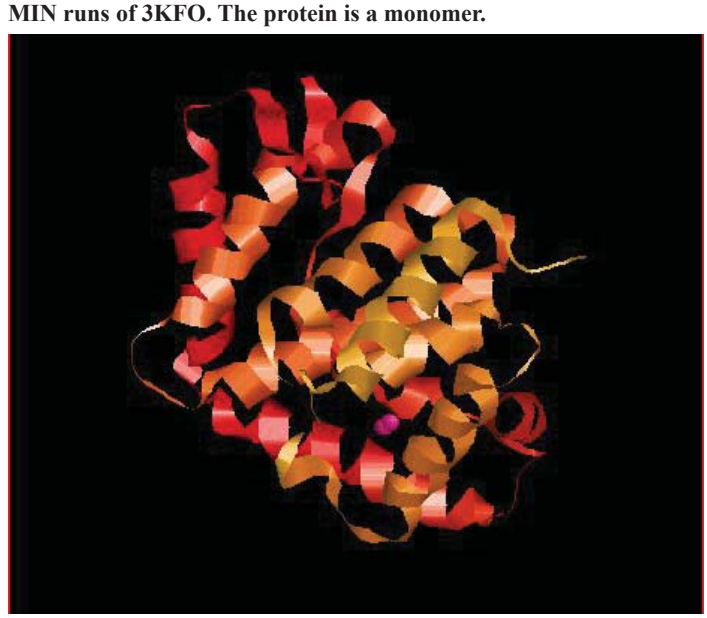

Figure 10. Monomeric SASREF result of 3KFO.

The last protein modeled was 3NF2. The Rg was 27.71 and in GNOM the first 12 points were left out. The D_{max} was set to 84 and the oliogomeric state of the protein was found out to be a dimer, but the XCR data showed a monomer. The results mimicked 3N4F's two CRYSOL runs where the first had a poor fit between the two curves and the second output was much better. In this case however, in the second CRYSOL run, an extra chain was added to the XRC data instead of removing chains. The DAMAVER results can be looked at in Figure 11, while Figure 12 contains the SASREF output. Both indicate the protein is a dimer.

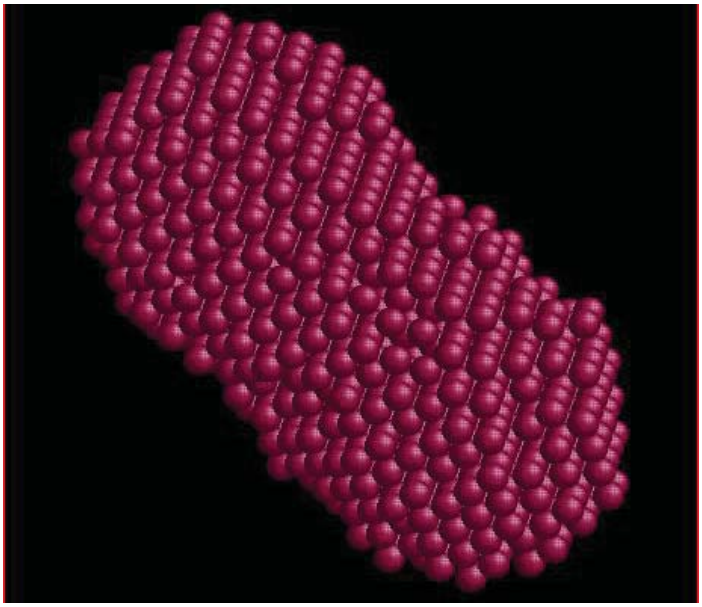

Figure 11. The average shape of 3NF2 found with DAMAVER of ten DAMMIN runs and three GASBOR runs. It contains the area for two protein chains.

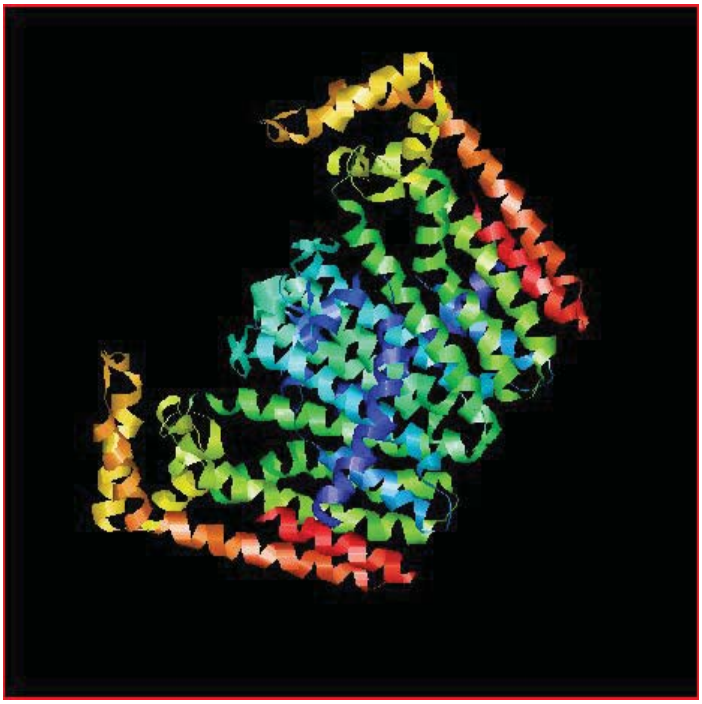

Figure 12. Above shows the SASREF result of the dimer of 3NF2.

IV. CONCLUSION

This experiment confirms the reliability of solution SAXS as a technique used to confirm the structure of a protein. When most structural genomics protein projects rely on XRC to confirm structure, SAXS allows scientists to address a fundamental piece of the puzzle not often established, the oligomeric state. The functional form of each protein discussed was found and modeled with little prior knowledge of them: 3N4F, a monomer, 3LKE, a trimer, 3KFO, a monomer and 3NF2, a dimer. This data can be used to further biological studies on these four specific proteins and for other closely related macromolecules. Even though there is a strong connection between protein structure and function, future progress in this field should focus on increasing the methods used to structure the abundance of sequenced molecules as well as refining the data and creating a level of standardization to support this data.

V. ACKNOWLEDGEMENTS

This project would not have been possible without the support of many people. I would like to thank my helpful mentor Dr. Marc Allaire for his expert guidance on this project and whose assistance was invaluable. Special thanks to Dr. Lee Newman who introduced to me this huge opportunity. Sincere gratitude is also due to my family for their continued and loving support and to all the friends I have made here this summer. I would also like to convey thanks to Brookhaven National Laboratory and the Department of Energy for providing financial means and a laboratory facility.

VI. REFERENCES

1. P. Bernadó, E. Mylonas, M.V. Petoukhov, M. Blackledge and D.I. Svergun, J Am Chem. Soc. 129 5656-5664 (2007)
2. G. Rhodes, Crystallography made Crystal Clear: A Guide for Users of Macromolecular models, (Academic Press, new York, 1993), pp.389
3. J.Y. Bottero, D. Tchoubar, J.M. Cases, and F. Flessinger, J Phys Chem. 86 3667-3673 (1982)
4. Y.K. Gupta, L. Yang, S. Chan, J.C. Samuelson, S. Xu, A.K. Aggarwal, J Mol Bio. 420 261-268 (2012)
5. P.V. Konarev, V.V. Volkov, A.V. Sokolova, M.H.J. Koch and D.I. Svergun, J Appl Cryst. 36 1277-1282 (2003)
6. M.V. Petoukhov, P.V. Konarev, A.G. Kikhney and Svergun, J Appl Cryst. 40 s223-s228 (2007)
7. D.I. Svergun, J Appl Cryst. 25 495-503 (1992)
8. M. Allaire, SAXS/WAXS Applications, Brookhaven National Laboratory Beamline X9 Workshop Handout (Unpublished)
9. D.I. Svergun, Biophys J. 25 2879-2886 (1999)
10. D.I. Svergun, M.V. Petoukhov and M.H.J. Koch Biophys J. 80 2946-2953 (2001)
11. V.V. Volkov and D.I. Svergun, J Appl Cryst. 36 860-864 (2003)
12. D.I. Svergun, C. Barberato and M.H.J. Koch, J Appl Cryst. 28 768-773 (1995)
13. M.V. Petoukhov and D.I. Svergun, Biophys J. 89 1237-1250 (2005)

Synthesis of [^{18}F]fluorosucrose based on enzymatic deacetylation of sucrose octaacetate

Caitlin Bennett
Department of Chemistry, Fordham University, Bronx NY, 10458
Alexandra Scavelli
Department of Chemistry, SUNY Albany, Albany, NY
Andrew N Gifford
Medical Department, Brookhaven National Laboratory, Upton NY, 11973

ABSTRACT

Since sucrose, the main sugar transported in plants, is such an essential compound for plants, there is a need to observe its movement through the plants and discover where it ends up. In order to do this, sucrose needs to be labeled with a radioactive isotope so that its movement can be successfully followed by Positron Emission Tomography (PET). The aim of this experiment is to react a specific site on sucrose with [^{18}F]fluorine, a PET isotope, to create [^{18}F]fluorosucrose. This particular reaction involved a protected form of sucrose that is commercially available that was reacted with an esterase enzyme to target one specific position on the molecule where the reaction can take place. This study took an in-depth look at the activity of specific enzymes and developed a full chart of data with all of the results. A new analogue of [^{18}F]fluorosucrose was discovered that had not yet been synthesized before.

I. INTRODUCTION

Sucrose is a disaccharide sugar with 8 hydroxyl groups, all with nearly identical reactivities. Using classical chemistry techniques to react with one specific hydroxyl group would not yield good results and might lead to poor reproducibility. The goal of this experiment is to react only one of the hydroxyl groups on sucrose with radioactive [^{18}F]fluorine in a way that is more dependable than the classical chemistry techniques. There have been other schemes to accomplish this same purpose; however, those involve complicated protection steps. With each protection and deprotection step, the overall product yield becomes much lower. While a fluorinated sucrose analogue has been created already by Card and Hitz[1] in 1985, my project takes a different approach for the synthesis. Some of the advantages of using [^{18}F]fluorine are that it has a long half-life compared with some other PET isotopes and is easily accessible. The half-life is 109 minutes allows for the reaction of transforming sucrose to fluorosucrose to successfully take place so that researchers have plenty of time to observe its movement through the plants. The information gained from this experiment will help researchers understand more about plant sugar transport and aid in the development of biofuels.

Most of the limits associated with this project were the very specific activity of the enzymes. Some were not as reactive as others, and some were too reactive. Since my reaction targets a very specific position on the molecule, it is difficult to influence a particular position because the products are based on the selective activity of the enzymes. Although I could not influence the enzymes selectivity, I could optimize results by choosing the best solvent system. Also, the restrictions of this experiment were that interpreting the H-NMR for a complicated structure such as sucrose is very difficult and I needed to rely on the literature for guidance.

II. METHODS AND MATERIALS

The goal of the first part of the experiment was to take a protected form of sucrose that is commercially available and to react it with an esterase enzyme. The enzyme activity targets one specific position on the molecule and allows regioselective deacetylation to take place. The product that results from this reaction is sucrose heptaacetate, which has 7 acetates and one hydroxyl group. This hydroxyl group is reacted with triflic anhydride. This structure allows the ^{18}Flourine to react quickly by SN2, because the triflate is a very good leaving group. The radiolabeled [^{18}F] fluorosucrose will be injected into plants to trace the movement of sucrose through the plant through either planar scintographic imaging or PET.

In order to optimize the amount of sucrose heptaacetate as a product of the reaction, the best reaction conditions were investigated through a series of test reactions. Various enzymes were tested in different solvent systems. 5.00 g of sucrose octaacetate was dissolved in 50 mL of DMF as a stock solution. Each test reaction was prepared with 5 mL of a different organic solvent. If the reaction was done in a mixture of Phosphate Buffer and DMF, 0.5 mL of the sucrose octaacetate stock solution was used, and if the reaction was done in diisopropyl ether, 50 mg of sucrose octaacetate was measured out directly. The reaction was incubated at 40°C with gentle shaking. The reactions all contained 5 mM $MgCl_2$ which acted as a catalyst. Liquid Chromatography-Mass Spectrum analysis was taken at two time points. The results from the traces showed the amount of sucrose octaacetate and sucrose heptaacetate, as well as any side products. In order to prepare the samples for analysis from the Liquid Chromatography-Mass Spectrum, I took a small sample of each test reaction and extracted it with an equal amount of ether. The product would dissolve into the ether layer but was separated from the enzyme.

Once the ether was dried off, the precipitate was dissolved in acetonitrile and 10 µL was taken and diluted into 1 mL of acetonitrile so that the concentration of the product was 0.1 mg/mL. The Liquid Chromatography-Mass Spectrum data told me the relative concentrations of each of the products and the mass to charge ratio so that I could determine if I had the right product based on the molecular weight. Overall, there were 16 different esterase enzymes that were tried in 5 different solvent systems, and 42 overall test reactions. Based on all of the information gathered from the test reactions, I developed a chart that gives each enzyme's reactivity. A summarized version of this chart can be seen in the Figure 1, 2, and 3 below.

Based on the results from the chart, I was able to single out the best conditions for this reaction to optimize the amount of sucrose heptaacetate. The reaction conditions that were used con-

sisted of sucrose octaacetate (0.500 g) with the enzyme Candida Rugosa (0.500 g) and 40 mg $MgCl_2$ in 30 mL of diisopropyl ether. The reaction was incubated for 10 days at 45°C with gentle shaking. My initial test reactions showed me that this reaction would take 100% starting material and in that time convert that to 46.7% of the product (sucrose heptaacetate). Based on the literature, the product of sucrose heptaacetate was believed to have a hydroxyl at the 4' position.[2] The sucrose heptaacetate was extracted into ether and water, separated, and purified from the side products using a Flash Chromatography Column. TLC analysis determined which fractions contained the desired sucrose heptaacetate product (0.110 g sucrose heptaacetate obtained). This was dissolved in 10 mL of dichloromethane and 0.4 mL pyridine and reacted on dry ice with 0.5 mL of triflic anhydride (100 mg sucrose heptaacetate triflate produced). Triflic anhydride, a very strong acid, makes it a perfect leaving group for the reaction with [^{18}F]fluorine. The sucrose heptaacetate (~5 mg) was dissolved in 0.5 mL of anhydrous DMSO. Radioactive K+ ^{18}F- was prepared in another laboratory and delivered to the Radiation lab in the Medical Department. It was added to 1 mg of K_2CO_3 and 10 mg of $K_{2.2.2.}$ and dried under Argon gas with three 2 mL portions of acetonitrile. The sucrose heptaacetate was added to the dried ^{18}F and reacted for 15 minutes in an oil bath at 100°C. The resulting product was purified with a C-18 sep pack and deacetylated with 0.6 M KOH. The resulting product was isolated [^{18}F]fluorosucrose. The sample was tested by radio-HPLC to confirm that the 18fluorosucrose product was obtained.

III. RESULTS

Of 16 enzymes tested, most showed no results over the course of the reaction time. A test done with just sucrose octaacetate in the phosphate buffer and DMF showed some spontaneous breakdown to sucrose heptaacetate over the 7 day monitored reaction time. Therefore, some of the results for that solvent system were only shown if they showed significant improvement over the system with no enzyme. The problem with most of the results from the Liquid Chromatography-Mass Spectrum data was that there were multiple peaks at 8.0, 8,5, and 9.1 minutes, indicating different heptaacetate products. These products were very similar because their only difference was one position on the molecule. Since the technology does not exist to separate the sucrose heptaacetate products that differ by only one position of the hydroxyl group, not much can be done with most of the data from the test reactions yet. Many of the results showed that there was not an impressive excess of one of the peaks over the others. However, out of the 42 test reactions, 4 showed good results, which means that there was an impressive conversion of starting material to the desired sucrose heptaacetate product with one sharp peak from the LC-MS with minimal side products. Out of all the enzymes tested, the best reaction was from Candida Rugosa in diisopropyl ether. Based on my analysis from the ^{1}H-NMR, it was confirmed that the deacetylation does occur at the 4' position, or the 4th Carbon of the fructose ring. Analysis shows that in the ^{1}H-NMR of the sucrose octaacetate, the 3', 3 and 4' hydrogens were combined as a multiplet. However, in the spectrum of the sucrose heptaacetate, the 3' hydrogen is slightly less shielded and therefore shifted upfield, and the 4' hydrogen is very much less shielded and shifts more upfield. The 3' of the heptaacetate product appeared as a distinct doublet. The literature confirms that our ^{1}H-NMR trace is identical to another trace of sucrose heptaacetate at the 4' position.[3]

Another enzyme, Candida Antarctica, also showed promising results in a short time period; however, there were some problems with reproducibility due to complications with the DMF. Initial analysis by ^{1}H-NMR shows that the reaction with Candida Antarctica removes the acetate from the 4' position, but further tests need to be done to confirm.

In the reaction of the sucrose heptaacetate triflate to 18fluorosucrose, there was a decent radiochemical yield for the product. In a total of 161.8 μCi, the radioactivity in the product was 22.3 μCi, which gave a 13.7% radiochemical yield. The radio-HPLC showed a sharp peak which is suspected to be the [^{18F}]fluorosucrose, but further investigation is being done.

IV. CONCLUSIONS

This experiment took the commercially available sucrose octaacetate and converted it to [^{18}F]fluorosucrose in three steps: (1) the translation of sucrose octaacetate to sucrose heptaacetate with one exposed hydroxyl group and 7 acetate groups, (2) the conversion of sucrose heptaacetate to sucrose heptaacetate triflate, and (3) the reaction with fluorine to create [^{18}F]fluorosucrose. The information discovered in this experiment about the reaction involving the esterase enzyme Candida Rugosa and the transformation of sucrose octaacetate to ^{18}Fluorosucrose is new. To our knowledge, the 4' position of sucrose has not been radio-fluorinated before. The next step for this project is to attempt to improve the radiochemical yield of the 4'-fluorosucrose and then inject the sample into a plant so that the movement of sucrose can be traced through plants. Future directions could also include looking at different positions of the [^{18}F]fluorine, for example the 1' versus the 4' to see if that affects the movement through the plant. This information will help researchers in the future gain more knowledge about plant sugar transport. The more we know about this topic, the more information with will have for the development of biofuels, which can be used as an alternative source of energy.

V. ACKNOWLEDGEMENTS

I would like to thank the Department of Energy for funding the research and the facilities at Brookhaven National Lab, and in particular the Medical Department, that had everything that I needed for my research to run smoothly. I would like to thank my mentor, Dr. Andrew Gifford, for helping me understand all of the background information and for his willingness to answer all of my questions. I would also like to thank Michiko Miura for giving me guidance and letting me double check some of my results with her.

VI. REFERENCES

1. Card PJ, Hitz WD. Synthesis of 1'-Deoxy-1'-Fluorosucrose Via Sucrose Synthetase Mediated Coupling of 1'-Deoxy-1'-Fluorofructose with Uridine-Diphosphate Glucose. *J. Am Chem Soc* 1984; 106:5348-5350.
2. U.S. Patent 5,445,951, "Regioselective enzymatic deacylation of sucrose esters in anhydrous organic media." 29 August, 1995.
3. Chang, Kung-Yao, Shih-Hsiung Wu, and Kung-Tsung Wang. "Regioselective Enzymic Deacetylation of Octa-O-acetyl-sucrose: Preparation of Hepta-O-acetylsucroses." *Carbohydrate Research* (1991).

VII. APPENDIX

Figure 1: Chart of the different enzymes and their amounts in different solvent systems and the resulting products of sucrose heptaacetate with the side product of sucrose hexaacetate and the amount of starting material, sucrose octaacetate, left. DiPE is diisopropyl ether and PB is a phosphate buffer with a pH of 7.

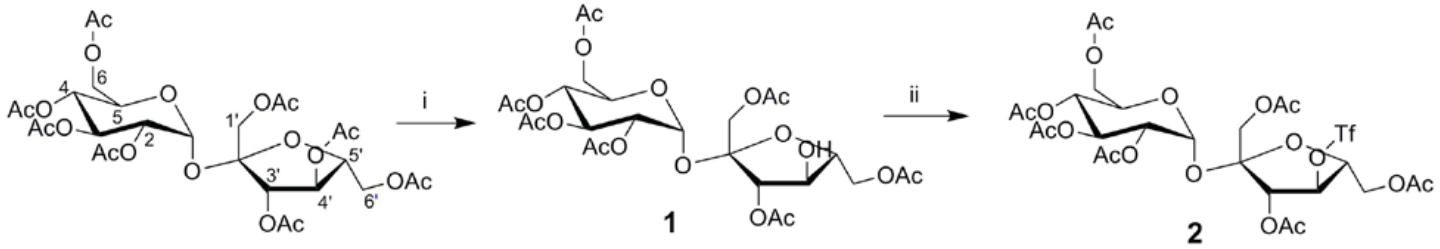

Figure 2: The overall reactions for this experiment, which was the conversion of sucrose octaacetate to sucrose heptaacetate (1) to sucrose heptaacetate triflate (2). i: different esterase enzyme in different solvent systems and ii: triflic anhydride.

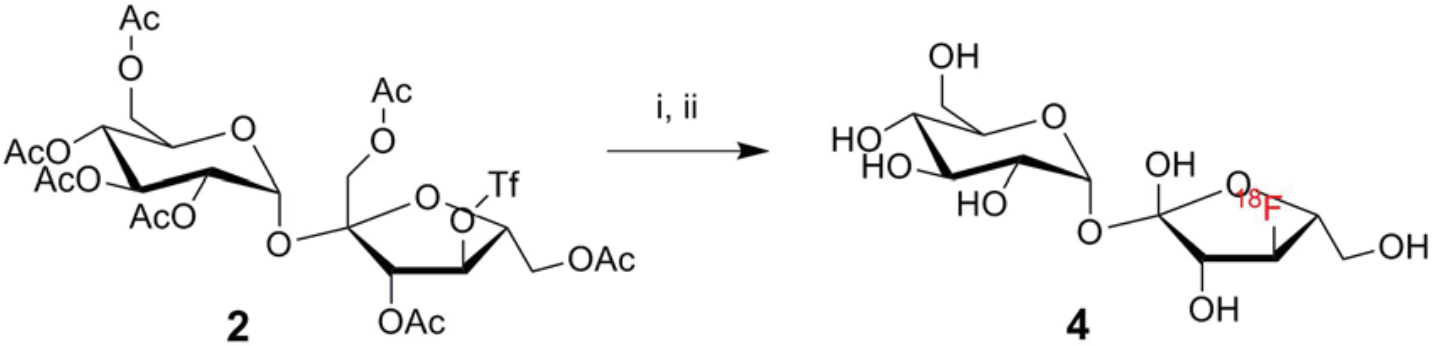

Figure 3: Conversion of sucrose heptaacetate triflate (2) to [^{18}F]fluorosucrose (4). i: [^{18}F]fluorine with $K_{2.2.2.}$ and K_2CO_3 and ii: KOH

Facilities and operations: utilities layout

Brian Bergh (University at Buffalo, Amherst, NY 14260)
Dennis Danseglio (Brookhaven National Laboratory, Upton, NY 11973)

ABSTRACT

Recurrent efforts to modernize Brookhaven National Laboratory aim to secure the future of scientific research. Project success demands upon extensive planning and documentation, with my own individualized concern dedicated to utilities layout. A construction proposal for the Interdisciplinary Science Building – Phase II focused on the relationships that govern sustainable energy, climate change, and ecosystems, details a footprint that engulfs four existing structures: buildings 437, 421, 355, and 179. A steam reducing station within Building 473 distributes steam to six additional buildings across Center Street. Alternate positioning of the reducing station and steam site preparation is necessary to ensure the continued supply of steam to the remaining buildings. Building 515, Information Technology, serves to house copious rows of data processing units. A system of chilled water pipes, in conjunction with Air Handling Units, is implemented to cool these units. Accurate layout and detailed AutoCAD drawings of all renovation proceedings are essential for future operations. Ultimately, projects involving utilities layout attempt to improve facility excellence and efficiency while minimizing necessary expenses.

I. Interdisciplinary Science Building II Utilities: Steam

A. Introduction

In an attempt to include scientific research in the relationships that govern sustainable energy, climate change, and ecosystems, Brookhaven National Laboratory has proposed the construction of the Interdisciplinary Science Building II (ISB-II). The building plans currently include an area of approximately 90,000 ft2 and four existing buildings. Since the DOE enforces a strict "one-to one" policy during construction; i. e., for any building to be constructed, a greater or equal area of land (ft2) must be demolished. The demolished property, however, may be assimilated from an alternate national laboratory. Since the four conflicting buildings represent a total area of 36,195 ft2, additional structures within BNL or other government laboratories must be allocated towards the project (Table 1).

Building Designation	Building Number	Area (ft2)
Staff Services/GARS/Post office	179	15,025
Contracts and Procurement	355	10,295
Structural Biology	421	5,980
Electron Beam Weld	473	4,894
	Total:	36,195

Table 1. ISB-II Area Offset

The positioning of existing utilities, specifically steam, presents multiple issues during site preparation. Unreduced steam at 125 psi is initially fed to Building 473 from MH-26. From this point, unreduced steam is distributed to three steam reducing stations located in Buildings 473, 421, and 478. The reducing stations decrease the pressure to 15 psi or less and supply each respective structure. Additionally, Building 478 subsequently dispenses reduced steam to five buildings: 449, 459, 460, 461, and 462. Due to the fact that 473 and 421 will be demolished to enable construction of ISB-II, an alternative means is required to supply the remaining buildings with steam. Likewise, an appropriate plan must be devised to deal with MH-73, which conflicts with the proposed location of the bridge between ISB and ISB-II.

B. Steam Line Placement Factors

Optimal positioning of the new steam lines should attempt to consider a multitude of factors: use of existing piping, accessibility, steam main capacity, and proximity to ISB-II construction zone. The solution should attempt to reuse existing piping in order to minimize expenses. The proposed site for ISB-II rests directly over Buildings 179, 355, and 473 while 421 resides in the expected location of the parking lot. Examination of steam lines in the surrounding area reveals three manholes in the vicinity of the contraction zone: MH-27, MH-26, and MH- 73. Previous concerns regarding MH-73 provide recommendations against its usage. Hence, it is preferred either to tap the existing line extending from MH-26 or to install an additional line from MH-27 to Building 478.The existing line from MH-26, however, traverses the proposed parking lot location and, thus, may present a possible hazard during construction. Additionally, examination of the manhole distances from the reducing station in 478 places MH-27 closer and would therefore require less piping. The drawing labeled "ISB-II M2" attached in Appendix A illustrates the approximate locations of steam piping in relation to the proposed site.

The programming report for the structure identifies that the main line along Brookhaven Avenue will be tapped to supply the building's stipulations. This requirement is largely due to an issue of capacity. While the 8" steam main along Bell Avenue may support 40,000 lbs/hr, the combined load of Bldgs. 449, 459, 460, 461, 462, 478 and ISB-II exceeds this capacity by approx. 7000 lbs/hr. Hence, steam for ISB-II must be supplied by an alternative source. The data for the combined loads of Bell Avenue is detailed in Table 2.

	Steam Load (lbs/hr)
Bell Avenue 8" Main Total Capacity	40,000 @ 6000 fpm
Expected ISB-II Load	12,760
Combined Load for Bldgs. 449, 459, 460, 461, 462 & 478	34, 287
Total:	47,047

Table 2. Bell Avenue Loads

Steam requirements for buildings 473 and 421 were neglected in anticipation of their demolition. Thus, the relocated manhole is obligated to only feed the six buildings immediately across Center Street.

Investigation of the issue surrounding MH-73 reveals that there are two primary concerns. Firstly, the manhole offers an unpleasant sight in relation to ISB. Secondly, the position of MH-73 interferes with a proposed bridge between ISB-I and ISB-II. Current investigations have revealed that steam lines from MH-73 feed Bldg. 464 (located directly beneath ISB-I). Thus, a substitute method must be devised which not only removes the existing manhole but also affirms the supply of steam to 464.

C. Conclusion: Steam

Examination of site factors and data provides the capability to arrive at a reasonable conclusion regarding steam line placement. Due to the proximity between the proposed ISB-II construction site and MH-26, it is favorable to implement MH-27 to meet Building 478's steam requirements. Pending an official cost estimate, new steam lines will be run from existing taps in MH-27 along the length of Center Street. This line will supply the steam reducing station in 478 with unreduced steam at 125 psi. New steam lines may utilize the existing lines connecting Buildings 473 and 478 in an attempt to minimize costs.

Conflicts surrounding MH-73 demand detailed cost estimates before an appropriate action route may be taken. Steam lines are anticipated to be run from the reducing station in ISB-II to 464, which would feed the building with reduced steam. Since Building 464 requires a steam supply during construction of ISB-II, a temporary means must be devised to heat the structure. While additional options are still being considered, site factors may be formulated together to devise two generalized routes to heat 464 during the construction of ISB-II. Steam lines from MH-73 may be used to feed 464 with steam throughout the construction process. Then, once the new supply from ISB-II is installed, MH-73 and the existing steam lines may be removed. In a similar manner, a portable boiler may be transported to the location to provide Building 464 with heat during ISB-II's assembly and likewise, removed once the new feed is completed. Both options fulfill the necessary requirements of the project and thus, ultimately depend on respective costs.

II. Bldg. 515 Information Technology Utilities: Chilled Water

A. Introduction: Chilled Water

Scientific experimentation throughout the laboratory generates considerable quantities of data on a daily basis. In order to process this information in a timely manner, appropriate computer centers were established. Building 515, Information Technology, serves to house numerous rows of data processing units. Computers, however, tend to radiate a substantial amount of heat and, therefore, must be cooled in order to prevent malfunction. Cooling is accomplished in Building 515 by means of a constant supply of chilled water (CHW) and a series of Air Handling Units. Yet, decades of rust build up and patch jobs require renovation in order to ensure the continued supply of conditioned air throughout the structure.

Piping lines previously provided Building 515 with chilled water from two sources: Building 510 and the 515 Blue Gene Line from the street. Proceedings of the renovation attempted to sever the supply of chilled water between the buildings, but leave the connection intact for use in future repair jobs. Additionally, sections of existing piping had to be replaced. The data processing units, however, demand a constant means of cooling. Hot taps and temporary hoses were implemented in various situations to ensure the continued supply of chilled water to the first floor data center during the stages of pipe replacement. The 510 chilled water feed enters the basement of the building from the north. The feed then diverges to the first floor on multiple locations to supply Liebert type CRAC (Computer Room Air Conditioner) Units. Chilled Water is additionally diverted to two AHU's (Air Handling Units), designated 7 and 8, which provide conditioned air throughout the building. In order to ensure the continued supply of chilled water to AC units 7 and 8 during the renovation, two temporary chillers and four temporary Air Handling Units (AHU) were situated in the alleyway between Buildings 515 and 510. The AHUs were then placed into economizer mode and a series of hoses were run through existing ducts in order to permit the continued supply of chilled air to the structure. The temporary AHUs and chillers were subsequently removed once the sections of pipe were replaced and existing AHUs were returned to their original mode.

B. Documentation

Proper documentation of the renovation proceedings and of the current state of chilled water feeds in the building provides an essential tool for future operations. Drawings of the feeds, however, were delayed due to employee time constraints. Hence, my task was to determine the proper layout of the Temp-Builts and As-Builts. As the titles suggest, the Temp-Builts depict the methodology used during the revamp while the As-Builts illustrate the current state of the piping system. Accurate documentation required significant communication between BNL employees. Project managers were regularly consulted to determine the specifications of individual components and arrangements. As the project progressed, frequent site visits became an essential element in the process in order to determine the relative positioning of piping and CRAC units. Prior to any drawing finalization, it was reviewed by the appropriate project manager in order to ensure a high degree of accuracy. Ultimately, the project culminated in a series of AutoCAD drawings grouped into two sections, Temp-

Builts and As-Builts, which depict the arrangement of chilled water pipes in the building at various stages of the revamp process. Both sets of drawings consisted of a total of five documents and were constructed with the intention of aiding future projects throughout the building.

C. Conclusion: Chilled Water Results

Intended results of the chilled water assignment were expected to solely consist on the Temp-Built and As-Built AutoCAD drawings. Additional fallouts, however, arose as the project progressed. Site visits proved to illustrate that numerous CHW values lacked appropriate labels. It was apparent that the tags were fading on existing values and absent for newly installed values from the revamp. Hence, a new labeling system was devised and the tags were installed. The two sets of drawings, however, proved to be the final results of the project. Additional details may be combined into the AutoCAD drawings to increase the spectrum of their effectiveness (i. e., ductwork supply vents and locations of data processing units). Ultimately, these drawings will enable future endeavors to proceed in an efficient manner and minimize expenses due to an unexpected error.

III. Appendix A

ISB-II Steam Line Layouts not available

Development of an electronic system for managing the change process for Brookhaven National Laboratory Policies and Procedures

Kiersten Blauer
Department of Mathematics, Southern Utah University, Cedar City, Utah 84720
Sabine Kessler
Quality Management Office, Brookhaven National Laboratory, Upton, New York 11973

ABSTRACT

The Standards-Based Management System (SBMS) Staff manages the change process for the Laboratory Policies and Procedures at Brookhaven National Laboratory (BNL). BNL develops these policies and procedures based on an evaluation of external requirements (i. e., directives and federal, state, and local laws). Currently, there are 639 applicable requirements in BNL's prime contract, with an average of approximately 10 requirements per month that need to be evaluated for applicability. Finding one applicable change could necessitate changes in more than one document. In order to effectively manage these changes, the SBMS Staff needs a more efficient system that integrates all elements of the editorial process. When there are changes, the current editorial process requires the subject matter expert (SME) and SBMS editor to interact via multiple software interfaces, each of which reside in a different system and are not integrated. This causes several problems, including:

- **Time-consuming effort for SMEs and SBMS Staff**
- **Data does not flow seamlessly from stage to stage inthe change process and systems do not track the stages**
- **Difficult and time-consuming effort to find metrics for reports**

As part of the continuous improvement of BNL's processes, the current SBMS change process will be enhanced by replacing some elements with a single electronic system that allows the data to flow directly between the SME and the SBMS Office. Using the agile development method, separate modules will be developed for each stage of the process. The new system will capture all information related to the modification of a document in a single interface. The modules include: the change request, all correspondence, the document's revision information, an implementation plan, the subscription information, all team members, an event/date timeline, and the archive, approval, and publication. Together, they provide an electronic representation of the SBMS business process. This will improve interaction between SMEs and SBMS, improve reporting capabilities, and provide a streamlined process to more efficiently manage changes to the Laboratory's policies and procedures. These improvements will work together to fulfill the DOE's mission for institutional excellence.

I. INTRODUCTION

Brookhaven National Laboratory (BNL) is one of ten national laboratories overseen and primarily funded by the Office of Science of the U.S. Department of Energy (DOE). As such, BNL has to abide by all DOE Directives, as well as Federal, state, and local laws. BNL develops its Policies and Procedures based on an evaluation of these external requirements. BNL uses the Standards Based Management System (SBMS) to ensure compliance with these requirements and to convey the policies and procedures to employees, visitors, and sub-contractors. Currently, there are 639 applicable requirements in BNL's prime contract, with an average of approximately 10 new or revised requirements per month that need to be evaluated for applicability. One change found to be applicable could necessitate changes in more than one document. The SBMS staff manages the change process for the Laboratory Policies and Procedures.

The SBMS staff supports the subject matter experts (SMEs) in creating the documents that are needed to meet requirements by providing editorial expertise, distributing the document for site-wide review and comments, and by providing process control, version control, editorial support, integration of content, and archiving.

The current management system for the change process requires the subject matter expert (SME) and SBMS editor to interact via multiple software interfaces, each of which reside in a different system and are not integrated. This is not efficient as information regarding SBMS documents is scattered among several system interfaces, and metrics and reports cannot be completed in a reasonable time frame.

In order to manage the change process more effectively, the SBMS staff needs a system that integrates all elements of the editorial process. As part of the continuous improvement of the Laboratory's processes, the current SBMS change process will be enhanced by replacing some elements in the current system with a single electronic system that allows the data to flow directly between the SME and the SBMS staff. Using the agile development method, separate modules will be developed for each stage of the process. The new system will, via an accordion menu, capture all information related to the modification of a document including: the change request, all correspondence, the document's revision information, an implementation plan, the subscription information, all team members, an event/date timeline, and the archive, approval, and publication of the revised or new document. All information related to such changes will be captured to provide an electronic representation of the SBMS business process in a single interface. This new system will be called the Change Package.

II. DEVELOPMENT METHOD

To develop the new Change Package, a team was assembled to work together using the agile development method. This team consists of a project manager, project lead, SBMS manager, senior editor, and software engineers. Agile development methodology provides many benefits that are suitable to this project. These include the ability to assess the direction of a project throughout development lifecycle, higher productivity, the ability to start one module's development before requirements for all modules is complete, and a faster time to completion. As this project is expected to be completed within a limited timeframe, the quick turn-

around time and ability to assess direction is very desirable. These benefits are achieved through regular cadences of work, at the end of which teams must present an increment of work. The teams will be working on different aspects of development including requirements, design, coding, testing/integrating, and deploying.

The new Change Package will be an extension of the current SBMS application. The current SBMS application's database will be broadened to incorporate an accordion menu, a timeline, a change request form, and to integrate all current interfaces into one interface. The SBMS' ColdFusion's platform and server will be re-used to develop the new change package, allowing the fastest development time possible.

III. CURRENT CHANGE/DEVELOPMENT PROCESS

The current change/development process is composed of several steps and several system interfaces (Figure 1). A Notice of Intent (NOI) is the first step in the change process. An NOI is a plan of action to revise, retire, or develop new SBMS documents. It is required for any change to an existing document or development of a new document excluding organizational title changes, correction of spelling errors, formatting, and non-working links. The SME completes the NOI and, for all major changes and new documents, assembles a review or development team. The SME or MSE submits the NOI, and it is automatically submitted to the SBMS Office. The SBMS Office reviews the NOI to determine the drivers, scope, development process, integration issues, the level of access protection, priority, impact, and implementation actions. The SME/MSE also contacts the Requirements Management Coordinator to discuss the drivers for major changes and new documents. If the SBMS office approves the NOI, the SME creates an implementation plan and drafts the document reflecting changes. The draft is then sent to the SBMS editor.

For all new documents, the SBMS editor emails the draft for a 10-day review to the SBMS department POCs and the review team on the NOI. The SME/MSE considers the reviewers' comments, and resolves all issues.

For all changes to or development of documents, the SBMS editor edits the draft document in Dreamweaver and returns it to the SME/MSE for their review and approval. Once the SME/MSE review and approve the document, the automated SBMS Document Approval Form is made available to the SME. The SME and/or the SBMS editor provide a revision history. The SME completes and submits the form concurrently to the MSE and Team Members/reviewers to obtain their approval. After all approvals are completed, the SBMS Document Approval Form is accepted by SBMS and the document can be published. Meanwhile, the SBMS editor must keep track of all correspondence regarding this change. This is done manually by copying and pasting all emails/call information into an MS Outlook task list. Also, they must send out a subscription message and/or lab-wide announcement (for new documents only) that reflects in a short summary the changes that are made (or description of new document), archive the document, update EDT, update the revision history, and update the database interface. Once all this is done, the SBMS editor will publish the document.

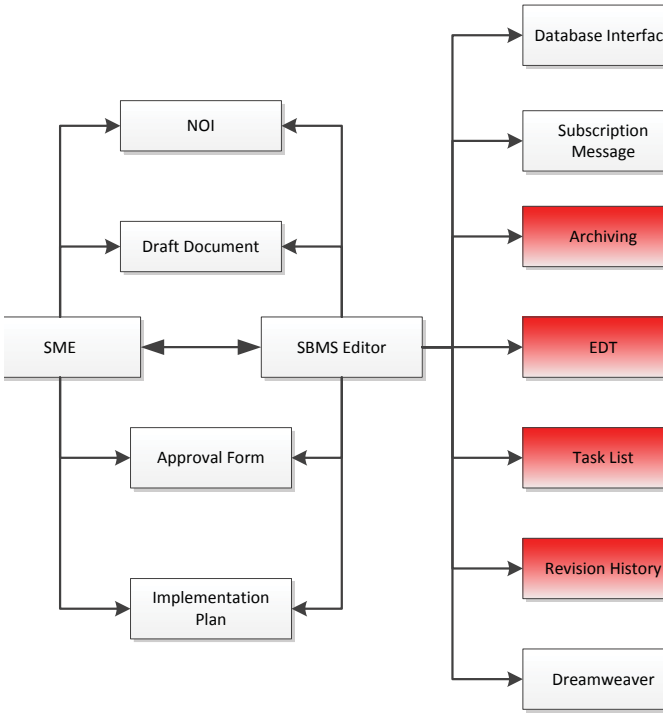

Figure 1. The model of the processes and systems used in the current SBMS process. The SME and SBMS staff communicate via an NOI, draft document(s), an implementation plan, and an approval form. The SBMS editor must document all correspondence and all changes regarding the change process in the database interface, subscription message, archiving, EDT, task list, revision history. They must make the actual change to the document using Dreamweaver.

A. Deficiencies

The current system, however simple as it may appear, has many deficiencies. One major flaw is that an NOI often times is never submitted. It is not required for many small procedures (minor changes). The second flaw is that the NOI was too long and had too many unnecessary steps for the SME to complete. Another huge imperfection is that during the editorial process there are too many system interfaces used. The SME and SBMS interact via the NOI, draft document(s), approval form, and the implementation plan, all of which are currently done separately and in separate interfaces. Once the change is finalized, the SBMS editor must then put all information back into the SBMS database, send out a subscription message, archive the document, put it in EDT, complete the outlook task list, fill out revision history, and then approve and publish the document. All of these are also in different interfaces.

Clearly, there are many unnecessary steps involved in the change process and far too many interfaces being used. Because everything is not in one place, the dates and information related to the documents are spread over several places/interfaces with no link between them. Thus, it is extra work and becomes complicated to correlate all the metrics regarding the changes made to a document for reports.

IV. CHANGE PACKAGE

The idea for the Change Package project was to create an electronic management system that essentially links all of the current systems into a single interface. This will allow information and metrics regarding the change to be found in one place. Due to

all of the complications with the previous method, the first step in redesigning the process was to replace the NOI with a form that the SME has to fill out for any and all types of change/modification to a document. This will serve as a starting place to allow every SME to be led to the same interface where all information regarding a change will be stored.

A. Change Request Form

We created the Change Request Form to fulfill these purposes. A user may start a Change Package and access the Change Request Form from three different places: from the SBMS home page, from any SBMS document, and from the Requirement's Management Tools in SBMS. Clicking on the "Change Packages" link, the SME will be presented with a list of change packages that belongs to his/her Management System. The SME will have the ability to continue editing a change package that was already started or start a new change package. If the user chooses to edit an existing change package, he/she will be taken directly to the change package interface. If the user chooses to start a new change package, he/she will be taken to the "change request" form. This form will automatically pull in the change request number, the name of the SME, and the management systems and documents that they have access to. The Change Request Form will ask the user to select the document they wish to make changes/modifications to or to create a new document. Depending on that selection, the user will be prompted to chose the corresponding management system, the name of document, the type of change made (major/minor), or if it is part of a review. They will then decide on team members. Depending on which departments are impacted by the change, the SME must choose a team member from several science departments and support divisions. They may then submit the change request form and be directed to the Change Package interface.

B. Change Package Interface

The Change Package interface will be an accordion menu that includes all information/metrics related to the change. The accordion menu will consist of the change request information menu, the correspondence menu, the event/date information manager/timeline menu, the revision information menu, the implementation plan menu, the subscription message menu, the draft/current document menu, and the approval/archive menu. Each of these menus will capture all information/metrics related to the change and will all be in one accordion interface. No information about the change will be stored anywhere else.

C. Change request module

This menu will show the type of change/modification being made: major, minor, new, or part of a review. It will also show a description of the change, the SME, the document in action, the change request number, and the revision number. This form will be available to edit if further changes need to be made.

D. Correspondence module

The correspondence form menu is the module that will be used to keep track of both out-going and incoming correspondence. It will replace the Outlook task list interface that is currently used to track correspondence. The change request form will automatically generate the first item in the correspondence form: an incoming message to SBMS that will inform the SBMS editor that a change request has been made. Any further correspondence between the SME, team members, and the SBMS editor will be manually added to the correspondence form. The SBMS editor will add to the correspondence list by completing the following requirements regarding the correspondence type: in to SBMS or out from SBMS, the date, who it is to or from, the subject, the text/information included in the correspondence, and any attachments. Once all the information has been completely added, the editor may press submit. This will prompt the question "Do you want this event to appear on the timeline?" If this event is information that is relevant to reports, then the editor will press "yes" and it will be added to the timeline with the subject line and date. Once "yes" or "no" is chosen, the event will then be added to the correspondence form as its own entry.

E. Event/time information manager module

The event/time information manager menu will be used to manage what information is shown in the change package timeline. This module is only available to the SBMS staff and is not available to the SMEs. There will be a "log" in the background of the event/date manager that captures the date of every action that is completed within the time frame of the change request. This will not be visible but instead will control which events are visible on the main module. The metrics that will be needed for reports will be the events that are captured on the timeline. The information that will be recorded in the event/date manager will come from three places: the change request form, the correspondence form, and the approval form:

1. Change Request Form: The event/date manager will capture the date the change request form is submitted and automatically label the subject as "Change Request Submitted."
2. Correspondence Form: The next event(s) that will be captured will all be decided upon directly by the SBMS editor and will be drawn directly from the correspondence form. Upon every action that is entered into the correspondence form, the question "Do you want this event to appear on the timeline?" is asked. If "Yes" is chosen, then the date of the action along with the subject line of that correspondence event will be automatically recorded into the event/date manager.
3. Approval Form: The last events that will be captured by the event/date manager are from the approval form. These dates include: the day the approval form is sent out ("Approval Form Sent Out"), the day that the first signature is received ("Approval Form 1st Signature"), and the day that the final signature is received ("Approval Form Final Signature"). The last date captured is the day the document was actually published. The approval form will be directly linked with the ability to publish and archive. Thus when "Publish and Archive" is clicked, the event/date manager will capture this date and automatically label the subject as "Published."

All of the events that are captured will then automatically generate a timeline which will depict all events in chronological order.

F. Revision information module

The revision information menu will be used to manage revision information for the change. This module will show the revision number and the revision information. The revision information will be editable to allow the SME/SBMS to edit the information that was changed in the document (note that once the subscriber message is sent out, the revision information will reflect

the subscriber message). The revision number will be based upon the revision number of the most recent version of the document. If a major change is made to the document, the new revision number will be the next whole number in sequence (i.e. 3.4 to 4.0). If the change is minor, the decimal portion of the revision number will be incremented one digit (i.e. 3.4 to 3.5). If a new document is created, the revision number will be 1.0.

G. Implementation plan module

The implementation plan menu will be used to manage the implementation plan for the change. This will be divided into three sections: the resource/implementation action, the department/division/person responsible for the action, and the date by which it will need to be done. During the course of the time that the document is being changed/modified, and before any changes can be published, the SME/team must fill out the implementation plan with any actions that will need to be done before and after the changes to the document are published.

H. Subscription message module

The subscription message menu will manage the subscription information for the change to the document. The information managed here is integrated with the revision information. Once the change request form is submitted, it will automatically populate the Subscriber Message module with the "Change Description" that the SME provided. The SBMS editor, however, has the option to edit the subscriber message. Only the SBMS editor will have access to the editing capabilities. Once the SBMS editor finalizes the subscriber message with the true description of the change that took place, it will be sent out for approval. This will also automatically update the revision information section of the Revision Information module with the subscriber message. The summary in the revision information will then be locked from making any further changes.

I. Draft/current document module

The draft/current document menu will be used to manage the current live and current draft documents related to the change. The current live document will be a link to the most current published version of the document that is being worked on. It will reflect the document most recently updated. The current draft document will be a link to the document draft site. This will only be available to the SBMS editor as this is where the changes/modifications to the document will be made. Once the changes made on the draft site are published, the current live document link will then reflect the newly changed document.

J. Approval/archive module

The approval/archive menu will be divided into four sections: summary, checklist, implementation actions, and signature. The summary section will be filled in automatically from the change request form with the name of the SME, the management system, the document title, the change request number, and the type of change made. The checklist section will reflect whether the document was done for a review, an implementation plan was created, and if it will be available externally. The implementation plan section will reflect any actions that will still need to take place once the changes are published and will be drawn from the implementation plan module. The signature section will require the signature of the SME and all team members. The names of all team members are automatically populated from the change request form. Once the editor sends out the approval form, the team members will all be prompted to give their signatures. Once all signatures are obtained, the editor may then publish and archive the document with the changes made.

V. CONCLUSIONS/IMPACTS

By creating an electronic system to incorporate all process elements necessary into a single accordion menu interface, all information related to a change will now be in a single place (see Figure 2). This new system offers many improvements, including:

1. Improve interaction between SMEs and SBMS
2. Reduction in the time required to generate reports
3. Menus will be based on the type of change to be made (major, minor, etc.) making it easier for SMEs and SBMS to decide what steps of the change process are applicable
4. Allow data to be entered once and flow through the entire SBMS process
5. Improve reporting capabilities
6. Single interface to manage the SBMS change process
7. Capture more information while requiring the user to provide less data
8. Provide an electronic representation of the SBMS business process

The Change Package electronic management system thus creates a flexible framework that not only improves the current change process, but also is flexible enough that all modules may be updated independent from each other. As such, the establishment of this operational and adaptable framework combines the best wisdom of all department stakeholders to maximize mission success, allowing for further adaptation in the future as required.

Isolation of *Chlamydomonas reinhardtii* mutants with low oil

Taryn Boucher, a) Chengshi Yan, b) and Changcheng Xub)
a) Department of Biology, Bucknell University, Lewisburg, Pennsylvania 17837
b) Department of Biology, Brookhaven National Laboratory, Upton, New York 11873

ABSTRACT

Renewable energy sources are in high demand in today's world due to growing environmental and economical concerns. Consequently, the potential to use microalgae as a precursor to biofuel production is an area of interest to scientists. However, before oil produced by microalgae can be used as a feedstock for biofuels, the genes that control oil production must be understood. The current study seeks to explore the genes responsible for oil production in *Chlamydomonas*. In order to find the genes that control oil production, however, mutants must be created that lack the ability to produce oil. Wild-type *dw15* strains and starch-mutant BAFJ5 strains of Chlamydomonas were used in this study as model systems. BAFJ5 *mutants* were transformed using *HindIII* and the mutants were screened for oil production. In ten weeks, over 800 single mutants were screened for oil production, and only two strains yielded low oil production. Future investigation on the two strains of interest will require further thin layer chromatography experiments, which are beyond the scope of this article.

I. INTRODUCTION

Accumulation of large amounts of oils by microalgae *Chlamydomonas reinhardtii* is a promising area in the study of biofuels as the oil is a potential feedstock for biodiesel production. Under normal conditions, *Chlamydomonas* is known to accumulate starch and oil in the form of triacylglycerol (TAG), with starch being the dominant storage product.[1-4] However, when the carbon supply is limited–such as under conditions of nitrogen starvation or in a mutant devoid of starch–oil becomes the main storage product.5

The biosynthetic pathway of TAG in microalgae starts with de novo fatty acid synthesis in the chloroplast, which can then be used directly in the chloroplast or can be transported to the ER where it becomes acylate glycerol-3- phosphate and produces phosphatidic acid (PA).[5-7] Next, PA is dephosphorylated to produce diacylglycerol (DAG), a precursor for the synthesis of membrane lipids and storage TAG.[5] The final step in the biosynthesis pathway is the conversion of DAG to TAG which is catalyzed by diacylglycerol: acyl-CoA acyltransferase (DGAT) and phospholipids DAG in microalgae.[5]

The current study investigates the genes that control oil production in the model algae *Chlamydomonas reinhardtii.* The role of TAG accumulation has been characterized at the molecular level in *Chlamydomonas*,[5] but the specific gene sequence responsible for oil production in nitrogen-limited conditions is still under investigation. The results from this study, although inconclusive, provide potential information about the genes that control oil production in *Chlamydomonas*. While over 800 individual colonies have been screened for oil content, only two mutants have been identified as having reduced oil production. Our results indicate that we are getting closer to finding the genes responsible for oil production.

II. MATERIALS AND METHODS

A. Growth conditions and transformation

The *Chlamydomonas* strains used were wild-type *dw15* and starchless mutant BAFJ5. The cells were grown to mid-log phase ($2x10^6$ cells/ml) on plates containing Tris-acetate-phosphate (TAP) liquid culture medium under continuous bright light (90 µE/m2/s) at 24°C on an orbital shaker for ten days.[8] Cells were pelleted at 6,000 rpm at room temperature for 5 min and then resuspended in fresh TAP by gentle pipetting to a concentration of $2x10^8$ cells/ml. Generation of insertion mutants was performed as described,[9] except cells were transported to 5 ml test tubes containing 0.4mm of sterile glass beads and 1 µg of linearized pHyg3 plasmid DNA (linearized with *HindIII*) and contents were suspended by vortex on top speed using a Vortex genie-2. Plasmid pHyg3 extraction was conducted using the IBI *Scientific* High-Speed Plasmid Mini Kit. Cells recovered overnight in a 25 ml sterile flask containing 10 ml of TAP medium with shaking (100 rpm). Cells were resuspended with fresh TAP and plated onto TAP 2% agar supplemented with hygromycin at 10 µg/ml. Cell viability was determined after 10 d of growth.

B. Lipid analysis

Chlamydomonas colonies that grew well in hygromycin were selected for and transferred to 96-well plates containing 2 mM TAP medium. The colonies were then kept under light in 24°C incubator for 7 d. Fluorescence was measured before and after Nile Red was added to each sample using a plate reader to generate ratios of oil accumulation. In addition, thin layer chromatography (TLC) was used to rescreen mutants for oil production.

III. RESULTS

Confirmation of pHyg3 plasmid extraction linearized with *HindIII* was confirmed using gel electrophoresis (Figure 1). The plasmid was digested to 1.7 kb. Additionally, BAFJ5 colonies grew well after 10 d of growth on plates containing TAP 2% agar supplemented with hygromycin (Figure 2). Nile red results for each plate tested yielded ratios of oil production by the individual colonies before and after Nile red was added and compared with the controls BAFJ5 and *dw15* being in wells H11 and H12, respectively (Figure 3). Ratios that were less than that of BAFJ5 (0.796532) are considered to have low-oil content. Low-oil colonies were then tested using TLC to confirm relative oil production (Figure 4). We have screened over 800 individual colonies in ten weeks and have identified at least two mutants with decreased oil content: strain B and strain D (Figure 4).

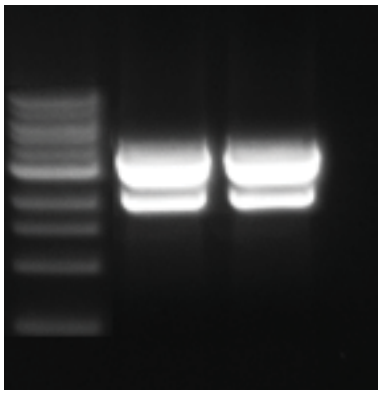

Figure 1. Gel electrophoresis of pHyg3 plasmid DNA cut with enzyme *HindIII* at 1.7 kb.

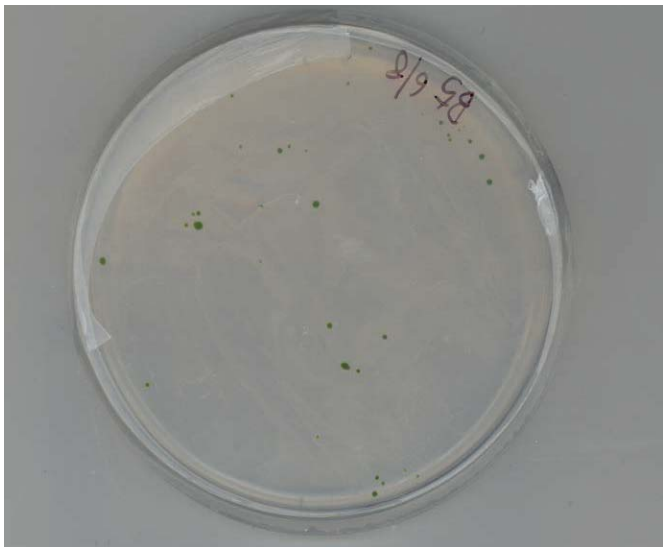

Figure 2. BAFJ5 transformation colonies after 10 d of growth. Plates are TAP 2% agar supplemented with hygromycin at 10 µg/ml.

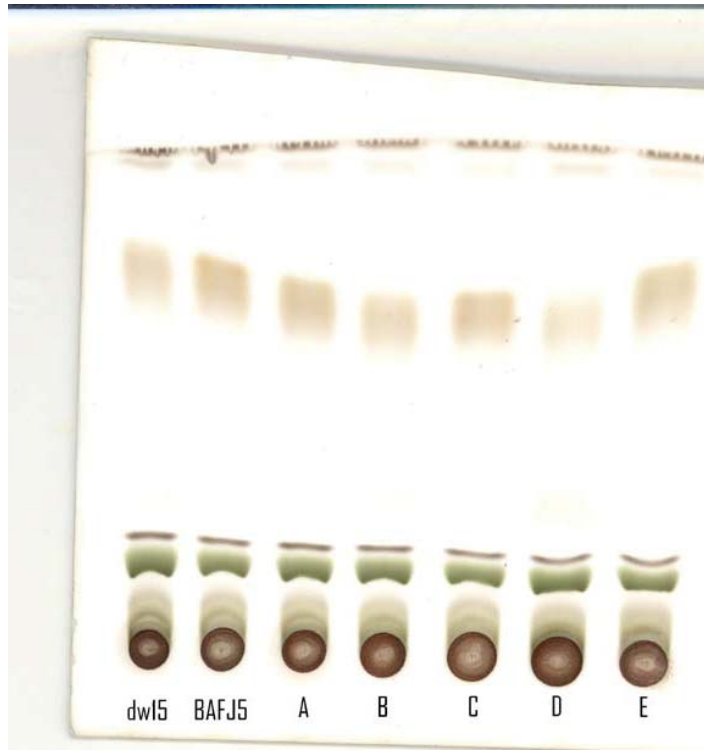

Figure 4. TLC plate with low oil mutants and controls *dw15* and BAFJ5. Strains B and D have low-oil content (TAG) compared to the controls, and are the strains that are of interest. Additional screening will be required to confirm oil concentration.

IV. CONCLUSION

Renewable energy sources are in high demand in today's world due to growing environmental and economical concerns. Consequently, the potential to use microalgae as a precursor to biofuel production is an area of interest to scientists. However, before oil produced by microalgae can be used as a feedstock for biofuels, the genes that control oil production must be understood.

The current study explored the genes responsible for oil production in *Chlamydomonas*. In order to find the genes that control oil production, however, mutants that lacked the ability to produce oil needed to be created. Wild-type *dw15* strains and starch-mutant BAFJ5 strains of *Chlamydomonas* were used in this study as model systems.10 BAFJ5 mutants were transformed using *HindIII* and the mutants were screened for oil production. In ten weeks, over 800 single mutants were screened for oil production, and only two strains yielded low oil production. Future

<>	1	2	3	4	5	6	7	8	9	10	11	12
A	0.94866	1.180291	0.980764	0.987618	0.911986	0.92416	1.040978	0.876276	0.714961	0.756864	0.922705	0.915487
B	1.059687	1.217061	0.928095	0.927829	0.9837	1.021044	0.829971	0.795437	1.00163	0.605601	0.80126	1.298629
C	0.741513	0.705672	0.736367	0.794343	0.96311	0.838467	0.860761	0.613567	0.810185	0.631813	0.773603	0.625352
D	1.040321	0.749918	0.828883	0.726646	0.825032	0.620013	0.71685	0.709201	0.69058	0.711654	0.68748	0.664983
E	0.77557	0.655275	0.660375	0.772957	0.652847	0.636271	0.875722	0.692673	0.82564	0.657789	0.661877	0.762124
F	0.66337	0.681715	0.648472	0.850214	0.758386	0.722652	0.674608	0.79159	0.697935	0.663958	0.730561	0.620991
G	0.636904	0.674759	0.668321	0.645521	0.636312	0.649958	0.608693	0.631739	0.656754	0.660603	0.705734	0.748598
H	0.624792	0.73989	0.646386	0.615709	0.625522	0.619508	0.654087	0.609791	0.679203	0.641976	0.796532	0.988281

Figure 3. Nile red results from Plate 2 of ratios before and after Nile red was added. Wells H11 and H12 were the controls, being BAFJ5 and *dw15*, respectively. Fluorescence measurement is based off of excitation wavelength (485 nm) and emission wavelength (535 nm) at 23.3°C. Wild-type *dw15* shows a higher oil yield than those of BAFJ5 (0.796532 to 0.988281). Low-oil yield is anything below BAFJ5 (0.796532). Additional screening for low-oil mutants is done by TLC.

investigation on the two strains of interest will require further TLC experiments.

V. ACKNOWLEDGEMENTS

I would like to thank my mentor, Dr. Chengshi Yan, for working with me and helping me with this project. I would also like to thank Dr. Jilian Fan, Dr. Changcheng Xu, and Dr. Zhiyang Zhai for giving me the opportunity to work in their lab. Thank you to the U.S. Department of Energy – Office of Science Education and BNL for their support.

VI. REFERENCES

1. Li, Y.T., et al. (2010) Chlamydomonas starchless mutant defective in ADP-glucose pyrophosphorylase hyper-accumulates triacylglycerol. *Metab. Eng.* 12: 387-391.
2. Siaut, M., et al. (2011) Oil aaccumulation in the model green alga Chlamydomonas reinhardtii: characterization, variability between common laboratory strains and relationship with starch reseves. B*MC Biotechnol.* 11: 7.
3. Wang, Z.T., et al. (2009) Algal aipid bodies: stress induction, purification, and biochemical characterization in wild-type and starch-less Chlamydomonas reinhardtii. Eukaryot. *Cell* 8: 1856-1868.
4. Work, V.H., et al. (2010) Increased lipid accumulation in the Chlamydomonas reinhardtii sta7-10 starchless isoamylase mutant and increased carbohydrate synthesis in complemented strains. Eukaryot. *Cell* 9: 1251-1261.
5. Fan, J., et al. (2012) Oil accumulation is controlled by carbon precursor supply for fatty acid synthesis in Chlamydomonas reinhardtii. *Plant Cell Physiol.*, doi:10.1093/pcp/pcs082.
6. Sirevag, R. and Levine, R.P. (1972) Fatty acid synthetase from Chlamydomonas reinhardi: sites of transcription and translation. *J. Biol. Chem.* 247: 2586-2591.
7. Moellering, E.R., et al. (2009) Molecular genetics of lipid metabolism in the model green alga Chlamydomonas reinhardtii. In *Lipids in Photosynthesis: Essential and Regulatory Functions.* Edited by Wada, H. and Murata, M. pp. 139-150. Springer, Dordrecht.
8. Harris, E.H. (2009) *The Chlamydomonas Sourcebook: Introduction to Chlamydomonas and its Laboratory Use,* 2nd ed, Academic Press, Oxford, United Kingdom.
9. Matsuo, T., et al. (2008) A systematic forward genetic analysis identified components of the Chlamydomonas circadian system. *Genes & Dev.* 22: 918-930.
10. Zabawinski, C., et al. (2001) Starchless mutants of Chlamydomonas reinhardtii lack the small subunit of a heterotetrameric ADP-glucose pyrophosphorylase. *J. Bacteriol.*, 183: 1069-1077.

Creating remote access capability for the LINAC Timing System and investigating electromagnetic noise conditions for the LINAC H- source

Adeel T. Butt
Department of Engineering, Stony Brook University, Stony Brook, New York 11790
Omar Gould
Collider Accelerator Department, Brookhaven National Laboratory, Upton NY 11973

ABSTRACT
The Linear Accelerator (Linac) of the Collider-Accelerator Department is a 200MeV proton source for Brookhaven Linac Isotope Producer (BLIP) and for the Relativistic Heavy Ion Collider (RHIC). The goal of the first project was to access the Linac Timing System remotely. Remote access will give us greater control on the operation and diagnosis of conditions of the Linac performance. The possibility of using an operating system compatible with the current network system will be evaluated; other methods will be explored. The goal of the second project was to investigate electromagnetic noise conditions for the Linac H- source. Investigating the noise conditions may provide a better understanding of the unexpected beam amplitude variations of the H- source. The transmission of signals between equipment for the H- source will be documented and analyzed.

I. PROJECT 1. Creating remote access capability for the LINAC Timing System

A. INTRODUCTION

The 200Mev Linac operates with a timing system with seven distinct user setups to control when the devices are triggered for the production of ion beam for each user. The User Interface for the Linac Timing System is currently utilizing C programming code working on Windows 95 which is not supported by the network. In order to have remote access the Operating System must be updated to the one which is supported by the network; i. e., Windows XP. Since operations execute differently in Windows 95 and Windows XP, updating the Operating System requires that those differences and the C code be addressed. In this paper we describe those differences, the problems encountered while upgrading, and the solutions to those problems.

B. METHODS AND MATERIALS

The Linac Timing Board is inserted in a Versa Module Eurocard (VME) chassis (Figure 1) which has a VME module (Figure 2) installed in it. The VME module is connected to the Peripheral Component Interconnect (PCI) card (Figure 3) installed in the computer through a Multisystem eXtension Interface (MXI-2) cable (Figure 4). MXI-2 has the capabilities to expand signals including triggers and interrupts.

First the operation of the Linac timing system was analyzed on the Windows 95 computer. After the analysis, the PCI board was transferred to a Windows XP computer.

All the required drivers and software were already installed on the XP computer. The software used is NI-VXI 3.5.1 from National Instruments. NI-VXI package includes

1. Resource Manager (Resman) which identifies all the devices in the main frame, ensures that devices pass their self-test, and allocates addresses to the devices;
2. The Interactive Control interacts with the Timing Board; and
3. Measurement and Automation Explorer (MAX) which allows users to configure National Instruments hardware and software, viewing devices and instrument connected to the chassis and executing system diagnostics.

LabWindows 4.0.1 was installed to compile and run the C programming code written for the Linac Timing System. This code is used to create the User Interface to communicate with the Linac Timing System; it contains User setups.

C. RESULTS AND DISCUSSIONS

The project of creating remote access capability for the Linac Timing System is in progress. The C programming code utilizes Interrupt Requests to access system diagnostics. The main hindrance in creating the remote access is with the Interrupt Request process. Interrupt Requests are the signals generated by the devices to gain the attention of the processor. Interrupts can be asserted and acknowledge but cannot be deasserted in Windows XP.

Initially it was thought that the problem could be the older version of the software we are using and also the software was installed before the hardware. A temporary XP computer was obtained; the plan was to install the hardware first and then the latest version of the software; i. e., NI-VXI 3.8. This plan didn't work as Windows XP installed its own driver for the PCI card. The steps taken while installing hardware and software on the temporary computer are as follows:

Hardware Installation
Installing PCI card

- Remove the metal bracket that covers the cutout in the back panel of the computer (Figure 5).
- Slowly push down on the top of the PCI; installing the PCI into any empty slot of the computer.
- Check installation.
- Attach the MXI-2 cable (end with white label) to inserted PCI card.
- Software Installation:
- For successful installation user must log into the computer as administrator.
- Browse to www.ni.com
- In the search box, search for NI-VXI 3.5.1
- Download NIVXI.zip file
- Extract and run the downloaded file

D. CONCLUSION

National Instrument was contacted for the interrupt issue; they suggested using LabView. Possible cause of this issue could be the version of LabWindows 4.0.1 we are using which supports Windows 95 only and is not compatible with Windows XP according to National Instrument forums. A newer version of LabWindows may provide a solution. There might be differences on how LabWindows 4.0.1 and current version of LabWindows works. If we get a new version of LabWindows, we would need to address those differences and make changes in the C programming code accordingly. This process is expensive and could be time consuming as well. A viable approach for this will be to use a proposed alternative to interrupts: polling to read data. In polling, the processor periodically checks each of its I/O devices to see if any of them have a request that it needs to handle. Changes need to be made in C programing code in order to use polling to access system diagnostics as an alternative to interrupts.

II. Project 2. Investigating electromagnetic noise conditions for the LINAC H- source

A. INTRODUCTION

The Linac Timing system controls triggering of Linac H- source. The Linac H- source is used for BLIP and sometimes use for experiments that require injection into the Booster Synchrotron at a lower beam intensity. The Linac H- source is showing an unexpected behavior in which the amplitude of the current drops abruptly and returns to its value after x number of pulses. This behavior is believed to be related to the electromagnetic noise. In order to launch an investigation on the noise conditions, all the signals present in the field needs to be documented.

B. METHODS AND MATERIALS

The first step to initiate the investigation on electromagnetic noise condition for the Linac H- source is to document all the signals present in the field. Since most of the signals were not labeled, I consulted with experts to identify those signals. The three main triggers related to the source are:

- Hydrogen Gas Discharge (HGD)

This pulse controls the valve that regulates the rate at which Hydrogen gas is discharge from its container to the source. Certain quantity of Hydrogen gas should be released in magnetron to react with Cesium and form Hydrogen ions.

- Discharge Rate of Magnetron (DRD)

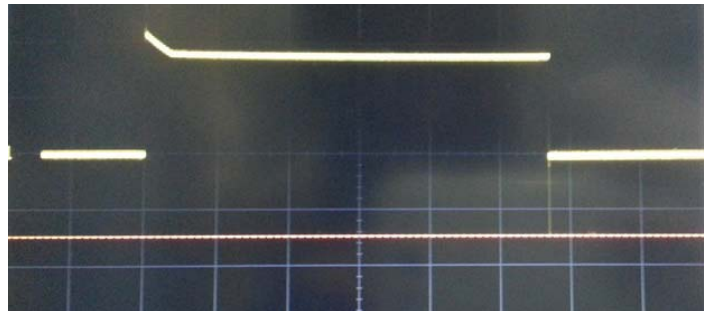

This pulse controls the valve to discharge Hydrogen ions that have been formed.

- Master Slave Pulse ‘A’ (MSP ‘A’)

This pulse tells the integrator when and where to make measurement of discharge voltage and current.

These triggers were examined using the digital oscilloscope to check if the noise was present. Microsoft Visio was used to create the block diagram which shows the origin of the signals and their transmission between the equipment.

C. RESULTS/DISCUSSIONS

The three main identified triggers originate from V102 (Figure 6) module as digital pulses and passed to Source Life Support System (Figure 7). Source Life Support System blocks all these pulses if one of them is missing and generates its own pulses to drive the H¬- source. These pulses are then passed to the Digital Light Transmitter (Figure 8) which converts them into light links that are sent to the Source High Voltage (HV) Rack. A digital light receiver in the HV rack converts the light links back to digital pulses and links to H- source. Noise was observed in the waveform of those pulses obtained by using an oscilloscope.

D. CONCLUSION

The unexpected behavior of the H- Source appears to be related to the electromagnetic noise present in the field equipment for the source. The H- Source required the documenting of its signal origins and destinations. It was necessary to gain knowledge of the signals in the field prior to investigating electromagnetic noise conditions. A block diagram (Figure 9) was created showing all the signals and transmission through the equipment. Waveform of pulses that originates from V102 module was analyzed. There is some noise present in each pulse. After consulting with experts, I came to the conclusion that the noise level observed in those pulses doesn’t affect the source as the variations are very low.

E. ACKNOWLEDGEMENTS

I wish to thank my mentor Mr. Omar Gould for his professionalism and generosity during the CCI program. I would also like to thank Mr. Mike Stegman, Mr. Tim Lehn, Mr. Brian Briscoe, Mr. Deepak Raparia, Mr. Frank Carlino and all the workers at building 930 for their help. Further, I would express my gratitude to the Office of Science Education, and all who continue to assist interns in that branch. Finally, I wish to acknowledge the hospitality and kindness of Brookhaven National Laboratory and the Department of Energy.

F. REFERENCES

National Instruments (NI), Getting Started with your VXI/VMe-PCI8000 Series and the NI-VXI software for Microsoft Operating Systems. March 1996.
National Instruments (NI), NI-VXI User Manual. July 1996.
National Instruments (NI), Getting Started with your PCI-based MXI-2 Interface for Windows 95/NT. September 1997.
National Instruments (NI), VME-MXI-2 User Manual. January 1996.
National Instruments (NI), Text Utilities Reference Manual. October 1993.
Peterson, Wade D. "The VME Handbook." Expanded Third Edition. VITA. Scottsdale, AZ. 1996.

G. APPENDIX

Participants:

Name	Institution	Role
Adeel T. Butt	Stony Brook University	Student
Omar Gould	Brookhaven National Laboratory	Mentor

Scientific Facility: Collider Accelerator Department.

Notable Outcomes: Created block diagram for Linear Accelerator H- source, showing all the signals present in the field and their transmission through the equipment.

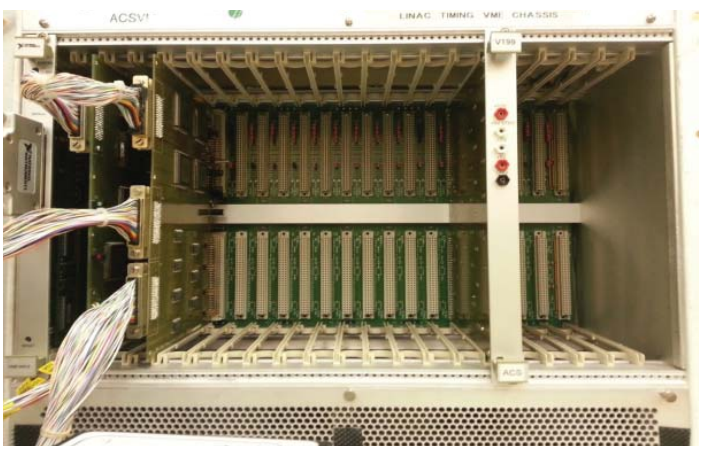

Figure 1 – VME chassis with VME module and Linac timing Board Installed

Figure 4 – MXI – 2 Cable

Figure 2 – VME Module. **Figure 3 – PCI card**

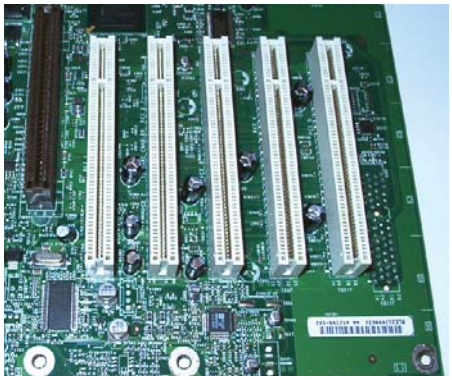

Figure 5 – Empty Slot of the computer for the PCI card

Figure 6 – V102 Module

Figure 7 – H- Source Life Support System

Figure 8 – Digital Light Transmitter

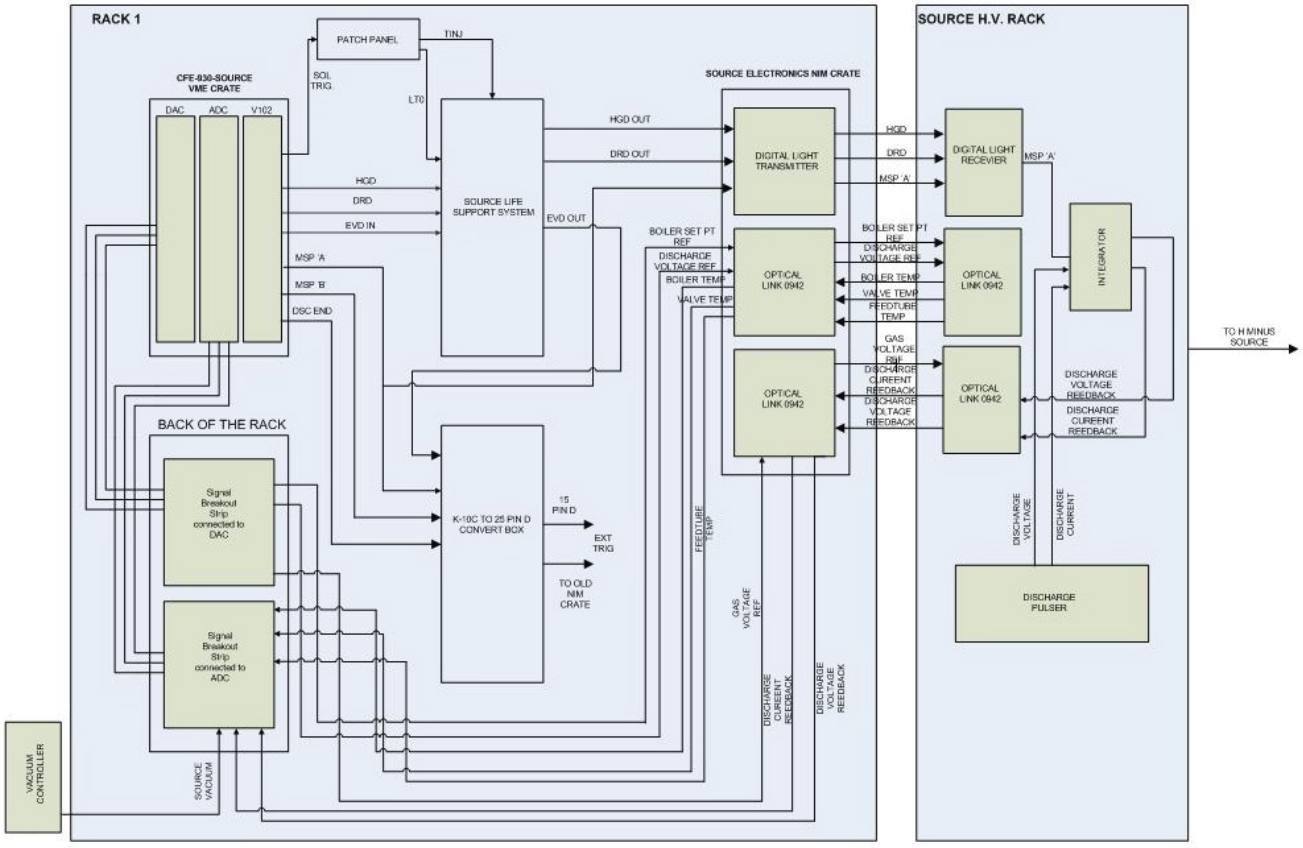

Figure – 9 Block Diagram for H- Source Signals

Characterization of cadmium zinc telluride radiation detectors grown by vapor phase method

Trevor Chan
College of Engineering, University of Alabama in Huntsville, Huntsville, AL 35758
Giuseppe Camarda
Nonproliferation and National Security Department, Brookhaven National Laboratory, Upton NY 11973

ABSTRACT

Throughout the years one of the main goals of the Department of Energy (DOE) has been to insure the integrity and safety of the country's nuclear materials and to advance nuclear non-proliferation. Through the researches done here at the Brookhaven National Laboratory's Nuclear Non-proliferation and National Security (NNS) department, the DOE is able to achieve these goals. The main focus of the NNS is to develop room temperature radiation detectors to monitor and track nuclear materials. Cadmium Zinc Telluride (CZT), one of the most promising materials for room-temperature radiation detectors, is a good radiation material candidate because it has the required material properties: high resistivity, high density, high atomic number, photosensitivity, and highly absorbent to x-rays. Like all of the other radiation detector materials, the CZT must be in extremely high quality so it can aid charge transport inside the material. The presence of extended defects like cracks, dislocation, and voids can have the potential to trap charges inside the material, resulting in poorly performing devices. With the help of a private company in England, NNS recently acquired CZT samples grown through vapor phase. To examine these crystals, the NNS department uses several different methods. The first uses optical and infrared microscopy to check for visual defects; the second, uses different x-rays at the National Synchrotron Light Source (NSLS) to examine the performance of the different samples and collect data on all of the non-visible defects the materials contain. One of the most interesting discoveries in these samples is that the defects on some of the samples are actually enhancing the performance of the detectors. The next goal of the NNS department will be to find out what is causing this strange phenomenon. For this summer, our department received several samples from an outside crystal grower in the United Kingdom, Kromek, who uses a special technique to grow their crystal. Instead of using the old melt-growth technique, they used a vapor phase growth technique. We have characterized their material and determined the quality of their crystals and the performance of their detectors and report back all the results back to Kromek. Vapor-phase grown crystals are grown by placing an atomic layer of cadmium telluride on top of an atomic layer of zinc telluride and continuing this process until the whole crystal is grown. By using this technique, the grown crystal has no Te inclusions and precipitates. Also due to the fact that the crystal can be grown without touching the ampoule walls, less stress is produced on the crystal while it is cooling down.

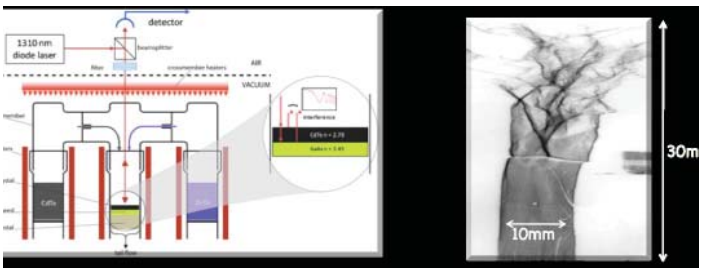

I. NTRODUCTION

In IR Microscopy the CZT crystals appears transparent to the infrared light because the band gap of CZT is ~1.45 eV, but the Te inclusions show up as dark masses (band gap of Te is ~0.2 eV). Te inclusions degrade a detector's performance because they trap the charge created by ionization in the CZT by the incoming photons (X-rays, gamma-rays). Fluctuations in total collected charge cannot be corrected electronically; therefore, the more Te inclusions there are in the crystal, the worse the performance of the detector fabricated from that crystal. The IR Microscopy method can count the number and size of Te inclusions in each volumetric region (or stack of images). Usually we measure 5 volumetric regions and then average the concentration of Te inclusions in each of the volumetric regions to finally estimate the concentration of Te inclusions per cm3. As shown below, IR Microscopy can project up to a 100 stack of images on one plane to find the concentration of Te inclusions per cm3.

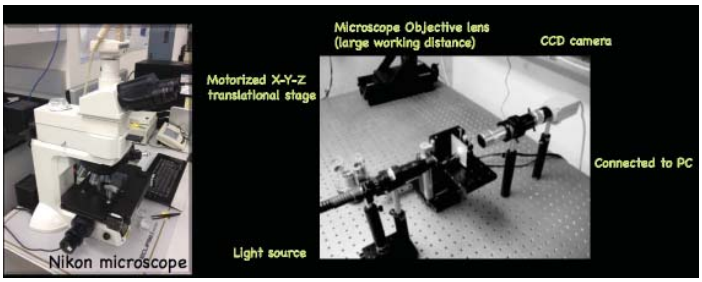

White Beam X-ray Diffraction Topography (WBXDT) uses beam energies ranging from 5 KeV to 54 KeV. The actual beam size is varied depending on the crystal area to be measured. WBXDT is very efficient and can take accurate diffraction images of detectors in only a few seconds. As shown in the figure below, the WBXDT image provides information on the crystalline structure and orientation of a detector. With the WXDT we can screen quickly CZT crystals to make sure they have only one domain and to see if there are extended defects in the crystal tested. We need high resolution X-ray films to see some extended defects and strains fields. Unlike other methods of analyzing CZT detectors, the WBXDT is very quick and nondestructive.

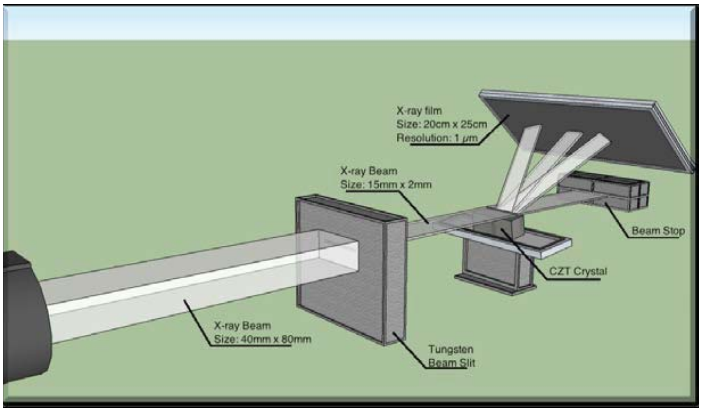

The Micro-scale Detector Mapping (MDM) method uses a monoenergetic X-ray micro-beam to map the whole area of the sample. As shown in the figure below, for each micro-area interrogated the energy spectrum is acquired, stored, and subsequently used to plot an X-ray response map. The X-ray mapping technique is the main tool that provides high spatial resolution, limited only by the diffusion (low in the case of X-rays) and lets us control the interaction depths of X- rays to avoid surface and polarization effects. With this technique each pixel on a pixilated CZT detector is analyzed up to a depth of 10 microns and an X-ray response map of the pixel is created to show dislocations, sub-grain boundaries, and the area where any charge collection is lost.

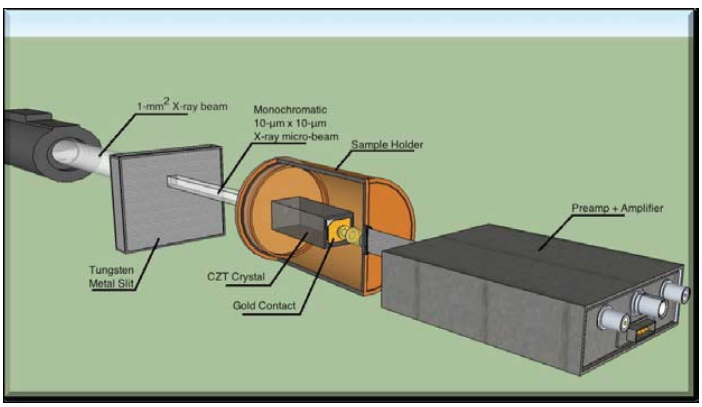

II. METHODS

In this experiment and analysis, characterization of two 10 x 10 x 2 mm3 CZT radiation detectors. The detectors measured are used as imaging devices. Some crystals might be impaired with material defects which cause non-uniformity in the electric field (E-field); therefore, aberrations of the image response can arise. This experiment characterized material defects and detector performance by using several techniques such as IR microscopy, White Beam X-ray Diffraction Topography (WBXDT), and Micro-scale Detector Mapping (MDM). After measuring the material defects by using IR and WBXDT, each device was then connected with the electronics inside a test box that measured the performance of each device using the beam-line X27B at BNL's National Synchrotron Light Source (NSLS). The X-ray response map showed images of this pixilated detector, and the charge electron is severely disfigured because of numerous crystal defects (multiple sub-grain boundaries and star-punching dislocations (white spots)). The crystal defects affect the charge transport and distort the E-field and thus severely hinder detector performance. The detectors tested don't match up to the standards of an ideal pixilated detector.

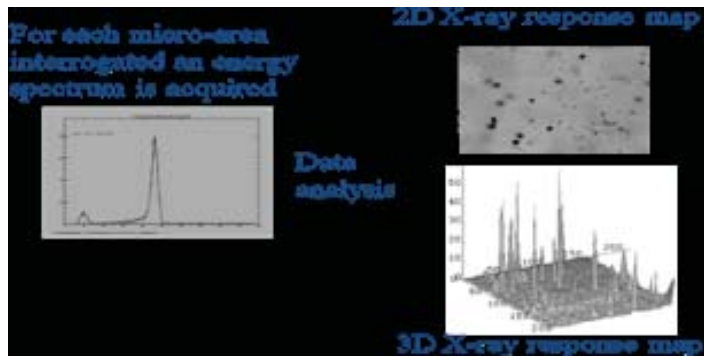

III. CONCLUSION

In conclusion, extended defects affect charge transport and detector performance. Sample d-3 is a better performing detector than c-6 because of the lower concentration of extended defects and better crystallinity. Also vapor phase growth method has made huge progress recently toward the production of higher quality and more economical single crystal CZT crystals.

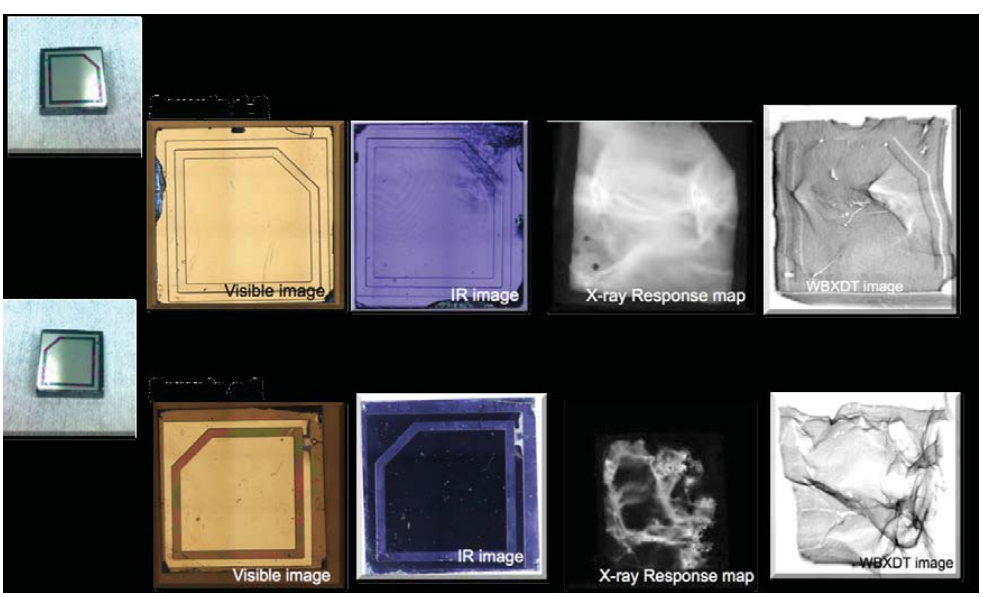

Investigation and confirmation of protein candidates interacting with *Arabidopsis* 4CL1

Morgan Campbell
Department of Biology, State University of New York at New Paltz, New Paltz, NY 12561
Sumar Hayan
Department of Biology, Stony Brook University, Stony Brook, NY 11794
Xuebin Zhang, Chang-Jun Liu
Brookhaven National Laboratory, Upton, NY 11973

ABSTRACT

Phenylpropanoid biosynthesis leads to the formation of a variety of phenolic metabolites such as flavonoids, benzenoids, and lignins which provide plant architecture and defense against environmental stresses. In the biofuel industry, lignin is an obstacle for production of renewable energy. Researchers are working to manipulate this pathway to disrupt lignin formation in cell walls, therefore increasing the conversion efficiency of biomass to biofuels. The key enzymes involved in every step of the phenylpropanoid pathway in *Arabidopsis thaliana* have been identified. Scientists at Brookhaven National Laboratory are focusing on the interacting partners of these enzymes to understand the regulatory mechanism at the protein level. 4-coumarate:coenzyme A ligase (4CL) is a key enzyme involved in the phenylpropanoid pathway. The present study aims to confirm the potential interactions between 4CL1 and twenty-one proteins identified by primary screening. 4CL1 was used as bait to screen the interacting partners in the yeast-two-hybrid system which detects protein-protein interaction by triggering the expression of reporter genes. Upon testing with a histidine synthesis reporter gene, we observed activation in all clones. To distinguish between genuine and false positive results, the interactions were further verified by monitoring the growth of yeast transformants harboring the "bait" and "prey" proteins in Adenine dropout medium and by observing the coloration. The adenosine triphosphate synthase subunit beta (ATPD) proteins were confirmed interacting with 4CL1. This is linked to its role in providing ATP for the reaction of 4CL in the phenylpropanoid pathway. Our experiment offers insight into metabolic organization between ATPD and 4CL, which can be applied to the disruption of lignin synthesis. Future research will be carried out through the analysis of ATPD knock-down mutant lines of *Arabidopsis.*

I. INTRODUCTION

Conducting in-depth research into the phenylpropanoid pathway in *Arabidopsis thaliana* is an important way for scientists to understand the details of lignin production. The phenylpropanoid pathway is a chemical pathway that involves many steps and numerous proteins that work carefully to produce lignin. All of the enzymes involved in this vital pathway have been identified and studied by scientists. 4-coumarate:coenzyme A ligase (4CL) is one of the key enzymes in the pathway whose properties are well understood. It is part of an early step in the phenylpropanoid pathway; it catalyzes the formation of 4-coumaroyl-CoA from 4-coumarate and CoA in a mechanism that involves the hydrolysis of ATP. 4CL1 is an isoform involved in the phenylpropanoid pathway in *Arabidopsis thaliana.*[2] In order to better understand and use such enzymes to manipulate lignin production, focus has now shifted to the proteins interacting with them. This includes the proteins which help the enzymes by providing substrates or by acting as modifiers. Protein-protein interactions involving 4CL1 were studied in this investigation. Twenty-one potential interacting partners that had been identified by primary screening were used to investigate these protein-protein interactions using the yeast-two hybrid method.

II. METHODS AND MATERIALS

A. Preparation of Yeast Competent Cells

AH109 yeast was plated overnight in a medium containing yeast extract, agar, peptone and dextrose (YPDA) at 30°C. One monoclone was inoculated overnight in 10 ml of YPD at 30°C with shaking. Five ml of culture was added to 100 ml of YPD for 4.5 hours at 30°C with shaking. When the OD600 value was between 0.2-0.3, the suspension was centrifuged at 3,000 rpm for 5 minutes, resuspended in 30 ml of sterile deionized water and then centrifuged similarly. The pellet was resuspended in 1.5 ml of Li/TE and transferred to an eppendorf tube, where the suspension was centrifuged at 3,000 rpm for 1 minute and resuspended in 500 microliters of Li/TE.

B. Yeast Two-Hybrid System

The yeast two-hybrid system is used as a way to detect protein-protein interactions. This is done by binding bait and prey proteins in order to activate reporter genes in yeast cells.[3] In this investigation, the enzyme 4CL1 was used as the "bait" and twenty-one potential interaction partners comprised the various "prey" proteins. The reporter genes that were expressed following a successful interaction included HIS3, ADE2, AUR1-C, and MEL1.1

C. Transformation and selection plates

Transformations were performed using the lithium acetate transformation protocol. AH109 yeast transformants consisted of the "bait" (DNA binding domain pGBKT7 containing 4CL1 cloned in frame with GAL4) and the "prey" (DNA activating domain pGADT7 expressing ATPD, AT1G11125, AT1G44160, AT2G22360, AT3G10910, AT4G26860, MYB4, or PPa5 as seen in Figure 1). Additionally, prey proteins were co-transformed with pGBKT7 empty vector which served as negative controls. PCR confirmed the successful transformation. The DNA was plated on two synthetically defined nutrition-deficient cultures mediums: SD-Leu/-Trp and SD/-His/-Leu/-Trp and incubated overnight at 30°C.[1]

D. Confirmation of genuine positive interactions

Once all protein complexes indicated self-activity, distinguishing genuine positive from false positive interactions was done by observing growth and coloration that resulted from the expression of the reporter genes on various dropout media.[1] Synthetically defined medium plates minus leucine, histidine, and tryptophan (triple dropout) were used with various amounts of

3AT, to suppress the expression of HIS3 reporter gene. SD/-Leu/-Trp medium supplemented with X-α-GAL (double dropout) provided blue coloration in successful colonies. SD-Leu/-Trp/-His/-Ade (quadruple dropout) selection plates provided a medium that would suppress the growth of yeast with false interactions, and a combination of these (SD-LTHA+X-GAL) was used for further confirmation of true interactions based on growth and coloration.

III. RESULTS

Primary screening indicated twenty-one candidates for a confirmation of a true interaction between ATPD and 4CL1. The plasmids were co-transformed with 4CL1 in AH109 yeast and via the yeast two-hybrid system, all the transformants grew on selective media (Figure 2). This indicates that self-activity was evident in all the candidates. To confirm if the interactions were genuine and not false positives based on non-specific interactions, 3-Amino-1,2,4-triazole (3AT) was used. Since the product of the HIS3 reporter, imidazole glycerol phosphate dehydratase is inhibited by 3AT, different concentrations of 3AT were used to suppress self-activation (Figure 3). In concentrations of 5 mmol and 10 mmol (3A and 3B), the growth of yeast that did not contain 4CL1 was visibly suppressed. In higher concentrations of 3AT (Figures 3E and 3F), inhibition exceeded the self activation threshold and suppressed the true interactions as well. The ATPD and 4CL1 interactions were then tested on SD-Leu/-Trp selection plates with X-α-GAL to confirm bait and prey interaction (Figure 4A). Since the yeast grew as blue colonies, there was a positive yeast two-hybrid interaction but no distinction between false and genuine interaction. ATPD and 4CL1 were then tested on SD/-His/-Leu/-Trp selection plates with 5 mmol of 3AT to suppress self-activity (Figure 4B). Genuine interaction was evident due to the visible colonies of yeast. Once genuine interaction was confirmed, the plasmids were then plated on SD/-Ade/-His/-Leu/-Trp and SD-LTHA X-GAL selection plates (Figures 4C and 5). The colonies without 4CL1 grew poorly if at all, whereas the yeast colonies with ATPD and 4CL1 grew well.

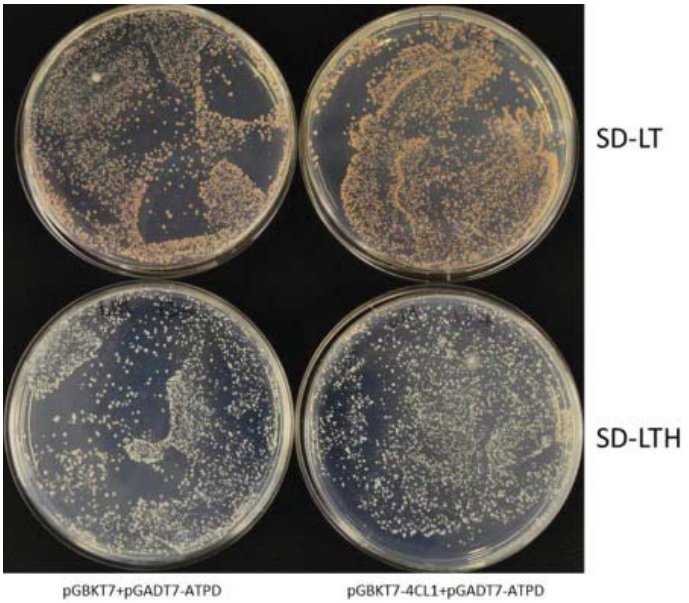

FIG 2. Results of protein-protein interactions between 4CL1 and a potential interacting partner in the yeast two hybrid system. The top two plates are Leu/Trp dropout plates. The bottom two plates are Leu/Trp/His dropout plates. Plates on the left contain yeast transformed with an empty pGBKT7 vector and the pGADT7 vector with an interacting partner (ATPD in these plates). These are the negative controls. Plates on the right contain yeast transformed with pGBKT7-4CL1 and pGADT7 with an interacting partner (ATPD on these plates).

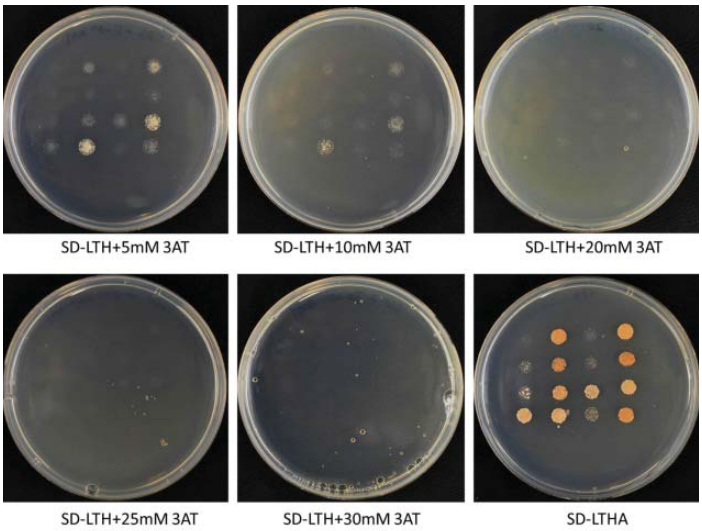

FIG 3. Growth of yeast on SD-LTH plates with varying concentrations of 3-Amino-1,2,4-triazole (3AT) to suppress false positive interactions. A. 5 mmol 3AT, B. 10 mmol 3AT, C. 20 mmol 3AT, D. 25 mmol 3AT, E. 30 mmol 3AT, F. 0 mmol 3AT; yeast was grown on SD-LTHA with no 3AT.

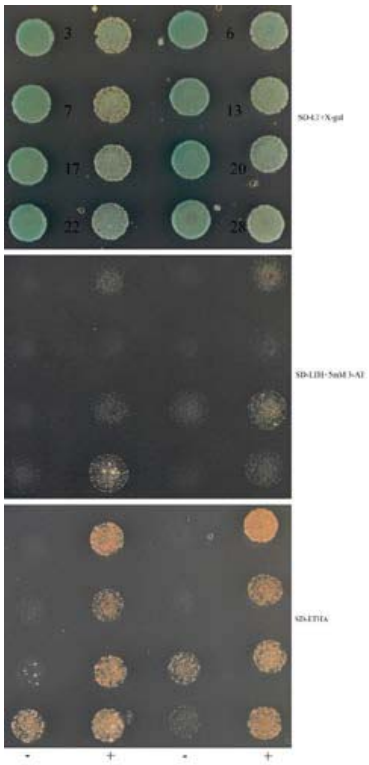

FIG 4. Testing of various reporter genes in the yeast. A. Yeast were grown on SD-LT+X-gal, in which the yeast will be blue if the reporter genes are expressed. B. Yeast were grown on SD-LTH+5 mmol 3AT, in which false positive interactions will be suppressed. C. Yeast were grown on SD-LTHA, which will also suppress false positive interactions. The first and third columns of each picture are yeast transformed without pGADT7-ATPD. The second and third columns are yeast transformed with pGBKT7-4CL1 and pGADT7-ATPD.

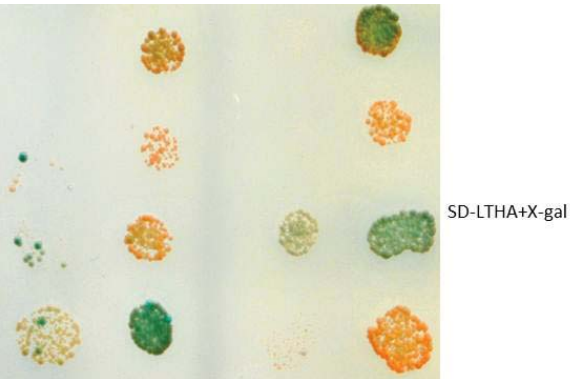

FIG 5. Growth of yeast transformants on quadruple dropout plates (SD-LTHA X-GAL).

IV. DISCUSSION

The expression of the reporter genes in Figure 2 suggests protein interactions in all samples, including negative controls. Since there was no 4CL1 present in these controls, this provides evidence of self-activation (false positive results) from some of the proteins investigated. Genuine positives are when both the bait (ATPD) and prey (4CL1) interact to activate the reporter genes (HIS3, ADE2, AUR1-C, MEL1). False positives occur when the prey (4CL1) activates the reporter genes in absence of the prey (ATPD). It was important to separate false positive results from genuine protein-protein interactions.

Varying concentrations of 3AT were used to hinder the expression of His3 in the yeast transformants in Figure 3. This caused yeast cells that were not harboring true interactions between 4CL1 and ATPD to be unable to express the gene and grow on the selective medium. By this method, we were able to observe which interactions were genuine positives.

After confirming these interactions, we tested the expression of other reporters in the yeast. The expression of reporter genes through successful interactions on medium containing X-gal causes the colonies to turn blue, as seen in Figure 4A. Genuine and false positives were able to yield these results.

The results of Figure 4B show how in yeast that do not have true interactions the suppression of histidine expression is severe. They will be able to grow in concentrations of 3AT up to 5 mmol. Only true interactions are able to survive higher concentrations, such as 25 mmol. Similar results are seen in Figure 4C, where yeast without 4CL1 have a more difficult time growing on SD-LTHA medium because they are unable to provide the necessary nutrients through the true expression of the reporter genes. The combination of these individual tests is seen in Figure 5. The yeast cells with genuine interactions were able to fully express all of the necessary reporter genes in order to grow on the SD-LTHA X-GAL medium. This indicates a stronger interaction between 4CL1 and ATPD, since they were able to grow on quadruple dropout media. This was the final confirmation that the interactions between 4CL1 and ATPD were genuine interactions.

V. CONCLUSION

4CL1 is a member of the 4CL family in *Arabidopsis*, which is involved in lignin formation and in the production of additional phenolic compounds in the phenylpropanoid pathway. ATPD is involved in the process of generating ATP, which is required to catalyze coenzyme thioesters in this pathway. By Investigating the proteins interacting with the enzymes in this pathway, scientists will be able to manipulate the pathway and, as a result, lignin production. The yeast two-hybrid method paired 4CL1 as bait to various prey proteins and observed their interactions via the expression of reporter genes. After results provided evidence of self-activation of prey proteins, the expression of various reporter genes was tested on double, triple, and quadruple dropout media in order to distinguish genuine from false positive interactions. Genuine interactions between *Arabidopsis* 4CL1 and various full-length and C-terminal ATPD were confirmed through this investigation. This understanding can be applied to future research involving the analysis of ATPD knock-down mutant lines of *Arabidopsis*.

VI. ACKNOWLEDGEMENTS

This work was made possible by the support of the US Department of Energy, National Science Foundation, as well as the Biology Department and Office of Educational Programs at Brookhaven National Laboratory. Special thanks are given to C.J. Liu and Xuebin Zhang for their support and instruction throughout the project.

VII. REFERENCES

1. Clontech Laboratories, Inc. Matchmaker Gold Yeast Two-Hybrid System User Manual. California: Clontech, 2010. Protein Interactions & Profiling. 30 Mar. 2010. Web. <http://www.clontech.com>.

2. Ehlting, Jurgen, Daniela Buttner, Qing Wang, Carl J. Douglas, Imre E. Somssich, and Erich Kombrink. “Three 4-coumarate:coenzyme A Ligases in *Arabidopsis Thaliana* Represent Two Evolutionarily Divergent Classes in Angiosperms.” *The Plant Journal* 19.1 (1999): 9-20. Print.

3. ”Two-Hybrid Screening.” Wikipedia. Wikimedia Foundation, 21 June 2012. Web. 31 July 2012. <http://en.wikipedia.org>

Electric field distribution nonlinearities in cylindrical and spherical plates in an electrostatic storage ring

Richie Chen
Department of Physics and Astronomy, Stony Brook University, Stony Brook, NY 11790
Yannis K. Semertzidis
Department of Physics, Brookhaven National Laboratory, Upton NY 11973

ABSTRACT

The proposed all-electric storage ring aims to detect the proton electric dipole moment (EDM) to an even higher precision than current EDM experiments. This experiment is of great interest to Brookhaven National Laboratory since EDM deals with the low-energy, high-precision frontier of particle physics which can possibly explore new physics beyond the current Standard Model. However, there may still be issues with the experiment. One of them is the limited acceptance of the particles in the storage ring. A.I. Papash, A.V. Smirnov, and C.P. Welsch's (PSW) *Non-linear and long term beam dynamics in an ultra-low energy storage rings* asserts that the electric field distribution nonlinearities in the storage ring is one of the factors that limit acceptance of particles. The results from their MAD-X tracking simulations using the OPERA computer code were benchmarked against the ELectrostatic Ion Storage ring, Aarhus (ELISA). A Fortran 77 program was used to perform tracking simulations similar to those using MAD-X. The electric field of cylindrical and spherical plates is dependent on the radius inverse and squared radius inverse respectively. Simulations of the cylindrical and spherical plates electric field is done with the exact functional form. The results from tracking simulations indicate that only at high initial angles are there radial nonlinearities. Even though there were radial nonlinearities, the radial nonlinearities are not as severe as PSW asserted. Therefore, the radius of the storage ring is not a huge factor in the limited acceptance of particles as they implied.

I. INTRODUCTION

Symmetry dictates that there should be an equal amount of matter and antimatter in the universe. However, the existence of matter demonstrates the broken symmetries. The electric dipole moment (EDM) can account for a symmetry violation source. The EDM is an intrinsic property of a particle. It is a measure of particle charge. A non-uniformly distributed charge on a particle produces has a nonzero EDM. The proposed Brookhaven National Laboratory (BNL) electrostatic storage ring aims to detect EDM of protons and deuterons to a sensitivity of 10^{-29} e · cm. This is at higher sensitivity than any current EDM experiments and can test theories beyond the SM. To illustrate how sensitive the instruments of the experiment are; suppose the proton was scaled to the size of the sun, measuring the EDM of the proton requires instrumentation sensitive to about 10 micrometers.

Asymmetry is the cause of excess matter over antimatter. They are attributed to the three discrete symmetries; charge conjugation (C), parity (P), and time reversal (T). C-symmetry is symmetry between particles and anti-particles. P-symmetry is mirrored symmetry. T-symmetry is time reversal transformation. The current SM of physics only has weak interaction CP violating source which accounts for some of the observed mass of the universe but not all. It is interesting to particle physicists to observe a non-zero EDM because it shows that parity symmetry and time reversal symmetries (P, T) are violated. Due to assumption that CPT symmetry is conserved, EDM is a CP violating source beyond the SM.

II. Experimental Method

The proposed all-electric storage ring, shown on figure 1, will indirectly measure the EDM of a proton by inducing an external electric field on the proton and observing the proton spin precession. Since the spin vector (s) is aligned with the EDM, this EDM (d) coupling to electric field (E) to determine spin is given by the equation (1).

$$\frac{d\vec{s}}{dt} = \vec{d} \times \vec{E} \tag{1}$$

Protons have a magic momentum and it can be fully utilized in an all-electric ring. Magic momentum is when the spin and momentum vector precesses at the same rate. If the spin is polarized before proton injection into storage ring, the magic momentum for protons maintains the spin vector and momentum vector parallel to each other horizontally. If a permanent EDM effect exists, then there will be a vertical precession of spin and momentum.3 This is shown on figure 2.

Measuring the EDM to a high sensitivity requires at least 1000 seconds.4 This is referred to as spin coherence time. Nevertheless, there may be factors influencing the particle storage times. A.I. Papash, A.V. Smirnov, and C.P. Welsch's (PSW) Non-linear and long term beam dynamics in an ultra-low energy storage rings asserts that the electric field distribution nonlinearities in the storage ring is one of the factors to the limited storage of particles. PSW found the dynamic aperture of the ELISA to be much smaller for the deflectors of spherical shape than the cylindrical deflectors. The decay rate is shown on figure 3. Ionized oxygen was used on ELISA and the number of ionized oxygen decreased exponentially and lost most of the particles in 60 seconds. PSW did tracking simulations and benchmarked it against the data collected from ELISA. Using Fortran, tracking simulations are performed under cylindrical deflectors and spherical deflectors with ELISA's radius and the proposed all-electric storage ring radius.

A Fortran editor and a compiler are used for program revision and program compilation. The Fortran program performs 4th order Runge-Kutta integration to solve beam and spin dynamics. Simulations with varying initial parameters were done such as momentum factor, different particle, energy and momentum of particle, radial and vertical electric focusing, angle, and cylindrical and spherical plates. Equations (2-5) of cylindrical plate and spherical plate electric field approximation are inputted into the Fotran program.6 All those parameters are done as a function of

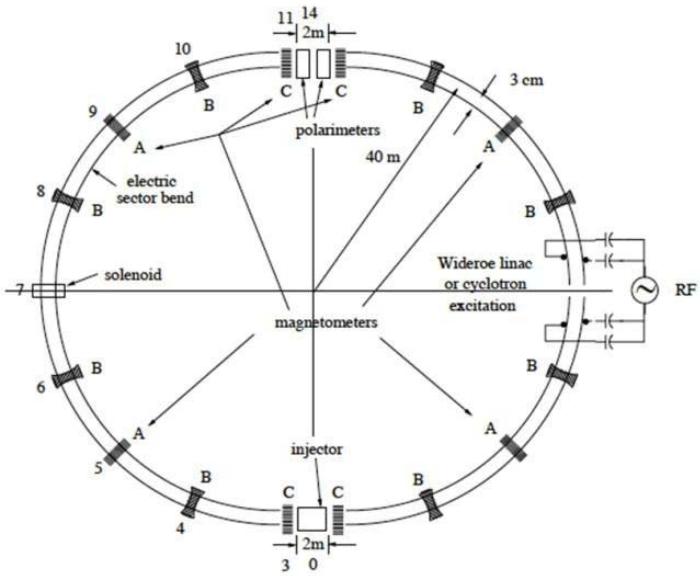

Figure 1.

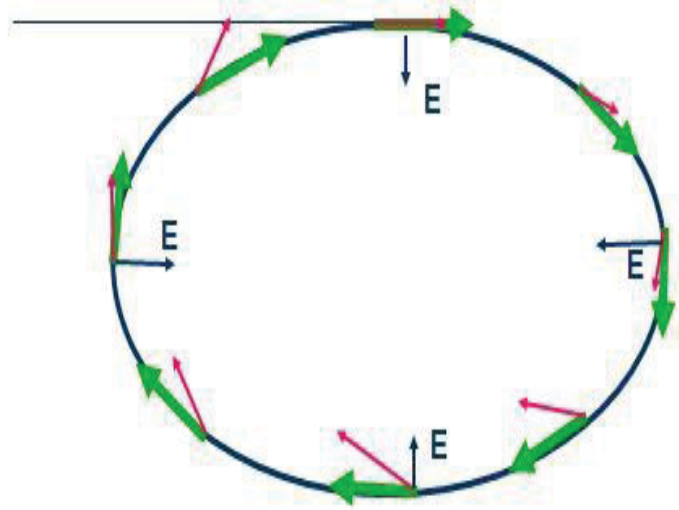

Figure 2.

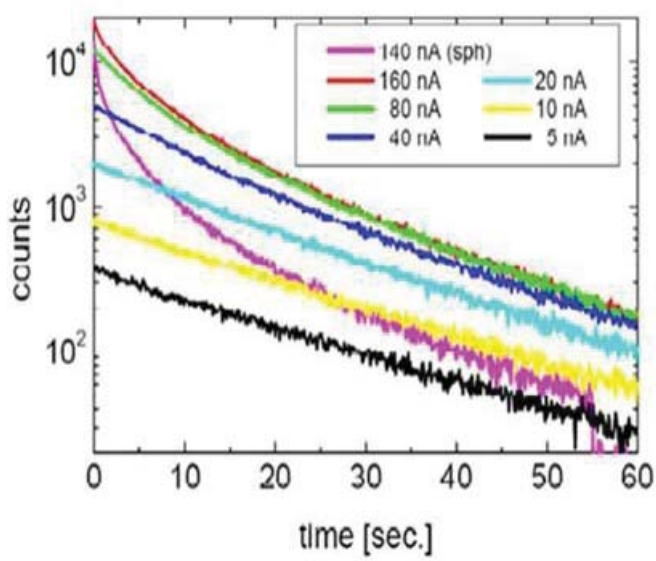

Figure 3.

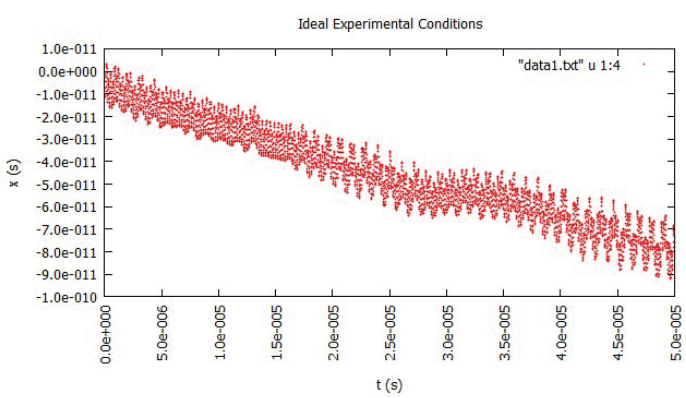

Figure 4: The ideal experimental conditions are protons traveling at the magic momentum with little to no momentum spread. Shown on the graph are minute oscillations of the particle to the order of 10 picometers, comparatively insignificant compared to the proposed 40 meter electrostatic storage ring.

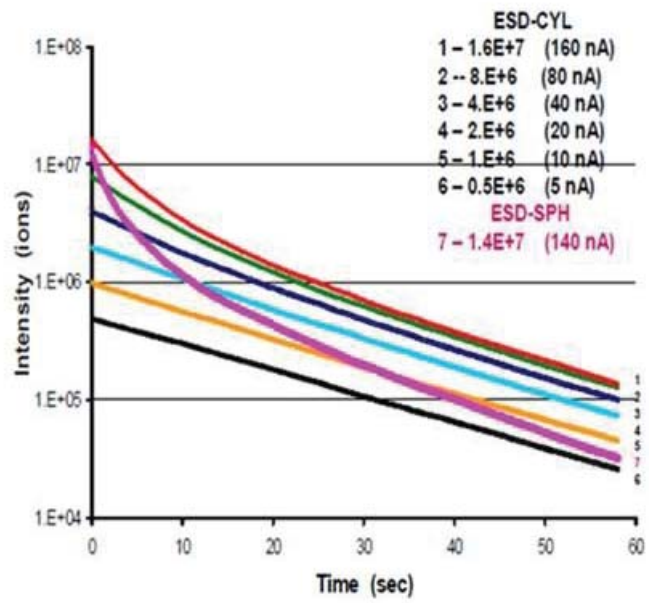

radius to see how initial parameters affect the acceptance of particles. The program data is graphed with. Data points were plotted mainly with phase space, Cartesian space, and radial location of particle as a function of time. The graphs are then inspected for nonlinearities.

Cylindrical Plates

$$E_R = E_0 \frac{R_0}{R} \tag{2}$$

$$E_y = 0 \tag{3}$$

Spherical Plates

$$E_R = E_0 \frac{R_0^2}{R^2}\left(1 - \frac{3y^2}{2R^2} + \frac{15y^4}{8R^4} + O(y^6) + \ldots\right) \tag{4}$$

$$E_y = E_0 \frac{R_0^2}{R}\left(\frac{y}{R} - \frac{3y^2}{2R^3} + O(y^5) + \ldots\right) \tag{5}$$

The nonlinearities are attributed to the higher order terms of the series expansion. The equations are inputted into the program along with the quadrupole electric field. These nonlinear term

may affect the acceptance of particles in the electrostatic storage ring. The cylindrical plates have a dependence of inverse radius. The spherical plates have a dependence of inverse radius squared.

I. Results

Tracking simulations of a proton at magic momentum with $\frac{\Delta P}{P} = 10^{-4}$ and electric focusing at 0.1 and different radii were performed.

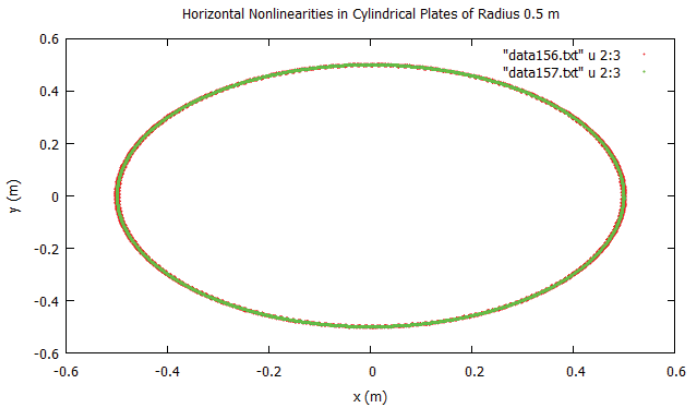

Figure 5 shows the horizontal electric field nonlinearities in cylindrical plates of radius 0.5 meters. The red plot is at the initial angle of 10^{-3} radians and the green plot at 10^{-2} radians.

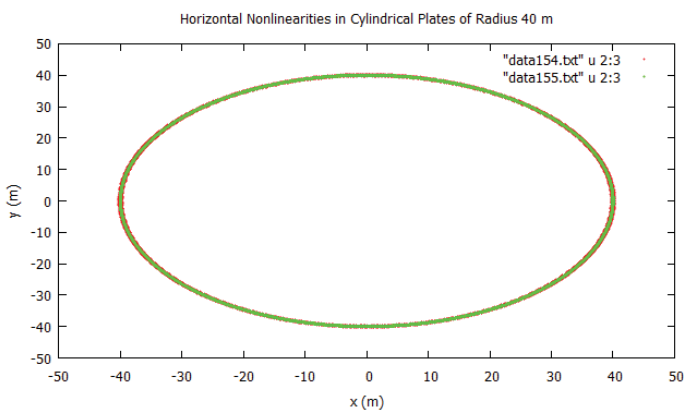

Figure 6 shows the horizontal electric field nonlinearities in cylindrical plates of radius 40 meters. The red plot is at the initial angle of 10^{-3} radians and the green plot at 10^{-2} radians. They almost overlap each other completely. Nonlinearities are not significant for both figure 5 and figure 6.

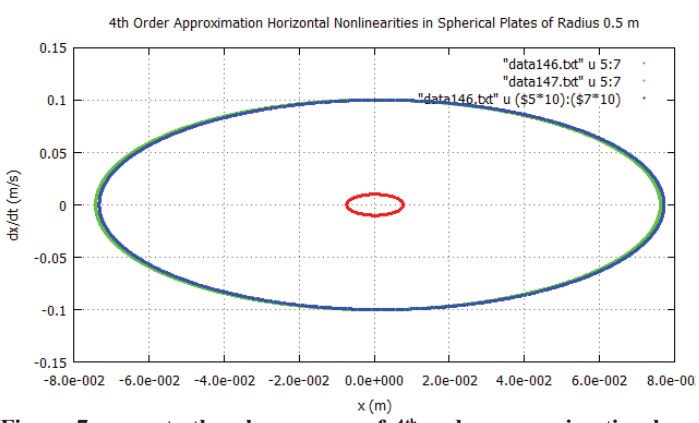

Figure 7 presents the phase space of 4th order approximation horizontal electric field nonlinearities in spherical plates of radius 0.5 meters. The red plot is at the initial angle of 10^{-3} radians, the green plot at 10^{-2} radians, and the blue plot is the red plot scaled by a factor of 10 to compare to the green plot. The blue and green does not directly overlap each other in the phase space plot. They are recognized as nonlinearities. Further plots with different axes are shown on figure 8 and figure 9.

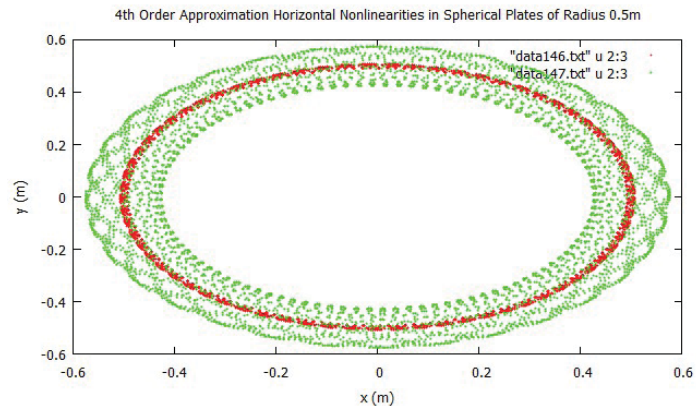

Figure 8 presents the simple x-y graph of 4th order approximation horizontal electric nonlinearities in spherical plates of radius 0.5 meters. The red plot is at the initial angle of 10^{-3} radians and the green plot at 10^{-2} radians.

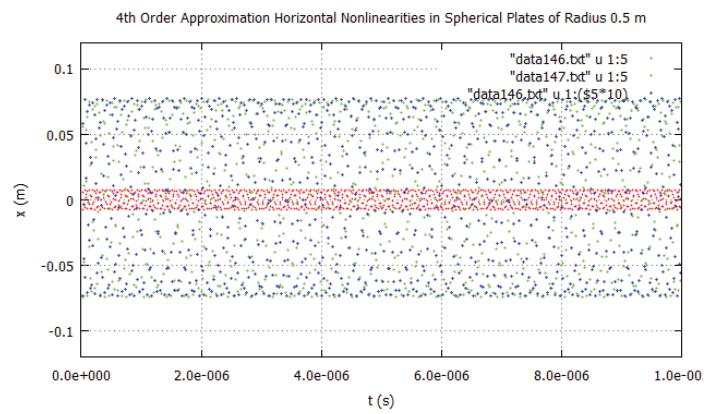

Figure 9 demonstrates the minute effect of nonlinearities in spherical plates of radius 0.5 meters. This is a time versus radial position of the particle graph. The red plot is at the initial angle of 10^{-3} radians and the green plot at 10^{-2} radians. The blue plot is scaled with a factor of 10 such that it can be compared to the green plot. A close inspection of the blue and green plotted data shows that the peak of blue is greater than that of green's and trough of blue is less than that of green's. These nonlinearities affect the particles by no more than a few percent.

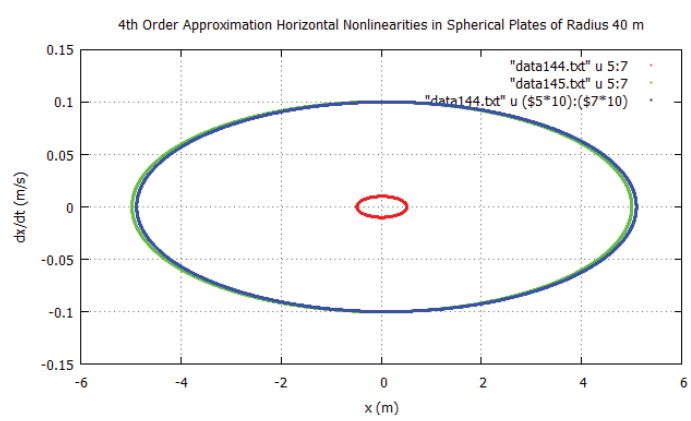

Figure 10 shows the phase space of the 4th order approximation horizontal nonlinearities in spherical plates of radius 40 meters. The red

plot is at the initial angle of 10^{-3} radians and the green plot at 10^{-2} radians. The blue and green does not directly overlap each other in the phase space plot. They are recognized as nonlinearities. Further plots with different axes are shown on figure 11 and figure 12.

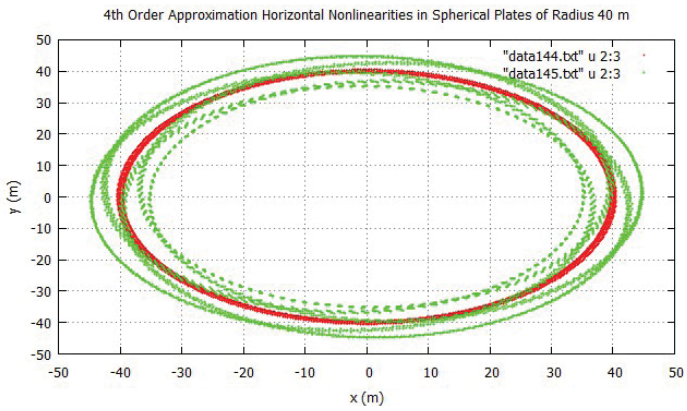

Figure 11 shows the simple x-y graph of 4th order approximation horizontal electric nonlinearities in spherical plates of radius 40 meters. The red plot is at the initial angle of 10^{-3} radians and the green plot at 10^{-2} radians.

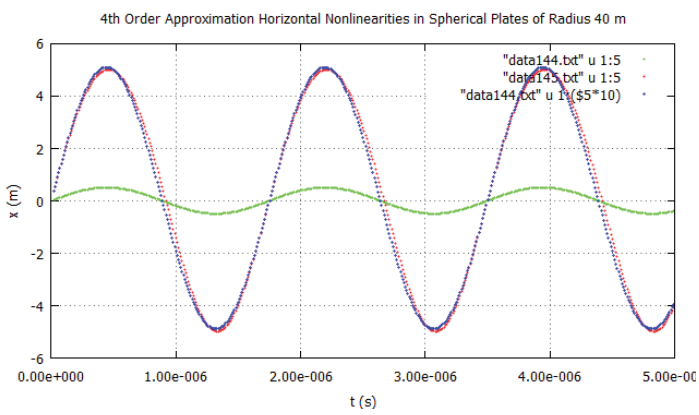

Figure 12 show that nonlinearities affect the 40 meter storage ring by no more than a few percent. This is a time versus radial position of the particle graph. The green plot is at the initial angle of 10^{-3} radians and the red plot at 10^{-2} radians. The blue plot is scaled with a factor of 10 such that it can be compared to the green plot. A close inspection of the green and red plotted data shows that the peak of blue is greater than that of red's and trough of blue is less than that of red's.

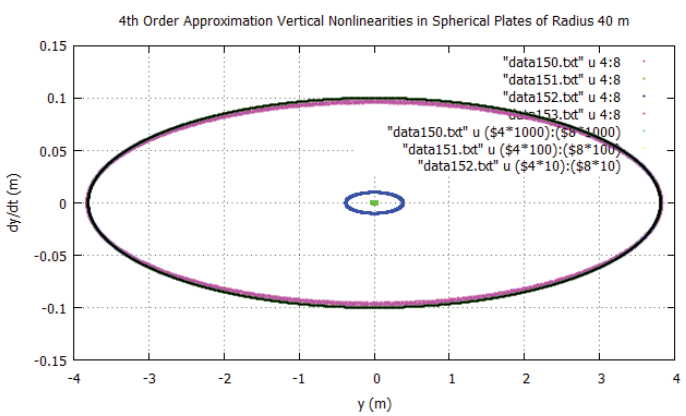

Figure 13 shows the 4th order approximation phase space vertical nonlinearities in spherical plates of radius 40 meters. The red plot is not shown due to the small size. Red, green, and blue plots are scaled to the size of the purple plot. Scaling them only shows one black plot because the scaled plots overlapped each other almost exactly due to the size of the graph. Fundamentally, it is a comparison between 10^{-4}, 10^{-3}, 10^{-2}, and 10^{-1} radians. The vertical nonlinearities does not have a huge influence over the particle.

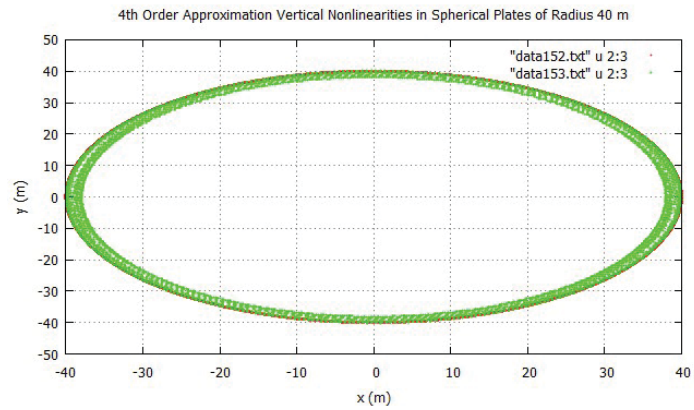

Figure 14 shows the simple x-y graph where the red plot is at an angle of 10^{-2} radians and the green plot at 10^{-1} radians.

II. Conclusion

Changing the initial angle of particle had a huge influence on electric field distribution nonlinearities especially for spherical plates. A large angle corresponds to a large equilibrium radius therefore the nonlinearities affect the particle more when displaced from equilibrium. For cylindrical plates, there were no graphically visible nonlinearities. The nonlinearities become more apparent for spherical plates at the scale of 10^{-2} radians. However, the experimental angle the proposed all-electric storage ring is at 10^{-4} radians. Furthermore, there seems to be more nonlinearity for a storage ring of a smaller radius due to greater nonlinear terms for the dependence of inverse radius. The horizontal and vertical nonlinearities are not as severe as stated by A.I. Papash, A.V. Smirnov, C.P. Welsch.

III. Acknowledgments

This research is made possible by The Department of Energy (DOE) Office of Science for funding SULI, the Science Undergraduate Laboratory Internship (SULI) for providing an enriching research experience, Brookhaven National Laboratory for serving as my host laboratory, Yannis K. Semertzidis for being a great mentor and guiding me throughout this research experience, William M. Morse for giving insightful mini-lectures, and Brandon Krouppa and Benjamin Kramer for their input in our interesting physics conversations.

IV. Works Cited

The Storage Ring EDM Collaboration. "A proposal to measure the proton electric dipole moment with sensitivity. (2011)

Yannis K. Semertzidis. "E-field radial and vertical dependence." (2011). Unpublished

A.I. Papash, A.V. Smirnov, C.P. Welsch. "Non-linear and long term beam dynamics in ultra-low energy storage rings."

Designing the electron Relativistic Heavy Ion Collider and Coherent electron Cooling Proof of Principle's 500 MHz systems

Shushanna Cherian
Mechanical Engineering, Stony Brook University, Stony Brook, New York, 11794
Joseph Tuozzolo
Collider-Accelerator Department, Brookhaven National Laboratory, Upton, New York, 11973

ABSTRACT

The Collider Accelerator Department (C-AD) at Brookhaven National Laboratory, is working to design the electron Relativistic Heavy Ion Collider (eRHIC) and the coherent electron cooling proof-of-principle experiment (CeC PoP). My engineering assignment entailed the layout of the major pieces of components of eRHIC's ring using Creo Elements/Pro three-dimensional (3D) computer-aided design software. Layouts consisting of superconducting energy recovery linacs, beam dumps, dipole magnets, quadruple magnets, and building layout for the supporting electronics were added into a 3D model of RHIC's 10:00 experimental area. This assembly allows the accurate evaluation of available space and the building modifications/additions needed. My CeC PoP assignment involved reconfiguring the 500MHz RF waveguides for the cavities to clear the superconducting magnets in RHIC, placing it into the 3D model of the 02:00 experimental area, comparing costs, designing a support frame and analyzing the frame using statics and mechanics of materials principles to prepare an engineering report for departmental approval.

I. INTRODUCTION

eRHIC will be the first fully polarized electron-ion (EIC) collider in the world. An electron ring and accelerator components will be added to the existing 10:00 experimental area of RHIC (Figure 1). Two stacked energy recovery linear accelerators (ERLs) will accelerate electrons that will collide with heavy ions or protons accelerating in RHIC's ring. The collider's purpose is to further explore matter and the "glue" that is suggested to control the heavy nuclei's internal structure.

CeC PoP will "cool" protons or ions at very high energies to allow more tightly packed beam bunches and more experimental collisions for eRHIC. The first components for this experiment, the 500MHz RF cavities, will be installed this fall at the 02:00 experimental area of RHIC (Fig. 2). The 500MHz system consists of two cavities that will supply energy chirps to the electron beam in order to lower the velocity of the electrons at the start of the bunch.

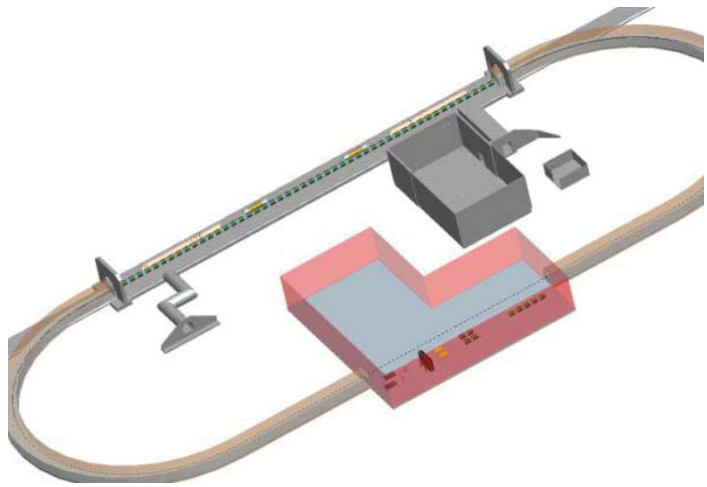

Figure 1: eRHIC Ring

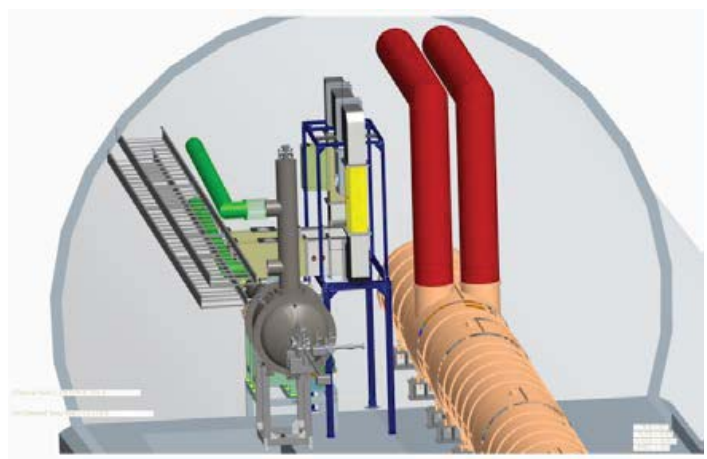

Figure 2: CeC PoP 500MHz System

II. THEORY/METHODS

For both projects, lead mechanical engineers and scientist supplied the necessary information to create 3D scaled models and assemblies using Creo Elements/Pro. Models of the 02:00 and 10:00 experimental areas as well as superconducting energy recovery linacs, beam dumps, dipole magnets, quadruple magnets of eRHIC, and the 500MHz system components were already created by members of the C-AD team. Subsequently any additional new components were modeled, such as eRHIC's ring, service building, concrete padding and shields--all components of the 500MHz system supporting frame. An assembly of eRHIC (Figure 1) was created and then added to the 10:00 experimental area as a subassembly.

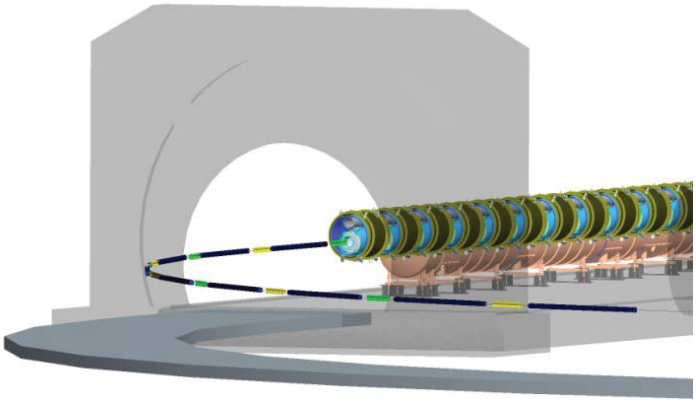

Figure 3: Magnets and Cryogenic Modules

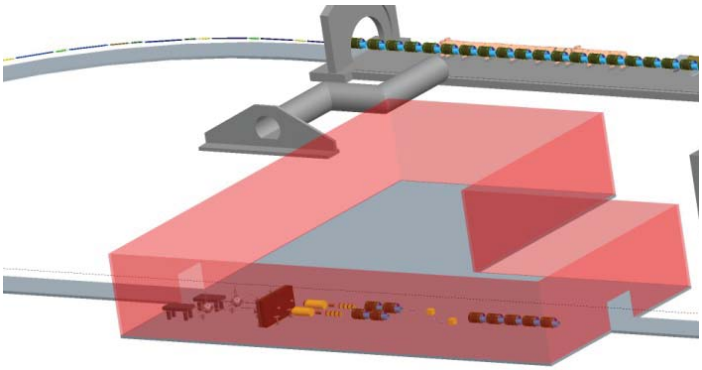

Figure 4: Service Building

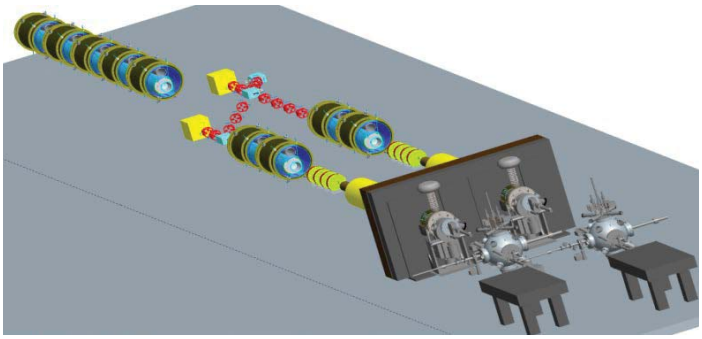

Figure 5: Linac Section

An assembly of the 500MHz RF waveguide configuration was created. Once the assembly was completed, a structural analysis was done to design a frame to support the waveguides, phase shifter, and both bi-directional weights. The center of gravity (CG) of each component in the RF waveguide configuration was found using Cero analysis tools and then located on 2D drawings of the configuration (Figure 6). A supporting frame was designed based on common axes of CG and high density areas. The manufacture used for the supporting frame is Unistrut. All the profiles of the components that were used were provided on the Unistrut website which was then imported into Cero and extruded. An assembly of the design was created (Figure 7) and added as a subassembly to the 500MHz RF waveguide system assembly (Figure 8), which was then added to the 02:00 experimental area assembly (Figure 2). Each member of the frame was individually analyzed using principles of statics and mechanics of materials.

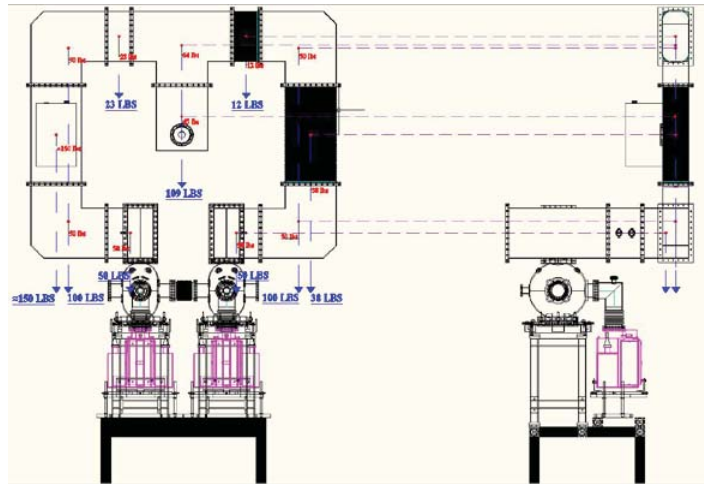

Figure 6: Center of Gravity

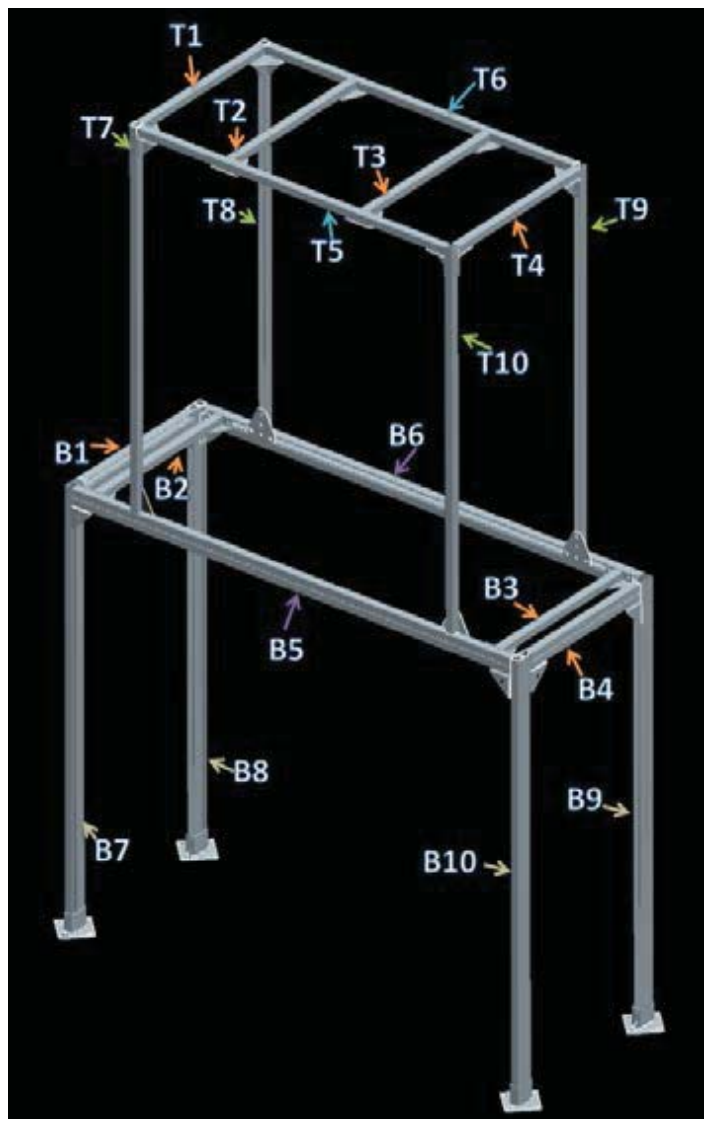

Figure 7: Supporting Frame

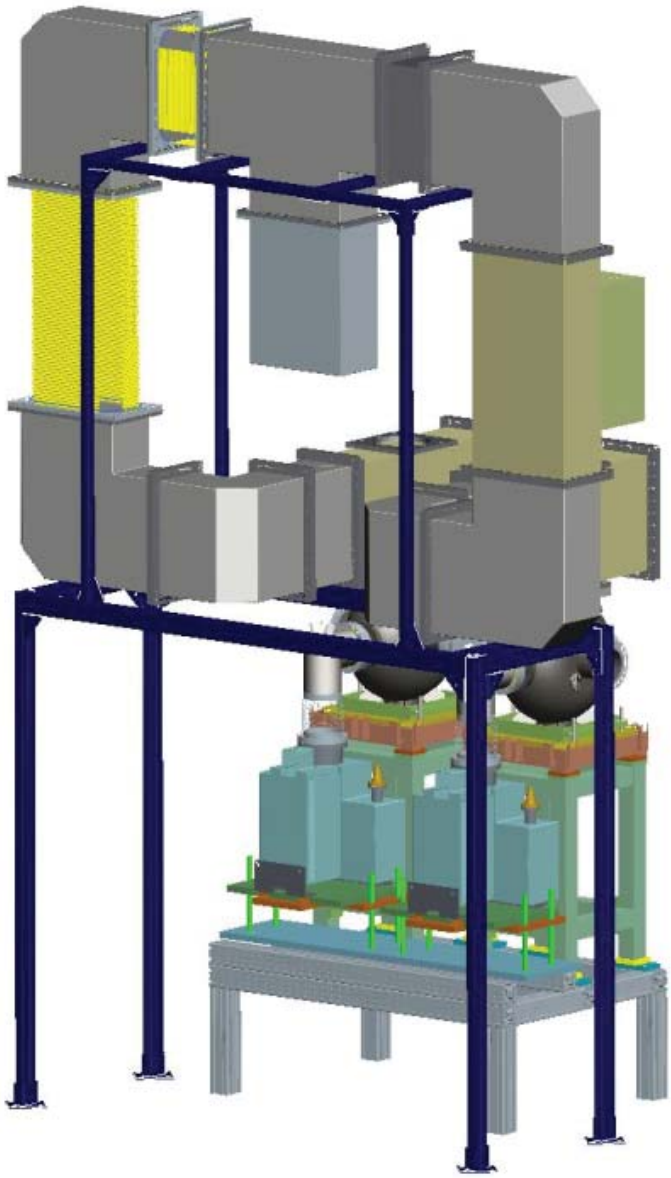

Figure 8: 500MHz RF waveguide assembly

A. 500MHz RF Waveguide Frame Analysis

Weights of the components in the 500MHz RF Waveguide configuration were received from the manufactures, Mega Industries. The remaining components such as the phase shifter and bi-directionals were over approximated. Maximum allowable uniform loads, moments, and deflections were found for every member based on their channel type and actual length using linear interpolation of the provided Unistrut values. Members of the supporting frame (as shown in Figure 7) were analyzed using point loads instead of uniformly distributed loads because these calculations would provide the worst case reactions, moments, and deflections.

Top members T1-T4 and Bottom members B1-B4 were analyzed using three different scenarios. The first scenario is represented by equations 1 through 4, where the point load is consider to be in the middle the beam. The second considers the actual distance of the load from each end of a fixed beam, as shown in equations 5-8. Lastly, calculations were done using a simple beam with the actual location of the load in equations 9-12. From these three different calculations, the highest value of reactions, moment, and deflection of each member were used to compare to the maximum allowable uniform loads and moments.

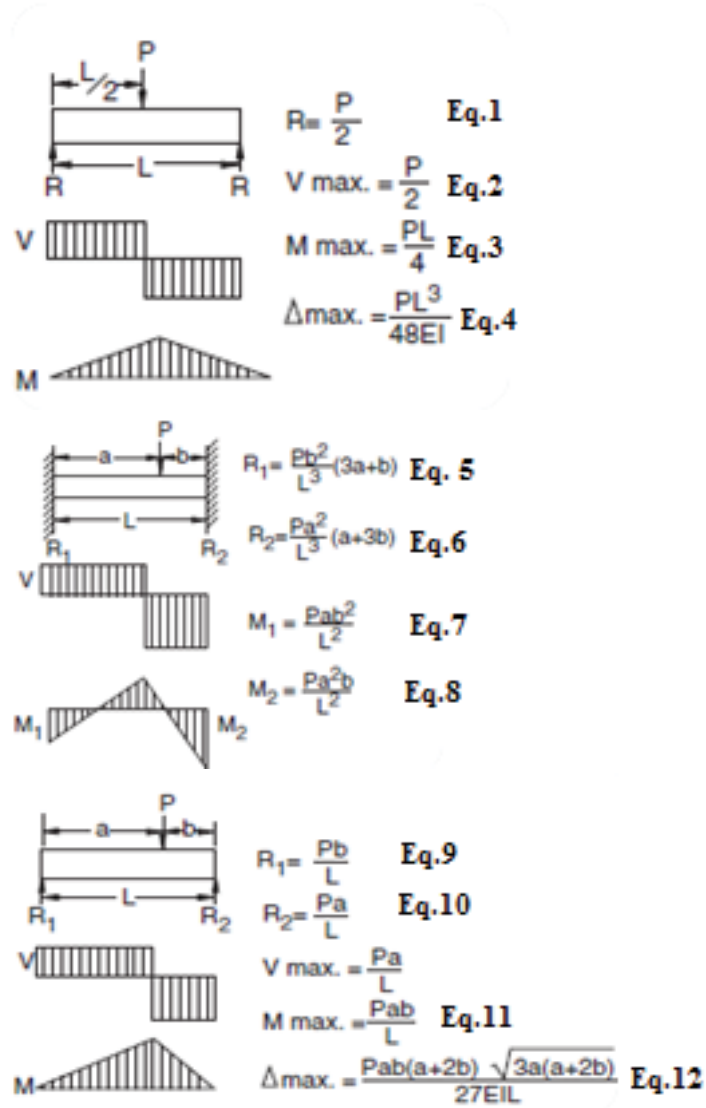

The two loads on T5 and T6 were taken to be the reactions of members T2 and T3. The loads were considered to be concentric with the beam rather than on one surface and equations 13-16 were used.

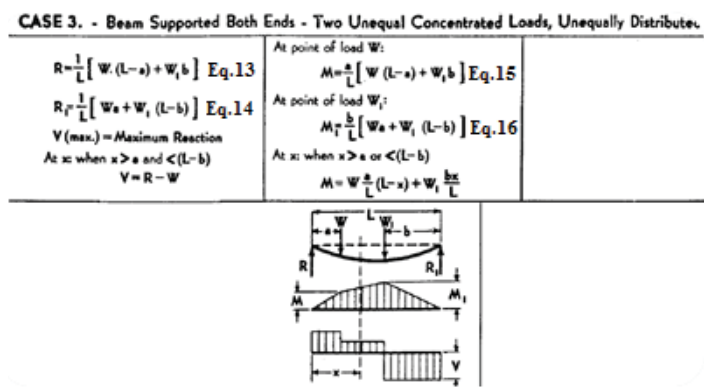

Column loads are applied to T7-T10 where a free top and fixed bottom support condition exist. From the Unistrut General Engineering Catalog – No.17 a value of the effective length factor based on end boundary conditions was given to be K=1.2, as shown in Figure 9. The critical buckling load was determined

from equation 17. Equation 18 was then used to find the critical stress. Equations 19 through 21 were used to calculate the maximum deflection, moment, and stress under conditions of eccentricity.

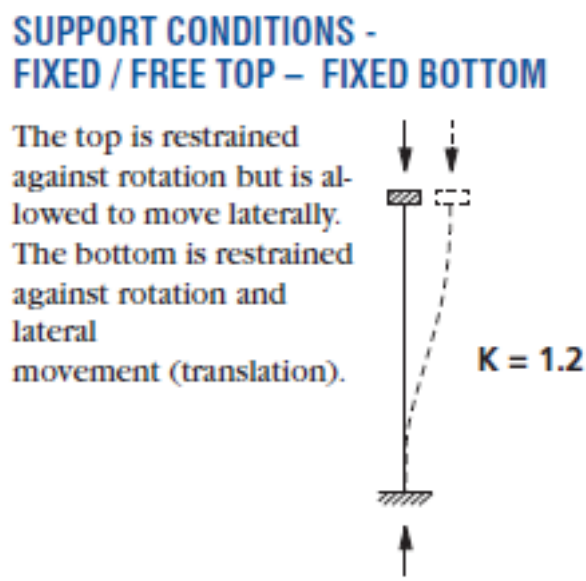

Figure 9: Support Condition

The critical buckling load P_{cr} for columns is theoretically given by

$$P_{cr} = \frac{\pi^2 E I}{(K L)^2} \quad \text{Eq.17}$$

$$\sigma_{cr} = \frac{P_{cr}}{A} \quad \text{Eq.18}$$

where, I = moment of inertia about axis of buckling

K = effective length factor based on end boundary conditions

ymax=e * (sec((π/2) * ((P/Pcr)^.5) -1))	Eq.19
Mmax P* (e + ymin)	Eq.20
σmax = (P/A) + (M/Sy)	Eq.21

For beams B5 and B6, the reactions at each end were found using the summation of forces under static conditions (Figure 10) using equations 22 and 23. The shearing forces and moments were derived at each point were a load is applied (equations 24-39).

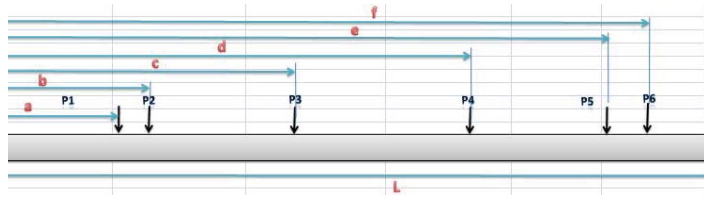

Figure 10: B5 and B6 free body diagram

ΣFy= 0 = P1 + P2 + P3 + P4 + P5 + P6 - R1 - R2	
R1 = P_{Tot} - R2	
ΣM_{R1}= 0 = P1*a + P2*b + P3*c + P4*d + P5*e + P6*f - R2*L	
R2 = (P1*a + P2*b + P3*c +P4*d + P5*e + P6*f)/L	Eq.22
ΣM_{R2} = 0 = P6*a + P5*b + P4*c + P3*d + P2*e + P1*f - R1*L	
R1 = (P6*a + P5*b + P4*c + P3*d + P2*e + P1*f)/L	Eq.23

Using the same methods, B5 and B6 were also evaluated for a hypothetical situation where a 300lb person would stand at the center of the beam as shown in Figure 11 (equations 40-59).

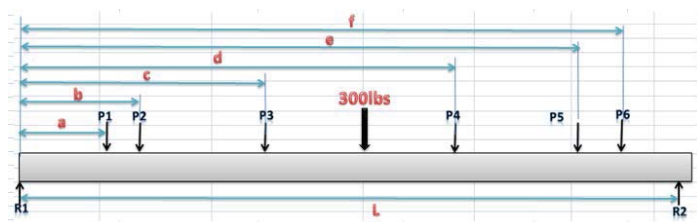

Figure 11: B5 and B6 hypothetical free body diagram

Mx & Vx
MR1= 0
VR1= -R1
MP1= -R1*a
VP1= -R1 + P1
MP2= -R1*b + P1*(b-a)
VP2= -R1 + P1 + P2
MP3= -R1*c + P1*(c-a) + P2(c-b)
VP3= -R1 +P1 + P2 + P3
MP4= -R1*d + P1*(d-a) + P2*(d-b) + P3*(d-c)
VP4= -R1 +P1 + P2 + P3 + P4
MP5= -R1*e + P1*(e-a) +P2*(e-b) + P3*(e-c) + P4*(e-d)
VP5= -R1 +P1 + P2 + P3 + P4 + P5
MP6= -R1*f + P1*(f-a) +P2*(f-b) + P3*(f-c) + P4*(f-d) + P5*(f-e)
VP6= -R1 +P1 + P2 + P3 + P4 + P5 +P6
MR2= -R1*L + P1*(L-a) +P2*(L-b) + P3*(L-c) + P4*(L-d) + P5*(L-e) + P6*(L-f)
VR2= -R2

Eq. 24-29

$\Sigma F_y = 0 = P1 + P2 + P3 + 300lbs + P4 + P5 + P6 - R1 - R2$
$R1 = P_{Tot} + 300lbs - R2$
$\Sigma M_{R1} = 0 = P1*a + P2*b + P3*c + 300lbs*L/2 + P4*d + P5*e + P6*f - R2*L$
$R2 = (P1*a + P2*b + P3*c + 300lbs*L/2 + P4*d + P5*e + P6*f)/L$
$\Sigma M_{R2} = 0 = P6*a + P5*b + P4*c + 300lbs*L/2 + P3*d + P2*e + P1*f - R1*L$
$R1 = (P6*a + P5*b + P4*c + 300lbs*L/2 + P3*d + P2*e + P1*f)/L$

Eq.40

Eq.41

The last set of member analyzed were columns B7 through B10. The columns were examined using the same conditions and equations as columns T7-T10.

B. 500MHz RF Waveguide Frame Results

All of the equations were computed in Excel. An input table was created for all members as shown in Figure 12. The orange cells indicate the required user input and are linked to their associated equations. The calculations for every member was evaluated and displayed in an output table shown in figure 13.

Moment values were compared to the channels' allowable moment values shown in Figures 14 and 15. The calculated maximum allowable uniform loads and deflections was then compared to values in Figure 16 that were found using linear interpolation based on individual member spans.

M_x & V_x
MR1= 0
VR1= -R1
MP1= -R1*a
VP1= -R1 + P1
MP2= -R1*b + P1*(b-a)
VP2= -R1 + P1 + P2
MP3= -R1*c + P1*(c-a) + P2(c-b)
VP3= -R1 +P1 + P2 + P3
M300lbs= -R1*L/2 + P1*(L/2-a) + P2*(L/2-b) + P3*(L/2-c)
VP4= -R1 +P1 + P2 + P3 + 300lbs
MP4= -R1*d + P1*(d-a) + P2*(d-b) + P3*(d-c) + 300lbs*(d-L/2)
VP4= -R1 +P1 + P2 + P3 + 300lbs + P4
MP5= -R1*e + P1*(e-a) +P2*(e-b) + P3*(e-c) + 300lbs*(e-L/2) + P4*(e-d)
VP5= -R1 +P1 + P2 + P3 + 300lbs + P4 + P5
MP6= -R1*f + P1*(f-a) +P2*(f-b) + P3*(f-c) + 300lbs*(f-L/2) + P4*(f-d) + P5*(f-e)
VP6= -R1 +P1 + P2 + P3 + 300lbs + P4 + P5 +P6
MR2 = -R1*L + P1*(L-a) +P2*(L-b) + P3*(L-c) + 300lbs*(L-L/2) + P4*(L-d) + P5*(L-e)
VR2= -R2

Eq.42-59

INPUTS

T1-T4

Span	Load Distances		Member	Load (lbs)
26.00	a (in)	9.00	T1	73.00
	b (in)	17.00	T2	31.50
			T3	42.50
			T4	62.00

Channel: P1000

T5, T6

Span	Load Distances	
62.52	a (in)	17.33
	b (in)	18.50

Channel: P1000

T7-T10

Span	K	e
71.36	1.20	0.92

Channel: P1000

B1, B4

Span	Load Distances		Member	Load (lbs)
22.75	a (in)	7.37	B1	200.00
	b (in)	15.38	B4	38.00

Channel: P1001C

B2, B3

Span	Load Distances		Member	Load (lbs)
25.50	a (in)	8.75	B2	100.00
	b (in)	16.75	B3	100.00

Channel: P1000

B5-B6

Span	Load Distances			Bi-Dirc Weight	100.00
89.21	Load	Distance	in		
	R1	0.00	0.00	Weight of Person	300.00
	P1	a	3.49		
	P2	b	12.53		
	P3	c	29.37		
	P4	d	60.20		
	P5	e	76.67		
	P6	f	85.71		
	R2	L	89.21		

Channel: P1001C

B7-B10

Span	K	e
79.65	1.20	1.68

Channel: P1001C

Figure 12: Input Table

OUTPUTS

Channel: P1000 — BEAM

T1		T2	
R1 (lbs)	52.81	R1 (lbs)	22.79
M1 (lbs*in)	474.50	M1 (lbs*in)	204.75
R2 (lbs)	36.50	R2 (lbs)	15.75
M2 (lbs*in)	474.50	M2 (lbs*in)	204.75
D max.	0.00	D max.	0.00

T3		T4	
R1 (lbs)	30.75	R1 (lbs)	44.86
M1 (lbs*in)	276.25	M1 (lbs*in)	403.00
R2 (lbs)	21.25	R2 (lbs)	31.00
M2 (lbs*in)	276.25	M2 (lbs*in)	403.00
D max.	0.00	D max.	0.00

Channel: P1000 — BEAM

T5		T6	
R1 (lbs)	25.57	R1 (lbs)	17.67
M1 (lbs*in)	443.07	M1 (lbs*in)	306.20
R2 (lbs)	27.97	R2 (lbs)	19.33
M2 (lbs*in)	517.28	M2 (lbs*in)	357.49
P1	22.79	P1	15.75
P2	30.75	P2	21.25

Channel: P1000 — COLUMN

T7		T8	
P	78.38	P	54.17
ymax	0.01	ymax	0.01
Mmax	72.69	Mmax	50.03
σmax	501.10	σmax	345.28

T9		T10	
P	50.33	P	72.82
ymax	0.01	ymax	0.01
Mmax	46.45	Mmax	67.47
σmax	320.63	σmax	465.23

Channel: P1001C — BEAM

B1		B4	
R1 (lbs)	150.58	R1 (lbs)	28.61
M1 (lbs*in)	1137.50	M1 (lbs*in)	216.13
R2 (lbs)	100.00	19.00	0.00
M2 (lbs*in)	1137.50	M2 (lbs*in)	216.13
D max.	0.01	D max.	0.00

Channel: P1000 — BEAM

B2		B3	
R1 (lbs)	72.76	R1 (lbs)	72.76
M1 (lbs*in)	637.50	M1 (lbs*in)	637.50
R2 (lbs)	50.00	R2 (lbs)	50.00
M2 (lbs*in)	637.50	M2 (lbs*in)	637.50
D max.	0.00	D max.	0.01

Channel: P1001C — BEAM

B5		B6	
R1 (lbs)	250.78	R1 (lbs)	103.63
R2 (lbs)	246.78	R2 (lbs)	100.87
Mx (lbs*in)		Mx (lbs*in)	
M_{R1}	0.00	M_{R1}	0.00
M_{P1}	-876.08	M_{P1}	-362.03
M_{P2}	-2484.75	M_{P2}	-846.67
M_{P3}	-4162.49	M_{P3}	-837.56
M_{P4}	-4151.10	M_{P4}	-820.87
M_{P5}	-2498.21	M_{P5}	-811.95
M_{P6}	-932.75	M_{P6}	-352.15
M_{R2}	-73.46	M_{R2}	0.26

With Weight of Person at center

B5		B6	
R1 (lbs)	400.78	R1 (lbs)	254.31
R2 (lbs)	396.78	R2 (lbs)	250.87
Mx (lbs*in)		Mx (lbs*in)	
M_{R1}	0.00	M_{R1}	0.00
M_{P1}	-1400.11	M_{P1}	-888.41
M_{P2}	-4364.28	M_{P2}	-2734.66
M_{P3}	-8567.96	M_{P3}	-5262.85
M_{Person}	-10847.24	M_{Person}	-7549.79
M_{P4}	-8501.19	M_{P4}	-5211.53
M_{P5}	-4378.09	M_{P5}	-2743.57
M_{P6}	-1456.81	M_{P6}	-934.05
M_{R2}	-73.46	M_{R2}	-59.94

Channel: P1001C — COLUMN

B7		B8	
P	401.35	P	203.63
ymax	0.06	ymax	0.03
Mmax	696.30	Mmax	347.38
σmax	1561.78	σmax	782.22

B9		B10	
P	119.87	P	275.39
ymax	0.03	ymax	0.04
Mmax	203.05	Mmax	472.66
σmax	457.97	σmax	1062.81

Figure 13: Output Table

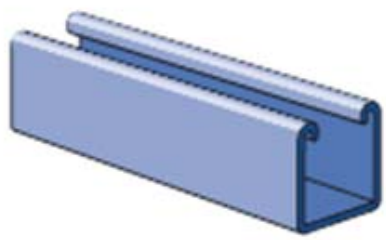

Wt/100 Ft:189 Lbs (281 kg/100 m)
Allowable Moment 5,070 In-Lbs (570 N•m
12 Gauge Nominal Thickness .105" (2.7mm

Figure 14: P1000 Properties

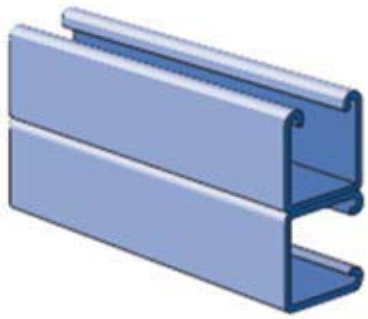

Wt/100 Ft: 378 Lbs (562 kg/100 m)
Allowable Moment 15,950 In-Lbs (1,800 N•m)
12 Gauge Nominal Thickness .105" (2.7mm)

Figure 15: P1001C Properties

III. CONCLUSIONS

eRHIC's assembly represents an accurate 3D model that will assist the C-AD team in evaluating their concepts and initiate corrections to reach a final detailed design. An engineering report for departmental approval is ready for the 500MHz RF waveguide supporting frame. Based on the result of the calculations, the supporting frame is structural sound. The properties of every member were designed not to exceed 70% of the maximum allowable properties. The 500MHz RF cavity system is accurately assembled in Creo, including all hardware, allowing for the first components of the CeC Pop's experiment to be ordered and installed.

IV. ACKNOWLEDGEMENTS

I would like to thank my mentor Joseph E. Tuozzolo for his help and guidance during my time at BNL this summer. His supervision and direction has made my time here an enhancing experience. Furthermore, I would like to thank the SULI program for giving this opportunity to take part in such an esteemed internship program.

- U.S. Department of Energy (DOE)
- Office of Educational Programs (OEP)
- National Science Foundation (NSF)
- Brookhaven National Laboratory (BNL)
- Collider Accelerator Department (C-AD)
- Louis Stokes Alliance for Minority Participation (LSAMP)

Structual Analysis Member T1-T4

Beam Loading	Span	Max. Allowable Uniform Load	Deflection at uniform Load
Through Linear Interpolation	26.00	1596.67	0.07
	Using Axis 1-1		
Moment of Inertia	0.185 IN^4		

Structual Analysis Member B1, B4

Beam Loading	Span	Max. Allowable Uniform Load	Deflection at uniform Load
Through Linear Interpolation	22.75	3532.29	0.01
	Using Axis 2-2		
Moment of Inertia (IN^4)	0.47		

Structual Analysis Member B2, B3

Beam Loading	Span	Max. Allowable Uniform Load	Deflection at uniform Load
Through Linear Interpolation	25.50	1620.00	0.07
	Using Axis 1-1		
Moment of Inertia (IN^4)	0.19		

Structual Analysis Member T5, T6

Beam Loading	Span	Max. Allowable Uniform Load	Deflection at uniform Load
Through Linear Interpolation	62.52	654.83	0.38
	Using Axis 1-1		
Moment of Inertia	0.185 IN^4		

Structual Analysis Member T7- T10

Column Loading	Span	Max. Allowable Load @ Slot Face	Max Column Load @ CG K=1.2
Through Linear Interpolation	71.36	2096.00	2429.87
	Using Axis 1-1		
Moment of Inertia	0.185 IN^4		
Section Modulus	0.202 in^2		

Structual Analysis Member B5- B6

Beam Loading	Span	Max. Allowable Uniform Load	Deflection at uniform Load
Through Linear Interpolation	89.21	1296.26	0.44
	Using Axis 2-2		
Moment of Inertia (IN^4)	0.47		

Structual Analysis Member B7- B10

Column Loading	Span	Max. Allowable Load @ Slot Face	Max Column Load @ CG K=1.2
Through Linear Interpolation	79.65	5333.13	7439.13
	Using Axis 2-2		
Moment of Inertia (IN^4)	0.47		
Section Modulus (in^2)	0.58		
Area (IN^2)	1.11		

Figure 16: Member Max. Allowable Properties

Analysis and Characterization of Viscous Biofuel Sprays Using Flash Atomization Techniques

Thomas Chiesa
Chemical Engineering, Stony Brook University, Stony Brook, NY 11790
Dr. Thomas Butcher
Sustainable Energy Technologies Department, Brookhaven National Laboratory, Upton, NY 11973

ABSTRACT

Spray atomization is a process by which a liquid is broken up into fine droplet sizes. Low viscosity fuels can be easily atomized with current nozzle technology, but as the viscosity increases the fuel fails to atomize into small enough droplets, which can lead to poor and incomplete combustion. The goal of the research is to use a technique called flash atomization to attempt to break up more viscous biofuels. Flash atomization uses the effect of phase change to help burst the viscous fuel into smaller droplet regimes just as it exits the nozzle. A binary liquid mixture is heated so that the more volatile liquid in the mixture will go into the vapor phase when the liquid is sprayed from the nozzle. In the Sustainable Technologies division at Brookhaven National Lab, nozzle spray characterization is being done on these viscous biofuels to adjust the spray atomization process to help burn more viscous fuels. This research is meant to help aid in the future transition to biofuel technology by ensuring that the fuels that are produced can be burned efficiently. Using a 3R Malvern Spraytec laser, the droplet size distributions were measured for different biofuel mixtures in order to see if the optimal droplet sizes could be achieved. In the experiments conducted 70, 80, 95, and 100% (by weight of glycerol to water mixtures) were heated and atomized with the laser to characterize the droplet distribution. The results showed that the Sauter Mean Diameter (SMD) of the spray decreases linearly at elevated temperatures. The SMD of a 95% glycerol-water mixture was found to have a minimum droplet diameter of 17 microns at 450°F, demonstrating that flash atomization is an effective method for viscous fuel break-up.

I. INTRODUCTION

Combustion engineering, the primary focus of this reearch, is the use of fuel chemistry, fluid mechanics, heat transfer, and thermodynamics to optimize flame quality and burning. The combustion of typical fuels such as oil, natural gas, and diesel fuels have been continually optimized over several decades, but a new challenge for combustion technology is on the rise with the introduction of biofuels. A potential problem with many biofuels is their high viscosity. Due to increased intermolecular polarity, many of the fuels tend to be thick and resist flow. This increased viscosity and surface tension causes major issues for combustion. A key aspect of combustion is spray atomization, the breakup of a liquid into fine droplets. Finer droplet sizes increase the surface area for combustion to take place and allow the flame to burn more fully and uniformly.

The experimental focus is on burning reagent grade glycerol. Glycerol is a byproduct of biofuel production. Much of the glycerol produced in the biofuels industry is used to make soaps, but there is a potential to burn glycerol and other viscous biofuels with the use of flash atomization techniques. This experiment has focused exclusively on glycerol because it is among the most viscous of all potential biofuels; consequently, if glycerol can be successfully burned, then most of the issues with burning viscous biofuels have been resolved. This research serves as a preliminary study of the effectiveness of the flash atomization of glycerol-water mixtures using a swirl nozzle under transient heat transfer conditions employing an in-line nozzle heater.

Typical combustion nozzles are designed to atomize relatively low viscosity fuels. Atomization can occur in jets or in sheets. The experiments conducted in this research deal strictly with swirl atomizers that are designed for liquid sheet breakup. Swirl atomizers have grooves and a conical swirl insert that transfers the forward momentum of the fluid into a centrifugal force forming a thin sheet against the nozzle wall.1

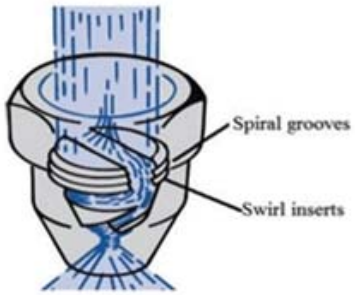

Figure 1. A depiction of the fluid mechanics through a swirl atomizer.[1]

The experimental focus is on burning reagent grade glycerol. Glycerol is a byproduct of biofuel production. Much of the glycerol produced in the biofuels industry is used to make soaps, but there is a potential to burn glycerol and other viscous biofuels with the use of flash atomization techniques. The reason for experimentation being done exclusively on glycerol is because it is amongst the most viscous of all potential biofuels, so if glycerol can be successfully burned, then most of the issues with burning viscous biofuels have been resolved. This research serves as a preliminary study on how effective flash atomization of glycerol-water mixtures are for a swirl nozzle under transient heat transfer conditions using an in line nozzle heater.

Sheet breakup is very effective because as a liquid sheet is sprayed, the liquid surface is sheared by the air causing it to oscillate in a distinct sinuous wave pattern [1].

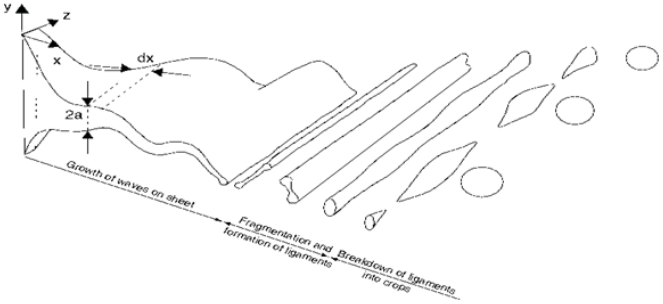

Figure 2. This wave pattern that is formed for conventional atomization.[2]

The wave pattern produces multiple nodes as the liquid travels through the air. These nodes act to weaken the surface of the liquid and eventually the sheet breaks into respective droplets with a diameter of the original liquid sheet.1 Flash atomization creates a rapid phase change of the more volatile component of the feed which allows for the target fuel in the mixture to be broken up. The kinetic energy of the flash boiling overcomes the surface tension of the liquid allowing fine droplets to form. The flash atomization process essentially enhances and accelerates the process of sheet breakup, taking full advantage of the instability of the liquid sheets at the nodes and elsewhere.

II. MATERIALS AND METHODS

The experiments conducted were based on measuring the droplet size distributions with a Malvern Spraytec Droplet Size Analyzer. The laser is a class 3R laser that uses the principle of Fraunhofer Diffraction to analyze the droplet size. The receiver collects the diffraction pattern using a concentric array of photodiode rings.3 The diodes are calibrated to certain droplet sizes so when a signal is transmitted to the receiver, the software can output the droplet size distribution.

Figure 3 - The Malvern Spraytec Laser [3]

Carlin Combustion Technologies, Inc., developed an in-line nozzle heater to help lower the viscosity of fuel oil in cold winter months. This allows for a cleaner burner startup that reduces emissions as well as the risk of nozzle fouling. This nozzle heater was used in the experiment to effectively lower the viscosity of the glycerol-water mixture and to attempt to flash the water component in the mixture. A thermocouple was attached to the surface of the nozzle so that a temperature sweep could be performed. Droplet distributions were taken continually as the temperature was gradually increased. This allowed for the observation of where clear transitions in droplet distribution and spray quality occurred.

III. RESULTS

Initially, the droplet size distributions were perplexing. The droplet analyzer appeared to indicate a distinct bi-modal distribution at elevated temperatures. At temperatures at or near the flash point of water, it was reported that over 50% of the spray (by volume) was larger than 500 microns. Droplets of this size would be catastrophic for combustion when an optimal spray is centered around only 30 micron diameter droplets. An even stranger characteristic of the spray distribution was that when the nozzle temperature increased, the sauter mean diameter or D[3][2] of the spray appeared to increase as well which strongly disagreed with theory. It was found that a two phase high density flow can result in erroneous data due to a distinct change in the index of refraction and multiple scattering of the cross-section of the spray.

Figure 4. Cross section of the laser beam through the spray at a superheated temperature

To combat this effect, multiple diode detector rings can be turned off so that the larger mode of the bi-modal distribution is effectively ignored, amending a well documented issue of what is called Beam Steering of two phase flows.4

After the diode ring corrections were accounted for, it was found that when large weight percentages of glycerol to water mixtures were sprayed through the swirl nozzle the results depict excellent atomization quality. The data collected by the Malvern Spraytec laser shows a distinct decrease in the D[3][2] as a function of increasing temperature. These results indicate that flash atomization is in fact occurring and the trend in droplet distribution is in agreement with theory.

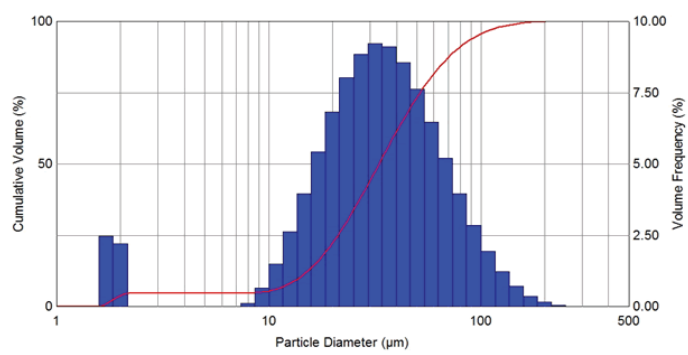

Figure 5. Droplet Size Distribution at 400°F

A high temperature droplet distribution is shown above for 95% Glycerol-Water sprayed at 450°F. At these conditions, the spray is centered around a droplet size of 34 microns with a small mode in the single micron range. The SMD for this spray is 17.2 microns.

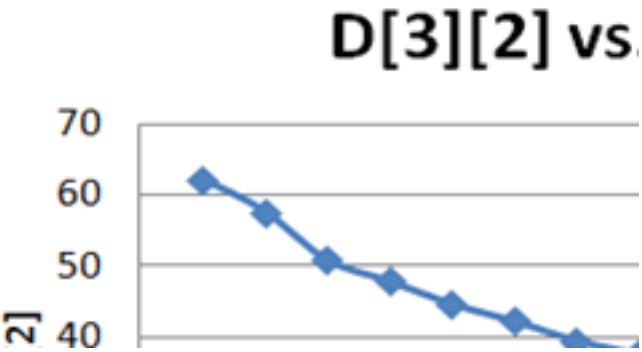

Figure 6. Sauter Mean Diameter vs. Temperature

Figure 6 displays a plot of D[3][2] vs. Temperature for a 95% percent by weight Glycerol-Water mixture. As the temperature is increased gradually, the Sauter Mean Diameter decreases, revealing a clear linear trend.

The nozzle spraying a high weight percent of glycerol to water indicates a clear correlation between increased temperature and viscosity. As the temperature was increased gradually, three distinct spray characteristics were observed before clear atomization took place.

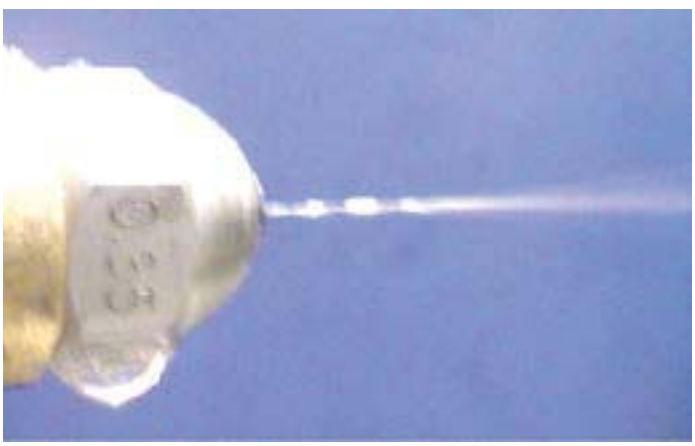

Figure 7. At 80-90°F, a linear liquid jet that appears to be swirling as it exists the nozzle orifice.

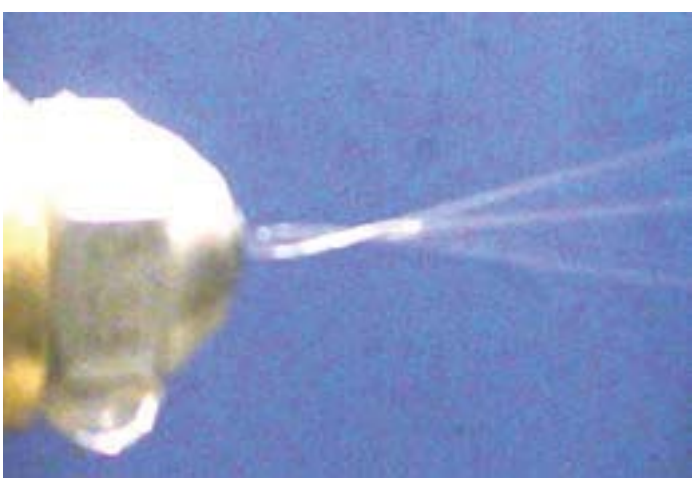

Figure 8. At 100 – 110°F, a clear swirling effect is occurring at the immediate exit of the nozzle orifice and after about a centimeter begins to break up into multiple streaming jets.

Figure 9. At close to 130°F, a sheet is visible emerging from the nozzle orifice. The Sauter Mean Diameter ranges from 98 to 70 microns. At higher temperatures, the sheet is no longer apparent.

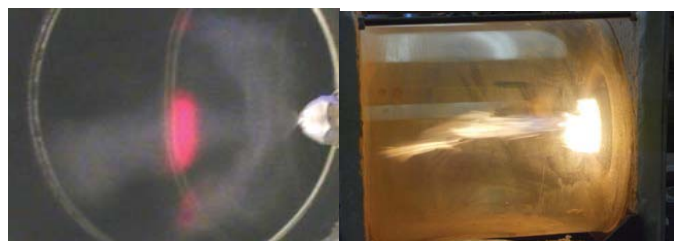

Figure 10. "Tulip" shaped atomization for water at superheated temperatures (Left), "Tulip" shaped flame for Ultra Low Sulfur Fuel when superheated by the Carlin Nozzle (Right)

The figure above depicts the heated nozzle assembly spraying water at 265°F. A clear "tulip" spray pattern is observed. The inner core of the spray develops a higher velocity flow than the outer most parts of the spray due to the elevated nozzle temperatures. One year prior to these experiments, Rebecca Trojanowski, now a staff engineer in the Sustainable Technologies Division at BNL performed fuel atomization and flame tests using the same heating element used in the current research. She observed a distinct "tulip" flame emerge from the heated nozzle assembly when spraying Ultra Low Sulfur Fuel. As can be seen from the two images above, the spray atomization at elevated temperatures clearly affects the flame shape and quality.

IV. CONCLUSION

According to droplet size measurements, the heated nozzle assembly allows for successful flash atomization of viscous fuels, and according to previous year's flame testing, burning glycerol appears feasible. The next step in developing this study is to find a way to reduce the "tulip" flame geometry. Although the atomization should be sufficient for burning, the flame quality is still a poor quality flame. Focus must be put on upgrading the flame quality to a healthier more uniform flame for efficient and reliable combustion. This may be done by finding an optimal temperature at which streaking of the flame does not occur or is less prevalent. Another possibility is to flash atomize with different nozzle geometries to reduce the high velocity core jet that is responsible for the streaking of the flame. Once this is achieved, the water in these experiments must be replaced by a volatile liquid that is combustible and miscible with glycerol.

V. REFERENCES

1. Ashgriz, Nasser. Handbook of Atomization and Sprays. New York, NY: Springer *Science+Business Media*, 2011. Print.
2. Dombrowski N, Johns WR, The aerodynamic instability and disintegration of viscous liquid sheets, *Chem,Eng.Sci.*18,203-214, 1963
3. "Particle Size Analysis, Zeta Potential Measurement, Rheology, SEC/GPC."Particle Size Analysis, Zeta Potential Measurement, Rheology, SEC/GPC. N.p., n.d. Web. 30 July 2012. <http://www.malvern.com>
4. D.Chaillou, V. Alaterre, X.Paubel, N. Marcono, B.Leroux, R. Tsiava, Characterization of fuel oil atomizers at industrial scale, 23rd Annual Conference of Liquid Atomization and Spray Systems, 2010

Development of the ion rapid cycling synchrotron

William Christie
Mechanical Engineering, Binghamton University, Binghamton NY 13902
Christian Cullen
Engineering, Brookhaven National Laboratory, Upton NY 11973

The summer of 2012 is the second consecutive summer that I've spent doing research at Brookhaven National Laboratory (BNL). During the summer of 2011, I learned about working as part of a team and progressing towards a goal in a field that does not always lay out a clear path of action. While the summer of 2011 was spent working primarily in the physics field with the polarimetry group, the summer of 2012 was spent entirely working in the mechanical engineering field developing models of large scale assemblies and solving physical problems that arise during the development of such large projects as the Ion Rapid Cycling Medical Synchrotron.

The Ion Rapid Cycling Medical Synchrotron (iRCMS) is being developed as a means to fight cancer. The basic premise behind the iRCMS is not a new one: particles of high energy are produced in the synchrotron and fired into patients' bodies, destroying cancerous growths. However, current medical synchrotrons are not powerful enough to focus the particles in a way that avoids damaging the patients' skin with rashes and scars. Additionally, current medical synchrotrons are fairly ham-fisted in their attempts to target cancerous growths that are moving within the patients' body. The iRCMS will be able to provide patients with effective cancer treatment while minimizing damage to the skin and also providing much more elegant targeting of moving cancerous growths. In all ways, the iRCMS will be advancement in medical accelerator technology.

My role in the development of the iRCMS was to take all of the components of the massive accelerator and create a working model of their layout along the beam line of the synchrotron using the mechanical engineering software ProEngineer. Because I was already quite familiar with the ProEngineer software, I was able to get to work on the layout of the iRCMS quite quickly. The layout began with six magnet girder assemblies. These were the largest, and arguably most important, components of the iRCMS and form the general shape of the iRCMS. Because each girder spans approximately sixty degrees, the iRCMS could have taken the shape of a circle if there were no need for more components. However, because there is so much more room required, the iRCMS is essentially in the shape of a circle that has been cut in half and stretched apart; it is two semi-circles attached by two long straight sections of beam line.

With the girders in place and the beam line formed, the next step was to populate the straight sections of the beam line with the many components that were required. A good amount of the components that would be required were already known and their dimensions already defined, but as the layout matured and became filled with more and more components, space issues arose and dimensions had to be changed. The first components placed onto the beam line were ten quadrupole magnets which serve the purpose of continually focusing the beam as it travels along the beam line. The placement of these quadrupoles along the beam line was thought to be well-defined when I first started working, yet as I worked on the layout of the components, it was discovered that documentation errors had led to poor dimensioning of the quadrupole magnets. Because various calculations hinged on the placement of these magnets, it was important to quickly determine their correct positioning along the beam line. After much back and forth discussion between the engineering and physics sides of the iRCMS group, the position of the magnets was solidified and I was able to place them into their permanent positions along the beam line.

The next component I placed into the assembly was the injection line for the iRCMS. This component was to be placed in the center of the stretched-circle shape and attached along the upper straightaway with the use of an injection septum. The injection line is where the particles originate from and where they are first focused and accelerated before being injected into the main beam line of the iRCMS. After I had placed the injection line and septum into the assembly, it was determined that an entire new injection system needed to be developed due to concerns with the physics requirements of the iRCMS. This new injection line would be shaped differently and would connect to the iRCMS beam line at a different location along the upper straightaway with the use of a completely different septum. As of now, the new septum has been designed and placed into the assembly while the new injection line is still being developed. It is likely that this new injection system will be complete and ready for addition to the iRCMS layout within a few weeks of my departure from BNL.

After the old injection line had been scrapped and a new injection system proposed, I began to populate the region where the new injection system would meet the main iRCMS beam line. This region is located on the far right side of the upper straightaway of the iRCMS. This is a particularly dense region of the beam line as there are a lot of required components for injection. First, a septum is required to bring the injection beam in line with the main iRCMS beam line. This septum was developed while I worked here and was the last component I placed in the assembly. After that, a beam position monitor (BPM) is required as instrumentation used to locate the beam inside the beam line. This component had not been designed when I began work here and I was chosen to design the component myself with the help of an instrumentation specialist, David Gassner. I quickly designed the component and placed it into the assembly without much issue. Next, a dipole corrector magnet, needed to correct the positioning and focus of the beam line and an injection kicker, was required to complete the aligning of the injection beam line with the main beam line. Finally, a vacuum valve was required at the end of the straight away in order to produce a vacuum in the curved section of the iRCMS, formed by the magnet girders. All of these components, combined with an already placed quadrupole magnet, were required to be in a section of the beam line that was not much more than a meter in length. It was difficult to make everything fit in a way that did not cause problems with the physics behind the accelerator; and so, I printed out a to-scale representation of the section of beam line and all of the required components. This allowed the physics group working on the iRCMS to fiddle with the positioning of each component until they found an order that would fit in this small section of the beam line and complete the required functions. After the order was solidified, it was fairly

simple to place the components into the assembly and prepare for the final model of the new injection system.

After the injection section of the beam line was complete, I turned my attention to the three sections between the magnet girders on both of the semi-circles of the stretched-circle shaped iRCMS. At first it was thought that these relatively small sections would need a vacuum valve, corrector magnet, BPM, and an ion pump, a device essential to maintaining vacuum along the arc. When all of these components were added to the assembly, it was clear that they could not fit in the section where they were required. Luckily, we were able to remove the vacuum valve from this region after we talked with the vacuum group and determined that a valve at both ends of the two straight away sections of beam line would be sufficient to keep vacuum along the arc. Even with the vacuum valve eliminated from this section, though, there were still space issues. The only clear solution was to reduce the length of the BPM. We had tried on our first design to make the BPM as short as possible while still maintaining its functionality, but the instrumentation specialist we were working with determined that the BPM could be made even shorter. After shortening the design to only 26 centimeters, we were able to fit the BPM, corrector magnet, and ion pump inside their required region.

The next step was to place the RF cavities into the assembly. These RF cavities are relatively long components, about one meter in length, and perform a function that is entirely unknown to me. When I first began working on the iRCMS, it was thought that the beam line would only require two RF cavities. Before long, though, it was determined that four RF cavities would be needed. Now, near the end of my time at BNL, there is talk of a fifth RF cavity. There seems to be little consensus currently on the RF cavity requirement, but I had very little issue adding the four confirmed RF cavities to the iRCMS assembly. The cavities are located on the lower straightaway of the iRCMS and their exact positioning upon that straightaway has yet to be determined. I have simply placed them within a section of the beam line that they will likely move about twenty centimeters from when their final location is solidified. The bottom straight away of the beam line is much less crowded than the top, so space concerns are not as frequent on the bottom straightaway.

After the cavities were placed into the assembly, there remained only the simple task of adding numerous corrector magnets, BPMs, and ion pumps to already well-defined positions along the beam line as I waited for components that were required but not yet designed. These components included the extraction and injection septums, the extraction and injection lines, the extraction kickers, wall current monitors, and sextupole magnets. Of these components, only the extraction and injection septums have been designed as of now. These were the last two components I was able to add to the iRCMS assembly. Development of the other components is still ongoing and will likely be completed shortly after I leave BNL.

I feel like I've learned a lot by working on the layout of the iRCMS. Although I was already very comfortable with the Pro-Engineer software, I became quicker at using its various functions as a result of picking up on some of the shortcuts embedded in the program. Additionally, I've learned a lot about the importance of communication and clarity when working with a large team to develop a structure. I've learned it can often be an exercise in frustration and wasted time to rely on emails for communication when you have the possibility to simply find the person you need to communicate with and talk to them in person. Finally, I've learned that things are rarely set in stone and that it is important to remain as flexible as possible and maintain engineering models in the same way.

Obviously, I learned a lot about my career field as well as what it means to work on a team, but I also feel that I was a good help to the laboratory. I feel that my work spurred on important discussions and brought to light some unsettling oversights that may not have been caught for months or years down the line had my work not uncovered them this summer. Additionally, although the iRCMS was the largest of my responsibilities this summer, I also spent a good amount of time working on the physical structure and support of two separate magnet measurement systems and developing an Excel spreadsheet programmed to help with a common heat transfer problems in the mechanical engineering field.

I would like to take this time to thank my mentor Chris Cullen who has made my experience here at BNL extremely painless and entertaining. Chris took the time to show me various parts of the lab I had never seen before and was very good about explaining things I may not have understood without making me feel like a clueless summer student. I learned a lot about having a career as an engineer and that is entirely thanks to Chris and his willingness to show me how he does the many things he is required to do around the laboratory.

Formal post-doctoral mentoring program proposal

Daniel Comas
SUNY Stony Brook University 11794
Maggie Sullivan
Brookhaven National Laboratory, Upton, New York 11973

ABSTRACT

In an effort to increase both productivity and career growth in an STEM environment, over the course of the past several weeks, I have researched and benchmarked Formal Mentoring Programs for post-doctoral scientists as well as its specific application to Brookhaven National Laboratory (BNL). Along with the benefits of such a program I have spent time outlining mentoring program goals that through my research I have found to be crucial to any successful formal mentoring program. This research has given illuminated aspects of Organizational Psychology and its applications in the workplace for me, but also fostered personal growth as this research has forced me to evaluate my summer mentoring program as well as the mentoring relationships I develop outside BNL. The proposed goals of this program are invaluably relevant to this as well as any other DOE sponsored scientific laboratory to help foster and retain young scientists as they try to find their own career path. In order to create an effective mentoring program it is first necessary to define explicitly the traits and tasks required by both the mentor and protégé for effective relationships. This time assessing Formal mentoring programs has been spent briefly canvassing key components and benchmarks of quality, and successful mentoring programs across the country. Using comparative tools, as well as several mentoring focused experiments, my objective has been to assess the feasibility as well as the worth of a formal mentoring program.

Before assessing the feasibility and worth of a formal mentoring program it is important first to give proper definitions to the moving parts within that program. What is a mentor? A mentor is an advisor who provides a non-competitive relationship in which the protégé can grow and develop their personal and career goals. What makes a good mentor? The character traits that make for a successful mentor are empathy, patience, friendliness, professionalism, compassion, experience, and most importantly responsiveness to the protégé. A mentor must engage the protégé, maintain an objective professional relationship, always be prepared for meeting with protégé, introduce the protégé to colleagues in the field, help navigate organizational politics, be open to receiving and giving feedback, and maintain an open availability to the protégé. Along with the characteristics of a mentor, there are also traits and qualities that are important when looking for a potentially successful protégé. A protégé should be enthusiastic, friendly, goal-oriented, professional, prompt, respectful, and flexible to the scheduling and style of the mentor. Along with these traits, it is important that any protégé take an active role in their mentorship; i. e., an active participating and pushing role is paramount to building a worthwhile and effective mentoring relationship.

Formal mentoring is not the only kind of mentoring. Informal mentoring "is a natural component of relationships that occurs throughout the society, in the workplace, as well as in social, professional, and family activities. Informal mentoring occurs in a relationship between two people where one gains insight, knowledge, wisdom, friendship, and support from the other." (Inzer and Crawford) Since this kind of mentoring occurs naturally, there is no need to form any sort of program to facilitate its growth. Whereas this is beneficial to both, the individuals involved as well as the productivity of the organization, there are potential deficiencies in a relationship formed natural and it is these issues that a formal mentoring program looks to remedy. Formal mentoring "differs from informal mentoring in several important ways: it is intentional; participants are held accountable; it is based on best practices to promote a high-quality, productive relationship; and it is available to all staff so that bias and unequal access, whether intended or unintended, is minimized." (Inzer and Crawford) One of the clearest benefits of a formal mentoring program is the ability of the program to spread its benefits equally to all individuals who could benefit from such a relationship. Instead of the needs of some falling through the cracks because they do not naturally form relationships with older more experienced potential mentors, this program allows pairing and matching based on a compatibility that allows all potential protégés the ability to enjoy the benefits of such a relationship.

In mentoring relationships there are also possibly toxic elements that can corrupt a potentially fruitful experience. Some important elements to remember about mentoring are the different kinds of relationships between individuals of higher experience in a field and those new to that field. One example of this typically is a coach and his employees or players. In a coaching relationship, the focus of the interactions between the coach and players is on functional growth. A coaching relationship focuses on increasing productivity and not long-term growth. A mentoring relationship is, however, growth-oriented. This type of relationship focuses on elevating this individual in the long run to more fully understand the personal and career paths that this individual should be on in order to maximize their performance and rewards they acquire from their employment. Not only growing protégés as workers but as people, and professionals in their field.

There are benefits for the individuals involved in a mentoring relationship, but this isn't the sole reason for an organization to implement a formal mentoring program. One such benefit in an increase in the retention rates of protégés. There was a marked decrease in the turn over percentage for post-doctorates who participated in a formal mentoring program. With differences as large at 41% to 79%, with a 38% increase in the success rate of post-docs becoming assistant scientists and the like, a formal mentoring program could ensure that Brookhaven holds onto the talent that it has helped to cultivate and continue to develop the laboratory's successes well into the future. (Insala)

Across all successful mentoring programs, as well as mentoring consulting firms, there seems to be some key components that are included in all models. One major component is

mentor and protégé training. With proper instruction for the mentor and protégé to be aware of what to expect in their relationship and how to address problems, there are several issues that could normally arise that can be avoided. Toxic relationships

that grow from a misaligning of goals between the mentor and protégé can be avoided by clearly stating goals for the relationship early on in its formation, thereby removing any doubt from either of them on what the other is looking for in the relationship. Also in case of a problem many of these programs have a support system that allows no-fault exit plans for the participants in the program in case there are issues with the relationship. With clearly set values and goals for the program, it is important that everyone involved in the program work toward the defined goals that the program manager and the committee have established for the growth and progress of the formal mentoring program as a whole. Without a mission statement or set values for all those involved, it is impossible for the group to work cohesively and aspire to the same goals. With goals, organization structure, and training for the mentor and protégé in place, now it is important that all of these pieces communicate well with each other and allow everyone to be updated on flaws or strengths in the current system, as well as how particular mentoring relationships are progressing so that any issues that may arise can be addressed. (Insala)

Although there are many hurdles to implementing a formal mentoring program, scientific research as well as personal testimonials point to so many advantages for an organization. With mentoring programs becoming more common in academic and scientific establishments in America as well as throughout the globe, the kind of personal and professional relationships that are brought about from programs such as these are such a great asset to not only the individuals involved but the organization as a whole. A formal program would provide equal access to a diversity of individuals, afford individuals with high quality relationships at the Lab, target needs of new postdocs, and continue the advance of Brookhaven National Laboratory as a scientific and educational facility.

I. Works Cited

Inzer, Lonnie D., and C.B. Crawford. "A Review of Formal and Informal Mentoring: Processes, Problems, and Design.." Journal of Leadership Education. 4.1 (2005): n. page. Web. 10 Aug. 2012. <http://www.leadershipeducators.org/Resources/Documents/jole/2005_summer/JOLE_4_1_Inzer_Crawford.pdf>.

James A. Wilson and Nancy S. Elman. The Executive,Vol. 4, No. 4 (Nov., 1990), pp. 88-94,Published by: Academy of Management
Article Stable URL: http://www.jstor.org/stable/4164981

"Benefits of Menotring Programs." http://www.mentoringtalent.com. Insala, 2012. Web. 1 Aug 2012. <http://www.insala.com/mentoring-benefits.asp>.

Bonetta, Laura. "Postdocs: Striving for Success in a Tough Economy." Science Careers. (2011): 1-5. Web. 3 Aug. 2012. <Http;//sciencecareers.sciencemag.org/career_magazine/previous_issues/articles/2011_08-26>.

Evaluation of the United States Support Program's Internship and Junior Professional Officer Programs

Jessica Cruz, Jade Patterson, and Susan Pepper
Brookhaven National Laboratory, Upton, NY 11973

ABSTRACT

The U.S. Support Program (USSP) to International Atomic Energy Agency (IAEA) Safeguards established a program of one-year paid internships for students and recent graduates. The program was in effect from 2002 until 2006 with a total of forty-one U.S. citizens and permanent residents placed in the IAEA. The USSP created a Junior Professional Officer (JPO) Program in 2005 that replaced the internship program at the IAEA. The JPO program creates opportunities for U.S. college graduates to become IAEA employees for a period of one to two years to help increase the effectiveness and efficiency of safeguards. The twent- three former and current JPOs work in varying fields such as software development, information collection and analysis, non-destructive analysis systems, and unattended monitoring systems. This paper will look at the impacts of the USSP internship and JPO program on the interns and JPOs, the U.S. government, and the IAEA. Academic backgrounds, past involvement in nuclear fields, program assessment, and post-program positions were recorded and analyzed through two studies using questionnaires sent to former interns and former and current JPOs. This paper will discuss the effects of the programs on the careers of the interns and JPOs, present the evaluations of the internship and JPO Programs, and report the recommendations for changes.

I. INTRODUCTION

The formation of the USSP internship and JPO programs created entry level positions for U.S. college graduates at the IAEA. Both programs allowed young professionals to work at the IAEA with little to no prior experience in safeguards. While the USSP internship program was open to students and college graduates, the JPO program required a college degree. JPOs were placed at the P1 or P2 level, were less than 32 years of age, and had zero to two years of prior experience. The internship program ran from 2002 until 2006 and consisted of 41 interns with varied academic backgrounds and work experiences. Similarly, the JPOs were a diverse group. As of July 2011, there were 23 former and current JPOs. This study was undertaken to assess the impacts of the intern and JPO programs to ensure that the financial investment made by the U.S. government was worthwhile.

II. BACKGROUND INFORMATION

The USSP was established in 1977 to augment the IAEA's regular budget for safeguard activities with U.S. sponsored expertise, equipment, and techniques. The USSP assists the IAEA in its mission to verify that nuclear material placed under IAEA safeguards is not diverted to non-peaceful purposes. The USSP is one of twenty-one Member State Support Programs that strive to improve the effectiveness and increase the efficiency of IAEA safeguards. The Subgroup on Safeguards Technical Support (SSTS) is the U.S. government interagency group that approves and authorizes funding for USSP tasks. The International Safeguards Project Office (ISPO), located at Brookhaven National Laboratory (BNL), performs the day-to-day technical and administrative project management activities for the USSP, including proposal solicitation, task progress and budget reporting, and technical oversight of tasks (Nook and Hoffheins, 2008).

The USSP's goal for the internship and the JPO programs was the formation of entry level positions at the IAEA, the provision of human resource support to perform basic yet essential work, and the creation of access to academic institutions as another source of USSP support to the IAEA (Pepper, Gaetano, and Lepingwell, 2003). The USSP and ISPO aimed to increase young people's awareness of job opportunities in the nuclear industry and nonproliferation. The USSP also intended to encourage interns and JPOs who participated in the programs to consider the IAEA for their future employment, bring their experience to government and national laboratories, and help further support the nuclear industry.

III. METHODOLOGY

Surveys were used to determine the impact of the internship and JPO programs on the IAEA, the U.S. government, and the interns and JPOs. Surveys provided a means to collect information regarding the experiences of interns and JPOs in a way that allowed for anonymity and openness.

The May 2011 survey of the internship program was the initial study. It was conducted under an independent study graduate course at the State University of New York at Stony Brook. This research used open-ended questions that addressed the backgrounds of the interns, individual experiences, and post-program opportunities. The JPO program study focused on the former and current JPOs as of the summer 2011. It took place from June to August 2011. The JPO study also used a series of open-ended questions that allowed the current and former JPOs to evaluate the impacts of the program.

A. Survey for the Internship Program

A questionnaire containing nineteen open-ended questions was prepared. The questionnaire was sent to all 41 of the former interns employed from 2002 through 2006. The interns were contacted via e-mail, cell phone, and Facebook. Five questionnaires were returned because of the lack of a current address and one intern declined to respond. Thirty-five completed questionnaires were received, yielding a 97% response rate from those who received the questionnaire. The returned surveys were addressed to people living overseas. It is assumed that the lack of response was due to the lack of a current address. The USSP had lost contact with these five individuals. However, the percentage returned was large enough to represent the entire sample of the population during the four years of the program.

B. Survey for the JPO Program

The research was conducted by an intern sponsored by the National Nuclear Security Administration's Next Generation Safeguards Initiative program and was modeled on the internship

study and questionnaire. Former and current JPOs were contacted through email and asked to fill out an attached questionnaire of twenty questions. The questions were open-ended with the exception of the two ranking questions, "What elements were most necessary to perform well in your JPO assignment?" and "Were you satisfied with your overall JPO experience?" One JPO was interviewed in person to further discuss his experience working in Vienna and his current employment. Questionnaires were sent to the 23 former and current JPOs. Twenty questionnaires were returned creating an approximate 87% response rate, as well as a strong foundation for analysis. The questions addressed the JPOs' educational and work background, their experiences while in the program, and their professional activities following the end of their assignments at the IAEA.

IV. RESULTS

The results of both surveys were analyzed through categorized Excel spread sheets. The results of the studies showed that the internship and the JPO programs benefited the U.S. government, the IAEA, and the interns and JPOs in different ways. The following sections will discuss the impacts of the programs on the U.S. government, the IAEA, and the interns and JPOs. Unless otherwise stated, the results reflect the status as of July 2011.

A. Benefit to the U.S. Government

The U.S. government has benefited from the internship and JPO programs by gaining well-informed citizens and employees through those who returned to the United States and used their IAEA acquired skills and education. The statistics presented in this section reflect an excellent return on the U.S. government's investment in the internship and JPO programs.

Thirty-four percent of the intern survey respondents went on to careers in U.S. government agencies, 20% took jobs at national laboratories, and 17% are working at the IAEA. Following the end of their assignments, a total of 40% of the former interns returned to the IAEA as staff members, Cost-Free Experts[1] (CFE), consultants, or JPOs for short or extended periods of time. These placements increased U.S. representation and contribution to the IAEA. Figure 1 illustrates the employment of interns as of May 2011. In approximately 2009, the SSTS determined that human resources are a high priority to ensure the IAEA has necessary expertise and capabilities in its workforce. Between the extra budgetary human resources of CFEs and JPOs, the SSTS believes that JPOs are the best investment because they have the potential to contribute to international safeguards for more years in the future. The USSP should continue to fund the JPO program to continue the preparation of young professionals for future positions with the IAEA Department of Safeguards.

Out of the twenty JPOs who responded to their survey, half already completed their assignments at the IAEA and half were currently employed at the IAEA. Of the ten former JPOs, six took jobs at the IAEA, one took a position at Oak Ridge National Laboratory, one at Canberra, another at a software development company, and the last took a job in publishing. Figure 2 illustrates the post program positions of the former JPOs. In March 2012, one intern, who was serving as a CFE, became a regular staff member. One JPO became a regular IAEA staff member in May 2012.

As of December 2011, one more JPO, who also served as an intern, joined the IAEA as a regular staff member increasing the percentage of former interns who work at the IAEA to twenty percent and the former JPOs who work at the IAEA to seven of the ten former JPOs. Also, one intern who started in 2002 left the IAEA in 2011 with only a short break in service during her nine year tenure. This maintained the percentage of former interns working at the IAEA at seventeen percent. Two of the former interns have since moved from the Department of Safeguards to the Department of Safety and Security. The programs enabled the IAEA to employ young professionals with the qualifications

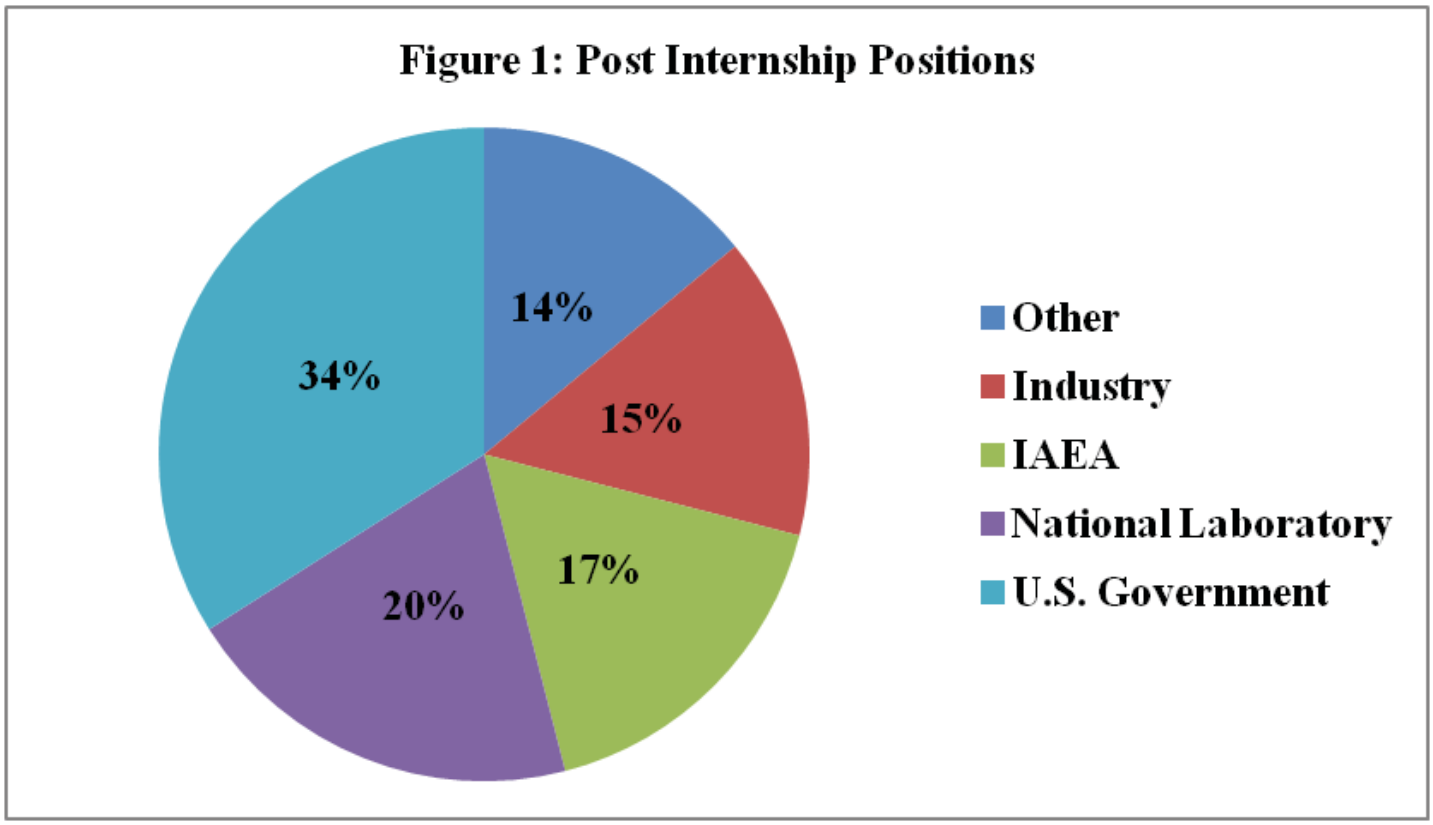

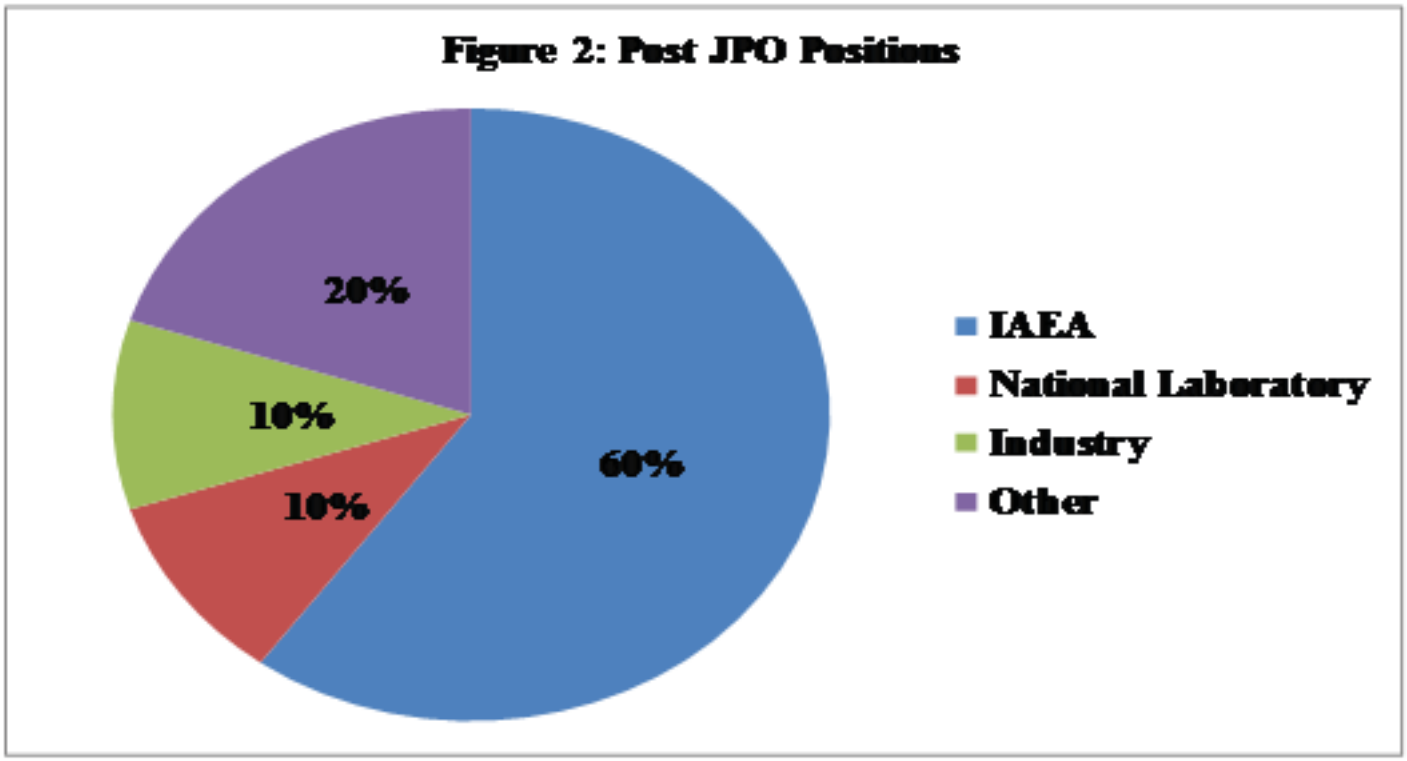

and skills to work on a variety of projects at no cost to the IAEA itself. These individuals were trained in the technical areas associated with the IAEA's work (e. g., nondestructive analysis, containment, surveillance, and information collection and analysis), creating a pool of applicants for future positions.

The typical cost of an intern was approximately $60,000 per year, including stipend and administration costs, although some interns were paid more based on education and work experience. Unlike interns who were the employees of and paid by BNL, JPOs are IAEA staff members and have the same privileges and benefits. This change corrected the issues that many interns spoke about, such as having to enter the Vienna International Center (VIC) through the visitor's entrance. Although it was not mentioned in the surveys, the JPO program offers medical and pension benefits. The typical cost of a JPO is about $140,000 per year, including salary, benefits, and program costs.

The employment of former interns and JPOs in government and national laboratory positions has brought skills and knowledge acquired at the IAEA to the United States workforce. Both programs also increased U.S. presence and representation at the IAEA during the assignment and led to hiring following the assignments. Alongside these benefits, the U.S. government and the USSP benefited through the creation of the internship and JPO Programs due to the growth in awareness of the nonproliferation industry and employment opportunities. Fifty-four percent of all intern respondents had not been involved in or had not considered the rewards of working in nonproliferation or in the nuclear industry prior to their internship. The remaining 46% were aware or involved through their university courses (nuclear engineering, physics, or nuclear non-proliferation). Towards the end of the internship, nearly all the interns wanted to continue working with the IAEA or expressed a desire to continue working in similar fields. Of the former and current JPOs, 90% were involved in nuclear related studies or fields prior to their assignment. Ninety percent were also aware of the IAEA prior to joining the JPO program. It should be noted that eight of the JPOs had been in the internship program and, therefore, would have had knowledge of nonproliferation and the IAEA prior to their assignments as JPOs. The JPO program created awareness of opportunities for 80% of former JPOs and similarly to the former interns, nearly all wanted to continue working with the IAEA or expressed a desire to continue working in similar fields. The U.S. government and the USSP benefited significantly from the internship and JPO Programs through a more aware and skilled American workforce.

B. Benefit to the IAEA

The interns and JPOs came from diverse educational backgrounds that brought interdisciplinary perspectives to IAEA assignments. Many of the former interns and JPOs hold degrees in engineering, political science, and computer science. All of the former and current JPOs hold bachelor degrees, as required by the JPO program. As of July 2011, 14 of the 23 JPOs hold at least a Master of Arts, a Master of Science, or a Master of Business Administration. Among the 14 JPOs who have Master degrees, one also has a Doctorate degree.

Prior to starting their internship, 60% of the respondents were not aware of the IAEA was or what it did. Although nearly all JPOs stated that they were aware of the IAEA prior to their assignment, the JPO program increased their awareness and understanding of the organization and its functions. After the internship and JPO programs, both interns and JPOs were more aware, for the experiences they had at the IAEA gave them a deeper understanding of the inner workings of the IAEA, the United Nations (UN) and international organizations in general, and recognition of the role they play in the international community. When asked "Did your experience change your perception of the United Nations Organization/IAEA?," a former intern responded: "Yes, working at the IAEA gave me a firsthand look at the driven people that are passionate about helping each other and creating safe nuclear energy. I had formerly thought that the UN was more bureaucratic in

Rating	Interns Out of 35 Responses	JPOs Out of 10 Responses
5- Experience far exceeded expectations	21	3
4- Experience exceeded expectations	8	1
3- Experience met all expectations	4	3
2-Experience met some expectations	2	3
1- Experience failed to meet Expectations	0	0

Table 1: Responses to the Question, "Were you satisfied with your overall JPO experience?"

nature, with little social or scientific impact on needy countries or people." A former JPO, who was also a former intern, stated that "before the internship, I was pretty unaware of the mission of the IAEA, so the internship and JPO certainly made me realize how important it is to work towards the IAEA's mission."

Eight interns who participated in the program have become JPOs, and several of the former interns and JPOs have become Cost-Free Experts after their assignments. As of July 2011, six of the former interns and six of the former JPOs are employees at the IAEA. The internship and JPO programs have helped the IAEA select staff members from a known pool of candidates. Also, their previous appointments shortened the learning curve because they had an understanding of the IAEA's procedures and because they were usually hired into positions related to their internship or JPO position. Both programs benefited by providing additional employees funded by the U.S. Support Program at no cost to the IAEA. The interns and JPOs are capable of working independently, perform basic yet essential work, and free more experienced staff members to focus on more complex work. After concluding their assignments, many of the former interns and JPOs entered the IAEA workforce as trained individuals, bolstered by their assignments.

C. Benefit to the Interns and JPOs

The survey indicated that the motivations for the respondents to participate in both programs were the opportunity to work for an international organization, to experience working in a multicultural environment, and to live overseas and experience a new culture. As one intern described, "For someone who has never even owned a passport, the internship allowed me not only to pursue my career on levels that I never would have imagined, but it also gave me an opportunity to travel and see the world. Due to financial constraints, I would not have been able to get this kind of hands-on international experience if it had not been for the USSP." A JPO stated, "I wanted to live in Europe and I was ready for a new experience. I also wanted to be part of a larger organization doing something helpful for humanity." Both programs provided opportunities for the interns and JPOs to gain new cultural and work experiences abroad. The programs offer a rare opportunity for young professionals to work abroad with a competitive salary.

Eighty-nine percent of the respondents answered that their participation in the internship program made them aware of new career opportunities and more specifically careers related to IAEA Safeguards, United Nations Organizations, national laboratories, and the U.S. Department of Energy. Eighty percent of former JPOs stated that their assignments at the IAEA made them aware of new opportunities within the nuclear industry. Seventy-one percent of the interns and 80% of the former JPOs tried to follow up on these opportunities to remain at the agency or in the field. Both programs allowed the participants to learn about and to try to participate in nuclear safeguards related positions at the IAEA, in the U.S. government, or in national laboratories.

All of the respondents stated that they have acquired new skills while working at the IAEA which were valuable and transferable to their current positions. Some of the skills identified were technical/work skills in information technology such as software configuration, database management, quality assurance and control, knowledge of the Carnegie Mellon² capability maturity model, web development, and programming. Others skills, such as open source collection techniques, knowledge of the nuclear fuel cycle, systems integration, information management and analysis, writing and communicating effectively, presentation skills, and the value of prototyping systems, were also listed. Many of the respondents placed emphasis on the importance of the interpersonal skills they acquired as a result of their experience at the IAEA such as teamwork, diplomacy in the workplace, cross-cultural skills, communication, and the ability to handle stress in dynamic work environment.

V. EVALUATION OF THE PROGRAMS

The internship and JPO programs proved beneficial by providing the participants with varied cultural exposure, experience within the nuclear field, networking opportunities, educational enhancement, and follow-up career prospects. Both of the surveys conducted found that the programs had positive effects on the IAEA, the U.S. government, and the participants. The intern and JPO studies asked, "Were you satisfied with your overall JPO experience?" Table 1 provides the results of this question.

Of the 35 intern respondents and the ten former JPO respondents, none ranked their program lower than a two. Sixty percent of the respondents felt that their overall experience as an intern at the IAEA far exceeded their expectations, 23% felt that it exceeded their expectations, 11% felt that it met their expectations, and 6% of the group answered that their internship experience only met some of their expectations. Of the ten former JPOs 30% of the respondents felt that their overall experience as an intern at the IAEA far exceeded their expectations, 10% felt that it exceeded their expectations, 30% felt that it met their expectations, and 30% of the group answered that their internship experience only met some of their expectations.

The differences in scores between the two programs cannot be explained in certainty, yet it should be noted that there were only ten former JPOs during the time of the study as opposed to the 35 intern respondents, providing more accounts of program experiences. Also, the internship program did not have a degree requirement, creating an otherwise unattainable opportunity for men and women who did not have the academic experience generally required within this field. This opportunity may have in-

fluenced program evaluation in the internship that did not reflect in the JPO study due to the higher academic requirements of the latter. One last possibility that may explain the difference in experience rating was that whereas 60% of interns did not know about the IAEA and its mission prior to their assignment, only 10% of JPOs were unaware. The greater awareness of the IAEA prior to their JPO assignments may have created a certain set of expectations that 60% of the interns did not hold.

The surveys of both the internship and JPO programs included the question, "What would you change about the program?" Many of the interns and JPOs wrote that they did not think their programs should change at all. A few of the interns and JPOs noted concerns that they felt were slight issues. Several former interns stated that they would have extended the length of their programs. An intern stated, "I would advocate for the program to be a bit longer (18-24 months)." Another intern wrote, "Make the intern a staff member with benefits." The formation of the JPO program addressed both these concerns for the JPO assignments range from one to two years and the positions came with benefits. Several former JPOs that responded to the questions sought aid in finding employment on return to the United States. One former JPO stated, "What would have made the JPO program even more attractive and meaningful is if there was a more systematic post-JPO job transition." Another stated that a potential improvement of the JPO program would be a reduction in the "time it takes between applying to the JPO program and notification." Although there were several changes proposed, it should be noted that 100% of the interns recommended the program based on their experiences in the internship program. All of the former JPOs also recommended the JPO program to others. Although the ratings varied between respondents and programs, both USSP groups had overall positive experiences and would recommend the programs to others.

VI. CONCLUSION

The results of the surveys which presented participants' opinions, backgrounds, and positions following their assignments allowed for an analysis of the programs' value to the U.S. government, IAEA, and the interns and JPOs. The internship and JPO programs received high ratings from the respondents who would all recommend them to others. The benefits to the stakeholders often overlap; for example, the skills and experience gained by the participants also benefit the U.S. and the IAEA. The preparation of the workforce benefits the IAEA, the U.S. government, and the individuals selected for employment by the agency. The internship and JPO surveys showed that the programs were of benefit to the U.S. government, the IAEA, and the participants themselves because of the creation of entry level positions at the IAEA, the development of experienced young professionals in the nuclear field, increased representation of the USSP at the IAEA, better awareness of the IAEA and international organizations, and a larger, better prepared work force for the Agency and the U.S. government.

Although this paper addressed the impacts of the USSP's internship and JPO programs, there is room for future research through follow-up studies on the recommendations given by the former interns and JPOs. The analysis was based on the responses of the former interns and JPOs, leaving open an opportunity to survey how the IAEA mentors and ISPO and SSTS view the benefits and rate the program.

VII. END NOTES

[1]Cost free experts are individuals whose work at the IAEA is sponsored by member states because the IAEA's regular staff lacks the expertise or the time required to perform the work.

[2] "CMMI (Capability Maturity Model Integration) is a [software development] process improvement approach that provides organizations with the essential elements of effective processes, which will improve their performance. CMMI-based process improvement includes identifying your organization's process strengths and weaknesses and making process changes to turn weaknesses into strengths." http://www.sei.cmu.edu/solutions/softwaredev/?location=main-nav&source=1395

VIII. BIBLIOGRAPHY

International Atomic Energy Agency Website, www.iaea.org.

Nock, C., &Hoffheins, B. (2008). "The U.S. Support Program to IAEA Safeguards — How it Works", presented at the INMM 49th Annual Meeting, Nashville, TN, July 2008.

Patterson, Jade. (2011). "The U.S. Support Program Safeguards Internship Program- Its Impact On the Careers of Interns and an Evaluation of the Internship Program."

Pepper, S., Gaetano, R., & Lepingwell, J. (2003) The Establishment of a U.S. Support Program Internship Program.

Pepper, S., & Osieki, C. (2006). Impact of the U.S. Support Program Safeguards Internship Program. "United States of America Support Programme and the International Atomic Energy Agency Department of Safeguards, Cooperation Arrangements and Guidelines," Revision 1, Valid: 2001–2003.

.

Evaluating the effectiveness of the current Tier 1 process

Clara S. Cuervo
Department of Engineering, Suffolk County Community College, Selden, New York 11784
Peter Eterno
Facilities and Operation Directorate, Brookhaven National Laboratory, Upton NY 11973

ABSTRACT

Managed by the Department of Environmental Safety and Health, the Tier 1 process consists of quarterly and/or yearly inspections of all facilities at the Brookhaven National Laboratory that check for deficiencies and/or code violations in accordance with the Department of Energy (DOE) Order 430.1B: Real Property Asset Management. This self-assessment process is vital not only to the safety of all employees, but also to the assurance of the uninterrupted continuity of current research projects and to maintain the readiness required to compete for new ones. At the beginning of FY 2011, a change in the procedure for Tier 1 was introduced. This research describes trends in the execution of work orders including the number generated, the number completed, the time needed to complete, the number cancelled, and the reason for cancellation. Toward this goal I have compiled and tracked work orders, and then analyzed the data by comparing the pre- and post- intervention periods. The outcome showed a sharp decline in the rate of completion of work orders in the post-intervention period. This research identifies flaws in the new process, suggesting that the change in the procedure could be a major reason for the breakdown of the Tier 1 process, and recommends strategies for corrective action.

I. INTRODUCTION

This research describes the trends in completion and cancelation of work orders of the Tier 1 process by comparing data for FY 2009, 2010, (immediately prior to the change in the Tier 1 Safety Inspection Process) with data from FY 2011and the first three quarters of FY 2012.

The Brookhaven National Laboratory has established a system of work area inspections by lines of organizations better known as Tier 1 inspections. This system provides a framework for the organization to document and track closure environment, safety, security, health and quality deficiencies and observations identified during walkthrough inspections of work areas.

The evaluation done in this research is limited to those Tier 1 deficiency inspections related to buildings, trailers, and other structures and facilities overseen by the department of Facilities and Operation (F&O) . This implies that approximately one third of all Tier 1 inspections were collected from the Computerized Maintenance Management System (CMMS) Maximo.

The Facilities Operation Center (F&O) provides computer programs designed to assist in the planning, management, and administrative procedures required for an effective maintenance and asset management process. Computerized Maintenance Management Systems (CMMS) enables the facility manager, subordinates, and customers to track the status of maintenance work on their assets and the associated costs for that work. CMMS are utilized by facilities maintenance organizations to record, manage, and communicate their day-to-day operations. The system provides reports to use in managing the organization's resources, preparing facilities key performance indicators (KPIs)/metrics to use in evaluating the effectiveness of the current operations and for making organizational and business decisions.1

Prior to the beginning of FY of 2011, if a deficiency or code violation was found, the Environmental, Safety and Health inspector sent a memo to the F&O. Here, the corrective action process started with the creation of work orders whereby the deficiency would be addressed according to a designated priority. Those work orders were sent to the Planner Estimator, the Building Manager, and the Supervisor where each work order was scheduled based on its priority and the budget needed to execute the work order. From here, the work orders were sent to the shops where the job would be completed within 30 days if the work order was a Tier 1 Safety, or 90 days if the work order was a Tier 1 Maintenance.

At the beginning of FY 2011, an organizational change was made which consisted of the creation of a new position that rolled together the responsibilities of the Planner Estimator, the Building Manager and the Supervisor into the Facility Project Manager (FPM). Each FPM plans, prioritizes, and authorizes work, and ensures that problems are resolved for the specific buildings that they are responsible for within a facility complex. FCMs manage budgets, reports, and planning for their complexes.2

The (CMMS) Maximo's report shows a list of work orders revealing their status as well as the time they took to complete. Based on the total number of work orders created per fiscal year, Figure 1 shows a very stable trend of the Tier 1 for safety inspections between the FY 2009 and 2010. It also indicates that on average its performance was approximately 99.4% effective, with 0.7% cancelation and 0% incomplete. An incomplete work order refers to a current status such as in progress, waiting for approval, waiting for planning, waiting for schedule, or waiting for material.

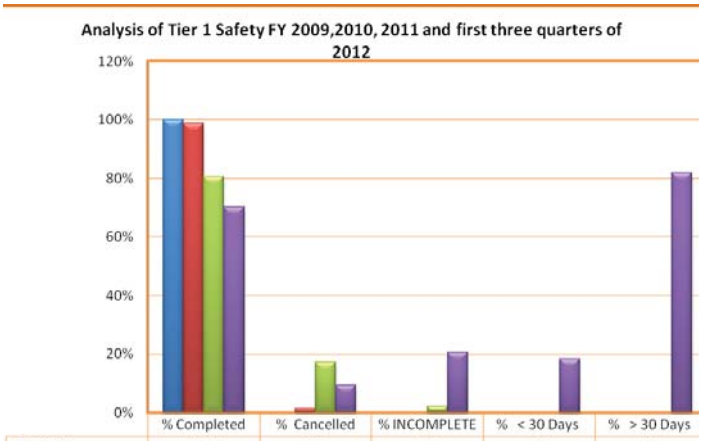

	% Completed	% Cancelled	% INCOMPLETE	% < 30 Days	% > 30 Days
FY 2009	100%	0%	0%	0%	0%
FY 2010	98.7%	1.3%	0%	0%	0%
* Change* FY 2011	80.8%	17.2%	2.1%	0%	0%
FY 2012	70.1%	9.3%	20.6%	18%	82%

Figure 1.

By FY 2011 the completion of work orders declined approximately 18 points, the cancelations of work orders increased approximately 16 points, as well as the non-completion of work orders increased only by 2 points. The most drastic decrease in performance is revealed on the first three quarters of FY 2012, where the cancelation of work orders dropped to 70.1%. Even though the percentage of canceled work orders looks low compared to the previous fiscal year, it is expected to be higher by the end of FY 2012. This prediction is assumed since the percentage of incomplete work orders drastically increased from one year to the next by 82% and they also had passed the 30-day period to finish and closed the work orders.

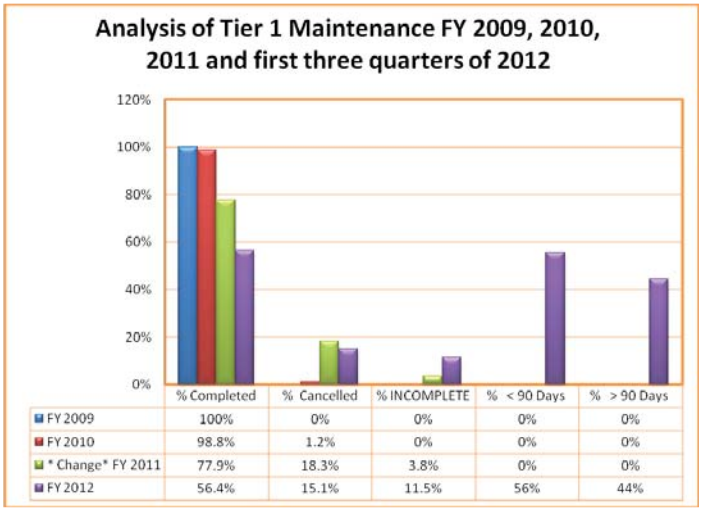

Figure 2.

A similar behavior is illustrated on Figure 2 for the Tier 1 maintenance inspections; however, comparing the data of the two previous charts, it is clear to see that there is a dramatic change in the percentage of completion and cancelation of work orders between FY 2010 and 2011, and even more between FY 2011 and 2012. This means that Tier 1 maintenance inspections have been less effective than Tier 1 safety inspections.

Finally, Figure 3 illustrates the analysis of the work orders cancelled through the same fiscal years shown on the previous charts. However, since there was no cancelation of work orders for the FY 2009 and very low (three) for the FY 2010, the analysis for those fiscal years has been omitted.

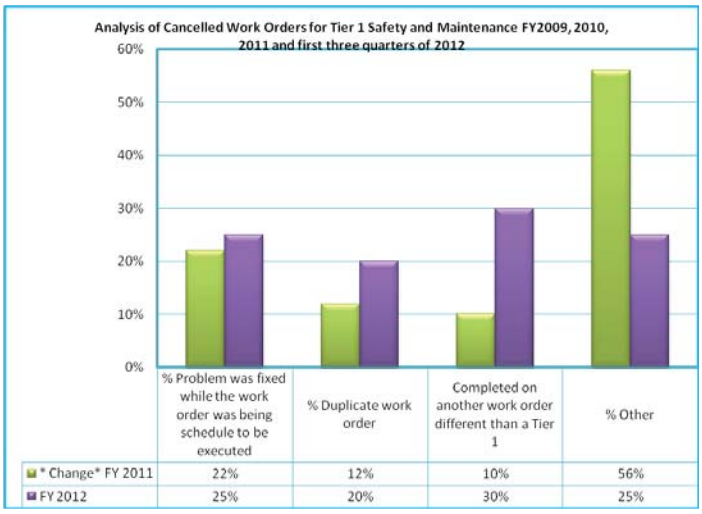

Figure 3.

The data for this chart was collected by manually searching on (CMMS) Maximo. It was found that there were several reasons for cancelation, but the majority of them fell under the categories illustrated in Figure 3.

This part of the research illustrates why the current Tier 1 inspection process has not been effective during the past two years. The first three categories have been increasing at a small rate,but the second and third category shows the highest increase. Therefore, there are still some issues that have not been corrected leading to a much less effective Tier 1 process.

II. CONCLUSIONS

This research shows that there is a sharp decline in the rate of completion of work orders for Tier 1 safety and maintenance inspections from FY 2010 through FY 2011. The completion rate went from 98.7 % to 70.1% on the Tier 1 safety inspections and from 98.8% to 56.4% completion for the Tier 1 maintenance inspections. Furthermore, the research also shows a dramatic increase in the rate of cancelation and non-completion of work orders.

Some issues need to be addressed in order to improve the effectiveness of the Tier 1 process. If safety is a major priority, the cancelation of work orders has to be reduced by:

1. Indicating on the Tier 1 inspection memo if the deficiency could be corrected at the time of inspection without creating a work order.
2. Making sure to include the work order number in the Tier 1 inspection memo if a Tier 1 emergency call is received by the clerks at the F&O to avoid duplicates.
3. Labeling Tier 1 findings only on work orders related to it as this will effectively track Tier 1 work orders for further evaluation.
4. Finally, mandatory training to all staff involved in this process regarding the utilization of the Computerized Maintenance Management System (CMMS) Maximo.

This evaluation clearly shows that the changes that probably helped to improve other areas involving the F&O have degraded the Tier 1 process, and it is expected that these trends will continue. However, a new Tier 1 database will be soon introduced and some of the issues mentioned before should be eliminated.

III. ACKNOWLEDGEMENTS

I would like to thank my mentor Peter Eterno as well as Michael Paquette and Keith Radich for the opportunity and guidance in this research. Furthermore, I would like to thank The Brookhaven National Laboratory and the Office of Educational Programs for letting me participate in the SULI program.

IV. FOOTNOTES AND REFERENCES

[1] Facility & Operation. 2012. 30 July 2012 http://intranet.bnl.gov/fo/.

[2] IFM. 2012. 30 July 2012 http://intranet.bnl.gov/ifm/faqs.asp

Design of beam line setup for high-charge state ions after radio-frequency quadrupole

Eric Cushing, Department of Mechanical & Nuclear Engineering
The Pennsylvania State University, University Park, Pennsylvania 16801
Masahiro Okamura, Collider-Accelerator Department
Brookhaven National Laboratory, Upton, NY 11973

ABSTRACT

Using TRACE3D, my project was to design the beam line setup after the beam is accelerated by the four-rod structure radio-frequency quadrupole (RFQ) so that we can analyze the emittance and current of every ion in a silver ion beam. I designed for Ag^{15+} in this project. I adjusted the position and magnetic field gradient of the quadrupoles using TRACE3D to have a beam diameter of less than 1.4 cm so that it will not only fit inside the 3.2 cm diameter quadrupole, but also fit inside a 3 cm diameter Microchannel Plate (MCP) with a large margin of error. The bending magnet's magnetic field will be scanned to analyze each charge-state's emittance and current. We expect to obtain a low emittance and a high current high charge state silver ion beam with the peak ion current to be centered around Ag^{15+}. I also compared and discussed the results of an RFQ modeling program PARMTEQ with experimental results.

I. INTRODUCTION

Accelerated heavy ion beams have many applications in high energy and nuclear physics and medical research. A good heavy ion beam will have high current and high charge state. At the laser ion source (LIS) department, we are researching how to provide high curren,t high charge, state heavy ion beams to a next generation accelerator. The current accelerators can handle ion beams at a level of ~1 mA. The ion beam comes from a ~1.5 J laser impacting a solid target leads to a beam that has high current, ~4 mA. Using TRACE3D, my project was to design the beam line setup after the beam is accelerated from 8.26 keV/u to 270 keV/u by the 100 MHz four-rod structure radio-frequency quadrupole (RFQ) so that we can analyze the quality of all the ions in a silver ion beam. The quality of the beam is characterized by emittance where the directionality and the size of the beam are taken into account. From an economic standpoint, it is important to keep the emittance of the beam low because a low emittance enables a smaller pipe to be used without losing any part of the beam. Because of space charge forces, the ion beam will naturally diverge after the RFQ. While a quadrupole can be used to focus the beam in both x- and y-directions, the beam cannot be focused in the beam line (z) direction because no forces act on the beam in that direction. A bending magnet can be designed to a specific charge-state by adjusting the magnitude of the magnetic field since the degree the ion is bent is directly proportional to the charge of the ion. Generally, emittance is conserved, but because a bending magnet is being used emittance increases. Because an experiment was already run and we obtained high current from C6+, we expect similar results with Ag^{15+} because Ag^{15+} ionization energy is 347.0 eV,[1] which is lower than C^{6+} ionization energy of 490.0 eV.[2]

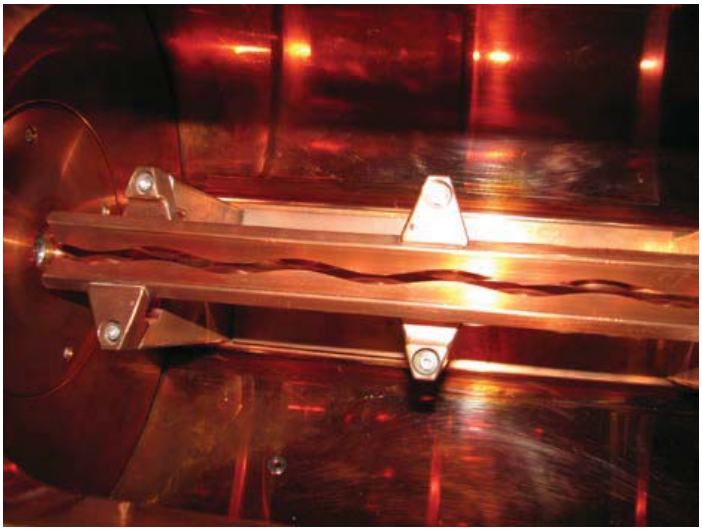

Figure 1. A picture of the four-rod Radio Frequency Quadrupole (exit)

A. How a rod radio frequency quadrupole works

Based on the structure of the rods, a four rod RFQ can be machined and designed to focus and accelerate the beam. Transverse focusing occurs from the shape of the electric field created by the quadrupole forces. By changing alternating polarity throughout the length of the RFQ, one can transversely focus the beam. With time dependent electric fields, one can accelerate the beam without decelerating it. When the particle moves a half period to the next electrode, the electrode will change polarity and so it will continue to accelerate the particle. As you can clearly see in Figure 1, the picture on the left has a longer period than the one on the right.

II. SCOPE AND OBJECTIVES

The objective of this project was to design a beam line setup after the RFQ to analyze the charge-state distribution, the emittance, and the current of the ions in ^{108}Ag. TRACE3D designed the bending magnet and quadrupoles to specific ions for analysis. However, a limitation of TRACE3D is that it assumes that all of the ions are the one it is designed for—in this case, Ag^{15+}. No doubt this factor will have some effect on it. Furthermore, PARMTEQ modeling software was used to get the exit emittance

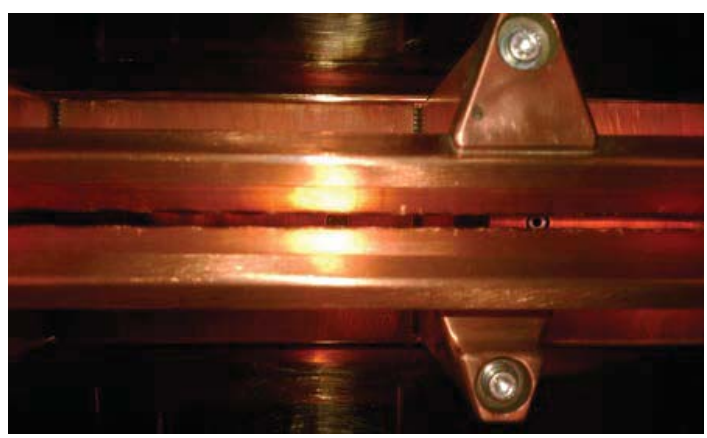

and current of Ag^{15+} after the RFQ. We tested the total current of the beam after the RFQ and compared it with the theoretical current of just one ion, Ag^{15+}, and found that the model gave a much shorter pulse. As shown in Figure 4 in the appendix, the theoretical pulse length was 0.31 ns Full Width Half Max (FWHM) of silver and the experimental was 3.44 ns FWHM of iron. While they are different ions, the shape of the current is expected to be the same[3] and the peak was normalized to the experimental peak. The short experimental pulse was the result of limitation that the PARMTEQ code can only track one charge state; whereas, in the experiment we are measuring the total current of all the charge states and will have a larger phase spread. Because the RFQ is designed for one charge state (Ag^{15+}) and the extraction voltage will cause different injection velocities at the beginning of the RFQ, the velocity of Ag^{16+} will be higher and will, therefore, oscillate around the synchronous particle in the RF bucket more. This means that the peak will be longer when you have several different charge state ions. Until I perform my experiment, we have no way of knowing the distribution of charge states in the ion beam. An ion with a lower charge state will be affected by the RFQ less than a higher charge state.

III. METHODS

TRACE3D models the beam envelope of a certain charge-state of the specified ion at known kinetic energy (270 keV/u, 29.404 MeV for silver) and input emittance. The user adds the necessary elements to the beam line and TRACE3D models what is expected for that charge state. I adjusted the parameters in TRACE3D until I found a suitable solution. In this model, I designed for Ag^{15+}. In order to obtain the input emittance (after the beam passes through the RFQ) we used PARMTEQ, which computes each particle's path through the RFQ. It outputs an Excel spreadsheet where a scatter plot of the emittance in each phase space can be obtained. As pictured in Figure 2, the longitudinal phase space is shown where the particle's energy and phase is graphed relative to the synchronous particle (the particle that will be accelerated to the desired energy). The red oval on the diagram indicates the RF bucket, or the stable region, and so we only want to consider the emittance of those particles. I calculated this value along with the associated TWISS parameters and used it in TRACE3D. TRACE3D uses five times the root mean square (RMS) emittance, $5\tilde{\epsilon}$. I also calculated the transverse emittance and TWISS parameters by using the same output data and equations[4] found in the appendix.

The last thing I had to do to start modeling the beam was to calculate the radius of curvature of the ion path inside the bending magnet as well as the magnetic field of the magnet. After taking measurements of the circular geometry, I calculated the radius of curvature to be 483 mm using the relationship found in the appendix. I then used the relationship[5] $B=m_0 v\gamma/q\rho$ to calculate the magnetic field to be 1.133 tesla designed for Ag^{15+}.

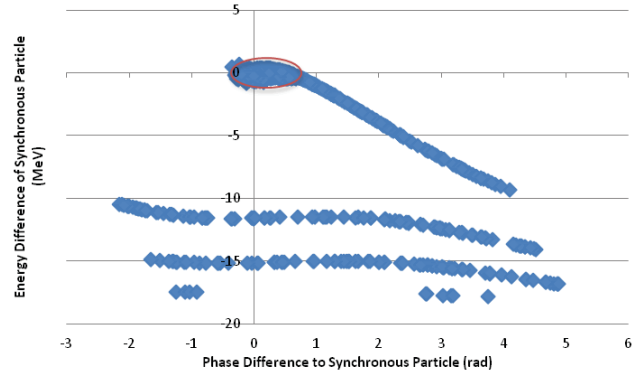

Figure 2: The longitudinal phase space where the RF bucket is shown by the red oval. The lost particles are outside the oval.

IV. RESULTS

In Figure 3 (b), the TRACE3D model for Ag^{15+} is shown by using the input file discussed in the methods section. There is concern that neighboring ion peaks may not be able to be resolved, and so the beam line must be designed for that. The distance between the centers of two neighboring ion peaks were found by using the relationship[6] $D=(\Delta P/P)\ \eta$, where η is the R_{16} value of the R transfer matrix in TRACE3D and represents the divergence function in meters. If D is greater than twice the x-radius, $2x_0=1.2$ cm, then there is enough distance between the neighboring peaks. In this case I found D to be 4.6 cm, which is more than enough to resolve the peaks. In theory, the neighboring ion will not even make it onto the MCP completely, and will be very easy to distinguish. This is shown in Figure 3 (a), where the red and blue lines indicate the paths of Ag^{15+} and Ag^{14+}, respectively and the distance between the lines at the MCP represent D. The beam profile in the y-axis comes out converging and the x-axis diverging. Soon, the beam profile in the y-axis over converges and starts to diverge while the beam profile in the x-axis continues to diverge. Thus, two quadrupoles placed close to the RFQ was required to prevent the two beam profiles from simultaneously diverging. A picture of the 32 mm quadrupole can be found in Figure 5 located in the appendix.

V. CONCLUSION

I conclude that a 1.133 Tesla magnet will be the appropriate strength to bend Ag^{15+} and that the distance between the center peaks of neighboring ions will be approximately 4.6 cm at the MCP. This allows for the peaks to have plenty of distance so that the resolution is good for analysis. We will scan the magnetic field strength to check the current of all the ions coming from the RFQ so that we can find the distribution. To check for lower charge states, the required magnetic field strength can be found by using the relationship in the methods section. After conducting the experiment, we expect to obtain the current graphs of the all the different charge-state ions. When a graph of the current distribution is made, the peak should be centered around Ag^{15+}. After this distribution is found, we could go back and check the accuracy of the PARMTEQ code by finding what fraction of the total current is $Ag1^{5+}$. Multiply that the total current by that fraction and we should obtain a current distribution similar to the one found in Figure 4.

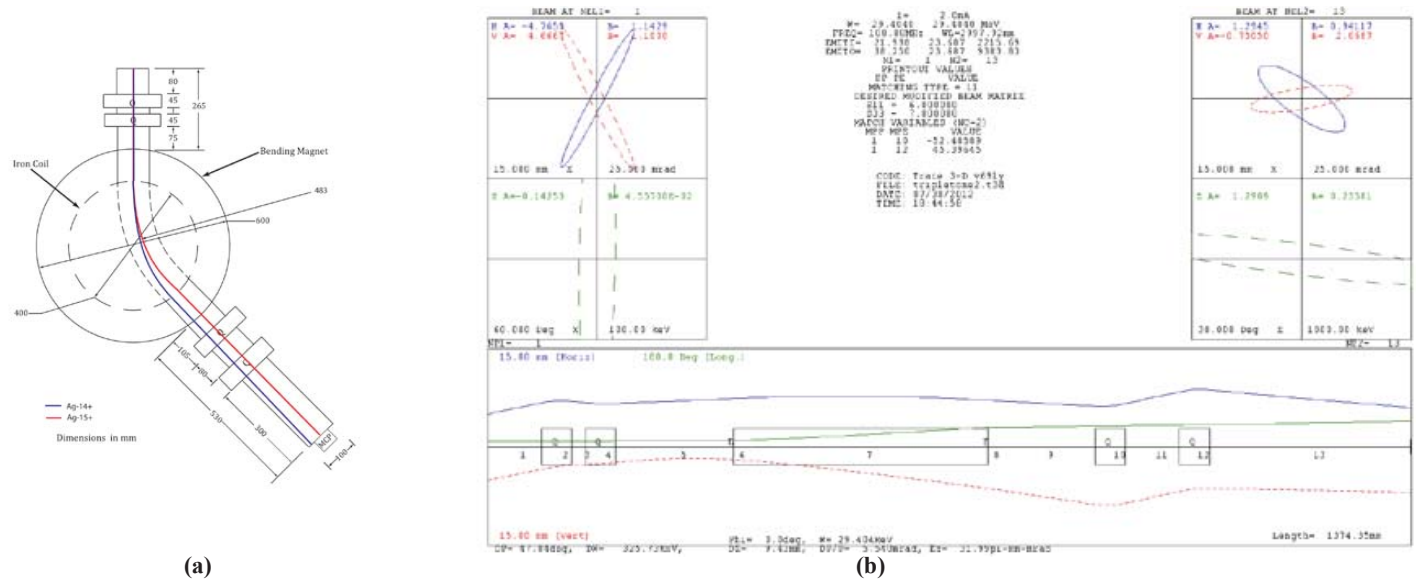

(a) (b)

Figure 3: The experimental setup is shown in (a) and the TRACE3D output is shown in (b).

VI. ACKNOWLEDGEMENTS

I thank my mentor Masahiro Okamura for his guidance throughout my project. I would like to thank Deepak Raparia for extensive conversations with him on numerous occasions about the use of TRACE3D software. Finally, I would like to thank my research group: Takayuki Yamamotto, Megumi Sekine, Takahashi Kazumasa, and Peter Jandovitz for assistance and educating me on the necessary background of lasers and plasma. I also thank the Department of Energy for sponsoring my internship.

VII. APPENDIX

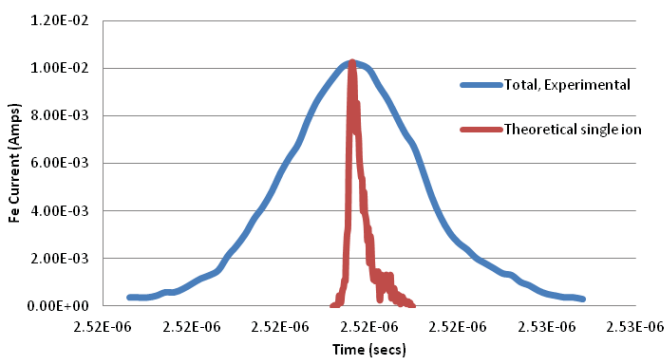

Figure 4: the relationship of total experimental current of iron versus an experimental single ion current of Ag^{15+}

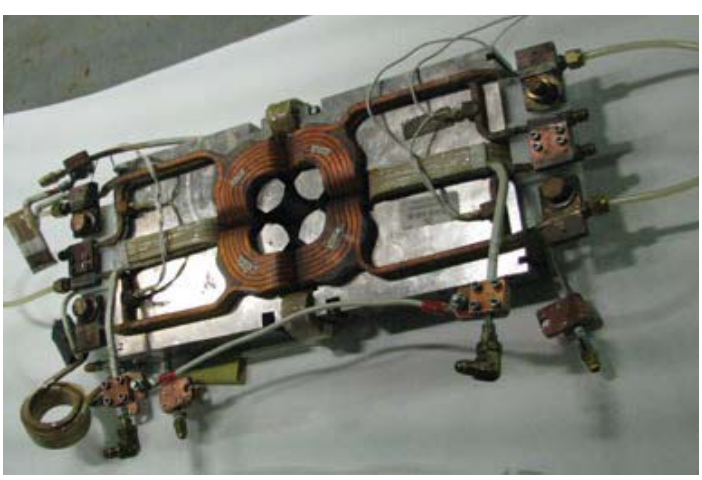

Figure 6: A picture of the 32 mm diameter quadrupole capable of obtaining magnetic field gradient of 68 T/m with an effective length of 45 mm.

A. Mathematical Formulae

1. Formulae used for emittance calculations and TWISS parameter calculations:

$$\dot{\epsilon}_x = \left(\overline{x^2}\,\overline{x'^2} - \overline{xx'}^2\right)^{1/2}, \quad \epsilon_x = 5\dot{\epsilon}_x, \quad \beta = \frac{\overline{x^2}}{\dot{\epsilon}}, \quad \gamma = \frac{\overline{x'^2}}{\dot{\epsilon}}, \quad \alpha = \sqrt{\beta\gamma - 1}$$

2. Formula used for the radius of curvature:

$$\rho = \frac{D}{\tan 22.5^\circ}, \quad D = \text{diameter of iron coil}$$

3. Formula used to scan the magnetic field:

$$B = \frac{m_0 v \gamma}{q\rho}$$

4. Formula used for resolution power of the peaks:

$$D = \frac{\Delta P}{P}\eta,$$

D=distance between peaks, P=momentum of particle, η=divergence function

Searching for the quantum chromodynamic critical point in relativistic heavy ion collisions

Mike Dai
Department of Electrical and Computer Engineering, Stony Brook University, Stony Brook, NY 11794
Jeffery T. Mitchell
Department of Physics, Brookhaven National Laboratory, Upton, NY 11973

ABSTRACT

The Pioneering High Energy Nuclear Interaction Experiment (PHENIX) is a particle detector located at the Relativistic Heavy Ion Collider (RHIC). Each year PHENIX collects tens of terabytes of data about the particles produced when nuclei collide at relativistic speeds. The purpose of our investigation was to use recently reconstructed PHENIX data to search for evidence of the quantum chromodynamic critical point, one of the primary objectives of the experiments at RHIC. Specifically, we scanned for fluctuations in particle multiplicity, total transverse energy production, and the ratio of antiprotons to protons produced as a function of transverse momentum at various RHIC collision energies. Many of these measurements had not yet been taken for these new datasets and were known to be monotonic at previous experimental settings. We looked for deviations from this behavior which would indicate that the system was in the vicinity of the critical point at one of these new experimental settings. Searching for these fluctuations is part of research that has been going on for many years, and has the potential to greatly increase our understanding of the theory of quantum chromodynamics if found. All work was done using the RHIC Computing Facility servers running the UNIX operating system. The ROOT data analysis package was used to perform most of the software operations necessary for our analysis including: Glauber Monte Carlo simulations, extraction of statistical information, data processing, and plotting the results. ROOT is a collection software libraries written in C++ and is heavily used within PHENIX's data analysis framework. As part of my work, I wrote and debugged the ROOT source code macros which were necessary to perform these operations and obtain our results. Our results show no significant evidence of critical behavior at these experimental settings and help to rule them out for critical behavior.

I. INTRODUCTION AND HYPOTHESIS

A. The quantum chromodynamic critical point

The quark gluon plasma (QGP) is believed to be a high energy phase of matter where individual elementary quarks and gluons exist completely deconfined from one another. The critical point in the theoretical QGP phase diagram is shown in Figure 1. It is thought that the QGP was the initial state of all matter in the universe moments after the big bang. The theory is that as the QGP cooled down, the constituent quarks and gluons recombined to form all matter present in the universe today.

The purpose of this investigation was to search for evidence of the quantum chromodynamic (QCD) critical point in the phase transition between the QGP and hadronic gas by analyzing data collected by the PHENIX detector. Finding the QCD critical point may help to explain much about the physical universe and the properties of matter. It will also provide firm evidence that the QGP is a distinct phase of matter. This search was done by examining the centrality dependent behavior of the total transverse energy production ($dE_T/d\eta$) and charged particle multiplicity ($dN/d\eta$), as well as the transverse momentum (P_T) dependent behavior of the antiproton to proton (P^-/P^+) ratio slope. Centrality is a measure of how head-on a collision is, and ranges between 0 (most central) and 1 (most peripheral). P_T refers to the magnitude of the transverse component the particle momentum at the time it hits the detector.

Because the baryon chemical potential of a system is not directly measurable, we instead scan for fluctuations in measurable quantities such as $dN/d\eta$, $dE_T/d\eta$, and the P^-/P ratio as indicators of critical behavior. The goal of our analysis was to examine how these measurable quantities behave as a function of collision energy ($\sqrt{S_{NN}}$). $\sqrt{S_{NN}}$ is also a measure of the amount of energy available to produce particles. A plot of a measurable quantity vs. $\sqrt{S_{NN}}$ is called an excitation function. The word excitation is used to indicate that in the vicinity of the critical point, the corresponding point on this function will be "excited" and deviate significantly from the rest. The data points for these excitation functions usually follow a monotonic distribution.[2] We looked for systems whose excitation functions did not follow a monotonic distribution as indications of critical behavior.

B. The PHENIX detector

Assembled in 1999, the PHENIX detector at RHIC has been operational for the past 12 years. The detector itself consists of a collection of detectors, or subsystems, each of which performs a specific role in the detection of particles and collection of data in response to a heavy ion collision. The name PHENIX originates from the fact that the detector is a resurrection of a number of particle detector engineering proposals which were not immediately approved during the assembly phase of RHIC. An image of the disassembled PHENIX detector and a cartoon of its subsystems are shown in Figure 2.

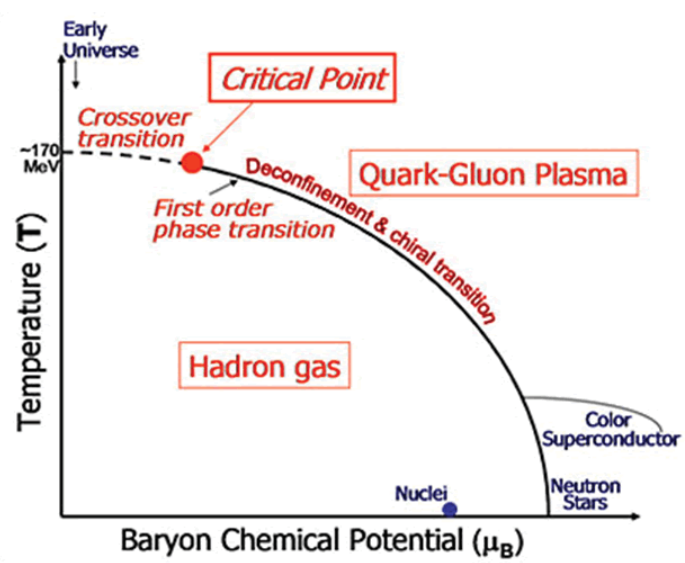

Figure 1. Theoretical QCD phase diagram for the QGP. Baryon chemical potential (μb) is analogous to pressure and is related to the baryon density of the system.[1]

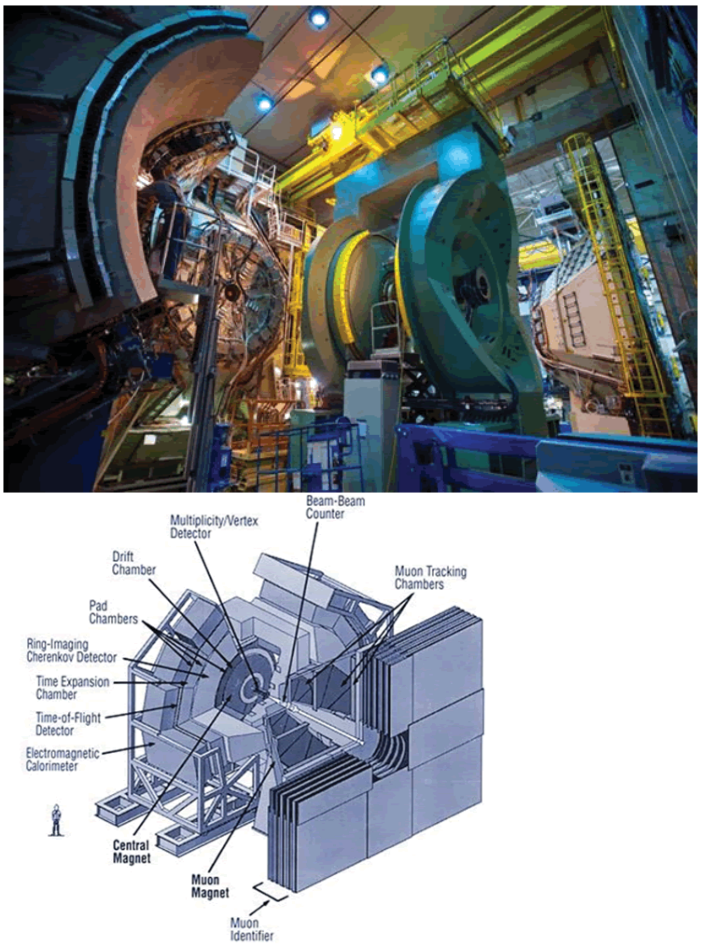

Figure 2. The PHENIX detector and its various subsystems.[7]

C. Computing at PHENIX

Most of my analysis work was done through remote connections to the RHIC Computing Facility (RCF) servers which run the UNIX operating system. These RCF machines are located in the physics building and have access to the software and data files which were necessary for our analysis.

MobaXterm is a commercial, Windows-based xterminal client which was used to establish simultaneous ssh connections to multiple RCF machines. This improved productivity by allowing the execution of parallel tasks in different xterminal windows and was essential due to the somewhat limited nature of the command line interface used in UNIX.

1. Data analysis at PHENIX

All of the raw ADC data from PHENIX's subsystems are recorded on magnetic tapes. The data stored on these tapes is reconstructed using various reconstruction algorithms for the purpose of obtaining event and particle track information. An event is a data structure which contains information about a collision which was recorded by the detector. Each event can contain multiple particle tracks. A particle track is subset of data in an event which contains information about a single particle as it moved through the detector. Each event has information associated with it such as where the event occurred, and how head on the collision was. Each particle track also has information associated with it which may include the particle trajectory, charge, energy and momentum. Other quantities, such as P_T and mass need to be calculated from the particle track information which was directly measured by the detector. All reconstructed data is saved to disks arrays at the RHIC computing facility. The amount of analyzable PHENIX

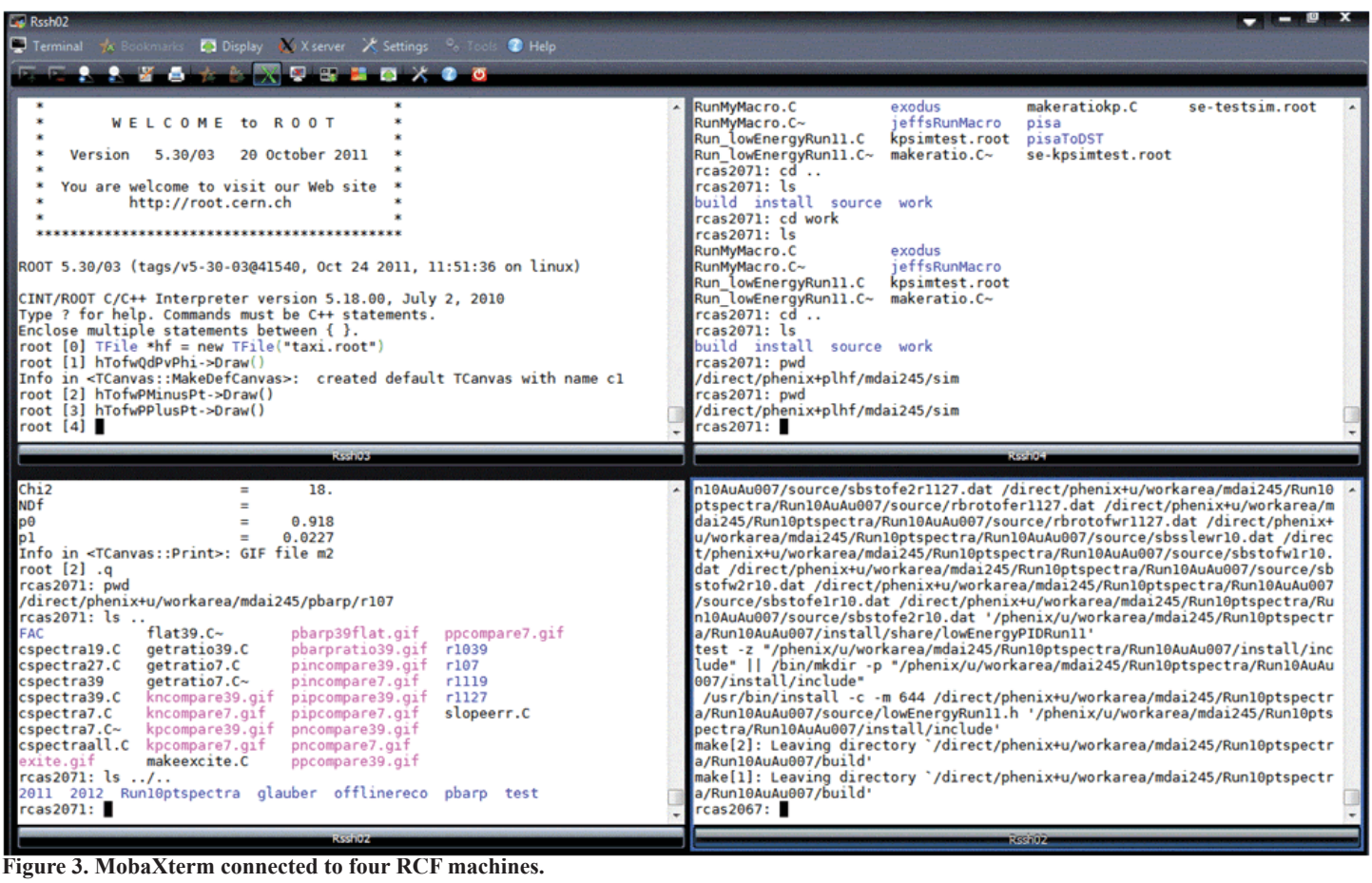

Figure 3. MobaXterm connected to four RCF machines.

data which is stored on these disk arrays is currently around 2.5 PB.

a. ROOT

ROOT is a program developed at CERN which consists of many object-oriented packages and libraries written in the C++ programming language. ROOT is capable of performing a wide range of computational and graphical tasks, as well as data analysis and simulation on large quantities of data. The base functionality of ROOT can be expanded by linking external libraries. ROOT is used heavily within PHENIX's data analysis framework. Examples of ROOT functionality are shown in Figure 4.

ROOT is capable of interpreting C++ commands in-line without the need for the user to first compile the source code. When more complex procedures are required, the user can write and execute a ROOT macro. These macros typically consisting of a single void function containing the necessary sequential commands to be passed to the ROOT interpreter. Data objects used by ROOT are stored in .root files. Objects which are created in a ROOT session, including those loaded from data files are stored in memory for the session and can be used for as long as the user does not quit ROOT. Appendix A shows a simple root macro I wrote which creates the bin-by-bin ratio of two histogram objects from a .root file and saves the result as a .gif image. A comprehensive list of root classes, member functions and associated UML diagrams can be found at http://root.cern.ch/root.

b. Analysis code

Analyzing data at PHENIX involves writing analysis source code which contains the procedure that describes what needs to be done with the data. A typical analysis code consists of a single class named for the analysis, constructor and destructor methods, an init() method, a process_event() method, and a reset_event() method. Additional methods may be introduced when required, but must also be member functions of the class.

Analysis code must be compiled before use and the user must set an environment variable which points to the location of the compiled code before running an analysis so that the framework can locate it. Once this is done, a ROOT macro is executed which begins the analysis process. This macro is called a run macro and creates an instance of the analysis and PHENIX's Fun4All analysis framework. This begins the analysis process as defined by the framework using the methods defined in the analysis class.

The dataset to be analyzed can be specified within the run macro or by passing the run macro text files which contain the names and paths of the relevant .root data files. These .root files contain data structures called trees which contain information about the events and particles recorded by PHENIX during a RHIC run. Multiple data files may exist for each RHIC run at a particular $\sqrt{S_{NN}}$ and species type, and are referred to as a dataset.

During a run of the analysis code, the init() method is called first, and only once per analysis session. Init() serves to initialize all member objects which are defined in the class. The process_event() method is then called once for each recorded event in the tree. The purpose of this method is to perform event and track selection, to apply data calibrations and offsets, and to fill various histograms with information about the events or tracks. A loop is contained within process_event () to process each particle

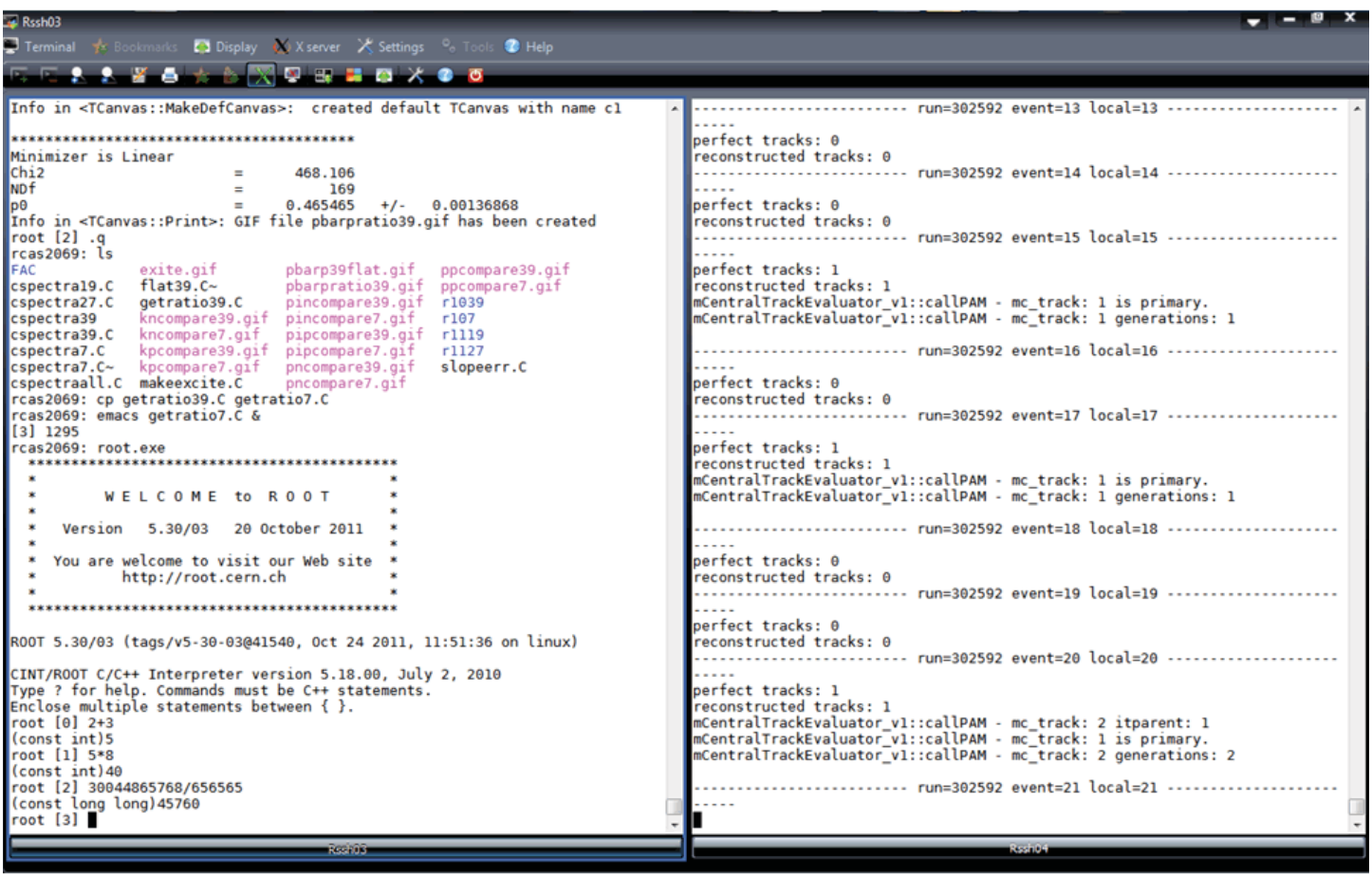

Figure 4. ROOT has a wide range of functionality which can be easily expanded. It can perform simple in-line computations (left), as well as Monte Carlo simulations (right).

track associated with every event. Reset_event() clears event and track information prior to processing a new event. All methods are called by reference in the analysis code to increase processing speed and efficiency.

Once there are no more events to process the analysis job is done, and an output .root file is written to disk. This root file contains the output histograms which can be used for physics analysis.

c. Analysis Taxi

Due to network constraints and the fact that the full data files need to be accessed from the data disk array each time an analysis is run, access to these disks is controlled to avoid I/O overload in the array. Only a fraction of the total data is made readily available for testing and debugging purposes. These files are called disk resident files. Running the analysis over an entire data set requires that the analysis code be submitted to the analysis taxi, which is a framework for submitting analysis jobs at PHENIX. The analysis taxi has access to all 2.5 PB of the data files stored on the data disk array and runs twice a week.

d. Testing and debugging

Some analysis tasks did not require a full dataset and were run using only the disk resident files. This was usually done for testing and debugging purposes. For example, in order to have analysis code accepted by the taxi, it had to pass a construct called the gate keeper. The gate keeper runs a bug checking program (valgrind) and a memory leak detector (insure) on the code. Before submitting any analysis code to the gate keeper for a taxi ride, the code needed to be manually debugged using both valgrind and insure over a disk resident sample for testing purposes. Any bugs or memory leaks had to be addressed before each taxi deadline. Memory leaks can be particularly hazardous in a method such as ProcessEvents() which may be called millions of times per analysis depending on the number of events in a dataset.

e. Regarding our analysis

Overall, three sets of analysis code were written for the three different types of measurements we were taking. The handling of different datasets as part of those measurements was done via an indexing system used in the code which passed a dataset index to the constructor of the analysis class, letting the analysis know what to do for each dataset. Analysis code is lengthy, typically consisting of several thousand lines of code. A template can be found in Appendix B along with a sample run macro in Appendix C.

The following sections detail the various methods which were used in our analysis. It can generally be assumed that each procedure was repeated multiple times, once for each dataset used. Any reference to "cuts" refers to event or track exclusion algorithm within the analysis code. For example, a cut on P_T > 2.5 GeV means that particles with a transverse momentum greater than 2.5 GeV were excluded from the analysis. As a result of such a cut, no histograms would be filled with an entry corresponding to a particle track with a calculated PT greater than 2.5 GeV.

II. METHODS AND MATERIALS

A. Total energy production measurements

The $dE_T/d\eta$ measurements were determined using the electromagnetic calorimeter (EMC) subsystem of the PHENIX detector. The EMC consists of 8 sectors, each one containing many electronic readout towers. When a particle strikes the EMC, several of the towers are fired which generate an EMC cluster. Each cluster has some energy associated with it and can be unpacked to determine how much energy is contributed by each tower in the cluster. The raw E_T measurements were calculated by summing the total energy from each tower. Of the 8 sectors shown in Figure 5, only the 5 active PbSc sectors of the EMC were used.

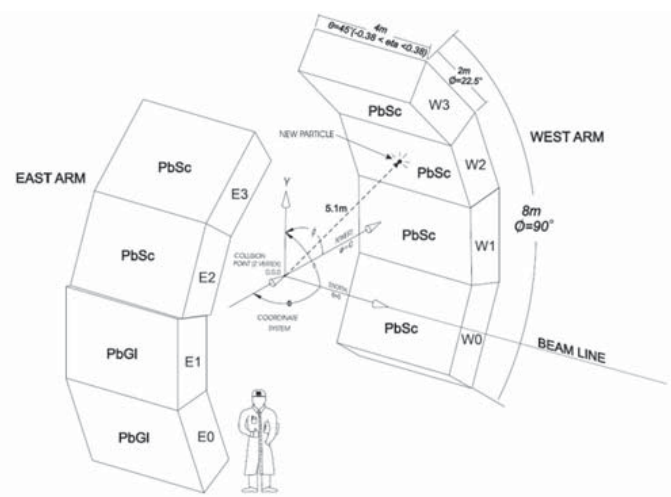

Figure 5. Layout of the EMC with respect to the PHENIX coordinate system.[3]

Tower map occupancy results:				
sector 0:	out = 647	good = 1981	total = 2628	pct good = 0.753805
sector 1:	out = 664	good = 1964	total = 2628	pct good = 0.747336
sector 2:	out = 741	good = 1887	total = 2628	pct good = 0.718037
sector 3:	out = 789	good = 1839	total = 2628	pct good = 0.699772
sector 4:	out = 1193	good = 3415	total = 4608	pct good = 0.741102
sector 5:	out = 1004	good = 3604	total = 4608	pct good = 0.782118
sector 6:	out = 721	good = 1907	total = 2628	pct good = 0.725647
sector 7:	out = 770	good = 1858	total = 2628	pct good = 0.707002
total:	out = 4332	good = 11436	total = 15768	pct good = 0.725266

Table 1. Dead and hot tower map results for sector 2 in 27 GeV Au+Au collisions.[4]

1. EMC calibrations

The raw transverse energy (E_T) required calibration to correct for several sources of systematic error before $dE_T/d\eta$ measurements could be made.

a. Dead and hot tower removal

The purpose of this correction was to remove dead or hot EMC towers from the analysis. 2D tower frequency histograms were created with one bin per tower arranged in the x-y geometry of the towers for each sector of the EMC. These histograms were filled with the number of times each tower contributed to a cluster. 1D hit frequency histograms were generated from these tower frequency histograms and fit to Gaussian distributions. Towers with a hit frequency more than 5σ from the mean were marked as dead or faulty in the analysis code and were not used. A sample summary of the dead or hot towers for Run 11 27 GeV Au+Au is shown below.

b. Sector-by-sector energy scale

Prior to measuring $dE_T/d\eta$, the analysis code was run once to determine the energy scale offset required to mitigate the energy losses which occur in the detector. The E_T distribution of each sector was multiplied by an energy scale factor prior to calculating the total E_T for an event. This scale factor was determined from a Gaussian fit of the invariant mass peak distributions of π^0 seen by each sector of the EMC. The mean of this peak was compared to the known π^0 mass. The correction factor was derived from this comparison.

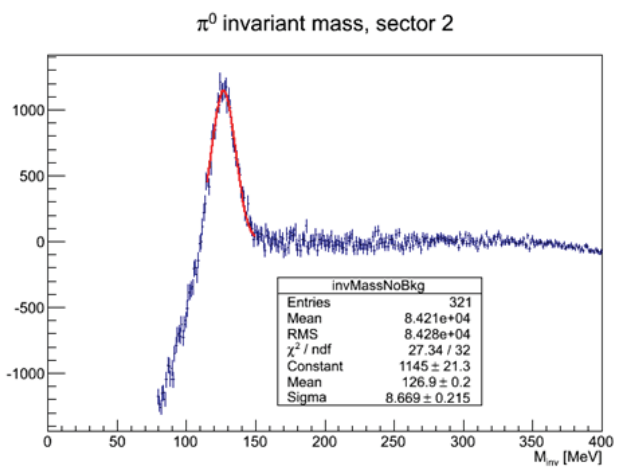

Figure 6. sector 2 π0 invariant mass distribution in Au+Au 27 GeV collisions fit to a Gaussian distribution.

2. dET/dη calculations

The analysis code was run once again with the calibrations applied. 16 1D E_T histograms were filled for each of 16 different centrality bins. These bins cover the range of 0% centrality to 80% centrality in 5% increments, and are used throughout this analysis to examine the centrality dependent behavior of the various measurable quantities. A sample of the resulting raw E_T distributions is shown in Figure 7. These distributions were integrated to determine the raw total energy production.

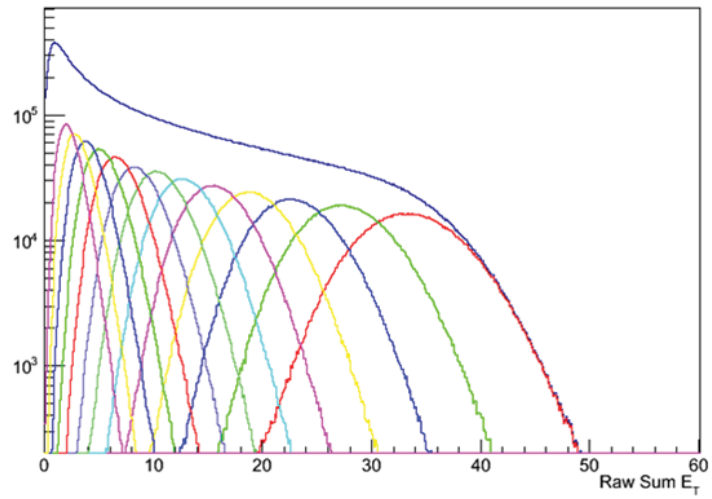

Figure 7. Overlapped raw ET distributions in 5% centrality bins + total in Au+Au 27 GeV collisions. A 0.1% background level is present in each bin, but not shown.

From the raw E_T measurement, the total transverse energy production is calculated:

$$\frac{dE_T}{d\eta} = E_{T,raw} \times k \times a \times t$$

where k is a correction factor which accounts for defects in the EMC, a is a correction for the actual EMC acceptance area, and t is a correction factor for the towers which were masked out.

3. Bjorken energy density estimates

The Bjorken energy density of each system was also estimated to determine the likelihood of QGP formation. The Bjorken energy density is calculated:

$$\in BJ = \frac{1}{A_o \tau} \frac{dE_T}{dy}$$

where A_o is the overlap area of the nuclei determined from the Glauber model and τ is the formation time, and dE_T/dy is $dE_T/d\eta$ times 1.25.[4]

4. Run-by-run quality assurance

3σ cut on: centrality, number of tracks, BBC total charge, total E_T and z-vertex

5. Event selection

Minimum bias triggered events

|z-vertex| < 30 cm for Au+Au collisions

|z-vertex| < 10 cm for Cu+Au collisions

Events with at least 2 hits in both BBC north and BBC south

6. Datasets used

200 GeV Cu+Au, 193 GeV U+U, 27 GeV Au+Au, 19.6 GeV Au+Au, 200 GeV Cu+Cu, and 62.4 GeV Cu+Cu

B. Charged particle multiplicity measurements

The dN/dη measurements were made using the beam beam counter (BBC) subsystem of the PHENIX detector. This subsystem consists of a pair of detectors--BBC North and BBC South--which are located in close proximity to the beam line and collision vertex of each event. The purpose of the BBC is to count the number of charged particles produced in each collision and to determine the centrality of each event. These charged particles are steered toward the BBC by the PHENIX central magnet. Our raw multiplicity measurements were directly determined by the number of charged particles which hit the BBC.

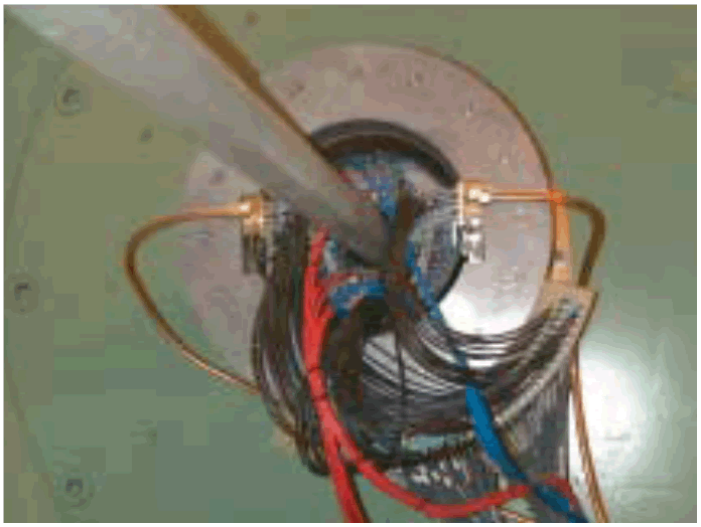

Figure 8. BBC south (donut shaped metal), beam pipe, and PHENIX central magnet (green).[7]

Sixteen 1D raw multiplicity histograms were filled for each of 16 centrality bins to examine the centrality dependent behavior of dN/dη. Samples of these histograms are shown overlapped in Figure 9 along with the total multiplicity distribution at 27 GeV.

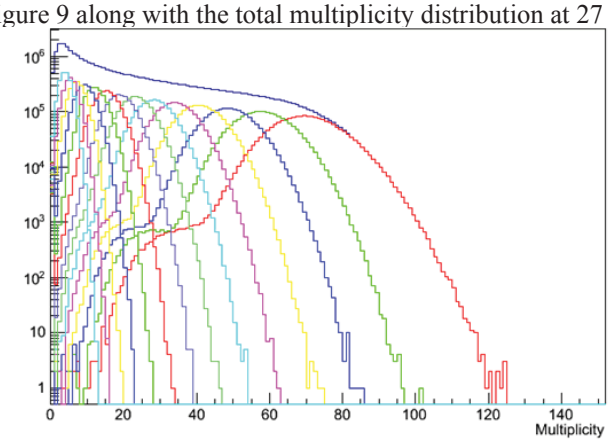

Figure 9. Overlapped raw multiplicity distributions in 5% centrality bins + total in Au+Au 27 GeV collisions.

1. Correction Factors

A set of correction factors needed to be applied to the raw multiplicity distributions before dN/dη could be determined.

a. Wire-by-wire drift chamber efficiency correction

This correction is required to correct for the wire-by-wire inefficiencies seen in the drift chamber (DCH) tracking subsystem. A 1D histogram is filled with the DCH ϕ-angle distribution of particles which hit the DCH. For each arm of the detector, the ϕ bin which contains the most particle hits is assumed to correspond to a grouping of DCH wires which are perfect. The value of this bin is then propagated to the rest of the bins within the ϕ-angle acceptance of the DCH. The resulting rectangles for each DCH arm are then integrated and summed. This sum represents the number of particles tracked by the DCH in the ideal case. This number is used to divide the actual number of DCH tracks to determine the necessary correction factor.

b. Tracking efficiency correction as a function of centrality

This correction is required to correct for the fact that the tracking efficiency of PHENIX is not uniform as a function of centrality. At higher centrality, the increased particle multiplicity tends to confuse the algorithms which are used to reconstruct event and particle tracks. The tracking efficiency drops as a result.

c. Charged particle in-flight decay correction

Some particles decay as they travel from the collision vertex through the detector which can add or subtract particles from the measured multiplicity. The appropriate correction factor for each $\sqrt{S_{NN}}$ was determined from a look up table.

2. Run-by-run quality assurance

3σ cut on: centrality, number of cgl tracks, BBC total charge, total ET and z-vertex

3. Event selection

Minimum bias triggered events
|z-vertez coordinate| < 30 cm for Au+Au
|z-vertez coordinate| < 10 cm for Cu+Au
|DCH z-coordinate| < 75 cm
Events with least 2 hits in both BBC north and BBC south
DCH track qualities of 31, 51 or 63

4. Datasets used

200 GeV Cu+Au, 193 GeV U+U, 27 GeV Au+Au, 19.6 GeV Au+Au, 200 GeV Cu+Cu, and 62.4 GeV Cu+Cu

5. Determining the number of participants using the Glauber Model

The number of participant nucleons (N_{part}) in an event is directly related to the centrality of the event. Between N_{part} and centrality, N_{part} is the more desirable quantity because it universally describes the amount of interaction in a collision, whereas centrality is a measure which was established at PHENIX. As such, most of our results will be presented in terms of N_{part} instead of centrality. A Glauber model Monte Carlo simulation program used to determine N_{part} information for each dataset. This program takes as an input the species type, RHIC collision energy and BBC trigger efficiency and outputs the required conversion tables.

The BBC trigger efficiency was determined by fitting a negative binomial distribution (NBD) to a probability mass function (PMF) describing the number of particles which were seen by the BBC in the ideal case. This PMF was also generated using the Glauber model by referencing real data. The actual number of hits seen by the BBC was compared to the probabilistic model to determine the trigger efficiency of the BBC. An example of such a PMF and a NBD fit is shown in Figure 10.

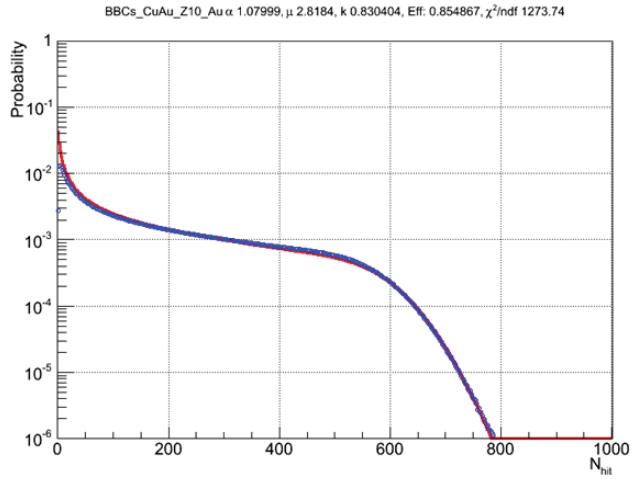

Figure 10. Simulated PMF for the number of particles which hit the BBC within a region of ± 10cm of the center of the BBC. The plot is drawn on log scale. The red line is the NBD fit.

C. Slope of the antiproton to proton ratio vs. transverse momentum measurements

The time of flight west (ToFW) subsystem of the PHENIX detector provides a time coordinate for the amount of time it takes a particle to travel from the collision vertex to the ToFW. It consists of 512 individual multi-gap resistive plate chamber strips. The position and layout of the ToFW are shown in Figure 11.

The timing information provided by the ToFW is critical in identifying charged particle species by their masses for the purpose of counting the number of each particle species seen in a given dataset. he mass squared of a particle can be calculated:

$$m^2 = \frac{tc^2}{l} - 1$$

where t is the time of flight of the particle from the collision vertex to the ToFW, c is the speed of light, and l is the path length of the particle trajectory through the detector.

1. ToFW timing calibrations

The raw timing data provided by the ToFW required several calibrations before it could be used to provide accurate particle identification (PID) information. This PID information was necessary for counting the relative numbers of P^- and P^+ at varying P_T. These calibrations included:

- A strip-by-strip slewing offset to correct for the errors introduced by flaws in its analog-to-digital converter and time-to-digital converter electronic systems
- A strip-by-strip timing offset to account for the non-uniform timing provided from different strips
- A strip-by-strip matching correction to correct for mismatches between particles and strip hits
- A run-by-run timing offset to account for changes which occured between the individual runs in a dataset (Au+Au 27 GeV only)

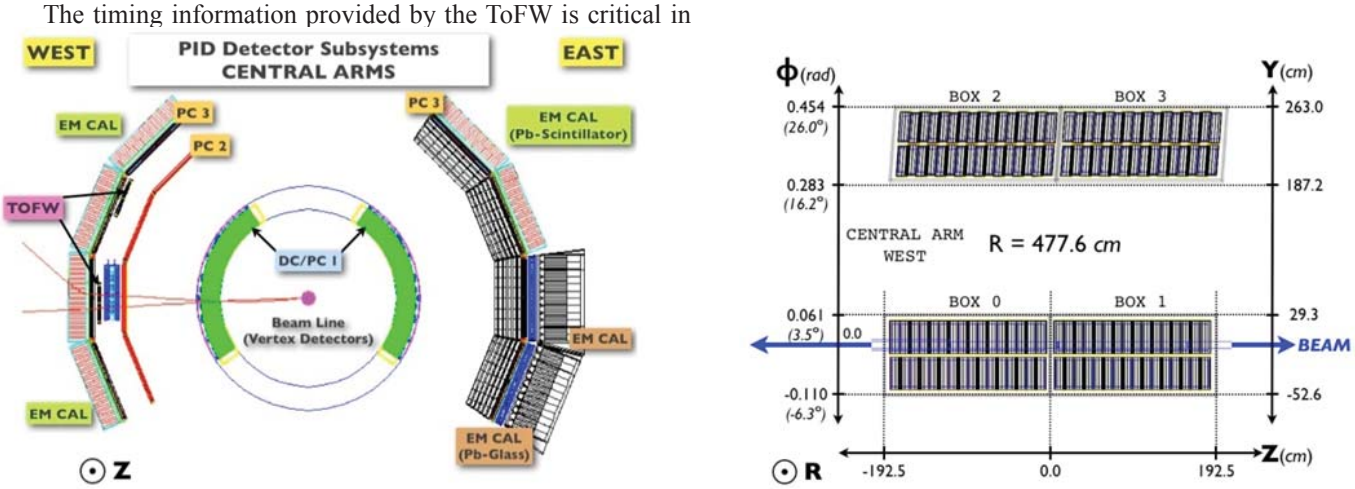

Figure 11. Position and layout of the ToFW detector at PHENIX. The acceptance area of the ToFW is relatively small.

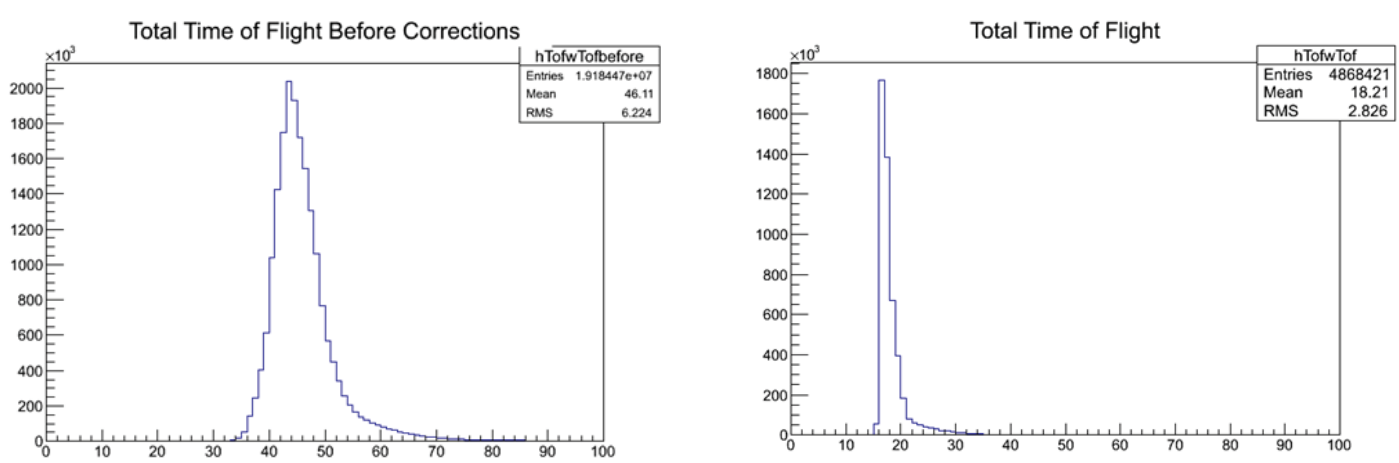

Figure 12. Time of flight (ns) before corrections (left) and after (right).

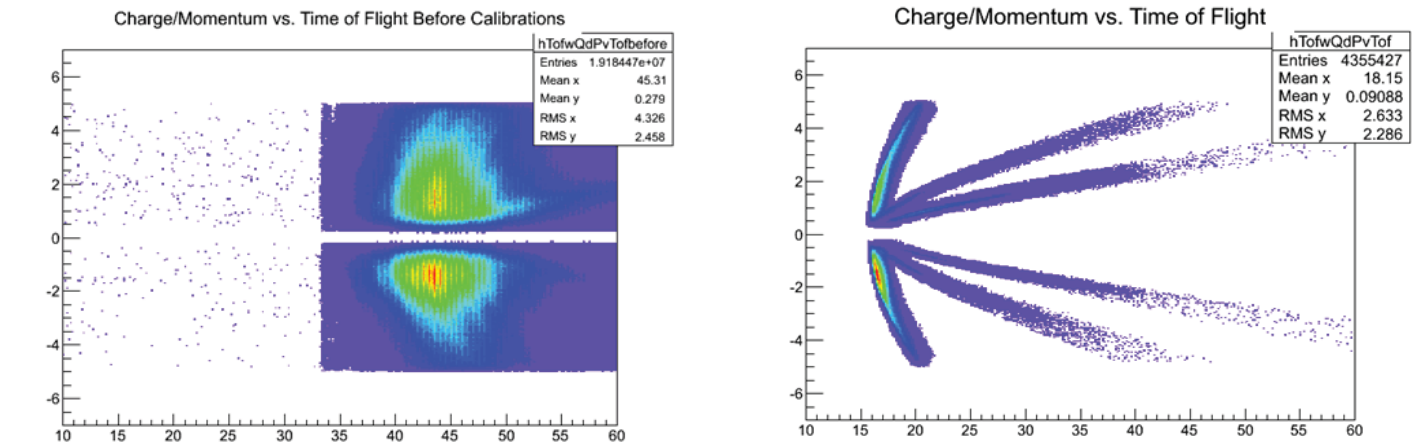

Figure 13. Charge divided by Momentum vs. ToFW ϕ-coordinate before fiducial cut (left) and after (right).

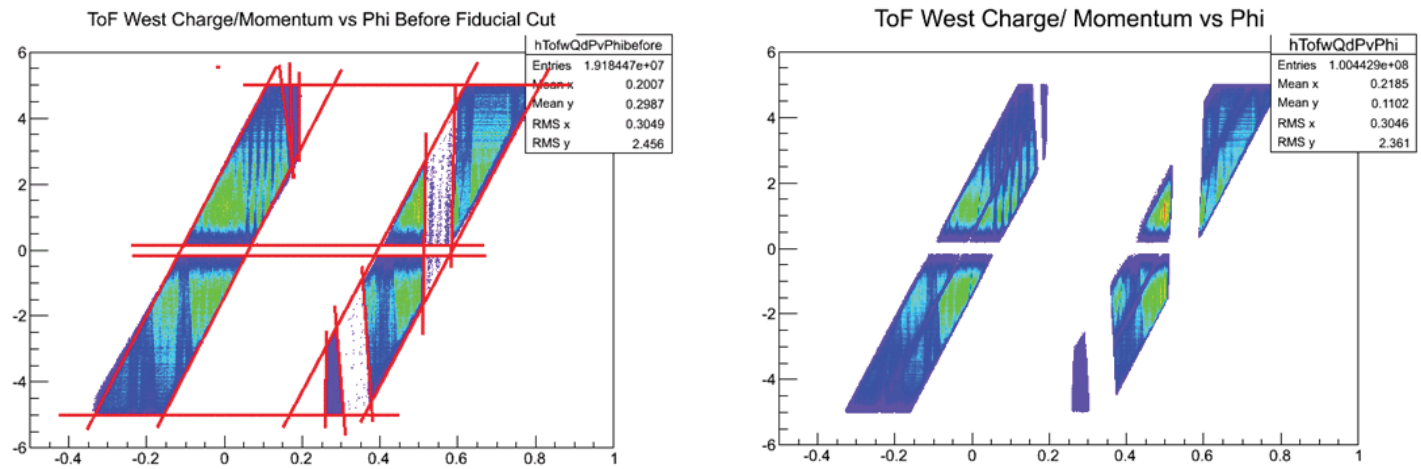

Figure 13a. Charge divided by momentum vs. time of flight before corrections (left) and after (right). The brightly colored bands represent charged π, K and P seen by the detector.

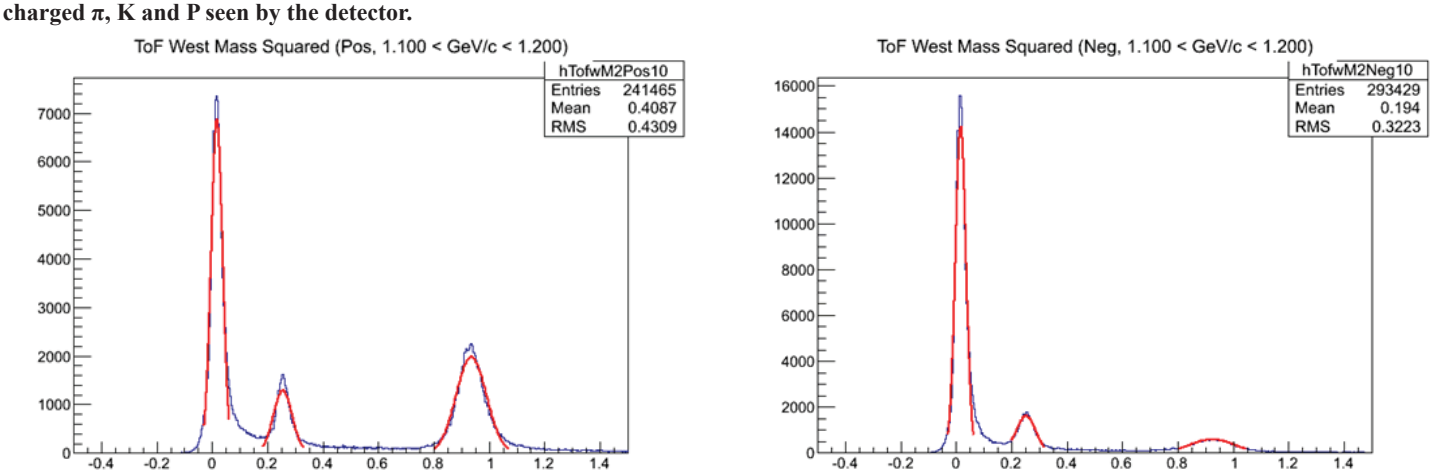

Figure 14. Positive (left) and negative (right) charged m2 distributions in PT bin 10. The red lines are Gaussian fits.

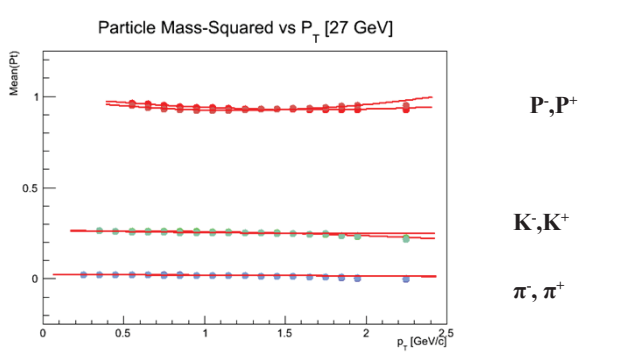

Figure 15. The red lines describe mass(PT) for P^+, P- ,K^+, K^-, π^+, π^- in Au+Au 27 GeV collisions.

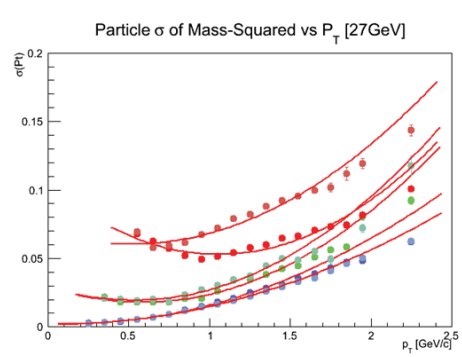

Figure 16. The red lines describe σ(PT) for P^+, P^- ,K^+, K^-, π^+, π^- in Au+Au 27 GeV collisions.

The ToFW timing calibrations were provided for us in the form of text data files. They were integrated into the code by adding the appropriate methods and loading the calibrations into the analysis code. The calibration of the ToFW is a lengthy process. A detailed procedure can be found in PHENIX Analysis Note: TOFW recalibration for Run8 dAu.[6] Figure 12 and Figure 13 show the cumulative result of the timing calibrations and cuts on the time of fight and PID information. The cuts will be described in later sections. These corrections were essential for accuracy in the mass calculations which were used to identify charged particle species.

2. ToFW fiducial cut

The purpose of the fiducial cut was to remove particle tracks which fell outside the actual ϕ-angle acceptance of the ToFW detector. These may include tracks from inefficient strips of the detector as well as unwanted background.

A set of linear equations were used to outline the geometric acceptance area of the ToFW in momentum and ϕ space. These equations were then used in the analysis code to cut out the unwanted tracks.

3. Particle Identification Functions

This section describes the process of developing the functions which described how the mass and standard deviation of the mass of the various particles seen by the ToFW behaves as a function of P_T for the purpose of counting the number of P^- and P^+ varying P_T necessary to measure the P^-/P^+ vs. P_T slope.

a. P_T bins

Eighteen 1D histograms were filled with the m^2 distributions of particles which hit the ToFW in 100 MeV/C P_T. bins ranging from 0.2 – 2.0 GeV/c for both positive and negative charged particles. Two additional 1D histograms were filled for charged particles falling in the 2-2.5 GeV/c P_T range, for a combined total of 38 1D m^2 distribution histograms. The m^2 peaks seen in these histograms, such as those which are shown in Figure 14, represent the three types of charged hadrons which are typically seen by the ToFW. These are π^-, π^+ ($m^2 \cong 20$ MeV), K-, K+ ($m^2 \cong 244$ MeV) and P^-, P^+ ($m^2 \cong 879$ MeV). These peaks were fit to Gaussian distributions for all 38 histograms in each dataset.

b. PID functions - mean(P_T) and σ(P_T)

The resulting mean and σ of these distributions are plotted as a function of P_T and fit to second order polynomials for each of the 6 charged particle species as shown in Figure 15 and Figure 16. These polynomials model the behavior of the mean and σ of the m2 distributions as a function of P_T, and are used to identify charged particles by their mass. These PID functions for $\sqrt{s_{NN}}$ = 27 GeV are shown in Figure 15 and Figure 16. The following pseudo code describes how these functions were used to identify charged particles:

If ($m^2 \geq$ mean(P_T)-2σ(P_T) && $m^2 \leq$ mean(P_T)+2σ(P_T))
  is[species] = true

where species can be π^+, π^-, K^+,K^-,P^+ or P^-. For example, if the mass of a negatively charged particle track was within ± 2σ of the expected mass of a P^- for a given P_T range, then it was identified as a P^- candidate.

c. Ambiguous track and background cut

A method of definitively identifying particle species was required because the PID functions did not account for overlaps in the Gaussian fits of the m2 distributions or unwanted background. An example this is shown in Figure 17. The particle tracks shaded in black are either ambiguous, such as the shaded region between the π and K mass peaks, or considered unwanted background, such as in the shaded regions around the proton peak. This functionality was implemented for each particle species by nesting another if statement within the previous statement, which removes these unwanted tracks using the PID functions of the other two particle types. A sample of the actual code which does this can be found in Appendix D.

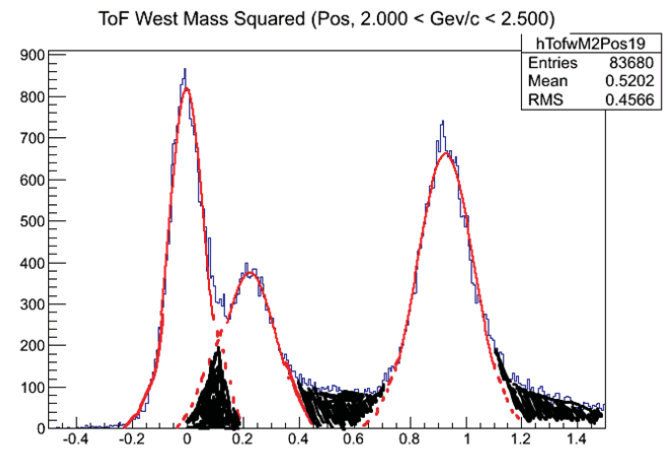

Figure 17. The purpose of the overlap and ambiguous track cut is to remove tracks in the shaded regions from the analysis.

d. P_T spectra and P^-/P^+ slope calculation

Using the PID functions, 1D particle P_T distribution histograms are filled from 0 to 5 GeV/c for each of the 6 particle species. These histograms are referred to as P_T spectra histograms. The P^-/P^+ ratio vs. P_T is obtained by dividing the P- P_T spectra by the P^+ P_T spectra. The slope of this ratio at each $\sqrt{s_{NN}}$ corresponds to a point on the excitation function of the P^-/P^+ ratio vs. P_T slope.

The slope was measured by fitting the ratio of the P^- and P^+ P_T spectra over a P_T range of 0.8-1.5 GeV/c for all datasets. This range was chosen because it covers a region in momentum space where timing resolution of the ToFW is at its highest. Sample P_T spectra for P^- and P^+ in the Au+Au 19 GeV dataset are shown in Figure 18.

4. ToFW acceptance corrections

The ToFW has a relatively small acceptance area compared to that of PHENIX. This is even smaller when compared to the spherical area around the PHENIX detector. The purpose of this correction was to obtain an analogue of the detector response as though it had perfect spherical coverage in the PHENIX coordinate system. This was to be done by using simulations and real data to determine a set of correction factors to multiply the P^- and P^+ P_T spectra by which would produce this response.

Unfortunately, the simulation software used to generate the appropriate correction factors was not functioning correctly. As a result, correction factors from a previous analysis had to be used. These correction factors were only applicable to the 7 and 39 GeV Au+Au datasets in the –+ PHENIX central magnet field configuration. These correction factors were generated as a function of P_T,

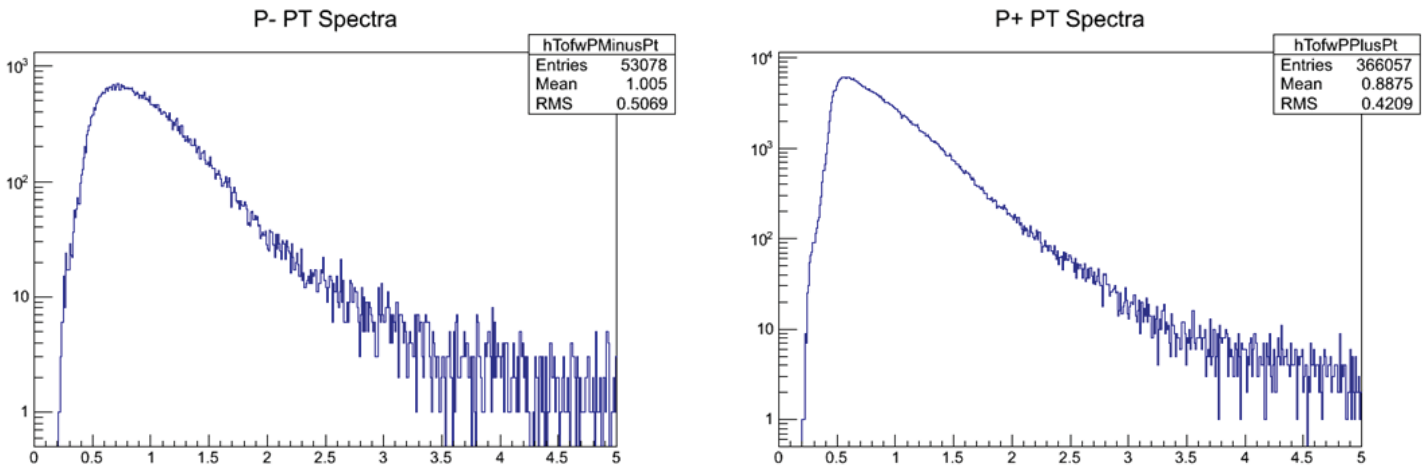

Figure 18. P^- P_T spectra (left) and P^+ P_T spectra (right) from 0 to 5 GeV/c in Au+Au 19 GeV collisions.

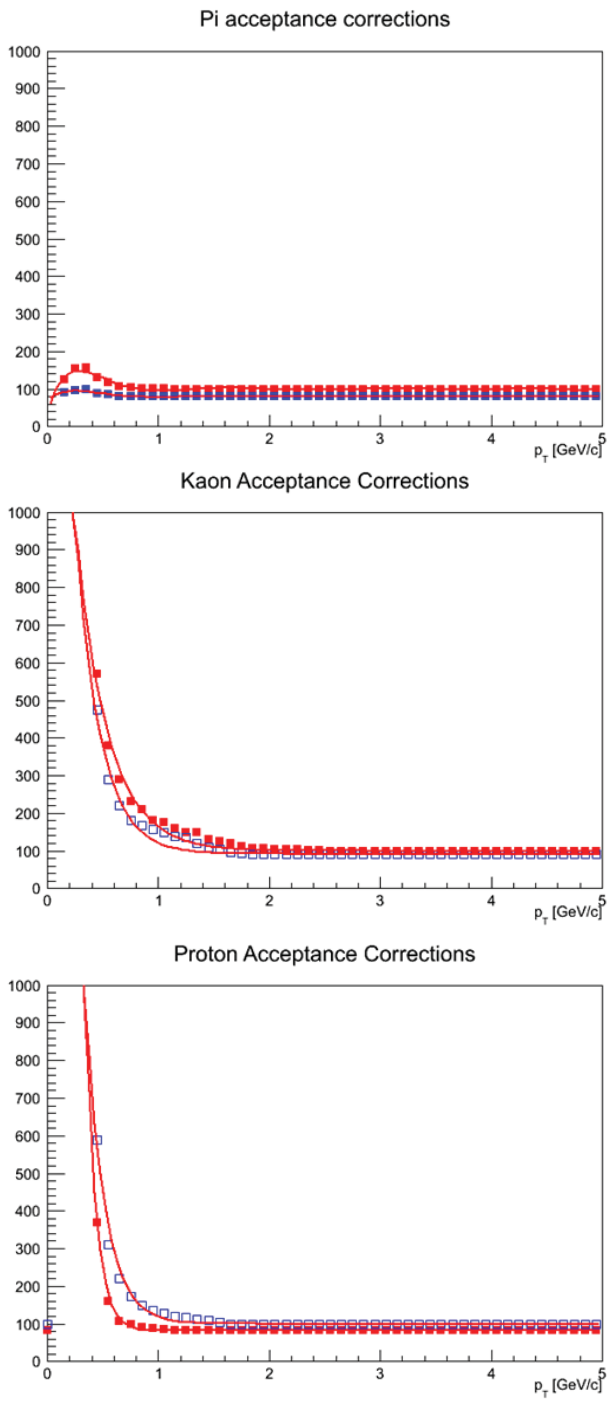

so applying them was a simple matter of multiplying histograms, however obtaining these histograms was not as strait forward.

The correction factors came in the form of histogram images found in a previous PHENIX analysis note,[6] but were not readily available as data objects which could be used in the code. Because of this, the correction factor histograms had to be reconstructed manually using the images in the analysis note as a basis.

For each particle species, a macro was created which created a blank histogram and then plotted the appropriate correction factors as a function of P_T. These correction factors had to be predetermined by eye and were input into the macro before running it. The resulting plots were fit to functions, either an nt^h order polynomial or a decaying exponential, which best described their behavior. The correction factors for each species are shown in Figure 19.

To apply the correction factors, a second macro which multiplied the P_T spectra for each of the 6 species by these correction factors was created. This macro read in the raw P_T spectra histograms from the analysis taxi output, cloned them, and then multiplied them bin-by-bin by the appropriate correction factor as a function of the P_T value associated with the center of each bin.

5. Event Selection

Minimum bias triggered events
Events with least 2 hits in both BBC north and BBC south
|z-vertez coordinate| < 30 cm

6. Track Selection

$0.2 \leq PT \leq 5$ GeV/c
|DCH z-coordinate | $\leq$ 75 cm
|ToFW Δz| and|PC3 ΔZ| $\leq$ 10 cm
|ToFW $\Delta\phi$| and|PC3 $\Delta\phi$| $\leq$ 1cm
Fiducial acceptance correction (7, 39 GeV)
ToFW bad strip rejection (19, 27 GeV)
Electron rejection

Figure 19 (Left). Manually reconstructed correction factors for negative (blue squares) and positive (red squares) charged hadrons as a function of P_T for P^+, P^- (bottom),K^+, K^- (middle), π^+, π^- (top). The red line is a function which describes how these correction factors behave as a function of P_0.

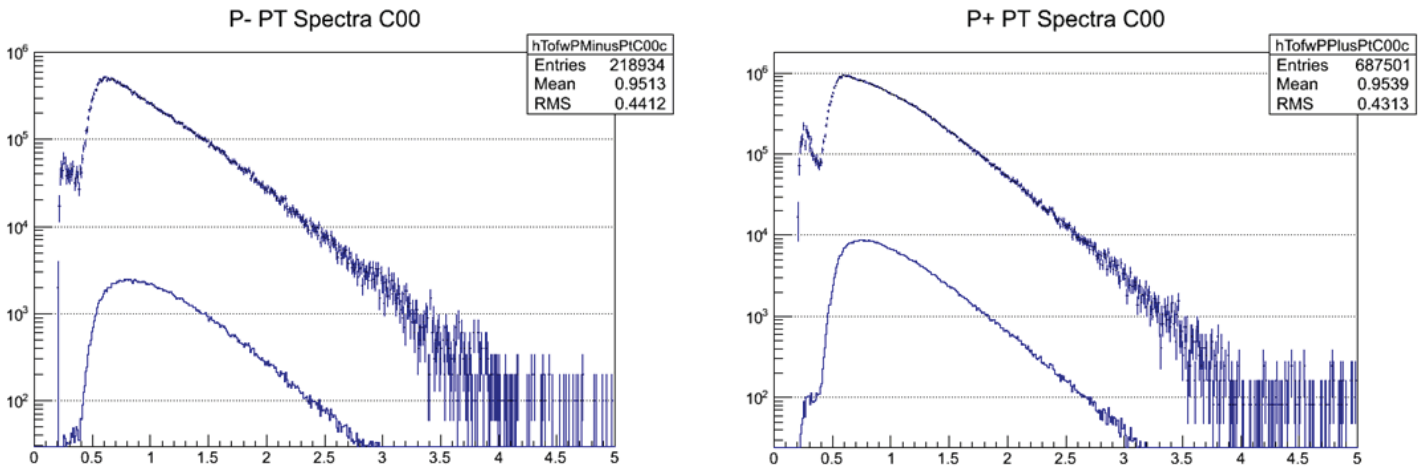

Figure 20. Overlay plots of the P^- (left) and P^+ (right) P_{T-} spectra both with and without the correction factors in Au+Au 39 GeV collisions. The corrected P_{T-} spectra are the larger of the two distributions shown on each plot.

7. Datasets used

7.7 GeV Au+Au, 19 GeV Au+Au, 27 GeV Au+Au and 39 GeV Au+Au

III. RESULTS

The $dE_T/d\eta$ and $dN/d\eta$ measurements are taken directly from our analysis note.[4] Our results for the 19.6 GeV Au+Au, 27 GeV Au+Au, 200 GeV Cu+Cu, 62.4 GeV, Cu+Cu 200 GeV and Cu+Au datasets are shown alongside existing measurements from other experiments at different $\sqrt{s_{NN}}$ for comparison purposes. The $dE_T/d\eta$ and $dN/d\eta$ results are presented as functions of N_{part} which is directly related to centrality (see materials and methods 5).The error bars in these plots represent statistical and systematic errors. All excitation functions are shown using only data from the 5% most central collisions for the best statistics.

A. Total energy production results

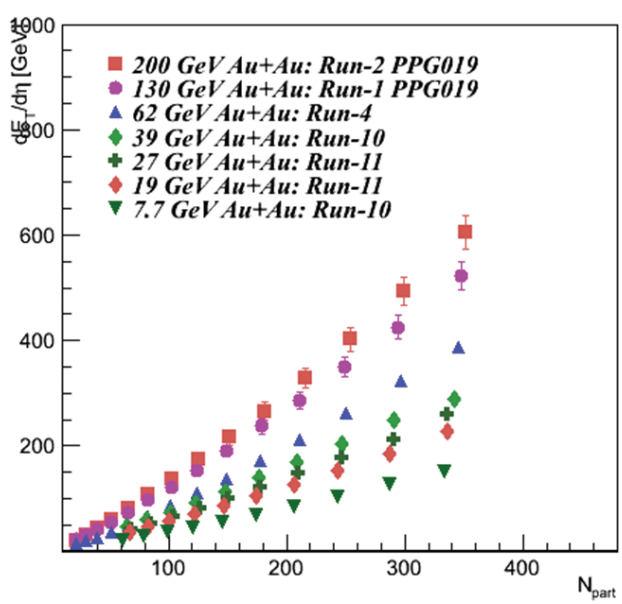

Figure 21. $dE_T/d\eta$ as a function of Npart for PHENIX Au+Au collisions. Higher N_{part} points represent more central collisions. Our measurements provide the 19 and 27 GeV points.

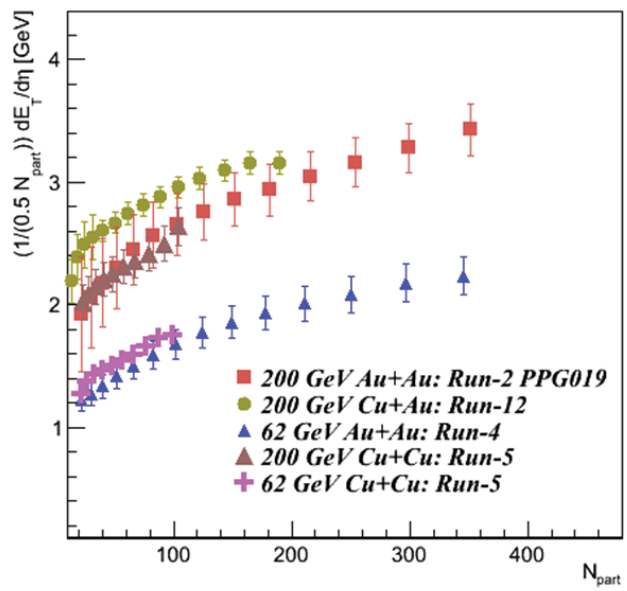

Figure 22. $dE_T/d\eta$ normalized by the number of participant pairs as a function of N_{part} for 200 GeV Cu+Cu and 62.4 GeV Cu+Cu collisions compared to Cu+Au and Au+Au collisions.

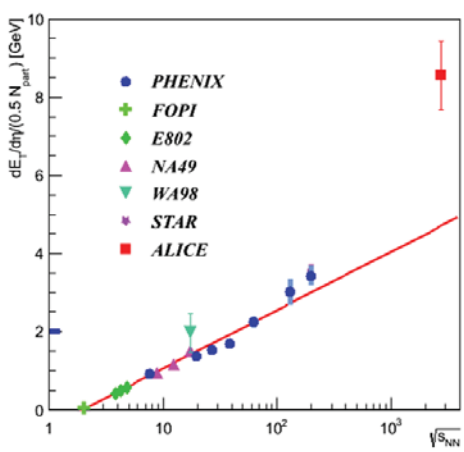

Figure 23. Excitation function of $dE_T/d\eta$ for the top 5% most central Au+Au. Our measurements provide the 19 and 27 GeV data points. The red line is a logarithmic fit to all points excluding the LHC points.

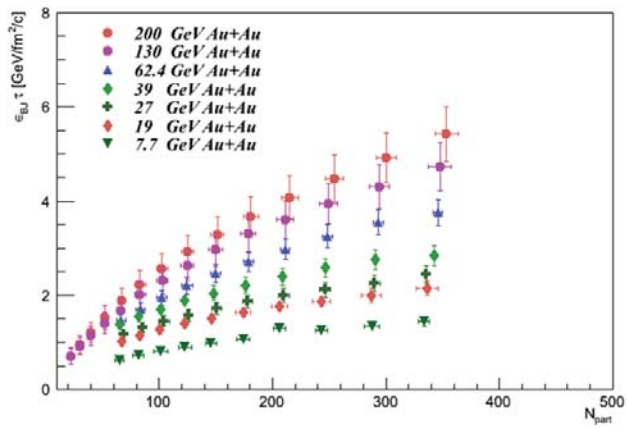

Figure 24. The estimated Bjorken energy density multiplied by the formation time as a function of N_{part} for all PHENIX Au+Au measurements. Our measurements provide the 19 and 27 GeV data points.

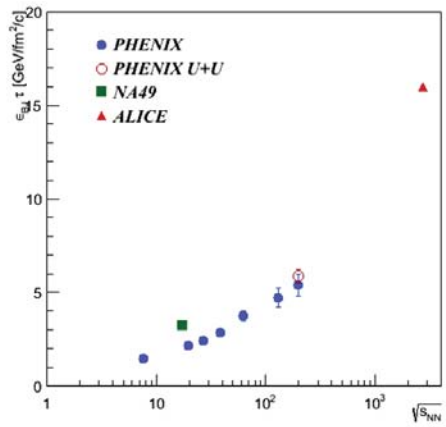

Figure 25. Excitation function of the estimated Bjorken energy in Au+Au collisions. The blue dots represent PHENIX Au+Au measurements. Our measurements provide the 19 and 27 GeV data points, as well as the 193 GeV U+U data point.

B. Charged particle multiplicity results

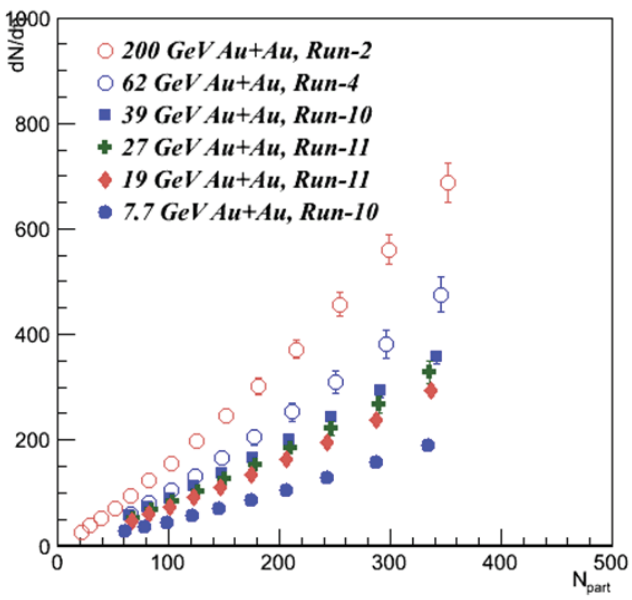

Figure 26. dN/dη as a function of N_{part} for PHENIX Au+Au collisions. Our measurements provide the 19 and 27 GeV points.

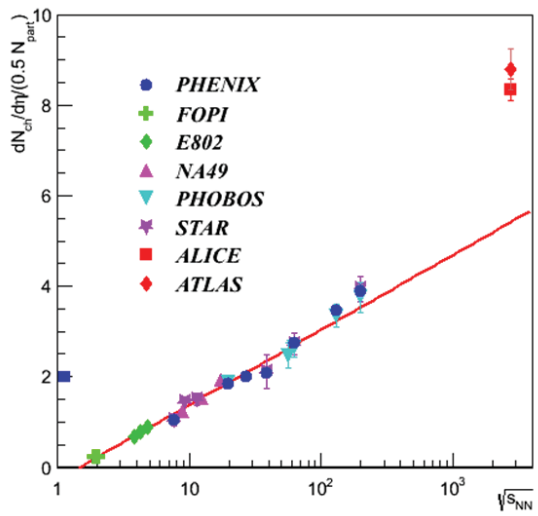

Figure 27. Excitation function for dN/dη normalized by the number of participant for the top 5% most central Au+Au collisions. The red line is a logarithmic fit to all points excluding the LHC points.

C. Antiproton to proton ratio vs. transverse momentum slope results

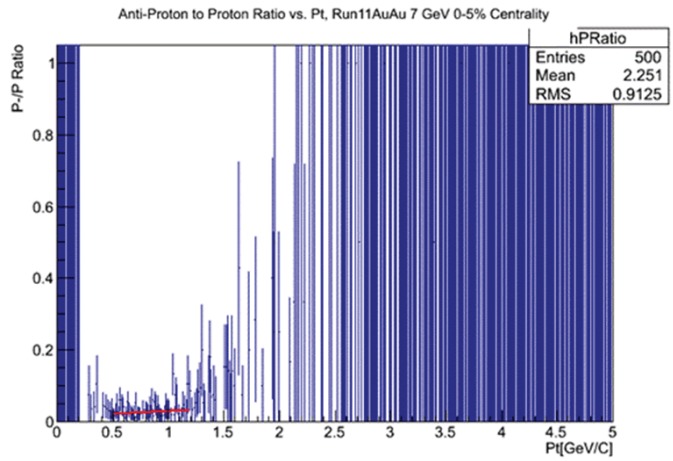

Figure 28. P^-/P^+ vs. P_T in Au+Au 7 GeV collisions. The red line is the fit which was used to measure the slope. The vertical blue bars represent statistical errors.

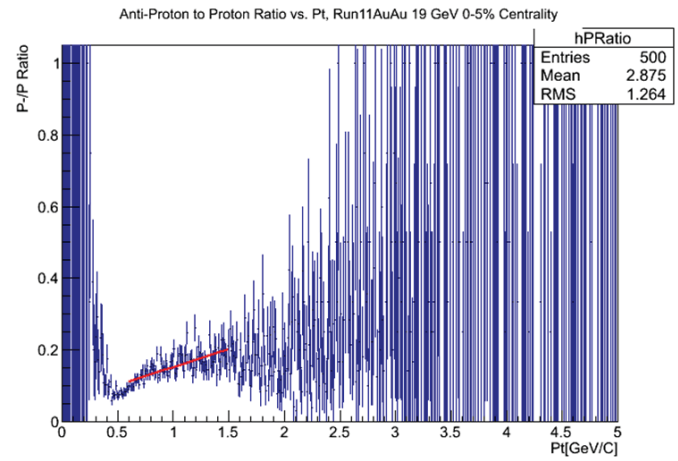

Figure 29. P^-/P^+ vs. P_T in Au+Au 7 GeV collisions. The red line is the fit which was used to measure the slope. The vertical blue bars represent statistical errors.

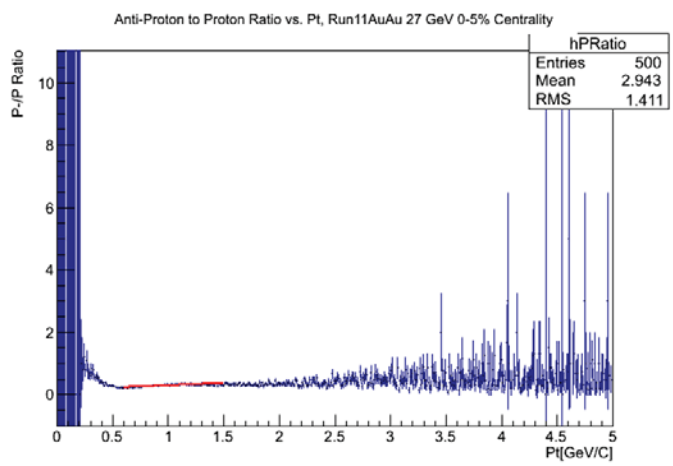

Figure 30. P^-/P^+ vs. P_T in Au+Au 7 GeV collisions. The red line is the fit which was used to measure the slope. The vertical blue bars represent statistical errors.

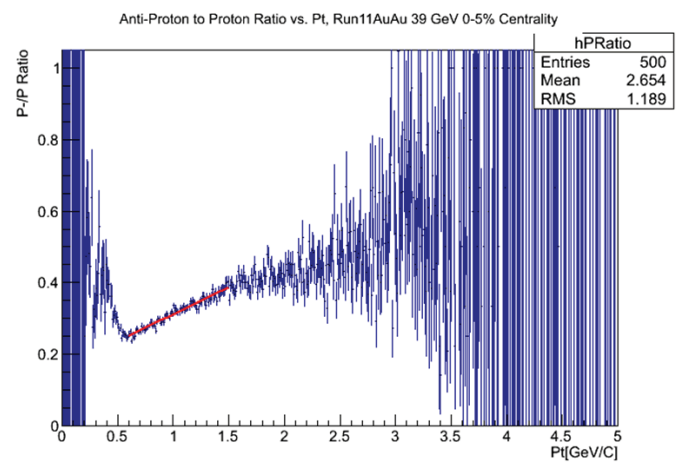

Figure 31. P^-/P^+ vs. P_T in Au+Au 39 GeV collisions. The red line is the fit which was used to measure the slope. The vertical blue bars represent statistical errors.

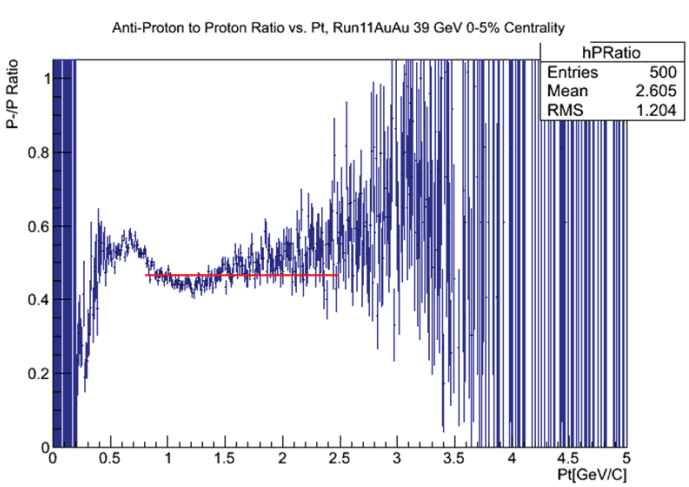

Figure 32. P^-/P^+ vs. P_T in Au+Au 39 GeV collisions with the ToFW acceptance correction (see Methods: C.4). The red line is used to illustrate that the slope flattens out as a result of the correction.

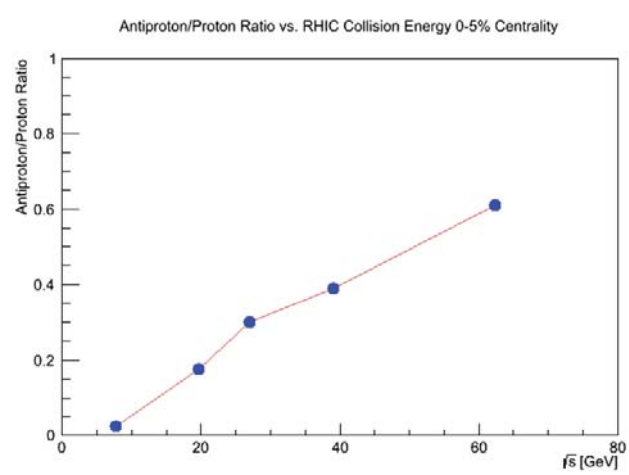

Figure 33. Measured P^-/P^+ ratio as a function of P_T. These are rough approximations determined through flat line fits of the P^-/P^+ vs. P_{T-} distributions. There are no error bars present.

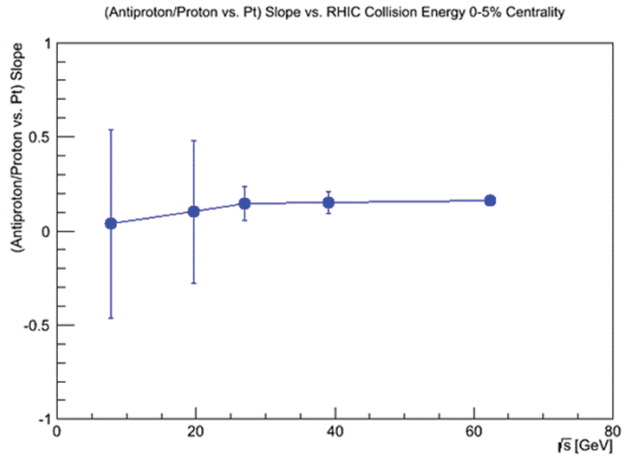

Figure 34. Excitation function of the P^-/P^+ vs. P_T slope in PHENIX Au+Au collisions. The uncorrected 39 GeV slope measurement is shown for consistency. The 62.4 GeV data point is added from a previous result. The error bars represent statistical errors.

IV. DISCUSSION AND CONCLUSION

The U+U 193 GeV results are not shown here because of inconsistencies with previous data which are likely the result of systematic error. Due to time constraints, the ToFW acceptance correction was not applied to all datasets in the PID analysis.

A. Discussion of $dE_T/d\eta$ results

The results in Figure 21 and Figure 22 show that the value of dET/dη increases monotonically with increasing centrality and $\sqrt{S_{NN}}$ in all datasets. A difference in the $dE_T/d\eta$ measurements in Au+Au and Cu+Cu collisions at similar $\sqrt{S_{NN}}$ is observed in Figure 22. This shows that the nuclei species plays a role in $dE_T/d\eta$. Heavier ions result in higher amounts of energy produced because they are more massive.

The excitation function of $dE_T/d\eta$ in Au+Au collisions is shown in Figure 24. This excitation function contains data points from several experiments along with our new 19 GeV and 27 GeV PHENIX measurements. Our new measurements agree well with the existing trend line. The large hadron collider (LHC) experiment point from ALICE does not follow the trend line because it was run at a much higher $\sqrt{S_{NN}}$. The $\sqrt{S_{NN}}$-axis in the excitation function is drawn on a log scale. The plot points at lower energies appear to be linear as a result. The point from ALICE shows that the excitation function of $dE_T/d\eta$ may actually follow an exponential distribution.

The Bjorken energy density estimate excitation function seen in Figure 25 is increasing monotonically with increasing $\sqrt{S_{NN}}$, and is consistently above 1.0. This is particularly interesting because 1.0 has been proposed as the lower threshold for QGP production. If this is true, then our results show that the QGP can be formed in at collision energies as low as 7 GeV.

B. Discussion of dN/dη results

Figure Figure 26 shows that the value of dN/dη increases monotonically with increasing centrality and $\sqrt{S_{NN}}$ in all datasets. The excitation function for dN/dη in Au+Au collisions shown in Figure 27 contains data from various experiments, as well as our new 19 GeV and 27 GeV PHENIX measurements. The distribution of these points looks very similar to that which is seen in the excitation function for $dE_T/d\eta$. Once again the points which come from LHC experiments, ATLAS and ALICE, do not follow the trend line.

C. Discussion of Antiproton to proton ratio vs. transverse momentum slope results

Figures 28 through 31 show the P^-/P vs. P_T distributions for each of the datasets used in this analysis. The large error bars in the high and low P_T ranges exist because of the relatively low number of particle tracks seen at these P_T. Low momentum particles are especially affected by the magnetic field which causes them to completely miss the detector in some cases. The line fits used to measure the slopes were done in the .6 GeV/c to 1.5 GeV/c P_T range for all datasets. This region in P_T was chosen because it is where the timing and momentum resolution of the ToFW and DCH provide the best statistics.

Figure 23 shows the P^-/P^+ vs. P_T distribution in 39 GeV Au+Au collisions with the ToFW acceptance correction. This is the simulated response of the ToFW with full spherical coverage in PHENIX's coordinate system. Due to time constraints, only the 39 GeV dataset had this correction applied. The resulting distribution can be observed to be flatter as a function of PT which is expected in a system which is not in the vicinity of the critical point.

The relationship between the P^-/P^+ ratio and $\sqrt{S_{NN}}$ can be observed in Figure 33. This plot shows that as the amount of energy available for particle production increases (the collision energy), so does the amount of antimatter produced as the result. The following relationship has been proposed to exist between the antimatter/matter ratio and $\sqrt{S_{NN}}$ in relativistic heavy ion collisions:

$$\lim_{\sqrt{S_{NN}} \to \infty} = 1$$

Our results are consistent with this.

The excitation function of the P^-/P^+ ratio vs. P_T slope is shown in Figure 34. The slope is seen to be nearly flat as a function of $\sqrt{S_{NN}}$ and that the value of the slope is consistently close to zero. None of the points appear to be excited. This is not indicative of critical behavior. The relatively large error bars $\sqrt{S_{NN}} = 7$, 19 GeV are due to the fewer number of particle tracks observed at these energies.

D. Concluding remarks

Overall, no significant evidence of the QCD critical point has been found in the various measurements and experimental settings considered in this investigation. All results also show good agreement with preexisting results and help to rule out these experimental settings for critical behavior.

E. Other Thoughts

Given additional time, I would have implemented the ToFW acceptance correction for all datasets in the P^-/P^+ vs. P_T measurements. I would have also wanted to examine how the P^-/P ratio behaves as a function of centrality, and whether or not it is consistent with the $dE_T/d\eta$ and $dE_T/d\eta$ results. I would have also liked to have been able to spend more time at the PHENIX detector helping with the repair of the Muon Arm Tracker (MuTr).

My interest and understanding in the field of particle physics, data analysis, and engineering have grown significantly since I began my summer internship at BNL. During my time here, I have developed valuable data analysis, programming and hardware repair skills which will surely come in handy in my future career as an engineer. I am very satisfied with my summer experience and consider myself to be very lucky to have had a chance to participate in such an exciting experiment.

V. ACKNOWLEDGEMENTS

This work was supported by the Department of Energy, Office of Science and the National Science Foundation. I thank my mentor Jeff Mitchell (BNL) and the Office of Education Programs at BNL for providing me with a wonderful summer internship experience. I would also like to thank Dr. Sheng Li Huang for providing the ToFW timing calibrations, as well as the Dr. Leitch and the rest of the MuTr group for allowing me to participate in the repairs of the MuTr south.

VI. REFERENCES

1. T. Nayak, "Search for the QCD Critical Point at RHIC: First Experience with Au-Au Collisions at 9.2 GeV," (2008). http://www.bnl.gov/rhic/news/040808/story3.asp.
2. M. A. Stephanov, "QCD phase diagram: an overview," (2006). arXiv:hep-lat/0701002.
3. R. Armendariz, "Phenix Analysis Note: 62.4 GeV Au+Au and 200 GeV Au+Au event-by-event E_T Distributions Measured in High Statistics, and Average E_T per Participant Nucleon in RHIC Run 4 Interactions," Unpublished analysis note (2004).
4. Jeffery Mitchell, Mike Dai and Mingxui Sun, "Phenix Analysis Note 1054 Global Measurements for Au+Au, Cu+Au, Cu+Cu, and U+U Collisions," Unpublished analysis note (2012).
5. PHENIX Collaboration "Systematic studies of the centrality and $\sqrt{S_{NN}}$ dependence of $dE_T/d\eta$ and dNch/dη in heavy ion collisions at midrapidity." The American Physical Society #034908 (2005). Print.
6. R. Belmont, S. Huang, "PHENIX Analysis Note: TOFW recalibration for Run8 dAu," (2010).
7. PHENIX Collaboration, PHENIX main page, (2012). http://www.phenix.bnl.gov.

VII. APPENDIX

A. Sample ROOT macro

```
//This macro performs the bin by bin division of two histograms and saves the result as an image
//file.

void getSlopeErr(const char* outFile = "test.root")

  //load .root file
  TFile *hf = new TFile("r1039/taxi.root");

  //Declare local variables. The binning here needs to be the same as hProtonPtC00
  Int_t nBins = 500;
  Float_t val1[500];
  Float_t err1[500];
  Float_t val2[500];
  Float_t err2[500];
  Float_t ratio[500];
  Float_t ratioErr[500];

  //create new 1D histogram object and label axes
  TH1D *hPRatio = new TH1D("hPRatio","Anti-Proton to Proton Ratio vs. Pt, Run11AuAu 0-5%   Cen-
trality",500,0.0,5.0);
  hPRatio->GetXaxis()->SetTitle("Pt[GeV/C]");
  hPRatio->GetYaxis()->SetTitle("P-/P Ratio");

  //Fill the new histogram with the ratio of two histograms contained in the .root file
  for (Int_t i=0; i<500; i++) {
    val1[i] = hTofwPPlusPtC00->GetBinContent(i);
    err1[i] = hTofwPPlusPtC00->GetBinError(i);
    val2[i] = hTofwPMinusPtC00->GetBinContnt(i);
    err2[i] = hTofwPMinusPtC00->GetBinError(i);
    ratio[i] = 0.0;
    if (val1[i] != 0.0) ratio[i] = val2[i]/val1[i];
    ratioErr[i] = (err2[i]/val1[i])*(err2[i]/val1[i]) +
      ((val2[i]*err1[i])/(val1[i]*val1[i]))*
      ((val2[i]*err1[i])/(val1[i]*val1[i]));
    ratioErr[i] = sqrt(ratioErr[i]);
    hPRatio->SetBinContent(i,ratio[i]);
    hPRatio->SetBinError(i,ratioErr[i]);
  }
```

```
    //Fit the resulting distribution to line
    TF1 *linefit = new TF1("linefit","[1]*(x-1.05)+[0]",0.6,1.5);
    linefit->FixParameter(0,0.160049);
    linefit->FixParameter(1,0.56);
    hPRatio->Fit("linefit","R");

    //save the histogram to a .gif file
    c1->SaveAs("pratioerrors.gif");
  }
```

B. Analysis code template

```
//Analysis code template. The class and class objects are declared in a separate header file.

#include <required libraries>

analysisname::analysisname(const char* outfile, int dsIndex)
{
  //constructor
}
analysisname::~analysisname()
{
  //delete objects here to free up memory
}
int analysisname::Init(PHCompositeNode* topNode)
{
  //Initialize Objects
  //load data files
}
int analysisname::ResetEvent(PHCompositeNode* topNode)
{
   //reset event and track nodes for each event
}
int analysisname::process_event(PHCompositeNode* topNode)
{
  //Get event and track information
  //Perform event cuts
  //Fill event histograms
  //Loop over all tracks for each event
  //Perform calculations
  //Perform track cuts & calibrations
  //Fill histograms which require track information
}
```

C. Sample run macro

```
  //The run macro instantiates the analysis code and the Fun4All data analysis framework,
//initializing the analysis process.
  void
  Run_lowEnergyRun11_0(const char* outFile = "test.root")
  {
    std::cout << "Run_lowEnergyRun11: loading liblowEnergyPIDRun11.so" << std::endl;
    int status = gSystem->Load("liblowEnergyPIDRun11.so");
    std::cout << "Run_lowEnergyRun11: Loading liblowEnergyPIDRun11.so returned status = " << status
<< std::endl;

    lowEnergyRun11 *le = new lowEnergyRun11(outFile,0);

    Fun4AllServer* se = Fun4AllServer::instance();
    recoConsts *rc = recoConsts::instance();
    se->registerSubsystem(le);
  }

  void
  InputData(std::vector<std::string>& inData)
```

```
{
  inData.push_back("CNT");
  return;
}
```

D. Except from PID analysis code

```
//This except from the PID analysis code shows how cuts are applied on a track by track basis //
within the loop over all particle tracks in the process_event() method. Cuts prevent unwanted //par-
ticle tracks from showing up in the output histograms
//Only the cuts for positive charged //particle species are shown.

int lowEnergyRun11::process_event(PHCompositeNode* topNode) {
.
.
.

//Particle track is a pion+ candidate if mass^2 is within 2 sigma(pt) of mean(pt)
if (m2tofw >= PiPMean - PiP2Sigma && m2tofw <= PiPMean + PiP2Sigma) {
       //Ambigous track cut, confirms that particle is a pion+ by removing kaon+ overlap
if (m2tofw <= KPMean - KP2Sigma){
  //Only fill these output histograms if the particle is confirmed to be a pion+
     hTofwPiPlusPt->Fill(pt);
     hTofwPiPlusPtM2->Fill(m2tofw,pt);
     hTofwAllPlusPtM2->Fill(m2tofw,charge*pt);
     hTofwAllPtM2->Fill(m2tofw,charge*pt);
     hTofwQdPvTof->Fill(ttofw,charge/ptot);
   }
 //Particle track is a kaon+ candidate if mass^2 is within 2 sigma(pt) of mean(pt)
 if (m2tofw >= KPMean - KP2Sigma && m2tofw <= KPMean + KP2Sigma){
//Ambigous track cut, confirms that particle is a kaon by removing pion and proton overlap
   if (m2tofw >= PiPMean + PiP2Sigma) {
     if(m2tofw <= PPMean - PP2Sigma) {
    //Only fill these output histograms if the particle is confirmed to be a kaon+
        hTofwKPlusPt->Fill(pt);
        hTofwKPlusPtM2->Fill(m2tofw,pt);
        hTofwAllPlusPtM2->Fill(m2tofw,charge*pt);
        hTofwAllPtM2->Fill(m2tofw,charge*pt);
        hTofwQdPvTof->Fill(ttofw,charge/ptot);

//Particle track is a proton+ candidate if mass^2 is within 2 sigma(pt) of mean(pt)
if (m2tofw >= PPMean - PP2Sigma && m2tofw <= PPMean + PP2Sigma){
//Ambigous track cut, confirms that particle is a proton by removing kaon overlap
   if (m2tofw >= KPMean + KP2Sigma) {
  //Only fill these output histograms if the particle is confirmed to be a proton+
     hTofwPPlusPt->Fill(pt);
     hTofwPPlusPtM2->Fill(m2tofw,pt);
     hTofwAllPlusPtM2->Fill(m2tofw,charge*pt);
     hTofwAllPtM2->Fill(m2tofw,charge*pt);
     hTofwQdPvTof->Fill(ttofw,charge/ptot);
      }
.
.
.
}
```

Fabrication and testing of sub-micron x-ray waveguides using anisotropic etch methods

Bianca Datta
Material Science & Engineering, University of Pennsylvania, Philadelphia, PA 19104

Kenneth Evans-Lutterodt, Ming Lu, Aaron Stein
Photon Sciences, Brookhaven National Laboratory, Upton, NY 11973

Abstract

X-ray waveguides were fabricated through the creation of narrow grooves in <110> silicon wafers. Wet KOH chemical etching techniques were utilized for this process. Prior to effective creation of devices, the fabrication methodology was optimized through experiments with nitride deposition, reactive ion etching, and electron beam lithography. Scanning Electron Microscopy was used for preliminary characterization and measurements. Waveguides were ultimately characterized using beam X-13B of the National Synchrotron Light Source. X-ray testing demonstrated functionality as light was effectively transmitted through the waveguide channels.

I. INTRODUCTION

The goal of this project was the production of a functional waveguide to be used to stabilize a beam of 12 KeV x-ray photons stemming from beamline X-13B of the National Synchrotron Light Source. Since beams produced by synchrotron light sources are initially irregular and riddled by interference,[23] a more stable x-ray beam can facilitate better imaging and diffraction, which would allow researchers to explore materials more accurately.

The typical refractive optics techniques used with visible or ultraviolet light are often ineffective for x-rays due to the small x-ray refractive index; and so, waveguides are used instead.[23] Waveguides utilize parallel reflective surfaces to compress and guide x-rays[21] to create a very parallel beam or to focus x-rays in very small dimensions.[24] For this process, smooth walls are crucial. Upon exiting the channel, the beam is smooth and lacks the interference residues initially present.[23] The waveguide only allows for the propagation of particular electromagnetic resonant modes,[24] so the exit beam consists of only a few channel modes.[23] These devices operate based on the total reflection that can be achieved due to the fact that refractive index for x-ray waves is always less than one.[24] Thus, the exiting radiation is very well confined, has a higher spatial resolution, and is more coherent than the entering beam.[23]

An increasingly greater fraction of novel x-ray photon based experimental techniques depend on sources with greater coherence. The more coherent a diverging beam is, the smaller is the apparent size of the source from which the beam comes. A wide, perfectly parallel beam can also be coherent because a lens can focus it down to a single spot, and the wider the parallel beam is, the smaller the size of the focused spot. A more coherent x-ray beam can be re-focused with a lens to put a greater fraction of that incident x-ray beam into smaller sized focused spots. Creating small x-ray beams allows scientists to investigate materials with better spatial resolution, and this often improves our understanding of the structure and composition of the material under study. Another example of a novel x-ray technique based on a coherent beam is that of a new imaging method called Coherent Diffraction Imaging (CDI). This imaging method is most effective when the illumination on the sample is perfectly coherent. While there are many synchrotron sources, only the most recently constructed sources have been designed with optimizing coherence as a guiding principle, and so most sources are only partially coherent.

One way to get a coherent beam from an incoherent source is to use a pinhole or slit to limit the spatial extent of the beam. An effective pinhole is an aperture cut in a sheet of material that is much thinner than the aperture size, and that allows beam in the open aperture of the pinhole to pass through unimpeded. Beam that is outside the defined open aperture is attenuated to zero intensity. Unfortunately, hard x-rays are very penetrating and so to attenuate the beam to zero intensity, one needs to make the material surrounding the aperture quite thick. Thus, for hard x-rays, it is difficult to make pinholes with small apertures; it is likely that the material is so thick that x-rays will bounce around between the aperture walls before exiting. An aperture in which the x-ray beam will bounce back and forth inside the walls of the structure is more correctly thought of as a waveguide.

Waveguides are well known from the radio frequency range with the wavelength of radiation in the centimeter (10^{-2}m) range, but are only just being considered in the hard x-ray range where the wavelength of radiation is in the 10^{-10}m range. The analysis of waveguides is most often discussed in the language of "modes." A mode can be thought of as an allowed path for light to pass through the waveguide. If incident radiation does not couple to allowed modes in the waveguide, the radiation will not pass through the waveguide. For a small enough waveguide, a only single mode will be supported, and in this case the radiation exiting the waveguide will behave as a completely coherent source. As the waveguide channel gets bigger more modes are supported, and the waveguide gets less coherent. Clearly the best waveguides will have small channels with smooth, highly reflective sidewalls.

Our x-ray waveguide design was a thin channel in a silicon wafer with smooth vertical walls with high x-ray selectivity. To create these smooth walls, we intended to perform chemical wet etching using potassium hydroxide (KOH) due to its tendency to etch silicon wafers anisotropically.

II. PROPOSED METHODOLOGY:

Chemical etching is a process by which portions of a substrate are selectively removed for microfabrication purposes. In wet chemical etching, a sample is immersed in a solution, typically an acid or base. Bulk silicon has a diamond cubic crystal structure in which the crystallographic directions are parallel to crystallographic planes.[18] For wafers with a {110} surface, the {111} planes are 90° from the wafer face, but not from each other.[18] These properties allow us to create deep moats in the

silicon. While wet etching can produce a wide array of shapes, for the purpose of waveguides, narrow grooves are the optimal result. Etching continues until the most densely packed plane of the crystal is reached. For silicon, this means that the <100> and <110> planes etch much more quickly than the most densely packed <111> plane which acts as an etch stop.[1] <110 planes> have one dangling bond at the surface, bond twice with atoms which each have three bonds, and bond once with atoms which have four bonds. As etching occurs, three bonds must be broken, two of which are weak due to the presence OH- groups. In contrast, the <111> planes have one surface dangling bond and three bonds with atoms which have four bonds each. For these planes, three stronger bonds must be broken to remove one atom from the surface, as opposed to the two weaker bonds and one strong bond in <110> planes.[15] In general, as the hydroxide concentration is increased, the etch rate of the {111} planes decreases.[19] Thus, for this project, <110> wafers were selected as the substrate and KOH was used as the etchant due to the anisotropy of KOH etches, which make it ideal for the creation of thin grooves. The etch reaction is as follows:

$$Si + 2OH^- + 2H_2O \rightarrow SiO_2(OH)_2^{2-} + 2H_2.$$

Etching is governed by the breaking of silicon-silicon backbonds as hydroxide ion bonds are formed, resulting in a transfer of electrons to the conduction band.[15] KOH typically exhibits high selectivity between the <110> and <111> etch rates.[2] As a result of this anisotropy and etch stop conditions, a circular pattern etches into a hexagon, which can be used for alignment purposes.

KOH is an optimal etchant for x-ray waveguide applications due to its high etch selectivity between the {110} and {111} planes, and because vertical {111} sidewalls that form can be used similarly to a mirror.[2] In order for the waveguide to function efficiently, the walls should act as vertical micromirrors, with large heights and high reflectivities.[20] Wet etching with KOH typically yields atomically smooth vertical surfaces and high aspect ratio trenches.[20] However, typically narrow channels etch at a much slower rate than wide channels, potentially due to crystal imperfections.[7] KOH tends to yield rough <110> bottom planes,[7] but if a rough surface is parallel to the direction of light propagation, it does not contribute to losses.[13]

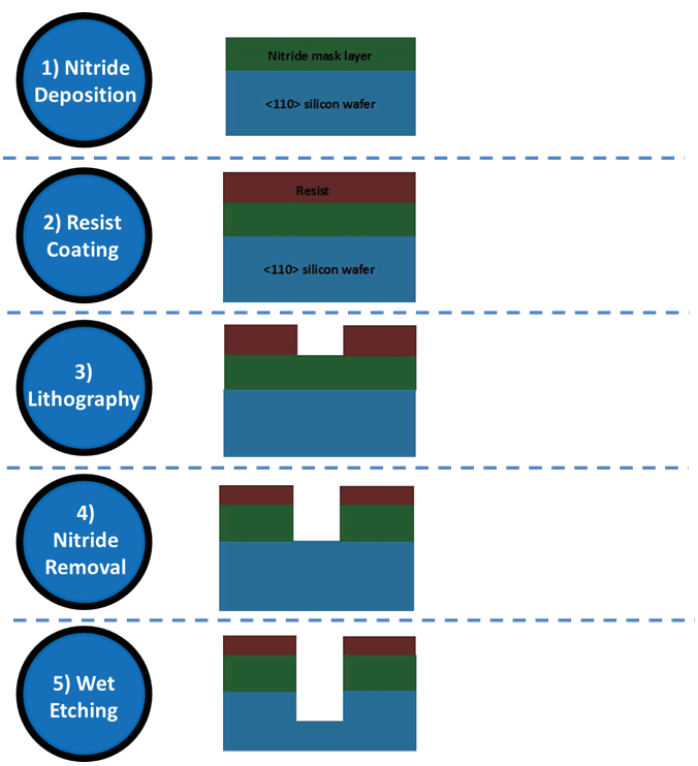

Figure 1: Diagram illustrating fabrication process

III. PROPOSED FABRICATION:

Due to the role of wet KOH as a powerful etchant, a mask layer is needed to protect the silicon wafer. For our purposes, silicon nitride (Si_3N_4) was used. Si_3N_4 theoretically acts as a perfect mask material. Thus, the first step of the proposed fabrication was to coat with wafer using a TRION Plasma-enhanced Chemical Vapor Deposition chamber.

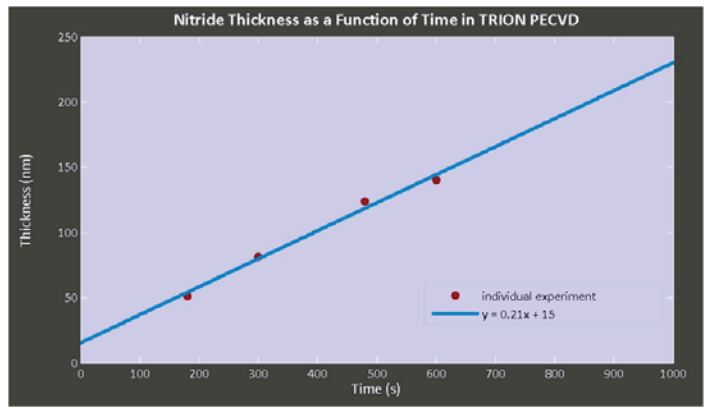

Figure 2: Nitride Thickness as a Function of Time in TRION PECVD

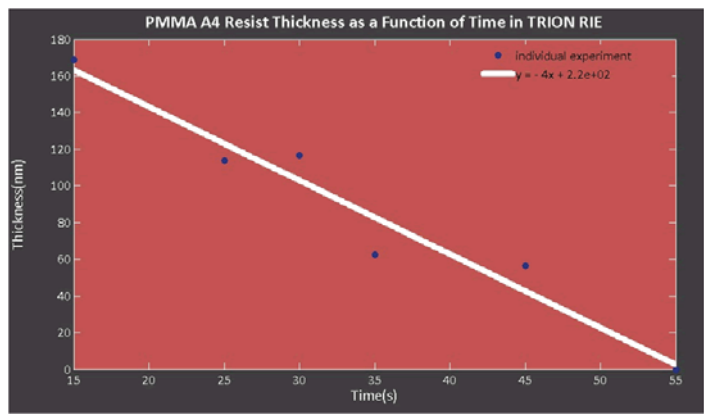

Figure 3: PMMA A4 Resist Thickness as a Function of Time in TRION RIE

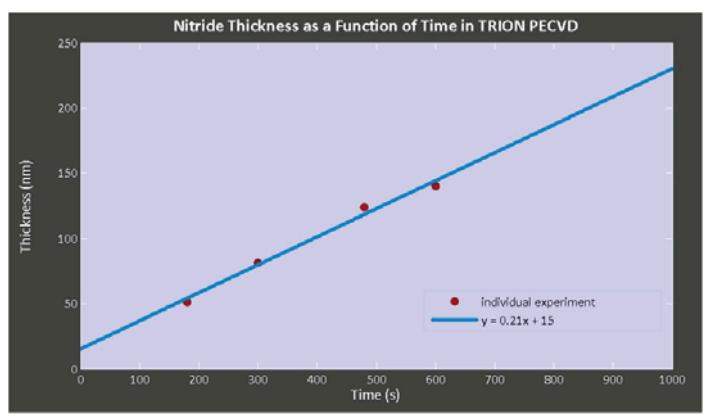

Figure 4: Nitride Thickness as a Function of Time in the TRION RIE

Before etching was conducted, the desired waveguide pattern had to be written onto the wafer to direct etching. Electron beam lithography was used to write the pattern. Electron beam lithography was selected instead of photolithography as it can be used to overcome the diffraction limit of light, allowing for more precise patterns with higher resolution.[17] Using a spincoater, a layer of polymethyl methacrylate (PMMA) A4 was placed on the wafer in a 243 nm thick layer. In later tests, PMMA A6 was to produce 571 nm films. After the pattern was written into the wafer, the resist was developed so that the pattern was exposed. In order for etching to occur, the mask nitride had to be removed in the patterned regions. A TRION Reactive Ion Etcher (RIE) was used to remove this nitride. However, as the resist had a higher etch rate in the RIE than the nitride, much of the resist was also removed in this process. RIE times had to be carefully monitored, as once the resist layer was eradicated the nitride began to come off. If the nitride layer became too thin, the wafer could get damaged by the KOH during the wet etching step.

In order to prevent this, we had to conduct tests to determine the thicknesses of films acquired as a result of different deposition conditions, and then use different RIE times to establish etch rates, the results of which are presented in Figures 2-4. Eventually we determined that depositing nitride in the PECVD for 3 minutes and 15 seconds yielded a film of optimal thickness of 75 nm. This wafer was eventually etched in the RIE for 50 seconds such that the exposed nitride layer could be removed, but some of the PMMA resist could be retained to ensure that the remaining nitride mask did not become too thin. The resist ultimately came off during the KOH etch.

IV. EXPERIMENTAL PROCEDURES:

Before any accurate wet etching could be conducted, some tests were needed to ensure the alignment was correct. Incorrect alignment could lead to underetching, in which lateral etching occurs in addition to vertical etching. For these first attempts, photolithography was used instead of the electron beam lithography we later employed. An initial KOH etch indicated that circular patterns resulted in hexagonal shapes. These hexagons were defined by two angles of 109° and four of 125.5°, as they were surrounded by four vertical {111} planes and two {111} planes inclined 35.5° to the wafer surface.[8, 15] This phenomenon could be utilized for alignment because corners of these hexagons could be

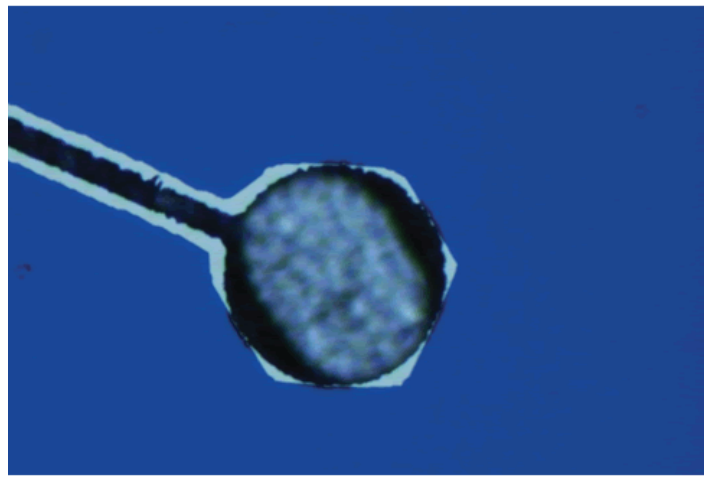

Figure 5: Etching Results on Wafer Patterned Using Photolithography

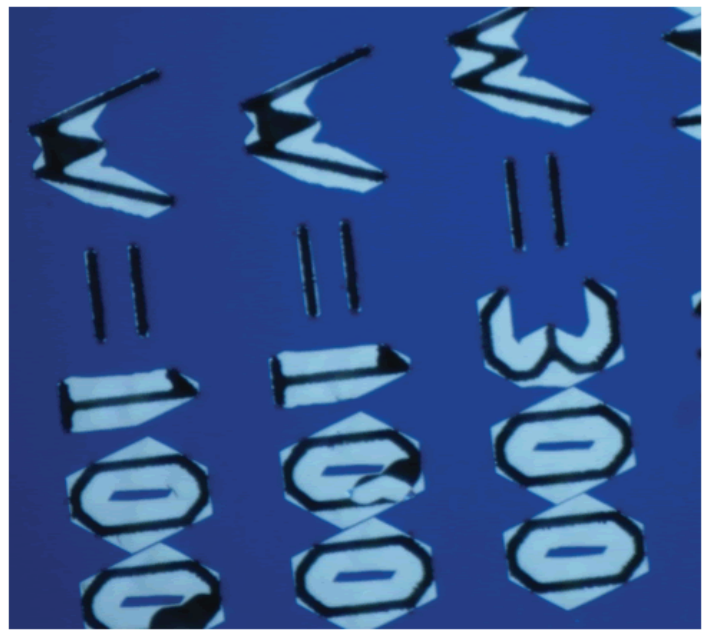

Figure 6: Further Evidence of Etching on Wafer

Etch Temperature (°C)	Etch Time (mins)	Result
35	660	width: 500-970 nm, depth: 9580-13100nm
50	14	width: 501-1480 nm, depth: 1440-2670 nm
60 (without stirring)	12	width: 523-1440 nm, depth: 2890-8030 nm
60	12	width: 700-820 nm, depth: 11000-11300 nm
65	12	width: less than 500 nm, depth: 1000 nm
75	12	width: 1580-1900, depth: 11000-11200 nm
80	3.75	depth: 9 um
85	12	width: 500 nm, depth: 1500-2000 nm
85	20	width: 3400 nm, depth: 30000-60000 nm
95	12	width: 600 nm, depth: 2000-3000 nm
100	6	width: 2500-5900 nm, depth: 55000-88000 nm

Table 1: Summary of wet etching experiments

guides for the location of [110] direction in <110> wafers.[8]

These effects were observed, as shown in the figures above, indicating that the wet etching process would be effective, allowing us to start on electron beam lithography rather than continue to experiment with photolithography produced patterns. Electron beam lithography allows for the creation of much smaller lines to serve as guides for narrower etches. For these patterns, the alignment method used was a fan pattern alignment. Underetching was expected for misaligned lines,[9] while the correctly aligned {111} planes have an etch rate close to zero.[12] In order to get truly vertical {111} walls, patterns needed to be correctly aligned with the <110> direction, as the sidewall always forms from plane with the slowest etch rate when aligned with the mask edge.[11] Thus, in these cases, etching stopped at the {111} planes.[10]

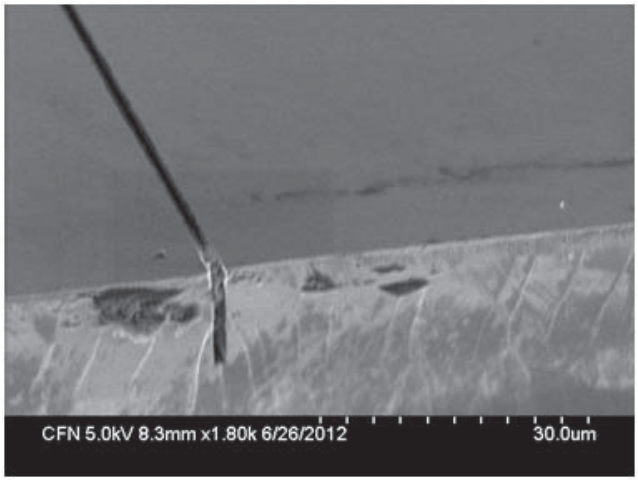

Figure 7: Etch Results of 75 degree, 12 minute Wet Chemical Etch using SEM

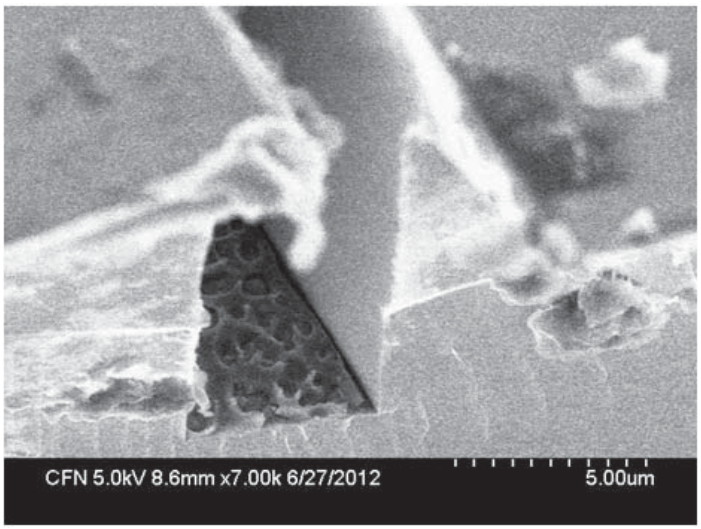

Figure 8: Demonstration of Atomically Smooth Vertical Sidewalls After Etching at 85 degrees for 20 minutes. Rough bottom and smooth walls clearly visible.

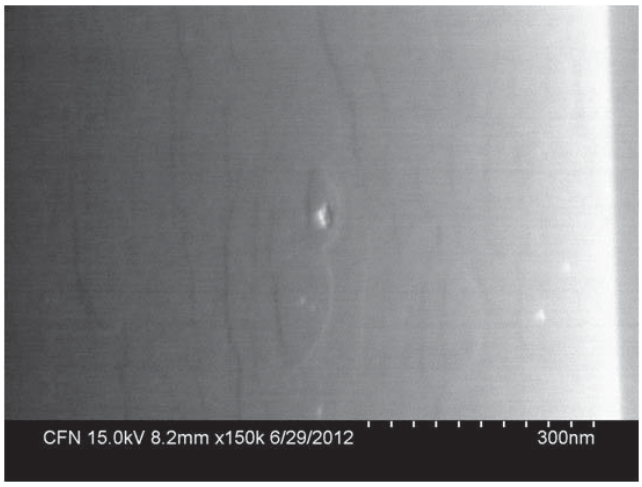

Figure 9: Detailed View of Atomically Smooth Walls After KOH Etching

Once the pattern had been written onto the substrate and the wafer had been prepared using the RIE, wet etching could be conducted. Etching was conducted on a hot-plate in a 500 mL beaker using a teflon-coated stir bar to ensure even heating and etching. The temperature was carefully monitored using a thermometer probe to ensure that heating was conducted evenly.

V. RESULTS AND DISCUSSION:

We established that stirring was a necessary part of the reaction as duplicating a 60° etch without stirring yielded channels of about half the depth, and said channels were much less cleanly formed.

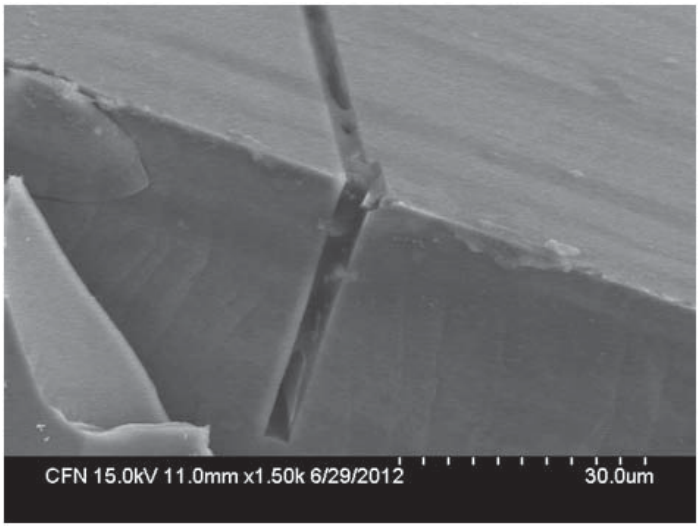

Figure 10: Results of Etching for 12 minutes at 85 degrees. Image taken using the SEM

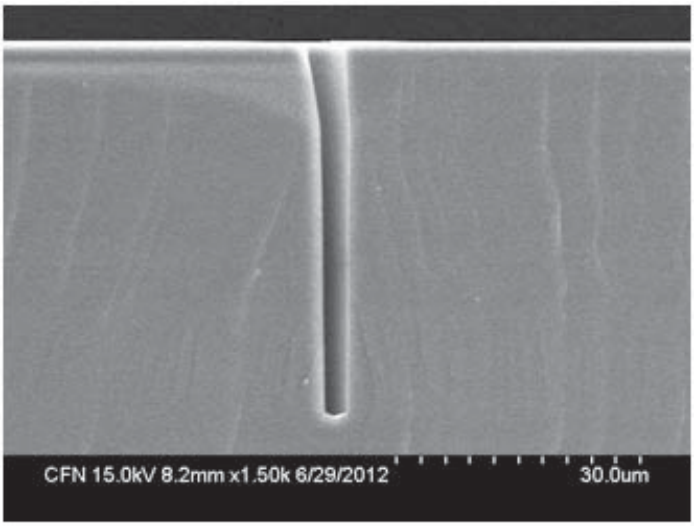

Figure 11: Further Results of the Same Etch Process

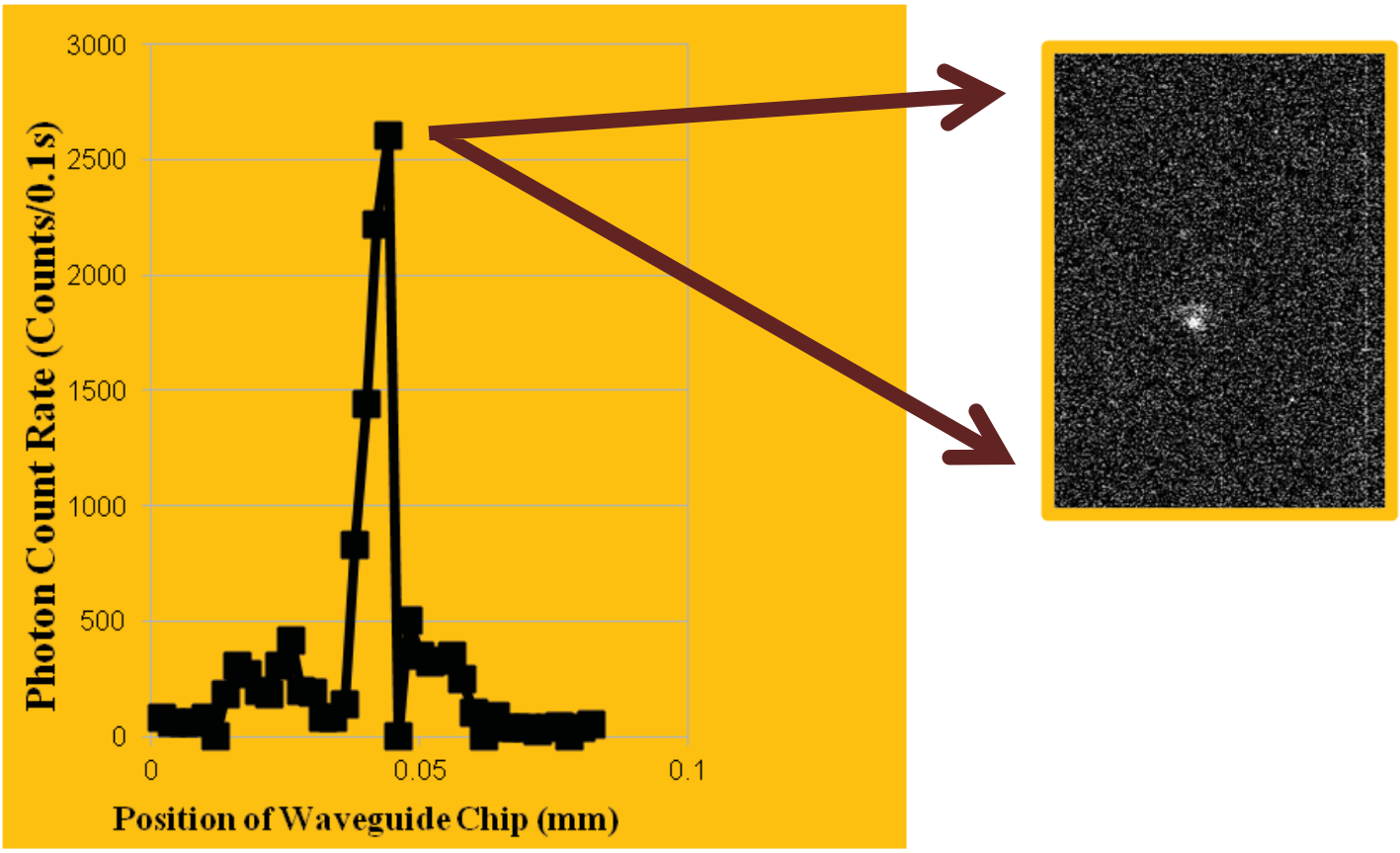

Figure 12: Demonstration of functionality using x-rays. The peak represents the bright spot where light passed through. The bright spot shown represents the point where the waveguide chip was aligned such that light propagated through.

After many experimental conditions were examined, functional waveguide devices were fabricated. The first set was created through a 75°C reaction carried out for 12 minutes, which yielded channels approximately 1.5 µm wide and 10 µm deep. The second set was etched at 85°C for 20 minutes, with channels about 3.5 µm wide and 30 - 60 µm deep. The final set was fabricated at 60°C for 12 minutes, with channels about 11.3 µm deep and 580-780 nm wide. Future sets were fabricated around 35 degrees for 11 hours, yielding channels of about 750 nm by 12 microns. We demonstrated that producing 200-300 nm wide channels is possible, but it is difficult to accurately produce channels of less than 100 nm.

These devices were then tested using the NSLS beam X-13 B of 12 KeV x-ray photon. The beam was lined up with the wafer surface and passed through the channel. We were able to see and record the beam on the other side of the waveguide, as indicated by a bright spot. Thus, the waveguides have been shown to be functional. Both wider channels and narrower channels proved effective, as wide channels were needed to initially clean up the beam, while narrower channels were more effective for waveguides.

What's next?

While functionality has been demonstrated, we would like to conduct more detailed x-ray characterization tests. X-ray optical tests will consist of setting up the waveguide as a secondary light source and evaluating the transmission, stability, and effective source size of the beam upon exit. Fabrication tests will also be continued to move towards 20 nm wide channels. Deep RIE etching may be used in the future, with KOH used to smooth the walls as a final step.

VI. ACKNOWLEDGEMENTS

This Summer Undergraduate Laboratory Internship (SULI) was supported and funded by the US Department of Energy, Brookhaven National Laboratory – Center for Functional Nanomaterial and National Synchrotron Light Source. We thank Aaron Stein, Fernando Camino, and Ming Lu for their assistance and support with fabrication, training, and cleanroom operations.

VII. REFERENCES

1. Ted J. Hubbard, MEMS Design:The Geometry of Silicon Micromachining. Diss thesis. California Institute of Technology, Pasadena, CA, 1994. Web. 21 June 2012.
2. Yuji Uenishi, Masahiro Tsugai and Mehran Mehregany, "Micro-opto-mechanical devices fabricated by anisotropic etching of (110) silicon," J. Micromech. Microeng. 5 (1995) 305-312.
3. Alexander H¨olke and H Thurman Henderson, "Ultra-deep anisotropic etching of (110) silicon," J. Micromech. Microeng. 9 (1999) 51–57.
4. Microchemicals (wet etching poster)
5. Photoresists.eu (microchemicals)
6. Kazuo Sato, Mitsuhiro Shikida, Takashi Yamashiro, Masaki Tsunekawa, Shunji Ito, "Roughening of single-crystal silicon surface etched by KOH water Solution," Sensors and Actuators 73 (1999)122–130.
7. Alexander H¨olke and H Thurman Henderson, "Ultra-deep anisotropic etching of (110) silicon," J. Micromech. Microeng. 9 (1999) 51–57.
8. Fan-Gang Tseng and Kai-Chen Chang, "Precise [100] crystal orientation determination on <110>-oriented silicon wafers," J. Micromech. Microeng. 13 (2003) 47–52.
9. T. D. James, G. Parish, K JWinchester and C A Musca, "A crystallographic alignment method in silicon for deep, long microchannel fabrication," J. Micromech. Microeng. 16 (2006) 2177–2182
10. G. Ensell, "Alignment of mask patterns to crystal orientation," Sensors and Actuators A 53. (1996) 345-348
11. Oliver Powell and H Barry Harrison "Anisotropic etching of {100} and {110} planes in (100) silicon," J. Micromech. Microeng. 11 (2001) 217
12. Don L. Kendall, "On etching very narrow grooves in silicon," Appl. Phys. Lett. 26, 195 (1975).
13. Kimmo Solehmainen, Fabrication of microphotonic waveguide components on silicon. Diss thesis. Helsinki University, Espoo, Finaland, 2007. Web. 15 June 2012.
14. Yue Kuo, "Reactive Ion Etching of PECVD Amorphous Silicon and Silicon Nitride Thin Films with Fluorocarbon Gases," J. Electrochem. Soc., Vol. 137, No. 4, April 1990.
15. H. Camon, Z. Moktadir, M. Djafari-Rouhani, "New trends in atomic scale simulation of wet chemical etching of silicon with KOH," Materials Science and Engineering B37 (1996) 142-145.
16. Irena Barycka, Irena Zubel, "Silicon anisotropic etching in KOH-isopropanol etchant," Sensors and Actuators A 48 (1995) 229-238.
17. "Electron Beam Lithography." Bostech Scientific Instruments and Technologies, 2011. Web. 06 Aug. 2012. <http://www.bostechltd.com/e_beam_lithography>.
18. Kenneth Bean, "Anisotropic Etching of Silicon," IEEE Transactions on Electron Devices, vol. Ed-25, no. 10, 1918.
19. Don L. Kendall, "A new theory for the anisotropic etching of silicon and some underdeveloped chemical micromachining concepts," J. Vac. Sci. Technol. A 8 (4), Jul/Aug 1990.
20. Daesung Lee, Kyoungsik Yu, Uma Krishnamoorthy, and Olav Solgaard, "Vertical Mirror Fabrication Combining KOH Etch and DRIE of (110) Silicon," Journal Of Microelectromechanical Systems, Vol. 18, No. 1, February 2009.
21. Schewe, Phillip F., and Ben Stein. "Tunable X-Ray Waveguide With An Air Gap." Physics News Update Number 415 - Story Tunable X-Ray Waveguide With An Air Gap. American Institute of Physics, 18 Feb. 1999. Web. 23 July 2012. <http://www.aip.org/pnu/1999/split/pnu415-2.htm>.
22. V.K. Egorov and E.V. Egorov, "Waveguide-Resonance Mechanism For X-Ray Beam Propagation: Physics And Experimental Background," International Centre for Diffraction Data 2003, Advances in X-ray Analysis, Volume 46.
23. "X-ray Waveguides Boost Resolution." Laser Focus World. N.p., 01 July 2005. Web. 23 July 2012. <http://www.laserfocusworld.com/articles/print/volume-41/issue-7/world-news/world-news/x-ray-waveguides-boost-resolution.html>.
24. "X-ray Optics." X-ray Physics. Institue for Photonics and Nanotechnologies, n.d. Web. 23 July 2012. <http://www.ifn.cnr.it/Groups/XRay/xray_optics.htm>.

Novel characterization techniques of scintillator detectors

Remy R. Devoe
University of Tennessee, Knoxville, TN
Giuseppe S. Camarda, Ryan Tappero, and Ralph B. James
Nonproliferation and National Security Department,B rookhaven National Laboratory, Upton, NY 11973

ABSTRACT

The Department of Energy is implementing technology to protect nuclear materials from weapons diversion through the NNSA funded NA-22 grant to the Nonproliferation and National Security (NN) Department at Brookhaven National Lab (BNL). The detector development group in the NN Department is developing room-temperature, high-resolution radiation detectors to observe and track nuclear materials. The research presented is on characterizing scintillator crystals received from Dr. Charles Melcher from the University of Tennessee. Using the x-ray beam capabilities of BNL's National Synchrotron Light Source (NSLS), LSO and YSO crystals developed by Dr. Melcher were tested for crystal defects and non-uniformities in the detector response. Correlating the observed defects with the detector's performance is the purpose of the research. Scintillation detectors have been predominately used in medical imaging, but because of poor energy resolution scintillators have been less desirable for use in gamma ray spectroscopy. The light yield should be maximized in these detectors to provide good resolution and also have a linear correlation of light output with energy deposited in the crystal. The X19C, X27B, and X27A beam-lines of NSLS were used in characterizing the crystal structure and detector response by performing White Beam X-ray Diffraction Topography (WBXDT), X-ray Response Mapping (XRM), and X-ray Fluorescence Microscopy (XFM) measurements. These measurements surprisingly reveal imperfections in the crystal on a microscopic scale. The first LSO crystal mapped in the X27B beam-line revealed striations that extend through the crystal. After performing the XFM measurements on the crystal at X27A, the striations were determined to be caused by varied concentrations of the activator ion Ce3+ that is responsible for scintillation. The non-uniformity of the crystal is likely to reduce the resolution of the detector and from these findings better techniques of crystal growth can be implemented. Through this process, I have learned how to use many instruments and facilities for scientific research.

I. INTRODUCTION

A. Background

Scintillator detectors have been used in medical imaging devices like PET and CT scans since the 1970s1 and have been used recently for radiation portal monitors to safeguard border crossings against smuggling. Radiation detection and measurement using scintillators have become popular due to the relatively low cost and availability of large volume scintillation material. The drawback of scintillator detectors is the poor resolution obtained from a gamma ray energy spectrum. The energy spectrum identifies what specific energy of radiation is coming from a source and with this information the identity of the radioactive material can be found. To obtain better resolution from scintillator detectors, the light output per unit of energy deposited must increase. The scintillation process begins when radiation, either a charged particle or uncharged photon or neutron, ionizes atoms within the scintillator. The recombination of the freed electron with an activator atom, usually a positively charged ion, causes the emission of a visible photon or light from the de-excitation of the electron. A photo-multiplier tube (PMT) coupled to the scintillator material collects the light and converts it to a current via the photo- electric effect. The current is processed in a circuit to produce a voltage pulse which is proportional to the energy deposited in the crystal.

B. LSO and YSO crystals

The scintillators used in the experiment are Lu2SiO5:Ce (LSO) and Y2SiO5:Ce crystals provided by Dr. Charles Melcher and his commercial collaborators. These crystals are both doped with a Cerium activator that produces a fluorescence photon with a wavelength of 420 nm. An ideal scintillator would have high luminosity, high density and atomic number, fast fluorescence decay time, and have an index of refraction close to 1.5.

II. EXPERIMENT

The experimental method of characterizing the scintillator detector's performance is by searching for crystal defects using white beam X-ray diffraction topography (WBXDT), X- ray response mapping (XRM), fluorescence lifetime imaging microscopy (FLIM), and micro X-ray fluorescence mapping (µXFM). Some of these methods have been used in Cadmium Zinc Telluride semi-conductor detector characterization2 and these experiments were the inspiration for trying these characterization techniques on scintillator detectors. These techniques allow for observation of the crystal on a microscopic level to reveal the homogeneities of the detector performance and crystal structure.

A. X-ray Response Mapping

The x-ray response mapping measurement is made at the NSLS X27b beam line. The detector's response is measured across the surface of the crystal facing the X-ray beam. The beam is collimated to an area of a few µm. The pixel is plotted on the image with a relative brightness corresponding to the channel number of the radiation peak of the X- ray beam. The higher the channel number, the greater the voltage pulse generated by the photo-multiplier tube which is proportional to the amount of light emitted from the scintillator. The dark regions have poorer luminescence than the bright regions due to concentration of activator dopant, Cerium.

B. White Beam X-ray Diffraction Topography

The X-ray beam is used to diffract off the surface of the crystal onto photographic film creating diffraction patterns. The image of the crystal should appear with the same dimensions as the crystal if it is uniform. If the scintillator crystal is not made of one continuous crystal structure, sub-grain boundaries will appear as dark lines in the crystal. If the crystal lattice orientation is different on both sides of the boundary, the diffraction pattern will show separation between the two crystal growth regions. Each volume of

crystal growth could have different characteristics like luminosity and decay time. Small features can also be seen like the Cerium striations and defects in the crystal.

C. Micro X-ray Fluorescence Mapping

The x-ray beam is collimated to a 10 µm area that, as in XRM, interacts within the material. The x-ray beam is able to ionize inner shell electrons leaving a vacancy that the higher energy electrons cascade down to fill. This process produces x-ray fluorescence that is characteristic to each atom. The material fluoresces and the emitted photons are counted for intensity by a 13 element high purity Germanium detector.

D. Fluorescence Lifetime Imaging Microscopy (FLIM)

The fast timing electronics and pulsed laser of the FLIM microscope allow for the measurement of fluorescence lifetime with pico-second resolution. The microscope uses a piezo stage to make the images with nano-meter resolution. The laser excites the sample and the fluorescence is collected by a microscope and recorded on a ccd. The images reveal regions of higher and lower fluorescence lifetime.

III. RESULTS

A. XRM Images

A crystal at a 45 degree angle was mapped using 25 µm area pixels to reveal striations across the horizontal axis. A zoomed in image is on the left showing the striations more clearly.

B. WBXDT Images

The crystal structure of each scintillator crystal is revealed using the WBXDT. The images show where the crystal separation occurs within the crystal. The uniformity of the crystal is sought after to make better performing detectors. The images below show the striation patterns observed in the XFM images as well as sub-grain boundaries.

C. µXFM Images

The image shows striations in Cerium concentration that correspond to the striations seen in the x-ray response mapping images. The scale on the right is in relative intensity of the Cerium fluorescence.

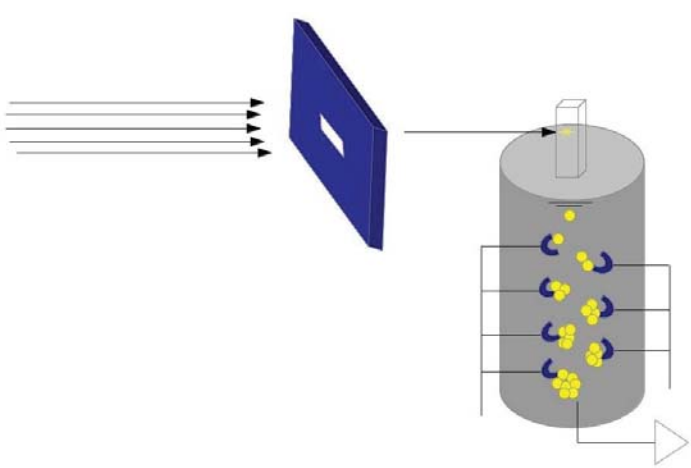

Figure 1. X-ray Response Mapping Diagram

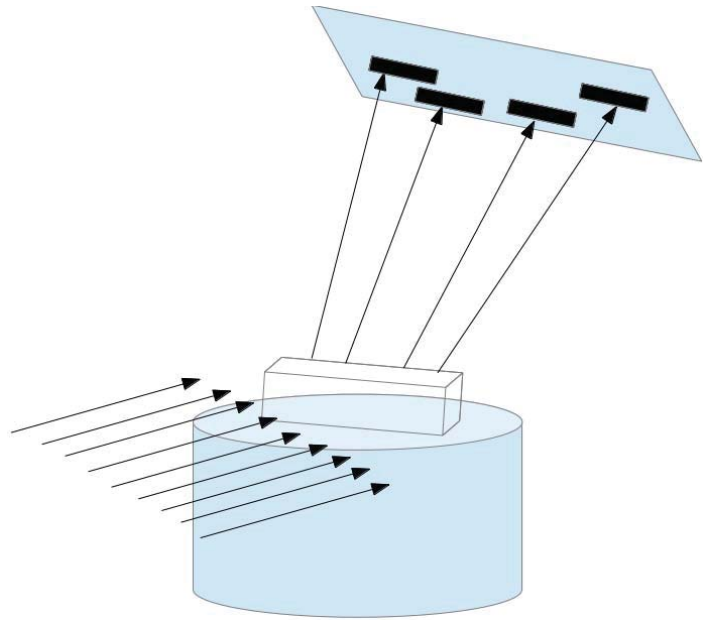

Figure 2. White Beam X-ray Diffraction Topography Setup Diagram

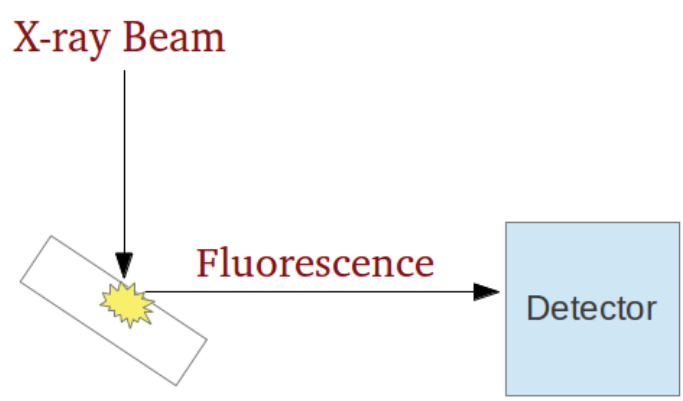

Figure 3. Micro X-ray Fluorescence Microscopy Setup Diagram

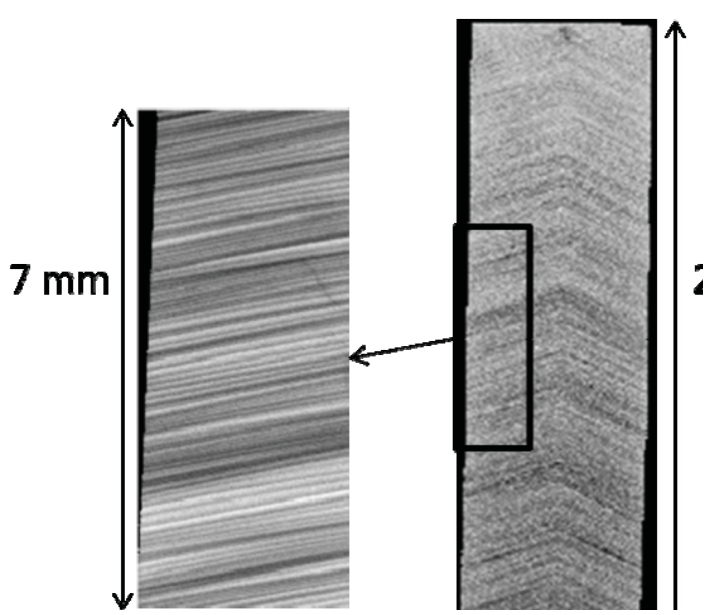

Figure 4. X-ray Response Mapping Images

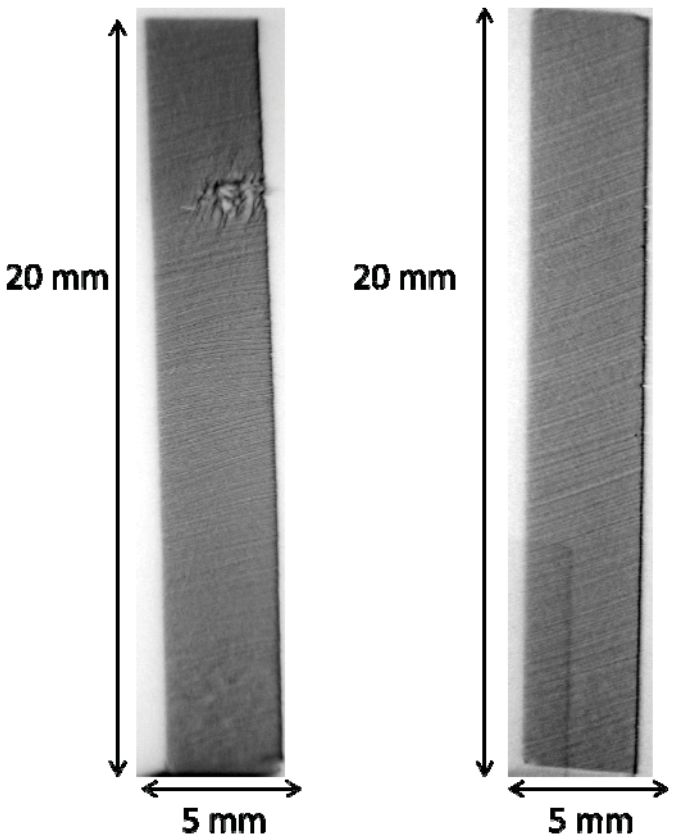

Figure 5. WBXDT Images Showing Striation Pattern

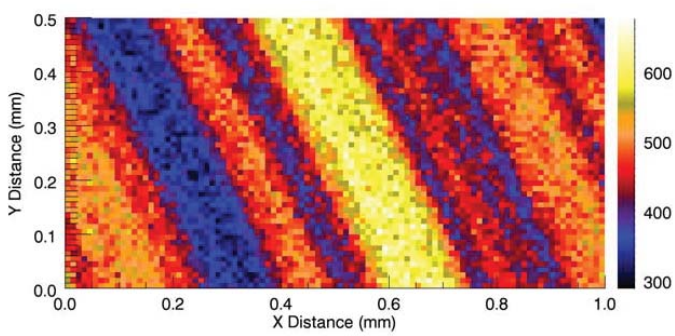

Figure 6. Micro X-ray Fluorescence Images

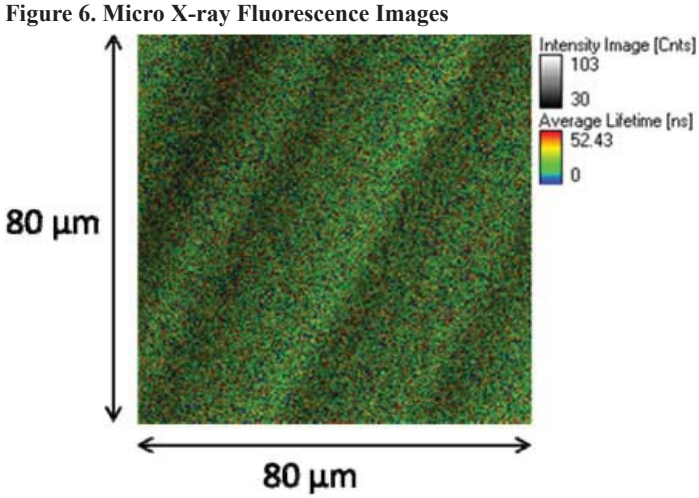

Figure 7. FLIM Image of Striation Pattern

D. FLIM Images

The images taken with FLIM are resolved with time and intensity. The longer fluorescence lifetimes are shaded in brighter colors and the shorter lifetimes in darker colors. The intensity is in gray scale like in XRM. The images above show the average fluorescence decay lifetime around 40 ns on the left and the FLIM image of a crystal area on the right.

IV. CONCLUSIONS

The LSO and YSO crystals show features in the crystal structure that were not observable using optical or IR microscopy. Using synchrotron radiation to create images with micron resolution revealed these non-uniformities and imperfections in the scintillator crystal. These defects could possibly be the source of poor energy resolution performance for these types of detectors and warrant more research into the detrimental effects on detector resolution of the scintillator crystal defects.

V. ACKNOWLEDGEMENTS

This work was supported by U.S. Department of Energy, Office of Nonproliferation and Verification R&D, NA-22.

Thanks to research carried out at the Center for Functional Nanomaterials, Brookhaven National Laboratory, which is supported by the U.S. Department of Energy,

VI. REFERENCES

[1] Bolotnikov, A.E.; Babalola, S.O.; Camarda, G.S.; Chen, H.; Awadalla, S.; Yonggang Cui; Egarievwe, S.U.; Fochuk, P.M.; Hawrami, R.; Hossain, A.; James, J.R.; Nakonechnyj, I.J.; Mackenzie, J.; Ge Yang; Chao Xu; James, R.B.; , "Extended Defects in CdZnTe Radiation Detectors," Nuclear Science, IEEE Transactions on , vol.56, no.4, pp.1775–1783, Aug. 2009 doi: 10.1109/TNS.2009.2019960 URL: http://ieeexplore.ieee.org/stamp/stamp.jsp?tp=&arnumber=5204719&isnumber=5204529

[2] Camarda, G.S.; Bolotnikov, A.E.; Yonggang Cui; Hossain, A.; Awadalla, S.A.; Mackenzie, J.; Chen, H.; James, R.B.; , "Polarization Studies of CdZnTe Detectors Using Synchrotron X-Ray Radiation," Nuclear Science, IEEE Transactions on , vol.55, no.6, pp.3725–3730, Dec. 2008 doi: 10.1109/TNS.2008.2004707 URL: http://ieeexplore.ieee.org/stamp/stamp.jsp?tp=&arnumber=4723818&isnumber=4723814

Usage and usability analysis of the Atmospheric Radiation Measurement program's web presence

Dan Ferguson
St. Joseph's College, Patchogue, NY 11772
Richard Wagener
Environmental Sciences Department, Brookhaven National Laboratory, Upton, NY 11973

ABSTRACT

The Atmospheric Radiation Measurement project (ARM) is Department of Energy (DOE) inter-laboratory project. Climate research facilities set up around the globe monitor and record atmospheric data from precipitation to multi-wavelength radiometric measurements with in situ and active and passive remote sensing instruments. The website for the ARM project is distributed and maintained by a number of DOE laboratories. Brookhaven National Laboratory maintains the primary web server, www.arm.gov, and initiated a project to determine the usage patterns with the goal of improving usability. Using the web tool known as Google Analytics (GA), we can more effectively know who is using the ARM's web site, why they are using it, how often they need it, and when it is needed. This invaluable information will help the people at BNL communicate with other DOE labs on how to improve the website for the user. Because the ARM site is spread over multiple DOE labs, making changes is a controlled and deliberate process that takes time and effort to implement. That is why GA is necessary to identify the changes that will be effective for the ARM site and to assess the impact of the planned changes. Over the past few weeks, GA has been used to test if the ARM site has fallen victim to system-wide glitches (test results were negative) to see if people were using the ARM site for requesting data, and to check how many people were getting caught in loops within the site. During this experiment, I have learned about large-scale websites, server technology, and human interaction with websites and the Internet as a whole.

I. INTRODUCTION AND HYPOTHESIS

The Atmospheric Radiation Measurement (ARM) Climate Research Facility's website www.arm.gov describes the measurement capabilities of ARM and is the primary means for discovering and ordering data of interest for visiting scientists. Scientists may pick from any research site, choose any number of instruments, and select any valid date range. These parameters are passed on to the ARM Archive (operated by Oak Ridge National Laboratory) to process an order for data and ship it out to the scientist who requested it. Additionally, the site provides links for accessing educational resources or submitting research proposals if someone wanted to use an ARM facility to conduct an experiment or a field campaign. Because the ARM website has a lot to offer, it is very difficult to keep track of how users use this site. Naturally, Brookhaven Lab wants the ARM site to be used for its intended purpose. But what if we cannot even measure the effectiveness of the ARM site? Recognizing this problem, the ARM researchers employed the powerful help of Google Analytics, Google's website statistics engine to track users from page to page as they navigated through the ARM website. Using Google Analytics, we were able to measure the effectiveness of ARM's website and suggest what kind of changes would need to be made to the site in the future.

II. METHODS AND MATERIALS

Google Analytics is simple to set up. It requires nothing more than a Google account, and a quick copy/paste of some readily available HTML code onto all of the pages you would want tracked. Since ARM used common styles throughout their pages, the tracking code was simply added to the common include file. The GA tracking code loads a JavaScript function that reports key statistics to the Google account that is linked to the web-site. The most obvious statistic is visitor count. However, Google Analytics employs a much wider variety of recording ability. It can also keep track of page visits, the percent of new visitors vs. returning visitors, the type of access point, the geographical location of the access point, even the keywords used to find the site. All in all, Google Analytics is a very comprehensive tool, even without optimizing some of its features. To track the data orders ARM received, we employed a GA feature called "Goals."

Google Analytics has a feature known as "Goal Setting," where the Google Analytics administrator will set up "goal pages." These pages are no different from any of the other pages on the site, except that when Google Analytics records a user on that page, a goal is completed. We have applied that principle to the receipt page of data ordering. Since data ordering is similar to e-commerce, there is a receipt for every order. By plugging the receipt's URL into the goal page, we were able to track the fraction of site visits when data was ordered. This same principle was applied to all research proposal forms begun as well.

III. DISCUSSIONS AND CONCLUSIONS

After the initial setup of Google Analytics on www.arm.gov, we noticed that at certain points a lot of visits were recorded as drop offs. We found that this was due to a change in domain. As a user goes to order data, they go from www.arm.gov to www.archive.ARM.gov. This change in servers caused a drop off in user counts and goal recordings. We then added the same GA token code to record all the visits to the www.arm.gov domain independent of the individual virtual host, and when goals were being processed, we recorded more hits than ever before.

A major topic of research was in finding how many people got caught in navigation loops within the website and never make it to one of our goals (order data, or submit research proposal). There are three main ways of accessing data orders: the "Instruments" tab, the "Measurements" tab, and the "Data" tab. While they all allow a user to order data, they just query the database differently. From the gathered data and our own navigation of the site, we have concluded the three methods of accessing data are so intertwined, it is impossible for a user to try to access data by staying within only one of the three sub-tabs. The user will invariably cross over to another sub-tab group, giving the appearance of

being caught in a loop. It was proposed that we combine the functionality of the three tabs into one tab, but the process involved is far too lengthy for any testing to be done during this ten week internship.

IV. ACKNOWLEDGMENTS

Thanks to the Department of Energy and Office of Science for funding this and other remarkable programs aimed at helping college STEM students find their path in the research world. Thanks also to Brookhaven National Labs for hosting these programs year after year. Thanks to the staff at BNL's Office of Educational Programs for organizing this program so well and for providing the interns with constant entertainment when the work day is through. And finally, thanks to the staff of the Department of Environmental Sciences, Scientific Information Systems Group, my host department, for helping me complete this research project.

Pefluorocarbon tracers: building industry potential and automated data management

Nathan Gubser
University of the Virgin Islands, St. Thomas, US Virgin Islands 00802
Terrance Sullivan
Department of Environmental Sciences, Brookhaven National Laboratory, Upton NY 11793

ABSTRACT

Deploying, capturing, and measuring perfluorocarbon tracer (PFT) gasses is a powerful technique used to comprehensively analyze both indoor and outdoor airflow as well as surface structure integrity. Brookhaven National Laboratory's (BNL) Department of Environmental Science has developed today's most comprehensive, precise, and environmentally sound tracer gas system. This tool is particularly relevant to the DOE's mission statement regarding public safety, energy conservation, atmospheric research, and indoor air quality. My contribution to this technology included two focal areas of product development. One effort entailed a review of building code and air parameter regulations as dictated by the American Society for Testing and Materials (ASTM), Leadership in Energy and Environmental Design (LEED), the American Society of Heating, Refrigerating and Air Conditioning Engineers (ASHRAE), the Environmental Protection Agency (EPA), and the National Fire Protection Association (NFPA). This review examined the possibility of a regulatory based need for precise physical testing such as BNL's PFT system provides. Findings indicated that there was currently no implicit demand for widespread PFT analysis in the building industry. However, it was concluded that this specialized tool will have applications in niche scenarios such as special use buildings, leak quantification, and design performance verification. My second area of focus employed Visual Basic coding to circumvent tedious manual processes in order to generate automated data calculations and graphic representations. This process takes gas chromatographic (gc) data files and establishes calibration curves from equations of best fit based on standard PFT concentrations. These calibration curves are then used to translate measurements of PFT samples from gc output into useful numeric data and automated plots of gaseous concentrations. Summarily, these efforts provide an expanded knowledge of building industry standards as well as a contribution that will provide a time and money saving method of analyzing PFT data.

Deploying, capturing, and measuring perfluorocarbon tracer (PFT) gasses is a powerful technique used to comprehensively analyze both indoor and outdoor airflow as well as surface structure integrity. Brookhaven National Laboratory's (BNL) continually evolving, multi-perfluorocarbon tracer (PFT) system, is the most advanced application of this practice. This paper will provide a general description of the PFT process and discuss two aspects of research and development pertinent to this product that were conducted throughout a ten week period. The first focus will explore this system's marketable potential in the commercial building industry with regards to its capabilities and industry based regulatory demand. The second area will discuss enhancements made to BNL's PFT data processing methodology.

Both of these endeavors were applied solutions implemented from a task-oriented problem solving approach process that started by finding a problem, working to understand the problem, developing an approach to the problem, and applying the solution. This is in contrast to an assembled arrangement of hypothesis, conclusion, methods, results, and a plentiful arrangement of clearly presented data. Both types of research experience are very valuable, yet I believe this difference to be an underrepresented quality typical to many engineering oriented undergraduate experiences. As I proceed to cover the components that entailed the problem scenarios approaches and results, I will do so more as a representation of a work experience and less so of a classical research endeavor.

Perfluorocarbon gasses are virtually non- existent in environmental air making them ideal for use as tracers. The term tracers refers to the action of following air travel by testing for their presence in an air sample according to the known location of their release. Their absence allows air samples to be collected with virtually no interference from pre-existing environmental PFT levels. Brookhaven's system consists of releasing up to seven known quantities of PFT gasses at known rates for known periods of time. The strategic placement of capillary absorption tube systems which are filled with filter suspended graphite capture spheres are organized throughout the release area of gasses. Upon completion of the gas release and absoprtion, these tubes are collected and taken for quantitative analysis using a uniquely modified gas chromatographer which is designed to specially handle these rare gasses.

Compared to other tracer gas technologies, BNL's PFT system is higher precision, environmentally cleaner system capable of studying more complicated scenarios. This system employs a superior gas chromatography technology that allows measurements up to a level of precision at parts per quadrillion versus the parts per trillion achieved through other methodologies. This greater sensory ability results in the deployment of smaller quantities of PFT than other methods which deploy greater gaseous quantities and are more harmful to the atmosphere. Furthermore, BNL's is able to deploy and analyze up to seven PFTs whereas most systems employ only one, and few are able to use as many as four. This creates the capability of studying a much more complex range of scenarios than other physical methods of verification.

This research's first focus was to ascertain whether commercial building regulations created an implicit demand for BNL's PFT technology. To explore this possibility, building system ventilation, indoor air quality, and climate control codes as defined by the American Society for Testing and Materials (ASTM), Leadership in Energy and Environmental Design (LEED), the American Society of Heating, Refrigerating and Air Conditioning Engineers (ASHRAE), the Environmental Protection Agency (EPA), and the National Fire Protection Association (NFPA) were reviewed.

This review took into account BNL's ability to evaluate various air flow properties. Building security was considered with regards to hazardous flow studies and building sensor placement efficiency. PFT can also interpret building envelope tightness, which is seen as increasingly important for environmental and energy-based reasons. This parameter describes the seal of a building's interior zones from the exterior, and though significant in

preserving energy, actually results in the reduction of indoor air quality as it is tightened. This calls for a greater quantity of indoor to outdoor and outdoor to indoor air exchange to be provided by ventilation systems. Here PFT aids in measuring of the ventilation performance of interzonal indoor airflow, as well as leak location and quantification within the ventilation systems. Additionally, various pressurization thresholds between room types and interzonal flow properties can be measured and/or verified.

BNL has, in the past, applied this technology in various applications within commercial buildings; however, these endeavors have persisted as niche scenarios or to service special use facilities. Still, this technology continues to improve while it is already the most powerful form available. Simultaneously, the building industry is evolving as well. As recently as 2008, regulations have been implemented that require regular and documented ventilation system upkeep. This is the first time that building management has been held responsible for the upkeep of the mechanical systems Additional codes, such as the relatively new LEED criteria, have developed to incentivize the development of higher energy design performance in the building industry. In fact, there are two specific areas where PFT technology is mentioned in LEED guidelines as an option for verifying specific airflow related criteria. However, despite indications of tightening regulatory measures and a trend towards environmental efficiency, there is no current requirement for a higher precision physical method of verifying and measuring any of these parameters. This review showed that equipment spacing, mechanical specifications, manufacturer design criteria, and computational fluid dynamic modeling are seen as sufficient avenues for satisfying industry requirements. With this knowledge, it can be expected that further niche services will develop. Additionally, as both this technology and industry standards advance, the time may come where BNL's PFT system can provide a much needed service in building air analysis.

The second focus of my research experience consisted of approaching a problem of how to best optimize a data managing process within the PFT system for BNL's Department of Environmental Science. This involved acquiring raw data output representing chromatographic measurements of PFT quantities and concentrations of sample gasses in the form of a comma delimited file. In addition to this, a comma delimited file from an automated sampling machine which held information crucial to the PFT data management process was developed and taken into consideration when designing this optimization. Furthermore, macros in Visual Basic that already described a portion of this data processing existed, which were to be included and utilized as an appendage to this overall design. With these considerations, a plan was developed to define what form of data output was desired.

The overall objective of this program would be to compute and output various calculations in both a tabular and graphical format, fit for both comprehensive analysis as well as formal presentation. Using the aforementioned comma delimited data files and through comparison to known properties extrapolated from known standard PFT mixtures these objectives are able to be accomplished. Measurements of samples and standards were recorded in electric units by the gas chromatographer and were then converted to more useful volumetric units. The standards were compared to known expected values which would help to calibrate this data in a way that could be represented by a polynomial equation in order to establish a line of best fit. The sample values were then refined according to this line of best fit and quantities were able to be to be understood in terms of rates location and presence. The assembly of this data included information describing expected standard values and deviation from that in terms of total quantity error and percent error, peak value calculations, associated time data, and concentrations. This program was then designed to output graphic information based on desired combinations of gas type and machine number.

This development is anticipated to supply a great level of benefits in terms of support for financial and manpower benefits when employed during an upcoming study. A series of seventy five hundred samples are slated to be gathered from throughout a subway system for an air flow and air quality study. Previously, capture data has been manually gathered and entered per sample and location and then combined with gas chromatograph information. This change in process will provide a great deal of support.

This research experience extended an opportunity to me wherein I was able to gain practical knowledge about building code regulations, advanced gas tracing methodology, dynamic integration of programming application, and the Visual Basic language. In return, I was able to provide a service that can settle an assumption by confirming that even though BNL's perfluorocarbon tracing methodology is a robust and powerful way of physically verifying air flow parameters, there is nothing strongly asserting that such a tool would have great demand. Additionally, I was able to approach a problem and incorporate a coordinated series of steps through a programming implementation to increase productivity. This allows employees the ability to spend more of their time on other important aspects. Additionally, the now automated processes will save costs associated with the handling, formatting, and output of crucial information.

Investigation of charge-coupled devices for the Large Synoptic Survey Telescope using Silvaco simulation software

Skyler Hagen
Ripon College, Ripon, WI 54971
Ivan Kotov, Instrumentation Division, Brookhaven National Laboratory, Upton, NY 11973

ABSTRACT

Brookhaven National Laboratory's Instrumentation Division is involved in the characterization of Charge Coupled Devices (CCD) for the Large Synoptic Survey Telescope (LSST). These are N-channel CCDs in 4k x 4k pixel format with a pixel size of 10 micron square and a CCD thickness of 100 microns. These CCDs, made on high resistivity (>3 kΩ·cm) silicon, are operated in a back-biased, over-depleted mode. LSST will require 189 individual sensors. The CCDs will not be built in-house, but will rather be purchased from vendors. Since vendors do not provide a simulation model that the LSST group can use to evaluate the electronic performance of the CCD sensors, this project entails the development of a CCD computer simulation using Silvaco software. The simulation being described is based on approximate CCD dimensions provided by the manufacturers' literature and communications with the LSST group. Although the various layer thicknesses and the general layout plan of these CCDs are well known, other parameters such as exact feature dimensions and processing recipes are not. Through these simulations, valuable data regarding inter-electrode capacitance, electric field, and operation of the CCD's read node reset transistor have been obtained. These data will be useful in determining sources of noise and various other electronic behaviors which occur during the image readout process.

I. INTRODUCTION

The first priority in simulating true behavior of the LSST CCDs is to develop a realistic structure exhibiting electrical and geometric properties similar to those seen in real devices. Many properties of the actual CCD sensors are known. If it can be seen that the simulation structure matches known parameters of the actual device, much more validity is given to simulation results in areas that are more difficult to directly measure in a physical device. Some examples of parameters which are difficult to measure directly are the capacitance between electrodes as a function of applied bias, depletion of the silicon substrate, and electron concentrations. These are all parameters which are available in the output from a Silvaco simulation.

Three main components of Silvaco's simulation software were used: Athena, Atlas, and TonyPlot. Athena, a process simulator, was used to generate the structure on which later tests would be based. Inputs to Athena come in the form of manufacturing processes and associated dimensions. An instruction set including material choices, doping concentrations, layer deposition, etching, etc. is processed by Athena. The result is a structure file. The second Silvaco component is Atlas, the device simulator. In addition to a structure file from Athena, Atlas requires instructions defining which electrodes to apply bias to, the size and quantity of bias steps, and which parameters to solve. Finally, Silvaco TonyPlot is an interactive graphic viewer which facilitates the graphical presentation of the results of Athena and Atlas. The program overlays a map of the structure with user-defined color gradients representing various solved parameters. Examples are Electron Concentration, Doping Concentration, Electric Field, and many others.

The Silvaco package used in these simulations is the two-dimensional version. Using the 2D version rather than 3D has its advantages and disadvantages. Clearly the 2D version is not as complex or computationally extensive as 3D. This directly results in less time spent computing (already on the order of several hours per simulation run on four processors). Using the 2D format, larger extended structures can be simulated. The time that would be required to do a 3D simulation of the CCD structure studied here would have taken an impractical amount of time, considering the quantity of parameters solved. However, 2D simulation is clearly not as accurate as 3D, especially in a structure as complex as a CCD. Output values such as capacitance and conductance are given as linear densities (Farads/micron, Siemens/micron), not absolute measurements. When the structure is assumed by the software to extend infinitely in its third dimension, as is the case with 2D Silvaco, some parameters cannot be accurately represented.

The initial structure had a number of features which were different from the structure studied here. It was similar in layout having 7 transfer gates, an output gate, and the reset metal oxide semiconductor field effect transistor (MOSFET) gate and drain. However the MOSFET was of the surface channel type. Source and drain were simply extensions of the N-channel, while the MOSFET channel region was left un-doped P-substrate. The channel stop originally consisted of a heavily doped P-type region, beneath the field oxide. Although the initial structure was sufficient to show electric field, it had shortcomings. Thus, the goal of this project has been to find more information and refine the structure further.

II. OVER-DEPLETED MODE

The CCDs for LSST are back biased to -70 volts in order to operate in over-depleted mode. Before any biases are applied to the CCD structure in Silvaco Atlas, there are electrons inherently present in the substrate from the N-doping performed in Athena. In this state, the silicon substrate behaves as a conductor inasmuch as no electric field is present throughout its depth. After an Atlas simulation run, structure files saved at each bias step may be viewed in the TonyPlot graphic display program. When the Electric Field gradient is displayed in TonyPlot, the magnitude of field may be graphed along a cutline drawn through the structure. The x-axis represents distance in microns along the cutline, and the y-axis shows electric field. As increasing potential is applied to the reset MOSFET drain (RD1) and backside window (W1), electrons are drawn out of the structure, and an electric field is created. The five plots of Figure 1 are Electric Field cutlines taken from TonyPlot. First, 0V on all electrodes is shown, followed by RD1 being raised to 18V. Finally, W1 is raised in three steps to

-70V. In the first plot, the horizontal scale includes only the top 10 microns. This plot shows that field is zero throughout the entire structure except the surface, where differences in doping of electrode materials inherently create fields. The four plots following show the entire 100 micron depth. As potentials are subsequently applied, the un-depleted portion where no field is present moves further from the top of the structure until it disappears. At this point a strong field is present in the entire substrate, indicating the device is in an over-depleted state.

III. CHANNEL BOUNDARY

The channel boundary, or p-stop, would normally run parallel to a pixel register or column. Because of the nature of this 2D simulation, that exact layout would not be possible. Instead, the pixel boundary was placed at the left-most end of the 7 transfer gates in the simulation. All the important properties of the p-stop can still be seen despite the difference in geometric layout. Two methods exist for creating a channel boundary. The first is to have an oxide formation above a break in the N-channel doping. A second method is a heavy P-implant. The initial structure had both of these, which was found to be redundant. A plot of potential along a horizontal cutline (Figure 2) shows a potential boundary created by this heavy p-stop.

To simplify the structure, the P-implant was removed leaving only a break in the N-channel below the field oxide. Although the potential barrier is not as great without the redundancy of both methods of channel boundary combined, the function is still the same as shown by the plot in Figure 3, after removal of the p-implant:

Figure 1. From top left: [RD=0V and W=0V], [RD=18V and W=0V], [RD=18V and W=-12V], [RD=18V and W=-42V], [RD=18V and W=-70V]; showing electric field as a function of depth in microns from CCD surface to window.

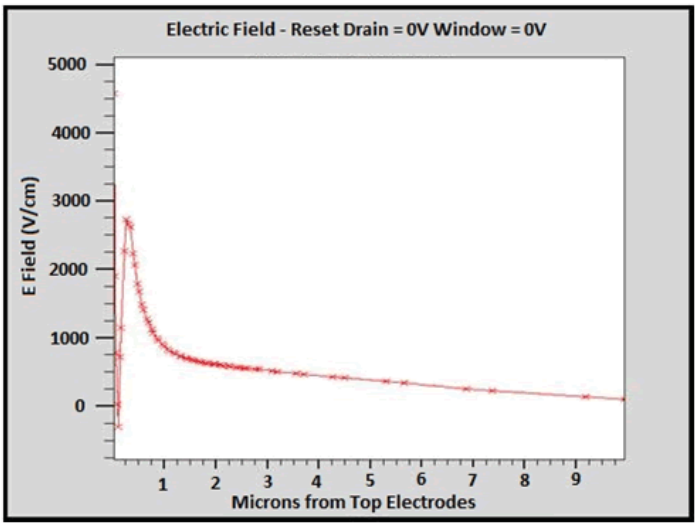

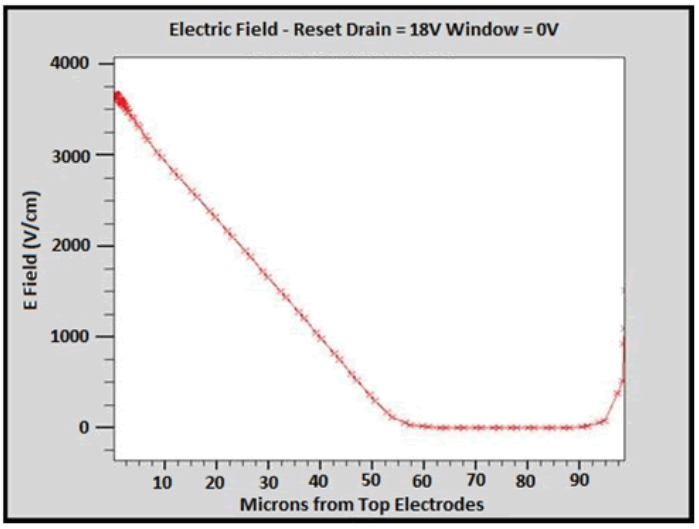

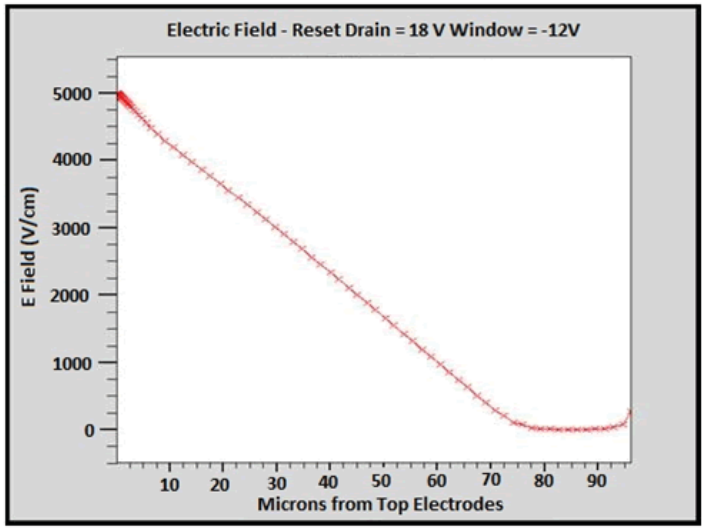

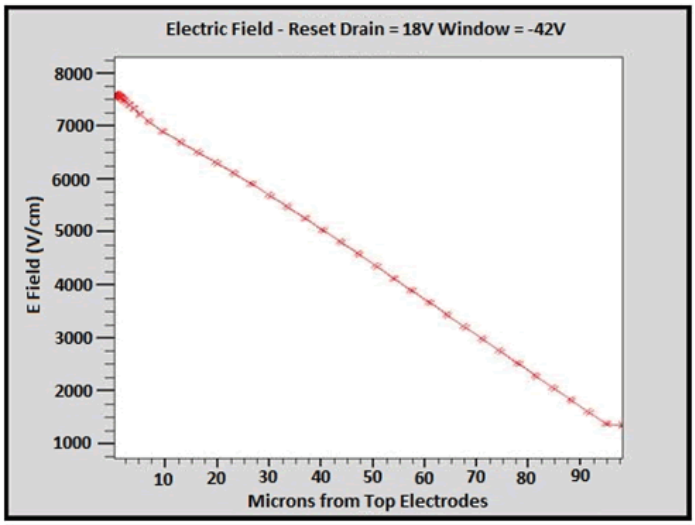

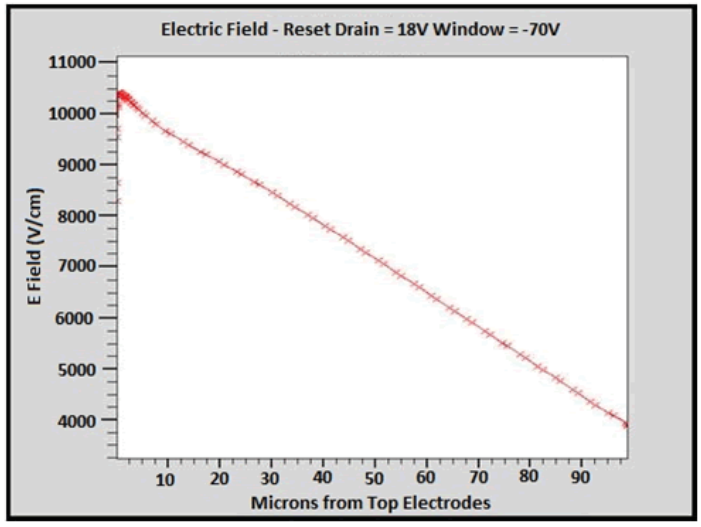

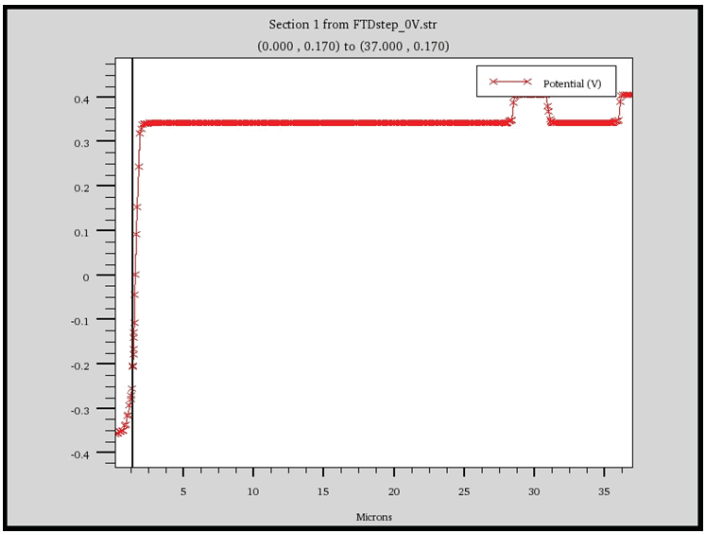

Figure 2. Break in N-channel combined with heavy boron P-implant produces strong electron barrier defining edge of pixel / channel

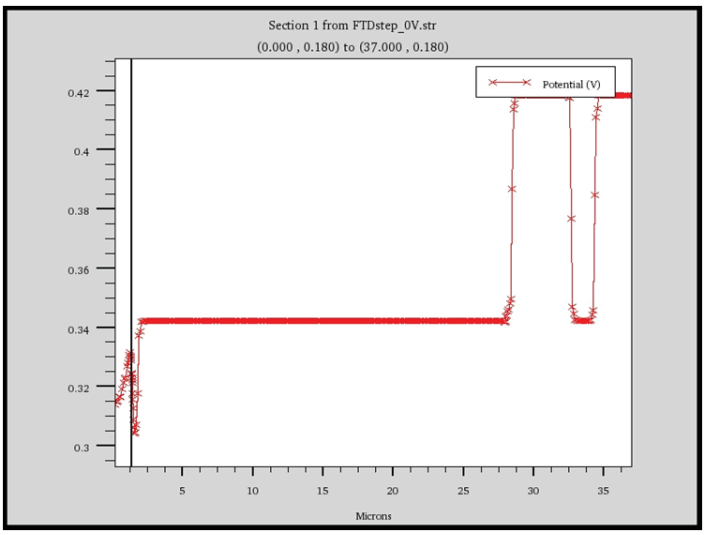

Figure 3. After removal of P-implant command in Athena, barrier is still present, though not as large. Note that potential of barrier does not extend in the negative direction as it did with P-implant.

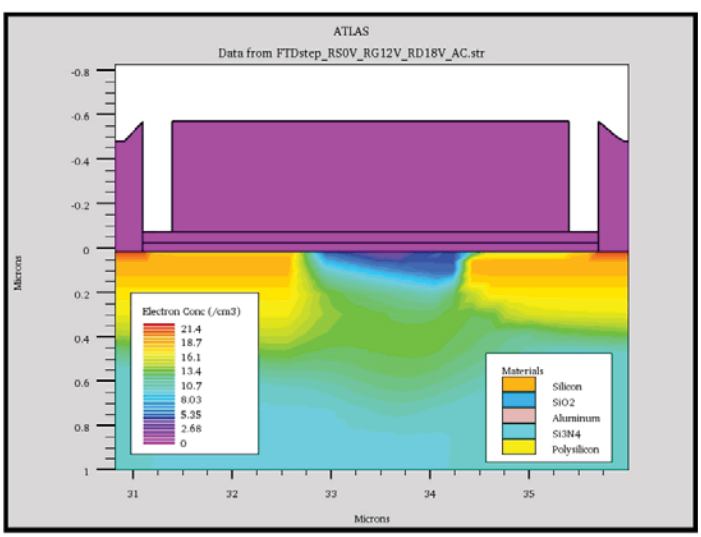

Figure 4. Structure of MOSFET is shown with color gradient representing electron concentration in channel region. The MOSFET is shown here with 12V applied to reset gate (RG1).

IV. RESET MOSFET OPERATION

After each pixel readout, the read node (RS1) must be reset to its baseline voltage in preparation for the following charge packet. The read node (source), reset gate, and reset drain form a MOSFET which accomplishes this purpose. The initial CCD simulation structure contained a surface channel MOSFET. The surface channel MOSFET operated well; however, it is known that the noise of surface channel devices is greater than that of a buried channel. Since the actual reset transistor is a buried n-channel device, this method was used in the more recent simulations. The basic structure of the MOSFET portion of the simulated CCD is shown in Figure 4. Specific properties such as doping profile and gate geometry of the commercially made devices are not known. The MOSFET must be "off" at a gate voltage of 0V, meaning no conducting channel is present. At 12V on the gate, a channel must form, connecting the source to the drain and equalizing their potentials in order to reset the read node. Results of simulation showed that there was little change in the conducting channel between 0V and 12V on the gate. A strong channel formed as gate voltage became very close to drain voltage (approximately 18V). One attempt was made to lower the "turn-on" voltage, commonly known as threshold voltage, by shortening channel length. The channel length is defined here as the length of N-channel region below the reset gate between source and drain N+ doped regions. Reducing the length of the channel was found to contribute little to lowering threshold voltage. Further studies will include the manipulation of doping concentrations and the ratio between N doping and N+ doping, in order to further refine threshold voltage characteristics.

V. SIMULATING FLOATING NATURE OF READ NODE

The CCD read node electrode is electrically connected only to the gate of the output amplifier transistor. As a MOS device, this transistor essentially presents infinite impedance to the read node. Thus, when the reset transistor is in its off-state, the read node must behave as a floating electrode. By default, Silvaco connects all electrodes to zero volts potential until they are raised to another defined bias. Because the FLOATING command within the Silvaco program requires that an electrode be completely surrounded by insulating material, this command could not be used for the read node which rests directly on the silicon substrate. Thus, Silvaco's external resistance command was used to insert a very high resistance (on the order 108Ω) between the read node and ground, effectively isolating it electrically such that it behaves as a floating electrode.

VI. CAPACITANCE AND CAPACITIVE COUPLING

Silvaco provides the option of applying an alternating current signal of a specified frequency to an electrode. When this is done, the program calculates capacitance and conductance between the electrode where the signal is applied and all other electrodes within the structure. Since clock signals are applied at high frequencies to gate electrodes in the CCD during image readout, capacitive coupling to the signal output is an important consideration. In the simulation discussed, the applied frequency was 500kHz which is an accurate approximation of real CCD clock signals. The output of the 2-dimensional calculation is in Farads/micron for capacitance and Siemens/micron for conductance. Capacitive coupling from clocked electrodes to signal electrodes can thus be

approximated given the values calculated. Some sample values are given in Figure 5.

Inter-Electrode Capacitance	
Electrode Pair	**Capacitance (Farads/Micron)**
G7 and RS1	0.590x10-3
OG1 and RS1	0.965x10-3
W1 and G7	5.750x10-3
RG1 and RS1	8.390x10-3

Figure 5. Representative values of capacitance. Note that values are given in linear density rather than directly in Farads. G7 is one of the seven transfer gates. OG1 is the output gate. RS1 and RG1 are the source and drain of the reset MOSFET, respectively.

Clearly these values derived from a 2D simulation may only provide ballpark estimates of actual device capacitance. Position and overlap of electrodes and N+ regions contributes a great deal to the inter-electrode capacitance. Because the exact geometry of these can only be estimated in simulation, capacitances derived must also be considered an approximation.

VII. CONCLUSION

A number of notable changes were made to the initial structure during this project. Though changing the reset MOSFET from surface to buried channel made the CCD structure more realistic, voltage to current characteristics now require adjustment. Capacitance values obtained should be used only in a relative sense. The ratios of capacitance between various pairs of electrodes is likely more accurate than actual values which could be computed by multiplying linear densities by appropriate length. It is clear that depletion is occurring in the simulated CCD as expected. Further work may include an investigation of localized electric field between electrodes. This could give an indication of combinations of bias voltage which, if accidentally applied to given electrodes, could create damaging electric field levels within the silicon.

VIII. ACKNOWLEDGEMENTS

Informative conversations with Graham Smith, Sergio Rescia, Justine Haupt, Konstantin Stefanov, and Andrew Clarke are greatly appreciated.

IX. WORKS CITED

D. Johns, K. Martin, Analog Integrated Circuit Design, John Wiley & Sons, New York, 1997.

J. R. Janesick, Scientific Charge Coupled Devices, The Society of Photo-Optical Instrumentation Engineers, Washington, 2001.

K. Nishiuchi, A Normally-Off Buried Channel MOSFET for VLSI Circuits, Electron Devices Meeting, International Vol. 24 pp 26-29, Fujitsu Laboratories Ltd., Kawasaki, Japan, 1978.

K. Ohwada, A High-Speed Buried Channel MOSFET Isolated by an Implanted Silicon Dioxide Layer, IEEE Transactions on Electron Devices, Vol. ED-28, No. 9, September 1981.

Weather instrumentation calibrations provide baseline data in the Long Island Solar Farm

Jonathan Haimoff
Nassau Community College, Garden City, NY 11530
John Heiser, Environmental Sciences Department, Brookhaven National Laboratory Upton, NY 11973

ABSTRACT

The Long Island Solar Farm (LISF), situated at Brookhaven National Laboratory (BNL), is capable of producing up to 32 megawatts of power for the Long Island grid. In an effort to provide researchers with a history of data that shows the effects of atmospheric conditions on the overall solar output of the LISF, BNL's Meteorological Services conducts routine maintenance procedures throughout the fields each year. Maintenance responsibilities include calibration and data collection of the instrumentation that report atmospheric conditions on any given day. Accurate, precise, and reliable readings were achieved through in situ and ex situ calibrations of meteorological instrumentation such as air, soil, and panel temperature sensors and relative humidity sensors. With these results, scientists are provided with a reliable history log for the future. By having a history log of atmospheric conditions and the total solar output in the LISF, scientists can refer back to recorded data in order to fix any problems that could potentially be posed in the future. Fluctuations of power levels from the LISF can be stabilized by knowing past conditions that can assist with predicting the effects of future atmospheric conditions. Consistent and accurate calibrations of instrumentation for atmospheric conditions associated with the LISF will pave the way forward for reliable solar energy to enter the marketplace for consumers in the long run.

I. INTRODUCTION

The LISF, a relatively new addition at BNL, is capable of producing up to 32 megawatts of power. Although the LISF may be able to power up to 4,500 homes at best, there are and will be times when energy produced by the solar panels may fall short of its carrying capacity since the surrounding environmental factors affect total solar energy output. In an effort to make solar energy as dependable as possible due to the weather effects on the panels, BNL's Meteorological Services conducts routine calibrations of weather instrumentation within the LISF to provide accurate and precise data readings of atmospheric conditions. These instruments record ambient air temperature, relative humidity, and panel temperature. Through instrumentation calibrations, Meteorological Services is continuing to provide other researchers with the necessary baseline data for how the solar farm operates in any and every weather condition. Through correlating the energy output of the solar panels to its ambient environmental conditions, future researchers can have a reference to look to in order to diagnose what may or can cause deficiencies in the energy that is provided to the Long Island grid. By having that reliable data history based on the weather effects at the solar farm, researchers can thus work to restore deficiencies in power based on those weather results. For example, if there were to be a sudden drop in energy, researchers could see why that energy has dropped based on the baseline weather data. Calibrations were done for Omega Platinum Resistance Temperature (PRT) sensors located at each of the 25 power blocks in the LISF in an ex situ setting. Those PRT's record the air temperature at a power block. Campbell temperature/ relative humidity sensors were calibrated in an ex situ setting. Finally, Omega photovoltaic panel temperature thermistors were calibrated in an in situ setting using an infrared temperature scanner as a reference. All ex situ calibrations were conducted in a lab using an ethylene glycol temperature bath.

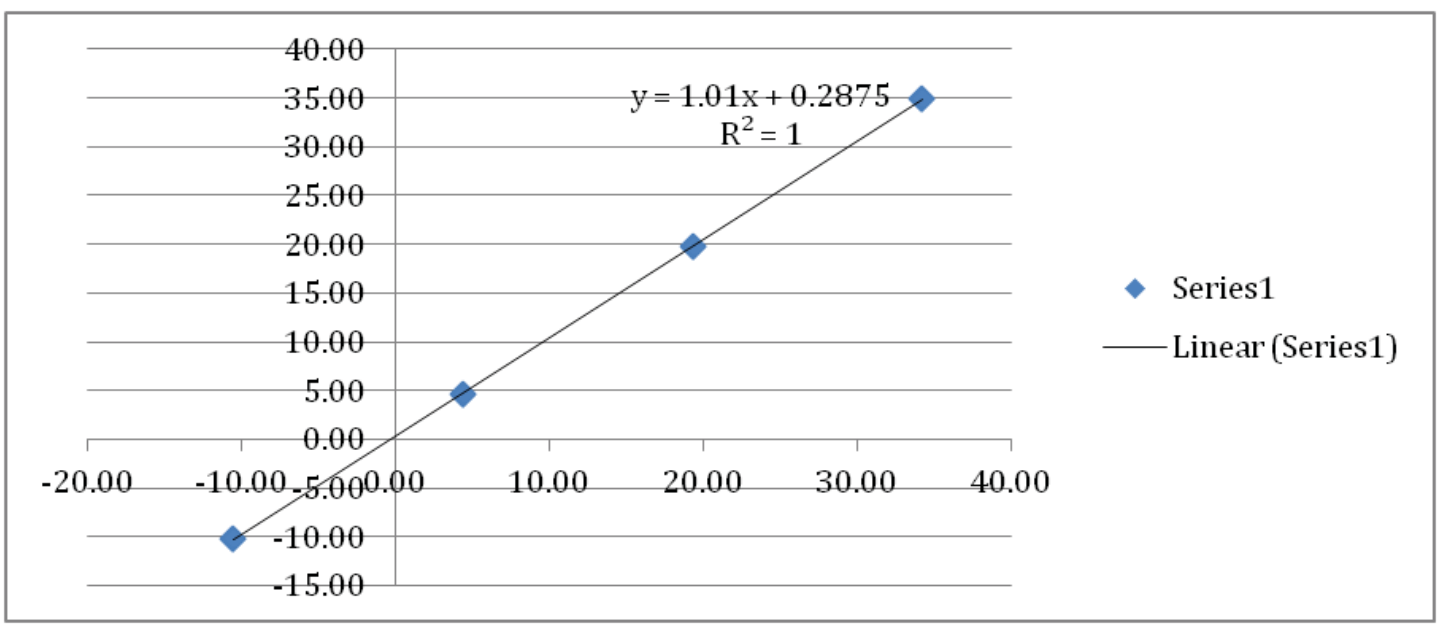

Figure 1. The graph of a platinum resistance temperature sensor that passed calibration

II. PROGRESS

The first group of instruments calibrated included the Omega platinum resistance temperature sensors that measure the air temperature at each of the 25 power blocks located throughout the LISF. Each sensor is connected to a CR-3000 data logger located in close proximity to the power block. The data loggers function as the record holder for each of the sensors. Data is stored, transmitted, and displayed by the data logger for each type of atmospheric sensor. Since the PRT calibrations require an ex-situ calibration setting, sensors of that type were cut down, unplugged and transported back to a laboratory. By using an ethylene glycol temperature bath, those PRTs were calibrated along with a reference probe at four distinct temperature levels. By comparing the test probe to the reference probe at -10, 5, 20, and 35 degrees Celsius, the probe's accuracy and precision in recording the temperature was tested. Probes that passed calibration recorded temperatures accurate enough by one tenth of a Celsius degree. An example of a calibrated PRT that passed accuracy and precision requirements by on tenth of a degree is depicted in the graph in Figure 1.

Sensors that failed to pass the accuracy and precision requirement were removed from service and replaced. The calibrated PRTs were transported back into the LISF and reinstalled at each of the 25 power blocks. Sensors will remain functional in the LISF until they are due for a recalibration. PRT calibrations are conducted each year. Meteorological Services keeps a log of all instrumentation in an electronic inventory tracker. Sensors that were removed from service were scanned with a Cipher Lab BNL barcode scanner. Each sensor that has been calibrated would be scanned to update the calibration date. All sensors that were brought back out into service also have been scanned in an effort to keep track of every instrument.

Omega panel temperature thermistor sensors record the temperature of a given panel at each power block throughout the day. Calibration of those 25 sensors required an in situ calibration setting. The procedure involved using a hand-held infrared (IR) temperature sensor. Using the data logger, the actual temperature of the panel read by the thermistor was recorded at precisely the same instant that IR sensor recorded the temperature of the same panel. These readings were done at three different time intervals from early morning to noon to ensure that the readings captured included the full range of maximum sunlight in a given day. Calibrations were only conducted on clear sunny days. Once all 25 thermistors were calibrated the results were graphed to check for overall thermistor accuracy and precision. In an ideal situation, the graph of a given temperature read by a thermistor should output the exact temperature value for the IR. When plotting many different temperature points, ideally the trend line should have a slope of exactly one showing the same value for thermistor vs. IR. In actuality, the results were graphed in Figure 2, producing a trend line that has a slope of precisely 1.002.

The results based on this graph provides evidence for Meteorological Services that the thermistors were calibrated to the accuracy and precision standards that produce reliable enough results to make conclusions that when weather conditions affect the overall panel temperature throughout a given day, the power levels produced by the solar farm can be explained by these results.

III. FUTURE WORK

Although solar energy overall has much room for improvement in its effectiveness in providing power to the globe, calibrations of weather instrumentation in the LISF will forever remain necessary for maintaining solar energy for what it has to offer today, and will play an even larger and more important role for the future of solar energy. Meteorological Services plans to continue to conduct routine calibrations of weather instrumentation as long as the LISF is still producing power. There are plenty of other weather instrumentation devices in the solar farm that provide researchers in other disciplines with necessary data for further study. Soil temperature probes are calibrated annually to provide data for ecology/conservation study applications. Total sky imagers are routinely calibrated as well. Sky imagers track cloud movement and make "now casting" the ability to predict cloud movements possible. This allows for the prediction of up to 30 minutes on how much energy is going to be produced by the LISF based on the cloud movement. It helps to maintain a constant energy grid by knowing ahead of time when there will be a dip in power produced so that adjustments can be made at lower costs of other energy sources.

IV. IMPACT ON LABORATORY AND NATIONAL MISSIONS

The mission statement of the National Photovoltaics Envi-

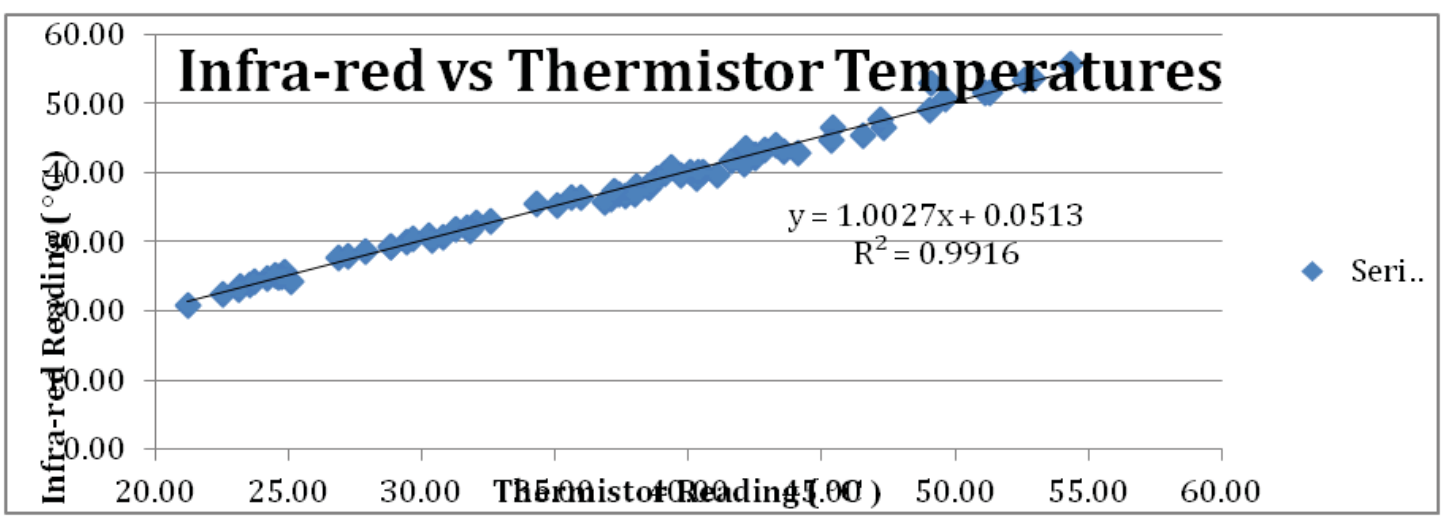

Figure 2. The relationship between IR temperature and thermistor temperature within calibration

ronmental Research Center at BNL says that it works to minimize environment health and safety impacts associated with current and future photovoltaic systems at the lab. In order to do that, it also works to minimize environment health and safety risks and associated costs. To do that, the lab must reduce uncertainties. By ensuring that the future of photovoltaics and solar energy has a reliable data history of the weather effects on the solar farm, uncertainties will be reduced as time goes on with consistent history records of weather in the solar farm. When doubt is eliminated and reassurance is established through routine calibrations, costs will decrease and safe renewable energy will not only continue to benefit people but the environment will be preserved, grow and benefit as well.

V. CONCLUSIONS

Solar energy may still have a lot more to offer the world with its growing potential. However, every small step that is taken to improve the quality of solar energy and its environmental impact will eventually build up to be a reliable source to count on in the future of solar energy. Twenty to thirty years from now, researchers will be able to look back to data from today with confidence in order to assess and solve problems, or expand and create new techniques in the realm of solar energy. Solar energy can and will evolve given today's urgent need for alternative energy sources into one of the world's most precious energy source. However, accurate and precise data involved in the solar plan must always remain consistent.

VI. APPENDIX

John Heiser	BNL	Project Advisor/ Principle Investigator	Conducts routine instrumentaion calibrations in the LISF
Laurence Milian	BNL	Environmental Sciences research member	Taught research interns how to conduct calibration procedures
Scott Smith	BNL	Environmental Sciences research member	Assisted in calibration parameters
Helen Bognato	UNC	SULI research intern	Assisted in actual calibration procedures of instrumentation and plotting data.
Lauren Herrera	SCCC	CCI research intern	Assisted in actual calibration procedures of instrumentation and plotting data

FACILITIES

- Brookhaven National Laboratory, Environmental Sciences Department, Building # 815
- Long Island Solar Farm at BNL

Study of electric field non-uniformity in Cadmium Zinc Telluride room-temperature, radiation detectors

Terance Harper
College of Engineering, Technology Alabama A&M University, Normal, AL 35762
Giuseppe Camarda and Ralph James, Non-Proliferation and National Security Department,
Brookhaven National Laboratory, Upton, NY 11973

ABSTRACT

For three decades, researchers have collaboratively worked on the improvement of Cadmium Zinc Telluride (CZT) as a room-temperature nuclear radiation detector material. This material offers a very promising way to fulfill the nuclear non-proliferation and national security goals important to the mission of the Department of Energy (DOE) and Brookhaven National Laboratory (BNL). Though researchers have made many advances with CZT through different transformative science and technology solutions, the reproducibility of the "perfect crystal" has yet to be accomplished, primarily due to the material inconsistences that directly affect the electric-field distribution. To investigate the non-uniformity in the electric-field distribution, we used different characterization experiments on two bar- shaped CZT crystals. One crystal was grown using the High Pressure Bridgman Method (HPBM) and the other with the Traveling Heater Method (THM). The National Synchrotron Light Source (NSLS) at BNL was utilized for Micron-scaled X-ray Detector Mapping (MXDM) along with White Beam X-ray Diffraction Topography (WBXDT). MXDM allows the researcher to apply an X-ray beam to a specific area of a crystal and record the corresponding signal output as an energy spectrum. To be able to see defects within the crystals, not seen with the naked eye, the NSLS was also used for WBXDT measurements of all sides of the crystals. Additionally, to check for surface damage, which can cause electron trapping, an optical microscope was used to take bright field micrographs. The results from the WBXDT and optical microscope were then used to compare results from the X-ray mapping system to see where the electric-field distribution inconsistences were occurring and why. These results will yield critical knowledge on how to improve the CZT crystal, so it can be implemented into the national security mission of our country and other countries toward nuclear nonproliferation, while giving me important research experience for my future educational and career endeavors.

I. INTRODUCTION

In principle, radiation detectors are simple devices that directly convert charge pairs generated by ionizing radiation, such as X-rays, gamma (γ) rays, and beta (β) particles, into electrical signals.[1] The devices presently used for portable gamma-ray spectroscopy are mainly scintillator counters and "portable" cryogenically-cooled high-purity germanium (HPGe) detectors.[2] For the past three decades, researchers have collaboratively worked on the improvement of Cadmium Zinc Telluride (CdZnTe or CZT), as a room-temperature nuclear radiation detector material. CZT is a very attractive material for room-temperature detectors because it has a wide band gap at $E_{gap} \cong 1.6$ eV which ensures high resistivity along with a high atomic number ($Z_{Cd} = 48$, $Z_{Zn} = 30$, and $Z_{Te} = 52$).[1, 3] This material is very promising way to fulfill nuclear non- proliferation and national security goals, monitor industrial processes, and improve medical imaging due to the very good resolution responses achieved thus far.

Though researchers have made many advances with CZT through different transformative science and technology solutions, the reproducibility of the "perfect crystal" has yet to be accomplished primarily due to the inconsistencies that directly affect the electric field distribution. A uniform internal electric field distribution is ideal to insure full electron collection, but due to defects within the crystal lattice, surface preparation, and tellurium precipitates or inclusions, this is not always achieved. To improve on the crystals defects, our crystal growers used two different growth methods--the High Pressure Bridgman Method (HPBM) and the Traveling Heater Method (THM)--which provide good control of the growth and produced large single crystals.[4] Along with controlling the growth, the growers also used their own unique fabrication techniques to control the surface properties of the detector. This preparation can influence the electrical field inside the device and can significantly affect transport properties, which in turn affect the induced signal at the electrode, if not executed properly.[5] Since researchers have improved and gained a better understanding of the correlations between various defects and the detector's performance, we were able to characterize these crystals.

To investigate the inconsistences in the electric field distribution, we used different characterization experiments on two bar-shaped CZT crystals in which both were 6 x 6 x 12 mm^3. One crystal was grown using the HPBM and the other THM, as well as two different surface preparation techniques. The National Synchrotron Light Source (NSLS) at Brookhaven National Laboratory (BNL) was utilized for Micron- scaled X-ray Detector Mapping (MXDM) along with White Beam X-ray Diffraction Topography (WBXDT). Additionally, to check for surface preparation and damage, an optical microscope was used to take Bright Field micrographs and Infrared (IR) micrographs of each side, including the anode and cathode. Here we report our findings, and discuss the factors affecting the electric field distribution.

II. EXPERIMENTAL TECHNIQUES

A. Micron-scale X-ray Detector Mapping (MXDM)

Micron-scale X-ray Detector Mapping is a unique technique that was developed at BNL's National Synchrotron Light Source (NSLS) at beamline X27B. With this technique (Figure 1a), we can deliver a fine collimated X-ray beam (10 x 10 μm^2), ranging from 7 keV to 40 keV, to a specific area of a CZT detector. Using a hybrid charge-sensitive amplifier followed by a shaping circuit and multi-channel analyzer (MCA), we are able to measure the spectral response in that specific area and extract the associated information, i. e., pulse height, photopeak position, and FWHM (Figure 1b). With using SPEC13 macro software, we can do a raster scan to control the translation stages and move the sample in the x- and y-directions. Hence, we can map the detector's energy

response (normally denoted by the photopeak's position) over the entire detection area.

Since the X-ray beam is very tiny, we can study how localized defects affect the detector's performance. This unique test cannot be done easily with a sealed radioactive source because, after fine collimation, its X- or Gamma-ray intensity is extremely low, and testing takes many days or months. However, with the bright, highly collimated X-ray at the NSLS, testing is rapid and easy. It takes only a few seconds to finish a test at one beam position, and a few hours (depending on the beam's size and the detector's size) to scan an entire detector.

For our detector mapping, we kept the collimation of the beam at 10 x 10 μm^2 for both the THM grown crystal and the HPBM grown crystal. The detector is positioned horizontally to a monochromatic 28 keV X-ray beam, as seen in Figure 1a. To excite the internal electric field of the crystal and to allow for full electron collection capabilities a bias voltage of 2000V was applied to the electrode, i.e. anode and cathode. Because a detector's response is related to charge collection, and is strongly affected by the internal electric field, such measurements yield information on the field's two-dimensional distribution. In the ideal case of a uniform electric field distribution inside a CZT detector, the resulting X-ray response map would display a pattern identical to that of the electrode used to read the signals.[6]

B. White Beam X-ray Diffraction Topography (WBXDT)

White Beam X-ray Diffraction Topography (WBXDT) measurements allow us to examine the distribution of defects and strains in CZT crystals. Brag's Law describes the principles of the operation of WBXDT as,

$\lambda = 2d \cdot \sin\theta_B$,

where λ is the wavelength of the X-rays, θ_B is the angle between the incident X-rays and the lattice planes of CZT crystal, and d is the interplanar distance between the adjacent lattice planes.[3] Beamline X19C at the NSLS was utilized to conduct topography of our two crystal samples.

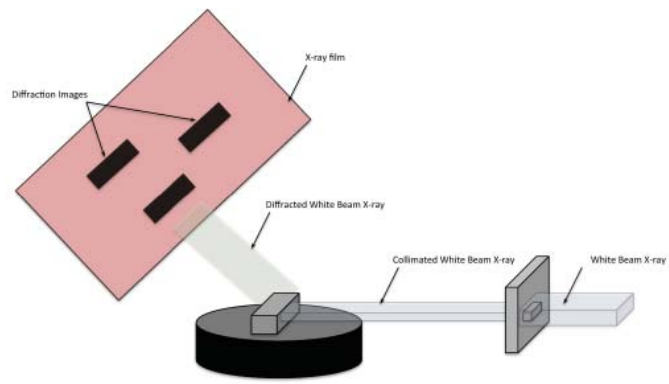

Figure 2. Schematic of WBXDT at x19c beamline in the NSLS

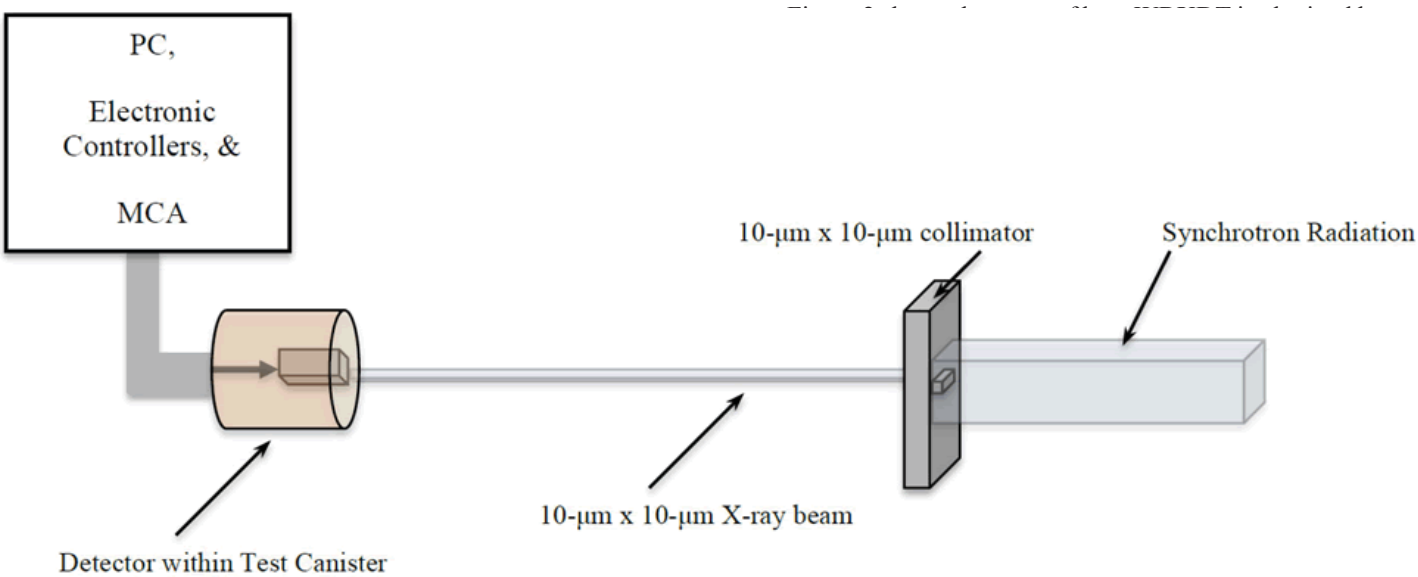

(a)

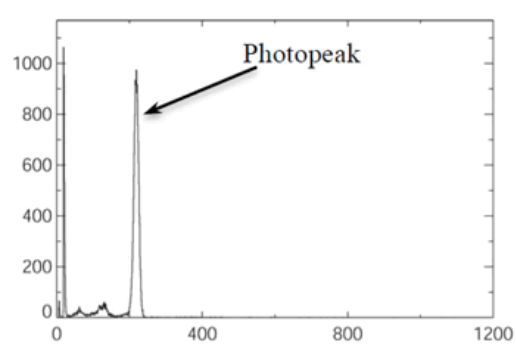

(b)

the anode of side surface C. But as the WBXDT is examined, the detector appears to have more extended defects that could cause electron trapping, whereas Figure 3 shows a more uniform internal crystal lattice.

To analyze the uniformity of the electric fields, x-ray response maps of the anode and cathode were measured for both detectors. The samples were tested with 28 keV of synchrotron radiation with a bias voltage of 2000 V at 100 µm steps. Figure 5 shows the x-ray response map of the anode and cathode of the HPBM detector with full charge collection, some charge trapping, and full charge trapping. On side A of the anode, full charge trapping occurred due to the chipped edge. When looking at the x-ray response map the squared uniform bright and light grey colors confirms that good surface preparation was utilized resulting in a focusing electric field for the HPBM detector. Overall, this detector shows good electron collection and a predominately uniform electric field. To further examine and support the assumption of a good surface preparation of this detector we took x-ray response maps of side surface C.

Figure 6 shows the relation of WBXDT and x-ray response maps for side surface C. The uniform light-grey color x-ray response map confirms that good surface preparation was

utilized resulting in a focusing electric field for the HPBM detector anode collection.

The same characterizing parameters were used for the THM detector to keep the data consistent, Figure 7 shows the x-ray response map of the anode and cathode of the THM detector with full charge collection, some charge trapping, and full charge trapping. When looking at the x-ray response mapping an assumption can be made that the entire area of the crystal is not collecting electron charges at 100% full performance, but instead at <100%. Two questions arise from the x-ray response maps; Why are sides A and D not linear to B and C? Is it due to the surface preparation that's causing the electron trapping? So to answer these questions we took x-ray response maps of side surface A and D to compare with the WBXDT and find out what's happening.

Figure 8 shows side surface A area where electrons are being trapped due to extended defects or surface damage. These consequent defects and surface damages are causing low electric field regions, therefore contributing to the non-uniformity of the anode collection. Also in the WBXDT of side surface A, one defect is seen towards the cathode of the crystal. This defect is causing substantial charge loss but isn't seen under the infrared micrograph nor the visible light micrograph. As shown in Figure 9, side surface D has a defocusing or weak electric field due to extended defects or surface preparation seen in the WBXDT and micrographs.

IV. CONCLUSION

As seen in Figure 7, the MXDM of the THM detector shows good electron collection through the volume, but there is severe charge loss near the edges due to electron trapping. To improve the detector's uniformity, the grower should improve their fabrication process of the surface. The fabrication technique the HPBM grower uses seems to be a better process due to their more uniform electric field. An improved fabrication process for the THM detector would increase the charge collection efficiency for better and more accurate radiation detection.

V. ACKNOWLEDGEMENTS

This work was supported by the U.S. Department of Energy, Office of Nonproliferation and Verification R&D, NA-22, Office of Science SULI Internship, BNL OEP, and Alabama A&M University. Also, special thanks to my mentor Giuseppe Camarda, Ralph James, Aleksey Bolotnikov, KiHyun Kim, Anwar Hossian, and Ge Yang.

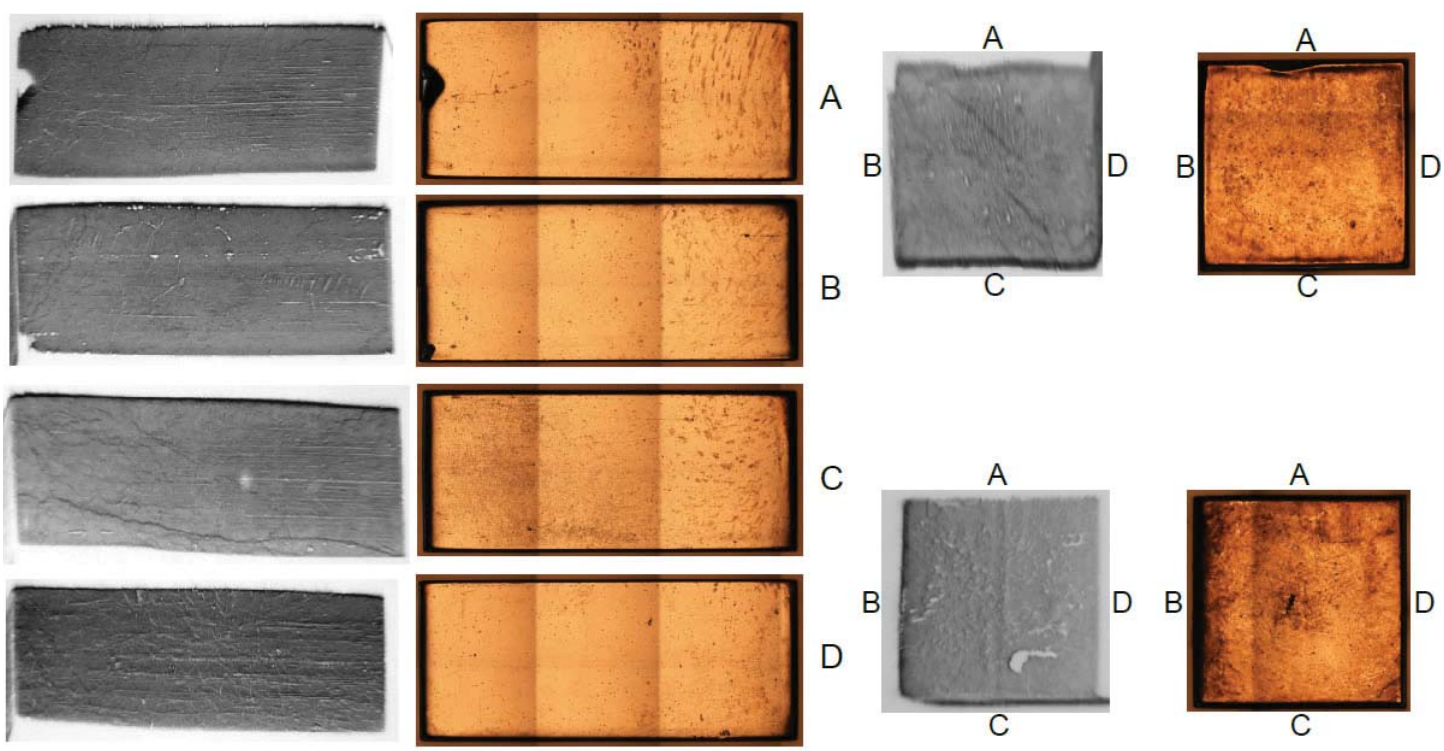

Figure 3. WBXDT & Micrographs of HPBM grown CZT Detector

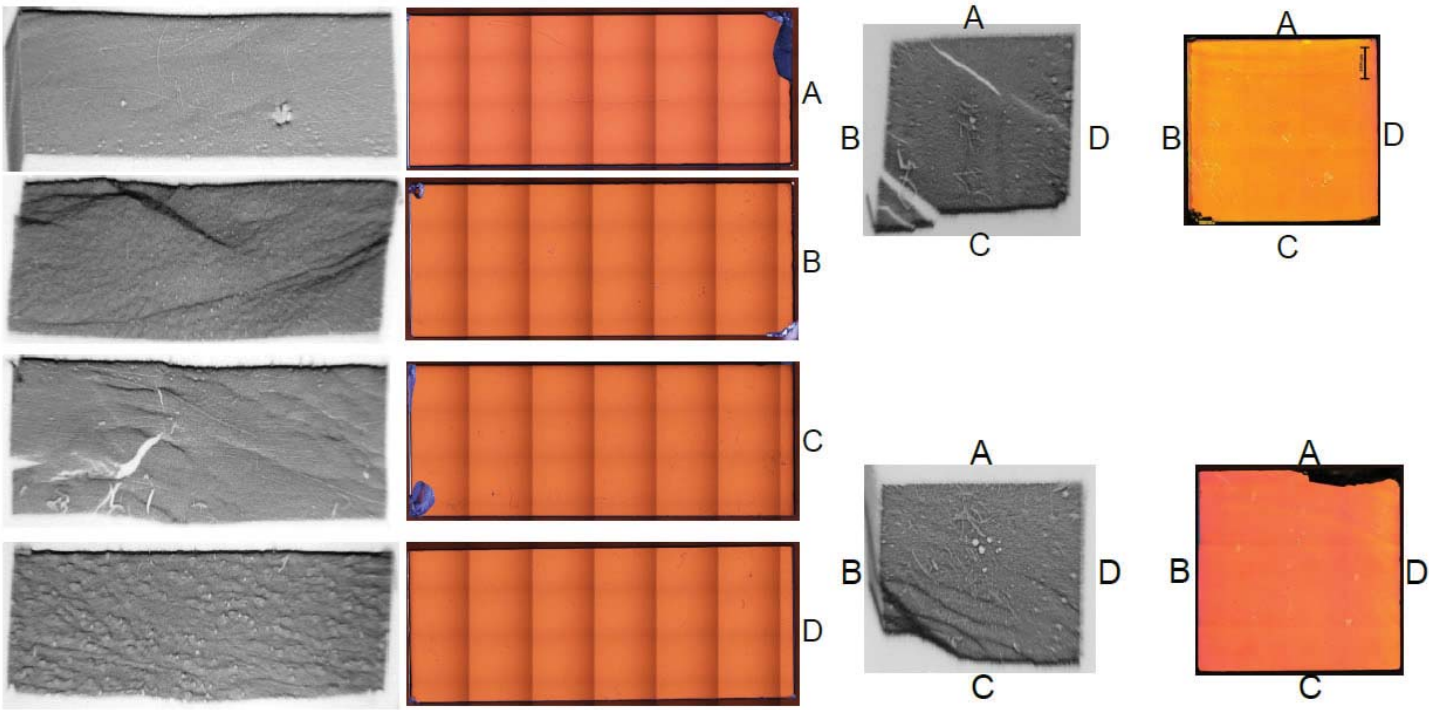

Figure 4. WBXDT & Micrographs of THM grown CZT Detector

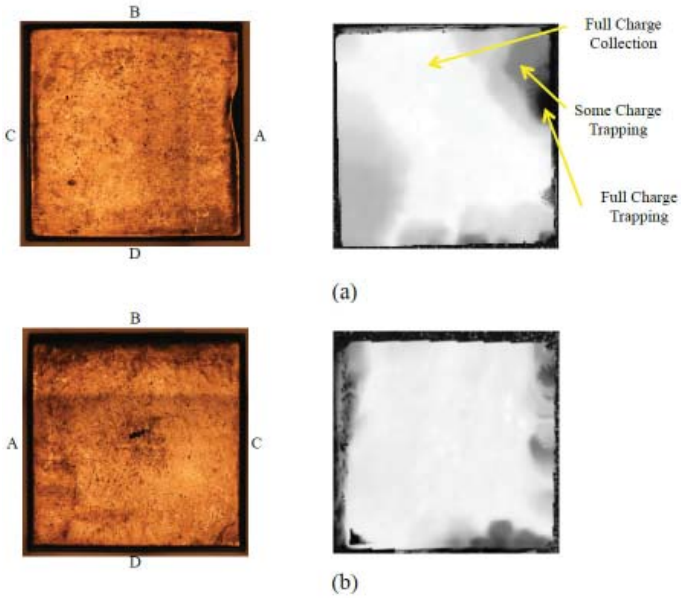

Figure 5. (a) Anode 1:1 Micrograph and MXDM; (b) Cathode 1:1 Micrograph and MXDM

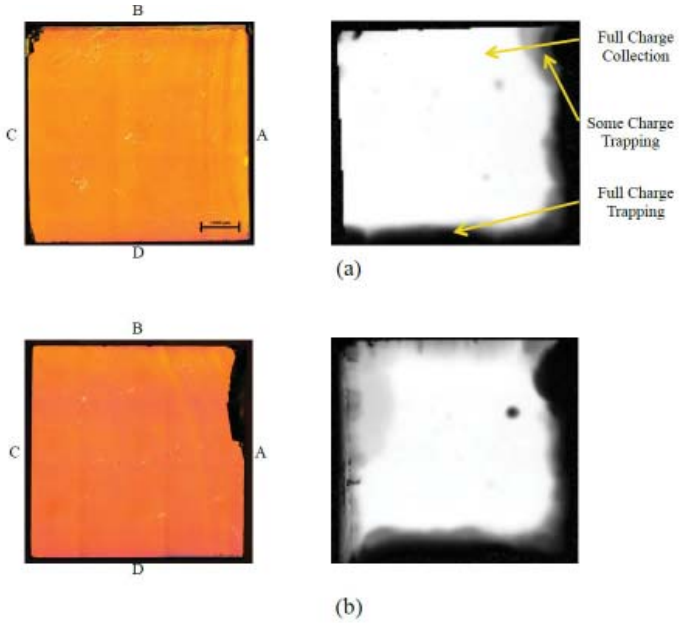

Figure 7. (a) Anode 1:1 Micrograph and MXDM; (b) Cathode 1:1 Micrograph and MXDM

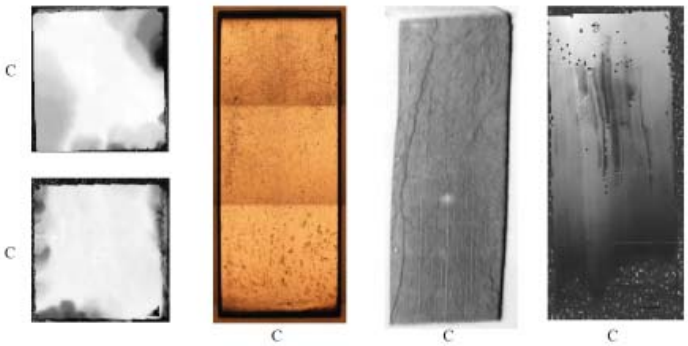

Figure 6. X-ray response maps of anode and cathode along with x-ray response map of side surface C of HPBM detector

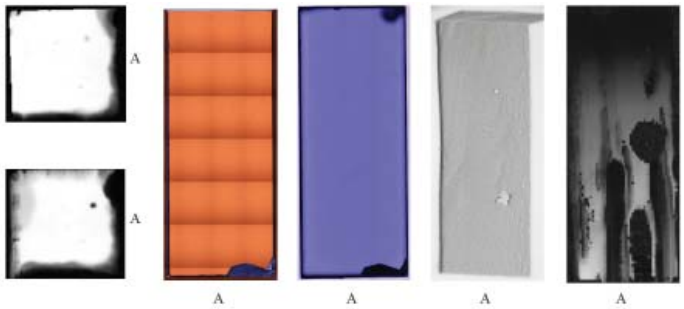

Figure 8. Side Surface A Examination

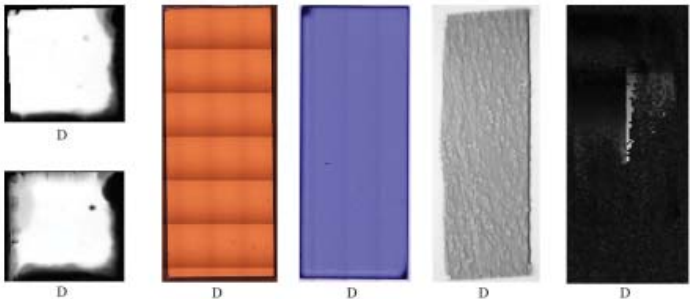

Figure 9. Side Surface D Examination

VI. REFERENCES

[1] G.A. Carini, G.S. Camarda, Z.Zhong, D.P. Siddons, A.E. Bolotnikov, G.W. Wright, B. Barber, C. Arnone, and R.B. James, "High-Energy X-ray Diffraction and Topography Investigation of CdZnTe", J. Electron. Mater. vol. 34, no. 6, pp. 804-810, 2005.

[2] G.S. Camarda, A.E. Bolotnikov, W. Chan, Y. Cui, R. Gul, A. Hossain, K. Kim, G. Yang, and R.B. James, "Hybrid Contacts for CZT Virtual Frisch-grid Detectors", Proc. of SPIE. vol 8142. Aug. 2011.

[3] A. Bolotnikov, G. Camarda, A. Hossain, K. H. Kim, G. Yang, R. Gul, Y. Cui, and R.B. James, "Development of CdZnTe Radiation Detectors", Presented at the 2011 IEEE Nuclear Science Symposium and Medical Imaging Conference, Valencia, Spain, October 2011.

[4] S.A. Awadalla, J. Mackenzie, H. Chen, B. Redden, G. Bindley, M.C. Duff, A. Burger, M. Groza, V. Buliga, J.P. Bradley, Z.R. Dai, N. Teslich, D.R. Black, "Characterization of detector-grade CdZnTe crystals grown by traveling heater method (THM)", J. Crys. Gro., vol. 312, no. 4, pp. 507-513, Feb. 2010.

[5] Q. Zheng, F. Dierre, J. Crocco, V. Carcelen, H. Bensalah,J.L. Plaza, and E. Dieguez, "Influence of Surface Preparation on CdZnTe Nuclear Radiation Detectors.," J. Applied Surface Science 257 (2011)

[6] G. Yang, A.E. Bolotnikov, G.S. Camarda, Y. Cui, A. Hossain, K.H. Kim, and R.B. James, "Electric Field Distribution of Cadmium Zinc Telluride (CZT) Detectors", Presented at the 2009 SPIE Optics & Photonics Conference, San Diego, CA, August 2009.

[7] A. Zappettni, L. Marchini, M. Zha, G. Benassi, N. Zambelli, D. Calestani, L. Zanotti, E. Gombia, R. Mosca, M. Zanichelli, M. Pavesi, N. Auricchio, and E. Caroli, "Growth and Characyerization of CZT Crystals by the Vertical Bridgman Method for X- ray Detectot Applications", IEEETrans. Nucl. Sci., vol. 58, no. 5, pp.2352-2356, Oct. 2011.

[8] Y. Cui, M. Groza, G.W. Wright, U.N. Roy, A. Burger, L. Li, F. Lu, M.A. Black, and R.B. James, "Characterization of Cd1-xZNxTe Crystals Grown from a Modified Vertical Bridgman Technique", J. Electron. Mater. vol. 35, no. 6, pp.1267-1274, 2006.

Sustainment of Meteorological Sensors on a Photovoltaic Solar Farm (Long Island Solar Farm)

Lauren Herrera
Suffolk County Community College, Selden, NY, 1784
John Heiser, Brookhaven National Lab, Upton, NY 11973

ABSTRACT

As the Department of Energy focuses its future on renewable energy, Brookhaven National Laboratory has a two hundred acre solar farm that converts the sun's radiation into electricity for over four thousand homes. Owned by BP Solar and MetLife, the Long Island Solar Farm (LISF) is the largest photovoltaic solar farm in the northeastern United States. The solar farm contains various sensors that monitor the meteorological conditions around the solar panels. These sensors track the wind, rain, sun's irradiance, barometric pressure, clouds, air temperature, panel temperature, and soil temperature--both inside and outside the solar farm, allowing scientist and companies the unique opportunity to collect a valuable data. An annual calibration of each sensor is needed, but maintenance and repair is crucial if an unexpected occurrence occurs. This research concerns the annual calibration of each sensor and the impacts the sensors data will have on observing the environmental effect throughout the solar farm during the next twenty years. Data collected will be used by BNL scientists, LIPA, and companies who will use solar energy in the future. Data observations made over the next twenty years can assists in anticipating future complications and ultimately find new ways to improve solar energy.

I. INTRODUCTION

As the country focuses its future on renewable energy, the Department of Energy will be contributing its share of solar energy research to the sustainable energy movement. Owned by BP Solar and MetLife, the Long Island Solar Farm (LISF) at Brookhaven National Laboratory (BNL) is the largest photovoltaic solar farm in the northeastern United States. This two-hundred acre solar farm converts the sun's rays into electricity for over four thousand Long Island homes. The Long Island solar farm is unique because of the different types of meteorological sensors that are located both inside and outside the solar farm. These meteorological sensors will monitor the meteorological changes, including cloud cover, at the solar farm for the next twenty years. The data being collected will hold valuable information about the problems large scale solar farms face. This research on the Long Island solar farm will shape the future of large scale solar energy.

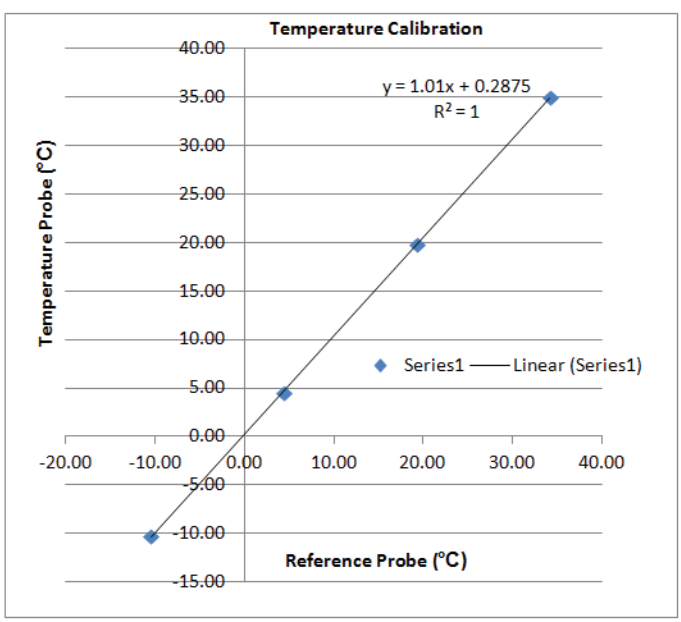

A large-scale solar farm can be any solar farm that has a net production capacity greater than 25MW. Using this cutoff, there are over sixty large scale solar farms in the world. As more and more people attempt to contribute to the sustainable energy movement, the numbers of large-scale solar farms will also rise in the next two decades. The long-term problems that may arise from such a large-scale solar farm are currently unknown. Even though we are attempting to recycle the energy, we might be destroying or helping the environment surrounding the solar farm.

With construction beginning in the fall of 2010 and ending in the fall of 2011, the 200 acre solar array of the LISF contains 164,312 crystalline solar photovoltaic (PV) modules and was built in collaboration with BP Solar, MetLife, the Long island Power Authority (LIPA), and BNL. Establishing a large-scale solar farm comes with many great benefits, chiefly its construction creates jobs for the community surrounding the area. The LISF produced over two hundred jobs ranging from construction workers and electrical engineers to horticultural workers who provided the plantings that were included in the project. The Long Island Solar Farm also contributed over $75,000 to the Long Island native life restoration.

The LISF was not only made plant friendly, but also animal friendly as well. Every seventy-five feet the fencing surrounding the LISF includes a small open hole to allow small mammals to pass through. The fencing also contain forty five degree angled corners to inhibit any deer from getting into the solar far, providing a deer free environment for the small mammals. The landscaping and planning of the solar farm was also built to protect the tiger salamanders.

In addition to the economical and plant and animal friendly

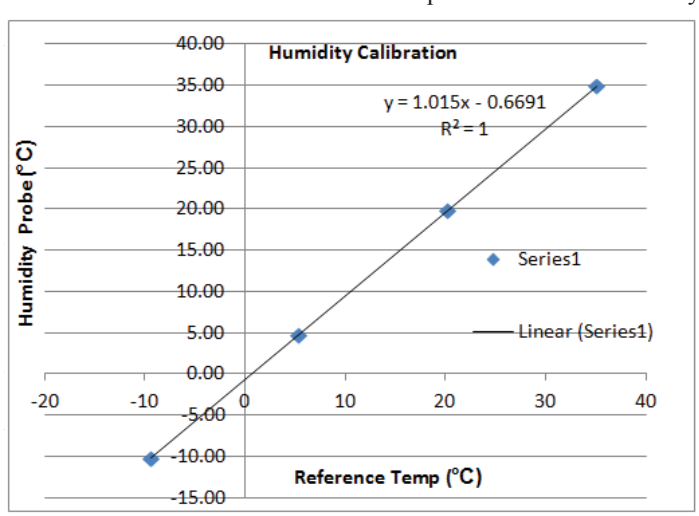

does not hit the area beneath a panel, it does strike the area the arrays causing a difference in soil temperature and thus raising the question of whether this soil temperature difference affects how animals adapt to this environment. Finally, over time our sensors will allow scientists to notice if there is a heat island affect that is changing the environment for small mammals.

III. SENSORS

The solar farm contains sensors that monitor different meteorological conditions. These conditions measure, solar radiance horizontal, solar radiance planar, soil temperature under the array, soil temperature between the array, air temperature, panel temperature, humidity, cloud cover, wind speed, wind direction, rain, and the sun's position. The annual calibration of all sensors is needed in order to maintain and collect accurate data to allow scientists to track how meteorological conditions affect large-scale solar farms.

IV. CALIBRATION METHODS

The air temperature sensors were calibrated ex-situ and those with a less than 3% error would pass calibration (Figure 1). The temperature sensor were placed into an ethylene glycol water bath and calibrated at -10 °C, 5 °C, 20 °C, and 35 °C.

The humidity probe was calibrated ex-situ and was placed in three different saturated solutions of $MgCl_2$, NaBr, and NaCl. Measurements were then taken at -10 °C, 5 °C, 20 °C, and 35 °C. Those humidity probes with a less than 3% error would pass calibration (Figure 2).

The thermistor was calibrated in-situ using an infrared scanner. If the temperature reading was more than a three degree difference, then the calibration would fail, but if it proved to be less than a three degree difference then the thermistor would pass (Figure 3). Statistical analysis proved that the thermistors passed. (See Appendices A, B, and C)

The rain gauges were calibrated in-situ; if proven to register more than a five percent error, then the calibration would fail.

V. CONCLUSION

All calibrations of the humidity probes, thermistors, and rain gauges passed. During the air temperature probe calibration, all initially passed, but due to a lightning strike, two air temperature probes failed during the second trail. It was concluded that the air temperature probes failed due to lightning striking the solar farm. The air temperature probes were replaced.

VI. FUTURE WORK

The annual calibration of the meteorological sensors insures the validity and accuracy of the data being collected. This data, to be collected over the next twenty years, will be used to assist the solar industry in foreseeing future problems, in ecology, technical, or climate research areas. Ultimately the data will provide key insights into the problems surrounding a solar farm, and prompt solutions that will improve the future of solar energy.

Appendix A.

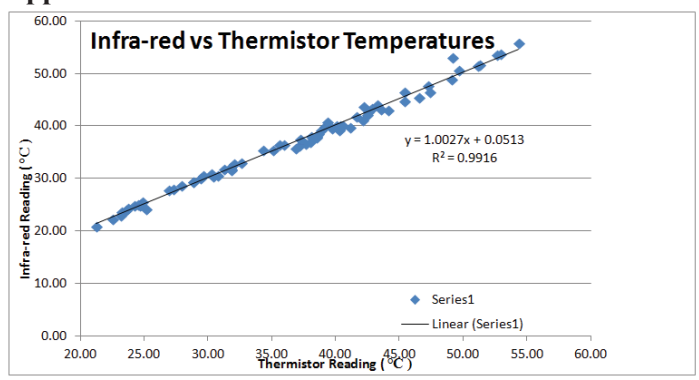

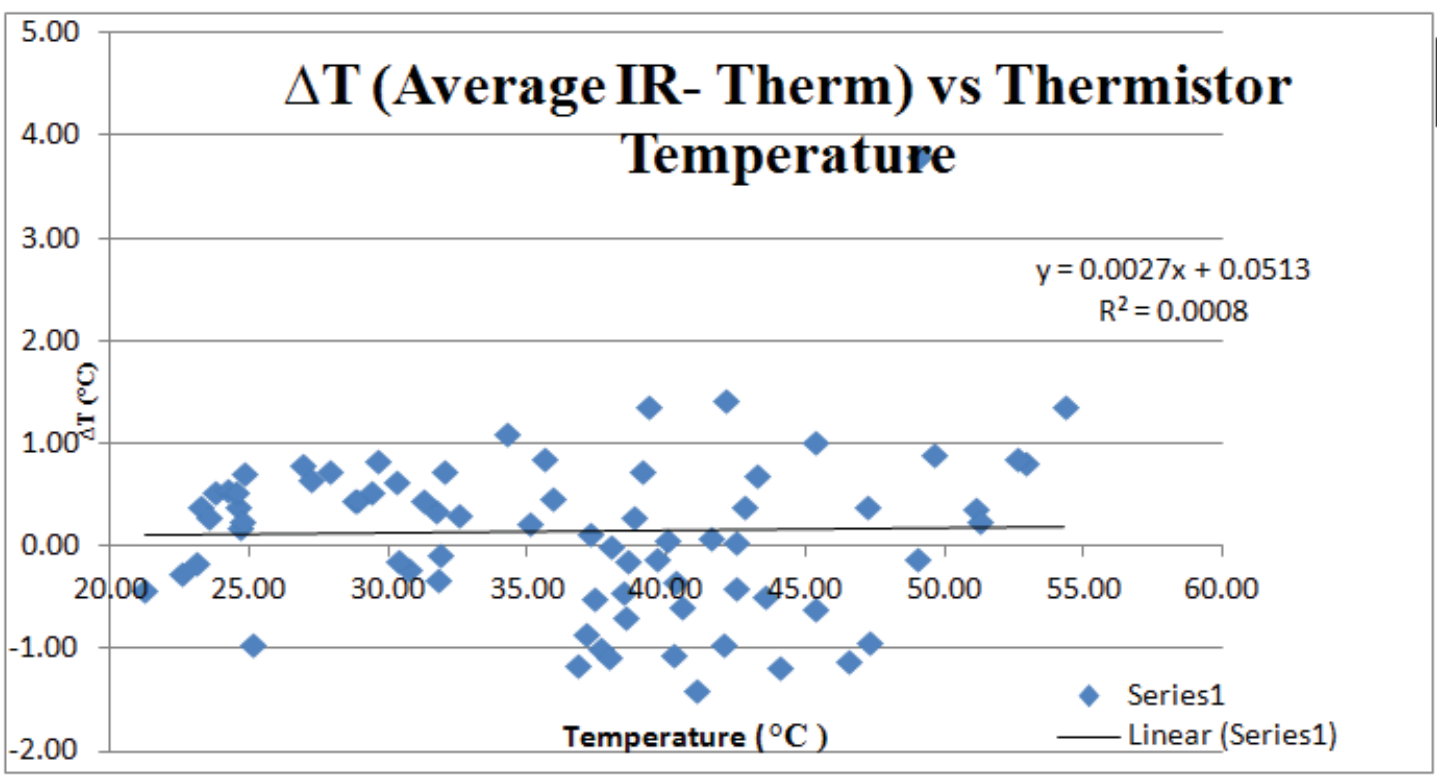

Appendix B.

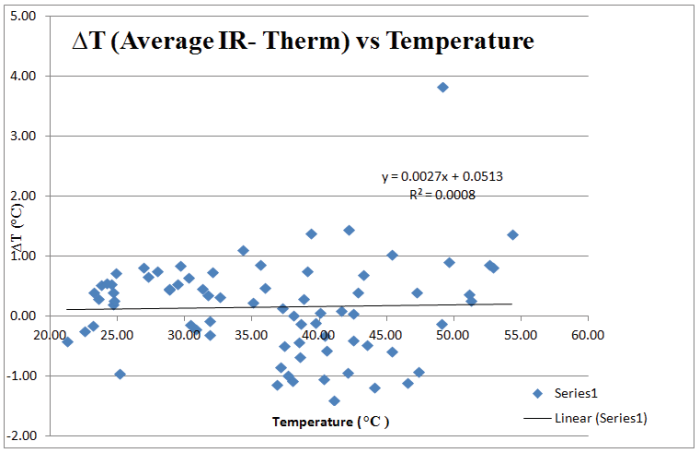

Appendix C.

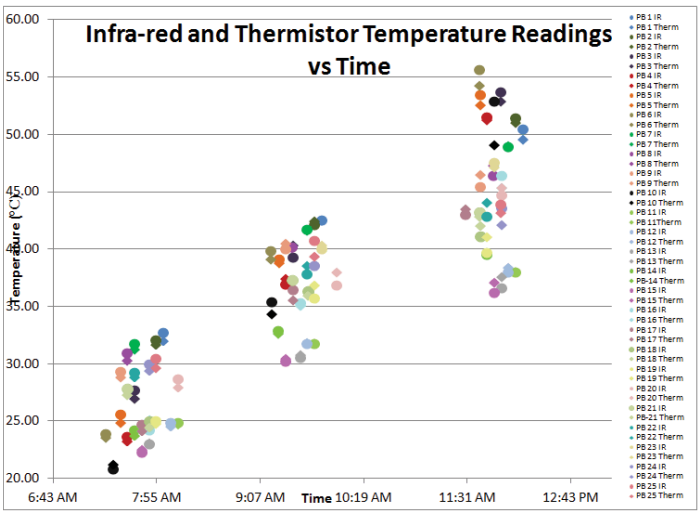

VII. REFERENCES

http://www.bnl.gov/GARS/SET/LISF.php

http://www.bnl.gov/envsci/envtech/

http://www.bnl.gov/video/index.php?v=236

http://www.bnl.gov/today/story.asp?ITEM_NO=2719

http://libn.com/2011/11/18/lipa-flips-switch-on-long-island-solar-farm/

Investigating the carbon monoxide effect on the platinum catalyst in a proton exchange membrane fuel cell

Andrew Hubert and Hazem Tawfik
Department of Mechanical Engineering Technology, Farmingdale State College, Farmingdale, New York 11735
James Wegrzyn
Department of Sustainable Energy Technologies, Brookhaven National Laboratory, Upton, New York 11973

ABSTRACT

An investigation of the performance of a Proton Exchange Membrane Fuel Cell (PEMFC), when exposed to hydrogen (H2) with varying concentrations of carbon monoxide (CO) found that the performance of the fuel cell was negatively affected in the presence of CO. As CO concentrations increased, the performance continued to decrease as a result of CO blocking active sites. To restore the PEMFC performance, CO must be oxidized from the catalyst. Regeneration was achieved using different methods of oxidation such as flowing hot air through the anode, exposing the catalyst to vaporized hydrogen peroxide (H2O2), introducing small electrical pulses to the fuel cell, and running the fuel cell in reverse. Flowing air at 50oC through the anode and exposing the catalyst to vaporized H2O2 were found to be the best methods of regeneration. This research demonstrated that a fuel cell, poisoned by CO, has the potential to regain most of its performance.

I. INTRODUCTION

As a result of rising energy costs and the negative impact of fossil fuels on the environment, research has increased in the area of clean alternative energy sources. More recently, considerable focus has headed toward the use of hydrogen fuel cells due to their fast start-up, low operating temperatures, and high efficiency. Fuel cells provide a cost-effective method of providing both heat and power for buildings and cars. For optimum fuel cell performance, the hydrogen gas must contain less than 10ppm of carbon monoxide. High production costs of hydrogen have led to its generation from the gasification of biomass which can be found in an overabundance locally and nationally. This biomass process (Figure 1) produces synthesis gas (syngas) containing high levels of CO, a known fuel cell catalyst poison even in trace amounts—as low as 10ppm--is adsorbed onto the catalyst surface.1

To reduce the amount of CO, syngas must first pass through the water gas shift (WGS) reaction where levels of CO are reduced to less than 2%. The WGS reaction combines steam with syngas, and in the presence of a catalyst, converts the CO to carbon dioxide along with increasing the amount of hydrogen. After the WGS, the treated syngas must flow through a hydrogen purification system, such as an electrochemical pump or a palladium membrane, where the hydrogen can be separated from the CO and allow pure hydrogen to flow to the fuel cell. However, if the hydrogen is not 100% pure, methods of regenerating the fuel cell's catalyst must be considered. Oetjen, et al., determined that performance degradation was noticeable after 5 minutes of exposure with the feed gas containing 100 ppm CO, with the cell reaching full poisoning after about 2 hours.2 This poisoning occurs due to the carbon monoxide blocking active catalyst sites for hydrogen to react. For catalyst regeneration, the CO must be oxidized in order to allow the catalyst to reactivate the blocked sites.

Figure 1: Systems of the biomass process that lead to the generation of pure H2

II. METHODS AND MATERIALS

A. Experimental Equipment

The experimental testing was performed using an aluminum bipolar PEMFC (Figure 2) provided by Farmingdale State College (Farmingdale, NY). The anode and cathode consist of a 50cm2 flow field with nine serpentine channels. The membrane electrode assemblies (MEAs), purchased from FuelCellStore.com with a 50 cm2 active area (Figure 3), are composed of a Nafion 115 membrane and have an anode and cathode loading of 4.0 mg/cm2 platinum black catalyst. The MEA also has an ETEK ELAT® gas diffusion layer pressed on top of the catalyst on both the anode and cathode.

The experimental setup, as shown in Figure 4, consisted of gas cylinders, an electronic load, a pressure regulator, and the fuel cell. The polarization measurements were taken using an electronic load provided by Green Energy Research Inc. (Figure 4). This allowed for an electrical current to be applied to the fuel cell that would give a voltage output reading. From the voltage (V) and current (I), the power (P) is calculated by using the equation P=IV. Tanks pressurized with hydrogen and carbon monoxide were used to feed the fuel cell with gas and examine the effects of CO on the catalyst. A pressure regulator was used to keep the anode gas feed at a constant 15psi while the cathode had constant air flowing and open to the atmosphere. All tests were performed with the fuel cell and feed gases operating at room temperature.

Figure 2: Farmingdale State College's patented aluminum bipolar plate

Figure 3: MEA purchased from FuelCellStore.com

Figure 4: Experimental Setup

B. Experimental Methods

To monitor the fuel cell's performance, a baseline with pure hydrogen was taken before every test using the electronic load. Once the baseline was established, catalyst poisoning and regeneration were tested on the fuel cell. Different, increasing concentrations of hydrogen mixed with CO were made to determine the effect that the CO would have on the fuel cell. Different concentrations of CO (1%, 5%, and 10%) with the balance as hydrogen were introduced to the fuel cell. Each with its own membrane, the fuel cell was operated with the CO mixtures to compare the cell to the baseline of pure hydrogen.

To monitor the effectiveness of the catalyst regeneration, the same process was carried out. The power was first measured with pure hydrogen to establish a baseline. The hydrogen and CO mixtures were introduced into the fuel cell, where other power curves were generated. After poisoning occurred, different methods of regeneration were applied to the catalyst. After regeneration, the fuel cell was tested again with pure hydrogen to compare the effectiveness of regeneration compared to the baseline hydrogen power curve.

C. Regeneration Methods

The hot air regeneration method consisted of using an AC power supply and a heater to treat the poisoned catalyst (Figure 5). The power supply was used to heat the heater that had air passing through it. Once the air reached 50oC, it was allowed to flow through the anode chamber of the fuel cell, where the poisoning had occurred. After one hour of hot air flow, the fuel cell was tested with the electronic load using pure hydrogen to determine how much of the catalyst was regenerated.

Figure 5: Hot Air Regeneration Setup

Regeneration using hydrogen peroxide (H2O2) was carried out with a hot plate to vaporize the H2O2 (Figure 6). Vaporization was to pass through the gas diffusion layer and reach the poisoned catalyst on the MEA. Once the H2O2 began to vaporize, the poisoned MEA was placed over the vapors for 10 minutes. After the 10 minutes, the fuel cell was tested again with pure hydrogen to determine how this regeneration method performed.

Figure 6: Hydrogen Peroxide Regeneration Setup

The reverse fuel cell regeneration method consisted of switching the anode and the cathode of the fuel cell (Figure 7). Instead of hydrogen flowing through the anode, it was now fed through the cathode. This was done to allow the hydrogen permeating back through the membrane would cause the CO to escape from the catalyst. The fuel cell was run in reverse for one hour and then tested as a regular fuel cell using pure hydrogen to determine how much the catalyst regenerated.

Figure 7: Reverse Fuel Cell Regeneration Setup (Anode & Cathode Switched)

The final regeneration method tested was by introducing small voltage pulses to the fuel cell (Figure 8). This consisted of connecting a DC power supply to the fuel cell. For two minutes, a 1.5VDC was applied to the fuel cell, followed by a .2VDC for an additional two minutes. This was done such that it would force the CO off of the catalyst. After the voltage cycle, the fuel cell was tested with pure hydrogen to evaluate the regeneration effect.

Figure 8: Voltage Pulse Regeneration Setup

III. RESULTS

The 50 cm2 aluminum bipolar PEMFC was tested under various conditions. Different gas mixtures with concentrations of CO and hydrogen were fed into the fuel cell to determine the effect of CO on the performance of the platinum catalyst. Figure 9 shows that just 1% of CO decreased the performance of the fuel cell to 54% of the baseline performance with pure hydrogen. The higher the concentration of CO, a greater decrease in performance is experienced as shown with the 5% and 10% CO concentrations. This decrease in performance is caused by the CO adsorbing onto the platinum catalyst and blocking sites for hydrogen reactions to take place. The greater the CO concentration signifies that more of the platinum catalyst will be poisoned and the performance will decrease.

Figure 9: The Effects of Different Concentrations of CO

Figure 10 shows the effect that the carbon monoxide has over time. A constant load of 30mA was applied, and every 30 seconds, the power was observed for a total period of ten minutes. Compared to the baseline with pure hydrogen, there was an instantaneous performance drop with CO present. Over the ten minute period, the pure hydrogen only dropped 0.05 W/cm2. However, with 1% CO present, the power dropped by 0.16 W/cm2, which is more than three times that of the pure hydrogen. This shows that CO has an instant effect on performance, and quickly poisons the platinum catalyst, even in a relatively small quantity.

Figure 10: Time Degradation Due to CO

To examine the effect of regeneration methods on poisoned catalyst, a new MEA was used for each experiment. After poisoning the MEA catalyst, a regeneration method was applied to the MEA. Figure 11 shows the effects that each regeneration method had compared to the original performance of an MEA using pure hydrogen. As Figure 11 depicts, the most successful regeneration method was flowing air at 50oC through the anode chamber where poisoning had occurred. This method rejuvenated the catalyst performance back to 86% of the original. The heat had facilitated the oxidation reaction with the oxygen in the air causing most of the CO to become CO2. The hydrogen peroxide also yielded decent performance recovery. With only 10 minutes of exposing the MEA to vaporized H2O2, the fuel cell regained 65% of the original performance. Like the hot air, the heat of the vaporized H2O2 facilitated the reaction of:

H2O2 + CO → H2O + CO2. However, operating the fuel cell in reverse and applying small voltages to the fuel cell also facilitated some regeneration (52% and 35%, respectively) of the original performance.

Figure 11: The Effects of Different Regeneration Methods on the MEA

IV. CONCLUSIONS

The data obtained proves that carbon monoxide has a negative effect on the performance of a PEMFC. As the CO concentration increases, the performance of the PEMFC will decrease. With a 1% CO concentration present in hydrogen, the performance decrease was more than three times greater over a ten minute period as compared to using pure hydrogen. After multiple methods of regeneration, it was concluded that the MEA has the potential for performance restoration. Flowing hot air through the anode, and exposing the MEA to vaporized H2O2 yielded the best results of 86% and 65%, respectively of the original PEMFC performance. These short term regeneration tests provide information that a fuel cell, once poisoned by CO, has the ability to be nearly restored to original performance.

V. ACKNOWLEDGEMENTS

I would like to express my appreciation to Dr. James Wegrzyn and Dr. Hazem Tawfik for their guidance throughout this summer internship. I would also like to thank the U.S. Department of Energy, the National Science Foundation, Brookhaven National Laboratory, Farmingdale State College, and Stony Brook University for allowing me to access their laboratories to conduct my research. I would also like to acknowledge the graduate students in Dr. Devinder Mahajan's laboratory at Stony Brook University.

VI. REFERENCES

1. K.K. Bhatia, C.-Y. Wang/Electrochimica Acta 49 (2004) 2333–2341.
2. H. Oetjen, V. Schmidt, U. Stimming, F. Trila, J. Electrochem. Soc. 143 (1996) 3838.

Generation and acceleration of a high charge state iron ion beam using a laser ion source and direct plasma injection into a radiofrequency quadropole (RFQ) linear accelerator

Peter Jandovitz
Collider Accelerator Department, Cornell University, Ithaca, New York 14853
Takayuki Yamamoto
Washio Laboratory, Waseda University / Collider Accelerator Department, Brookhaven National Laboratory, Upton, New York 11973
Eric Cushing
Collider Accelerator Department, Pennsylvania State University, University Park, Pennsylvania 16802
Masahiro Okamura
Collider Accelerator Department, Brookhaven National Laboratory, Upton, New York 11973

ABSTRACT

Accelerated heavy ion beams have numerous applications in high energy and nuclear physics research, medicine, and possibly as cost-effective drivers of inertial fusion for energy. A laser ion source with the direct injection of the plasma into a radiofrequency quadropole (RFQ) linear accelerator is one effective way of generating high-intensity, low-emittance, heavy ion beams. At the Brookhaven National Laboratory Linear Accelerator, an iron plasma was generated by exposing a solid iron target to a high powered (~1.5 joule) laser. The charge state distribution and current of the plasma were determined using an Electrostatic Ion Analyzer (EIA) and a Faraday cup, and it was found that the distribution was centered around 13+ and the current at the RFQ opening was calculated to be 17 mA. The plasma was directly injected into an RFQ linear accelerator at different injection and vane voltages. A peak bunched, accelerated current of around 10 mA was detected, with a DC peak average of 3.4 mA.

I. INTRODUCTION

The Direct Plasma Injection Scheme (DPIS) is an approach to creating a high-intensity ion source that has been investigated recently and is composed of three stages with three associated components. The process starts with plasma generation from a laser ion source. A high voltage cage and nozzle then extract and inject the ions into an radiofrequency quadropole (RFQ) linear accelerator which captures, focuses, bunches, and accelerates the ions into an intense beam.

A laser ion source generates a plasma by irradiating a solid target with a high power laser. Particles evaporate and are stripped of electrons by the inverse Bremsstrahlung process. The charge state distribution is determined by the temperature of the plasma, which is determined by the power density of the laser. Higher charge states can be created by increasing the laser power or decreasing the laser spot size by focusing the beam. Laser ablation plasma has a high density compared to other ion source plasmas because it is generated from a solid as opposed to a gas that most other ion sources use. The overall current produced by a laser ion source can be much greater than conventional sources produce because of this key difference. Laser ion sources should also produce beams with low emittance. Because the plasma expands perpendicularly from the target, the initial phase space area of the beam is limited.

Radiofrequency quadropole (RFQ) linear accelerators are common first stage accelerators that are capable of focusing, bunching, and accelerating an ion beam. RFQs are composed of 4 vanes or rods in a quadropole configuration that switch polarity at a radio frequency. The quadropole provides a transverse focusing force, and spatial modulations in the rods provide a longitudinal force. However, statically there is no net acceleration through the RFQ because the modulations produce equal accelerating and decelerating longitudinal fields. With the polarities switching at a known frequency, the spatial modulations can be designed so that a "synchronous" particle, of a certain mass, charge state, energy, and phase, always experiences the accelerating force at exactly the same phase with respect to its modulation in time. RFQs are designed so that particles faster than the synchronous particle experience a slightly weaker accelerating force, and slower particles experience a slightly stronger one. This leads to bunching of the ion beam. The output current of an RFQ will resemble the input waveform, except it will oscillate to zero at the RF frequency.

Most RFQs are designed with very precise injection currents in mind and so generally have transmission efficiencies above 90% in practice. The RFQ used here is designed with DPIS in mind, and the first guess at transmission efficiency is 30%. Such a low efficiency is acceptable because the extremely high current density of the laser ion source makes it so that the output at the RFQ should still be much more intense than any other methods of similar scale. There are two main reasons for the low transmission efficiency: 1) The injection current is imprecise since the plasma is freely expanding in three dimensions; and so, only low emittance ions will be accepted into the RF bucket; and 2) The RFQ has a much more aggressive acceleration scheme than others. It achieves this by using a larger "modulation factor," which determines the depth of the spatial modulations. Deeper modulations allow for more efficient acceleration, but the different geometry introduces nonlinearities that can cause more ions to be lost.

II. METHODS AND MATERIALS

A 10 ns laser pulse was sent to one of two target chambers. The ablated plasma traveled down the corresponding vacuum pipe and had either its current measured at a Faraday cup, its charge

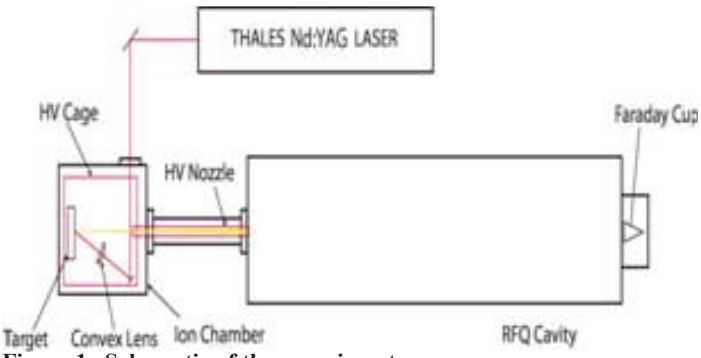

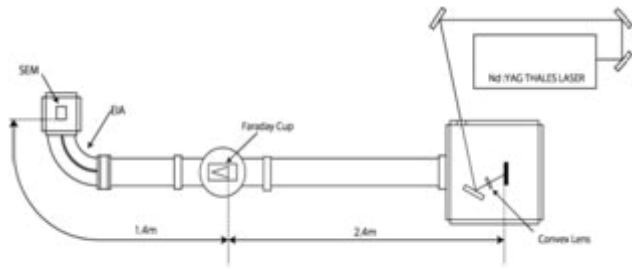

Figure 1: Schematic of the experiments.

distribution measured at the Electrostatic Ion Analyzer (EIA), or its accelerated current measured at a Faraday cup after the RFQ. Secondary electron multiplier (SEM) signals were analyzed using Origin software peak detection. Arrival times were calculated using a Microsoft Excel spreadsheet and the equation for radial motion. Linear interpolation and other data manipulations as well as plotting were performed with Python.

A THALES SAGA Nd:YAG 1064 nm laser was used, with the power delivered to the target measured to be around 1.5 joules over the length of the pulse. The laser was aligned to pass through a 25 mm diameter, 10 cm focal length lens in one of the two target chambers. The target was a 99.99% pure solid iron plate. A three dimensional mechanical manipulator was used to scan through target z-position to optimize laser focusing, and to move the target in the x or y direction by 1 mm after each shot to provide a fresh surface for plasma ablation. The RFQ used has four rods powered by a 100.100 MHz radiofrequency power supply. It is designed for a 1/6 charge to mass ratio and has 144 "cells" (1/2 period spatial modulation) and is 2 meters long. The required injection energy is 8.26 keV/u, and exit energy is 270 keV/u.

In order to analyze the charge state distribution of the plasma, an EIA was used where different voltages were applied to a curved section of the beamline that ended with an SEM. Particles are bent along a radius of curvature that is determined by the particle's charge to mass ratio and velocity, and the applied voltage. Thus, for a given applied voltage, only particles of a given velocity for a specific charge to mass ratio will reach the SEM and produce an electrical signal. Therefore, it is possible to determine the charge state that caused a signal simply by looking at the time it occurred. Then, by scanning through a range of voltages, it is possible to check for signals from particles traveling at some range of velocities, and from that paint a complete picture of the pulse.

III. RESULTS

Figure 2 shows the charge distribution of the plasma in coulombs and the relative abundances of particles. The distribution is centered around 13+. H+ makes up an appreciable percentage of the particles, which shows that the sample was not pure.

Figure 3 shows the current waveform before and after the RFQ. The current at the opening was obtained from the unaccelerated Faraday cup data by assuming that current density scales as L-3, where L is the length the plasma has drifted, and that current density is constant in the 1 cm diameter Faraday cup aperture and the 4 mm diameter injection nozzle opening. The upper right corner of the second graph shows a magnified version of the accelerated beam peak. The RF bunching expected is readily apparent, with peaks separated by the expected 10 ns. The unbunched waveform seen is the result of unaccelerated particles. The peak accelerated current reaches almost 10 mA, with the DC average over 4 periods calculated to be 3.78 mA.

IV. CONCLUSION

A laser ion source with direct plasma injection into an RFQ linear accelerator is a very effective way of generating intense heavy ion beams. This RFQ's acceleration to 270 keV/u within 2 meters is one of the most aggressive accelerators in use, and it appears to have been successful in accelerating a large amount of iron ion current: 3.78 mA DC compared to hundreds of microamperes obtained using conventional methods.2 This was the first successful acceleration of iron using this RFQ, which was

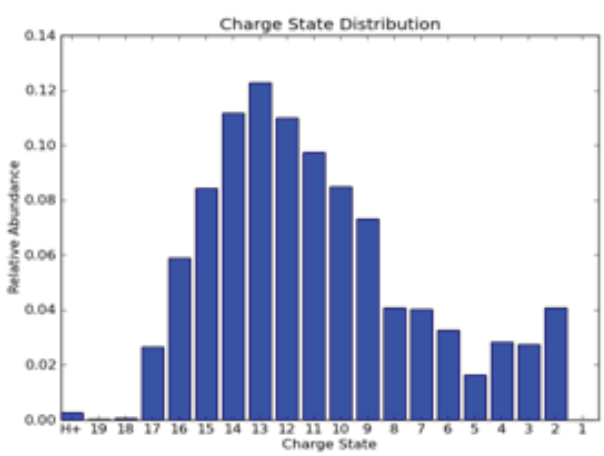

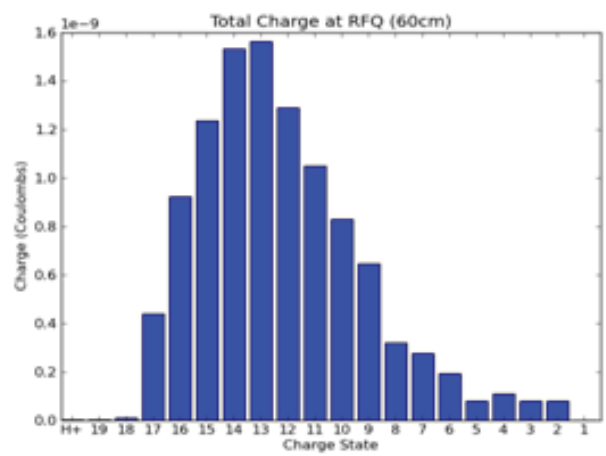

Figure 2:

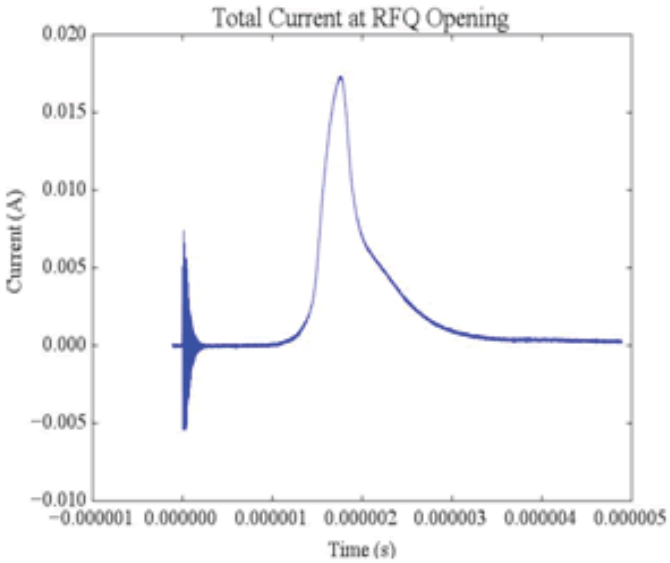

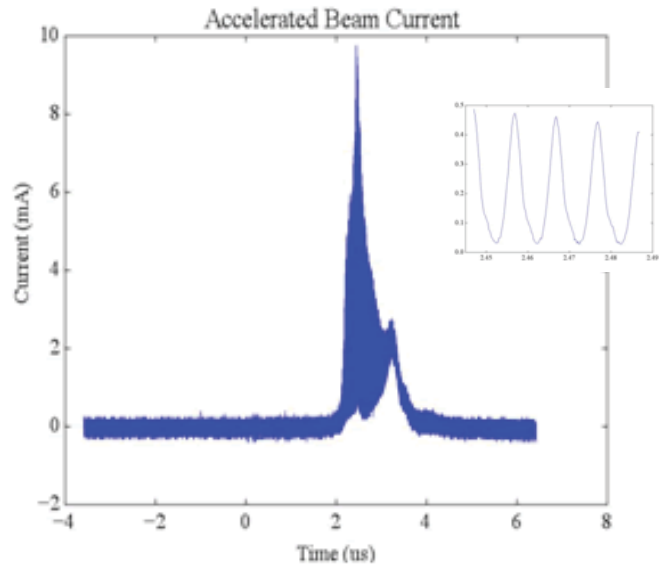

Figure 3.

designed for highly charged silver. The success suggests that this method is fairly robust and versatile.

Unlike most other RFQs which are designed with transmission efficiencies of over 90% in mind,3 the overall efficiency of this RFQ is 21.8%, comparatively very low. This is because of the aggressive injection scheme as well as the low energy charge states present in the plasma. In this case, 53.5% of the total charge of the plasma was of a high enough energy to be accelerated by the RFQ. Ignoring the low energy charge states gives an actual transmission efficiency of 40.8%, higher than the predicted 30%. This is still much lower than most other RFQs, but the extremely high current density of the laser ion source more than makes up for it.

V. ACKNOWLEDGEMENTS

I would like to thank the Department of Energy for their tremendous support for science, specifically for their SULI program which supports young people interested in science. I would also like to thank my mentor, Dr. Masahiro Okamura for his guidance and ideas, Brookhaven National Laboratory for the opportunity to work there and its excellent environment, facilities, and staff, and finally, my lab group, without whom this work would not be possible.

VI. REFERENCES

1. J. Y. Benitez, et al. “Recent progress on the superconducting ion source VENUS,” Review of Scientific Instruments 83 02A311 (2011)
2. T. Thuillier et al. “Roadmap for the design of a superconducting electron cyclotron resonance ion source for Spiral2,” Review of Scientific Instruments 83 02A339 (2011)
3. Dechoudhury, S. “Design and development of a radio frequency quadrupole linac postaccelerator for the Variable Energy Cyclotron Center rare ion beam project,” Review of Scientific Instruments 81 023301 (2010)

Using plant oils as an alternative fuel source

Trevor Johnson
West Virginia University, Morgantown, WV 26505
Changcheng Xu, Brookhaven National Laboratory, Upton, NY 11973

ABSTRACT

Throughout my summer internship at Brookhaven National Laboratory I have been conducting research on the Arabidopsis plant by manipulating certain genes to determine their function in the plant's lipid production. In our research, we have attained four mutants from EMS-induced mutations. Among them, one was generated from the wild type Col (M19-4) while the other three mutants (M7-23, M10-2 and M10-28) were generated from the fad6 mutant that is deficient in prokaryote-pathway (chloroplast pathway) biosynthesis of unsaturated fatty acids and, therefore, depends on the supply of unsaturated fatty acid from the eukaryote-pathway (ER pathway). The mutant M19-4 shows a higher accumulation of TAG and is recessive in term of genetics. A gas chromatography assay showed that mutants, M7-23, M10-2, and M10-28 have significantly different fatty acid profiling from fad6. The four mutants are very valuable for gene mapping. The following is a brief process of gene mapping: F2 plants resulting from a cross between the mutant and the L er ecotype were screened based on higher oil content or a pale green phenotype respectively. At least 50 plants identified from each screen are for rough mapping using 17 SSLP markers which disperse evenly along the 5 chromosomes of Arabidopsis. Once a loosely linkage marker is found, the fine mapping is carried out by selecting more markers and DNA sequencing.

I. INTRODUCTION AND HYPOTHESIS

In today's society, fuel has become an increasing concern for people around the world. With oil having such a limited supply, it has not become a reliable fuel source. This is why scientists are looking into many other possible bio-fuel sources. Many potential sources have been discovered, but none are as promising as the oils produced by the Arabidopsis plant.

My mentor Changcheng Xu assigned me to conduct research with Zhiyang Zhai, a Ph. D. graduate from Cornell University. Our focus was to discover the genes responsible for producing the plant oils in the Arabidopsis plant. These plant oils hold great potential as an alternative bio-fuel source. In order to determine which genes function in the plant's lipid production, we induced certain mutations into the genes to characterize the role the gene plays. We have attained four mutants so far: M19-4, M7-23, M10-2, and M10-28. Each mutant will be analyzed further to find out its value in the plant's lipid production process. We used EMS-induced mutations because they produced point mutations in the genome that are randomly distributed in the genome. Point mutations are single base pair mutations in a gene. These mutations may lead to a complete or partial loss of gene function. We utilize a wide range of laboratory techniques to manipulate, isolate, and identify these genes.

II. METHODS AND MATERIALS

We first had to plant Arabidopsis seeds in soil pots and allow them to grow in a 22 °C gross chamber in the greenhouse for about a week. Once the plants grew a sufficient amount, the cotyledons were removed from each mutated plant. The mutated plants had a distinguishable yellow color. The cotyledons were then added to a DNA Extraction Buffer inside of a tube and the cotyledons were ground up. This grinding process released all of the DNA into the buffer. Ethanol must then be administered to each tube as well. The tubes were finally placed into a 22 °C refrigerator to allow complete DNA extraction.

When extraction was completed, the ethanol was completely removed from all the tubes and a TE buffer was subsequently added to each tube. This procedure prepared the DNA for a Polymerase Chain Reaction (PCR), a technique used to amplify specific DNA.

After amplification was completed, the genes were then run through an Agarose gel in a process called Gel Electrophoresis separates the genes based on size. Gel Electrophoresis sends an electrical current through the Agarose gel and since DNA is negatively charged, it will travel to the positive end of the gel. Smaller DNA segments travel further because the gel is not able to impede their movement as effectively as the larger ones. We used a 4% Agarose gel and examined it under UV light where the genes showed up as bright fluorescent bands.

We also utilized Western blotting to view the protein-protein interaction of the specimen. Proteins were stained with antibodies specific to the target proteins.

Thin Layer Chromatography (TLC) is a chromatography technique used to separate mixtures. A thin layer of an absorbent material, usually silica, is used to coat a sheet of glass. The sample is applied to the plate and a solvent mixture is drawn up the plate via capillary action. Because different samples ascend the TLC plate at different rates, separation is achieved.

III. RESULTS

Thus far, we have identified the TGD-4 gene in the Arabidopsis plant to be an essential part of the oil production process. In our research we have attained four mutants from EMS-induced mutations. Among them, one was generated from the wild type Col (M19-4) and the other three mutants (M7-23, M10-2 and M10-28) were generated from fad6 mutant which is deficient in the prokaryote-pathway (chloroplast pathway) biosynthesis of unsaturated fatty acids and, therefore, depends on the supply of unsaturated fatty acid from eukaryote-pathway (ER pathway). The mutant, M19-4, shows higher accumulation of TAG and is recessive in term of genetics. GC assay showed that mutants, M7-23, M10-2, and M10-28 have significantly different fatty acid profiling from fad6.

IV. DISCUSSION AND CONCLUSIONS

While we have made tremendous advancements in alternative bio-fuel research throughout this summer, it will require some more time, patience and diligence to further analyze the function of the four mutants. We are currently examining the roles of these

four mutant genes, M19-4, M7-23, M10-2 and M10-28, hoping that some of these genes reveal more evidence of the lipid production pathway of the Arabidopsis plant. The discovery of the TGD-4 gene was a huge first step in our research. These genes hold a huge potential for the bio-fuel industry. The discovery of the oil producing genes will create a much more efficient and environmentally-friendly transportation method for the entire world.

V. ACKNOWLEDGEMENTS

I would like to thank Changcheng Xu (Mentor) and Zhiyang Zhai for their guidance and leadership throughout my Summer Undergraduate Laboratory Internship experience. They have made it a worthwhile experience for me.

Optimizing the Geometry of the Focusing Horn Magnets in the Long-Baseline Neutrino Experiment Beamline

Jacob Kiefer
Cornell University, Ithaca, New York, 14853
Mary Bishai
Brookhaven National Laboratory, Upton, New York, 11973

ABSTRACT

We report the results of our simulations for electron neutrino appearance at the far detector in the proposed Long Baseline Neutrino Experiment experiment as a function of the geometry of the focusing horn magnets and a cylindrical graphite target located one kilometer before the near detector. The current setup of the beamline is a target distance of 45cm, with a horn current of .20 MA in both horns, and a horn spacing of 6m. We used the horn shape of the existing Neutrinos at the Main Injector (NuMI) horns at Fermilab. The 0-15 GeV neutrino energy range optimal horn/target geometry and currents for maximum electron neutrino flux are: the target located 50cm before horn 1 in the beamline, spacing between the horns at 10m, and .30 MA current for both horns using the NuMI horns. For the more important neutrino energy range of 0-2 GeV where oscillations are more readily observable, however, the optimal horn/target geometry and currents are: the target located 0cm target before horn 1 in the beamline, horn spacing between horns at 6m, and .22 MA horn current for both NuMI horns. These optimizations provide a significant yield, increasing the current capabilities of the NuMI beamline by 32.0 for 0-15 GeV and and 23.8 for the 0-2 GeV neutrino energy case. Additionally, there is an intersection of the two optimal regions with a setup using a target distance of 30-40cm before horn 1 with a horn current of .28-.30 MA that gives an increase in yield of 18.9 over 0-15 GeV and 14.9 over 0-2 GeV. In the horn current optimization, the best currents are: .4 MA horn 1 and .5 MA horn 2 for 0-15 GeV and .25 MA in both horns for 0-2 GeV. The 0-15 GeV horn current optimization give a 53.8 increase, while the 0-2 GeV optimization gives a 13.2 increase in electron neutrino yield when compared to .20 MA in both horns.

I. INTRODUCTION

In the path forward for neutrino physics, a few major pieces of information are still missing. Two of the most important bits are the hierarchy of the three neutrino masses and a parameter that governs neutrino properties called the CP angle.[1] The discovery of this information would revolutionize not only neutrino physics as we know it, but also possibly how physicists view the entire universe. Indeed, neutrino physics could contain explanations for why there is a disparity in the amounts of matter and antimatter in the universe, among other perplexing puzzles modern physics faces.[2]

In an effort to determine these very important characteristics of neutrinos experimentally, the Long Baseline Neutrino Experiment (LBNE) has been proposed.4 Because the proposed experiment is so large and costly, many preliminary simulations need to be run to determine the most optimal and technically feasible solutions to achieve the desired results. The basic premise behind neutrino production in the current NuMI beamline is as follows: a high intensity proton beam is accelerated to high energy and hits an 80 cm long cylindrical graphite target with radius of 6mm, producing positively and negatively charged pions that spew out in all directions.[3] These pions are focused into a beam by the two focusing horn magnets, which are parabolic in shape and have large currents running through them.[3] Depending on the sign of the current through the horns, the focusing horn magnets bend the trajectory of the positive or negative pions so that they travel in the desired path toward a detector.3 Positive pions decay into positive muons and muon neutrinos, and negative pions decay into negative muons and muon antineutrinos.[1]

The LBNE beamline is the next generation of the NuMI beamline, and plans to add optimizations to increase the neutrino events detected and to increase sensitivity to the unknown neutrino parameters.[4] In the LBNE, a long cylindrical decay pipe is added, in order to reduce the background and give the LBNE very good signal to background ratio and, therefore, high statistics [4] As they are travelling through the decay pipe, the pions decay into neutrinos in the direction of their momentum vector. 1 These neutrinos then travel approximately 1300 km before they hit a very large detector made of liquid argon buried in the Homestake Mine located in South Dakota .[4]

II. FLAVOR OSCILLATION

One of the key characteristics about neutrinos is their apparent ability to oscillate between flavors. The three flavors of neutrinos that we know about so far are electron, muon, and tau neutrinos, each corresponding to a partner charged lepton in the standard model.[1] This oscillation is a result of each neutrino being a different superposition of three quantum mechanical mass eigenstates, each of which are only slightly different from each other. These mass differences cause the phases of the quantum mechanical mass states to propagate at a different rate, thus resulting in a changing mixture of the masses as the neutrino travels through space and therefore flavor oscillation .[1]

There are two modes of neutrino propagation that are of interest in the LBNE: muon neutrino to electron neutrino oscillations, and muon neutrino to muon neutrino survival .[4] The neutrinos produced by the proton beam hitting the target are muon neutrinos and throughout their trajectory toward the far detector, there is a finite probability that these muon neutrinos will oscillate to electron neutrinos. By measuring the number of muon and electron neutrinos detected at the far detector, we can discern information both the CP violation of neutrinos as well as the hierarchy of the three masses .[4] The probabilities of each of the oscillation and survival modes occurring are given by the following equations:

$$P(\nu_\mu \to \nu_\mu) = 1 - \sin^2(2\theta_3)\sin^2(1.27\Delta m_3^2 \frac{L}{E}) \quad (1)$$

$$P(\nu_\mu \to \nu_e) \cong \sin^2 2\theta_3 T_1 - \alpha \sin 2\theta_3 T_2 + \alpha \sin 2\theta_3 T_3 + \alpha^2 T_4 \quad (2)$$

$$T_1 = \sin^2\theta_3 \frac{\sin^2[(1-x)\Delta]}{(1-x)^2} \quad (3)$$

$$T_2 = \sin\delta \sin 2\theta_2 \sin 2\theta_3 \sin\Delta \frac{\sin(x\Delta)}{x} \frac{\sin[(1-x)\Delta]}{(1-x)} \quad (4)$$

$$T_3 = \cos\delta \sin 2\theta_2 \sin 2\theta_3 \cos\Delta \frac{\sin(x\Delta)}{x} \frac{\sin[(1-x)\Delta]}{(1-x)} \quad (5)$$

$$T_4 = \cos^2\theta_3 \sin^2 2\theta_2 \cos\Delta \frac{\sin^2(x\Delta)}{x^2} \quad (6)$$

with $\alpha \equiv \Delta m_2^2 / \Delta m_3^2$, $\Delta \equiv \Delta m_3^2 L/4E$, and $x \equiv 2\sqrt{2} G_F N_e E / \Delta m_3^2$

where $\sin^2\theta_{ij}$ are the neutrino mixing parameters, $|\Delta m_{ij}^2| = |m_i^2 - m_j^2|$ are the absolute values of the neutrino mass differences squared, L is the distance traveled by the neutrino, E is the neutrino's energy, and G_F is the Fermi coupling constant.[1] The mixing parameters and mass differences are known precisely. The values used for this simulation shown in Table 1, with the length to the far detector as L = 1300 km and the neutrino energy output by the simulator.[4] There are three major factors that affect the flavor oscillation probabilities: the value of δ_{cp}, the ordering of the masses, and whether the particle in question is a neutrino or an antineutrino.[2] The following plots in Figures 1 and 2 show the variations of the probability curves with respect to these three variables.

III. EXPERIMENTAL SETUP AND PROCEDURE

With this general knowledge of neutrino physics, our task was to explore the effects of target position with respect to the horn, and horn current on the electron neutrino yield at the far detector using the GEANT4 LBNE simulator. GEANT4 is simply a large simulation package that was developed to simulate the passage of particles through matter.[6,7] The parameter space for optimizing the horn geometry is complicated since many factors determine how well the magnets can focus the pion beam.[4] The parameters that we varied to explore the neutrino yield were: tar-

Parameter	Value
$\sin^2 2\theta_2$	.869
$\sin^2 2\theta_3$	1.00
$\sin^2 2\theta_3$	.100
Δm_2^2	+7.59 eV
$\lvert \Delta m_3^2 \rvert$	2.32 eV

Table 1: Values used for mixing parameters and mass differences for neutrinos. [1]

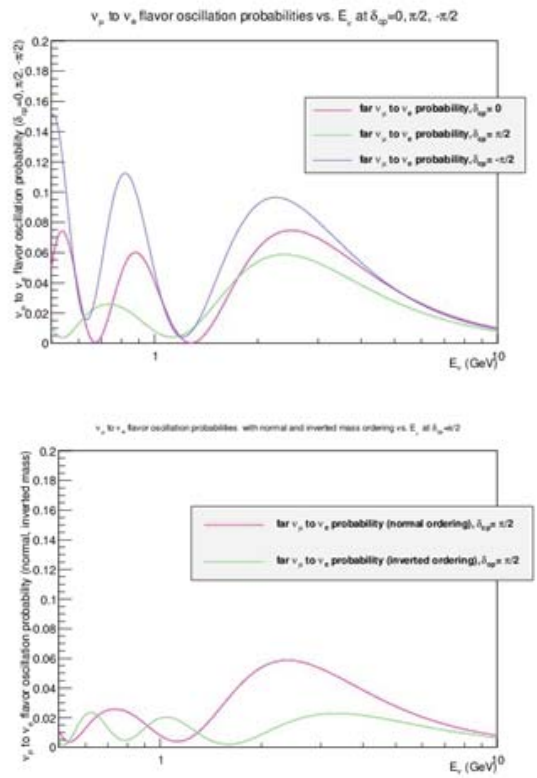

Figure 1: Neutrino flavor oscillation probability curves changing with respect to the δ_{cp} and the mass ordering.

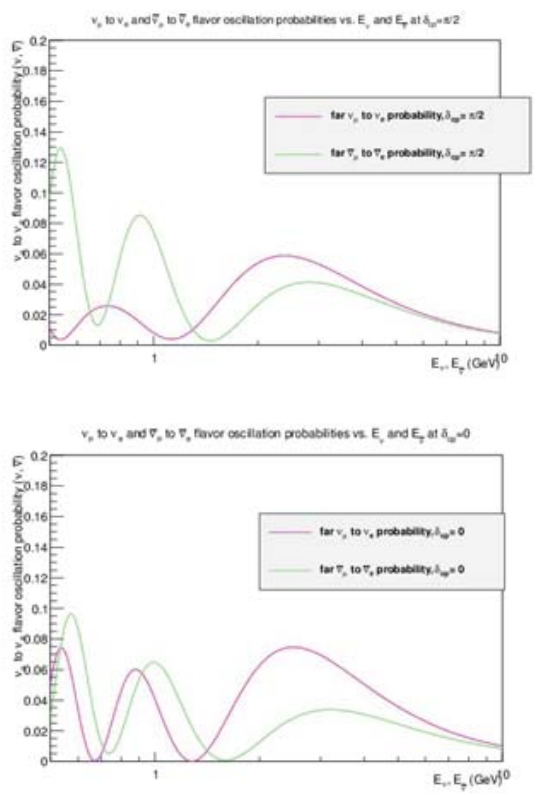

Figure 2: Neutrino flavor oscillation probability curves changing with respect to neutrinos/antineutrinos for two different values of δ_{cp}.

get distance from horn 1, horn current (both holding the same and varying with respect to the other), and horn distances from one another as shown in Figure 3.

Using a Monte Carlo procedure, we varied different parameters in the input file to the GEANT4 simulator, ran the simulation of 2 500 000 protons for that specific target distance, horn currents, horn spacing, etc, and analyzed the output files using a PyROOT interface.[6,7,8] To verify that the GEANT4 simulations were correct, we simulated the neutrino flux results for both the near and far detector from the MINOS experiment.[3] GEANT4 and PyROOT produced plots that were within 10^{-20} of the measure neutrino interaction rate in the MINOS near detector depending on the neutrino energies.[3]

Though the focusing horn parameters were varied from simulation to simulation, the general projected experimental setup for LBNE remained the same for each simulation. As such, the total mass of the far detector was 10 kilotons, with detection efficiency of 80 for electron neutrinos and 85 for muon neutrinos, and fiducial mass considered to be 100 total mass.[4] The simulations also were scaled to 1×10^{21} protons on target.[4] The cross-section for neutrinos used was $.667\times10^{-42}$ m^2/GeV/nucleon neutrino energy.[1]

With these experimental parameters and the varied horn geometry, the simulator would calculate, among other outputs, the energy and parent particle weight for each neutrino. PyROOT would then plot a histogram of the distribution of neutrino events for each flavor over the energy spectrum of 0-15 GeV for that instance of the simulation.[8] In order to visualize the two flavors of neutrinos on the same histogram as shown in Figure 4, the electron neutrino distribution plot is multiplied by a factor of 10, which is noted in the legend of the plot. Additionally, since the value of the CP angle is unknown, the histogram is plotted for three values of the CP angle, δ_{cp} 0, $\pi/2$, $-\pi/2$.

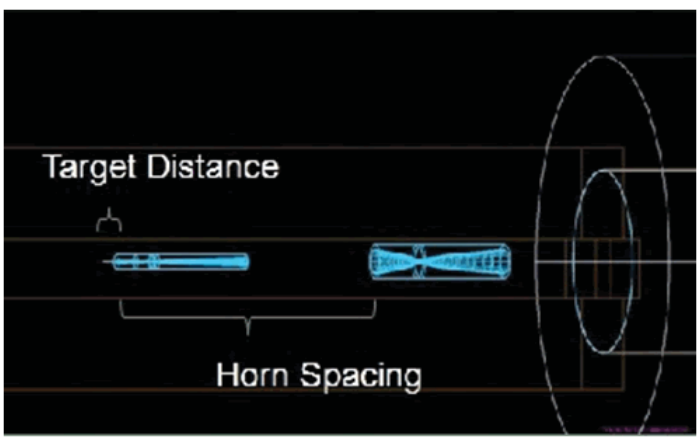

Figure 3: The conventions for measuring target distance and horn spacing.

From these distribution plots, an integrated number of electron neutrino events as well as an fit comparing $\delta_{cp}=0,\ \pi/2$ (in terms of neutrino events, where $\delta_{cp}=0$ is taken as expected value and is observed over 0-6 GeV) is taken for the whole energy spectrum as well as the interval from 0-2 GeV. The 0-2 GeV energy interval is the region where the effects of flavor oscillation are most apparent due to the larger differences in the probability curves as seen in Figures 1 and 2.[2] The following equations were used to calculate the χ^2 fit:

$$\chi^2 = \sum_{k=1}^{n}(O_k - E_k)^2/E_k \tag{7}$$

$$\tilde{\chi}^2 = \chi^2/d \tag{8}$$

with O_k as the observed value, E_k as the expected value, $\tilde{\chi}^2$ as the reduced chi squared, and d as the degrees of freedom or, in our case, the number of bins from 0-6 GeV: 24.[5]

After they are calculated, the integrated numbers of neutrino events and χ^2 values are then extracted for several iterations of simulations with various input parameters for the horn geometry and plotted against the geometric parameter that was varied in order to find maxima and then compared to the simulated values of the current LBNE beamline setup. The current LBNE setup is a target distance of 45 cm, 0.20 MA in both horns, and a horn spacing of 6 m. 4 In maximizing the electron neutrino number, we are trying to increase the amount of event data we receive from the LBNE. By maximizing χ^2, we are finding the regions of the phase space where we have the most sensitivity to variances in δ_{cp}.[4] The most important of these studies was optimizing the target distance in combination with the horn currents with the same current. These results are plotted below in Figure 5.

IV. RESULTS

The extracted results for varying the horn current versus the target distance upstream from horn 1 for both the 0-15 GeV energy spectrum and 0-2 GeV in terms of electron neutrino flux are shown below for $\delta_{cp}=0$. The shapes of the contours do not change with δ_{cp}, so we can extract an optimal geometry from these plots even though the total integrated number of electron neutrinos varies.

From Figure 5, we see that the optimal geometry and currents are: 50 cm target distance and .30 MA horn current for 0-15 GeV and 0 cm target distance and 0.22 MA horn current for 0-2 GeV. These optimizations give an electron neutrino yield increase of

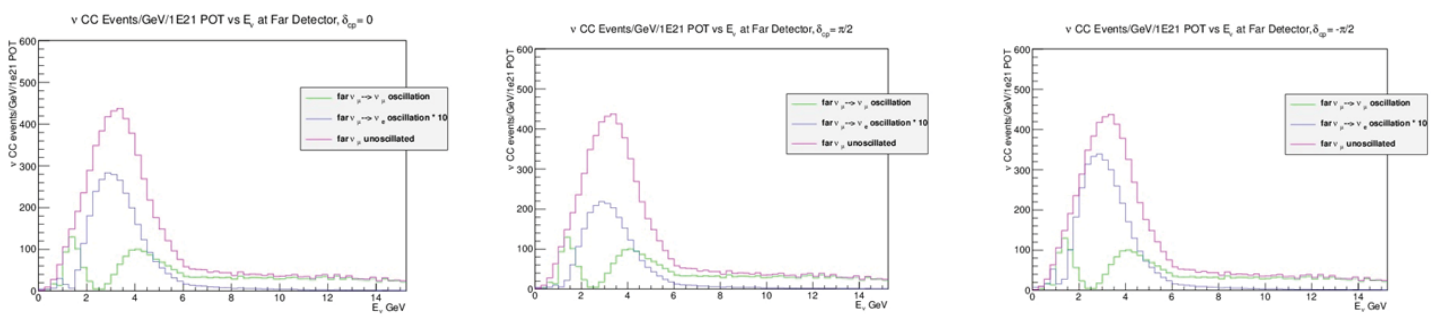

Figure 4: Neutrino event distributions over the 0-15 GeV energy spectrum for three values of δ_{cp} for 10 cm target distance and 0.25 MA horn current at 6m horn spacing.

32.0 and 23.8 respectively.

The extracted results for the χ^2 fit of the horn current versus target distance are shown in Figure 6, yielding a large region with high sensitivity to δ_{cp}.

Another important variable that determines the neutrino flux at the far detector along with horn current and target distance is the horn spacings with respect to one another. The current setup of the LBNE beamline has the horn spacing at 6 m. Figures 7 and 8 show the number of electron neutrinos as a function of horn spacing with the target at a distance of 10 cm and 45 cm, respectively.

From these plots, we see that for 0-15 GeV the optimal horn spacing is 10 m which gives a 17.6 increase in electron neutrino yield over the current setup, and for 0-2 GeV the optimal horn spacing is 6 m (the current beamline setup), therefore, giving no increase in the yield. We also see that the same trend occurrs both when the target is and is not inserted in horn 1.

In determining the optimal configuration for horn current, target distance, and horn spacing, we see that for integration over the 0-15 GeV energy spectrum, the optimized geometry is 50 cm target distance, 10 m horn separation, and 0.30 MA in both horns.

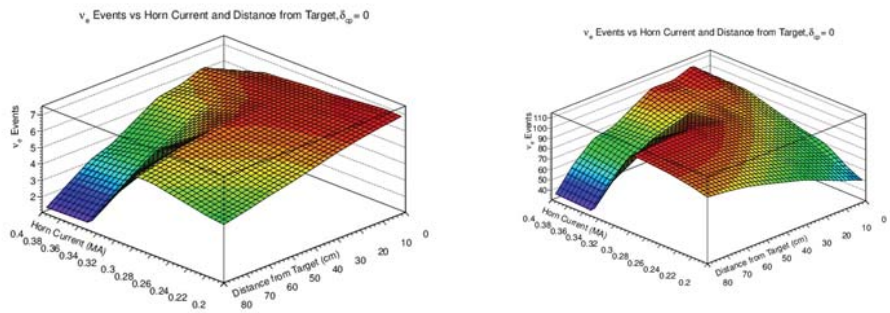

Figure 5: Electron Neutrino Events versus horn current and target distance over the 0-15 GeV interval and 0-2 GeV interval, respectively, with $\delta_{cp} = 0$. The horn spacing is fixed at 6m.

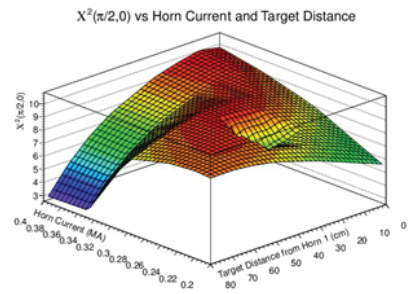

Figure 6: χ^2 fit comparing $\delta_{cp} = 0,\ \pi/2$ versus target distance and horn current. The horn spacing is fixed at 6m.

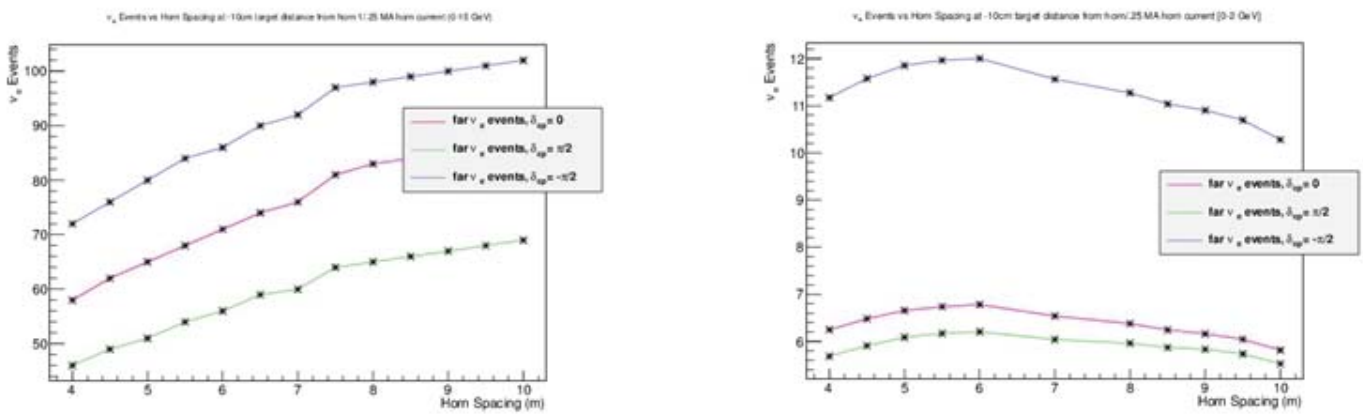

Figure 7: Neutrino events vs. Horn Spacing with target 10cm from horn 1 and 0.25 MA horn current over the 0-15 GeV and 0-2 GeV energy ranges, respectively.

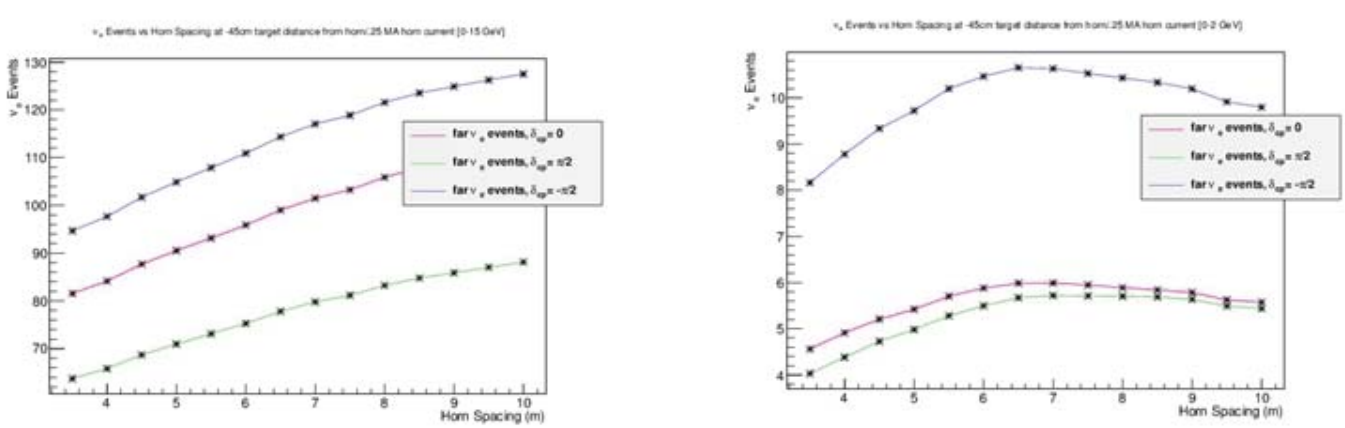

Figure 8: Neutrino events vs. Horn Spacing with target 45cm from horn 1 and 0.25 MA horn current over the 0-15 GeV and 0-2 GeV energy ranges, respectively. The same trend is seen when the target is and is not inserted.

This complete optimization gives a total increase in electron neutrino flux yield of 56.7%. For integration over the 0-2 GeV energy range, the optimal solution is much different: 0cm target distance, 6m horn separation, and 0.22 MA horn current. This 0-2 GeV optimization gives a total increase of 23.8%. This vast change in optimal geometry comes from the different requirements of focusing softer pions for the low energy range than simply just focusing as many pions as possible at whichever energy scale.[4] This difference can also be seen in the neutrino distribution histograms for both of the optimal cases when compared to one another:

From the plots shown in Figure 9, we see that the peak of the distribution is at a higher energy for the whole spectrum than the peak of the narrow 0-2 GeV energy spectrum. Additionally, we see that there are much different oscillatory properties of the muon neutrinos in the two different energy range optimal cases, as predicted by the probability curves in Figures 1 and 2. In addition to this, there is also a region where the two optimal regions overlap at 30-40 cm target distance and 0.28-0.30 MA horn current in both horns. As a measure of the approximate gain, at 30 cm target distance and 0.28 MA (a point in this region)we see a gain in electron neutrino yiel of of 18.9% for 0-15 GeV and 14.9 for 0-2 GeV, both at 6 m horn spacing. From this optimal intersection, the neutrino yield can be tuned by changing the horn spacing.

After finding the optimal target distance versus horn current and horn spacing, we held the target distance and horn spacing constant at 45 cm and 6 m, respectively, and varied the currents in horn 1 and horn 2. The plots in Figures 10 and 11 show electron neutrino events and the χ^2 fit versus horn 1 and 2 current.

We see from the varied horn current plots that for 0-15 GeV the optimal horn currents are 0.40 MA for horn 1 and 0.50 MA for horn 2 and 0.30 MA and 0.30 MA. These optimizations give electron neutrino yield increases of 53.8 and 13.2 respectively. Additionally, we see a large area in the χ^2 plot where we have good sensitivity to δ_{cp}. Although these optimizations exist, they would be very difficult to implement not only due to the limitations of the horns themselves at very high current, but also because of the cost of separate power supplies for each horn. The 0-2 GeV optimization is within design feasibility, but the 0-15 GeV is far beyond the reach of current horn technology. A much more reasonable optimization is that of the target distance, current, and horn spacing.

V. CONCLUSION

We find that the most feasible solution is to optimize the horn current (keeping both the same), target distance, and horn spacing. The optimal arrangement for 0-15 GeV is 50 cm target distance, 10 m horn spacing, and 0.30 MA current in both horns. The optimal arrangement for 0-2 GeV is 0 cm target distance, 6 m horn spacing, and 0.22 MA current in both horns. These produce a electron neutrino yield increase of 56.7 and 23.8 when compared to the original LBNE beamline setup of 45 cm target distance, 6 m horn spacing, and 0.20 MA current in both horns. In short, we see a significant increase in events as compared to the current setup of the LBNE beamline with these changes. There is also an intersection of these two optimal regions around the range of 30-40 cm target distance and 0.28-0.30 MA at 6 m horn separation, which give electron neutrino yield gains of 18.9 for 0-15 GeV and 14.9 for 0-2 GeV simultaneiously. Additionally, we see that these opti-

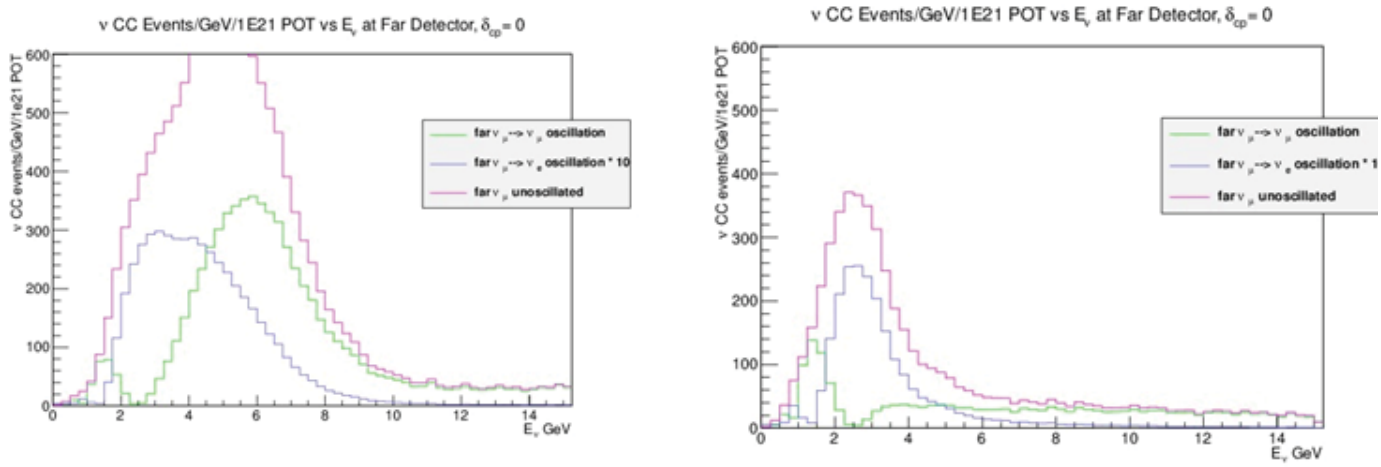

Figure 9: Neutrino Events vs. Neutrino Energy for the optimal cases over the 0-15 GeV spectrum (with 10 m horn spacing) and 0-2 GeV, respectively.

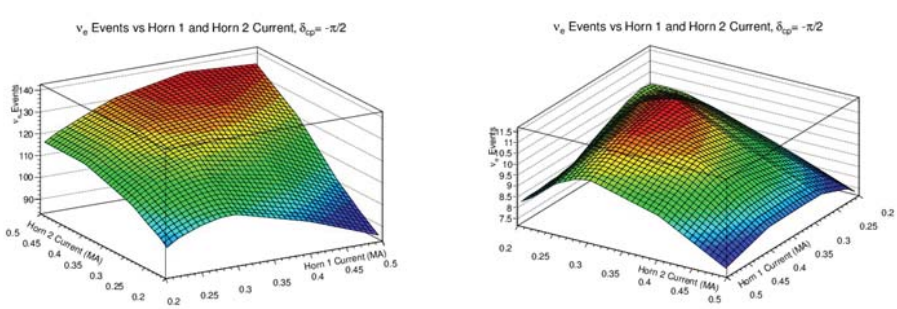

Figure 10: Electron Neutrino Events vs. horn 1 and horn 2 current over the 0-15 GeV spectrum and 0-2 GeV, respectively, with $\delta_{cp} = \pi/2$; target distance of 45 cm and horn spacing at 6 m.

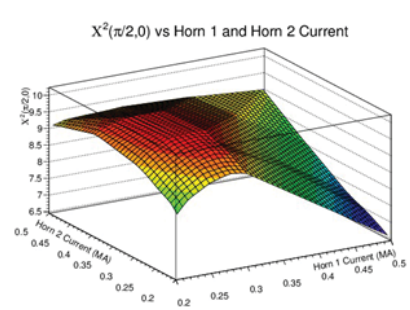

Figure 11: χ^2 fit comparing $\delta_{cp} = 0,\ \pi/2$ versus horn 1 and horn 2 current.

mizations are the same independent of the CP angle, which makes these technical designs viable for any value of the parameter and thus simplifying the design possibilities. Modifying the existing horns so that the LBNE horn geometry matches these optimizations as closely as possible is an extremely cost-effective way to achieve drastic gains in neutrino production over the course of the experiment. Implementing these changes would certainly give the LBNE the best chance possible to discover the values of the CP angle δ_{cp} and the mass hierarchy of neutrinos and give physicists a much deeper understanding of the universe and our place in it.[4]

VI. REFERENCES

[1]K. Nakamura et al. (Particle Data Group), "The Review of Particle Physics". J. Phys. G 37, 075021 (2010).

[2]R.N. Mohapatra et. al. "'The Theory of Neutrinos: A White Paper".Rept.Prog.Phys. 70 (2007) 1757. arXiv:hep-ph/0510213v2.

[3]P. Adamson et al. [MINOS Collaboration] "Search for the disappearance of muon antineutrinos in the NuMI neutrino beam." FERMILAB-PUB-11-357-PPD, BNL-96122-2011-JA, Phys. Rev.D84:071103,2011. arXiv:1108.1509

[4]T. Akiri et al. [LBNE Collaboration] "The 2010 Interim Report of the Long-Baseline Neutrino Experiment Collaboration Physics Working Groups" arXiv:1110.6249

[5]John R. Taylor *An Introduction to Error Analysis: The Study of Uncertainties in Physical Measurements.* University Science Books (1982).

[6]S. Agostinelli et. al. "Geant4 - a simulation toolkit" Nucl. Inst. Meth. A 506, 250 (2003).

[7]J. Allison et. al. "Geant4 developments and applications." IEEE Transactions on Nuclear Science 53 No. 1, 270 (2006).

[8]Rene Brun and Fons Rademakers, "ROOT - An Object Oriented Data Analysis Framework", Proceedings AIHENP '96 Workshop, Lausanne, Sep. 1996, Nucl. Inst. and Meth. in Phys. Res. A 389 81 (1997).

Structural design of a high-temperature, superconductor, cosine theta coil

Christopher Kolz
Watson School of Engineering, Binghamton University, Binghamton, NY 13902
Jesse Schmalzle and Michael Anerella
Superconducting Magnet Division, Brookhaven National Laboratory, Upton, NY 11973

ABSTRACT

Typically, the Superconducting Magnet Division at Brookhaven National Laboratory develops superconducting magnets that are constructed using a cable of low temperature superconducting material. Recently, new High Temperature Superconductor (HTS) tape has been developed which has the following advantages:

- **Refrigeration expenses are drastically reduced since HTS can operate using liquid nitrogen cooled to 77 K, rather than liquid helium cooled to 4 K.**
- **The material is capable of operating at higher magnetic fields.**
- **The material processing is simpler and cheaper.**

Most HTS coil applications to date have utilized simple "pancake" type solenoid or racetrack coils. However, most particle accelerators utilize "cosine theta" style coils (coils which wrap around a cylindrical beam tube) which are more efficient magnetic designs. This project involves designing cosine theta test coils utilizing HTS tape, as well as winding tooling to be used to fabricate and test the HTS coils. In order to accomplish this task, Pro/ENGINEER (three-dimensional, computer-aided design software) was used to develop detail drawings of the necessary winding tooling and the magnet design itself. This design consists of two center posts located on a single mounting tube for the tape to be wound on, appropriate clamping devices, and tooling with two degrees of freedom, responsible for attaching the coils to the winding machine. HTS tape application is still in its early stages--the first two small scale test coils based on this design are to be made and tested simultaneously by the end of summer 2012. Production of these coils is a predecessor to the creation of the first large-scale magnet of its type.

I. INTRODUCTION

Cosine theta coils are commonly used in particle accelerators including the Relativistic Heavy Ion Collider (RHIC) at Brookhaven National Laboratory (BNL). Cosine theta describes the behavior of the magnetic field density with respect to an angle relative to the midplane of the magnet. As the angle approaches 90 degrees, the magnetic field density gets closer and closer to disappearing. This follows a cosine model in which cosine of 90 degrees is 0 and cosine of 0 degrees is 1. Conventionally, the Superconducting Magnetic Division (SMD) at BNL constructs these superconducting magnets using low-temperature, superconducting cable. Each cable is developed from a multitude of superconducting wires wound together, which are then combined to create relatively flat strips.

Recently, professional engineers and physicists have suggested that constructing these cosine theta coils for use in particle accelerators using high temperature superconductor (HTS) tape may be more versatile in its application. This is due to how this high temperature superconducting material can operate at liquid nitrogen temperature of about 77 K, rather than at 4 K resulting from the use of liquid helium in low-temperature superconductors. This drastically reduces refrigeration expenses. The material is also capable of operating at higher currents, thus allowing for more control of the magnetic field particularly due to the greater potential strength of this field. Since a flat piece of superconductor is simply plated for insulation, manufacturing this material is also much cheaper, making this option much more attractive.

II. PROJECT DESCRIPTION

The mechanical engineering department of the SMD at BNL was tasked with designing a small-scale cosine theta coil that uses the HTS tape. Since this material has not been used in magnet production to date, this design will act as a prototype for application on a much larger scale in order to see the feasibility of the fabrication process. Characteristically, a cosine theta coil consists of various coil segments, located at numerous angles in order to keep the magnetic field density as consistent as possible. Figure 1 represents a cross section of a modern cosine theta coil where various segments can be seen.

Since the prototype is simply a small-scale test model, only two of these segments are to be constructed and tested simultaneously. This includes the segments located directly at the midplane and farthest from the midplane: the two extreme cases. The given dimensional constraints for this project are as follows:

1. The tape used will be 0.157 inches wide and 0.006 inches thick.
2. The mounting tube should be approximately 2 feet long with a 2 inch outer diameter.
3. The center posts should be approximately 1 foot long and the inner piece should fit between the outer piece(s).
4. The HTS turns for the current block should go from 70 degrees to about 50 degrees from the midplane.
5. The HTS turns for the midplane current block

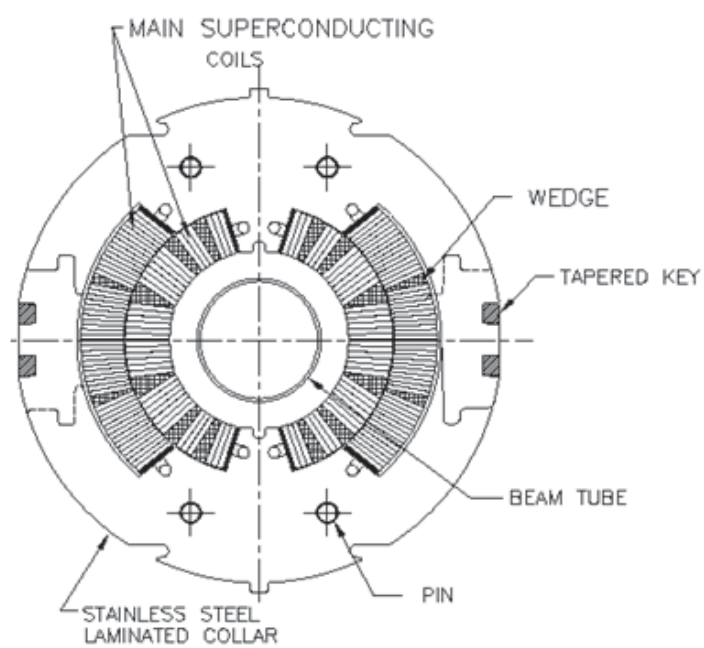

Figure 1. Cross section of a completed cosine theta coil using low temperature superconducting cable[1]

should go from 20 degrees relative to the midplane to approximately the midplane itself.

6. The spacer for the midplane current block should only be as wide as necessary, so that the pole turns can be inserted if it is in place.

The current block is defined as the segments of superconducting cable that lay against each other and the pole piece represents what is known as the center post. The pole is responsible for locating the angle of the windings and is the component that each turn is wound on. Additional initial parameters include that adjustable length arms are needed at each end to hold the turns in place as the turns are wound, approximately 40 turns of HTS tape are to be looped on each of the two coil segments, the materials must be non-magnetic, and the path of the turns must be considered. The path of each winding must be reflected since at the ends, the turns will want to flare out because of the angle they must take to traverse from side to side. This is due to how the bottom of the tape will rest against the mounting tube and how the top of the tape will take its own path. However, the length of each perimeter must be equivalent since the tape is non-deformable.

Essentially, the purpose of this project is to see if it is possible to build a full-scale superconducting magnet using HTS tape. This project is the first phase seeks to determine if a feasible design can be discovered. Using the completed design, the first step is to practice winding with inexpensive stainless steel tape. This step will determine if the winding is possible. The next step will be to wind the magnet with the HTS tape in order to test it as a functional magnet. Here, apprehension arises from the properties of the superconducting material itself. Within the tape resides superconducting material that is approximately a mere micron thick. The rest of the tape consists of supportive and insulating plating. The properties are of concern because the metal possesses characteristics that are similar to glass. In other words, the tape must be wound so that this glass-like metal doesn't fracture. Since the physical material is so thin, bending the tape should not cause too much alarm, but it is important to keep in mind that there is a minimum turn radius that can be made. Since the tape is so thin, the challenge is figuring out a way to get the cable to lay and turn properly on the mandrel. If the first phase is successful, the second phase will take this process and adapt it to a completely functional magnet that can be used for future research.

III. DESIGN PROCESS

This design process had two main considerations: the magnet itself and the tooling required to wind it. The magnet specifications were described in the project proposal, making the engineering simpler with regard to having more constraints to follow. As stated in the project description, the dimensions were specified, as well as those of the center posts. Here, the specified lengths and angles determined the overall setup of the magnet itself. Given the parameters regarding the tape, the entire magnet could principally be modeled and subsequent designs could be based on that model. In order to accomplish this design task Pro/ENGINEER (three-dimensional, computer-aided design (CAD) software) was used to dynamically modify the physical layout and develop appropriate detail drawings to be used in the manufacturing process. Figure 2 represents the magnet in its most basic form.

This figure represents the basic layout of the magnet to be tested. It should be noted that this image excludes the hardware used to bolt the poles to the mounting tube and pieces to hold the tape in place for additional support. The HTS tape shown is just a crude model of the path it will take. During the design process, it was decided that the turns will be allowed to take whatever path they choose. This is primarily owed to the difficulty of modeling this via the software package used. Mainly, the path is generally unknown. An estimate was made by modeling the first winding using Pro/ENGINEER. However, in order to do this, an initial shape for the ends needed to be assumed. Since this was merely an assumption, the accuracy of this representation was questionable. As a result, the importance of an accurate depiction was determined to be negligible. Instead, the final product will show what sort of path each turn will follow for future advances with this technology. The tape shown in this model is solely in place to give an idea of the magnet's structure. Nonetheless, the tape modeled is still functional in the sense that its thickness and angles emulate that of the proposed magnet. The holes were determined as additional design changes were made. From this standpoint,

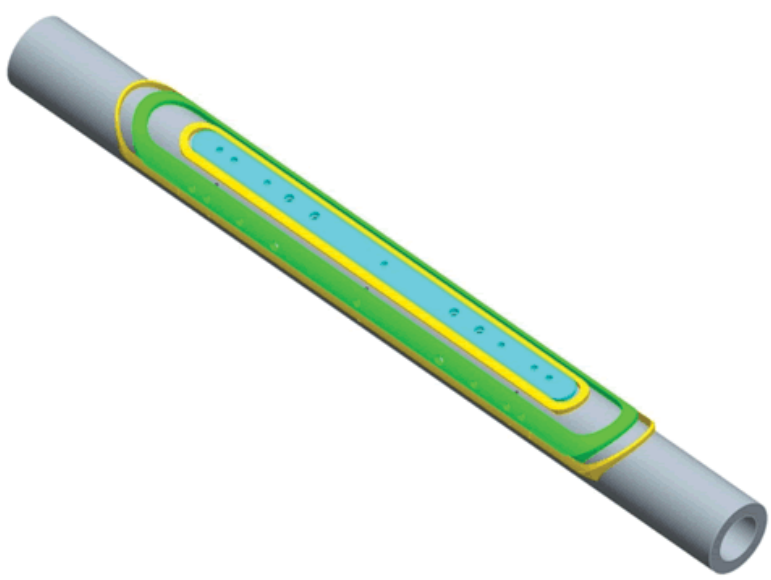

Figure 2. HTS cosine theta coil layout

each strip contains three holes that were used to secure the poles to the mounting tube. This requirement controlled the necessary thickness of the mounting tube so that the appropriate holes could be tapped. The ends of the poles were rounded, merely to avoid forcing the turns to begin on a sharp corner, also assisting to guide the turn.

To get to the product portrayed in Figure 2, each coil segment must be made separately. The inner pole will first be secured to the mounting tube and will be wound with the appropriate tooling. The tooling will be removed so that the magnet can be wrapped in Kevlar before curing it in an oven, with the intention of keeping the components tightly in place. This part of the process is done to fuse each of the turns together by activating the thermoset adhesive on the Kapton insulation. Intermediately, strips of metal called side pushers will be bolted against the turns to hold the tape in place. Once this is complete, this coil segment will be removed and the process will be repeated for the outer coil segment. Upon completion of these steps, the coils will be arranged as shown in Figure 2, using the suitable hardware.

The principle idea that encompassed the winding process was that a programmable rotating shaft will be used to wrap each of the coils. During this process, tooling was required to attach the magnet to this particular rotating shaft and after each half turn, the magnet will need to be rotated to the appropriate angle about its own axis. The tape will be put under tension beside the winding machine, making the winding process occur in a vertical orientation. The two issues that needed to be addressed included designing the tooling to attach the magnet to the winding machine with the two discussed degrees of freedom and designing clamps that would be concentric with the mounting tube in order to hold the tape down after each half turn. The tape will be clamped on one side and wound on the other. After each half rotation, the one side will be unclamped so it can be wound while the other side is clamped in order to be held in place.

Of the two required pieces of tooling, the clamping device was the first part to be designed. The tooling for the winding machine was designed in accordance to the magnet design in combination with the clamp design. Ideas for a new clamp were generated and eventually scrapped for a new, more cost-effective plan. It was found that existing clamps used for the RHIC magnets served the same purpose. These clamps were much larger, but were able to be modified to a much smaller scale so that many of the same parts could be used. Production of this part has been completed and the functionality has been tested. Figure 3 includes an image of the original clamp and an image of the modified clamp.

The next step was to design the tooling that would attach the magnet to the rotating shaft of the existing winding machine. An image of the machine can be seen in Figure 4.

The magnet is to be attached to the end of the rotating shaft so that it rotates in a vertical, upright orientation. Given the fact that a large adjustable chuck will be used, it was decided that an oversized sleeve would be a sufficient way to attach the tooling to the rotating shaft via the chuck. From here it was also determined that the magnet could most effectively be grabbed from the two ends of the mounting tube, since a major concern was interference during the rotation about its own axis. Two end pieces were added to the structure in which an oilite bearing on each end would insert into the inner diameter of the mounting tube. Holes were put into one end of the tube at appropriate angles so that a pin could be used to lock the tube in place. These angles were the 20 and 70 degrees specified for the angles of the center posts. A CAD model of this tooling is displayed in Figure 5.

This was the final step in the design process. The completed assemblies for the two coil segments with all of the components can be seen in Figures 6 and 7.

IV. CONCLUSION

Detail drawings for all parts were completed and approved by professional mechanical engineers. As of August 6, 2012, the components required to wind the inner cosine theta coil have been made and winding is expected to begin in the near future. The tooling has been attached to the winding machine and the coil has been prepared for the winding process. By the end of August 2012, the feasibility of HTS tape application will be determined depending upon the outcome of the winding of the two test coil segments. If successful, a large-scale prototype coil design will be made. The current progress can be seen in Figure 8.

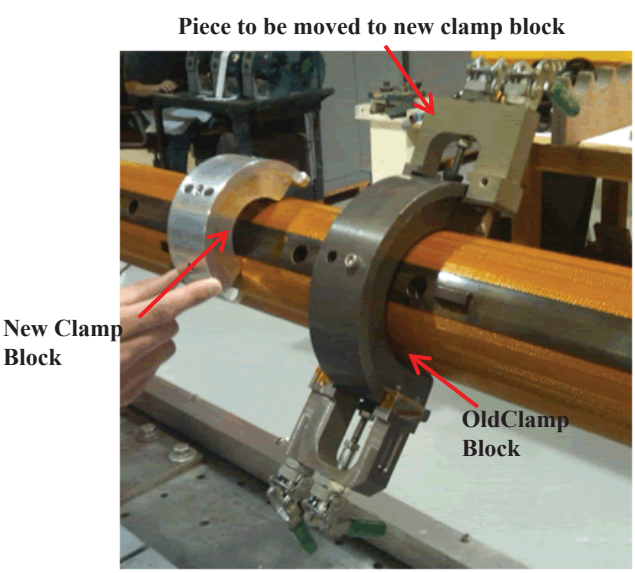

Figure 3. Photograph of the original and modified clamps

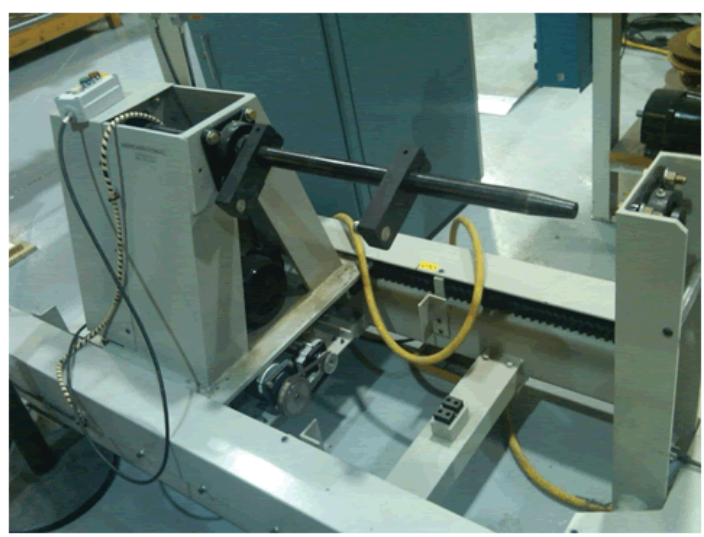

Figure 4. Photograph of the existing winding machine

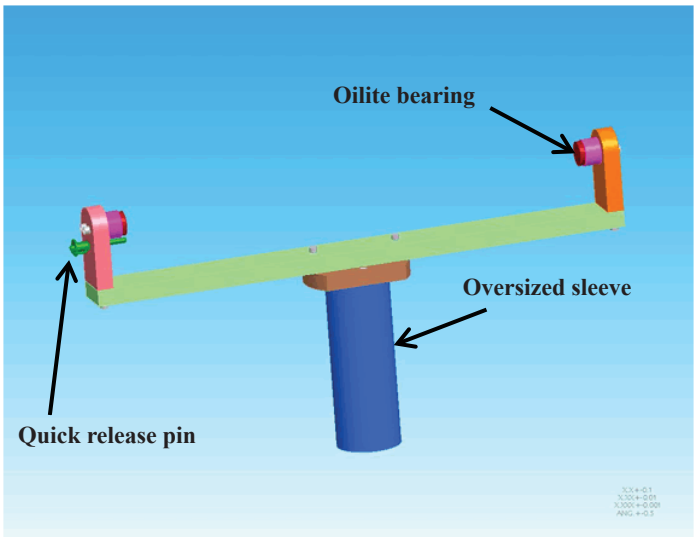

Figure 5. CAD model of the winding tooling

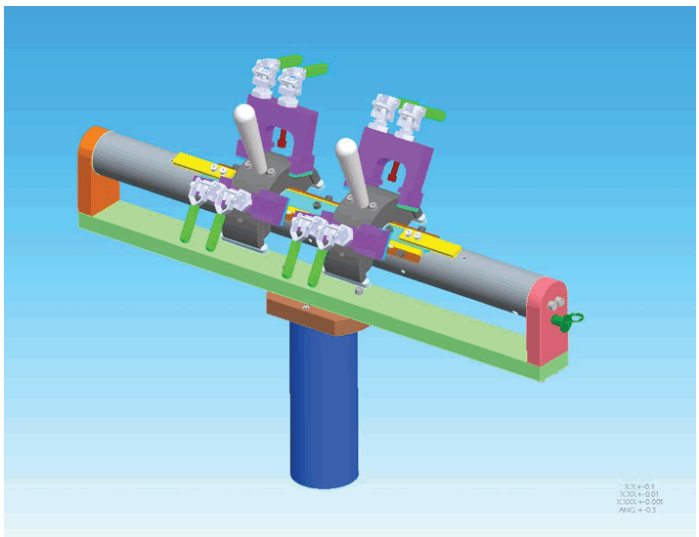

Figure 6. Inner coil segment: complete assembly

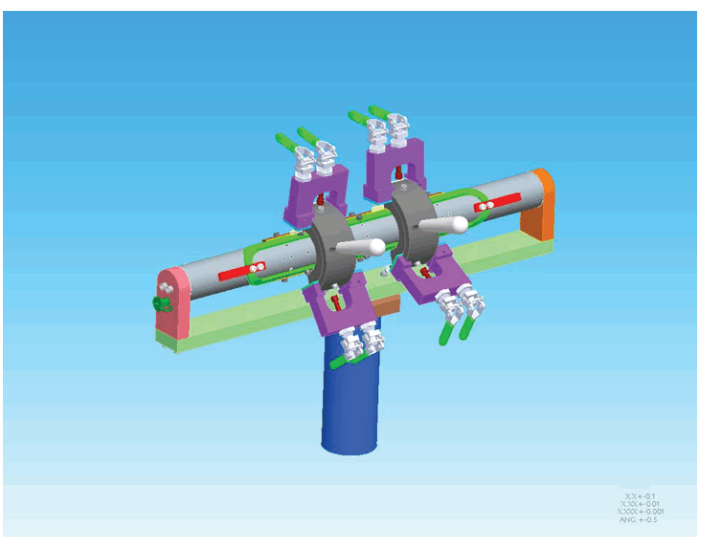

Figure 7. Outer coil segment: complete assembly

V. REFERENCES

Gupta, R., & Jain, A. (2006, January). A One Week Course On: Superconducting Accelerator Magnets. Retrieved July 15, 2012, from Brookhaven National Laboratory: http://www.bnl.gov/magnets/staff/gupta/scmag-course/uspas06/RG06/rg-uspas06-lecture01.pdf

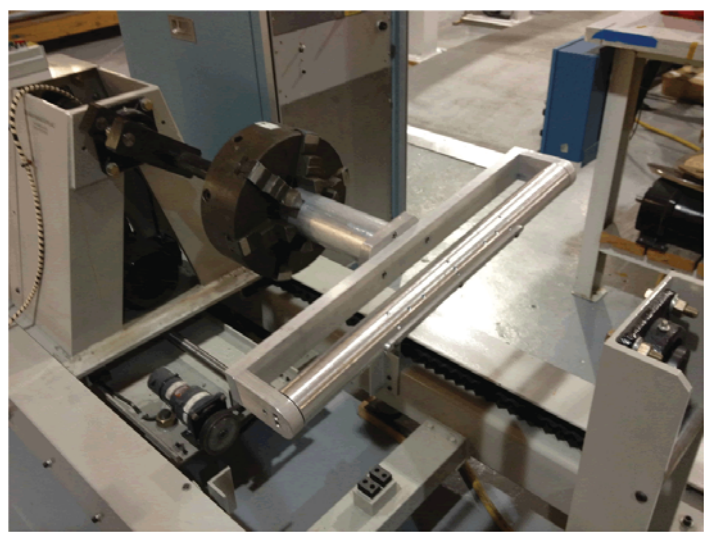

Figure 8. Progress as of August 6, 2012: inner coil preparation

An in-depth analysis of the RF Wien-Filter spin-phase correlation of the Proton and the Deuteron for the Electric Dipole Moment using an electrically and magnetically focused precision storage ring.

Benjamin Kramer
Villanova University, Villanova, PA, 19085
Yannis Semeritzidis
Brookhaven National Laboratory, Upton, NY, 11973

ABSTRACT

The proposed storage ring Electric Dipole Moment (EDM) collaboration for Brookhaven National Laboratory proposes to refine the previous measurement of the EDM for the proton by a sensitivity of five orders of magnitude. This would results in a magnitude of a value that is sensitive to 10^{-29} e*cm. It is necessary to research how the EDM effect of the deuteron and proton are affected by the spin-phase correlations of the particle within the storage ring when electromagnetic fields are used to communicate the effects applied to the particle. I adapted a program, previously constructed by Yannis Semertzidis, in order to analysis these simulations and determine the spin-phase correlation for the EDM of the proton and deuteron. This program incorporates the use of radial focusing Wien-Filter that uses electric and magnetic fields to isolate the EDM of the particle, an incorporated phase analysis subroutine, a spin procession isolation subroutine, and a formatting ability in order to analyze the particle through different spin planes. Using my written program, adapted for FORTRAN 95, it was possible to analyze the spin-phase correlations for the deuteron and proton, assisting in the calculation of a more precise value of the EDM. The results have shown the critical relationship between the spin precession and phase relation, such that the spin and momentum must be collinear to produce the greatest EDM effect. In addition, the results from the program for an EDM in an electrically focused storage ring illustrated differences between the proton and deuteron resulting in a clearer understanding of the EDM and further knowledge on the effects in an electric storage ring. This is the proposed ring type for the EDM experiment BNL hopes to pursue. The direct impact of the refined value for the EDM of the proton will result in a more in-depth understanding of the unequal amounts of matter versus anti-matter in the universe; justifying physics beyond our current construct of the Standard Model. This research provides the collaboration with a clearer understanding of the correlation of the particles spin-phase relation and assists in the refinement of value of the EDM of the proton.

I. Introduction

From introductory physics to even the most complicated quantum mechanics the conservation laws are engrained in physicists' minds. Symmetry is critical to the balance of life and almost all of physics. That being said, it is expected that our world should be made up of equal parts matter and anti-matter. However, through research and other experiments, it has been realized that our universe is made up of much more matter than expected. The Standard Model currently would describe a universe in which the night sky is would be almost entirely pitch black. The current construct of the Standard accounts for some of this imbalance of matter through weak charge conjugation and parity violations (CP violations) of particles. However, this imbalance is nowhere near the observed imbalance and is not a sufficient explanation of the universe. The Electric Dipole Moment (EDM) of the proton may be able to provide a strong CP violation to explain this imbalance

The EDM is the separation of center of mass and center of charge of a particle. Because of this separation the particle is able to deviate and under certain conditions be analyzed to calculate this distance of separation. This experiment hopes to observe a non-zero EDM. A non-zero EDM is intriguing because it illustrates a parity and time violation (PT violation, also recognized as a CP violation). This violation would support a strong violation that could assist in accounting for the imbalance of matter and antimatter in the universe. Under the current idea that CPT must be conserved, the EDM would support a CP violating source that is beyond our current construct of the Standard Model. This experiment hopes to refine the current value of the EDM for proton to an order of magnitude of 10^{-29} e*cm in order to observe a non-zero EDM and justify physics beyond the standard model. A refinement of this value would allow theorists to rule out extraneous physical particle models for physics beyond the Standard Model. This experiment is specific enough that if the proton were the size of the sun, the EDM value (difference between center of mass and center of charge) would be approximately 8 micrometers.

This paper will be segmented in four major sections the RF Wien-Filter, Spin-Phase, the Magnetic Ring, and the Electric Ring. My research specifically applies to the spin-phase correlation of the proton and deuteron under the effects of the RF Wien-Filter in a magnetic storage ring and then an electric storage ring. In order to produce this research an adapted version of Yannis Semertzidis' "Radial_E_field\B_field_RFE.f"[1] for FORTRAN 77 program was utilized as the framework for my own program. The original program as used in order to analyze a particle in either a magnetic or electric storage ring. The new program took this old program and broke it down into two different programs, one for a purely magnetic storage ring and the other for a purely electric ring, and also was written for FORTRAN 95. Following this adaptation a section of code was added to introduce the Wien-Filter into the program. Then a section was added to introduce the effect of a desired phase misalignment of the particles spin and momentum. This way the desired phase could put initialized, the Wien-Filter initiated and the research would produce data the represented the relationship between the spin and phase of the particle, and its effect on the EDM. From this research it will be determined under which conditions an EDM effect may be achieved and in which way to maximize this effect. The EDM, represented by d is represented by equation 1.

$$\frac{d\vec{s}}{dt} = d \times \vec{E} \tag{1}$$

The rate at which the spin precesses is equivalent to the cross product of the EDM and the electric field. Thus through the analysis of the particles spin over time the value of the EDM is calculable. This research of the spin-phase correlation for the proton and deuteron under the conditions of the RF Wien-Filter will assist in achieving the goals of the Brookhaven EDM collaboration, to refine the value of the EDM for the proton to a value of 10^{-29} e*cm.

II. RF-Wien Filter

The Lorentz force is the force a particle experiences due to the effect of both the magnetic and electric field. This force is calculated by the product of the charge of the particle and its velocity, crossed with the magnetic field, then added to the product of the charge and electric field (2).

$$\vec{F} = q\vec{E} + (q\vec{v} \times \vec{B}) \qquad (2)$$

It was discussed in Yannis Semertzidis' report[2] that a "magic" combination of magnetic and electric fields within a storage ring could result in a Lorentz force of zero could be achieved, causing the particle to travel in a straight line unaffected by the electric or magnetic fields. These results[2] also imply that the configuration of electric and magnetic radial focusing have no effect on the EDM. Seen in resultant figure 1(below) these three different cases illustrate the critical effect of the Wien-Filter. In red, the effect is seen of just the radial electric field on the effective radius. In green, the effect is seen of just the radial magnetic field on the effective radius. And finally, in blue the effect when the radial electric filed are additive, resulting in a non-oscillating effective radius. It is also important to note that these results hold true for an electric ring as well. According to the same study[2], the purely electric case works and does not need or result in the effect of the Wien-Filter. This is due to the lack of a g-2 precession and due to the fact that this Wien-Filter is being used under the same resonance conditions[2] (Note: These conditions lie outside the scope of this research but are mentionable for a more detailed account of the research). Due to this effect, according to Semertzidis[2], these results justify that the Wien-Filter does not have any effect on the EDM, however keeps the effective radius constant, allowing for the interpretation of the data and probing of the EDM effect.

III. Spin-Phase Correlation

Spin-Phase is the relationship between the intrinsic spin of a particle and its momentum. Spin-Phase refers to the angle by which the particle's spin and momentum are misaligned. This is to this phase angle by looking at the relationship between spin-phase and the EDM effect it is determinable which case will result in the maximum EDM effect. By isolating the spin in different planes and observing the x, y, and z components of the particles spin, it will be possible to view the EDM effect and provide the collaboration with an in-depth understanding of the effect of the particles spin. It is important to research how the spin is affected under these conditions, as the spin precession is critical to the value of the EDM, as illustrated in (1). This spin misalignment also plays a critical role in the Brookhaven collaborations proposal for the all-electric ring. Understanding this spin-phase relationship allows the analysis of the components of the particles spin. As discussed by Yuri Orlov,[3] it is possible to freeze the spin in one direction as long as the Lorentz forces are kept equal to zero, which is done and describes by figure 1. This infers that the spin can be oriented in the direction of any component desired. This allows for the analysis of the spin in the x, y, and z directions to determine if there is any EDM effect under certain conditions.

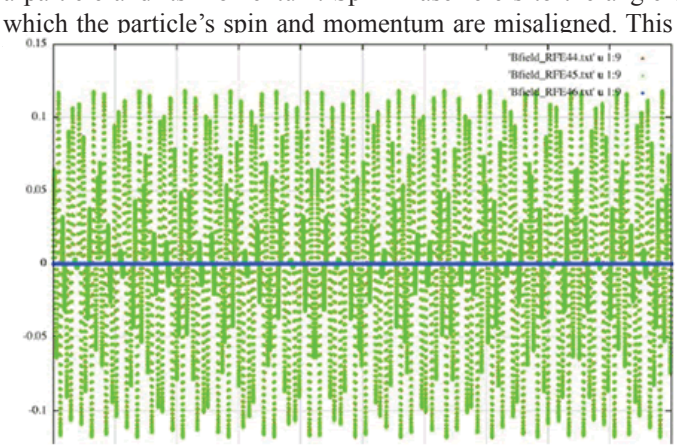

Figure 1 – Graph of Effective Particle Radius (rad) vs. time (s). This illustrates the effect of the Wien-Filter on the particles path.

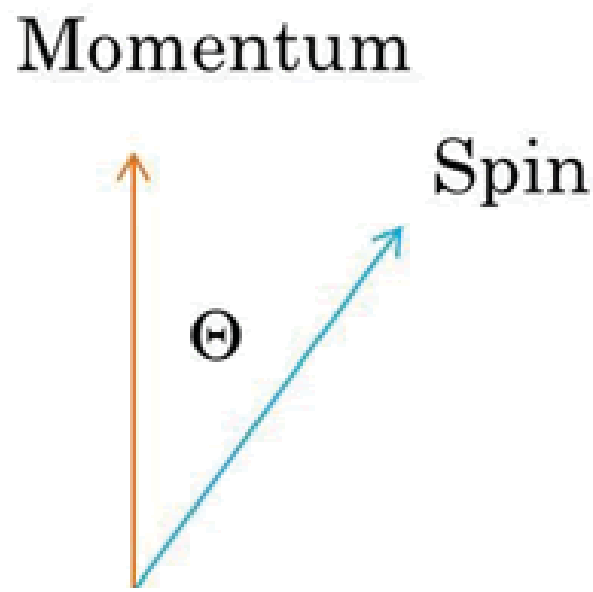

Figure 2 - Illustrates what is meant by phase. The angle between the orientation of the spin and momentum

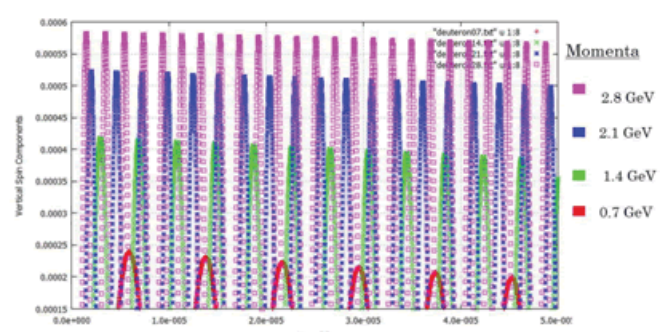

Figure 3 - The vertical spin component of the Deuteron (rad) vs. Time (s) at varying momenta. Observed EDM effect is seen by the slope of the vertical spin amplitude as a function of time

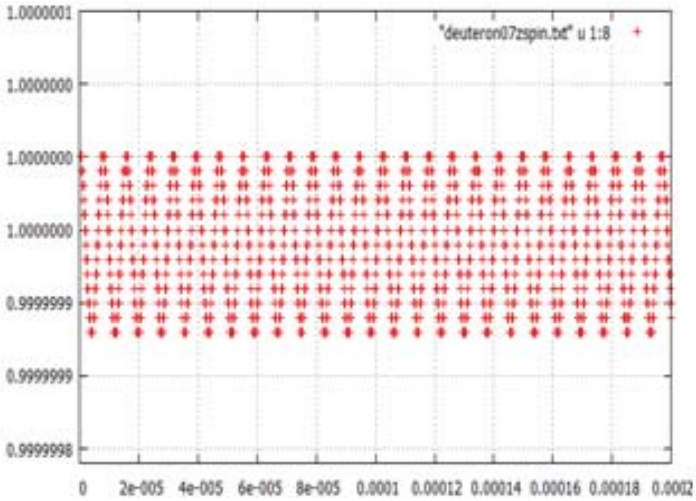

Figure 6 - When the spin is frozen in the X-direction and the vertical (expected) spin component is visualized. There is no EDM effect observed in this or any other components.

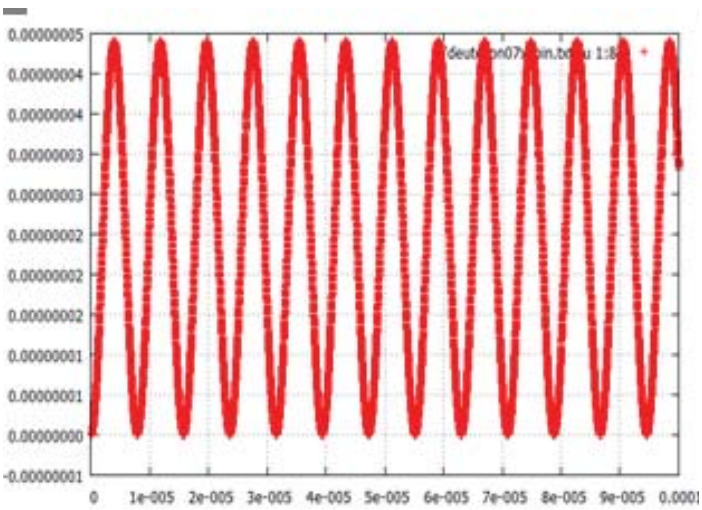

Figure 6 - Spin frozen in the y-direction, observing the vertical component. The vertical component is the only component that illustrates an EDM effect.

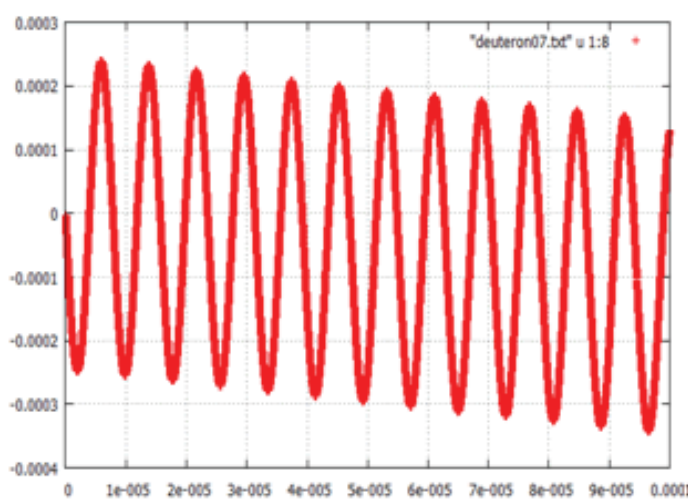

Figure 6 - When the spin is frozen in the Z-direction and vertical spin component is visualized. There is no observed EDM effect. It is also important to note that there is no EDM effect in any other components.

With the ability to freeze the spin in any desired direction and the Wien-Filter allowing the research to probe the EDM effect, the research will produce accurate sensitive data.

IV. Magnetic Ring

Under the conditions of a magnetically focused storage ring the results were fruitful in illustrating the expected results and how the spin-phase correlation is related to the EDM effect. The program was adapted to incorporate both magnetic and radial electric fields that affected the EDM of the particle. This would result in the Lorentz force being zero, and the application of the Wien-Filter within the ring.

A. Deuteron

The data collected below represent the results verifying the presence of an EDM effect on the Deuteron. This verifies that the reconstructed program works and can replicate results of previous cases and research. Figure 3 illustrates the various cases of deuteron at varying momenta. Since the deuteron does not have a "magic" momentum, which is define as the momentum at which the spin and the momentum precess at the same rate, varying the momentum results in varying EDM effects. The EDM effect is observed as the slope of the vertical amplitude of the spin component over time. This verifies the program functions as expected as well as provides initial data for the verified EDM of the deuteron. The next step of to orient or "freeze" the particles spin in one direction and see how the EDM is effect or any change in the EDM effect produced. As is seen in figures 4 and 5 when there are certain RF conditions that produce no EDM effect. However, there are certain RF conditions that do, such as when the z-spin component is observed, when the particles spin is frozen in the y-direction figure 6. All of this collected data represents the deuteron at 0.7 GeV in a 20 m radius storage ring with the Wien-Filter on. From these and other results it is seen, in the magnetic ring, that when the particle has any y-direction component there is an observed EDM effect. This would indicate that in order to observe an EDM effect the spin must contain a y-component. The next step in the research is to analyze how the spin-phase correlation affects the EDM and the results, in order to produce the largest and most observable EDM effect. To analyze these results the program took each frozen spin component and tested the results at angle from 0-3/2. Although we took data from each component it became clear that when the spin was "frozen" in the y-direction the largest EDM effect was observed. Ultimately, observed in figure 7, it was concluded that when the spin and momentum are parallel and anti-parallel (phase equal to 0 or) the maximum EDM was observed. It is also observed that when the particle lacks and y-component that no EDM effect is observed, this is illustrated by figure 8. These figures illustrate that the maximum EDM effect is achieved when the spin and momentum are collinear in direction, resulting in a spin-phase angle of 0, and when the spin is "frozen" in the y-direction. These results will hold true and only the critical findings will be noted.

B. Proton

The results from the proton are upheld with the results of the deuteron. When the spin is "frozen" in the y-direction and the spin-phase angel is zero the maximum EDM effect is observed for the proton in figure 9. Agreement is also seen in figure 10, where the proton is oriented with a spin-phase angle of /4. It is then ob-

served a decrease result in the EDM effect when the particle is out of phase with the momentum. It is clear from these results that an EDM effect is achievable within the magnetic storage ring under certain RF conditions. In addition it is observed that the maximum EDM effect is observed when the spin-phase angle is 0 and when the spin is "frozen" in the y-direction.

However, unlike the deuteron an additional EDM effect is seen for the proton. When the spin is "frozen" in the z-direction the particle naturally precesses out of the z-plane due to the EDM of the proton. The y-component of the spin increases linearly over time, illustrating a growing y-component. This is an observable result that has been looked for by the German COSY ring, partner witht he Brookhaven EDM collaboration. These results from this interesting result are seen in figure 11.

V. Electric Ring

The electric ring enforces different RF conditions which shifts the EDM effect and calls for edits to the written program. The program was then adapted to incorporate a purely electric ring, similar to the one that is in the proposal for Brookhaven's EDM experiment. In this experiment counter rotating particle beams are used to probe the EDM.[4] This experiment forces a shift in the analysis of the EDM and in which ways the effects are observed and defined. Below is a simplified schematic,[5] figure 12, of the proposed all-electric Brookhaven EDM experiment.

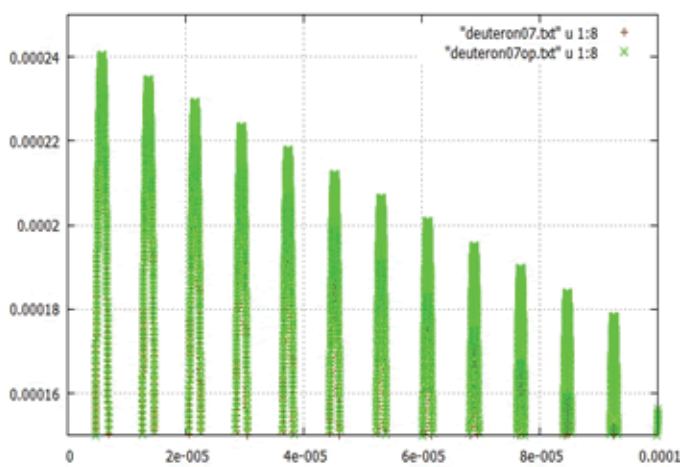

Figure 7 - Spin Component (rad) vs. Time (s) -Vertical spin component observed when the spin is "frozen" in the y-direction and the particle is in phase (angle equal to 0) and out of phase (angle equal to [(1/4)*pi]). Illustrates maximum EDM at phase angle 0.

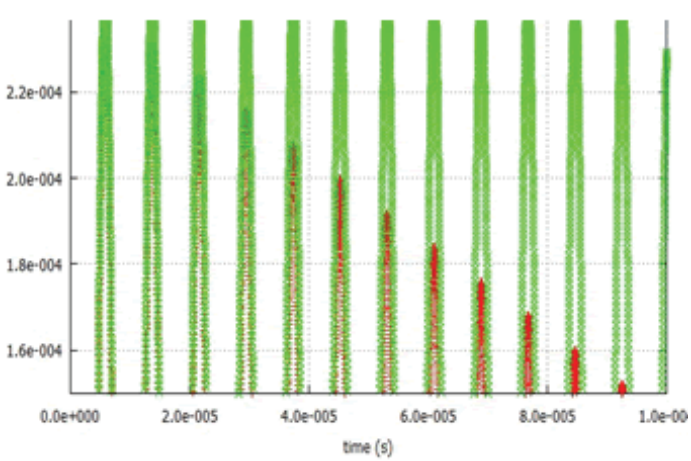

Figure 8 - Spin Component (rad) vs. Time (s) - Vertical spin component observed when the spin is frozen in the y-direction and a phase angle of 0 and pi. In green at angle pi, illustrates no EDM effect.

A. Deuteron

For the deuteron we see the same EDM effect where the spin-phase angle is 0 and the spin is "frozen" in the y-direction. Similar to the magnetic ring, the EDM effect is observed in the z-component of the spin. As time progress the slope of the vertical oscilla-

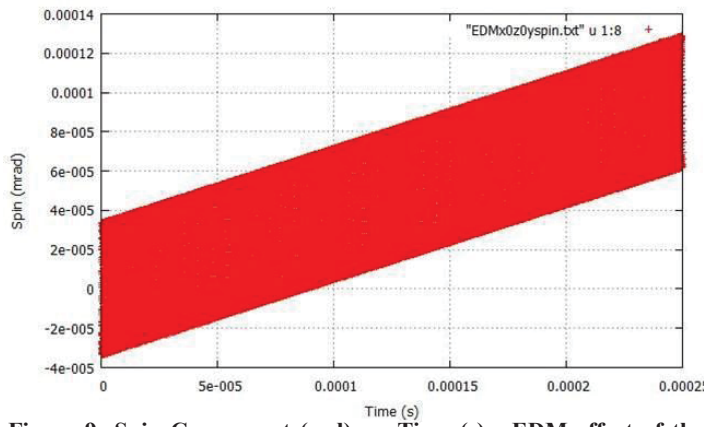

Figure 9- Spin Component (rad) vs. Time (s) - EDM effect of the proton where spin is "frozen" in the y-direction.

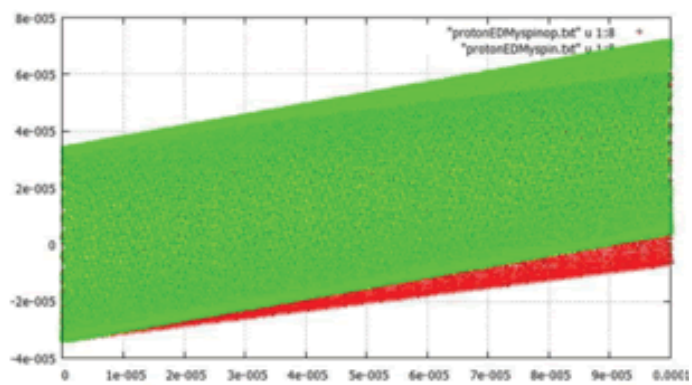

Figure 10 - Spin Component (rad) vs. Time (s) - Green represents the EDM of the proton with a spin-phase angle of 0, and the red a spin-phase angle of pi/4.

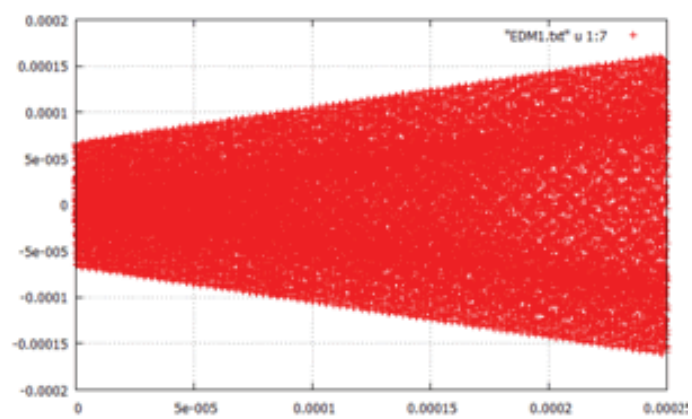

Figure 11 - Spin Component (rad) vs. Time (s) - The spin is "frozen" in the Z-direction and the y-component is observed, illustrating a growing component over time. Resulting in the particles precession out of the z-plane due to the effect of the EDM by the German COSY ring, partners with the Brookhaven EDM collaboration. These results from this interesting result are seen in figure 11.

tions represents the EDM. Figure 12 represents the EDM effect on the Deuteron under the appropriate maximum EDM conditions.

B. Proton

The proton produces the expected results, reaching the maximum EDM effect with a phase angle of 0 and the spin "frozen" in the y-direction (figure 13). This represents the "classic" EDM experiment for an all-electric ring. There are no oscillations in this graphs spin precession due to the lack of the magnetic field in the storage ring, and the RF conditions due the ineffectiveness of the Wien-Filter in an all-electric ring. Figure 14 shows the horizontal spin component of the proton in the all-electric ring when the spin is "frozen" in the z-direction. Once again, the particle precesses of the z-plane over time as the horizontal component grows linearly.

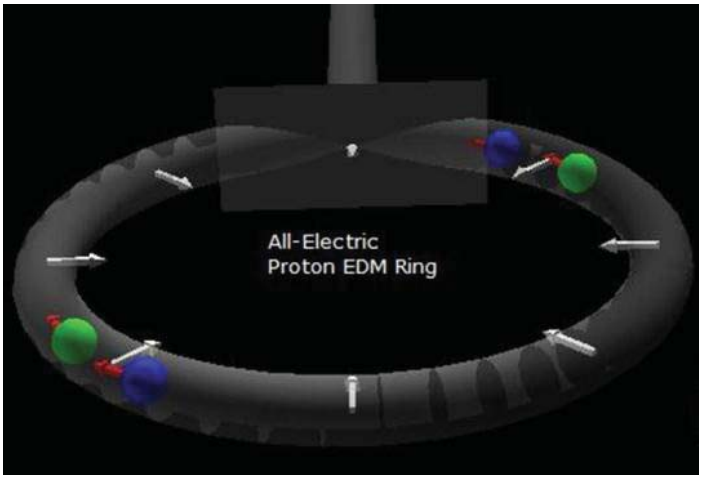

Figure 11 - Schematic of the all-electric EDM storage ring proposed by Brookhaven collaboration. Produced by co-worker Rolph Phillips

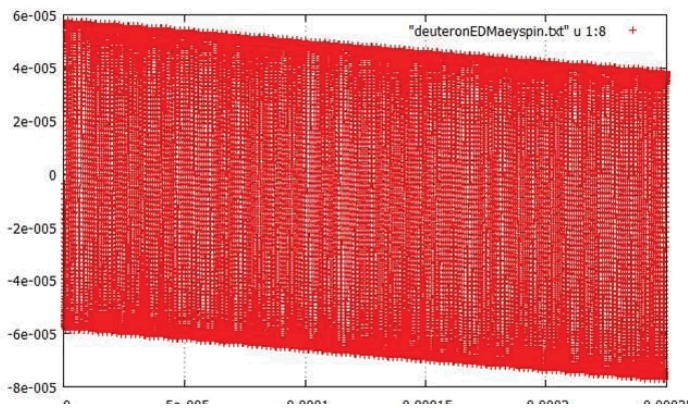

Figure 12 - Spin Component (rad) vs. Time (s) - The Deuteron EDM effect in the all-electric ring resulting in the expected EDM effect seen in the slope of the vertical oscillations over time.

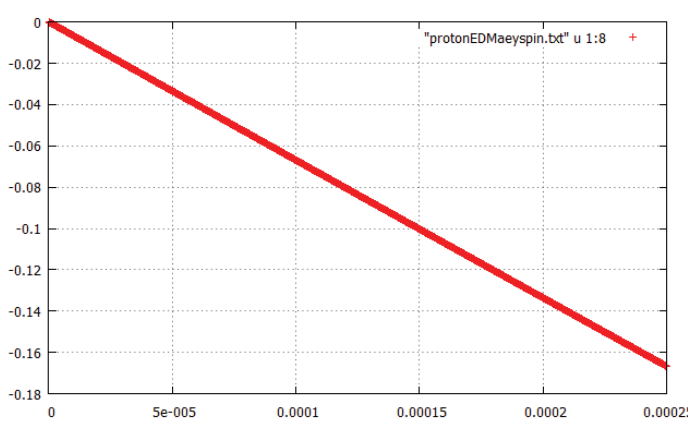

Figure 13 - Spin Component (rad) vs. Time (s) - The vertical spin components of the proton as a function of time to illustrated the clear EDM effect, this is the "classic" EDM effect

VI. Conclusion

The overarching goal of this research was to obtain a detailed understanding of the spin-phase correlation in order to gain a greater understanding of its impact on the EDM effect and provide the collaboration with the data from the simulation in order to assist in the refinement of the value of the EDM of the proton to an order of 10-29 e*cm. In conclusion this research provides the collaboration with experiment results that illustrate the RF conditions that produce the greatest EDM effect and result in most refined data. It also justifies the theoretical research of the Wein-Filter and "frozen" particle spin. This data will and has assisted in the knowledge the collaboration needs to progress with their research proposal and experiment.

VII. References

1. Y. Semertzidis, "Radial_E_Field\Bfield_RFE.f", Program, Janurary 2012 (unpublished)
2. Y. Semertzidis, " The RFB, RFE resonance and the Lorentz force", EDM Note, March 2012
3. Y. Orlov, "On the partially-frozen-spin method", EDM Note #21, March 2012, available at https://npvm.ceem.indiana.edu/elog1/EDM+notes/21
4. V. Anastassopoulos " A proposal to measure the Proton Electric Dipole Moment with 10-29 e*cm sensitivity by the storage ring EDM collaboration", Proposal, October 2011. Print.
5. R. Phillips "pEDM VI", Program, July 2012 (unpublished)

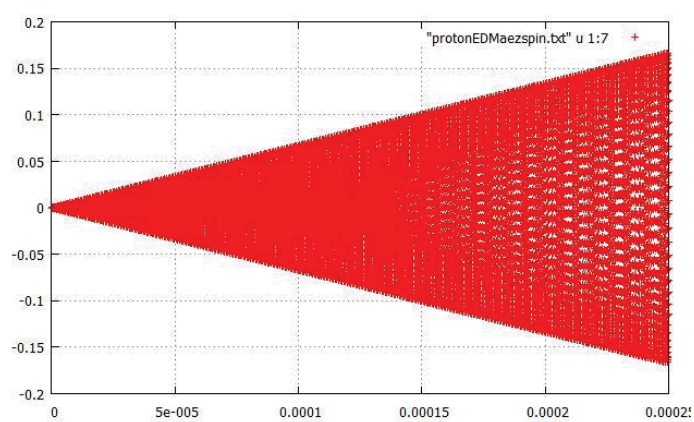

Figure 10 - Horizontal Spin Component (rad) vs. Time (s) - Proton EDM effect when the spin is "frozen" in the z-direction. This graph illustrates the linear growth of the horizontal (y) component of the particle over time.

Protein crystallization with Lysozyme-NAG binding

Benjamin Le
Department of Biomedical Engineering, Georgia Institute of Technology, Atlanta, 30318
Christian Roessler
Biology Department, Brookhaven National Laboratory, Upton, NY 11973

ABSTRACT

While x-ray protein crystallography is a useful tool in the structure-based drug design and discovery process, one shortcoming can be seen in the rate of throughput. The current process used for protein crystallography is relatively slow because it is a multistage, delicate process, which is completed manually. Under the leadership of Alexi Soares, Christian Roessler, and Brookhaven National Laboratory's Photon Sciences Department, one facet of work that is being done by the Serial Protein Crystallography project is geared towards correcting this throughput deficiency with the development of an automated, acoustic droplet ejection (ADE) system that will streamline crystallography research. It is important to improve the efficiency of this process because of the transition from the technologies available at the NSLS I (Nation Synchrotron Light Source) to what will be available at the NSLS II. Diffraction data will be collected orders of magnitude faster at the NSLS II facility. Therefore, to utilize the new technology efficiently the process of protein crystallography needs to move towards a streamlined, automated process. In order to do this, experiments were designed and are being implemented to gain an understanding regarding the kinetics of the ligand N-acetyl-D-glucosamine (NAG) and how it behaves when interacting with protein N-acetylmuraamide glycanhydrolase (lysozyme). Numerous lysozyme protein crystal samples have been grown, mounted, and processed using the X-12C and X-25 beamlines located in the NSLS I. These experiments will be used to validate whether the method of acoustic droplet ejection can be utilized for protein crystallography. To do this, an understanding of the protein-ligand binding interactions must be obtained, and the work that I am doing contributes to that understanding. My specific efforts have been focused on deriving a graph that demonstrates the relationship between crystal size, ligand soak time, and NAG occupancy. This will be useful in that there is currently little published information directly related to this information. Additionally, once this graph is developed, it will help users to predict and understand the occupancy of very small proteins that will be used in the acoustic droplet ejector system. If successful, this system could have a significant impact on drug design and discovery since the increased throughput is several orders of magnitude greater than that of current methods.

I. INTRODUCTION

During the drug design process, one design methodology, structure-based design, relies on understanding the three dimensional structure of a protein and using that knowledge to predict and identify protein behavior. Given that it is critical to know the three-dimensional structure of a protein while using this design method, it becomes clear that x-ray crystallography is an important tool in the drug development process. At Brookhaven National Laboratory (BNL), the Biology and Photon Sciences Departments are collaboratively doing research involved with using x-ray crystallography to facilitate protein modeling. Studies are being done to understand the binding behavior of the ligand N-acetyl-D-glucosamine (NAG) to the protein N-acetylmuraamide glycanhydrolase (lysozyme). More specifically, research is being conducted to understand the binding rates and kinetics of the NAG and lysozyme protein crystals' interactions since a comprehensive knowledge regarding the rate of binding of NAG to lysozyme will provide insight into the viability of an acoustic droplet ejection (ADE) system for protein crystallography. One procedure that is currently being used at BNL mounts individual protein crystals by hand onto micorbatch crystal mounting tips. Given that the protein crystals are typically very small, only about 50-200 µm for typical lysozyme crystals, it is often a difficult and time-consuming task to mount protein crystals. To overcome this, an ADE system that is automated to both grow as well as move protein crystals onto a data collection platform is being tested.1 This is significant in that using this method would greatly increase the through put by several orders of magnitude. However, a caveat to this new method is that only very small amounts of media can be moved using acoustic dispensing. Therefore, if this method is to be used, a thorough understanding of protein-ligand binding and what drives the kinetics is necessary because that information will be used as a means to determine if other protein-ligand soaks can be used by the acoustic drop ejection system.

II. METHODS

Lyophilized hen egg white lysozyme proteins, as well as other reagents were purchased from Sigma-Aldrich.[1] Several procedures were tested while attempting to discover specific conditions that would grow protein crystals of a specific size and quality. Understanding conditions in relation to the protein crystallization phase diagram was critical to predicting the various conditions that were optimal for crystal growth (Figure 1).

We found that hanging drop method accompanied with micro-seeding to grow tetrahedral lysozyme crystals that ranged from 50 microns 480 microns was effective. By varying the buffer concentration, salt concentration, and protein concentration a variety of crystals sizes could be produced.

Lysozyme was dissolved into a solution of 20 mM sodium acetate at a pH of 4.6 to form a protein solution of concentration 70 mg/ml. This mixture was then filtered using a 0.22 micron syringe filter and centrifuged for ten minutes. The seeding solution used was the mother liquor taken from a tube containing proteins that were grown using batch method. The batch method was carried out by mixing 2.5 ml of a 70 mg/ml lysozyme protein solution with 2.5 ml of a buffer solution (buffer solution was 100 mM sodium acetate and 6% (w/v) sodium chloride). With this mixture a hanging drop method was used to grow crystals in six by four well plates. A 1 ml solution of sodium acetate and sodium chloride solution was placed in each well. The concentrations of sodium acetate were varied in each well, spanning a range of 50-100 mM and incremented by 10 mM between each well. This was achieved by mixing two intermediate solutions together in individual wells. One intermediate solution contained 10 ml of 100mM sodium acetate and 6% (w/v) sodium chloride and another held 10 ml of 0 mM sodium and 6%(w/v) acetate solution.

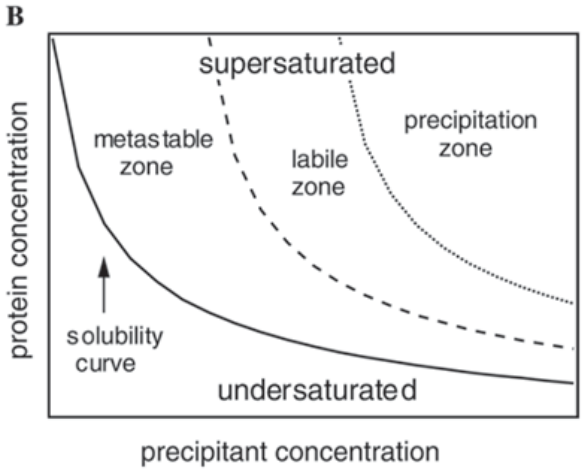

Figure 1: Phase diagram shows the change in solubility of a protein with the change in precipitate concentration.[2]

These two intermediates were then combined at specific ratios to reach the desired concentrations. 2 µl of well solution, 2 µl of protein solution, and 2µl of seeding solution was then combined on a cover slip, which was then sealed on top of an individual well. The formulation of the crystals occurred within less than 24 hours and each drop contained hundreds of crystals of sizes varying from 50µm-150µm.

These lysozyme crystals were then soaked in a 50 mM NAG and mother liquor solution for times that ranged from 0-900sec. These crystals were then mounted on micorbatch crystal mounting tips and were cryogenically frozen in liquid nitrogen into either 'canes' or 'pucks' (see Figures 2 and 3). These storage devices where then placed in the hutches at the National Synchrotron Light Source's (NSLS) X-12C or X-25 beamlines where x-ray diffraction data was then collected using a ADSC Q210 CCD detector and a Pilatus 6M detector respectively. The protein crystals were graphically controlled using the CBASS program and the data that was collected was processed using the program HKL-2000.[3]

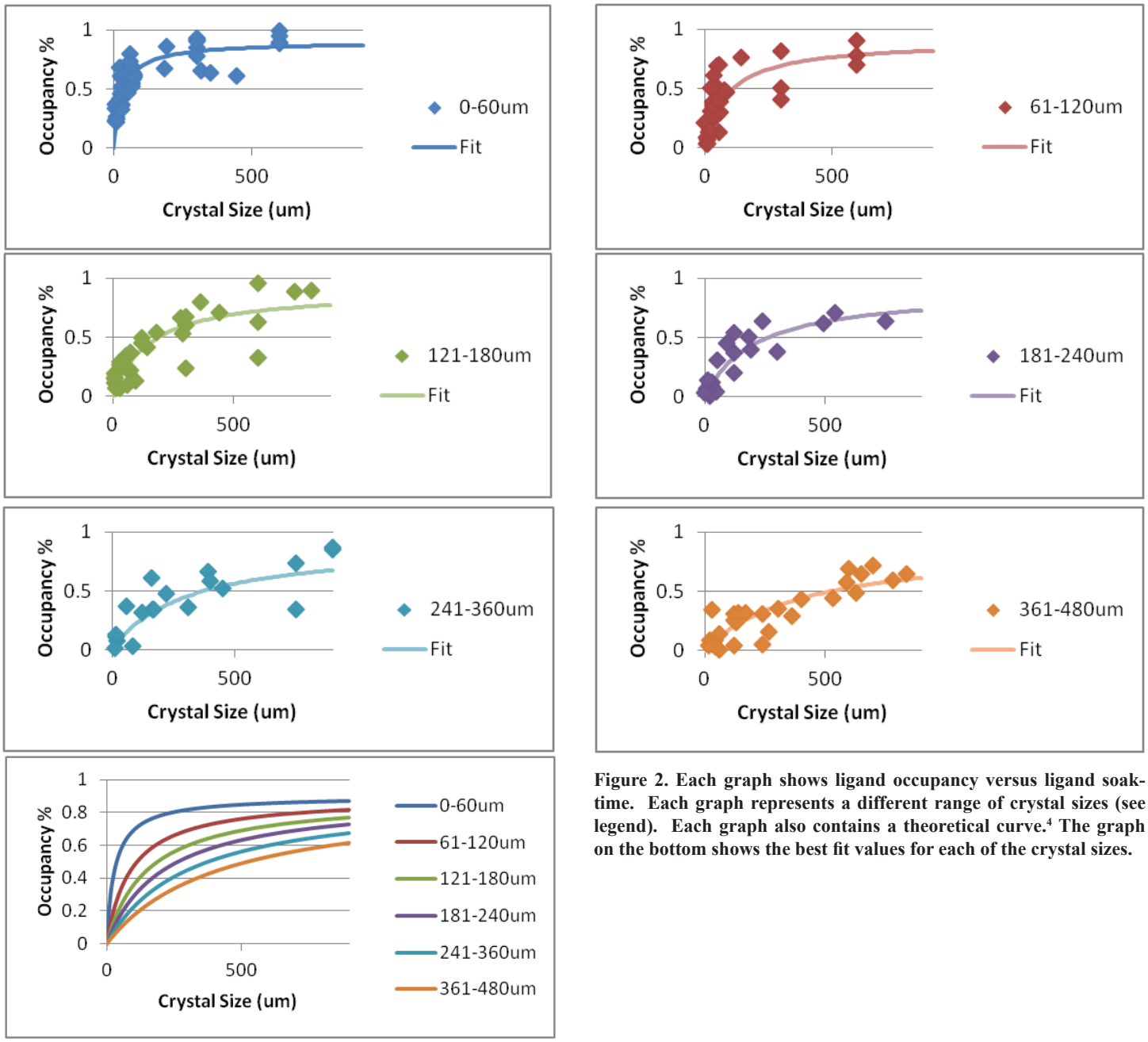

Figure 2. Each graph shows ligand occupancy versus ligand soak-time. Each graph represents a different range of crystal sizes (see legend). Each graph also contains a theoretical curve.[4] The graph on the bottom shows the best fit values for each of the crystal sizes.

III. RESULTS

Based on 218 data sets of NAG bound lysozyme crystals that were collected, a correlation between crystal size and occupancy and NAG soak time and occupancy was found. Data sets were organized into ranges because individual crystals did not necessarily share the precise size or dimension as other crystals. On the whole, the results indicate that crystal size was inversely proportional to the percentage of occupancy, while the NAG soak time was directly proportional to the percentage of occupancy. For instance, the results show that for a lysozyme crystal of 60µm or smaller, 50% occupancy was reached within approximately 30 seconds; however, as the crystal increased in size so also did the soak time necessary to reach 50% occupancy.

The occupancies were found to fit the curve

$$O = O_{max}\left(\frac{t}{t + S\left(t_{\frac{1}{2}}\right)}\right)$$

where O represents the occupancy of the fitted line, O_{max} is the occupancy limit after an extended soak in NAG, t is the soak time, and $t_{1/2}$ is the theoretical soak time for a 1 µm crystal to reach 50% occupancy. Omax was determined to be 90.7% and $t_{1/2}$ was 0.800 s/µm. These two values were found using a least squares algorithm. The overall mean discrepancy between the predicted and observed occupancy was 12.77%.

The occupancy of NAG in each lysozyme crystal was then determined using two different programs REFMAC and PHENIX.[5,6] All data that was used was modified to reflect a resolution of 1.6 Å. REFMAC was used to continually alter occupancy until a temperature factor was refined to 28 Å^2. Two different methods in PHENIX were used to determine occupancy. One way was fixing the B factor to refine occupancy for data at 1.6 Å. Another method was to use all the diffraction data and refine both the temperature factor and the occupancy.[7]

IV. DISCUSSION

The final goal of this research sought to verify the claim that acoustic drip ejection will be a superior technology in relation to the methods currently used in protein crystallography. To do this several parameters and assumptions were taken into account. For instance, several factors make lysozyme a desirable model protein for these experiments since, in many ways, lysozyme can be viewed as the upper bound on binding in relation to other proteins. The rationale being that because it is relatively more difficult for lysozyme to achieve high occupancy, if it is determined that sufficient occupancy can be seen in lysozyme crystals of the sizes that will be used in the ADE system, then the ADE system will be a superior technology to test other proteins because of its high rate of throughput.

Lysozyme crystals, which have about 1nm wide channels, have relatively small channels relative to other proteins.[8] These small channels, which permeate the protein crystal structure, act as pathways for ligand diffusion. Therefore, typical diffusion behavior indicates diffusion into the lysozyme protein crystal will be slower due to the small channel size. Another reason that lysozyme can be treated as the upper bound because of its relatively high dissociation constant in the lysozyme-NAG complex. The K_D values were determined to be 20-23 mM[9]. In drug design it is typical for drugs to have K_D values less than $1 < 10^{-9}$ M[10]. These factors make lysozyme an underestimate for ligand binding relative to many other proteins. Therefore, the occupancy-soak time curves generated by the experiments done at BNL's NSLS serve as an upper bound on what one could expect for the values found in other proteins of a similar size and soak time.

There are still other factors to take into account when considering what drives ligand binding. For instance, because the ADE system will be using small volumes of liquid, the evaporation rate of the liquid that the protein crystals are suspended in is important to take into account. In the experiments done in this research, sufficient volumes of liquid were used so that the evaporation of the suspension media did not drive NAG diffusion into the lysozyme crystal; however, with the use of the ADE system that may not be the case. In terms of our results, this is a positive characteristic because it is another factor that causes the lysozyme-NAG results to be an underestimate of occupancy. This indicates that other protein-ligand should theoretically achieve higher occupancy values within short amounts of time. Another factor to consider is that the sizing of each lysozyme crystal was subjective. While each crystal was sized as accurately as possible, the fact that each specimen was not completely uniform on all dimensions as well as factoring in human error made it impossible to size the crystals with one hundred percent accuracy. The sizes of the crystals were accurate to about ±5 µm. This inaccuracy does not greatly impact the accuracy of the results because, as seen in Figure 2, the occupancy results were taken from a range of crystal sizes. Lastly, the method to determine occupancy and refinement of the date should also be taken in to account. Given that the programs of HKL2000, PHENIX, and REFMAC are used to process experimental data, each user has to change vary numerous parameters to refine the x-ray data which affects the final occupancy value. In addition, many other programs can be used to determine occupancy instead of the ones listed here.

V. CONCLUSION

These results demonstrate a necessary component for the success of ongoing efforts to greatly increase the rate of data collection from NSLS II. This kind of incremental work can be an important part of transformative, paradigm-changing research. If NSLS II can be leveraged by ADE technology, it will dramatically increase speed and quality of crystallographic data collection. In particular, drug discovery projects involving ligand search will be much faster and more productive. The use of ligands in crystallography is very important for drug discovery as well as improving data collection. Every drug begins its life as a ligand. The faster ligands can be discovered, the faster drugs can be developed. By analyzing lysozyme crystals of different sizes and with different NAG soak times, we were able to study the effect of ligand soak time and crystal size on ligand occupancy. We found that there is an inverse relationship between crystal size and occupancy and a positive relationship between ligand soak-time and occupancy. Furthermore, we found that crystals of 60um or less had occupancies of 50% or higher after 30s, which is insufficient time for drying to occur and damage the crystals. Our research has helped to identify the soak times necessary for small crystals, which are the future of crystallography.

VI. ACKNOWLEDGMENTS

Data for this study were measured at beamlines X12C, X25, and X29 of the NSLS. Financial support comes principally from the Offices of Biological and Environmental Research and of Basic Energy Sciences of the US Department of Energy, and from the National Center for Research Resources (P41RR012408) and the National Institute of General Medical Sciences (P41GM103473) of the National Institutes of Health.

VII. REFERENCES

[1]A. S. Soares, M. A. Engel, R. Stearns, S. Datwani, J. Olechno, R. Ellson, J. M. Skinner, M. Allaire, and A.M. Orville, "Acoustically Mounted Microcrystals Yield High-Resolution X-ray Structures." Biochemistry 50 (21), 4399–4401 (2011).

[2]N. Asherie, "Protein crystallization and phase diagrams" Science Direct. Methods 24 (2004)

[3]Otwinowski, Z. & Minor, W. (1997). *Methods in enzymology*, edited by Charles W. Carter, Jr. pp. 307-326: Academic Press

[4]S. Geremia, M. Campagnolo, N. Demitri, L.N. Johnson, "Simulation of Diffusion Time of Small Molecules in Protein Crystals." Structure 14 (3), Pages 393–400 (2006).

[5]M. Winn, M. Isupov and G.N.Murshudov, "Use of TLS parameters to model anisotropic displacements in macromolecular refinement." Acta Cryst. D57, 122-133 (2000).

[6]P. D. Adams, P. V. Afonine, G. Bunkóczi, V. B. Chen, I. W. Davis, N. Echols, J. J. Headd, L.-W. Hung, G. J. Kapral, R. W. Grosse-Kunstleve, A. J. McCoy, N. W. Moriarty, R. Oeffner, R. J. Read, D. C. Richardson, J. S. Richardson, T. C. Terwilliger and P. H. Zwart, "PHENIX: a comprehensive Python-based system for macromolecular structure solution." Acta Cryst. D66, 213-221 (2010).

[7]K. Cole, C. Roessler, M. Allaire, B. Le, A. Tieman, E. Benson-Xu, E. Mule, C. Birone, M. Brown, J. Hernandez, S. Neff, A. Orville, R. Sweet, A. Soares. "A linear relationship between crystal size and small molecule diffusion time observed crystallographically: implications for in-situ fragment library screening using acoustic droplet ejection" In Press (2012)

[8] K. Seemann, R. Kiefersauer, U. Jacob, B. Kuhn, "Optical pH Detection within a Protein Crystal" Journal of Physical Chemistry.DOI 10.1021 (2012)

[9] K. Hiromi, T. Kawagishi, M. Ohnishi, "Kinetic studies on the chemical modification of Lysozyme by N-Bromosuccinimides and its protection by substrates and analogs". Biochemistry. 81 1583-1586 (1977)

[10]Kent S. Gates. "Equilibrium Binding and the Role of "Weak" Binding Forces in Drug Action." Departments of Chemistry & Biochemistry, University of Missouri-Columbia.

Determination of distribution coefficients for the Zion Solutions nuclear power plant decommissioning project

Emily Leonard
Department of Engineering, Stony Brook University, Stony Brook NY 11790
Sung Paal Yim
Department of Chemistry, Korea Atomic Energy Research Institute, Daejeon, South Korea
Terry Sullivan, Larry Milian, and Paul Kalb
Department of Environmental Sciences, Brookhaven National Laboratory, Upton NY 11973

ABSTRACT

Zion Solutions of Illinois is working to decommission an out of service nuclear power plant in order to construct a new, clean facility on the property. A series of preliminary predictive calculations must be completed as part of this decommissioning process to determine the contamination threshold of potential toxins before the groundwater will exceed the Nuclear Regulatory Commission's radioactivity limits. To complete these calculations, Zion Solutions must acquire the site-specific distribution coefficient for each contaminant. The coefficient is a ratio of the radioactivity before and after the groundwater contacts the geological media. The radioactivity decreases upon contact due to the ability of the ground to sorb the radioactive isotopes. The amount of the isotopes that the ground will sorb varies based on particle size, mineral content, and the biological properties of the geomedia. Zion Solutions asked the Engineering/Environmental Department of Brookhaven National Laboratory to find and report the distribution coefficients for five potential contaminants.

I. INTRODUCTION

Located on the Lake Michigan shoreline in Zion, a town in northeastern Illinois, the Zion Nuclear Power Station was retired in 1998 after generating power for over 20 years. Decommissioning a nuclear power plant requires a plan for the proper removal and disposal of radioactive materials and its subsequent accumulated contamination. The proposed, decade- long decommissioning project for the plant in Zion began in 2010. Energy Solutions provides services for the decommissioning of nuclear power plants around the world. They help to safely process, dispose or recycle radioactive waste and contamination. Zion Solutions, a sub division of Energy Solutions, was created to head the project for this unused nuclear reactor. The company will strictly follow all Nuclear Regulatory Commission's (NRC) rules and regulations for the safety of the workers, the public, and the surrounding environment. The NRC is a private branch of the United States government established to enforce safe limits and the set of laws established for the use of radioactive materials, the proper disposal of radioactive waste, and the commissioning and decommissioning of nuclear power plants. The purpose of setting regulations for decommissioning standards is to release the previous nuclear power plant property for either unrestricted use or restricted conditions, and to retire their licenses. The ultimate goal of the Zion plant decommissioning is to construct a new facility on the property that is a completely energy- efficient, Green building. The specific use of the building has not been publicized yet, but will "provide a new era of beneficial use" as stated on the project's webpage.[1]

Radioactive atoms are characterized by unstable nuclei due to an excess of internal energy. In a natural effort to attain stability, energy is spontaneously distributed out of the atom by radioactive decay. Radiation is classified into two different categories based on whether or not the decay process releases enough energy to remove electrons from other atoms. Non-ionizing radiation does not have adequate energy, but the more dangerous form, known as ionizing radiation, emits enough energy to remove electrons. Ionizing radiation can be released as electromagnetic waves (gamma or x-rays), subatomic alpha and beta particles, neutrons, or any combination of these types. Radioactive danger depends on the type of exposure rather than the amount. Certain forms of radioactive decay, such as internal alpha particles and neutrons, have a greater potential for severe biological damage and serve as more of a risk than the other types of radiation in high doses.

It is in the best interest of Zion Solutions to avoid environmental contamination from leftover radioactive sources in the power plant that could place the surrounding population at risk. Accordingly, all workers must complete a series of preliminary calculations before any serious work on the plant can be done. These assessments are executed to determine the negative biological impact of potential contaminants that may be released during the decommissioning process. For instance, the calculations will be able to predict how the contaminants will move through the ground and in what way the environment could help to hinder the contamination of large bodies of water in the area.[2]

To complete these calculations accurately, the decommissioning team needs to acquire the coefficients of distribution for all the potential radioactive contaminants. This coefficient is a ratio of the radioactivity before and after contact with geologic material (geomedia).

Geomedia describes the site-specific types of soil, clay, rocks, etc. characteristic of the stratum through which groundwater will flow. The ground has the ability to sorb radionuclides as the water percolates through. The term "sorption" includes both absorption and adsorption; that is, when particles are being taken up by volume and when particles adhere directly to a surface, respectively. The method of particle retardation is unimportant because the coefficient demonstrates the trend of delayed migration of the radioactive materials.

Due to the nature of geomedia and groundwater, no two sites will have the same mineral balance, particle size, chemical composition or other biological properties. The value of the distribution coefficient strongly depends on these characteristics; therefore, the geomedia, groundwater and any other materials in question must be sent into the lab from the site.

Zion Solutions has asked the Environmental Sciences division of Brookhaven National Laboratory (BNL) to complete a series of tests based on a standard model that will determine the distribution coefficients of five different radionuclides. Zion Solutions sent large samples of the groundwater and geomedia, as well as cement remnants from the plant that may also play a role in sorbing potential contamination. BNL ordered the radionuclides that were desired by the plant, which included Strontium-85, Iron-55, Cobalt-60, Cesium-137 and Nickel-63.

II. METHODS

The standard method that we followed was ASTM C1733-10, Distribution Coefficients of Inorganic Species by the Batch Method. Once the shipments of geomedia and cement were received, the large portions of the geomedia were spread out to a depth of about 2-3 cm in order to air dry and the cement blocks were crushed up with a hammer. Our team analyzed the particle size of the cement and geomedia samples using sieves, and after determined the moisture content through the Sartorius Model MA 30 Moisture Analyzer.

Once the preliminary tests were completed, the two cement and two geomedia samples were each weighed out in three sets of 1-5 g portions (mass recorded to the nearest hundredth) and placed in nalgene sample bottles. Five separate stock solutions of groundwater spiked with the respective radionuclide were prepared. The standard calls for a 25:1 liquid to media ratio, and BNL chose to use the smallest option in the range of media mass required to minimize waste. For each radionuclide, three standard solutions were made without media for radiochemical analysis, and three test samples per type of media. There was a total of 72 sample bottles: 4 media samples and 5 radioisotopes tested in triplicate with 12 standards sans media solutions. The groundwater solution was added to the media containing sample bottles and all the mixtures were agitated using a shaker table in order to simulate the water percolating through the soil.

The amount of time for the distribution coefficient to reach its true value by sorbing the maximum amount of radioisotopes varies due to the sorption characteristics of the media and the kinetics of relevant reactions. To be certain that an accurate coefficient value has been obtained, a preliminary batch test was conducted. Five standards without media and five spiked groundwater and media samples were made up and tested at various times. Since there will be more than one aliquot of liquid removed, a larger 25:1 solution to media ratio was prepared. The coefficients were calculated at each interval and graphed until the standard deviation was less than the desired precision of the values. Once this point was reached, the unique times were noted for each isotope. The results served as a guideline for the lengths that specific test bottles were left on the shaker table for the data collecting portion of the experiment.

Once the agitation was complete, the bottles were left to separate out until the water was once again visibly clear. Temperature and pH readings were taken and recorded. The supernatants were syringed out and filtered through a 0.45 μm hydrophilic filter into a Liquid Scintillation vial, and each was tested by the Liquid Scintillation Counter (LSC) for an after- contact radioactivity count. The standards were also filtered and tested using the LSC for the before contact measurement.

The calculations for the coefficient of distribution requires the volume of spiked groundwater, the moisture content and the before and after counts of the radioactivity. The difference in the counts represents the decrease in radioactivity due to the number of sorbed radioisotopes. The equation for the distribution coefficient (Kd) is the following:

$$Kd = \frac{((A - B)V)}{(Ms*B)}$$

Where:
A = initial count before contact, the average of the three samples in counts per minute (cpm)
B = the final count after contact with the media, the average of the three samples in cpm
V = volume of the solution in milliliters
Ms = mass of media corrected for moisture content in grams

For each radioisotope, 12 distribution coefficients were calculated (4 types of media combinations each tested in triplicate). These coefficients are entered into a spreadsheet along with the other collected data for each specific combination.

III. CONCLUSIONS

Due to the nature of this experiment, the procedure cannot be started until the shipments of geomedia and groundwater arrive. Unfortunately for our team, all the necessary materials from Zion Solutions have not yet arrived at Brookhaven. However, this did not stop us from getting everything prepared so when the barrels arrived, we could hit the ground running. Through this preparation process, I learned a lot about the behind the scenes aspects of national laboratory experiments, especially the safety precautions that are taken to ensure the safety of the scientists and the environment. I saw the Radiological Work Area be determined and set up, as well as went through extensive training to work with radioactive dispersible materials.

Even though I was unable to conduct the bulk of the experiment during my time here, the Environmental Sciences Department at BNL has conducted tests using a similar standard model for different companies multiple times in the past. I was able to read through all of these reports and get a good idea of the trends of some of the isotopes that were used in tests in the past. For instance, Cesium-137 has a tendency to be sorbed very readily by the common organic substances found in many soils. In a study conducted in 2008 by BNL, the coefficients for Cesium-137 were the highest of all the isotopes. It is expected that similar results will be found at the conclusion of the Zion Solutions sorption study.[4]

Two concrete cores arrived at the lab in my final week. These make up two of the four different types of media that will be tested for sorption contribution. They were labeled "B1-01107-CJVCCV-001" and "B2-08101-BJFCCV-A016." For simplicity in labeling, we referred to them as "B1" and "B2", respectively, and the images of the two as received can be seen in the appendix in figures 3 and 4. In order to be in workable shape for the experiment, the cores had to be size reduced so that the particles could pass through a 2 mm sieve, according to the standard. This was completed using mechanical force from a hammer (figure 5). Once the concrete was the correct size, the moisture content was found using the Sartorius Model MA 30 Moisture Analyzer.

When the experiment is completed, a report will be written up and sent back to Zion Solutions articulating the observations and ultimately the results of the calculated distribution coefficients for

all five isotopes. The outcomes are compared with previous sorption studies and literature information to make sure that the coefficients follow the relative trends.[3] Zion Solutions will then use the coefficients to accurately complete their preliminary predictive calculations for a safe decommissioning of the Zion Power Plant.

IV. ACKNOWLEDGEMENTS

I would like to thank my mentor, Paul Kalb for trying so hard and succeeding in making my experience at Brookhaven this summer so valuable and rewarding despite so many obstacles in the project process. I would also like to thank Larry Milian, Sung Paal Yim, and Terry Sullivan for their guidance and efforts in making the most of my time here. Finally, I am so appreciative of the staff of the Office of Education and the Department of Energy for giving me this amazing opportunity.

V. REFERENCES

[1]"A Powerful Transformation. Zion Solutions" <http://www.zionsolutionscompany.com/>.

[2]"Standard Test Method for Distribution Coefficients of Inorganic Species by the Batch Method1." *Designation: C1733 – 10* (2010.)

[3]P. D. Kalb, L. Milian, C. Dodge, *Determination of Site-Specific Distribution Coefficients For Pail C. Rizzo Associates Final Report for Sorption Study No. 3*. (2010)

[4]P. D. Kalb, C. Dodge, L. Milian, *Determination of Site-Specific Sorption Coefficients for Soils from the Proposed Berwick Unit 1 Nuclear Power Plant*. (2008)

VI. APPENDIX

Figure 1: Various sieves that will be used for particle analysis

Figure 2: The shaker table that will be used to simulate the groundwater percolating through the geological media

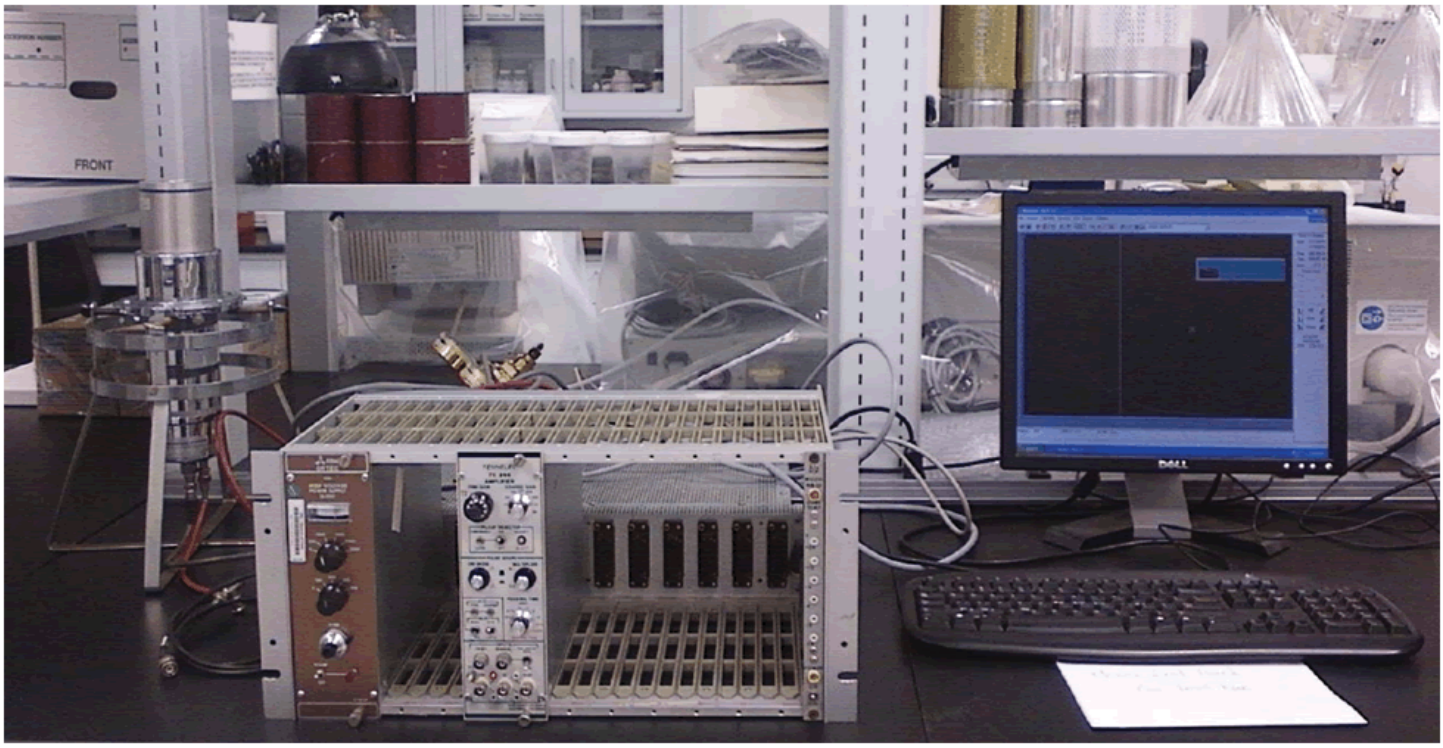

Figure 3: The Liquid Scintillation Counter will be used for radiochemical analysis

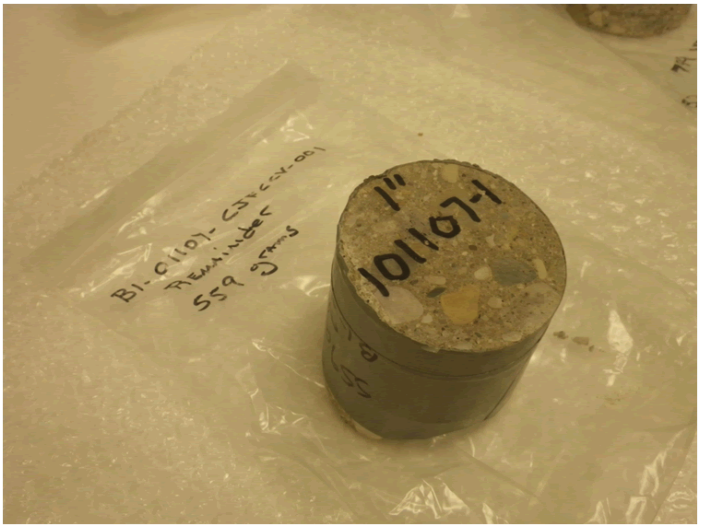

Figure 4: the B1 labeled cement core from Zion

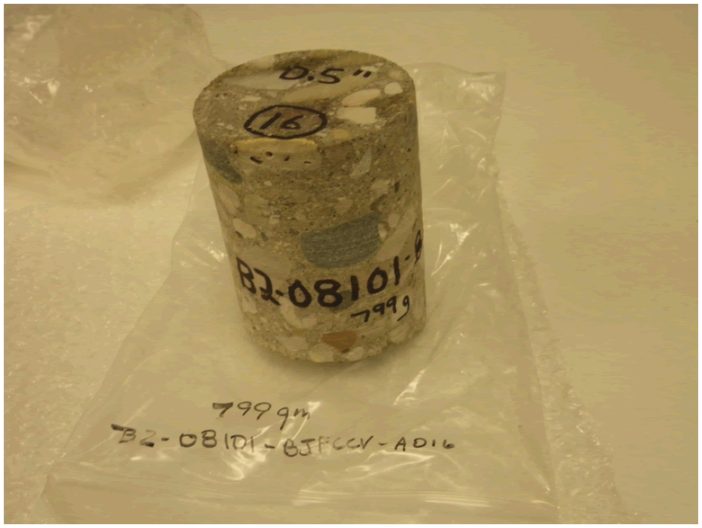

Figure 5: the B2 labeled cement core from Zion

Figure 6: The rocks and size reduced cement sample

Extended defects in Cadmium Zinc Telluride crystals grown by the High Pressure Bridgeman method and the Traveling Heater Method

Matthew Marshall
University of New Mexico, Albuquerque, NM
Jamie Butcher
SUNY Geneseo, Geneseo, NY
Matthew Petryk
Huntington High School, Huntington, NY
Aleksey Bolotnikov
Brookhaven National Laboratory, Upton, NY

ABSTRACT

Currently work is being conducted at Brookhaven National Laboratory (BNL) to look into Cadmium Zinc Telluride (CZT) crystals as a promising material for room-temperature, semiconductor detectors that produce a good spectral resolution. While CZT detectors exhibit high performance capabilities in many practical tasks, the presence of extended defects such as Te inclusions and subgrain boundaries drastically degrade the spectral resolution and detection efficiency. Although Te inclusions arise during the crystal growth process, the inclusions can be prevented through proper growth techniques; still, subgrain boundaries cannot be eliminated completely from the crystal. There are two methods used for growing commercial detector grade CZT crystals: the High Pressure Bridgeman (HPB) method and Traveling Heater Method (THM). The research being conducted at BNL uses Infrared Transmission (IR) Microscopy and White X-ray Beam Diffraction Topography (WXDT) to observe and understand the difference in the Te decorations resulting from each growth method. The IR imaging is a useful technique that gives the total concentration and size of the Te inclusions by mapping the distribution of Te inclusions. WXDT is employed to better understand the geometry of the crystal by showing extended defects and twin grain boundaries by using the Bragg diffraction. Utilization of these two methods appears to show THM is the more successful method for growing crystals with a reasonable size distribution of Te inclusions. This study is helping expand the groups understanding of how inclusions and subgrain boundaries are formed and which growth method is preferred for the reduction of Te inclusion distributions and other extended defects during the crystal growth process. This project has proved to be beneficial with expanding my knowledge of CZT crystals and how small inclusions, primarily accumulated inside subgrain boundaries, can have a hampering effect on energy resolution. This knowledge will be advantageous for graduate school because I plan on doing work with radiation detection and research experience with new semiconductor technology will help me immensely.

I. INTRODUCTION

The detection of gamma rays is an important aspect relating to national security and nonproliferation, and CZT crystals are promising room-temperature, semiconductor detectors that offer reasonable spectral responses. However, CZT crystals have extended defects that arise during the growing process that hinder the spectral resolution. These defects are: Te inclusions and subgrain boundaries. The defects, mainly the Te inclusions, can trap charge from an applied bias, which affects the resolution output of the spectrum. Subgrain boundaries accumulate Te inclusions along their boundaries but these cannot be prevented during the growing process.

Presently, there are two methods that are being investigated that would minimize the inclusions that arise inside of CZT crystals. These two methods are the HPB method and THM. In the HPB method, crystals are grown from a melt of nearly equal quantities of cadmium and tellurium, with a small cadmium excess. The cadmium excess generates high vapor pressure that requires a growth furnace with a special design. The crystal grows at high temperature, above 11000 C, at a high growth rate of few millimeters per hour. Zinc addition increases the crystal's band gap and electrical resistivity; therefore, it reduces the detector's spectral broadening by dark current noise. HPB yields high quality detectors; however, the crystal uniformity is limited, and the detectors' yield is low due to a large concentration of inclusions but no other extended defects.[1] THM utilizes chlorine-doped crystals that grow from tellurium solution. The ratio of cadmium to tellurium within the solution determines its melting point, and therefore also the temperature of crystal growth. The temperature is usually adjusted in the range of 650–700°C. The low growth temperature limits the growth rate to typically a few millimeters a day.[2] THM produces high quality detectors because of low concentrations of Te inclusions, but extended defects, mainly prismatic defects (areas with polycrystalline materials) that occur, lower the detectors yield. The HPB method does not have a large concentration of prismatic defects but THM crystals develop significant sized defects during its growth process. The origin of such defects is unclear. Two possible explanations are: 1) caused by a high pressure built inside inclusions;[3] and 2) moving dislocations interact with inclusions or precipitates.[4] The slow growth rate and prismatic defects that arise within the crystal are the main disadvantages of this method, but high quality crystals and detectors have been made by this method.

For this experiment, we analyzed crystals grown from two different companies, where Company A uses the HPB method and Company B uses THM. We analyzed the crystals using IR imaging, WXDT, and Etch Pits Analysis. IR imaging is able to give the concentration of the Te inclusions, and WXDT gives a greater insight inside the crystal and can reveal where subgrain boundaries and extended defects occur in the crystal. These boundaries accumulate high local concentrations of impurities, which trap charge carriers at a high rate due to the relatively high density of the trapping centers.[5] Etch Pits uses a Nakagawa solution (H2O:H2O2:HF) to reveal prismatic defects within the crystal and the prismatic defects relative size. Prismatic defects are more likely to trap charge than inclusions. This experiment should give

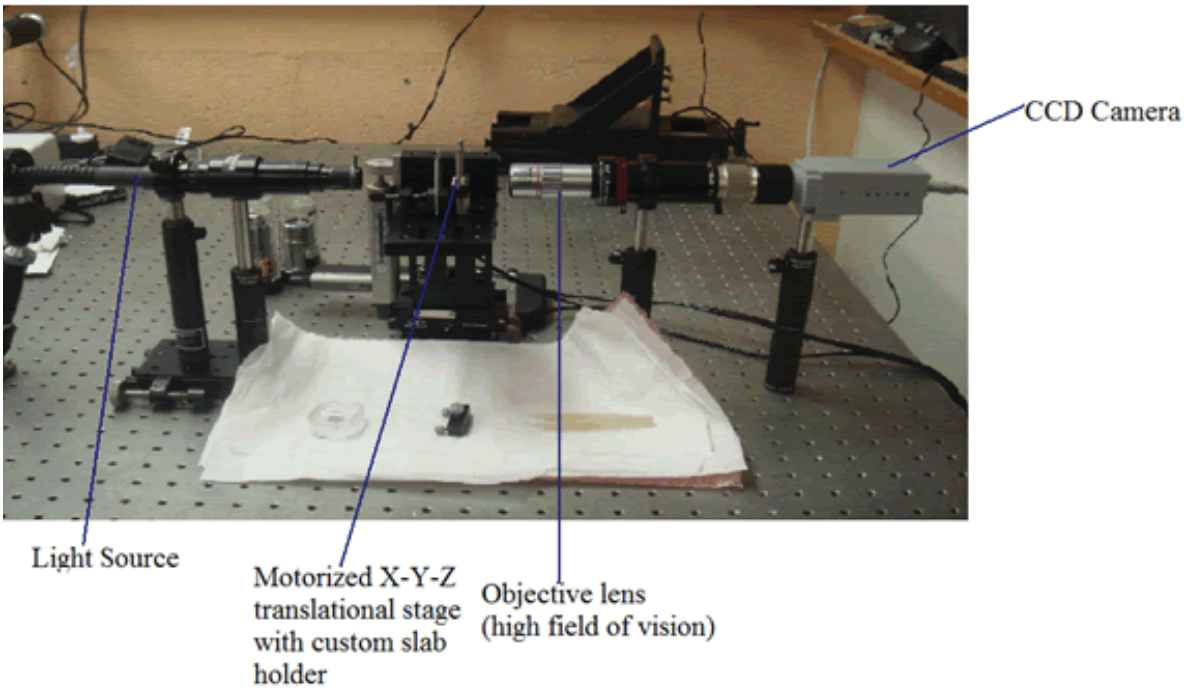

Figure 1. IR Transmission Microscope setup

insight into which growth method is the best at limiting extended defects within the crystals.

II. MATERIALS AND METHODS

A. IR TRANSMISSION MICROSCOPE

The IR Transmission Microscope has a motorized X-Y-Z translational stage that allows for the sample to be viewed in one-, two-, or three-dimensional scans by using a CCD camera, 7.8 x 10.6 mm^2, sensor area 2208x3000 pixels, and 3.5x3.5 μm^2. The camera was used in this experiment to take a five-point scan. It moved to five different spots along the x-axis of the crystal and traversed through the crystal in the z-direction for a predetermined number of steps. This data was then acquired in stacks of images, each focused at different depths of the crystal, and the images were analyzed with Interactive Data Language (IDL), a computer program, to identify inclusions and their sizes throughout the length of the crystal.

B. WHITE X-RAY DIFFRACTION TOPOGRAPHY

WXDT was utilized in this experiment for imaging the crystal's defects, mainly subgrain boundaries and extended defects. WXDT is based on the following principles: x-rays incident on the surface of a crystal scatter with an angle according to Bragg's Law:

$$n\lambda=2*d*\sin(\theta) \quad (1)$$

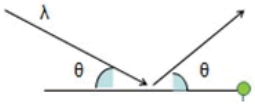

Figure 2a. Illustration of Bragg's Law. θ is defined as the angle between the plane of the crystal surface and the incident x-ray

A perfect crystal surface would reflect a collimated beam of x-rays at the same angle at all points, however defects on the surface cause changes in the scattering angle of some of the rays. With proper placement of x-ray sensitive film, an image of surface defects can be obtained. This method allows the imaging of dislocation bands (sub-grain boundaries and dislocation walls) in the crystal which are exiting from the surface..

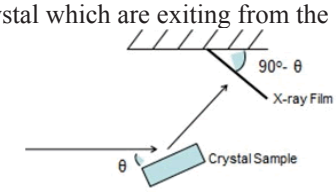

Figure 2b. Illustration of the proper placement of the crystal surface and industrial x-ray film with respect to incoming beam

III. RESULTS

The IR images below were produced after analyzing the data with IDL. From inspection of the two graphs, it is clear that the THM grown crystals have fewer concentrations of Te inclusions and the size of the inclusions stay relatively small. The crystals being analyzed are 6x6x15 mm^3 so a crystal with large inclusion diameters leads to significant charge loss and is detrimental to the spectral response.

The lower concentration of inclusions can be more easily corrected for incomplete charge collection (ICC). This means that the spectral resolution better approaches the Fano-factor, the theoretical limit for spectral resolution, for CZT detectors. Based off the IR imaging, THM offers a better chance thus far at higher spectral resolution.

The images shown below were taken from WXDT. It can be seen that THM grown crystals have a high concentration of prismatic defects. These defects are more threatening to the overall spectral response of the crystal compared to inclusions, and cannot be corrected for ICC. Both methods seem to have similar subgrain boundaries.

Using Nakagawa solution, Figure 5 was produced. It reveals dislocations on the THM grown CZT surface. The effect of etching depends on the crystallographic surface orientation and surface preparations.

IV. DISCUSSION AND CONCLUSION

In our research, we compared crystal quality of CZT material grown by THM and the HPB method. The results indicate that THM is the better method for growing crystals with small concentrations and sizes of Te inclusions. The size of the inclusions rarely exceeds 20 micrometers. However, there are high concentrations of big prismatic defects that arise from THM and these defects are more prone to trapping charges and therefore are more detrimental to the crystal than inclusions. As seen by Figure 5, the defects occupy a 1x1 mm^2 area, which is significantly larger than the space inclusions occupy, and they lead to ICC that cannot be corrected reducing the overall spectrum. It is suspected extended defects could have a larger effect on the spectral resolution. As for subgrain boundaries, both methods are very similar. More research is needed to conclude if the presence of high concentrations of Te inclusions or prismatic defects are worse for the overall spectral response of the detector before the better growth method is known. We will have to fabricate and test more detectors and then analyze the resulting data to determine on average what crystal growth method produces the best spectral response.

A recommendation for future work would be to use more pure Cd, Zn, and Te. This might reduce inclusions and defects in the growth process. Also, exploring other growth options or electron correction methods to correct for ICC events. The progress made with CZT crystals other the past few years has been remarkable, and I am sure that soon a growth method will be found that will alleviate inclusions and other extended defects from the crystals.

V. REFERENCES

[1]P. Fougeres et al , "J. Crystal Growth", 184-1313, 1998

[2]R. Triboulet, "Prog. Cryst. Gr. Char. Mater.", 128-85, 1994

[3]R. D. S.Yadava et al., J. Electron. Mater 21, p. 1001, 1992

[4]P.B. Hirsh, J. Inst. Metals 86, p. 7, 1957

[5]Bolotnikov, A.E. et al. , "Performance Studies of CdZnTe Detector by Using Pulse Shape Analysis", Proc. of SPIEE, BNL-74873-2005-CP., 2005.

VI. ACKNOWLEDGEMENTS

I would like to acknowledge Dr. Ralph James, his team and the NNS department for all their help this summer. Further, I express my gratitude to the Office of Education for this opportunity to come to BNL to study this summer, and for being accommodating throughout. Finally, I express my thanks to the Department of Energy for funding this summer program and allowing me to learn vital skills that will assist me in my future career.

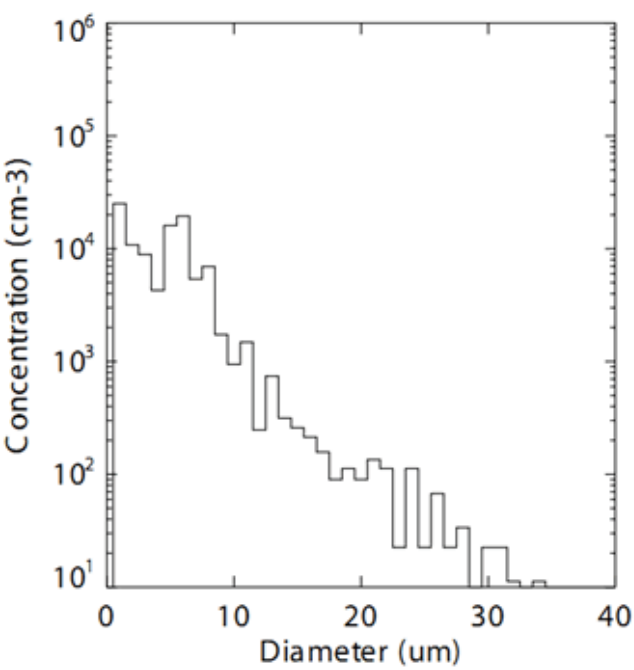

Figure 3a. Concentration of Te inclusions from a HPB grown crystal

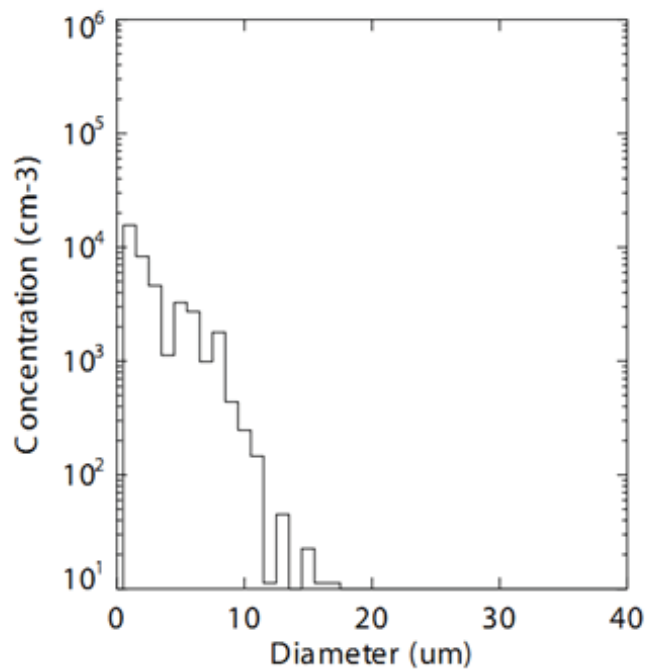

Figure 3b. Concentration of Te inclusions from a THM grown crystal

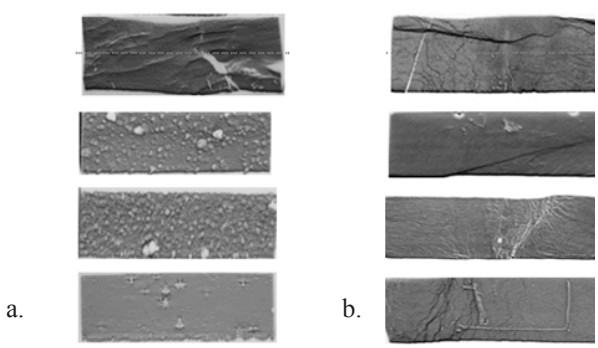

Figure 4. (a) HPB grown crystals (b) THM grown crystals

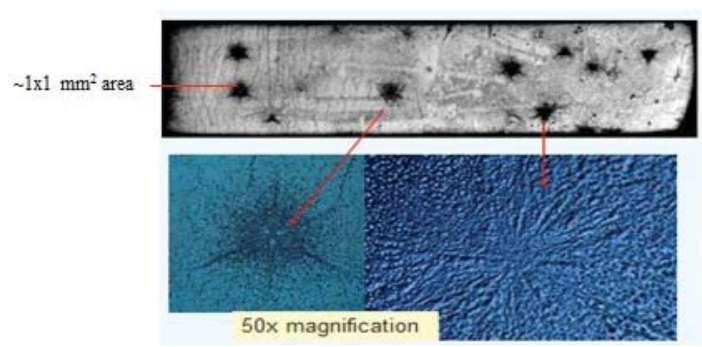

Figure 5. Nakagawa solution to reveal dislocations in the THM grown crystal surface

Temperature and vibration isolation system design for the multilayer Laue lens deposition system

Jesse A. Miller
Department of Photon Sciences, California State University Fresno, Fresno, CA 93740
Raymond Conley
Department of Photon Sciences, Brookhaven National Laboratory, Upton, NY 11973

ABSTRACT

A type of nanofocusing optic known as a multilayer Laue Lens (MLL) is the optic of choice for the National Synchrotron Light Source II (NSLS-II) since the MLL allows for a higher level of x-ray nanofocusing relative to other types of lenses. The fabrication system for the MLL is the NSLS-II MLL deposition system which utilizes a capacitance manometer to measure the pressure inside of the chamber. Those measurements are then used to dictate the mass flow of various gases that are used in the machine to serve as a medium for lens growth. Because the capacitance manometer is sensitive to temperature and vibration stimulation, it was necessary to design and fabricate a temperature and vibration isolating system that mitigated any erroneous measurements taken from the manometer. Results from the temperature and vibration isolation system show that the design isolates and maintains a set temperature within a tenth of a degree and mitigates vibrational noise.

I. INTRODUCTION

The temperature and vibration isolation system for the multilayer Laue Lens (MLL) deposition system was designed in order to address issues associated with temperature and vibration stimulation while growing MLLs. MLL growth is dependent upon the measurements taken from the capacitance manometer that the temperature and vibration isolation system is focusing on isolating. Both theoretical and experimental analysis was performed in order to determine design solutions for the isolation system.

Readings taken from the capacitance manometer in October of 2011 show a significant amount of noise due to vibration as well as a large discrepancy in the data due to temperature fluctuation in the deposition lab room. These readings indicating the aforementioned discrepancies are shown below.

Figure 1 shows a progressive drop in ion voltage as well as a significant amount of noise in the readings. This is indicative of consistent vibrational stimulation to the capacitance manometer. A voltage drop due to temperature fluctuation in the deposition lab room can also be seen in measurements taken on the same date.

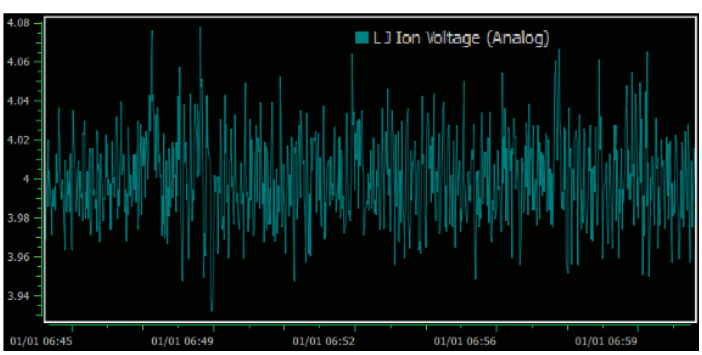

Figure 1. Pressure Noise due to Vibration Stimulation from October 2011

Figure 2 shows a large "scoop" out of the data from the capacitance manometer. The major drop in ion voltage shown in figure 2 is consistent with temperature variation within the lab room of the deposition system.

II. DESIGN OBJECTIVE AND CRITERIA

In short, the design objective of the temperature and vibration isolation system for the MLL deposition system is to mitigate, as much as possible, the vibrational effects on the readings garnered from the capacitance manometer in the system while also maintaining a set temperature immediately around the manometer with at least a one tenth degrees Celsius accuracy.

In order to design an effective temperature and vibration isolation system for the capacitance manometer, it was necessary to analyze any constraints and limitations that may influence the design. It was necessary first to identify any design requirements of the isolation system. Design requirements for the isolation system are listed in the table below.

In order to design the isolation system it was also necessary to consider any limitations that the geometry and environment of the deposition system placed upon any potential design solutions. In particular, any temperature and vibration stimulation present near the capacitance manometer needed to be measured along with any physical constraints that limited the isolation frame geometry.

The deposition system is subject to vibrations caused mostly by four cryogenic vacuum pumps that are used to pump various

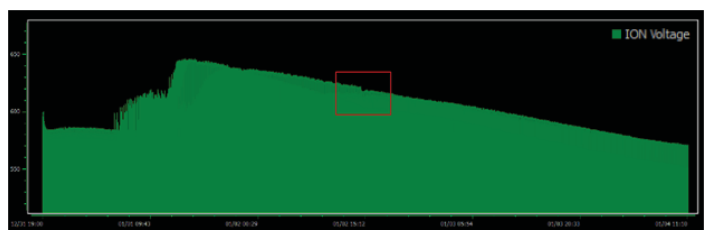

Figure 2. Pressure Variation due to Temperature Stimulation

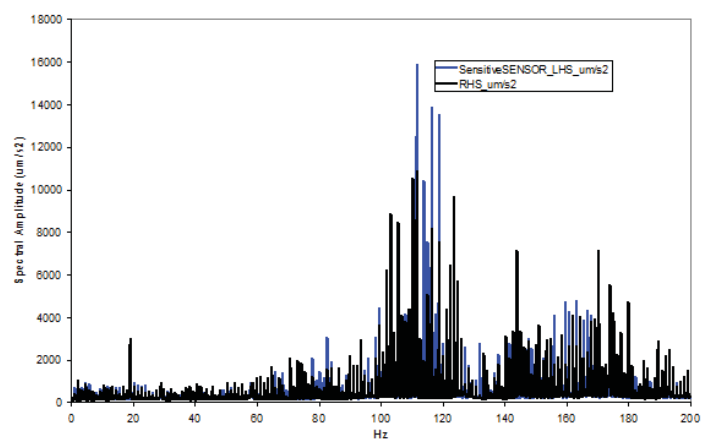

Figure 3. Average Spectra of Vibration Recorded at Different Segments of Deposition Chamber

Table 1. Design Requirements
Temperature immediately around the manometer is able to be controlled within 0.1°C
Any vibration translated to the manometer is minimized through the use of vibration isolation mounts.
Any parts to be machined are designed in such a way that they are easily fabricated.
Temperature isolating enclosure is largely translucent.
Easy access to small screw located at the top of the manometer.

gasses. The excitation frequency output from the vacuum pumps was recorded using two accelerometers positioned at two separate locations on the deposition system. Results garnered from the vibration measurement device indicate that the excitation frequency near the capacitance manometer is mostly between 100 and 200 Hertz. Figure 3 shows the vibration spectra from two different sensors that were placed on the deposition chamber.

Figure 3 shows measurements of vibration that were taken in July 2012, by Simos from Brookhaven National Laboratory. Its data is composed of measurements from two different gauges placed at different locations on the deposition chamber. It was impossible to place sensors exactly on top of the capacitance manometer; therefore, it was necessary to place sensors at approximate locations and then average the results. The data shown above indicates that most of the vibration is in the 100–200 Hz range, and it is this range of frequencies that were of the most concern for damping.

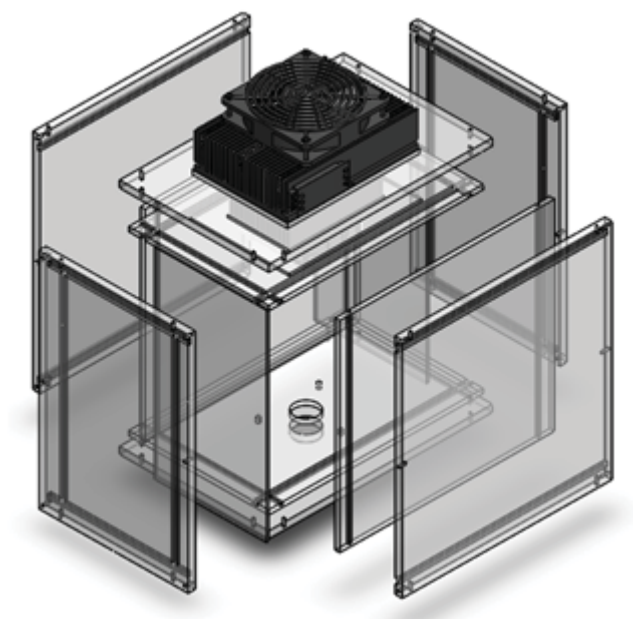

Figure 4. Enclosure Exploded View

III. DESIGN ITERATIONS AND SOLUTIONS

Once analysis of design constraints and criteria was performed, it was necessary to formulate design solutions to satisfy those constraints. Since the design process is iterative and, therefore, yields multiple results, it is up to the engineer and the rest of the design group to analyze design solutions and decide which one is best. Initial design solutions for the temperature isolating enclosure mainly consisted of a single walled acrylic enclosure that would be mounted to a metal frame and then connected to the existing frame for the deposition system. Eventually, a double walled acrylic box with outer dimensions of 8 inches by 13 inches by 12 inches, and inner dimension of 10 inch by 5.75 inch by 10.25 inches was selected for the enclosure as shown in Figure 4.

This initial concept has only one pair of support arms made from 0.25 inch thick, 1.25 inch wide 6061 T6 Aluminum at various lengths. Note that Aluminum at this thickness, width, alloy and temper was used in the final design and construction of the support frame for the enclosure. This design also utilizes a mounting plate for the vibration isolation mounts that is outside of the enclosure. This initial frame design was only mounted to the enclosure at one location per side of the enclosure, and was mounted a nominal distance forward of the center of mass of the enclosure. For a more stable support frame, it was necessary to have a frame that mounted to the enclosure in a symmetrical fashion, and was

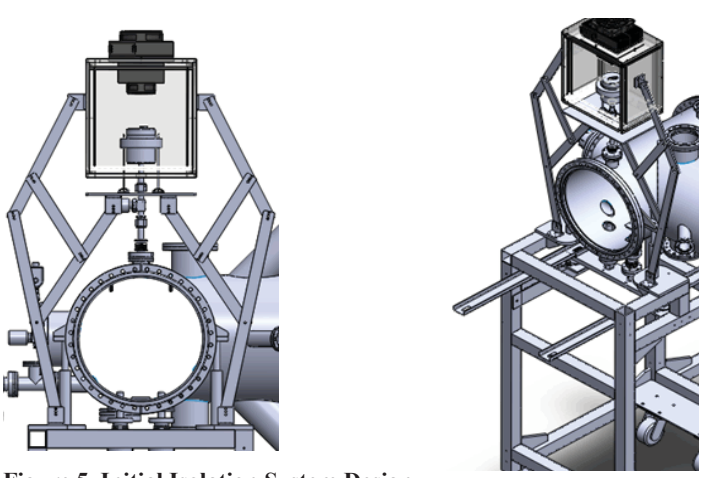

Figure 5. Initial Isolation System Design

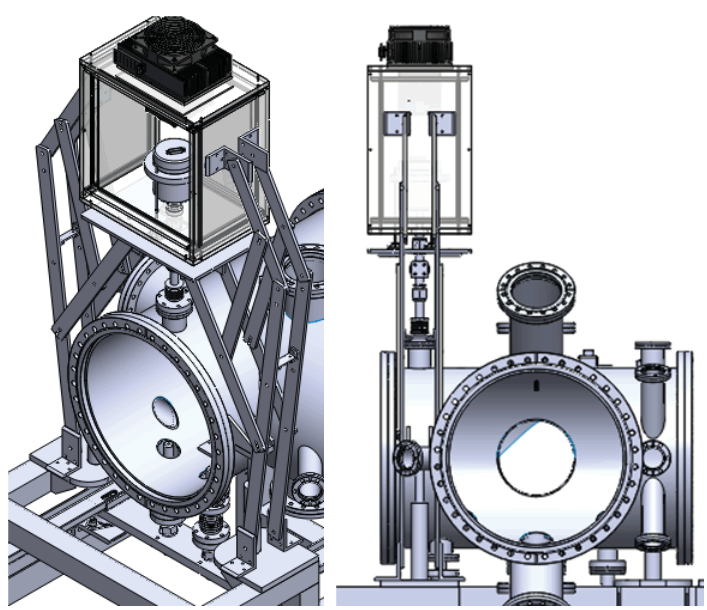

Figure 6. Intermediate Isolation System Design Iteration

as rigid as possible. Also, mounting the vibration isolation mounts outside of the enclosure was deemed to be unnecessary, so mounting the isolators inside of the enclosure was designed for in future design iterations. Shown in Figure 5 is an example of the intermediate isolation system design iteration.

The above intermediate design iteration sports a more robust support frame for the temperature isolating enclosure than the initial frame and enclosure design iteration. As can be seen above, the support frame for the intermediate design has two sets of arms that are connected to the enclosure symmetrically. The fact that the support frame is symmetrical about the central axis of the enclosure allows for the enclosure to be balanced and not potentially cause more vibrational problems due to an unbalanced situation. The vibration isolators are in the same configuration in this iteration as they were in the initial design iteration, which is they are 120 degrees from each other on a 1.875 inch radius circle situated at the inside bottom center of the enclosure. Finally, after making corrections to the support frame for the temperature isolating enclosure, and locations and types of the vibration isolators, a final isolation system design was achieved.

The design iteration in figure 7 was fabricated and attached to the deposition system. Geometrically, the final frame design is far simpler than any other design. Linkage lengths were all made to be relatively simple values. A significant amount of tolerance for the mounting holes was necessary because the frame was designed to be symmetric about the center axis of the main chamber and the floor of the deposition chamber is very slightly out of level. The amount of tolerance on the mounting holes for the support frame allowed construction of the support frame and mounting to the enclosure to be very simple.

IV. COMPONENT SELECTION

Components selected for the temperature and vibration isolation requirements were chosen based on their abilities to fulfill the aforementioned design requirements. The temperature controller used in the design is the TE tech AC-046.[1] Being used in conjunction with the AC-046 is the TC-48-20 from TE tech.[2] The AC-046 is an air cooler that communicates with a temperature controller in order to either heat or cool a given enclosed space. In this case, the AC-046 is communicating with the TC-48-20. The TC-48-20 temperature controller uses user specified proportional derivative integral (PID) settings in order to control the temperature response of the system. A user can set the proportional bandwidth, integral gain, and derivative gain to various values in order to alter how quickly and how accurately the temperature controller and air cooler control the given temperature in an enclosure. Figure 8 shows a temperature response graph after several changes made to the PID settings of the temperature controller.

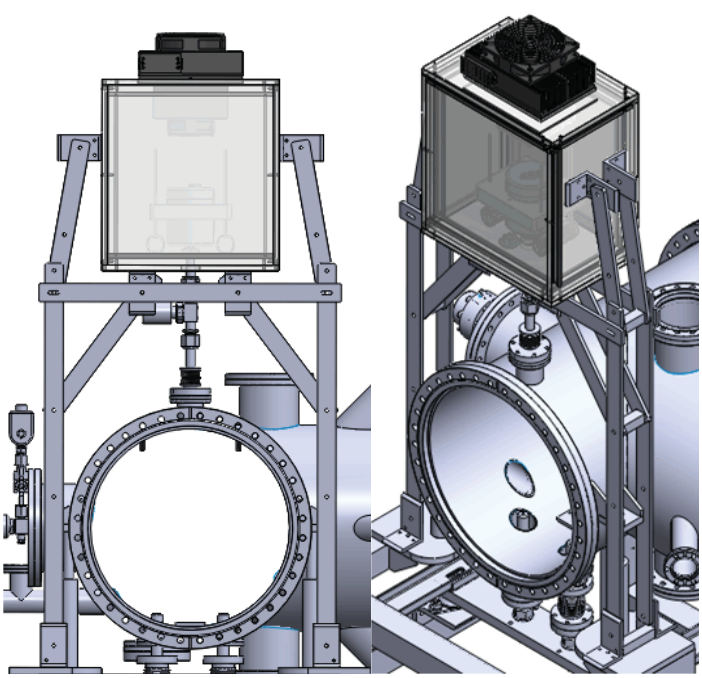

Figure 7. Final Isolation System Design Iteration

Note that TE Tech[1] software was used to acquire the data that is depicted in Figure 8. Figure 8 shows how the temperature isolating enclosure responded to changes in PID settings in ambient air with a temperature of 22 °C. The changes in PID settings are indicated by red circles. The blue line indicates set point temperature, while the yellow line shows the temperature read from a thermistor attached to the heat sink of the AC-046, while the green line shows the temperature read from a 15 kΩ thermistor suspended in the enclosure. Changes to the PID settings were made at the indicated times on the graph. Upon observation, it can be seen that after the first change to the PID settings, the temperature response of the system seemed to oscillate more about the set point temperature. In order to select vibration isolators, it was necessary to analyze the data shown in Figure 3, the weight of the components that the isolators were to support, as well as the amount of damping that was desired for the system.

In order to select vibration isolators, it was necessary to get an estimation of the weight of all of the components that the isolators were to support, as well as the amount of force pulling down on the manometer due to vacuum. The manometer was explicitly weighed using a standard scale. In order to find the weight of the manometer clamp being used to secure the manometer, SolidWorks solid modeling software was used. SolidWorks allows for a user to find the mass of any given object once a material has been assigned to that object, in the case of the manometer clamp, that material was 6061 T6 Aluminum. The total weight that the vibration isolators would have to support came out to be 7.88625 pounds. Once the system weight was found, standard vibration analysis equations were used in order to find the necessary spring constants of the vibration isolators. All equations used are shown below.

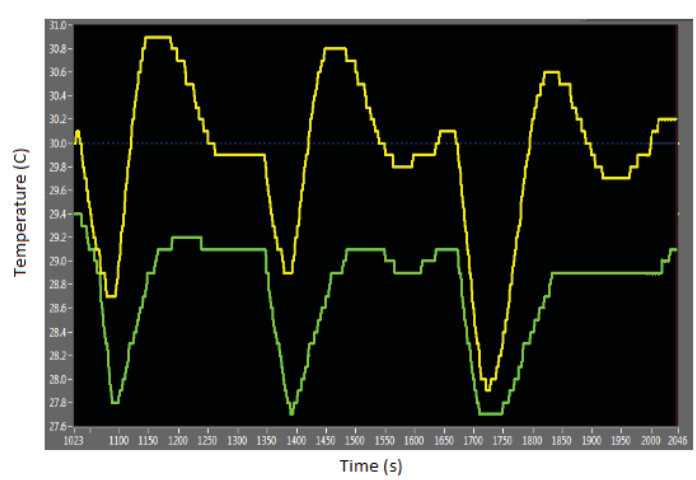

Figure 8. Temperature Response under Various PID Settings

$$(1)\quad f_n = 1/2\pi * \sqrt{(K * g/W)}$$

$$(2)\quad \delta = \sqrt{(3.13/f_n)}$$

$$(3)\quad K = W/\delta$$

The selected vibration isolators after analysis was performed had spring constants of 18 lb. /inch.[3]

V. RESULTS

The temperature and pressure response of the capacitance manometer after the isolation system had been attached showed a marked improvement when compared to measurements taken prior to the isolation system being attached. In terms of vibration, the noise in the measurements of pressure taken from the capacitance manometer decreased by a factor of 2 to 3. In terms of temperature isolation, the enclosure isolates temperature much better than expected. The temperature isolating enclosure maintains a set point temperature within a tenth of a degree at a very stable level. Figure 9 shows the comparison between pressure measurements before and after the isolation system being attached to the deposition system.

Note that in Figure 9, the spike in the data is due to removing the air controller from the enclosure and letting ambient air "reset" the temperature inside of the enclosure. Upon observation, it can be seen that the noise in the data is greatly decreased. Temperature control is indicated by the following graph.

Figure 10 shows the temperature within the enclosure being controlled within a tenth of a degree over the course of seventeen minutes. The set point temperature in the above case was 39.1°C. The measured temperature still tends to oscillate about the set point and overshoot the set point at times but is still plenty reliable. An image of the final design is shown if Figure 11.

VI. CONCLUSIONS

Since the temperature and vibration isolation system was able to isolate the temperature and vibrational noise that is depicted in measurements taken from the capacitance manometer, the design is a success. The aforementioned design requirements of reducing vibration and isolating temperature to within a tenth of a degree were met.

VII. ACKNOWLEDGEMENTS

I would like to thank my mentor Ray Conley for the guidance and continued help throughout the course of the summer. I would also like to thank James Biancarosa, Nathalie Bouet, Dennis Kuhne, Kenneth Lauer, Nate Simos, and Ruchik Bhatt for all of their help throughout the design and fabrication process of the temperature and vibration isolation system for the MLL deposition system. I would also like to thank the Department of Energy and Brookhaven National Lab for facilitating a rewarding and challenging experience through the 2012 Summer SULI internship program.

VIII. REFERENCES

[1]"Temperature Controllers", TE Technologies. <http://www.tetech.com/Temperature-Controllers/TC-48-20.html>

[2]"Air Coolers", TE Technologies. <http://www.tetech.com/Air-Coolers/AC-046.html>

[3]"Vibration Mounts-Cable Isolators." Vibration Mounts. Web. July-Aug. 2012. <http://www.vibrationmounts.com/Store.asp?Page=RFQ/VM05024.htm>.

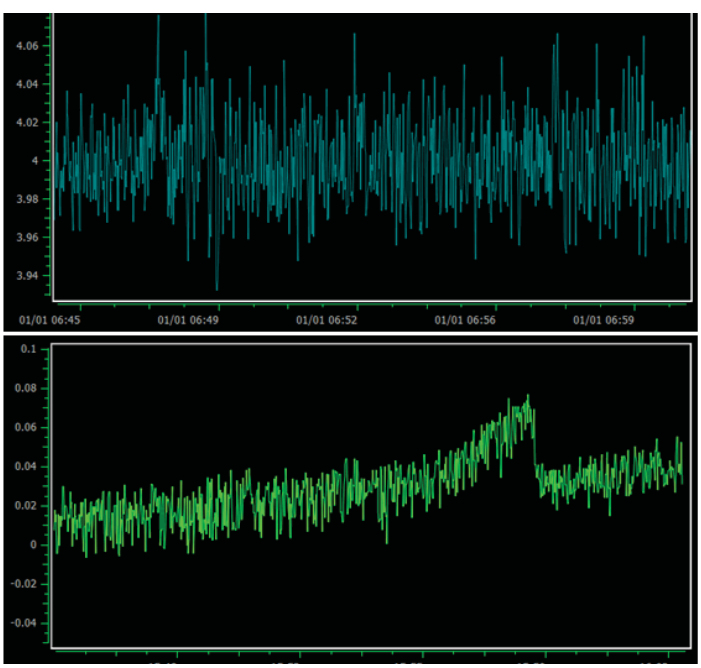

Figure 9. Comparison of Pressure Measurements; original data (top), data after enclosure was installed (bottom).

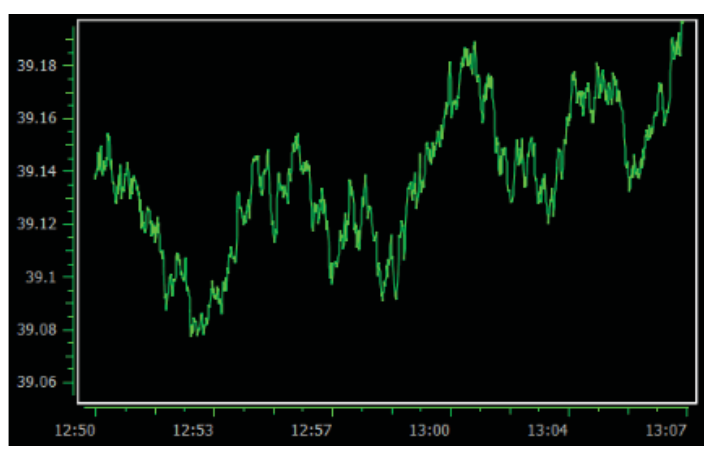

Figure 10. Comparison of Pressure Measurements

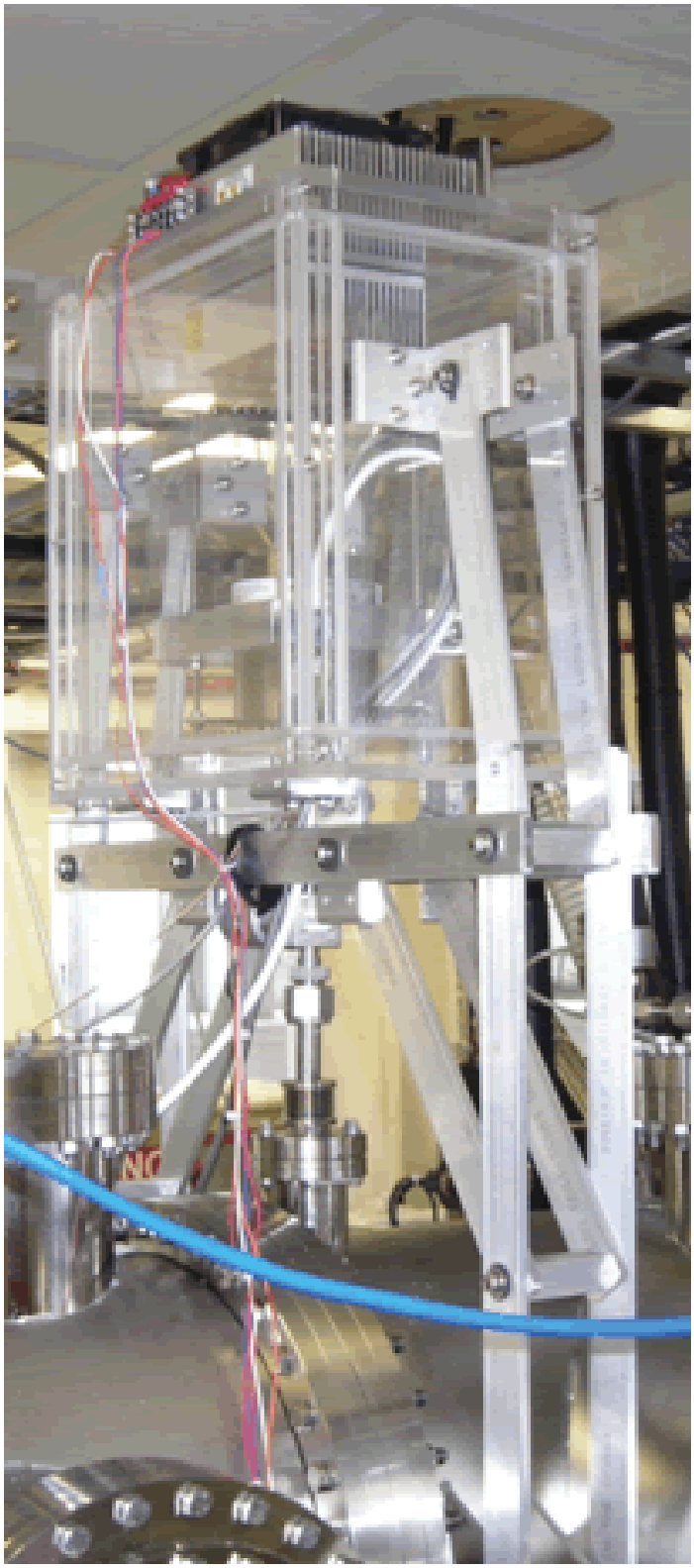

Figure 11. Fabricated and Constructed Design

Programming a low-voltage distribution controller board

Louie-John Mistretta
Worcester Polytechnic Institute, Worcester, MA 01609
Steve Boose
Brookhaven National Laboratory, Upton, NY 11973

Abstract

The Low Voltage Distribution Controller is an embedded system consisting of various electrical components that can control the power supplied to different channels, read analog voltage and current values, and report them as digital values to a host. The process of programming this board requires the knowledge of how each individual component works and, furthermore, how they all function together as a system. Using debugging features of the compiler and tools such as an oscilloscope, the board can be properly programmed to read the current and voltage values off of each channel on twenty distribution boards, each consisting of ten channels (two-hundred channels, four-hundred readings) once every second or less. This board will also feature Ethernet upgrades that improve the speed and efficiency of the board.

I. Introduction

The low voltage distribution system is a system that controls the power distribution to High Energy Physics detectors within PHENIX from a host computer. This system allows the host to control individual channels as well as check to make sure each component is working properly by gauging its voltage and current readings. In context, many of these sensors will be shielded within the PHENIX confines. If an individual sensor breaks or malfunctions during one of the runs, no one has access to the sensor to repair it. This system allows you to turn off that individual sensor while the rest of the sensors continue to run. During the process of the updating PHENIX, the low voltage distribution system is going to be upgraded in order to increase the system's speed, reliability, flexibility and standardization.

II. Updates

The major updates that were made to this system include a new microcontroller and Ethernet connection capabilities. The new microcontroller is a PIC32 microcontroller as opposed to the PIC24 that was used in the previous system. The PIC32 is much faster than the PIC24 running at 80 MHz and has a 32-bit ALU instead of a 16-bit ALU. It also has many more pin out options (100 pins, 80 input/output pins) that increase its functionality. The Ethernet connections are an upgrade over the old rs485 connections since Ethernet connections are inherently more stable and faster than rs485 connections. An Ethernet-based system includes features such as collision detection multiple access and a higher resolution checksum. An Ethernet-based system also allows a host device to be added to any node within the private LAN system. In the previous system, there was only one computer connected at the end of the system that could control it, now any host device that complies with MODBUS TCP/IP protocol can be added as a host.

III. Process

Before programming the Low Voltage Distribution Controller, one must know how the system functions. It is good to know the functionality of each individual component as well as how the system works as a whole. In order to obtain this information, one must diligently study the schematics of each board and the datasheets of each component. After this step, you can begin to test individual components of the board to check for functionality and finally bring it all together into functioning system.

A. Overall system (Figure 1)

The overall design schematic for the Low Voltage Distribution system is relatively simple. The PIC32 microcontroller at the heart of the system receives commands (sent from the host in MODBUS TCP/IP protocol) through the ENC624J600 Ethernet chip, processes the command and then sends it out to the Low Voltage Distribution Card. The command is sent to the digital logic of the Distribution Card and the desired output is implemented. If a voltage or current reading is requested, it will be registered locally and then read from the Distribution Card back to the controller. The PIC32 processes all of the information and sends it back through the Ethernet chip to the host which will display the data. The host software that is going to be used is the Kepware Technologies OPC MODBUS server.

B. Low Voltage controller (Figure 2, 3)

The Low Voltage Controller Board is the main board in the system. It controls the rack of distribution boards and contains the PIC32 microcontroller. The PIC32 is the device that controls all of the inputs and outputs from the board by coordinating the digital logic components with chip selects, clock sources and data input.

The main function of this board is to appropriately send out commands that will allow the user to select individual boards and channels and furthermore turn them on and off. The LV Distribution board and channel select outputs are controlled by a serial output channel, Serial Peripheral Interface 1 (SPI1). A 24-bit data word is sent from the PIC32 into a series of three contiguous shift registers (74HC595/SO). The shift registers take in the serial data and output it as parallel data. The board selects and the commands are tied together in the 24-bit data word, the first 20 bits control the board selects (each bit is a board) and the last four bits represent a command. The first 20 bits of parallel data are then sent into tri-state octal buffers (SN74ABT540) that invert the signal. Each of the 20 bits is sent out to its corresponding board as a BDSELx. The last 4 bits (the command bits) are sent to a hot-swapable quad RS485 driver that will take the inputs and produce the same output as differential RS485 signals (CHSELx+ and CHSELx-). The remaining four bits in the buffer are driven by digital outputs from the microcontroller that illuminates bi-directional LEDs, the Heartbeat LED and IO LED. The CHSELx outputs are sent to all of the boards but will only be registered in the boards that are selected by the BDSELx outputs.

C. Distribution Card (Figure 4, 5, 6)

Each distribution card will receive seven inputs: SCK+,SCK-, SDO+, SDO-, CHSEL0+, CHSEL0-, CHSEL1+, CHSEL1-, CHSEL2+, CHSEL2- and BDSEL. It will output SDI+ and SDI-. The three CHSELx inputs are sent to a quad line receiver (LTC1519). The "Ax" inputs will be CHSELx+ and the "Bx" inputs will be CHSELx-. The fourth input is the BDSEL. The outputs of the corresponding CHSEL inputs are sent to a 3-8 inverting de-multiplexer (74HC138) and the BDSEL output is sent as the chip select. The de-multiplexer will take a three bit input and output an eight bit value that contains a "0" at the location of the value of the three bit number. For example, an input of "101" will produce the output "11011111." Five of the eight outputs are connect as inputs to other digital logic components and the other three are left unconnected. The codes and outputs are as shown in Table 1 below.

These signals are then sent to a sixteen bit serial-in, parallel-out shift register where ten of sixteen bits are used to switch output LV channels. The serial data comes from the SDO+ and SDO- signals that are sent into a transceiver (LTC1685). The transceiver converts the incoming differential SPI signals to uni-polar signals for use on the LV Distribution board. This data line is put into an AND gate (74HC08) with the BDSEL and sent to the shift registers. The shift register clock is treated in a similar manner but is in an AND gate with the inverted RW_SR- signal. The SET_SR- signal is simply inverted and sent to the shift registers. A non-inverted RW_SR- signal is sent to the control input of the double-throw analog switch (SN74LVC1G3157-1Q). This component switches the serial output SPI sources between the channel select shift registers and the analog-digital converter.

All of the voltage and current signals are connected to a 32 input analog multiplexer (ADG731BSU). The first ten inputs are voltage readings from the channels and the eleventh channel is the main low voltage supply input, VMAIN. Starting at input seventeen, the next 10 inputs are current values. The inputs are multiplexed from a serial input after the chip is selected using CS_MUX_ISO-. The analog values are then sent to the analog-digital converter (AD7685) that will return a digital representation of the analog input.

IV. Programming

After a full understanding of the schematics, you can start writing useful C code. The first step is to properly configure the board. Configuring the oscillators and clock (80 MHz) is essential to running any code. Each microcontroller port that is being used must have a defined port direction (input/output) and function (digital/analog). Since we are using the Serial Peripheral ports, they must be configured (8 bits). The Parallel Master Port (PMP) must also be configured since it has dual use, both as a 16-bit PMP and as serial peripheral interface 2. Finally, the interrupts need to be set to trigger on the change notice inputs and on timer 4.

In order to make the process of programming the board simpler, two debugging features were implemented. An OLED screen was connected to the second serial data port. This display allows us to view important information stored in control registers while the program is running. Rotary encoders were also added to allow manual entry of values during run time.

Now the actual coding can begin with a simple function that selects boards. The boardSelect(int BD, int Channels) was made to send the board select values and the commands out on the serial data port. Building on a series of boardSelect commands we can construct a function called selectChannel(int BD, int Channel). This function selects the given board and sends out the correct series of commands (chip selects, clocks, data) in order to send the value of Channel into the second layer of shift registers on the distribution board. Similar to the selectChannel function, a series of boardSelects are used to create the function readADC(int BD, int Channel) that will read the given voltage or current. readADC() can then be expanded on to create the readBD(int BD) function which will read all of the current and voltage values on each channel on the selected board and save the values in an array. Since it is not a given that all of the boards will be in place, the checkBD(int BD) function was written to make sure the board actually exists. This is done by writing a value to the channel select shift registers on the board and then reading them back. If the value is returned, the board exists. The status of existing boards is stored in an unsigned long integer with each bit 0-19 corresponding to boards 1-20. With all of these functions combined we can create an interrupt every .05 sec that will read a valid board and store the values. If the next board does not exist, it will recursively check for the next board during the same interrupt.

This interrupt system is essential to the functionality of the low voltage distribution system. If the processor is constantly reading analog values then it will be bogged down and won't be able to execute other commands. The board also needs time to communicate with the host and process information.

V. Conclusion

Upon the completion and installation of the new Low Voltage Distribution System, the PHENIX experiment will gain much more efficiency when controlling their High Energy Physics detectors. The system is able to meet all of its timing requirements and is relatively responsive to changes in power supply control. There will also be extra features that were not in the original design such as the ability to add a host anywhere in the system and error solving features that come with using the Ethernet proto-

3-bit Code	8 bit Output	Signal	Function
000	00000001	CLR-	Clears the shift register
001	00000010	CS_ADC-	Selects the analog-to-digital converter
010	00000100	CS_MUX-	Selects the analog multiplexer
100	00010000	RW_SR-	Enables shift register clock
101	00100000	SET_SR-	Enables output in shift register
011,110,111	00001000,01000000,10000000	NC	Not connected

Table 1.

col. At this point in time, Low Voltage Distribution Controller is functional with the exception of the Ethernet MODBUS TCP/IP driver. This function is yet to be fully implemented.

VI. Acknowledgements

I would like to thank all of the people and organizations that made this summer internship possible for me including: Don Lynch, Steve Boose, and Sal Polizzo. I would also like to thank the United States Department of Energy, the Brookhaven National Laboratory, and the PHENIX group for facilitating my work.

VII. Works Cited

"16-Bit, 250 KSPS PulSAR ADC in MSOP/QFN." Analog.com. Analog Devices, n.d. Web. <http://www.analog.com/static/imported-files/data_sheets/AD7685.pdf>.

"3-to-8 Line Decoder/demultiplexer; Inverting." Nxp.com. Nxp Semiconductors, n.d. Web. <http://www.nxp.com/documents/data_sheet/74HC_HCT138.pdf>.

"52Mbps Precision Delay RS485 Quad Line Receivers." Datasheetcatalog.org. Linear Technology, n.d. Web. <http://www.datasheetcatalog.org/datasheet/lineartechnology/15189fa.pdf>.

"8-bit Serial-in, Serial or Parallel-out Shift Register with Output Latches; 3-state." Nxp.com. N.p., 12 Dec. 2011. Web. <http://www.nxp.com/documents/data_sheet/74HC_HCT595.pdf>.

"LTC1685 - 52Mbps, Precision Delay, RS485 Fail-Safe Transceiver." - Linear Technology. N.p., n.d. Web. 10 Aug. 2012. <http://www.linear.com/product/LTC1685>.

"LTC1688CS Pdf, LTC1688CS Description, LTC1688CS Datasheets, LTC1688CS View ::: ALLDATASHEET :::." LTC1688CS Pdf, LTC1688CS Description, LTC1688CS Datasheets, LTC1688CS View ::: ALLDATASHEET :::. N.p., n.d. Web. 10 Aug. 2012. <http://pdf1.alldatasheet.com/datasheet-pdf/view/70817/LINER/LTC1688CS.html>.

"Quad 2-input AND Gate." Nxp.com. Philips Semiconductor, n.d. Web. <http://www.nxp.com/documents/data_sheet/74HC_HCT08.pdf>.

"SINGLE-POLE DOUBLE-THROW ANALOG SWITCH." Ti.com. Texas Instruments, n.d. Web. <http://www.ti.com/lit/ds/symlink/sn74lvc1g3157.pdf>.

"SN74ABT540 Pdf, SN74ABT540 Description, SN74ABT540 Datasheets, SN74ABT540 View ::: ALLDATASHEET :::." SN74ABT540 Pdf, SN74ABT540 Description, SN74ABT540 Datasheets, SN74ABT540 View ::: ALLDATASHEET :::. N.p., n.d. Web. 10 Aug. 2012. <http://pdf1.alldatasheet.com/datasheet-pdf/view/27495/TI/SN74ABT540.html>.

"PIC32MX460F512L." PIC32MX460F512L. Microchip Technology Inc., 2009. Web. 31 July 2012. <http://www.microchip.com/wwwproducts/Devices.aspx?dDocName=en534177>.

"ENC424J600 Datasheet." ENC424J600 Datasheet and Application Note, Data Sheet, Circuit, Pdf, Cross Reference | Datasheet Archive. Microchip Techonology Inc., 2009. Web. 31 July 2012. <http://www.datasheetarchive.com/ENC424J600-datasheet.html>.

"Modbus Organization." Modbus Technical Resources. Modbus Organization Inc., n.d. Web. 31 July 2012. <http://www.modbus.org/tech.php>.

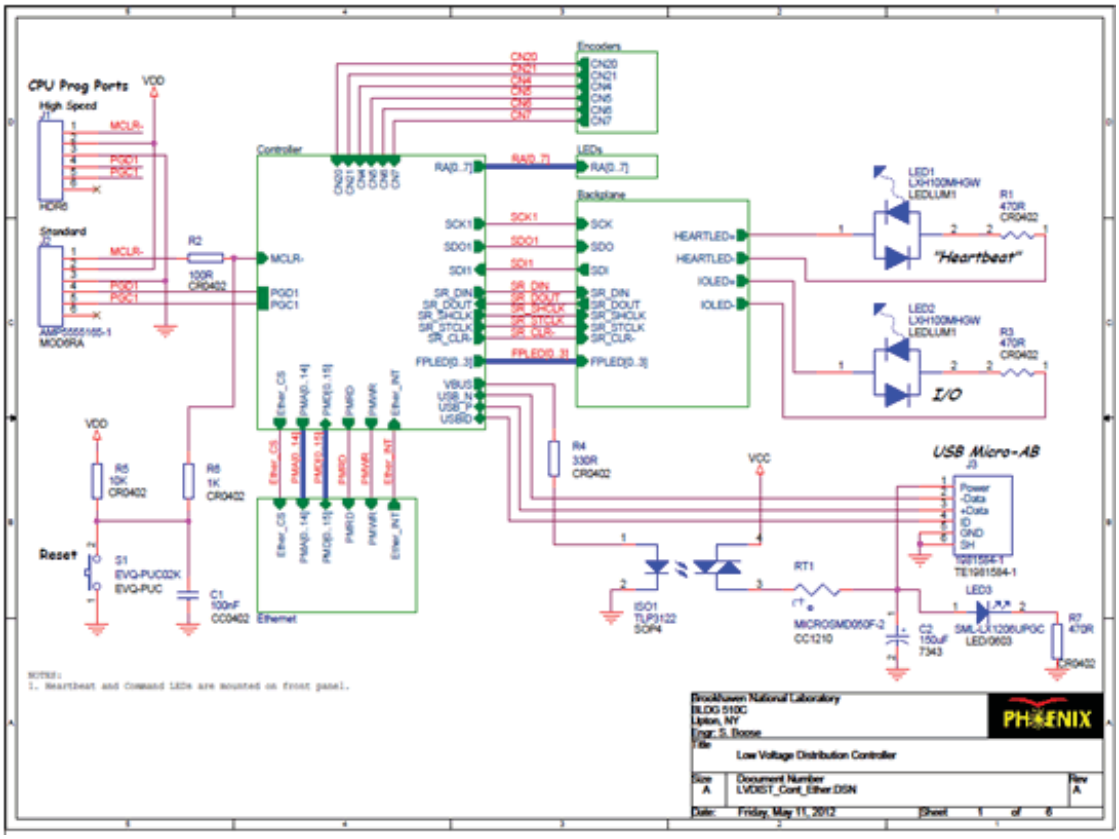

Figure 1: Overall Schematic

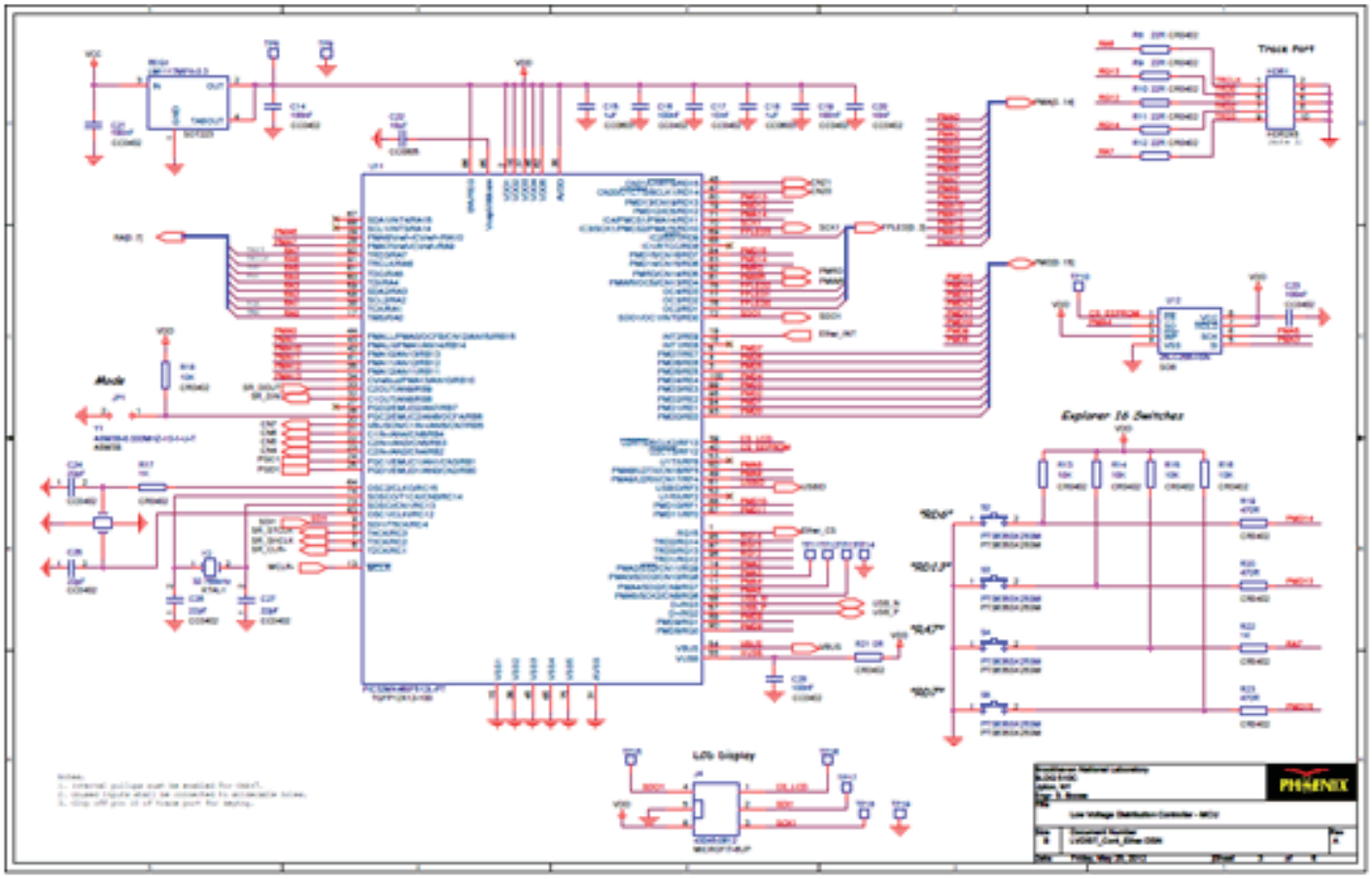

Figure 2: PIC32 and Port Assignments

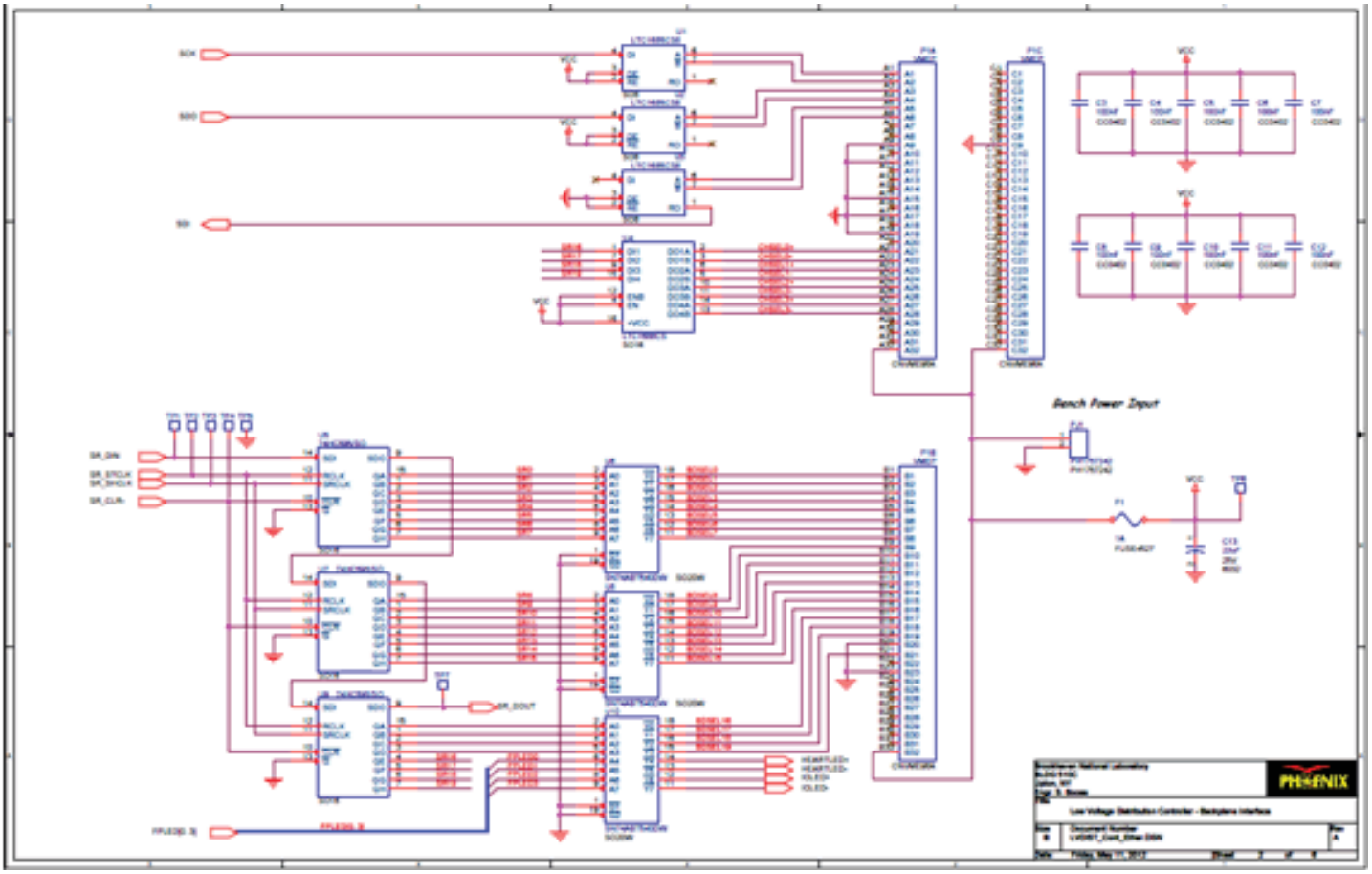

Figure 3: Board Select Shift Registers

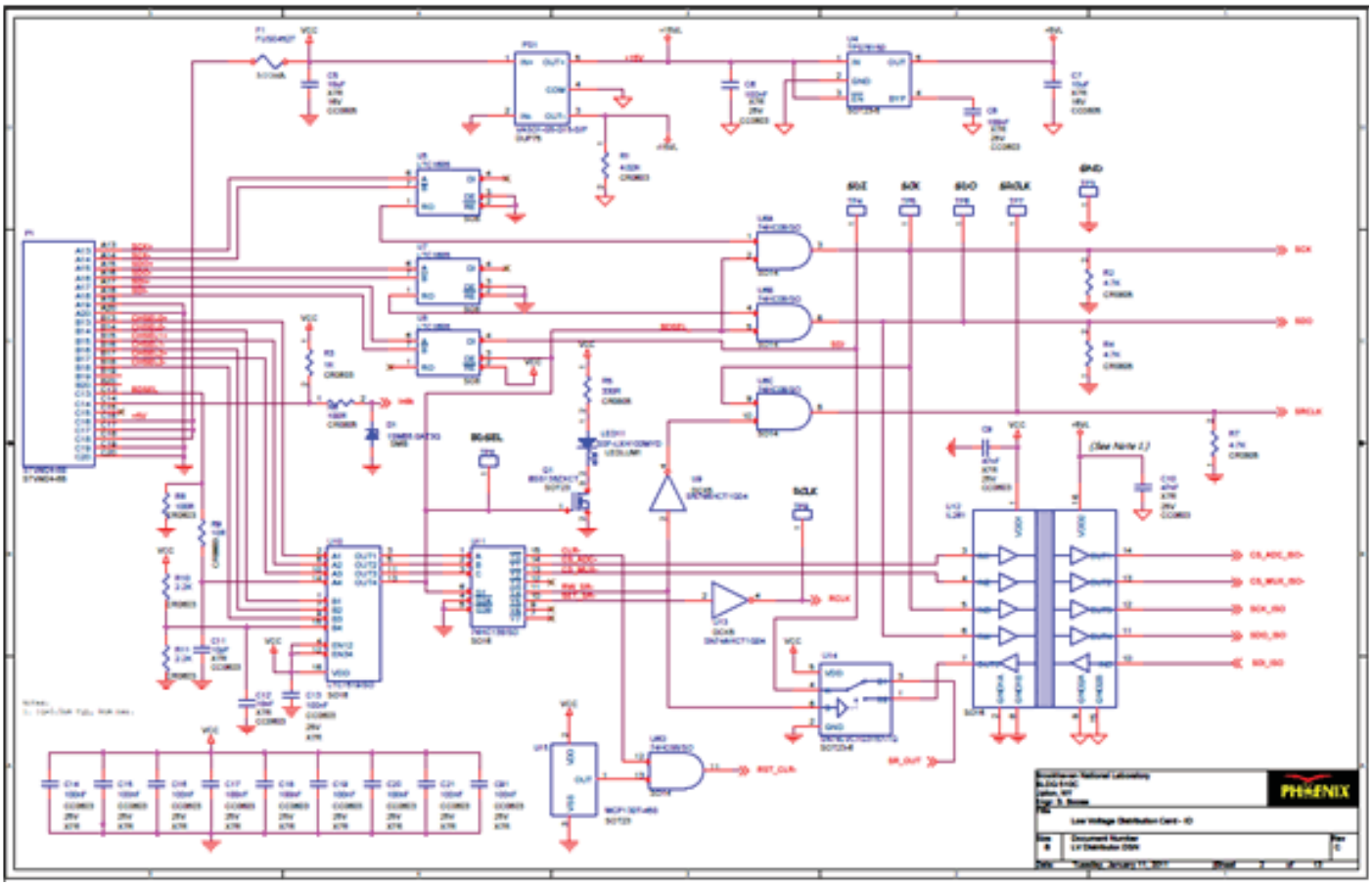

Figure 4: Command de-multiplexer, serial data control

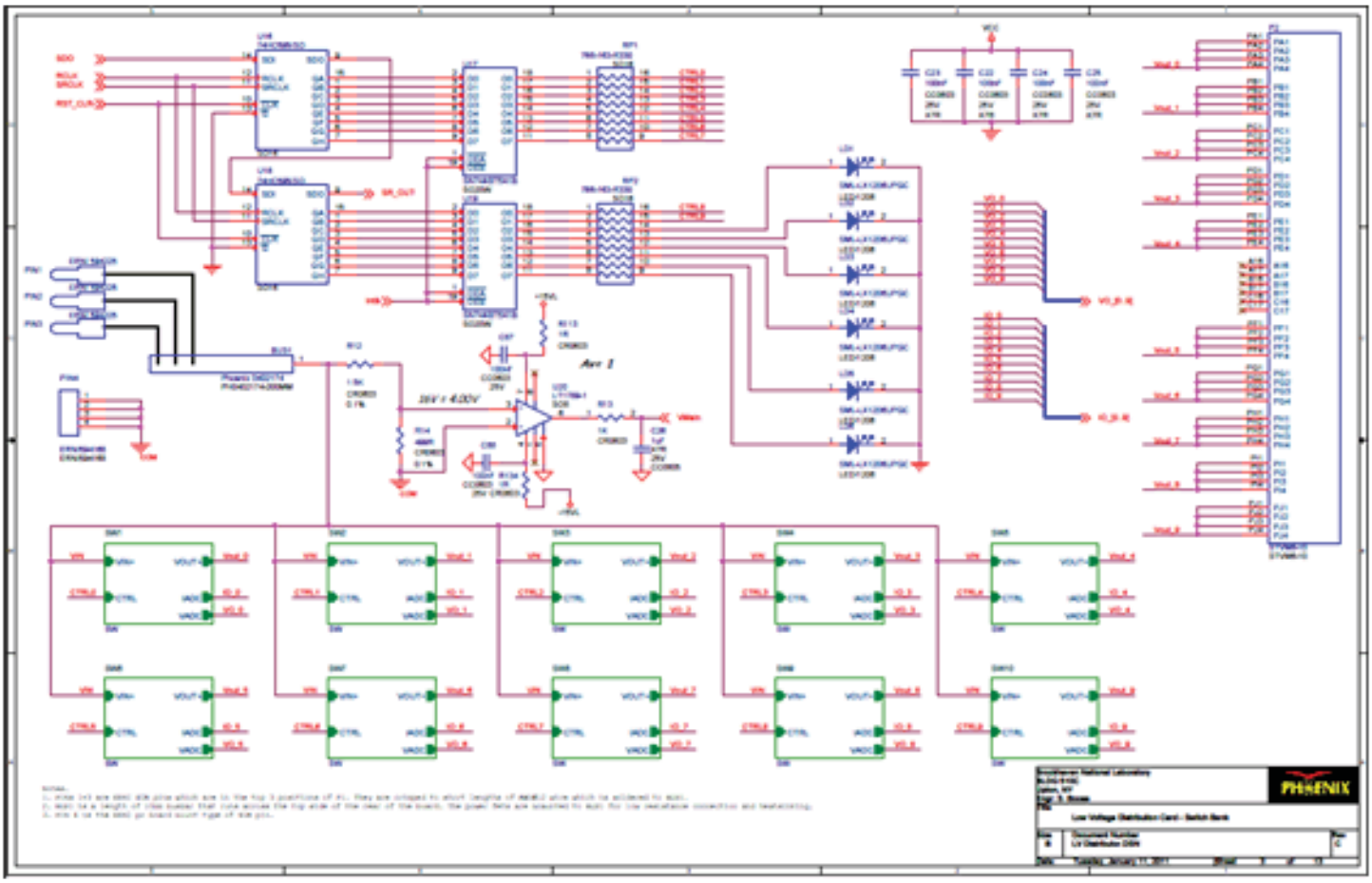

Figure 5: Channel Select Shift Registers, Power Distribution

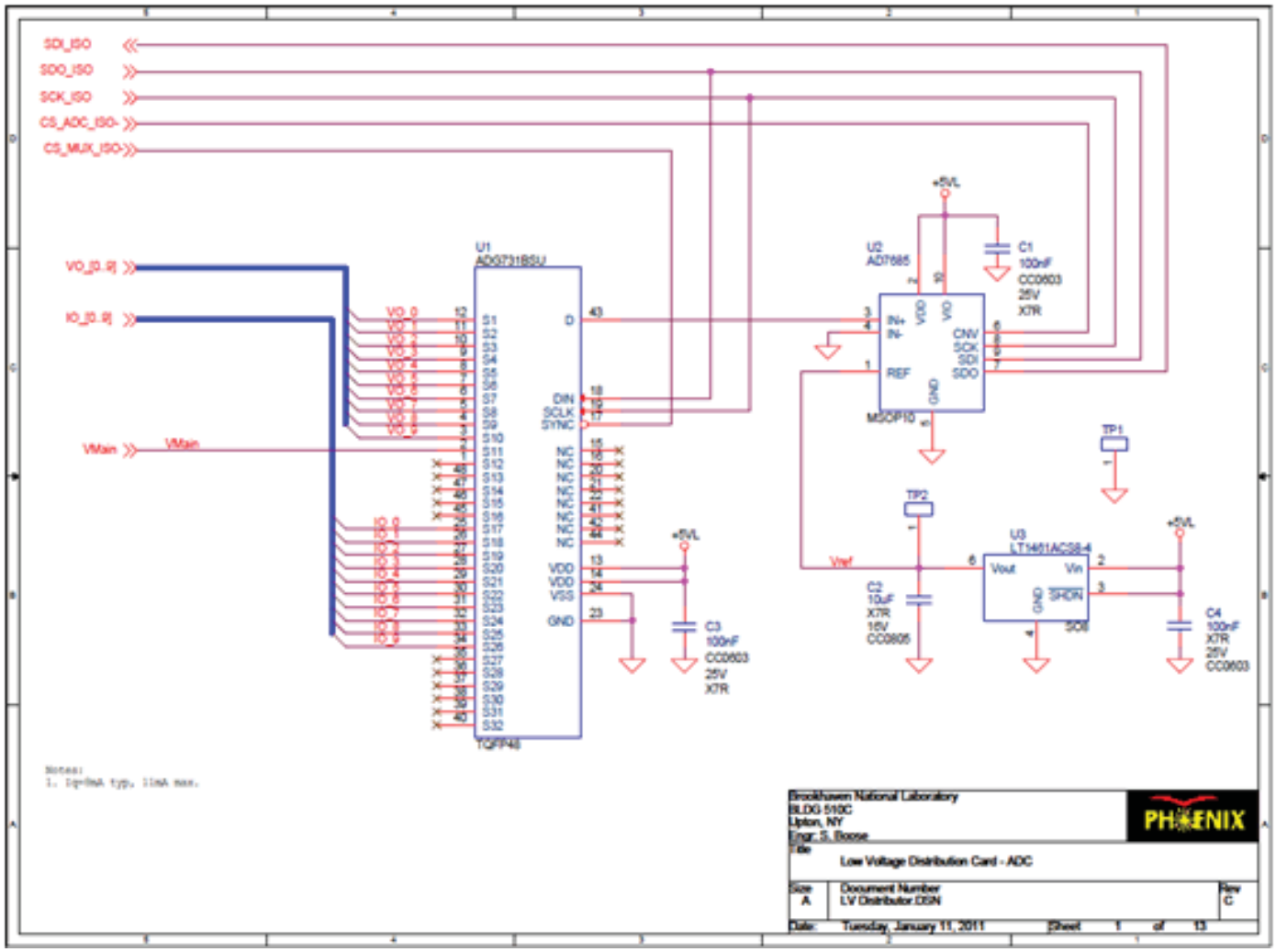

Figure 6: Analog Multiplexer, Analog-digital Converter

Comparison of the linearity of an energy dispersive detector with fluorescent ion chamber for x-ray spectroscopy

Ahmad Mohammad
Oregon State University, Oregon
Vincent Castillo
Brookhaven National Laboratory, Upton

ABSTRACT

To find the count rate limit of a photon counting detector when it starts deviating from the current integrating detectors, we need to compare the photon counting detectors with the current integrating detectors in the fluorescence mode of X-ray Absorption Spectroscopy. The results of the project shows that the count rate limit varies in a specific pattern with the width of the x-ray beam line, and this will enable us to predict the count rate limit at any width. Those results will help other scientists to more reliable data from vortex detectors in the future.

I. INTRODUCTION

Due to the importance of x-ray absorption spectroscopy in elemental and chemical analysis, different types of detectors are used to get the spectroscopy data such as an ion chamber, Canberra's Passivated Implanted Planar Silicon (PIPS) detector and a photon counting detector. In this experiment, we will compare the data taken from two of the detectors: PIPS detector and photon counting detector and find the count rate limit of the photon counting detector when it starts deviating from the PIPS detector.

The basic principle of these two detectors is the same as that of silicon drift detectors, a type of solid state detector where electron-hole pairs are produced as the beam goes through the detector. The main difference of our interest between the detectors is that the PIPS detector records electrical signals from individual interactions averaged together, forming a net current signal, while the photon counting detector record each individual quantum radiation that interacts with the detector.

The problem with the vortex detector is that it does not give reliable data at high counting rates. That's why we are going to find at what count rate the vortex detector will give reliable data.

II. METHODS

We will target a sample with an x-ray beam line and use the PIPS detector to get x-ray absorption spectroscopy data. The sample that is going to be used for the experiment is copper oxide. Than, using the same sample, we will use the vortex detector to get x-ray spectroscopy data. However, when we use the vortex detector we are going to vary the width of the beam line from 0.5 mm to 5 mm and get several data for each width. After that, using Athena software, the data for each detector will be transformed to k space. From the k space graph we will find out at which count rate the data overlaps. The transformation is done using the Extended X-ray Absorption Spectroscopy (EXAF) equation to find the oscillation as a function of wave number χ (k):

$$\chi(k) = \sum_j \frac{N_j f_j(k) e^{-2k^2\sigma_j^2}}{kR_j^2} \sin\left[2kR_j + \delta_j(k)\right]$$

where f(k) and δ(E) are scattering properties of the atoms neighboring the excited atom, N is the number of neighboring atoms, R is the distance to the neighboring atom, and σ^2 is the disorder in the neighbor distance. k is the wave number of the photon-electron and is found from

$$k = \sqrt{\frac{2m(E - E_0)}{\hbar^2}}$$

where E_0 is the absorption edge energy and is the electron mass.

We'll start with the beam line width of 0.5 mm. In figure 1, the data from PIPS detector and the data from the four channels of the vortex detector averaged together are compared. As we can see, the two data are very similar at low count rates in the k-space graph. However, the data from the four channels of the vortex detector start to deviate from the data from the PIPS detector, but not significantly, at some count rate.

III. RESULTS

When the beam line width was 0.5 mm, as it is shown in figure 1, the two data from the PIPS detector and Vortex detector deviate from each other and the count rates for the first, second, third and fourth channels were 53497, 52304, 50851, and 54602 respectively. When we increased the beam line width to 0.7 mm, we see in figure 2 that the two data overlap each other and the count rates for the first, second, third, and fourth channels were 71259, 70249, 66794 and 72585 respectively. Having increased the beam line width to 1 mm, the situation was similar to that of the 0.5 mm beam line width and the count rates for the first, second, third, and fourth channels were 80598, 79441, 75408, and 81979 respectively. With a beam line width of 1.5 mm (as shown in in figure 4), the two data were totally different due to the irrelevant noises caused by external factors. Thus, this measurement will be ignored. With a beam line width of 2.0 mm (figure 5), we see that two data also deviated from each other and the count rates for the first, second, third, and fourth channels were 162633, 160988, 149842 and 167422 respectively. The same thing happens with a beam line of width of 2.5 mm (figure 6) where the count rates for the first, second, third and fourth channels were 187011, 187718, 172755, and 195429 respectively. The same thing happened also with beam line widths of 3.0 mm, 3.5 mm, 4.5 mm, and 5.0 mm where for the 3.0 mm beam line width the count rates for the first, second, third, and fourth channels were 210059, 211716, 194263, and 222354 respectively; the 3.5 mm beam line width the count rates for the first, second, third and fourth channels were 233341, 232854, 212457 and 246306 respectively; the 4.5 mm beam line width the count rates for the first, second, third, and fourth channels were 264319, 265613, 239298, and 296332 respectively; and

for the 5.0 mm width the count rates for the first, second, third, and fourth channels were 276221, 279712, 249958, and 296332 respectively.

IV. DISCUSSION AND CONCLUSION

Since the only beam line width at which the data from the PIPS detector overlaps with the data from the Vortex detector is 0.7 mm, the vortex detector will work best at this width. Apparently up to about 70,000 counts / channel the Vortex detector is as good as PIPS detector. Although, more measurements should be made to increase the preciseness of the data in this experiment, we did not have enough time to do them.

V. ACKNOWLEDGEMENTS

I would like to thank my mentor Dr. Syed Khalid for helping and guiding me throughout my project. I would also like to thank my co-worker Wahaj Saleem for helping me with Athena software, as well as the staff at the National Synchrotron Light Source who have helped me with using the beam lines. I would also like to thank the U.S. Department of Energy, Office of Science for the unique opportunity they gave me here at Brookhaven National Laboratory. Finally, I would like to thank all the nice workers at the lab for their kindness.

VI. REFERENCE

D. C. Koningsberger, and R. Prins. *Xray Absorption: Principles, Applications, Techniques of EXAFS, SEXAFS, and XANES, in Chemical Analysis*. John Wiley & Sons, 1983. Print.

Knoll, Glenn. *Radiation Detection and Measurement*. 4th ed. John Wiley & Sons, 2010. Print.

M. Newville. IFEFFIT: interactive EXAFS analysis and FEFF fitting. Chicago: J. Synchrotron Rad., 2001. 322-324. Print.

B, Ravel, and M. Newville. *ATHENA, ARTEMIS, HEPHAESTUS: data analysis for X-ray absorption spectroscopy using IFEFFIT*. Chicago: J. Synchrotron Rad., 2005. 537-541. Print.

FIGURES

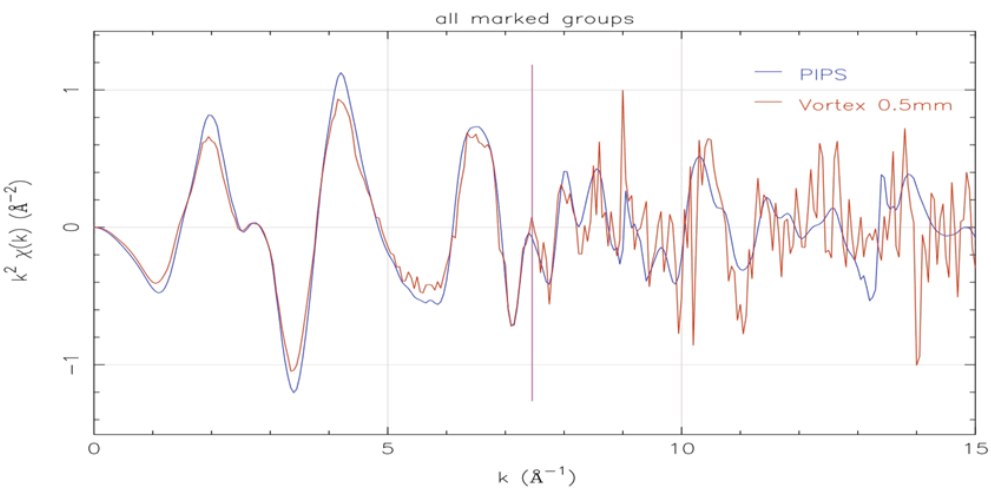

FIG. 1. Graph of the data from the PIPS detector and the data of the vortex detector with beam line width of 0.5 mm. The count rates for the first, second, third and fourth channels were 53497, 52304, 50851 and 54602 respectively.

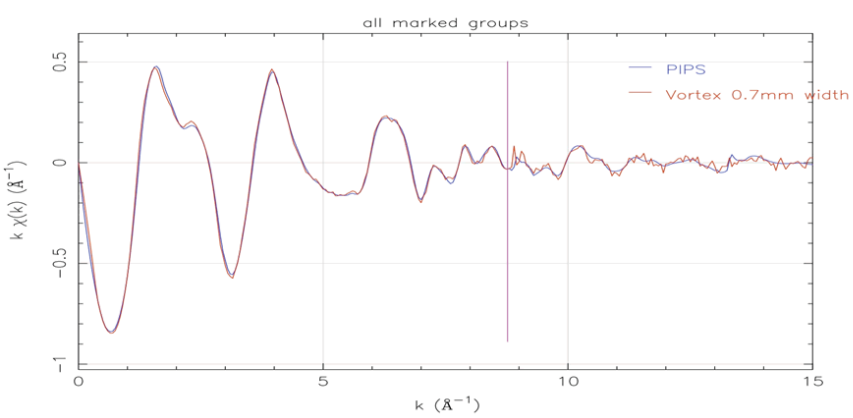

FIG. 2. . Graph of the data from the PIPS detector and the data of the vortex detector with beam line width of 0.7 mm. The count rates for the first, second, third and fourth channels were 71259, 70249, 66794 and 72585 respectively.

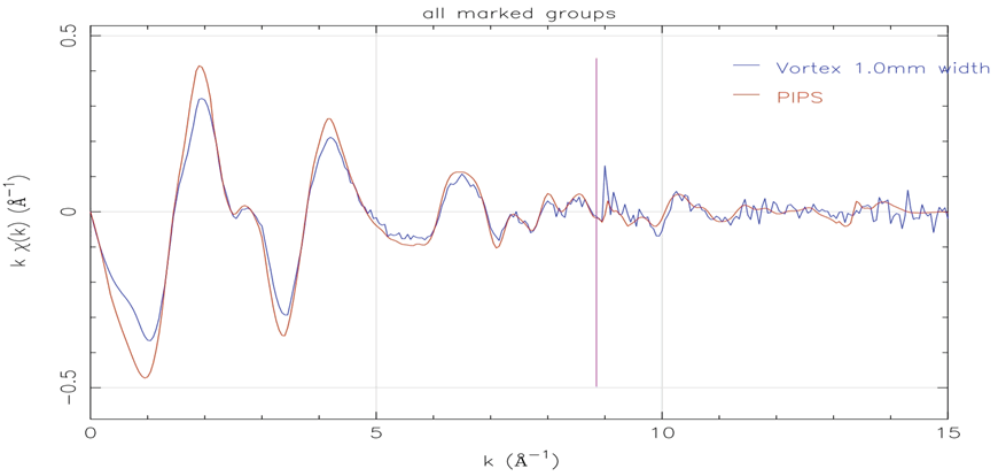

FIG. 3. Graph of the data from the PIPS detector and the data of the vortex detector with beam line width of 1.0 mm. The count rates for the first, second, third and fourth channels were 80598, 79441, 75408 and 81979 respectively.

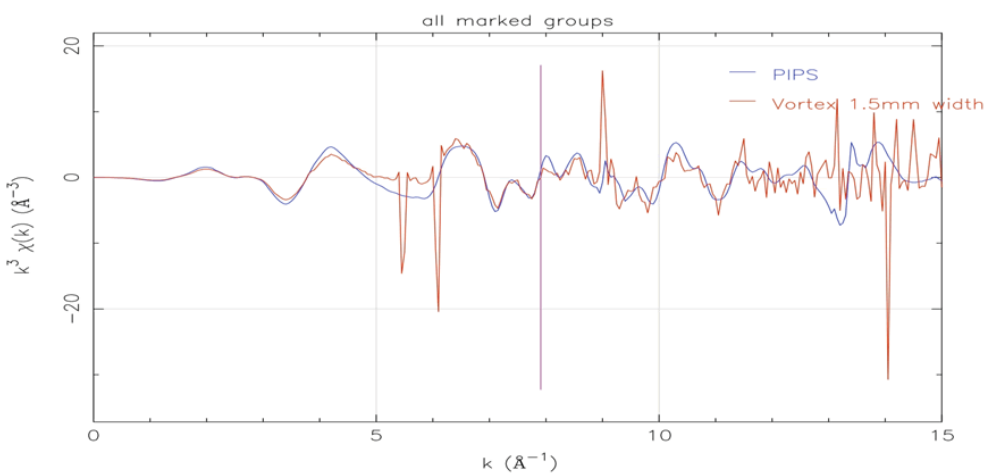

FIG. 4. . Graph of the data from the PIPS detector and the data of the vortex detector with beam line width of 1.5 mm. Due to the random noises, this measurement will be omitted.

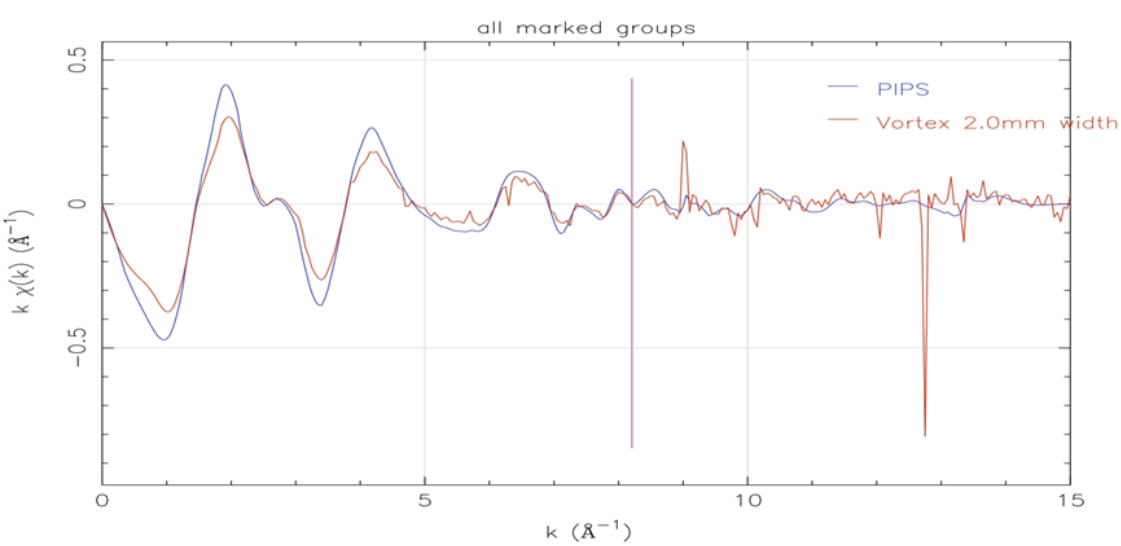

FIG. 5. . Graph of the data from the PIPS detector and the data of the vortex detector with beam line width of 2.0 mm. The count rates for the first, second, third and fourth channels were 162633, 160988, 149842 and 167422 respectively.

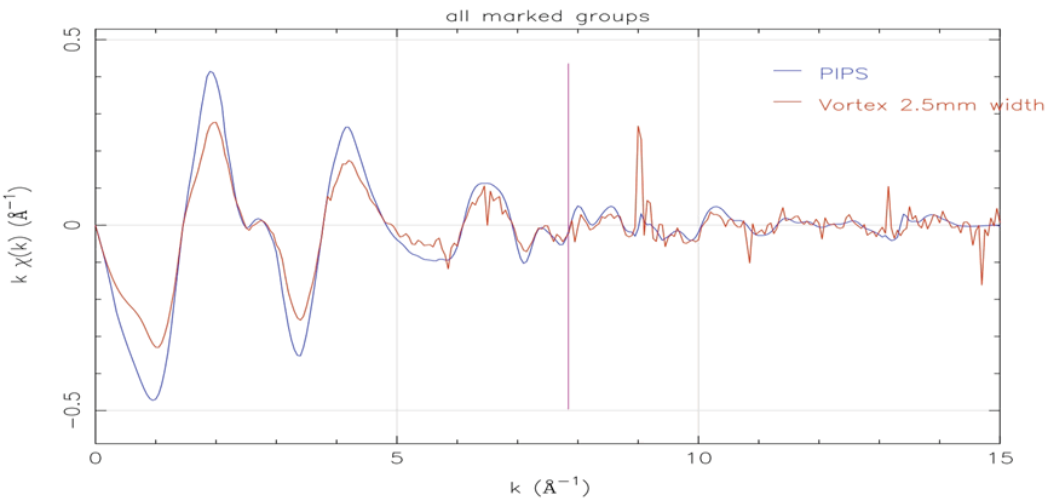

FIG. 6. . Graph of the data from the PIPS detector and the data of the vortex detector with beam line width of 2.0 mm. The count rates for the first, second, third and fourth channels were 187011, 187718, 172755 and 195429 respectively.

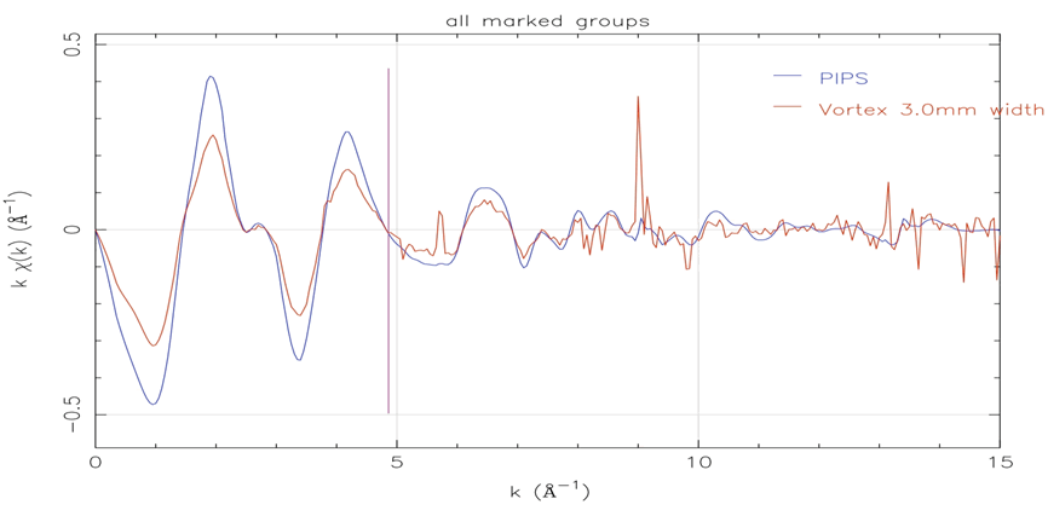

FIG. 7. Graph of the data from the PIPS detector and the data of the vortex detector with beam line width of 3.0 mm. The count rates for the first, second, third and fourth channels were 210059, 211716, 194263 and 222354 respectively.

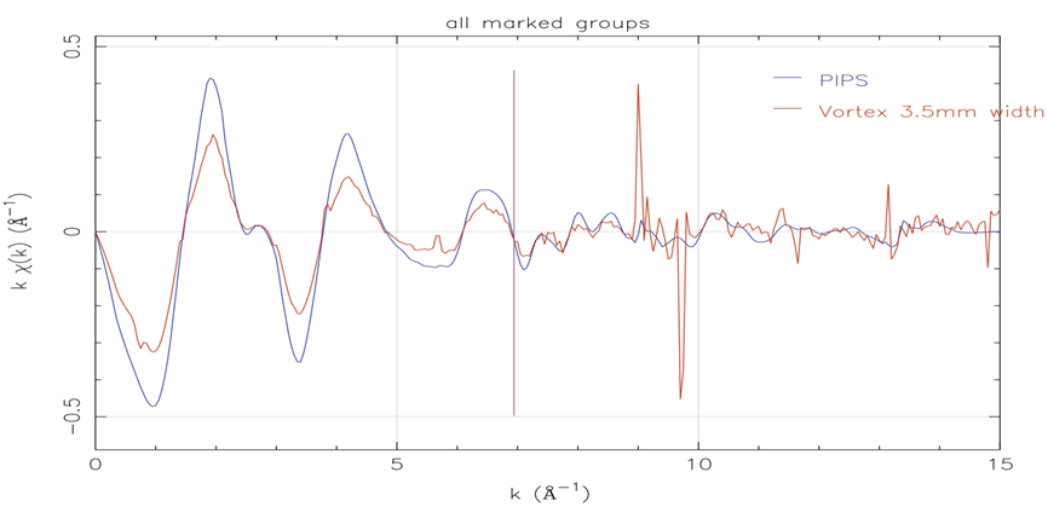

FIG. 8. . Graph of the data from the PIPS detector and the data of the vortex detector with beam line width of 3.5 mm. The count rates for the

first, second, third and fourth channels were 233341, 232854, 212457 and 246306 respectively.

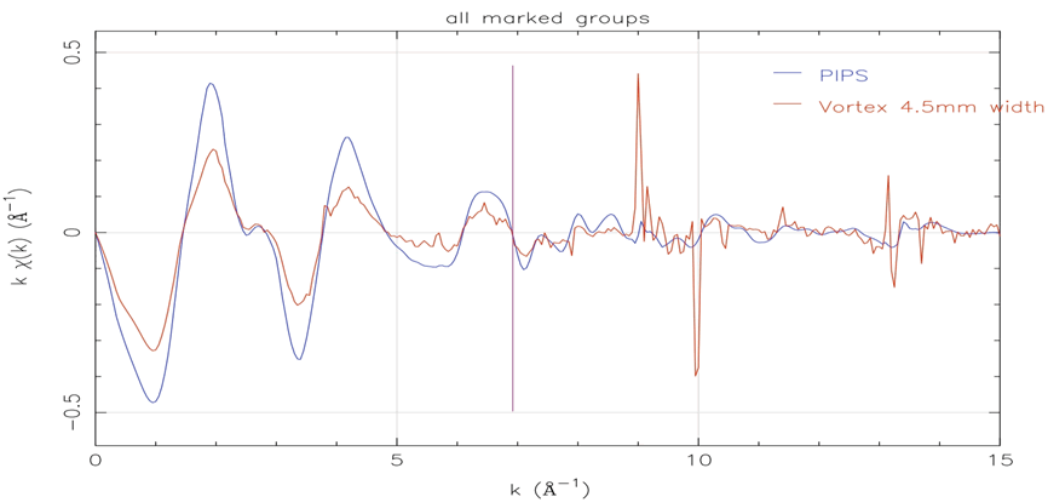

FIG. 9. . Graph of the data from the PIPS detector and the data of the vortex detector with beam line width of 4.5 mm. The count rates for the first, second, third and fourth channels were 264319, 265613, 239298 and 296332 respectively.

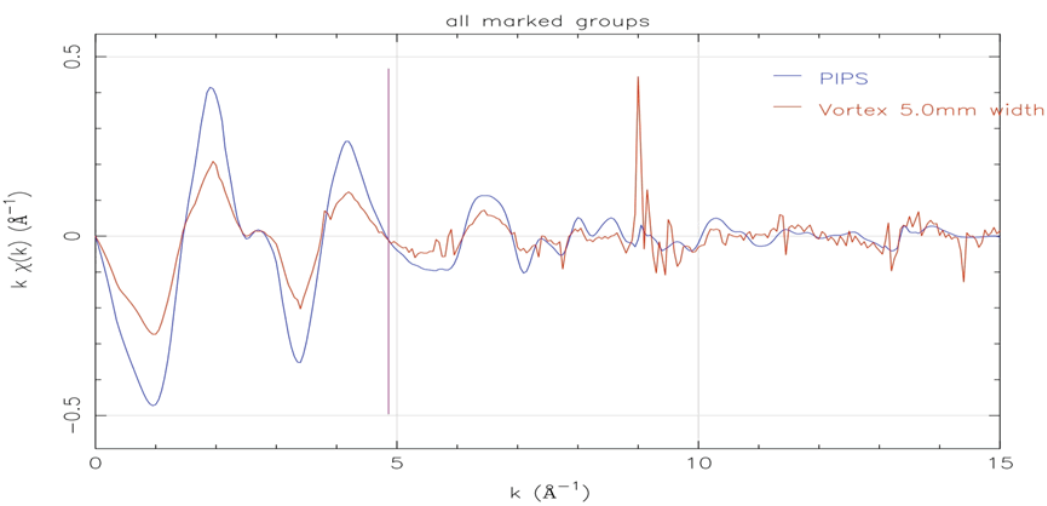

FIG. 10. . Graph of the data from the PIPS detector and the data of the vortex detector with beam line width of 5.0 mm. The count rates for the first, second, third and fourth channels were 276221, 279712, 249958 and 296332 respectively.

Brookhaven Atmospheric Tracer Sampler: Fabrication and Revision

Juan Mojica
Tallahassee Community College, Tallahassee, FL 32304
Adam Batley
Tallahassee Community College, Tallahassee, FL 32304
Lezou Dali
Stony Brook University, Stony Brook NY
April McCray
Tallahassee Community College, Tallahassee, FL 32304
John Heiser and Scott Smith
Environmental Sciences and Sustainable Technology, Brookhaven National Laboratory, Upton, NY 11973

ABSTRACT:

The Brookhaven Atmospheric Tracer Samplers (BATS) are being redesigned as the original, thirty-year-old units have become outdated, increasingly unreliable, and challenging to maintain. Further, the older internal electronic components are failing and replacement parts are increasingly difficult to find. The BATS units sample tubes, made from stainless steel, make it difficult to assess the integrity of the adsorbent (Ambersorb) and are difficult to rebuild and replace. Also, the old BATS units are based on an old air pumping technology that is difficult to adjust and does not hold the flow rate at an acceptable precision making it difficult to achieve high quality field data. In contrast, the new BATS units are based on current technology that will give a more reliable and flexible sampling unit. The stainless steel tubes have been replaced with glass tubes that can be easily assessed and/or replaced. They have a mass flow meter and pump controller which will result in accurate and precise flow rates over an operational range from 0 to 450 sccm. Every sample can be set with a specific start time, flow rate, and duration to allow for any kind of special circumstances. In addition, sampling data is logged for quality assurance and can be monitored in real time, locally on an LCD screen or via wireless internet. The new BATS units have on-board GPS for time synchronization and recording location information which is especially useful for coordinating multiple samplers.

Brookhaven Atmosphere Tracer Samplers (BATS) are being redesigned after thirty years. Due to the fact that the old BATS samplers are based on technology from the late 1970s and early 1980s, the units have become unreliable and also take a great deal of time to keep in good repair. In addition, the old BATS unit internal electronic components are failing and replacement parts are increasingly difficult to find. Further, the BATS units sample tubes are made from stainless steel which makes it difficult to assess the integrity of the Ambersorb and stainless steel sampling tubes are also difficult to rebuild and replace. Finally, the old BATS units are based on an old air pumping technology that makes it difficult to adjust the flow rate and also sustain the flow rate at an acceptable precision essential to achieving high-quality field data. In contrast, the new BATS units are based on current technology that will result in a more reliable and more flexible sampling unit that it uses glass, Capillary Adsorption Tube Sampler (CATS) tubes that can be easily assessed and, if need be, easily replaced. Also, the new BATS units will create electronic files containing all the important sampling data a project may require and have mass flow control which will result in accurate and precise sampling flow rates from 0 to 450 sccm, which means every sample can be set with a specific start time, flow rate, and duration to allow for any kind of special circumstances. Mass flow rate, temperature, and pressure are continuously logged for quality assurance and can be monitored in real time, locally on an LCD screen or via wifi. The new BATS units allow for GPS time synchronization and recording of location information. This is especially useful for coordinating multiple samplers. These are key requirements in terms of operation which can also encourage and promote science literacy.

Scientists at Brookhaven national Laboratory (BNL) are interested in how contaminants behave in very complicated urban canyon environments like New York City. The new BATS which BNL has revised and updated are currently in production. Our role was to assemble and test the new production type air samplers, which will be used during the summer of 2013 to collect and record air samples. We have been working on getting the parts ready before assembling them. This includes cutting, stripping, cramping, and soldering wires.

Each unit is equipped with wireless internet. This allows for remote control of each individual unit, remote calibration, wireless data collection, and allows for geolocation capabilities. The BATS units are smaller in dimension, lighter in weight, and waterproof due to the use of Pelican cases.

Glass sample tubes have replaced the previous metal sample tubes. Each has a unique barcode for ease classification. They are reusable, easier to replace, and allow collected samples to be processed faster. The previous visual output of ticker tape has been replaced with an LCD screen. This allows for real-time, less codified, viewing of output.

Previously the sampling rate, flow rate, and duration were programmed in advance and could not be altered without reprogramming the sampler. Now even the most tedious or intricate program changes can be made via onboard controls, LCD screen, or by way of wireless Internet, i.e. laptop, tablet, or smart-phone.

A mass flow meter and pump controller result in accurate and precise flow rates over an operational range of 0 to 450 sccm. Every sample can be set with a specific start time, flow rate and duration to allow for any kind of special circumstances. Sampling data is logged for quality assurance and can be monitored in real time.

The new BATS units have onboard GPS for time synchronization and recording location information which is especially useful for spatial analysis of collected data.

The overall design improvements allow for more sensitive testing, enhanced durability, and result in an easier to use air

sampler. Future experiments will greatly benefit from the higher sensitivity to life, smaller size, lighter weight, and waterproof enclosure.

Regarding the use for future work of the BATS

The beginning of the process of experimentation for future work will take place on the island of Manhattan, New York, in which Perfluorocarbon Tracers (PFTs) will be released from a centralized point on the island. PFTs are colorless, odorless compounds that consist of a carbon and fluorine atoms joined by covalent single bonds. These compounds are chemically inert, non-flammable, and have no biological effects. This process will help BNL better understand how an airborne compound moves through an urban area with consideration for elevation, wind speed, wind direction, weather conditions, time of day, and more; depending on the type of spatial analyses to be performed, all of these factors will be used BNL to better understand the "flow" or movement of particles through an urbanized environment due to buildings and other structural components, such as subway vents or sewers, that may affect the movement of compounds through the city landscape.

Another proposed experiment for future work is utilizing the BATS to locate, contain, and remove the airborne dielectric fluid sources in subway tunnels throughout Manhattan. By placing the BATS in subway tunnels, the BATS could act as passive sensors to alert transit authorities of the presence of dielectric fluid. The technology could even be specialized or slimmed down for similar airborne substance detection purposes.

While there are numerous benefits and impacts resulting from redesigning the Brookhaven Atmospheric Tracer Sampler, the primary focus has been creating a highly versatile and portable sampler that can stand the test of time, be repaired with ease, maximize accuracy of data, improve the data collection process, reduce data processing time, and serve as a catalyst toward future tracer sampler technologies.

The aforementioned design improvements positively impact BNL and subsequent studies. Utilizing a mass flow meter means samples will be taken with greater consistency and higher precision than previous samplers, resulting in more precise data. Wireless synchronization results in greater incorporation of time and spatial location in collected data. Wireless control results in greater operational flexibility for varying field conditions. The use of barcodes means less time processing samples. The use of glass for sample tubes instead of the previous metal sample tubes reduces sample corruption due to corrosion or galvanic response.

Overall, this focus on improvement results in a greater quality of collected data of interest to more than merely environmental sciences groups, government agencies, or disaster preparedness committees.

So after more than thirty years of unquestioning and faithful service the old BATS are finally being replaced by a lighter, sleeker, and more efficient design. These new designs will be more reliable and will allow for much less time being wasted on repair than their predecessors. The new internal electronic components will be more easy and simple to replace than ones of old and with the fact that the technology is newer the replacement parts will be much less of a hassle to acquire. With the switch from stainless steel collection tubes to glass collection tubes there will be a more efficient methodology of changing tubes out of the BATS and reusing the tubes without degrading the integrity of the Ambersorb used within the tubes. The redesigned models will have a more user friendly aspect that will allow the air pump technology to be more adjustable, allowing the flow rate to be more precise and adequate for whatever the users' need, which will allow for more accurate data from the field. With all of these improvements the new systems will be far superior than that of old, plus there will be new additions to the system such as LCD screens for more real time, quality assured data that can be seen in the field and Wifi capabilities that will allow users' to track the progress of experiments from a desktop, laptop, smart phone, or other hand held devices. Plus with GPS capabilities time synchronization and location information can be tracked and assessed more easily. With these additions and improvements upon the old BATS system operations, the encouragement and promotion of science literacy will help ensure America's security and prosperity through environmental means.

Manual calibration system simulations for the Daya Bay neutrino experiment

Alyssa Montalbano
Department of Physics, Applied Physics and Astronomy
Rensselaer Polytechnic Institute, Troy, New York 12180
Zeynep Isvan
Department of Physics
Brookhaven National Laboratory, Upton, New York 11973

ABSTRACT

The Daya Bay Neutrino Experiment searches for the disappearance of electron antineutrinos from the Daya Bay Nuclear Power Plant to measure neutrino oscillation parameters. The antineutrino's energy can be reconstructed through measuring the energy of the final state neutron in inverse beta decay (IBD). The antineutrino detectors identify electron antineutrinos by their characteristic IBD in the detector's active volume of Gadolinium-doped liquid scintillator. The Manual Calibration System (MCS) is an apparatus which can insert a radioactive source into the liquid scintillator at a large range of positions. By measuring the position dependent response to a known radioactive source, the detectors can be calibrated with great accuracy to improve the precision of the oscillation measurement. Simulated data is generated using software that studies the effect that the MCS's geometry and materials have on the detectors' signal. We analyze this data to predict the impact its deployment is expected to have on the oscillation measurement.

I. Why are we interested in Neutrinos?

Neutrinos are ellusive particles within the Standard Model of physics. They are electrically neutral and are known to have mass, which is not measured but is constrained to be small. They interact solely via the weak interaction, giving them a small probability of interacting with matter. There are three types, or flavors, of neutrinos (ν_e, ν_μ, ν_τ) and each is associated with a charged lepton of the same flavor: electron, muon and tau particles. While neutrinos have mass, each flavor does not have definite mass; instead, the mass eigenstates (ν_1, ν_2, ν_3) are mixtures of the flavor eigenstates. Neutrino flavor oscillation is the quantum mechanical phenomenon by which a neutrino created as one flavor can be measured some distance away to be a different flavor. When neutrinos are measured away from a single-flavored neutrino source, there is a non-zero probability that the measured neutrinos are not what is expected if the neutrino stayed in one type and did not mix with the other flavors, or *oscillate*. The probability of flavor change depends on the neutrino's energy and the distance it travels. Measuring the parameters that govern the oscillation allows us to answer fundamental questions about both neutrinos and the universe. All matter has corresponding anti-matter. Studying neutrino and antineutrino oscillation independently could help us understand the matter-antimatter imbalance. It is believed that matter and anti-matter were created in equal amounts during the Big Bang, but it is not fully understood why the universe that we see is dominated by matter. If neutrinos and antineutrinos behave differently, it could be the explanation for the matter-antimatter imbalance. Oscillation experiments have made progress measuring several properties of neutrinos with precision, but their masses remain unknown. In addition, the order of their masses, that is, if ν_3 is heavier or lighter than ν_2, is unknown. Measuring these remaining neutrino properties with precision not only answers questions about neutrinos but also allows us to search for new physics beyond the Standard Model.

II. A Neutrino Oscillation Search at Daya Bay

Neutrinos have an extremely small probability of interacting. In order to see interactions we need a large source of neutrinos and also a very large, dense target. These requirements are fulfilled in the Daya Bay experiment.[2] The source of electron antineutrinos are the Daya Bay Nuclear Power Plant (NPP) and Ling Ao NPP in Daya Bay, China. Figure 1 shows the layout of the experimental halls which house the water pool and the anti-neutrino detectors (AD).

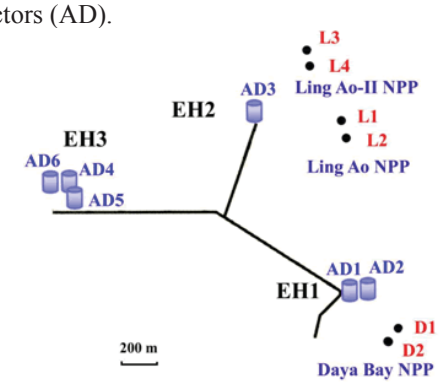

Figure 1: Layout of the Daya Bay experiment.[1]

There are two near halls, one near each NPP in order to detect the neuturino flux close to the source before traveling. Each houses two ADs. Situated about two kilometers away from both sets of nuclear reactors is a far hall with four ADs, which measures how many antineutrinos have remained as electron antineutrinos. This disappearence of electron antineutrinos is the signal that showcases neutrino oscillation. Neutrinos are detected by their inverse beta decay (IBD) which occurs when the antineutrino from the power plant interacts with a proton, producing a neutron and a positron.

$$\overline{\nu_e} + p^+ \rightarrow n^0 + e^+ \qquad (1)$$

The positron then annihilates with an electron nearby and creates two characteristic gamma rays (γ) each with 511 KeV of energy. The neutron then is captured by another atom. In the case of Daya Bay, it is ideally captured on a Gadolinium (Gd) atom, which releases another γ at about 8.05 MeV when it de-excites. We choose to use Gd because it is a neutron rich element as the 64th element in the periodic table, with isotopes that are in excess of 90 neutrons. This makes it a good, dense target for the antineutrinos to interact with. The first photons from the e^++e^- annihilation is a prompt signal, and the second photon from the Gd

atom is the delayed signal. The energy and position of the original antineutrino interaction is reconstructed from these signals' information. Inside of each hall there are multiple massive ADs. Inside of each AD is the fiducial volume of Gd-doped liquid scintillator where the neutrinos interact. The light created by IBD is captured by the photomultiplier tubes (PMTs) which cover the top, bottom and sides of the cylindrical ADs as homogeneously as possible.

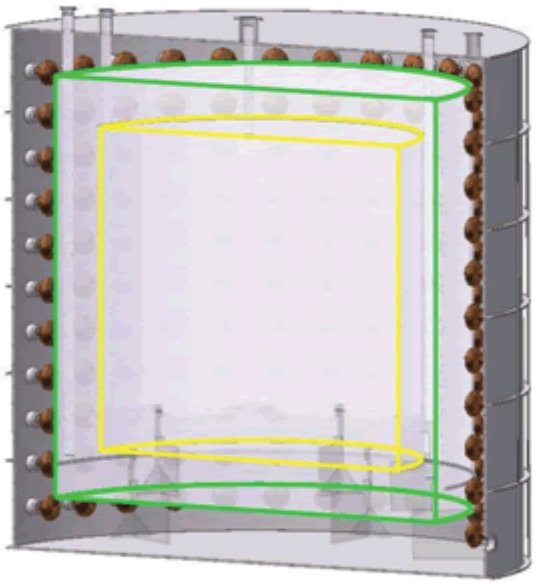

Figure 2: A cross section view of an AD. At the center is the Gd-doped liquid scintillator, right outside is the liquid scintillator between acrylic vessels and then the mineral oil with photomultiplier tubes are mounted on the inside walls of the stainless steel tank.[3]

The Daya Bay experiment has recently measured one of the oscillation parameters, which governs the oscillation from electron to muon and tau neutrinos, to be $\sin^2 2\theta_{13}=0.089 \pm 0.010(stat.) \pm 0.005(syst.)$.[4] The next step is to understand the detector's uncertainties better so that the errors can be reduced and a more precise value can be measured.

III. The Manual Calibration System

Because one of the main objectives for the Daya Bay experiment is to measure θ_{13} which is a small number, the measurements must be very precise. The experiment has very low systematic and statistical uncertainties but aspects of the experiment's uncertainties can be understood better and improved. It is important to have good resolution in obtaining the energy and understand the uncertainities in the energy so that we can improve our measurement of θ_{13}. The survival probability of an electron antineutrino traveling a distance L can be given as in equation (2) below.

$$P(\bar{\nu}_e \rightarrow \bar{\nu}_e); 1-\sin^2(2\theta_{31})\sin^2\left(1.27\frac{\Delta m_{13}^2 L}{E}\right) \qquad (2)$$

E is the antineutrino energy, and $\Delta m_{31}^2 = m_3^2 - m_1^2$ is a known variable that is measured precisely.[5] L, the distance from source to detector, is measured precisely from a geographical survey. Improving the precision of the energy measurement will improve the measurement of the parameter we search for, in$^2 2\theta_{13}$. Equation (3), is a simplified description of how Daya Bay measures the survival probability.[4] On the left hand side of this equation is the number of electron antineutrinos detected at the far detector ($N_n(E_\nu)$) over the number detected at the near detector ($N_n(E_\nu)$). These are the direct observables. On the right side of the equation is first the number of protons in the far detector ($N_{p,f}$) over the number in the near detector ($N_{p,n}$) as well as the distances of the near (L_n) and far (L_f) detectors from the source. These four variables were optimized when designing Daya Bay, and are measured precisely. This leaves the efficiencies of the detectors ($<\varepsilon(E_\nu,r)>$) and the survival rates of the antineutrinos ($P_{survival}(E,L)$) in the equation, which are both dependent on the antineutrino's energy. To improve the measurements we need to know the efficiency and energy scale. We do this by an energy calibration.

$$\frac{N_f(E_\nu)}{N_n(E_\nu)} = \frac{N_{p,f}}{N_{p,n}}\left(\frac{L_n}{L_f}\right)^2\left(\frac{<\varepsilon_f(E_\nu,r)>}{<\varepsilon_n(E_\nu,r)>}\right)\frac{P_{survival}(E,L_f)}{P_{survival}(E,L_n)} \qquad (3)$$

In order to reduce errors and uncertainties, the MCS is designed to create an energy scaling map inside of a detector in order to better understand and reduce the errors.[7] The MCS makes a direct measurement of the efficiency of the detector, thereby removing the uncertainty tied with the Monte Carlo simulations. If employed in an AD the MCS's benefits are to provide constraints on different models as well as to help us understand the neutron capture on Gd efficiency and energy non-linearity better. Certain mechanical efficiencies have been canceled out because we are comparing near data to far data. If the MCS is placed inside a near detector it can be useful for absolute reactor flux measurements, absolute neutrino rate and spectrum measurement.[8] The manual calibration system is designed to be able to scan the entire fiducial volume of the vessel. Physically, the system is made of two long arms. The vertical arm has another arm on a hinge that can rotate 90 degrees from being vertical to being perpendicular to the first arm. The horizontal arm has a fork that sticks to the opposite side of the source when perpendicular, and when vertical that locks into the other arm. When the horizontal arm is locked in the normal position, it can be rotated a full 2π.[9] The radioactive source is contained within a Teflon capsule that runs along the horizontal arm via a stainless steel wire that is connected to the two ends of the horizontal arm. The wire shortens and lengthens to change the radial positions. Its position can be controlled to within one centimeter. The materials are self contained to avoid contaminating the liquid scintillator.[9]

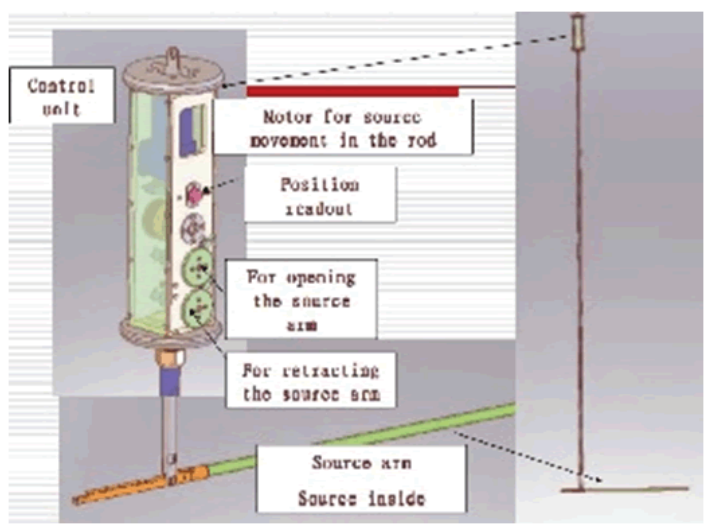

Figure 3: Diagram of the MCS. Included are close ups and labelling of the motor source which will be situated above the detector and used by the operators, as well as the source arm. [6]

Plutonium-13 Carbon (PuC) was chosen as the radioactive source because it has multiple lines to calibrate detected energy and gamma ray efficiency, as well as provide a tagged neutron source, allowing the efficiency of neutron capture on Gd to be studied. The PuC source enables three components of the neutron detection efficiency to be explored better, neutron-Gd (nGd) capture fraction, spill-out and delayed energy cut, thereby allowing the detector efficiency errors to be reduced.[10]

IV. Capture Ratio

The nGd capture ratio is a measure of how many neutrons are captured by the Gd atom compared to the total number of neutron captures. There are other possible capture targets for the neutrons, among them Hydrogen. When operating the MCS, there are even more possible targets introduced by the materials the MCS is composed of. There is a cut made to determine the nGd captures.[4] This cut must be well understood as to make sure that a significant portion of the signal is not being cut and that too much background isn't introduced. Since the pathway by which we obtain the count of antineutrino lies with the neutrons captured by Gd, we need to know how many out of all of the neutrons are actually captured so that we can reverse engineer how many neutrinos there were originally.

V. Simulations

First we simulated the geometry of the MCS inside of an AD to see simulated results and effects. This was done using Monte Carlo (MC) methods within a module created for the Nuwa.py system used for Daya Bay analysis. The simulation,[10] created by Wenquiang Gu, acts as a generator for the PuC source. The generator is highly attuned to provide an accurate gamma energy spectrum as well as a neutron energy spectrum. This was done at multiple positions inside the detector in order explore the position dependence. We chose these points,[11] seen in Table 1, to best illustrate and study the variation of detector response to changes in the position of the PuC source independently in the radial, angular and z directions. The center of the cylindrical detector is defined as the origin.

The simulation works by creating a neutron source and following the particles it creates as they move through the detector. This includes the physical geometry of the MCS and takes into account the physical, optical and other properties and how they will effect the particles passing by. This is possible because we inputed not only the geometry of the MCS but also the material it is made out of. This simulates what we call shadowing and optical effects of the MCS. PMTs receive their signal through photons, light, therefore there are literal shadowing effects that prevent light from following the path it would have taken without the MCS as a physical obstruction in the way. We are studying the effect that this has on the signal. Because the detector relies on light as its signals, the optical properties of the casing in which the light travels through can alter the path. The index of refraction for the arms can cause an effect when light passes through the arms. We study the effect this has on the signal. Now that we see the simulated result with the MCS, we remove it from our simulations so that we can understand what changes the MCS caused. We call these the bare source simulations. The module merely generates the PuC source and isn't blocked in any way by the MCS. This closely resembles what would happen during an actual physics run without the calibration unit. By comparing these simulations at the various points we can see the position dependent efficiency and the effects the MCS causes, the difference between the bare source and with the MCS. Since the PuC source is encapsulated, there are many new targets to capture the neutrons while it is in the detector. The acrylic, stainless steel and Teflon all provide possible capture targets which not only skew the Gd capture ratio but also cause false positives. These false positives can make it hard to interpret the data from the calibration run without understanding the processes from the MC simulations. Since it is a MC program, we have access to the true identity and properties of particles unlike in actual data. From this we isolated the real nGd captures, like what we aim to do with calibration and run-time data. Because the simulation outputs its data like a detector's readout we can make cuts on the simulated data like we would on real data. By doing this, we will be comparing the efficiency of tagging real nGd captures from an analysis of the readouts with real nGd captures known from the true MC information.

VI. Analysis and Results

Events that fit the following criteria were included in the analysis sample:

1. The particle was a neutron
2. The capture target was Gd
3. The signal was a delayed signal
4. If there was more than one particle seen in the time window, then the above criteria must apply to at least one particle

The first step was to identify the neutrons that we knew were really neutrons according to the Monte Carlo (MC) truth information provided. Furthermore, we required that the simulation saw that the neutron was captured on Gd using the MC truth information. We made time cuts in order to ensure that the interaction seen is the delayed signal. All graphs included at least 100,000 simulated events and were time-scaled to one minute of runtime. The events were simulated in cylindrical coordinates with ($r(mm)$,

r (mm)	φ(°)	z (mm)	r (mm)	φ(°)	z (mm)	r (mm)	φ(°)	z (mm)
0	0	0	300	22.5	0	600	22.5	1350
120	22.5	0	300	112.5	0	600	22.5	500
300	22.5	0	300	202.5	0	600	22.5	0
600	22.5	0	300	292.5	0	600	22.5	-500
1000	22.5	0				600	22.5	-1350
1350	22.5	0						

Table 1: Points at which the simulations were run, with the origin at the center of the detector. Chosen to study the effects of varying the radius, angle and height of the source independently.

φ(°),*z*(*mm*). Multiple points were chosen to clearly illustrate the difference between with the MCS and without the MCS (i.e. bare source). In Figure 4, we show these selections for the bare source for three different sets of data which highlight the radial, angular and height dependences. Next, we show the comparisons for the same cuts with the MCS, seen in Figure 5. Different radii can be found in Figure 6, different angular positions can be found in Figure 7 and different depths can be found in Figure 8. The nGd capture ratio was calculated for various positions with the MCS simulated. This was done by calculating the fraction of IBD events selected with the above selection and fall between 6 MeV to 12 MeV to the entire spectrum. The results can be found in Table 2.

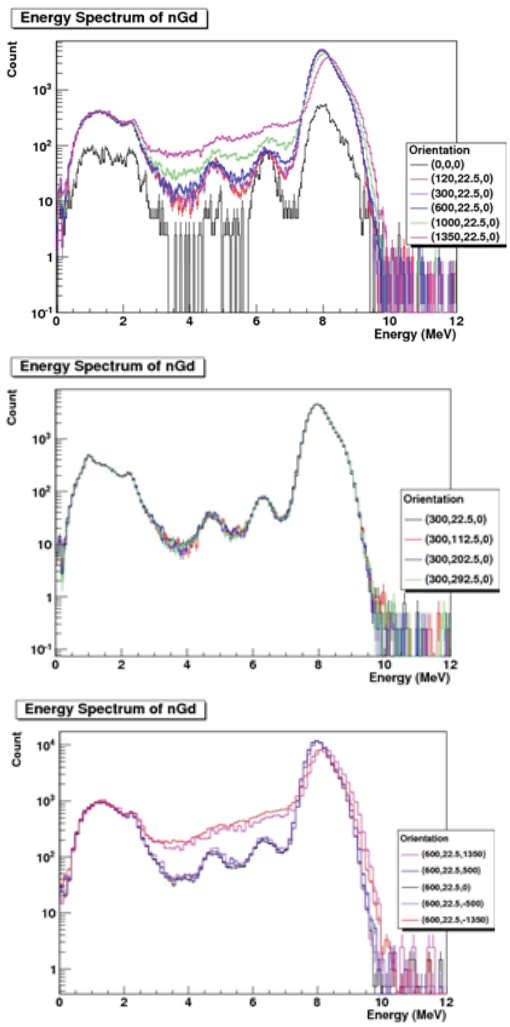

Figure 4: nGd captures based on MC truth information for a bare PuC source. Done for varying radii (top), angles (middle) and depths (bottom).

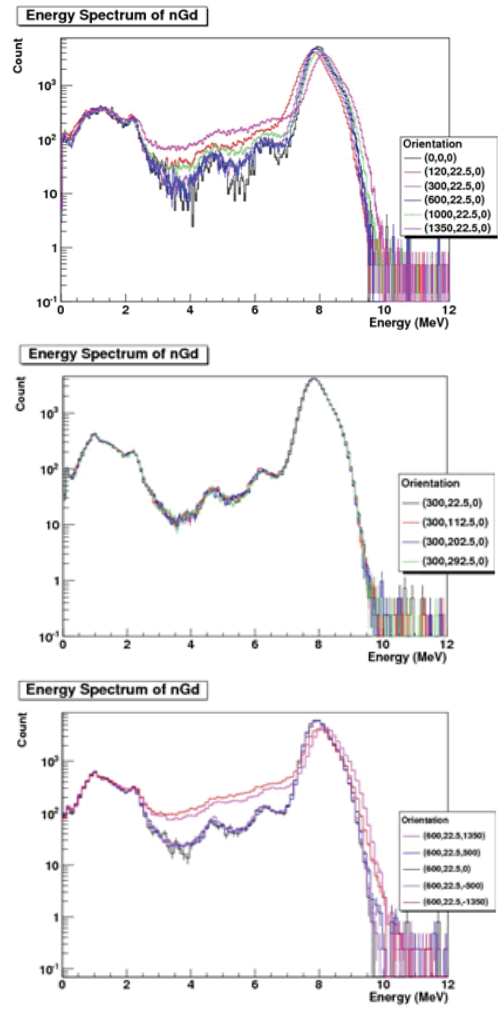

Figure 5: nGd captures based on MC truth information for a PuC source inside the MCS. Done for varying radii (top), angles (middle) and depths (bottom).

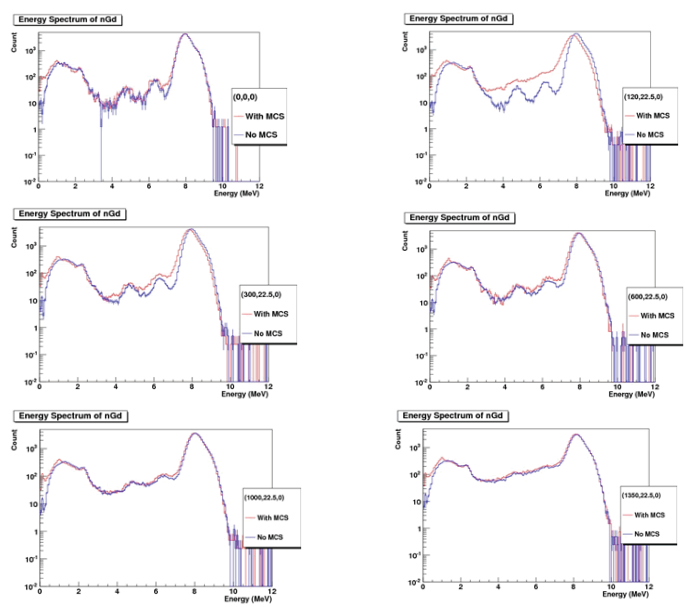

Figure 6: Comparison of the energy of nGd captures with and without the MCS at various points in the detector with varying radial positions. Positions are in cylindrical coordinates, left to right, top to bottom: (0,0,0), (120,22.5,0), (300,22.5,0), (600,22.5,0), (1000,22.5,0), (1350,22.5,0). Red is with the MCS, blue is without.

VII. Discussion

Certain trends can be concluded from the graphs. The data is inconsistent with any angular dependence. The data is consistent, however, with a radial dependence. As the radius is moved out further from the center of the detector, the energy peak in the spectrum for nGd captures, which should be centered at 8.05 MeV, shifts towards higher energy and spreads out with increased width. There are fewer captures when at the extremes of the detector, as well as when the source is partially covered by the MCS at r = 120 mm. This also applies to the extremes of the detector in the z direction. There are some errors involved in isolating true neutrons with the simulation. Our method relies on delayed signals and there can be some accidental coincidences when more than one event is recorded in the same time window. This is an expected error because PuC is a very active source. For this study, we made use of a combination of truth and data selection vari-

nGd capture ratio with MCS	Percent Difference	Position (r(mm), ϕ (°), z(mm))
.573 % ± 0.170 %	0.7 %	(0,0,0)
.738 % ± 0.085 %	0.7 %	(120,22.5,0)
.590 % ± 0.079 %	1.4 %	(300,22.5,0)
.636 % ± 0.140 %	0.8 %	(600,22.5,0)
.988 % ± 0.082 %	0.6 %	(1000,22.5,0)
.912 % ± 0.092 %	1.0 %	(1350,22.5,0)
.590 % ± 0.079 %	1.4 %	(300,22.5,0)
.696 % ± 0.079 %	1.4 %	(300,112.5,0)
.548 % ± 0.079 %	1.4 %	(300,202.5,0)
.628 % ± 0.079 %	1.5 %	(300,292.5,0)
.636 % ± 0.140 %	0.8 %	(600,22.5,0)
.300 % ± 0.080 %	1.0 %	(600,22.5,500)
.171 % ± 0.080 %	1.1 %	(600,22.5,-500)
.444 % ± 0.090 %	0.8 %	(600,22.5,1350)
.400 % ± 0.094 %	1.2 %	(600,22.5,-1350)

Table 2: The nGd capture ratio for the various points with the MCS including the percent difference from the bare source simulation. The position is given in cylindrical coordinates.

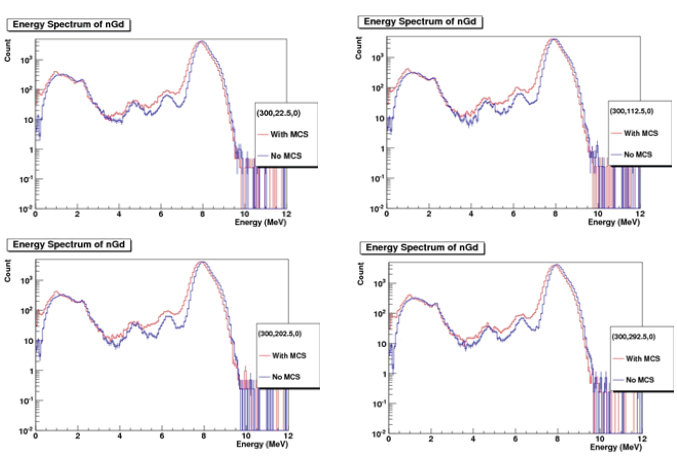

Figure 7: Comparison of the energy of nGd captures with and without the MCS at various points in the detector with varying angular positions. Positions are in cylindrical coordinates, left to right, top to bottom: (300,22.5,0), (300,112.5,0), (300,202.5,0), (300,292.5,0). Red is with the MCS, blue is without.

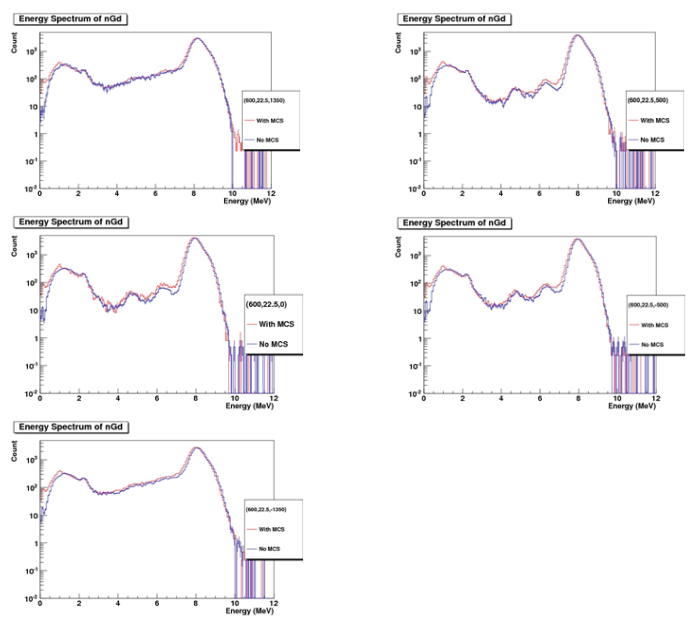

Figure 8: Comparison of the energy of nGd captures with and without the MCS at various points in the detector with varying depths. Positions are in cylindrical coordinates, left to right, top to bottom: (600,22.5,1350), (600,22.5,500), (600,22.5,0), (600,22.5,-500), (600,22.5,-1350). Red is with the MCS, blue is without.

ables. We knew the particle was a neutron and the capture target was Gd because of the Monte Carlo truth. The delayed signal, however, is in the form of data from the read-out of the detector. We made an energy cut of IBD candidates between 6 MeV to 12 MeV to isolate nGd captures, and they were divided by all events to get the nGd fraction. In this situation, the nGd capture ratio in an ideal world would be 85%.[1,4] Instead, we are in a real world and we look for the similarities of this fraction between with and without the MCS. We want them to be close, to show that we understand the effects the MCS can have and to be confident in our results. When we calculated the nGd ratio for the simulations we found that in general ratios with the MCS are a little bit smaller than without the MCS. This is expected because the MCS introduces more materials that causes more non-Gd captures than bare. There was never a percent difference between the two scenarios that exceeded 1.5%. This leads to our conclusion that the shadowing or non-Gd capture effect of the MCS is not prohibitively large, meaning that the data from MCS deployment will indeed be useful and improve our calibration.

VIII. Future Work

The MCS is scheduled to be used in one detector for approximately 30 days of running this summer.[12] In order for its deployment to be fully utilized, we need to better understand this difference in nGd at the different positions. That way, the calibration can depend on where in the detector the interaction occurred. We aim to repeat these results without making use of any information that the MC provides that the data does not. We aim to make a good set of selection criteria that will come as close as possible to how well we can do with MC. When are satisfied with the selection we can apply it to the actual physics calibration run with the MCS and be confident of our results.

IX. Acknowledgments

I would like to thank my wonderful mentor, Zeynep Isvan, for hosting me this summer. Many thanks to the Department of Energy for funding the SULI program and to the Brookhaven National Laboratory's Office of Educational Programs for their assistance and making sure the program ran smoothly.

X. References

[1]F.P. An, et al., "A side-by-side comparison of Daya Bay antineutrino detectors," arXiv:1202.6181

[2]The Daya Bay Collaboration, Technical Design Report (v2), (2008)

[3]The Daya Bay collaboration, A Precision Measurement of the Neutrino Mixing Angle θ_{13} Using Reactor Antineutrinos At Daya Bay (2006)

[4]F. P. An et al., "Observation of electron-antineutrino disappearance at Daya Bay," Phys. Rev. Lett. 108, 171803(2012) arXiv:1203.1669

[5]P. Adamson et al., "Measurement of the neutrino mass splitting and flavor mixing by MINOS," Phys. Rev. Lett., vol. 106, p.181801, 2011

[6]The Daya Bay collaboration, Overview of the manual source deployment system, (2011)

[7]J. Liu, "Physics Rationale Behind the Manual Calibration System," Daya Bay DocDB-6174

[8]J. Liu, "Reconsideration of physics cases for MCS," Daya Bay DocDB-7790

[9]X. Ruan, "Manual calibration system engineering drawings," Daya Bay EngDB-249

[10]W. Gu and J. Liu, "PuC source studies," Daya Bay DocDB-6700.

[11]J. Liu, "Proposed scanning points in MCS dry run," Daya Bay DocDB-7892

[12]H. Band et al., "Joint Schedule for Summer Shutdown," Daya Bay DocDB-8210

[13]D. Motta, "Search for the θ_{13} neutrino mixing angle using reactor anti-neutrinos," arXiv:hep-ex/0702003v1

Designing the hadron calorimeter

Patrick Montalto
College of Applied Sciences, Stony Brook University, Stony Brook, New York 11794
Don Lynch
Nuclear Physics, Brookhaven National Laboratory, Upton, New York 11973

ABSTRACT

The Pioneering High Energy Nuclear Interaction Experiment (PHENIX) consists of using the Relativistic Heavy Ion Collider (RHIC) to collide particles at speeds near those of the speed of light. The PHENIX experiment has been currently operating for more than a decade and serves to help researchers develop a better understanding of the elementary particles that make up matter. A new design was recently proposed, called sPHENIX, or "Super PHENIX." The main body of work that I conducted at Brookhaven National labs consisted of designing a newly proposed detector for the PHENIX/sPHENIX experiment. This design will consist of a set of new detectors that will greatly increase the ability of PHENIX to detect particles. This proposed set of upgrades is currently in the early stages of development. One of the new detectors proposed is the hadron calorimeter. This device records the energy associated with hadrons, particles that are tracked after a collision in the RHIC. The device consists of a series of steel plates oriented in a circular fashion. This circular plate formation contains scintillating material, special material that will detect the presence of hadrons after a beam collision. The scintillating material is to be wedged between steel plates and will completely encompass the interaction point of the beams. It was necessary to design a detector that would be hermetically sealed. This was needed to avoid any particles from being undetected. Therefore, the geometry incorporated with designing such a device is complex. The main portion of my work involved designing the proper way to produce, construct, and support the hadron calorimeter and the other proposed sPHENIX detectors. CAD software was used to design and analyze the proposed design. Various design iterations were done to aid in the future development of the calorimeter and it's supporting structures.

The PHENIX experiment has been running for over a decade. It is one of the largest of four experiments that have taken data at the Relativistic Heavy Ion Collider.

PHENIX is an exploratory experiment for the investigation of high energy collisions of protons and heavy ions. The experiment is specifically designed to measure direct probes of the collisions such as muons, photons, and electrons. The main goal of PHENIX is to discover and study a newly identified state of matter called the Quark-Gluon Plasma.

Recently, a series of massive upgrades for PHENIX were proposed. This series of upgrades is called "Super PHENIX," or sPHENIX. One component proposed for sPHENIX is a new particle detector, the hadron calorimeter.

Calorimeters are a fundamental device in the study of particle physics. Their main function is to measure the energy associated with particles. When particles enter the calorimeter, a particle shower is usually initiated. The energy of these particles is then deposited in the calorimeter. This data is collected and then measured. A calorimeter can be designed to measure the entire containment of the particle shower or just a sample. Calorimeters work by using the total absorption of particles to measure the energy and position of the incident particles or jets. The calorimeter will absorb the particles, resulting in cascades of interactions. These are called showers. A majority of the incident particle energy is subsequently converted into "heat." However, no temperature is measured in particle detectors. Characteristic interactions with matter, such as atomic excitation and ionization, are used to generate a detectable effect via particle charges.

Hadron calorimeters are designed to measure particles that interact through the strong nuclear force. These particles, called hadrons, are particles made of gluons of quarks. Examples of such particles include protons, neutrons, pions, and kaons. Hadron calorimeters also provide indirect measurement of the presence of particles like neutrinos and other non-interacting and uncharged particles.

The hadron calorimeter finds the particle's position, energy, and arrival time using the layers of steel as an "absorber" and fluorescent, "scintillator" materials, producing a rapid light pulse when it passes through. Optic fibers then collect up the light produced and feed it into the readout boxes where the photodetectors amplify the signal.

There were significant obstacles when attempting to design the hadron calorimeter. It was important that the designs were structurally sound while still meeting the physics requirements of the experiment it will be used in. The high precision required with these particle physics experiments increases the difficulty of satisfying these requirements. Computer-aided design software was used to produce design iterations for evaluation. These designs were analyzed and crucial to the development of the hadron calorimeter. Design constraints included cost, size and spacing, and ease of fabrication and assembly. Some of these, including cost and fabrication, required a specialists input.

While preliminary design work was done, further design iterations are still required, as is comprehensive stress analysis to verify that the designs are capable of being assembled so that they can also support the inner devices of the sPHENIX experiment.

There were many design constraints when working on the hadron calorimeter. In order to account for these constraints during the design process, it was necessary to have discussions with other technicians, engineers, and scientists working on the calorimeter. This process was critical to the development of my final design iteration. Limited materials were necessary to begin work on designing the components of the hadron calorimeter. A computer with Autodesk Inventor software provided all the necessary tools. Inventor was used to design and draft the outer support structure and the structures that would assemble the calorimeter. Inventor allowed one to produce drawings that were sent off to steel manufacturers. Many visual aids and tutorials were used and provided help when attempting to relearn the program and develop an understanding of how to produce drawings for engineering design and manufacturing. This would provide the insight needed to properly manufacture and assemble the proposed design, as well as develop an understanding for the associated cost. Having a manufacturer's opinion on a design is crucial. Their insight and knowledge of the material and its production can be the difference between finalizing a design or creating a completely new one. Specifically, Atlas Tool and Die, based out of Illinois, was contacted. They had done work for PHENIX and other projects at

Brookhaven National Laboratory earlier; therefore, their reputation was one of excellence.

It was necessary to create support for the entirety of the sPHENIX experiment. This includes the hadron calorimeter itself, the electromagnetic calorimeter, the VTX, and the solenoid magnets. These devices take up a large volume and an equally large mass. The adjacent plates, both the inner and outer segments, of the hadronic calorimeter had to be connected. Another design constraint was allowing enough clearance on the outer and inner portions of the calorimeter. There will be cables and readout devices mounted on these surfaces, so it was important to develop a structure that saved space. Lastly, the calorimeter needed to be modular. This means it needed to be capable of being taken apart with ease and allow people to access what is inside, such as the electromagnetic calorimeter or the VTX, during maintenance as well as allow access to the inner parts of the sPHENIX experiment, such as the solenoid magnets.

It was also important to develop an understanding of how to manufacture the plates and support structures. Drawings were sent off to a steel company that would analyze the structure and determine the most affordable way to meet the standards associated with the experiment. One of the fabrication methods hypothesized involved extruding a blank of the overall shape of the four hadron calorimeter plates, where a wire EDM would be used to cut the slots in between them. Creating the plates individually was also discussed; however, welding would have to be used to join the inner, outer, and adjacent plates together. While possibly more cost-effective, the structural effects and anomalies created through welding all of these plates would compound over the entirety of the plate assembly and inhibit our ability to meet specific tolerances.

Multiple design iterations yielded the design seen to the left. The initial designs consisted of large brackets that connected each group of four plates. However, these plates took up too much outer and inner surface area with not enough clearance for the readout devices. This design then evolved into a new design, one allowing more clearance and having an outer support structure. However, the spoke design was too intricate and unnecessarily complicated and limited access to the top of the device from multiple angles. This is when a staggered connector design was implemented. Also introduced was a connector with simply one "spoke" that would connect to an outer support structure, saving both space and material.

PHENIX has operated at Brookhaven National Laboratory for over a decade. "Super" PHENIX will be implemented toward the latter half of this decade and consist of many upgrades to the existing system. It will nearly double the efficiency in recording particle showers and interactions and will be of great benefit to the scientific community and toward the understanding of the quark-gluon plasma – the superfluid being examined currently by PHENIX. The hadron calorimeter is a critical component of this upgrade and the functionality of the sPHENIX experiment heavily depends on the capabilities of the hadron calorimeter and the support structure to properly contain the experiment assembly.

Acknowledgements

I personally want to acknowledge Don Lynch, Rich Ruggiero, Melvyn Morris, and Mike Stegman for all of their insight and guidance during this process.

Development of a parametric model for the Super Pioneering High Energy Nuclear Interaction Experiment hadronic calorimeter scintillator design and fabrication

Ammar Morgan
Physics Department, Stony Brook University, Stony Brook, NY 11790
Don Lynch
Physics Department, Brookhaven National Laboratory, Upton NY 11973

ABSTRACT

This project, the Super Pioneering High Energy Nuclear Interaction Experiment (sPHENIX) is the intended successor to the Pioneering High Energy Nuclear Interaction Experiment (PHENIX) project. The sPHENIX project will contain upgraded hardware intended for the detection of sub-nuclear particle resulting from heavy ion collisions. As a researcher/designer, my responsibilities included 3-D AutoCAD Inventor drawing and design, engineer and technician collaboration, and calorimeter research. Coming into the SULI program, I had a fundamental understanding of 3D CAD drawing systems. After consulting with PHENIX experts and referencing the work of others, I have been able to utilize the technique known as parametric drawing to allow rapid recreation of a family of similar drawings by simply updating parameters. Using parametric drawing, the details of the drawings can be related to one another by using a common reference file, commonly known as a Microsoft EXCEL file. The EXCEL file enables convenient editing, as necessary. Personal accomplishments related to the sPHENIX project, include both completed and partially completed drawings for the upgraded calorimeter components. The tasks that were assigned to me were in the developmental stage when I received them and I advanced their design concepts. The knowledge that my work, in the end, may contribute to the advancement of a project, such as sPHENIX, is truly, a great opportunity. My work, here, may allow for convenient modifications to be made in the future, as necessary. The PHENIX project serves as a tool of research and development for Brookhaven National Laboratory and the Department of Energy. My time here has given me exposure to a new level of professionalism, the acquisition of new engineering/design techniques, as well as a high level professional work experience.

When a new design for a project is being developed, it is important to have a sense of direction for where the project is going. The same can be said about any attempt in trying something new. The Physics Department at Brookhaven National Laboratory (BNL) is in the process of developing the Pioneering High Energy Nuclear Interaction Experiment (PHENIX) project into what is to be known as the Super PHENIX (sPHENIX) project. This upgrade, from PHENIX to sPHENIX, involves dramatic swaps and changes for the current detector used in the PHENIX project. In order to maintain some of the aforementioned sense of direction that every new project needs, new designs and prototypes will have to be made.

If we were to view the entire upgrade from PHENIX to sPHENIX as many small parts that make up a whole, then one of these small parts is the design and developed of the Hadronic Calorimeter Scintillator. The Hadron Calorimeter (HCAL) measures the energy of hadrons, particles made of quarks and gluons; for example, protons, neutrons, pions, and kaons. Additionally it provides indirect measurement of the presence of non-interacting, uncharged particles such as neutrinos.1

The development of these new designs and prototypes is what we will be discussing. The main focus of my time here during the summer was to create, using tree-dimensional computer drawing software, a parametrically dimensioned model of the scintillators that are to be used in sPHENIX.

The scintillators that are to be used in the prototyping are cut into tiles. Figure 1 illustates what we start out with. From there, we divide the piece shown above into 22 different tiles. There will be 11 tiles that will be on the upper portion of the piece and 11 tiles that will be on the lower portion of the piece. The tiles that will be on the upper are to be about double the size of the tiles that are to be on the lower portion. Once the tiles have been cut, there will be grooves that will be cut into the tiles. The upper and lower potion tiles have official names which are the Outer Hadronic Calorimeter (Outer HCAL) and the Inner Hadronic Calorimeter (inner HCAL). Together, they are known as the Hadronic Calorimeter (HCAL). The scintillator tiles alone do not make up

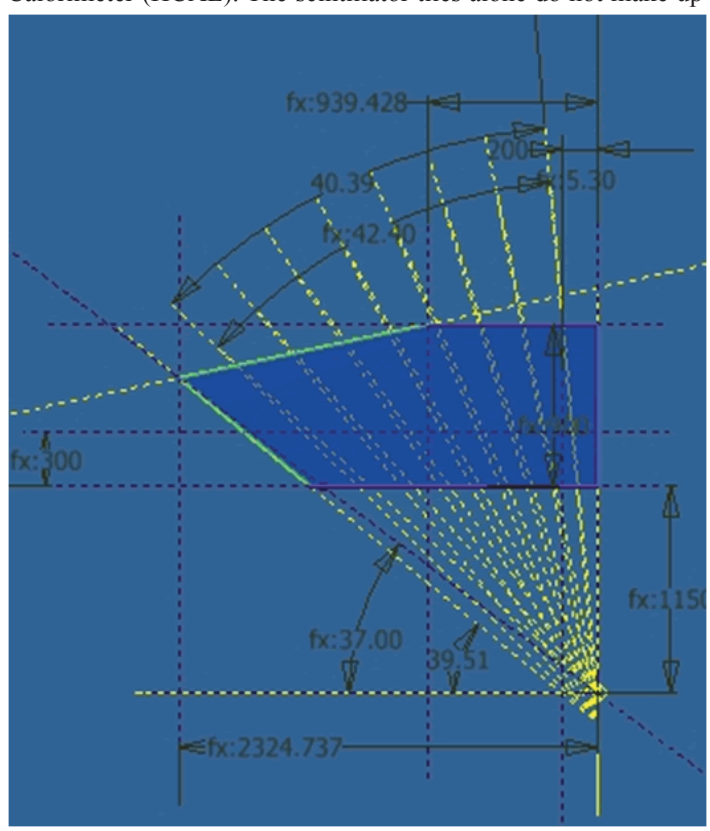

Figure 1

what is to be known as the HCAL, rather, the scintillator tiles in combination with the steel casings that they are to be placed in make up what is to be known as the HCAL. Displayed below are four pictures. Figures 2a and 2b illustrate the front and side views of the steel casing that the scintillator tiles will fit inside of. Figure 2b shows small gaps, and it is inside of these small gaps that the scintillator tiles will fit. Together they form a segment of the HCAL. Figures 2c and 2d show what the complete HCAL looks like, which comes as a result of a 360 degree rotation.

The grooves will be made for the purpose of holding wave shifting fiber optic cables. These wave shifting fiber optic cables gather any light that fluoresces from the scintillator tiles as a result of being struck by charged particles. The nature of these wave shifting fiber optic cables is such that any light that hits the cable is only allowed to be released through the tips of the cable. This allows for an efficient collection of light. The light that is collected and sent to a photo collector connected to a data recorder. Once sufficient data has been recorded, the data is then analyzed. Figure 3 shows a picture of the wave shifting fiber optic cables making their way to the photo collector as they leave the scintillator tiles.

Now, to get back to what was mentioned before regarding a parametrically dimensioned model, I will describe what a parametric model is. A parametrically drawn model is a model that pulls numbers from a reference file. The numbers that are pulled are the same numbers that are used to dimension the model. The dimensioning of a model takes places with a computer-aided design (CAD) program. The CAD software that is used in this project is Autodesk Inventor, and the reference program used in conjunction with Autodesk Inventor is Microsoft Excel. The beginning stage of a parametrically drawn model, used in this project, is to first create the general shape of the intended model. After the general shape has been created, the user dimensions the drawing by selecting a dimensioning program from the CAD program and then selects the desired parts from the model that need dimensioning. Once the necessary parts have been selected, a dimension editing function is selected. What happens next is crucial in making a successful parametric model. Once the dimension editing function has been selected, the user proceeds to entering in a key reference name for a desired measurement. This key reference name that is used must be identical to the name given in the reference file. One might ask, how, exactly, does one connect a CAD drawing program to a reference file such as Microsoft Excel? In the case of Autodesk Inventor, the answer is by way of a special function known as parameters, found under the management tab. The user must select the parameter function and then link the appropriate Excel file. Once the Excel file has been linked, the user can then proceed to follow the procedure, given above, for inputting key reference names.

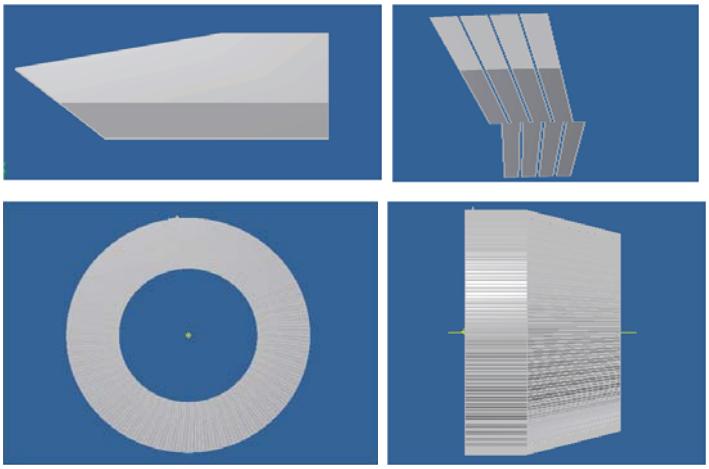

Figure 2 a, b, c, d

The outcomes produced during the summer are presented in the pictures that follow. (Figures4-1, 2, 3, 4)

Designs 1 and 2 are very similar. Design 2 was made in response to critiques made by senior engineers and physicists. Key differences between designs 1 and 2 are the angles at which the fibers exit the scintillator, the amount of fiber used, and the oscillation pattern exhibited on the scintillator tiles. Design 1 has fiber optic cables that exit at 90 degrees while design 2 has fiber optic cables that exit at approximately 15 degrees. The taper that the fiber takes after every bend in design 1 results in a considerable increase in the amount of fiber used relative to design 2. Lastly, design 2 uses phase shifted oscillation pattern of 90 degrees while design 1 follows an oscillation figure 8 patter with a phase shift of 0 degrees. Designs 3 and 4 differ from designs 1 and 2 as a result of a single side embedment used in designs 3 and 4, rather than the dual side embedment used in designs 1 and 2. Benefits of this are a considerable decrease in the amount of fiber used. Once might ask why single side embedment could not have been used for designs 1 and 2, and the answer is because one of the constraints for the design is appropriate horizontal symmetry. In order for designs 1 and 2 to maintain appropriate horizontal symmetry using single side embedment, the oscillating patters of either side would have to be placed on one side only. If this happened, the fiber optic cables would have to cross many times, and this may result in non-reliable data. When design 3 was made, complete cost effectiveness was the target rather than a balance of performance and cost-effectiveness. Design 3 utilizes a deeper cut into the scinitillator tiles which allows for a center positioning of the fiber. Design 4 was made in an attempt to maximize both performance and cost-effectiveness. Design 4 utilizes oscillation as well as single side embedment. The oscillation allows for efficient area coverage and the single side embedment allows for decreases fiber usage. Unlike designs 1 and 2, design 4 utilizes an oscillations that moves horizontally rather than vertically. Therefore, the constraint of horizontal symmetry is satisfied by simply centering the grooves on the tile. Closer inspection of the given scintillator tiles, shown below, may suggest that the centering of the tile grooves may become more difficult as we move to the left.

While this is true, figure 5 will only represent half of the complete HCAL before it is to be revolved 360 degrees to become what is shown below. And so the horizontally symmetrical constraint is satisfied.

From this point, possible next steps are to manufacture the design and proceed to testing . Depending upon test results, the appropriate design will be chosen or modified.

The difficulties faced in this project were finding designs that have appropriate coverage while also staying in accordance with placed constraints. My overall experience here has been enriched through the acquisition of the parametric modeling technique of which I was previously unaware.

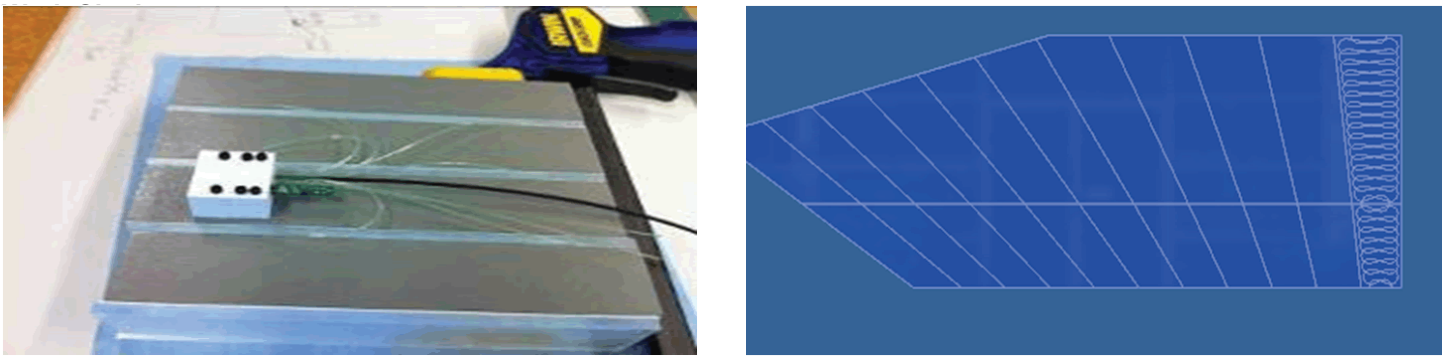

Figure 3

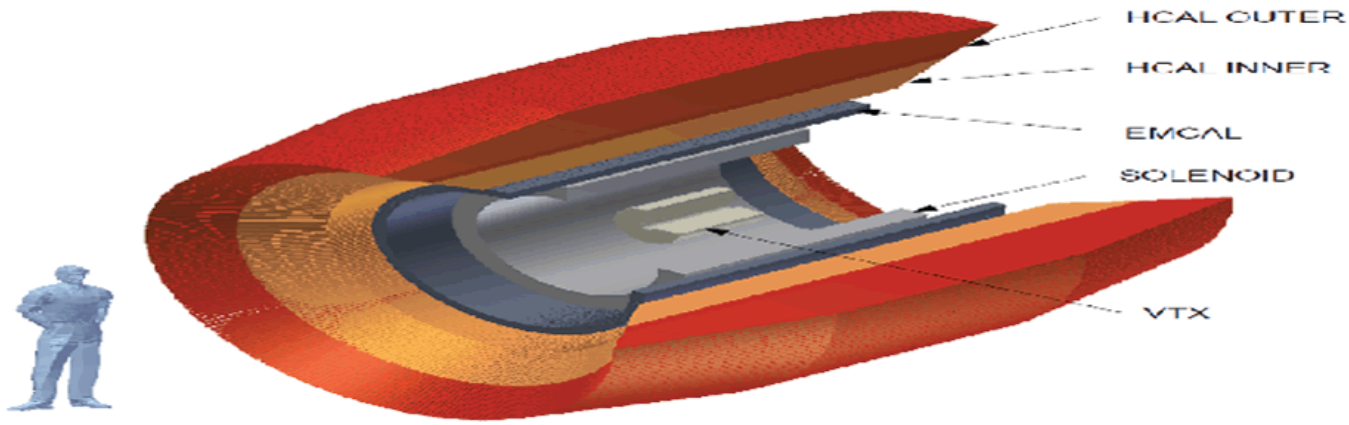

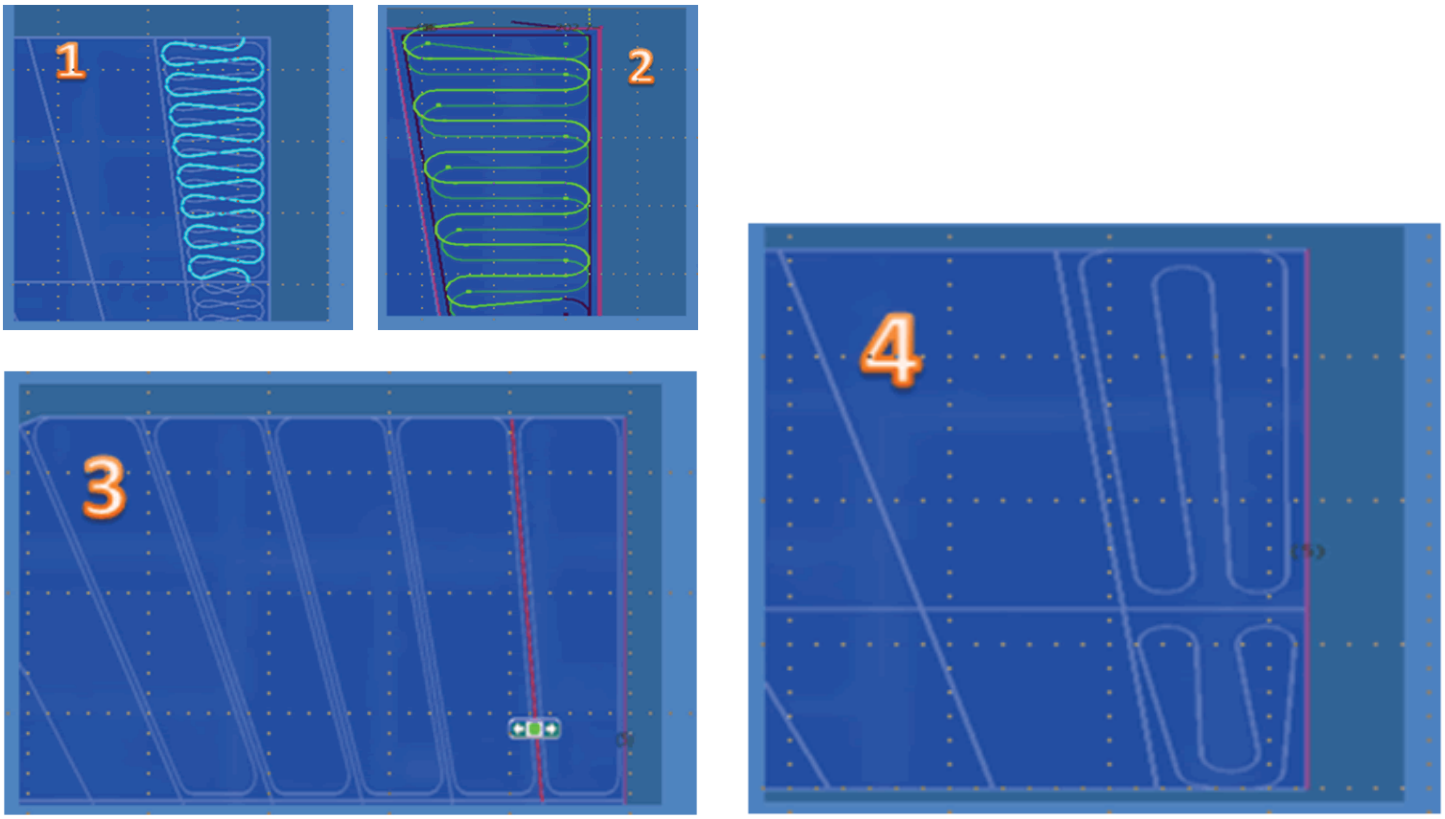

Figure 4: 1, 2, 3, 4

Characterization of indium iodide (InI) crystals for room-temperature radiation detector applications

J. Mwathi, A. Kassu
Department of Technology, Alabama A&M University, Normal, AL 35762
A. Hossain, K. H. Kim,
Brookhaven National Laboratory, Upton, NY 11973

ABSTRACT

Indium iodide (InI), a compound semiconductor with a high atomic number and a wide band gap, has a relatively low melting point (351 ˚C), low vapor pressure, good mechanical properties, and does not exhibit a solid-solid phase transition between its melting point and room temperature. Its wide band-gap energy enables it to detect low-noise operations at and above room temperatures. These physical aspects suggest that indium iodide is a very promising material for fabrication of room-temperature, x-ray and gamma-ray detectors. While there are many different methods of growing indium iodide crystals, we focused mostly on crystals grown using the zone melting method and the Czochralski method. The following steps were taken in the InI crystal preparation: mechanically polishing of the InI crystal with different grit size papers and chemical etching using two different chemical solutions. Hydrogen bromide and hydrogen peroxide (HBr+H2O2) in the ratio of 10:1were used to etch the crystal grown by zone melting while a 2% bromine methanol solution was used to etch crystals grown by the Czochralski method to determine which chemical would be ideal for chemical etching. After the etching process was complete the next step was to take optical and infrared images using an optical/IR microscope to view most of the defects on the crystal surface including scratches and different chemical reactions that happened during the chemical etching process. By comparing the images we were able to determine which chemical was suitable for the etching process. We concluded that the 2% bromine methanol solution was the best to use in chemical etching. We also used the infrared microscopy to determine the inclusions and voids in the crystals. From the images obtained we learned that the crystal grown using zone melting method had more inclusions than the crystal grown using Czochralski method; and thus, the later would be the ideal crystal to use in detector fabrication. There is high demand for compact, cost-effective, high-performance room-temperature radiation detectors in many areas, including homeland security, medical imaging, and astrophysics.

I. INTRODUCTION

The Czochralski pulling process is the most valuable and cost efficient method for producing large, oriented, single crystals of group IV and III-V semiconductors. However, there have been only a small number of reported attempts to use the Czochralski process for growing wide band-gap compound semiconductors, needed for the room temperature operated gamma-ray detectors. Indium Iodide (InI) crystals are being considered as the future of room-temperature radiation detectors. This is due to their characteristics: Indium Iodide is a compound semiconductor with a wide band-gap, high atomic number, and high density. It has a higher photon stopping power for x- and gamma-rays than germanium (Ge) or CdTe. Most compound semiconductors used for fabrication of radiation detectors are very toxic and pose occupational poisoning and environmental pollution hazards, but Indium Iodide is less toxic than all other materials used in radiation detector fabrication. There is a high demand for compact, cost-effective, high-performance, room-temperature radiation detectors in many areas, including homeland security, medical imaging, and astrophysics. In this experiment we determine a number which crystal growth method produces the best crystal for detector fabrication and which chemical solution is the best for chemical etching.

II. MATERIALS AND METHODS

We focused on crystals grown using zone melting method and Czochralski method and compared the different defects in crystals from both methods of growing. We started by preparing two different InI crystal surfaces. The first step was to polish the crystal using different grit size papers (1200, 100, 800) then move on to fine polishing using AL2O3 micron polishing powder (0.9µm and 0.5µm) to make the crystal smooth and eliminate most surface scratches and defects.

The next step was the chemical etching. We used two different chemical solutions to etch each InI crystal: Hydrogen-Bromide + Hydrogen peroxide and Bromine-Methanol. We gradually changed the ratio of the chemical concentration since some of the ratios used turned out to be too concentrated and reacted with the crystals and caused more defects. We etched crystal A in 2% Bromine-Methanol and crystal B in (10:1) Hydrogen Bromide + Hydrogen Peroxide. Each crystal was etched for 20 seconds then rinsed with methanol and air dried using nitrogen gas.

After chemical etching we viewed the crystal under a Nikon multi-functional microscope and later took infrared images of the crystals. This enabled us to view inside the crystal bulk and view inclusions, voids, and any other defects. As shown from the diagrams below, we could measure the size of inclusions and voids.

Surface roughness affects the detector's functionality; and so, before depositing the contact on the crystal it was crucial to make the crystal as smooth as possible. Surface roughness was determined using an optical profilometer to measure small surface variations. A typical profilometer can measure small vertical features ranging in height from 10 nanometers to 1 millimeter. The measurements are analyzed and a 3D image of the crystal was produced. The 3D image has a y-axis color scale. Different colors show how deep a certain part of the crystal is; for example, in the images below the deepest surface of the crystal is represented by the color blue while the highest surface of the crystal is represented by the color red. A roughness scale interpreting the surface roughness of the 3D image is also produced.

We used a different infrared microscope to take images of the crystals. This microscope took several images of the crystal from one surface to the other surface. This images are the compiled using a software that plots a 3D replica of the crystal showing inclusion distribution throughout the crystal.

Crystal (C), grown by a zone melting method, was used to determine whether chemo-mechanical polishing (CMP) would produce a smoother surface than just using chemical polishing. So after mechanically polishing, the crystal was placed on a smooth polishing cloth and a Hydrogen Bromide + Hydrogen Peroxide+ Ethylene Glycol solution was added and the crystal was mechan-

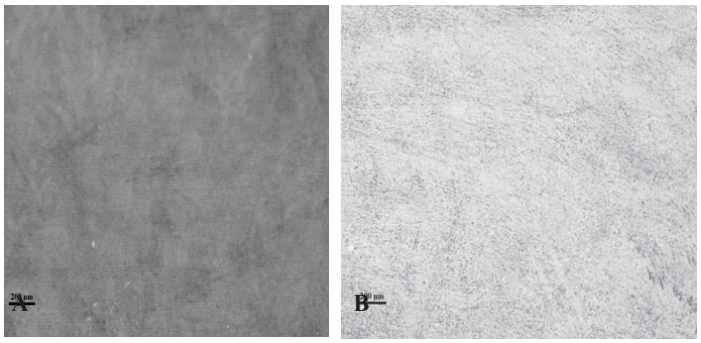

Figure 1. Polished crystal: A. Indium Iodide crystal grown by Czochralski method, mechanically polished; B. Indium Iodide crystal grown by zone melting method, mechanically polished

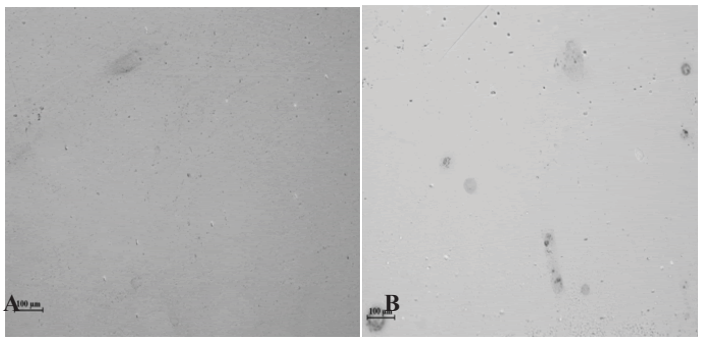

Figure 2. Chemical Etching: A. Crystal grown by Czochralski method etched in 2% Bromine Methanol; B. Crystal grown by Zone melting method etched in 10:1 Hydrogen Bromide + Hydrogen Peroxide

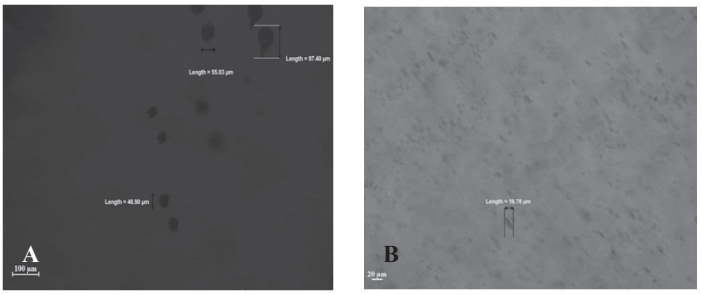

Figure 3. Infrared Images: A. Crystal grown by Czochralski method etched in 2% Bromine Methanol infrared image; B. Crystal grown by Zone melting method etched in 10:1 Hydrogen Bromide + Hydrogen Peroxide infrared image.

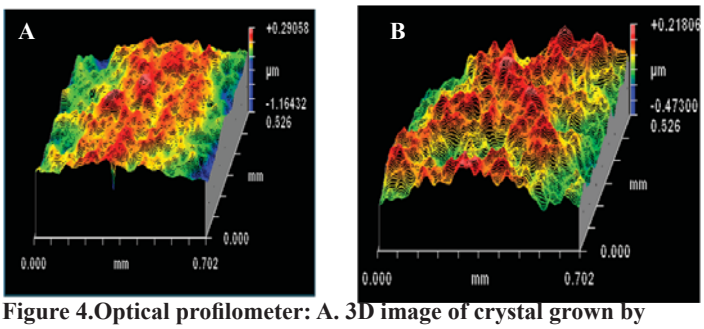

Figure 4.Optical profilometer: A. 3D image of crystal grown by Czochralski method optical profilometer reading; B. 3D image of crystal grown by zone melting method optical profilometer reading.

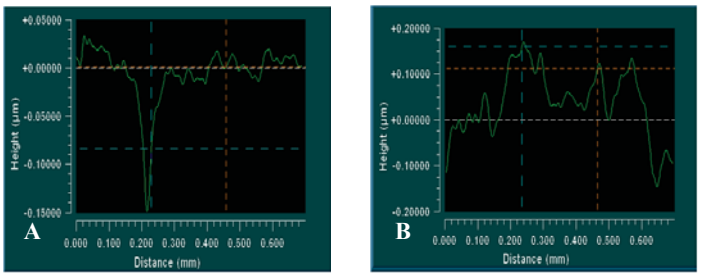

Figure 5. Optical profilometer: A. Roughness scale of crystal grown by Czochralski method optical profilometer reading; B. Roughness scale of crystal grown by zone melting method optical profilometer reading.

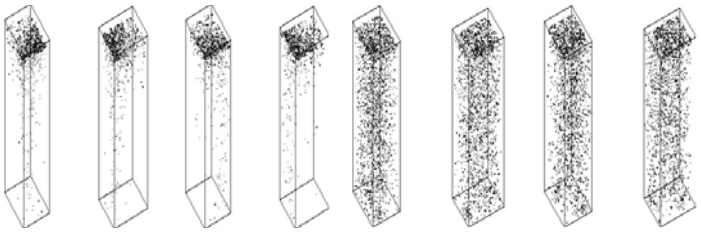

Figure 6.3D crystal replica: A. 3D replica of a crystal grown by Czochralski method. B. 3D replica of a crystal grown by zone melting method.

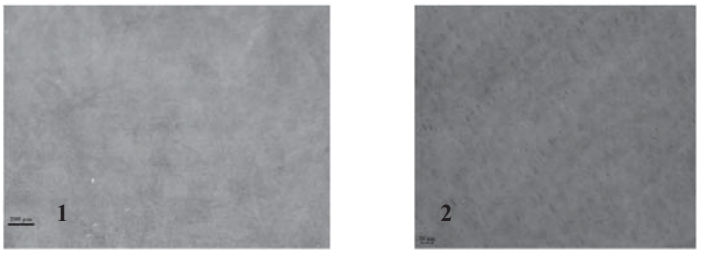

Figure 7. Chemo-mechanical polishing: 1. Optical image of crystal C after chemo-mechanical polishing; 2. Infrared image of crystal C after chemo-mechanical polishing.

ically polished for 20 seconds. It was then rinsed off in methanol and water and air dried using nitrogen gas. Optical and infrared images of this crystal were taken as shown in the images below.

III. RESULTS

From the above experiments and tests, we learned a lot about the three different crystals. By using different solutions we were able to determine which chemical solution would be ideal for the chemical etching process. From the figure 4 and figure 5 optical profilometer readings, we were able to determine which crystal had the smoothest surface. Crystal (A) which was etched in 2% Bromine Methanol had a smoother surface than crystal (B) which was etched in Hydrogen Bromide + Hydrogen Peroxide. From figures 3 and figure 6 we concluded that crystal (A), grown using the Czochralski crystal growth process, had fewer inclusions than crystal (B) grown using a zone melting method. Crystal (C) which was chemo-mechanically polished appeared to have a really smooth surface from the optical microscope view as shown in figure 7.

IV. DISCUSSION AND CONCLUSION

From the above experiments, we could determine which crystal would be ideal to make a detector. Crystal A, which was grown using the Czochralski method and etched in 2% bromine methanol, would be the best crystal to use in making a detector since it has fewer inclusions; hence, fewer electrons would get trapped and thus a better reading would be acquired if a radiation source was introduced.

V. REFERENCES

Hossain, K. H. Kim, A. E. Bolotnikov, G. S. Camarda, Y. Cui, G. Yang, and R. B. James "Characterization of Indium Iodide (InI) Crystals for Room-Temperature Radiation Detector Applications"

D. Nicoara, C. Bertorello, G.A. Slack,, A. G. Ostrogorsky, M. Groza and A. BurgerIllinois Institute of Technology (IIT), Chicago, IL 60616 "Czochralski Growth of Indium Iodide crystal."

Modulation enhanced diffraction

Max Osmulski
Vanderbilt University, Nashville, TN 37235
Eric Dooryhee and Jonathan Hanson
Brookhaven National Laboratory, Upton, NY 11973

ABSTRACT

The goal of this project was to prepare for the use of the Modulation Enhanced Diffraction (MED) technique at the X-ray Powder Diffraction (XPD) beamline at the National Synchrotron Light Source II (NSLS II). This included writing software capable of analyzing the data generated by such experiments. Using simulated data in addition to preliminary data taken recently at the X7b beamline in the current NSLS, such software was written using MATLAB. The use of MED will expand the capabilities of the XPD beamline for future study in several areas; for example, the data we have taken from the experiments at the NSLS studied the water-gas shift reaction on Cu-CeO2. This reaction is important for processes involved in things such as hydrogen fuel cells.

Modulation Enhanced Diffraction (MED), a relatively new and promising technique, will increase the sensitivity of the X-ray Powder Diffraction (XPD) beamline at the NSLS-II to the structural changes in materials which would otherwise be largely hidden by noise. Tracking the part of a structure that changes over time would ordinarily require very sensitive instruments. Using MED, it is possible to view the time evolution of a crystal structure in operando and separate the contributions of different parts of the crystal structure. The theory behind MED has already been developed, e. g., by periodically varying a stimulus to the material, a periodic response in the diffraction pattern that is dependent on both the frequency of the stimulus and twice the frequency of the stimulus appears. Analyzing these two separate frequency components allows for the separation of partial diffraction contributions. This process can lead to gaining a high signal-to-noise ratio for the active part of the material that would otherwise be hidden.

Most of my work on a day-to-day basis was done using the MATLAB programming language. The experiments I ran with Jon Hanson at NSLS were performed at the X7b beamline, utilizing much of the equipment available to us there. Some coding was done in Spec# to control the different parts of the experiment. The sample was mounted in front of the detector where we could adjust the temperature of the sample as well as pulse different gases through the sample. The gases were flowed through a bubbler to keep the sample 'wet' (in the presence of water) throughout both experiments. The gas valves were controlled by the program written in Spec# and alternated at specific intervals. The gases flowing out of the sample were examined using a residual gas analyzer (RGA). My work was largely based on the work done in several papers in which the theory and mathematics behind the MED process were detailed. These papers are listed in the below.

Experiment 1

Both experiments were conducted at the X7b beamline at the NSLS. For both experiments we used a sample of copper ceria (Cu-CeO2) which was heated and exposed to water and a periodically changing flow of gases. The gases then flowed out of the apparatus and into the RGA, where the makeup of the gases could be analyzed. For the first experiment, we pulsed gases as follows at 200°C:

Helium	15 minutes
Carbon monoxide	20 seconds
Helium	15 minutes
Oxygen	20 seconds

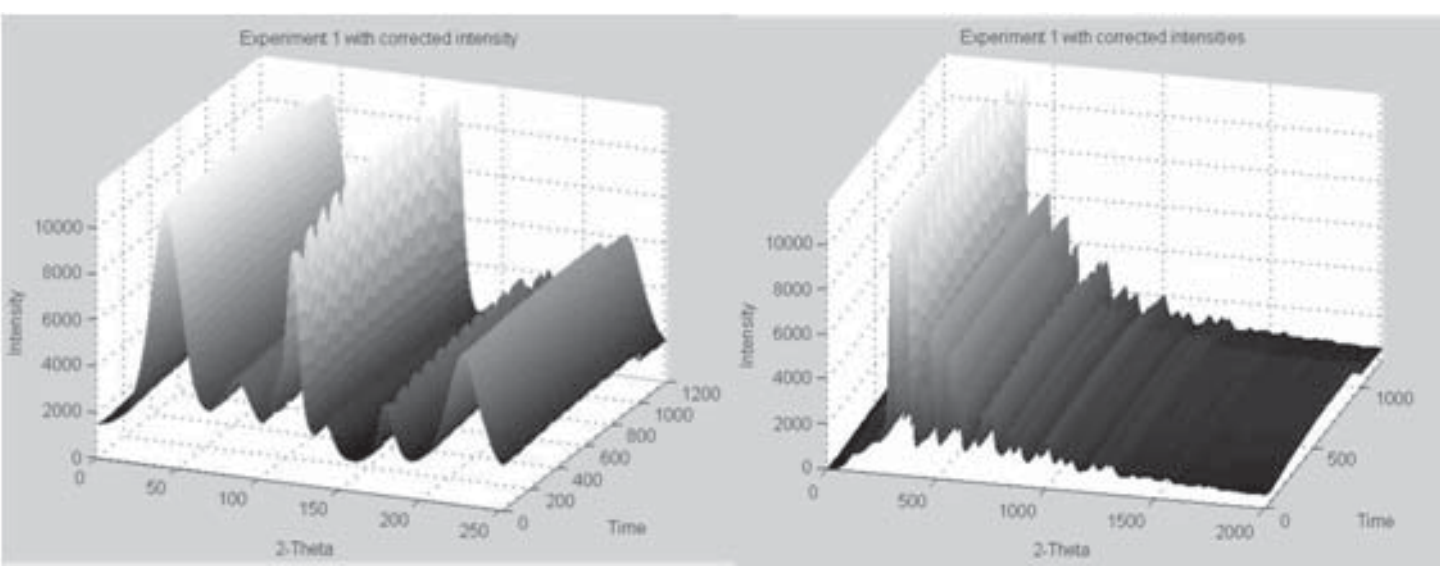

Figure 1. The above graphs also illustrate one of the improvements of the MATLAB program over the previous IDL program used to graph the data – the above right graph has been corrected for the intensity counts. Over the course of the experiment, the number of counts received by the detector begins to fall off as the synchrotron uses the electron beam, which causes the intensity of the peaks to diminish over time. This is solely from the machine, not something in the sample, so we can use the counts to correct for this effect.

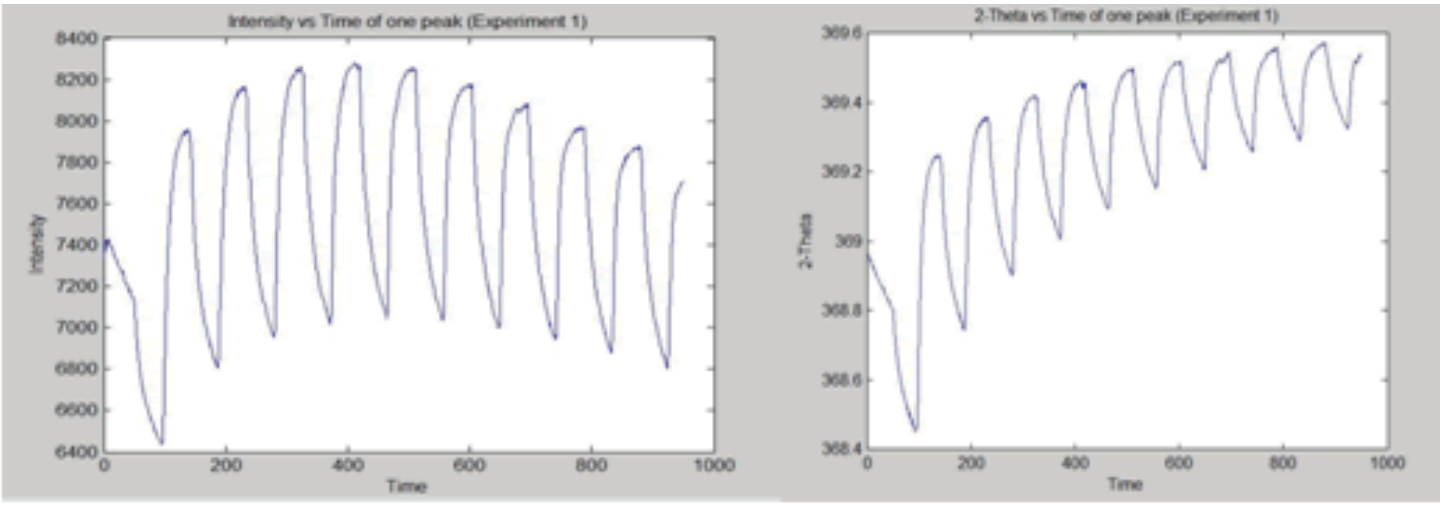

Figure 2.

This process was repeated numerous times and a diffraction pattern was taken every 20 seconds. The periodic stimulus from the gas alternately oxidizing and reducing the sample caused changes in the diffraction pattern as can be seen in figure 2. Some of the peaks had easily visible changes in intensity. While harder to see, the peaks also shifted their position in 2-Theta. Figure 3 shows the change in intensity (left) and 2-Theta location (right) of a single peak over time where the periodic response to the periodic stimulus can easily be seen.

Experiment 2

The second experiment, which also used a copper ceria sample, followed a slightly different procedure. Prior to beginning the data taking, the sample was heated to 300°C and then exposed to carbon monoxide for an hour to fully reduce the sample from the start. The sample was cooled back down to 200°C, and for this experiment, the gas pulses were changed. In the first experiment, it was unclear whether the water-gas shift reaction was occurring or if the pulse of oxygen was simply reoxidizing the sample; and so, we removed the oxygen phase. Instead, we alternated 15 minute pulses of Helium and 20 second pulses of Carbon Monoxide. This time, the RGA showed clear evidence of the water-gas shift reaction. In figure 3, it is hard to see any shifts in intensity, but in the figure to the right of the same peak as was examined in the prior experiment, it is easy to see the periodic change in 2- Theta. This reiterates the usefulness of MED; it shows just how sensitive the technique is to very small changes in 2-Theta (<0.1% changes in 2-Theta).

REFERENCES

Chernyshov, D., van Beek, W., Emerich, H., Milanesio, M., Urakawa, A., Viterbo, D., Palin, L. and Caliandro, R. "Kinematic diffraction on a structure with periodically varying scattering function" Acta Cryst. (2011). A67, 327-335.

Urakawa, A., van Beek, W., Monrabal-Capilla, M., Galán-Mascarós, J., Palin, L., and Milanesio, M. "Combined, Modulation Enhanced X-ray Powder Diffraction and Raman Spectroscopic Study of Structural Transitions in the Spin Crossover Material [Fe(Htrz)2(trz)](BF4)†" The Journal of Physical Chemistry C (2011) 115 (4), 1323-1329

Urakawa, A., Burgi, T. and Baiker, A. "Sensitivity enhancement and dynamic behavior analysis by modulation excitation spectroscopy: Principle and application in heterogeneous catalysis" Chemical Engineering Science, (2008) Vol. 63, No. 20. pp. 4902-4909

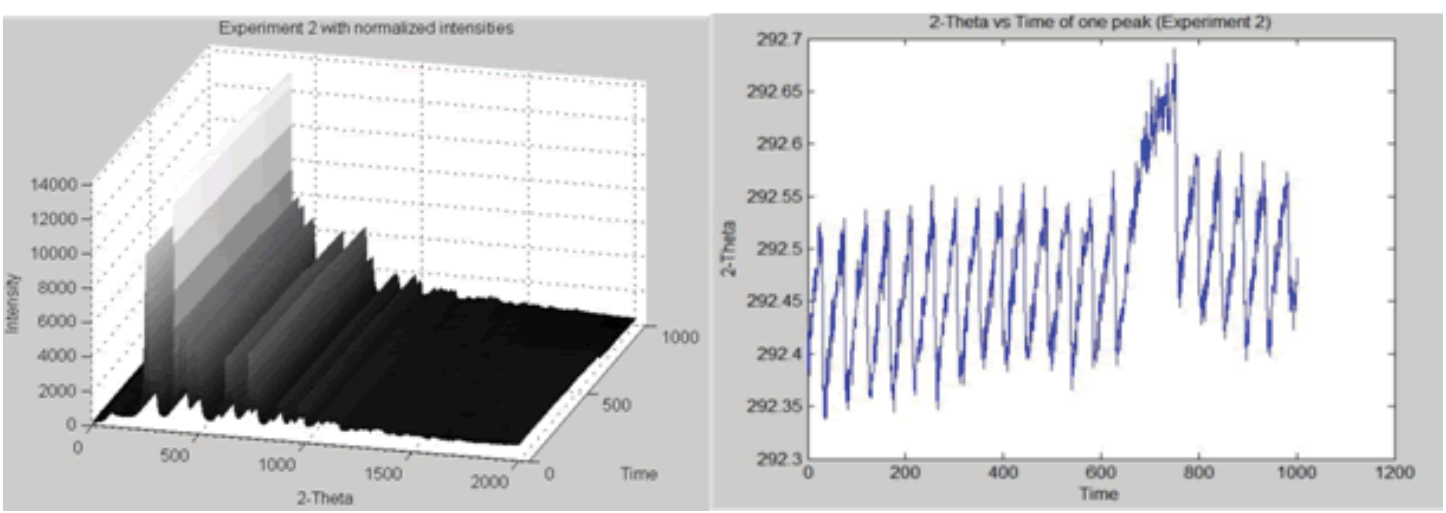

Figure 3.

Mechanistic investigation of novel ruthenium π-arene water oxidation catalysts

Nicholas Patterson
Chemical and Molecular Engineering, Stony Brook University, Stony Brook, NY 11794
Jonathan Hull
Chemistry Department, Brookhaven National Laboratory, Upton, NY 11973

ABSTRACT

Clean sources of dihydrogen and hydrogenated fuels can be developed through artificial photosynthesis research. Artificial photosynthesis uses sunlight to split water into protons and electrons, and then combines them to make fuel. The high energy barrier (1.23 eV) of water oxidation and the complexity of the reaction's kinetics are two obstacles encountered during artificial photosynthesis. In order for this reaction to be practical, a suitable catalyst is needed to lower the energy barrier using a reasonable mechanism. Our current research aims to analyze the catalytic abilities and characterize the reaction mechanisms of various novel water oxidation catalysts (WOC). Understanding the mechanism of these WOCs allows us to rationally tune a catalyst's properties to increase its effectiveness. In this study, three different WOCs were synthesized with slight variations of their ligands in order to vary the catalyst's electronic effects. This allows us to evaluate whether donor or acceptor ligands are better WOCs. Visible spectra were recorded as the pH was varied in order to determine the pK_a of the aquo ligand. It was found that the most electron donating ligand correlated with the highest pK_a and the highest catalytic rate. Electrochemical studies were also done in order to make a Pourbaix Diagram for each WOC. These determinations tell us the properties of the WOC, and give us insight to the possible mechanism of the reaction. To prove catalysis of the process O_2 measurements were taken in a closed system. It was found that catalytic water oxidation did occur for one of the complexes. We propose that this is because of a high Ru^V oxidation potential.

I. Introduction

With rising oil demand and depleting oil reserves, renewable energy research is a high priority; however, many of these energy sources cannot provide a fuel that can be stored or transported. Our approach is to oxidize water (Eq. 1); then use the resulting protons and electrons to create a combustible liquid fuel such as, but not exclusively, dihydrogen or methanol (Eq. 2 and 3).

$$2H_2O \rightarrow 2H^+ + 2e^- + O_2 \quad (1)$$

$$2H^+ + 2e^- \rightarrow H_2 \quad (2)$$

$$6H^+ \; 6e^- + CO_2 \rightarrow CH_3OH \quad (3)$$

A significant challenge to water oxidation is the high reaction barrier (1.23 eV). In order for water oxidation to be practical, a suitable catalyst is needed to lower the energy barrier. This can be done using homogenous or heterogeneous water oxidation catalysts (WOC). Heterogeneous WOC are robust and easy to fabricate; however, it is more difficult to characterize their mechanism and rationally predict their properties. Our current research aims to design new homogeneous WOC, and to characterize the mechanism by which they operate. We chose to look at three similar but moderately tuned WOC. The three catalysts have a molecular formula of $[Ru(bpy)(L_{3n})(OH_2)]^{2+}$, where L_{3n} is one of three tridentate ligands that we have named HMB, TMB, and Bz (Fig. 1). These ligands were chosen to systematically examine the effects of adding electron donating or withdrawing π-arene ligands to the WOC.

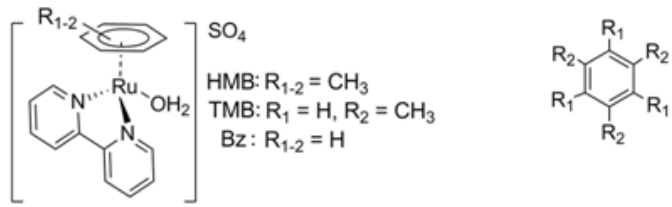

Figure 1. Complexes used in this study.

II. Methods

Determination of the various redox potentials of each WOC were acquired via cyclic- and square-wave voltammetry during a pH titration. Typically, 3 mg of catalyst were dissolved in 3 mL of 0.40 M Britton-Robinson buffer (1.9 M HMB). The solution was then titrated from pH 2 to pH 12 by adding 15 µL aliquots of NaOH which changed the pH by approximately 1 pH unit intervals. Using an Epsilon potentiostat to scan from -200 to +1800 mV and recording the redox peaks at each pH, a Pourbaix Diagram was constructed for each catalyst.

To determine the pK_a value of the catalysts, UV-Visible Spectroscopy was taken using an Agilent UV-Visible Spectrometer during a pH titration. A stock solution of 8.3 mL of 1 mM catalyst in water was prepared for this experiment. 100 mL of Britton-Robinson buffer starting at pH 1.8 was taken and 2.0 mL of 1 M NaOH was added to the buffer to yield a pH 5.8 solution. 3.6 mL of buffer was pipetted into a cuvette and 0.40 mL of catalyst solution was added prior to recording the spectrum. Through the addition of 0.20 mL of 1 M NaOH the buffer solution was then titrated approximately 1 pH unit and the same process was repeated until pH 12 was reached. This allowed us to see the spectral changes that occurred as the pH varied.

The rate of the catalytic reaction was measured with an O2 sensor. The first step in this process was to dissolve the catalyst (varied concentration from 0.05 mM to 1.0 mM) into 2.25 mL of 1.0 M HNO3. The reaction vessel was then degassed under Ar for 45 minutes to allow equilibrium with the solution. The terminal oxidant chosen for these oxygen measurements was cerium ammonium nitrate (CAN.) After dissolving 629 mg of CAN into 5 mL of 1.0 M HNO3 the solution was degassed by bubbling Ar through the solution for 30 minutes. Using an airtight syringe the CAN solution was injected into the vessel containing the catalyst. The reaction vessel was held at a constant temperature of 19.6°C for all experiments. By keeping the system closed and starting with a degassed vessel we knew that any oxygen detected by the probe was a product of the water oxidation.

III. Results

A. Electrochemistry

Cyclic voltammetry and square-wave voltammetry were used to find the redox potentials of HMB, TMB, and Bz. As the donor power of the ligand increases the higher the $Ru^{III/II}$ and $Ru^{IV/III}$ couples; however, the opposite is true for the $Ru^{V/IV}$ couple. This is likely the result of proton coupled electron transfer, as discussed below.

	HMB	TMB	Bz
$Ru^{III/II}$ couple, mV vs. NHE	452	429	396
$Ru^{IV/III}$ couple, mV vs. NHE	1136	1086	1050
$Ru^{V/IV}$ couple, mV vs. NHE	1520	1626	1730

Table 2. These peaks were recorded at pH 3 by square wave voltammetry.

B. Pourbaix Diagram

The results from the square wave and cyclic voltammetry (Fig. 3--5) show that through the lower parts of the pH range the $Ru^{III/II}$ and $Ru^{IV/III}$ redox peaks are pH dependent. An analysis of the Pourbaix Diagrams (Fig. 4--6) shows the pH dependent lines have a slope of approximately a -59 mV/ pH unit. This is characteristic of a Nerstian one electron per H+ reaction, and is helpful in determining the speciation of the catalytic intermediates.

As electron donating groups are added to the π-arene ligand, the $Ru^{V/IV}$ potential decreases. Since the Ru^{V} oxidation state must be reached in order for water oxidation to occur, this is likely the reason that the catalytic water oxidation is fastest for the HMB complex.

C. pKa Determination

The pK_a of the aquo ligand on each catalyst was determined through a spectral titration (Eq. 4.).

$$Ru^{II}\text{-}OH_2 \rightarrow Ru^{II}\text{-}OH + H^+ \qquad (4)$$

After the spectra (Fig. 9–11) were taken a Δ Absorbance versus pH plot (Fig.12–14) was constructed using multiple wavelengths from each WOC spectral titration. The wavelengths with the largest Δ Absorbance were graphed. This plot was graphed using the Origin 8 software package and fitted using sigmoid line fits to the data series. The midpoints of the sigmoid lines occur at the pK_a of the aquo ligand of the complex. It was found that the HMB had the highest pK_a (8.44), followed by TMB (7.81), and then Bz (7.25).

D. Oxygen Measurements

Oxygen was detected for the HMB complex; however, it was not detected using the other complexes. This is due to the high $Ru^{V/VI}$ potential of the TMB and Bz complexes. Since Ce^{IV} has an oxidation strength of 1.61 V vs. NHE, it is not a strong enough terminal oxidant to chemically oxidize the TMB and Bz WOC to their respective Ru^{V} oxidation states.

The HMB complex did show O_2 evolution proving that it does in fact work as a WOC. Multiple concentrations of the HMB catalyst were tested to observe if the initial rate of reaction was dependent on the catalyst concentration. A first order rate constant was determined as expected when a plot of initial rate versus concentration of WOC was graphed (Fig.15).

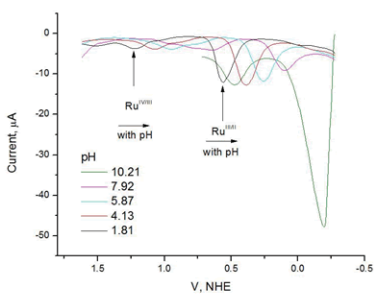

Figure 3. Square-wave voltammetry scans from a pH titration done using the HMB catalyst. Scans were taken from -200 to +1800 mV versus NHE.

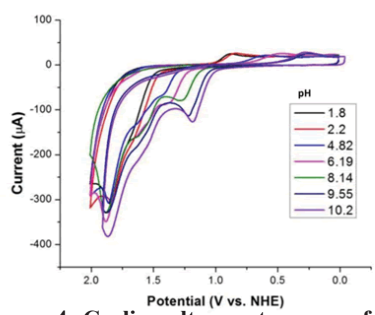

Figure 4. Cyclic voltammetry scans from a pH titration done using the TMB catalyst. Scans were taken from -200 to +2000 mV versus NHE.

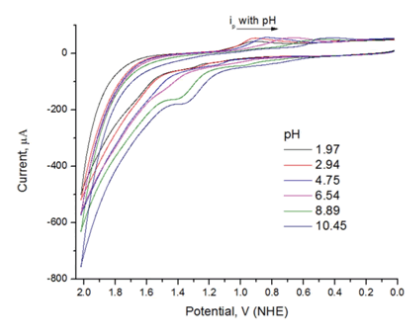

Figure 5. Cyclic voltammetry scans from a pH titration done using the Bz catalyst. Scans from 0 to 2000 mV versus NHE.

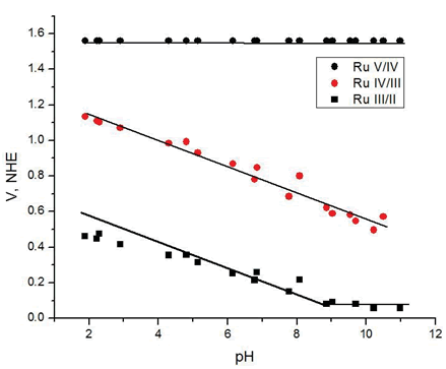

Figure 6. Pourbaix diagram for the HMB WOC. Note the $Ru^{V/IV}$ couple is shown just above 1.5

$[Ru(TMB)(bpy)(OH_2)](NO_3)_2$ Pourbaix Diagram

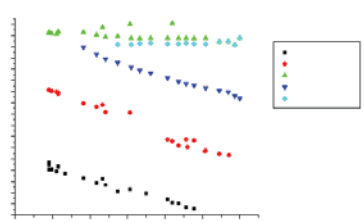

Figure 7. Pourbaix diagram for the TMB WOC. Note the $Ru^{V/IV}$ couple is shown at approximately 1.6 V. The extra peaks on the graph are due to new species that still must be studied further; however, the $Ru^{III/II}$, $Ru^{IV/III}$, and $Ru^{V/IV}$ couples all appear to behave similarly to the other catalysts.

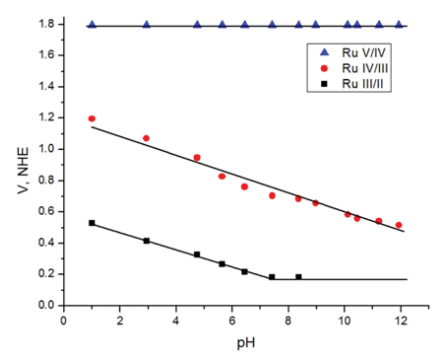

Figure 8. Pourbaix diagram for the Bz WOC. Note the $Ru^{V/IV}$ couple is shown just above 1.7 V.

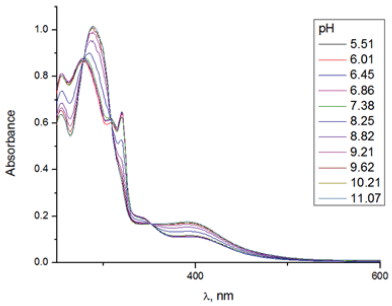

Figure 9. Spectral titration of HMB complex from pH 5.5 to 11.

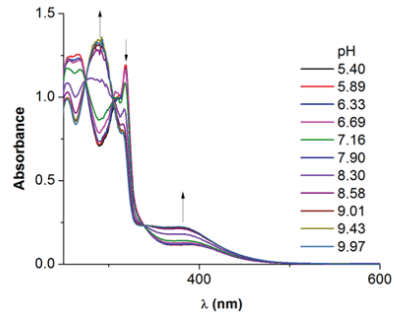

Figure 10. Spectral titration of TMB complex from pH 5.4 to 10.

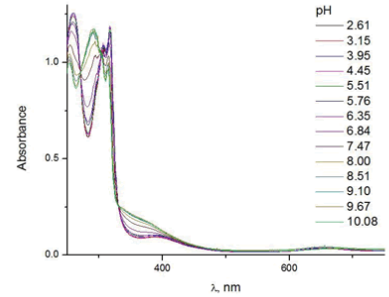

Figure 11. Spectral titration of Bz complex from pH 2.6 to 10.

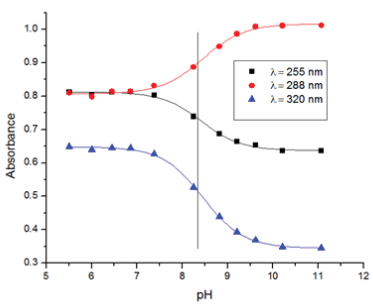

Figure 12. Sigmoidal fit for the HMB complex to determine the pKa value. This graph shows that the pK_a of the aquo ligand on this complex is 8.44.

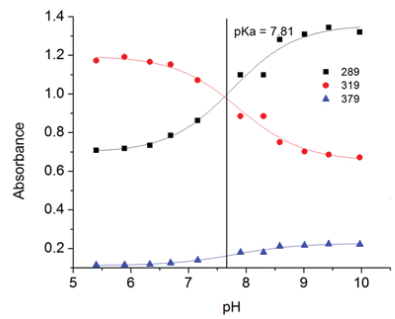

Figure 13. Sigmoidal fit for the TMB complex to determine the pKa value. This graph shows that the pK_a of the aquo ligand on this complex is 7.81.

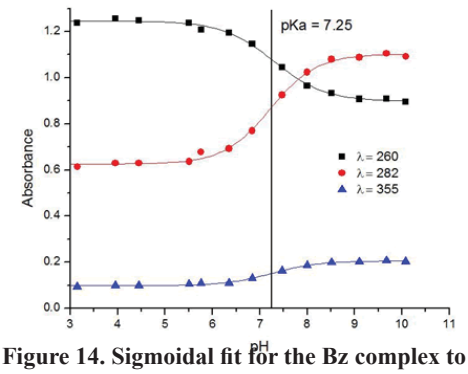

Figure 14. Sigmoidal fit for the Bz complex to determine the pKa value. This graph shows that the pK_a of the aquo ligand on this complex is 7.25.

IV. Conclusions

We have characterized the ionization and redox behavior of the HMB, TMB, and Bz complexes and have shown that at least one is active in catalytic water oxidation. The pKa's vary in the order $pKa_{Bz} < pKa_{TMB} < pKa_{HMB}$, while the E^0 for the $Ru^{V/IV}$ is approximately 0.2 V larger for the HMB complex than the Bz with TMB falling approximately in the middle. These effects are due to the HMB having the greatest electron donating effects. This difference in energy was expected based on the Lever parameters. Electrochemical studies are in progress. These measurements hold an electrical potential across the catalyst solution as an oxidant as opposed to using a chemical oxidant with a limited oxidation potential such as CAN. We believe that these measurements will allow us to prove the catalytic abilities of the TMB and Bz complexes as well.

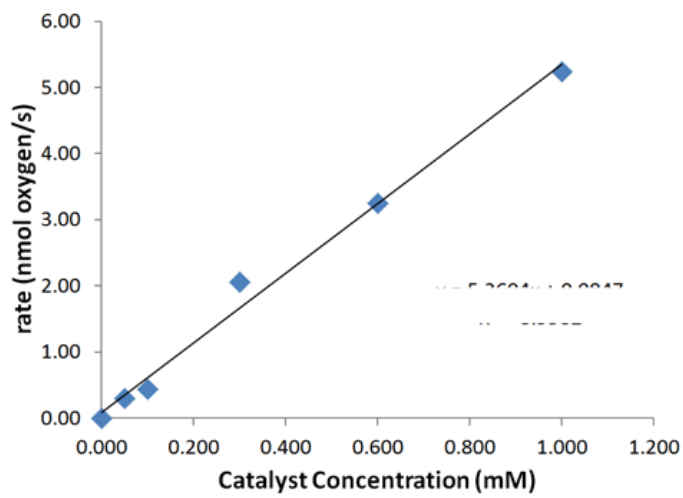

Figure 15. A plot of initial rate versus time. The oxygen measurements above used the HMB WOC. The WOC concentrations range from 0 M to 1.0 mM. All reactions took place in 1 M HNO3 at 19.6°C.

Optimization of the Copper Zinc Alumina catalyst for the low-temperature water gas shift reaction

Alexandre Pereira and Hazem Tawfik
Mechanical Engineering Technology, Farmingdale State College, Farmingdale, New York 11735
James Wegrzyn
Sustainable Energy Technologies, Brookhaven National Laboratory, Upton NY 11973

ABSTRACT

The performance of Copper Zinc Alumina (CZA) in reducing CO levels was tested in a single-stage, packed-bed reactor designed to carry out the water gas shift (WGS) reaction. A syngas simulation of 20% CO, 20% H_2, 10% CO_2 and 50% N_2 flowed through 100 grams of CZA concurrently with a constant distilled water flow rate of 20--23 ccm for each test. Temperature, residence time, and catalyst particle size were the main testing parameters. Decreasing the catalyst temperature, particle size, and residence time resulted in a decrease in CO reduction in the gas stream. The highest CO reduction occurred when using a 3.1 mm catalyst particle size, a catalyst temperature of 250°C, and a 0.78 sec residence time. These conditions allowed for a 92% reduction of CO content in syngas. Such a system is desirable in a pure H_2 production system as it increases the lifetime of H_2 purifiers, by reducing CO poisoning.

I. Introduction

The insecurities associated with the high demand of oil-based fuels have led our nation to search for safe, economical, and renewable sources of energy. Hydrogen (H_2), a suitable alternative energy source, has a high specific energy and can be used efficiently in fuel cells to produce combined heat and power. H_2 is not found in pure form in nature and must, therefore, be extracted using processes such as biomass gasification. The gasification process produces a biogas mixture, or synthesis gas (syngas), that contains varying levels of Nitrogen, Oxygen, Methane, Carbon dioxide, Hydrogen, and Carbon monoxide (CO). Numerous applications require a pure stream of H_2; therefore, H_2 purification systems such as electrochemical separators are used to separate H_2 from other gases. The catalyst of these purification systems decreases in efficiency when exposed to CO; therefore, the CO content in syngas must be reduced to allow for the longevity of these H_2 purifiers. To achieve this reduction of CO content in syngas, the water gas shift (WGS) reaction should be used.

The WGS reaction has the following chemical equation:[1]

$$CO + H_2O \Leftrightarrow CO_2 + H_2 \quad \Delta H = -41.1 \text{ kJ mol}^{-1}$$

Catalysts are often used to facilitate and enhance the reaction kinetics. Catalytic performance and activity in the WGS process is sensitive to temperature, residence time, catalyst particle or granular size, and the steam to CO ratio. Copper Zinc Alumina (CZA), a low-temperature shift catalyst, was acquired in order to test its performance at reducing CO in a stream of syngas composed of 20% CO, 20% H_2, 10% CO_2, and 50% N2. In addition to reducing CO, the WGS also increases the H2 content in syngas. For each mole of CO converted, one mole of H_2 is produced. As a result, H_2 content in syngas can almost double if the majority of the CO is converted into CO_2 using this gas simulation for the WGS reaction.

The parameters that were tested during this experimental work were the catalyst's temperature, the residence time of the syngas in contact with the catalyst, and the particle size of the catalyst. The results acquired will be used to develop a full scale WGS system for the Farmingdale State College Biomass System. The biomass system--a downdraft gasifier, a WGS system, an H_2 purifier, and a 5 kw proton exchange membrane fuel cell--will convert wood-chips into combined heat and electrical power (Figure 1).

A CZA catalyst was selected for the WGS system of the Farmingdale State College Biomass System because it is offered commercially at the low cost of $84/kg (Alfa Aesar), it maintains most of its catalytic activity after shutdown/startup operations

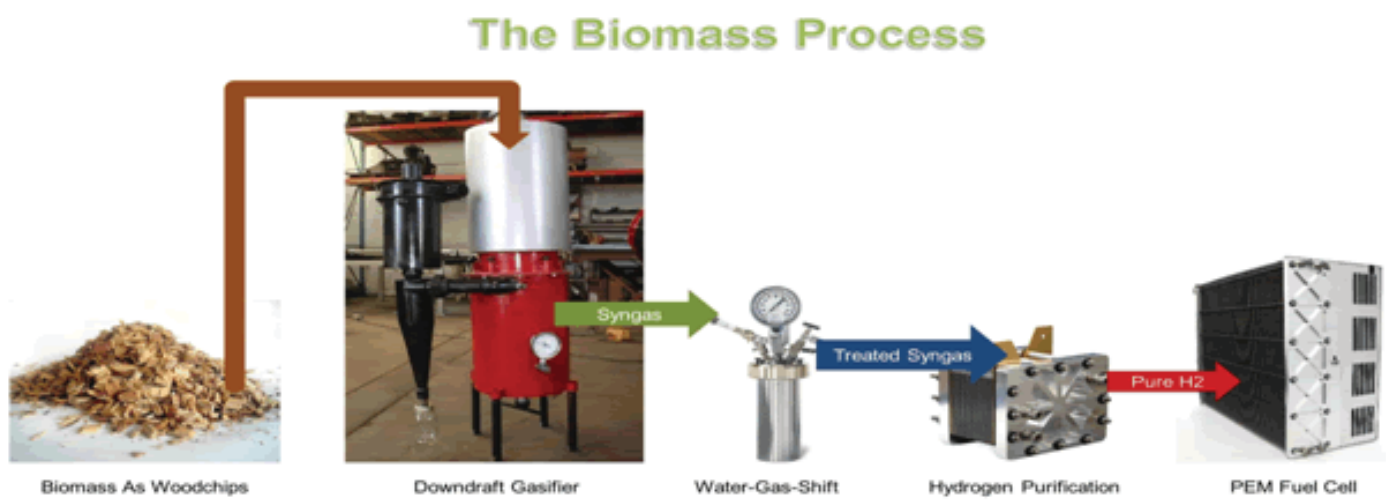

Figure 1: Simple layout of the Farmingdale State College Biomass System

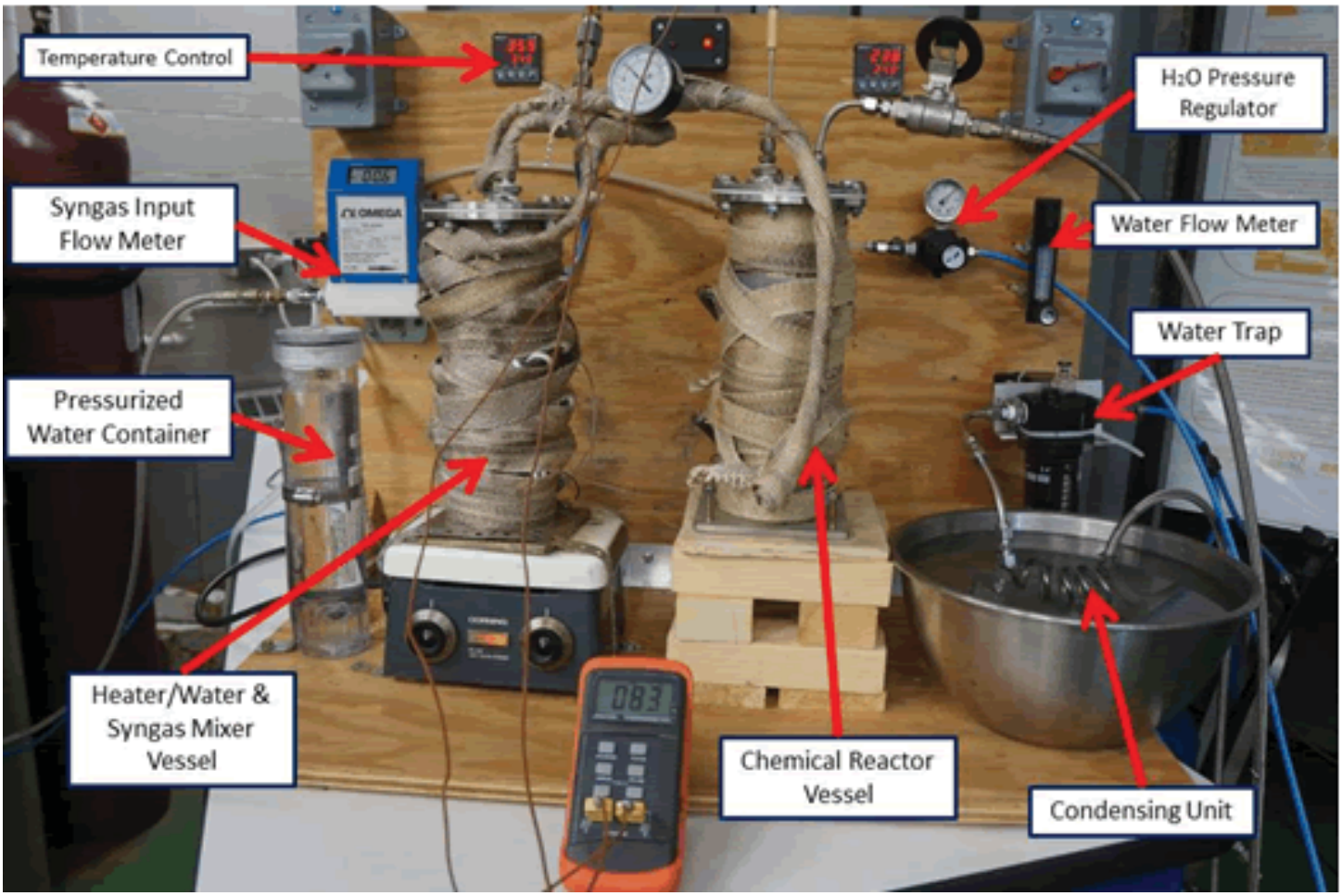

Figure 2: WGS system to test the performance and activity of CZA

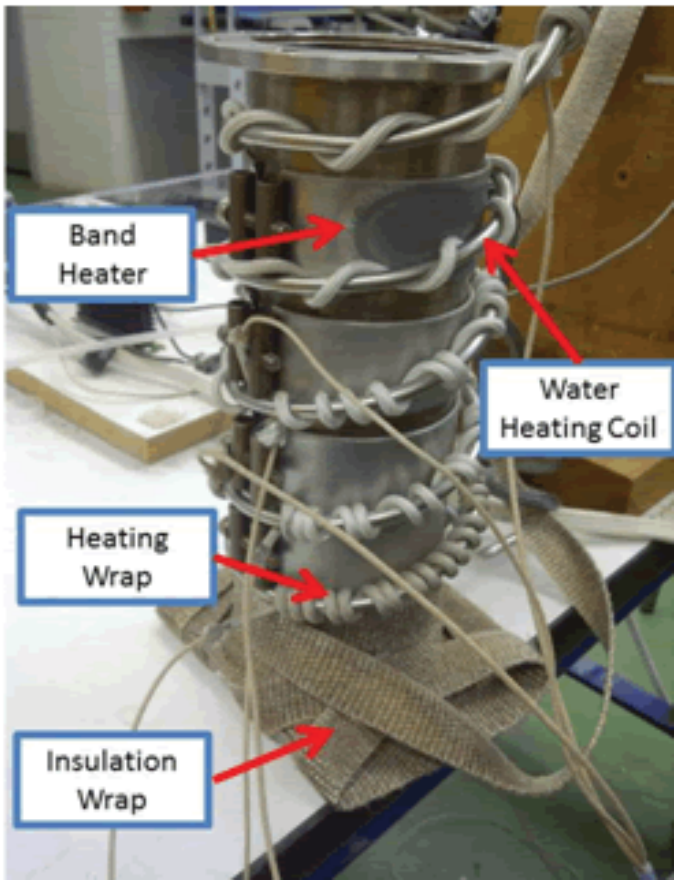

Figure 3: Heater/water & syngas mixer vessel

in the presence of water,[2] its performance decreases about 10% for every 900 hours on stream,[3] and it has a Hazardous Material Identification System (HMIS) rating of 0, 1, and 0 designated for health, fire, and reactivity. In addition to all of these favorable features, CZA is also more active than other platinum-based, low-temperature shift catalysts in the temperature range of 200°C to 250°C.[4] High catalytic activity allows for a low quantity of a

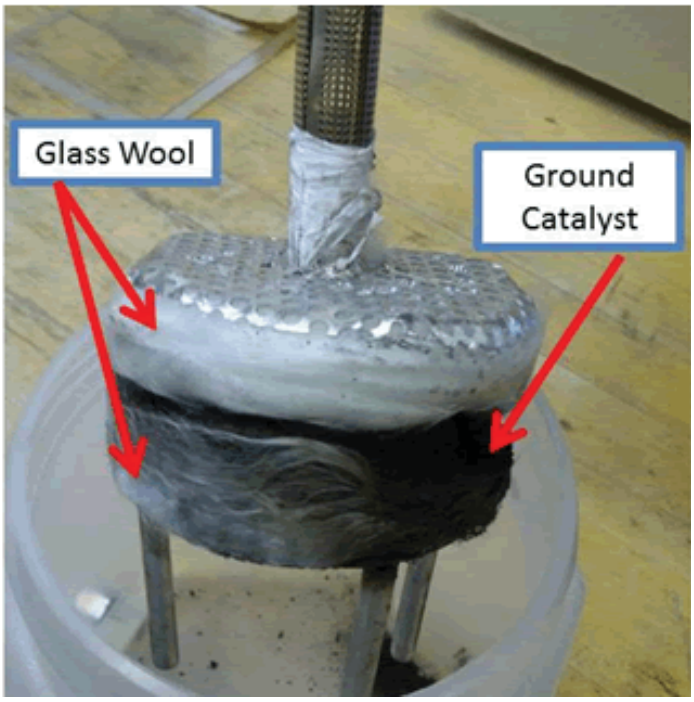

Figure 4: CZA catalyst sandwiched between glass wool

catalyst to be used to achieve a high CO reduction in syngas. This minimizes the pressure drop of the system. The only disadvantage of using CZA is that it becomes pyrophoric, when active, upon exposure to an oxidative environment. This results in permanent reduction in performance.[4]

II. Methods and Materials

A. Experimental Equipment

To test the activity and performance of CZA in the WGS reaction, a single-stage packed bed reactor design was considered for its simplicity and durability. The system, as shown on Figure 2, was composed of a pressurized distilled water container, a heater/water and syngas mixer vessel, a chemical reactor vessel, a water heating coil (Figure 3), a condenser, and a water trap. Heat was supplied to the vessels using a hot plate and six band heaters regulated by feedback control systems. Other parameters were monitored using a water flow meter, a syngas flow meter, and four temperature thermocouples. One thermocouple was installed on each vessel to monitor and maintain the surface temperature at the desired level, another was used to monitor the gas temperature between the heater/mixer and the chemical reactor, and the fourth thermocouple was used to monitor the temperature of the catalyst inside of the chemical reactor. The CO content in the output gas, after passing through the packed bed of CZA (Figure 4), was monitored through samples collected by a 10μL gas tight syringe and examined using a Thermal Conductivity Detector (TCD) gas chromatograph with a Molsieve 13X column.

B. Experimental Procedures:

One hundred grams of CZA, supported by glass wool, was loaded in the chemical reactor. The catalyst particle size was tested at 3.1 mm and was also ground to 0.5 mm to examine the effects of increased surface area. The CZA catalyst was composed of 50% Copper Oxide, >25% Zinc Oxide, <25% Aluminum Oxide, and a balance of Graphite. Once the catalyst was loaded and the system pressure-tested, both vessels were purged of gaseous impurities three times with 30psig of pure H_2. For one hour, the vessels were progressively heated, in a closed system, until their respective temperatures were reached. Pure H_2 was maintained inside both vessels during heating at a pressure of 15-20 psig. When the desired temperatures were reached, syngas and distilled water were allowed to flow through the catalyst.

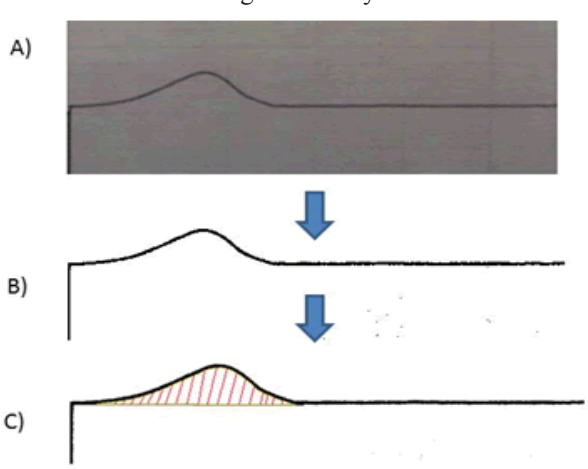

Figure 5: Modification of gas peak curve using ImageJ: A) Original picture of gas peak, B) Image modified to allow ImageJ to detect curve, and C) Area under the curve computed by ImageJ using pixel counts.

In all tests, the water flow rate was maintained at 20-23 ccm. Syngas flow rates used were 3, 10, and 20 SLPM resulting in a residence time of 0.12, 0.24 , and 0.78 seconds and a steam to CO ratio of 29:1, 9:1, and 5:1 respectively. The relatively small distilled water flow rate range was selected for simplicity as the work of Chen, et al., showed that increasing the steam to CO ratio past 4:1 did not result in a significant increase in WGS performance.1 Gas samples were collected when the catalyst reached 200°C, 225°C, and 250°C; at each temperature, the residence time was also tested. An average of three gas samples were collected for each combination of temperature and residence time, and each test was repeated for precision. The data collected was then used to establish graphs to illustrate and analyze the effects of the changing parameters of the WGS reaction.

C. Data Analysis

As previously mentioned in the experimental equipment section, post WGS samples were analyzed using a gas chromatograph. A strip chart recorder, connected to the gas chromatograph, recorded the quantity of individual gases by making curves based on voltage changes and the feed rate of the paper. The specific strip chart recorder employed did not have an automated feature to determine the area under the gas peaks curves. These areas are necessary to determine the percent composition of specific gases, such as the content of CO in the sample, etc. ImageJ software was used to determine these areas. A digital copy of the recording had to be made in order to enable ImageJ to compute the areas using pixel counts. Subsequently, the digital recordings had to be modified for ImageJ to recognize the gas peak curves (Figure 5). The same software was also used to find the average particle size of the CZA catalyst (Figure 6).

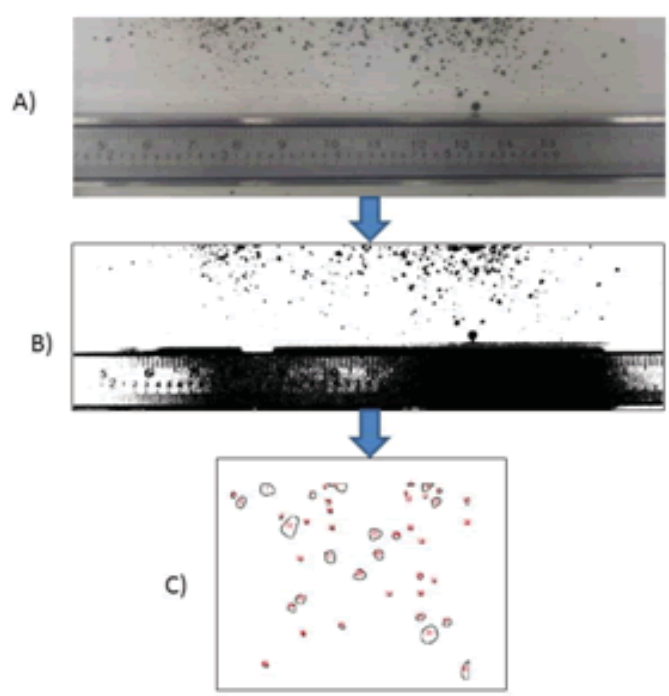

Figure 6: Use of ImageJ to determine particle size: A) Original picture of catalyst particles, B) Image modified to allow ImageJ to detect particles, and C) Area of particles were found and averaged

III. Results and Discussions

A. CO Content Reduction in Syngas vs. Temperature

The utilization of the CZA catalyst was tested in a low-temperature shift reactor. An increase in temperature, from 200°C to 250°C, resulted in a considerable reduction in the CO content in the syngas. Figure 7 illustrates the results obtained from testing the catalyst at varying temperatures and residence times. At each residence time, an increase in temperature was shown to increase the percentage of CO reduction. This indicates that the CZA catalytic activity increased with temperature within the 200°C to 250°C range. Figure 7 also shows that there is a relatively smaller increase in performance when increasing the catalyst temperature from 225°C to 250°C with a peak at 250°C. This observation, also evident in Figure 8, indicates that the peak activity of the CZA is near 250°C.

B. CO Content Reduction in Syngas vs. Residence Time

The residence time of the syngas in contact with the catalyst was found to be one of the most crucial factors in CO reduction. At 200°C, changing only the residence time of the syngas from 0.12 sec to 0.78 sec resulted in an increase in CO reduction from 70.4% to 88% respectively. This relation was expected as the catalyst would have more time to react with the CO. A similar, yet less heightened behavior was recorded at 225°C and even more so at 250°C as shown on Figure 8 below. This indicates that the rate of the WGS reaction slows down as the CO content in the syngas is lowered. Additional testing at residence times close to 0.78 secs would be required to determine if a longer residence time is beneficial. It is expected that any further increase in residence time will not result in a significant CO reduction. This expectation is based on the equilibrium line of the WGS reaction using CZA demonstrated by Guo, et al.[2]

C. CO Content Reduction in Syngas vs. Catalyst Particle Size

Usually, increasing the surface area of a catalyst results in a faster reaction. For this reason, the CZA catalyst was ground to a 0.5 mm mesh diameter and tested at 0.78 sec residence time. Figure 9, below, shows a comparative graph of the results attained when testing, under the same conditions, for CO content reduction using 0.5 mm and 3.1 mm catalyst particle size. At 250°C, 100 grams of the 3.1 mm catalyst particle size was able reduce 33% more CO than 100 grams of the catalyst ground to 0.5 mm. This result was unexpected. However, after reviewing published literature, we note that Guo, et al., concluded that increasing the Copper surface area had no relationship to the WGS reaction.[2] Instead, the Copper-Zinc interface sites are found to be responsible for the WGS reaction. Therefore, grinding the CZA catalyst must have reduced the amount of Copper-Zinc interface sites, resulting in the poor WGS performance experienced. This suggests that in order to see the benefits of having a smaller particle size, the catalyst should be synthesized, and not ground to the desired smaller particle size.

IV. Conclusions

The experiments conducted showed that the CZA acquired was most active and near its maximum activity around 250°C. A 92% reduction of CO, by volume, is achievable with the following parameters: a catalyst temperature of 250°C, a residence time of 0.78 sec, a steam to CO ratio of 5:1, and 100 grams of CZA with a non-ground particle size of 3.1 mm. A greater residence time would have most likely resulted in a very small increase of CO reduction. Under the same conditions, 100 grams of CZA ground to 0.5mm, converted 33% less CO than the 3.1 mm catalyst. This reduction in catalytic performance was a result of reducing the Copper-Zinc interface sites by grinding the catalyst. Therefore, in order to experience the benefits of a decreasing particle size, the catalyst should be synthesized and not ground to a smaller particle size.

V. Acknowledgments

I would like to express my gratitude to Dr. James Wegrzyn, Dr. Hazem Tawfik, and the graduate students at the biofuels lab, in Stony Brook University, for their sincere guidance during this wonderful summer internship. I also want to thank the Office of Educational Programs at Brookhaven National Labs along with Farmingdale State College, Stony Brook University, the U.S Department of Energy, and the National Science Foundation for this golden opportunity to conduct research.

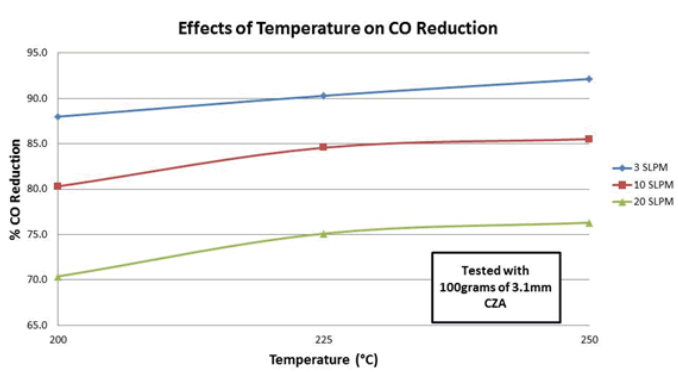

Figure 7: Shows how a change in temperature affects the performance of CZA in reducing the percent of CO in syngas.

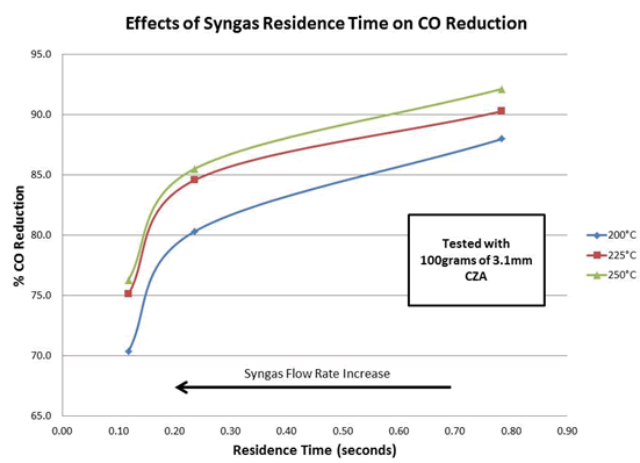

Figure 8: Shows how a change in residence time affects the performance of CZA in reducing the %CO in syngas.

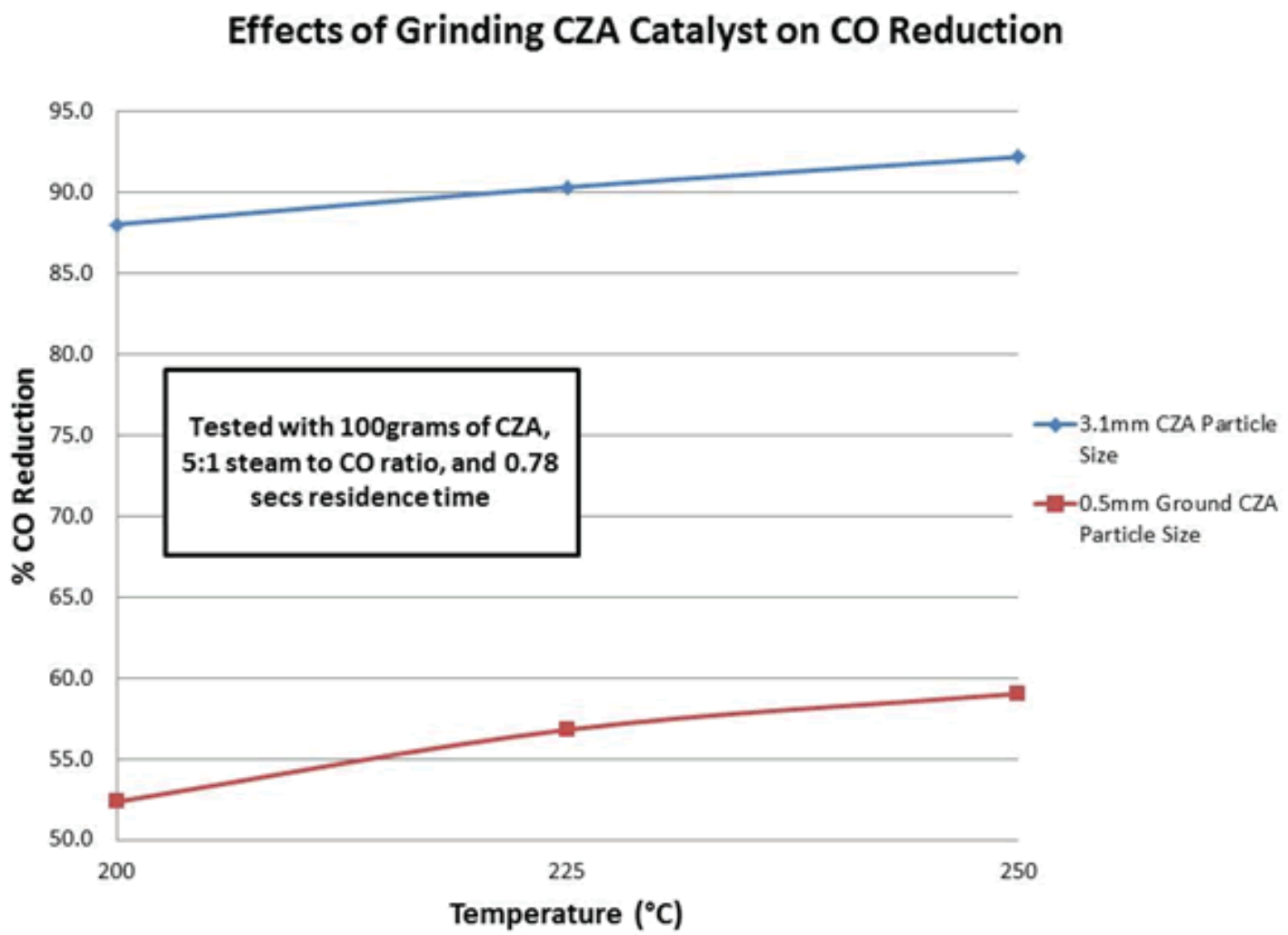

Figure 9: Shows how a change in the catalyst's particle size affects the performance of CZA in reducing the %CO in syngas.

VI. References

[1]W.-H. Chen et al. / Energy Conversion and Management 49 (2008) 2801-2808

[2]P.-J. Guo et al. / Catalysis Communications 10 (2009) 1252-1256

[3]J. R. Mellor, N. J. Coville, A. C. Sofianos, R. G. Copperthwaite, Appl Catalysis 164 (1997) 185

[4]R. Kam et al. / Chemical Engineering Science 65 (2010) 6461-6470

Increased prefrontal gray matter volume in structural MRI of cocaine abstainers at 6-month follow-up

Amanda Pflumm
Psychology Department,Washington & Jefferson College, Washington, PA 15301
Muhammad A. Parvaz and Rita Z. Goldstein
Medical Research, Brookhaven National Laboratory, Upton NY 11973

ABSTRACT

During my time here at the Brookhaven National Laboratory, I focused on a longitudinal study using voxel- based morphometry to compare the structural magnetic resonance imaging (MRI) scans of individuals with cocaine use disorder (CUD) at a baseline (with 14 days of abstinence) and at a 6-month follow-up. Using a similar study design (including abstinence length, follow-up duration and subject sample), prior functional MRI studies performed by the neuropsychoimaging group showed improved activation in brain regions associated with motivation and self-regulation. Therefore, for the current study, we hypothesized higher gray matter volume (GMV) of the brain structures associated with better emotional and cognitive functioning. Our results show significant bilateral GMV increases in the prefrontal cortex (including the inferior frontal gyrus, directly implicated in inhibitory control) at the 6-month follow-up as compared to baseline. Thus, our results show improved structural integrity of the prefrontal brain structures implicated in self-regulation following longer term abstinence. By conducting this study, I have gained knowledge and experience in working with human subjects' data, human subjects' safety, and the confidentiality of the subjects' personal information. I have also learned a great deal about teamwork and using the in-house neuroimaging expertise and applying it to learn new and important information about the effects of longer term cocaine abstinence on brain structure. This experience is completely in-line with DOE's mission of "educat[ing] new generations of scientists, engineers, technicians, and researchers." This experience has helped me understand the benefits of research in the medical world, and has inspired me to pursue higher education in biomedical sciences and eventually pursue it as a career.

I. Introduction

Drug addiction is a disease where the motivation to procure the desired drug overpowers the drive to achieve other non-drug related goals (Goldstein & Alia-Klein, et al., 2007). Individuals with substance abuse disorders display an array of deficits when compared to healthy controls. Many times, individuals with substance abused disorders show the most prominent deficits in areas of executive functioning (Alia-Klein & Parvaz, et. al., 2011).
Specifically, individuals with cocaine use disorder (CUD) demonstrate poor response inhibition, impaired-decision making skills, deficits in abstract reasoning and nonverbal problem solving, and auditory and visual impairments (Connolly & Foxe, et al., 2011). Response inhibition, decision making skills, and reasoning and problems solving have all been linked to be products of the prefrontal cortex (Alia-Klein & Parvaz, et. al., 2011). In other words, the prefrontal cortex is the area of the brain that is responsible for producing these higher functioning tasks.

Prior research has generally centered its focus on the functionality impairments of different substance use disorders. For example, an fMRI study with CUD subjects hypothesized that after a protracted period of abstinence, the CUD subjects would gain back some of the functional abilities that they had loss due to the excessive use of crack/cocaine. The study used a Stroop Task which measures inhibitory control--a product of the prefrontal cortex—to examine the subjects at a baseline scan and at a 6-month follow up scan. At baseline, Stroop scores were lower than scores demonstrated by healthy controls; however, after remaining abstinent for 6-months, CUD individuals showed significant improvements in their Stroop Task scores. This fMRI study demonstrated enhanced performance in functionality after a 6-month abstinence compared to baseline (Moeller SJ, Tomasi D, et al.).

Similar to individuals with cocaine use disorder, individuals with alcohol use disorder show similar deficits in functions that the prefrontal cortex is responsible for producing. A prior study using alcohol abuse individuals reported decreased gray matter volume (GMV) in the frontal lobe of alcoholics at baseline; however, after a 6--9 month period of abstinence the follow-up scans revealed increases in GMV of the frontal lobe. This study revealed structural increases after a period of abstinence rather than functional increases. The structural increases after the abstinence period suggest that alcoholics can regain some of the GMV that is damaged during years of abuse (Cardenas VA, Studholme C, et al.).

For the purpose of this study we wanted to examine if CUD individuals could regain any of the GMV lost during their years of use. While previous research demonstrated that it was possible to regain functionality that was lost, we wanted to see if there were structural gains that corresponded with the functional gains. Also, it was shown in a study using individuals with alcoholism that some of the individuals gained back GMV after 6--9 months of abstinence as compared to baseline (Cardenas VA, Studholme C, et al.). We wanted to examine if after a period of abstinence, individuals with cocaine use disorder also demonstrated increased GMV in the prefrontal cortex.

II. IMethods

A. Participants

Twenty-two individuals with cocaine use disorder participated in this study. The demographics of these individuals can be seen in Figure 1. The average age of participants was about forty-three years old. The majority of the participants were high school educated, African-American, and Caucasian. Fourteen males and seven females participated in the study. The average age of onset of cocaine use was about twenty-seven years old, with an average use of about five times a week. Participants were examined by a physician and a psychologist for MRI contraindications. For example, participants who had a major psychiatric disorder, major physiological disorder (i. e., cardiovascular dis-

ease), metal in the body, or loss of consciousness for less than 30 minutes were excluded from the study. Participants underwent a series of examinations at both baseline and the 6-month follow-up. Not only did they undergo MRI scanning, but participants were also evaluated using indicators that included neuropsychological tests, IQ, Beck's Depression Inventory, Craving questionnaire, and an Addiction Severity Index.

B. Imaging/Preprocessing

All images were structural MR T1 weighted, 3 dimensional modified driven equilibrium Fourier transform (3D-MDEFT) images acquired using a 4-Tesla Varian/Siemens scanner with SONATA gradient set (Shown in Figure 2). The scan time was about 15 minutes. Regional GMV was acquired using voxel based morphometry (VBM). Before VBM analysis images underwent a sequence of three preprocessing steps: step one, reorientation where the raw MRI image is reoriented over the X, Y, and Z axis so that each image is facing the same way and can be aligned with one another; step two, normalization were the image is normalized in accordance with the MNI (Montreal Neurological Institute) coordinates; and step three, the images are segmented into gray matter, white matter, and cerebral spinal fluid. For the purpose of this study we focused on the gray matter. The gray matter was then smoothed with a $10mm^3$ Gaussian Kernel.

C. Analysis

Regional GMV was acquired using voxel based morphometry (VBM). VBM uses voxels to label and recognize specific areas of brain matter: gray matter (GM), white matter (WM), and cerebral spinal fluid (CSF). For the purpose of this study, VBM computed a voxel-wise comparison of gray matter volumes. VBM was performed using the VBM8 toolbox in SPM8 using MATLAB. Segmented gray matter images from the baseline and 6-month follow-up were compared to determine regions with significant differences. Clusters were considered significant if $p<.05$ (FWE) with cluster sizes <20 voxels. GMV of significant clusters were extracted and compared statistically in SPSS using paired t-tests.

III. Results

Comparing the baseline and 6-month assessments, we found that areas with increased GMV were structures in the refrontal cortex which included the left and right inferior frontal gyrus, and the right superior frontal gyrus. Interestingly, we also found that at the baseline, the left and right ventral medial orbitofrontal cortex was larger than at the 6- month measurement. That there would be any GMV larger at baseline as opposed to at 6-months was a very unexpended result. Results are better demonstrated in Figures 3 and 4.

	Participant Demographics
	Baseline
Age (yrs)	42.6 ± 7.3
Race	7/12/1/2
Education	11.5 ± 3.7
Gender (Male/Female)	14/8
Verbal IQ (WRAT third edition)	92.1 ± 13.7
Nonverbal IQ (Matrix)	11 ± 3.2
Beck's Depression Inventory	5.6 ± 7.4
	Elements of Drug Exposure
	Baseline
Age of onset	27.1 ± 9.2
Cocaine use (yrs)	14 ± 8.2
Days since last drug use	103.3 ± 134.9
Cocaine Abstinence days	145.6 ± 189.7
Cocaine use days/week	4.2 ± 2.8

IV. Conclusions

In this study we demonstrated an increase in dorsolateral prefrontal cortex GMV (especially bilateral IFG) in treatment seeking CUD from baseline to 6-months. Our results are in accordance with previous fMRI studies that demonstrate increased cognitive performance in CUDs with longer term abstinence. Previous studies showed the increases in functionality after a baseline to 6-month period of abstinence; our results show a corresponding increase in structure from baseline to 6-month.

Larger Ventromedial Orbitofrontal Cortex (VMOFC) GMV at baseline compared to 6-months follow-up are consistent with an fMRI study showing increased VMOFC activity in individuals with Obsessive-Compulsive Disorder compared to controls when performing an error-response task which was linked to impulsivity. A previous study used positron emission tomography to demonstrate hyperactivation in the OFC of amphetamine and opiate abstainers when making risky-decisions. Perhaps at baseline the CUD were more impulsive in risky decision making than after the period of abstinence.

In the future it we would like to increase our sample size so that our results are even more robust than they already are. We would also like to examine longer time periods rather than just 6-months. For example, we are interested in seeing if the GMV increase remains, continues to increase, or perhaps thresholds and stops or maybe decreases at periods of 12 and 18 months. Furthermore, it is difficult to examine CUD subjects for such long period of time, because unfortunately, the relapse rate is high and we can no longer use the subjects if they return to using cocaine in a full-blow relapse.

Figure 2. 4-Tesla Varian/Siemens scanner used here in the Medical Department at the Brookhaven National Laboratory.

Larger GMV at 6-months

Larger GMV at Baseline

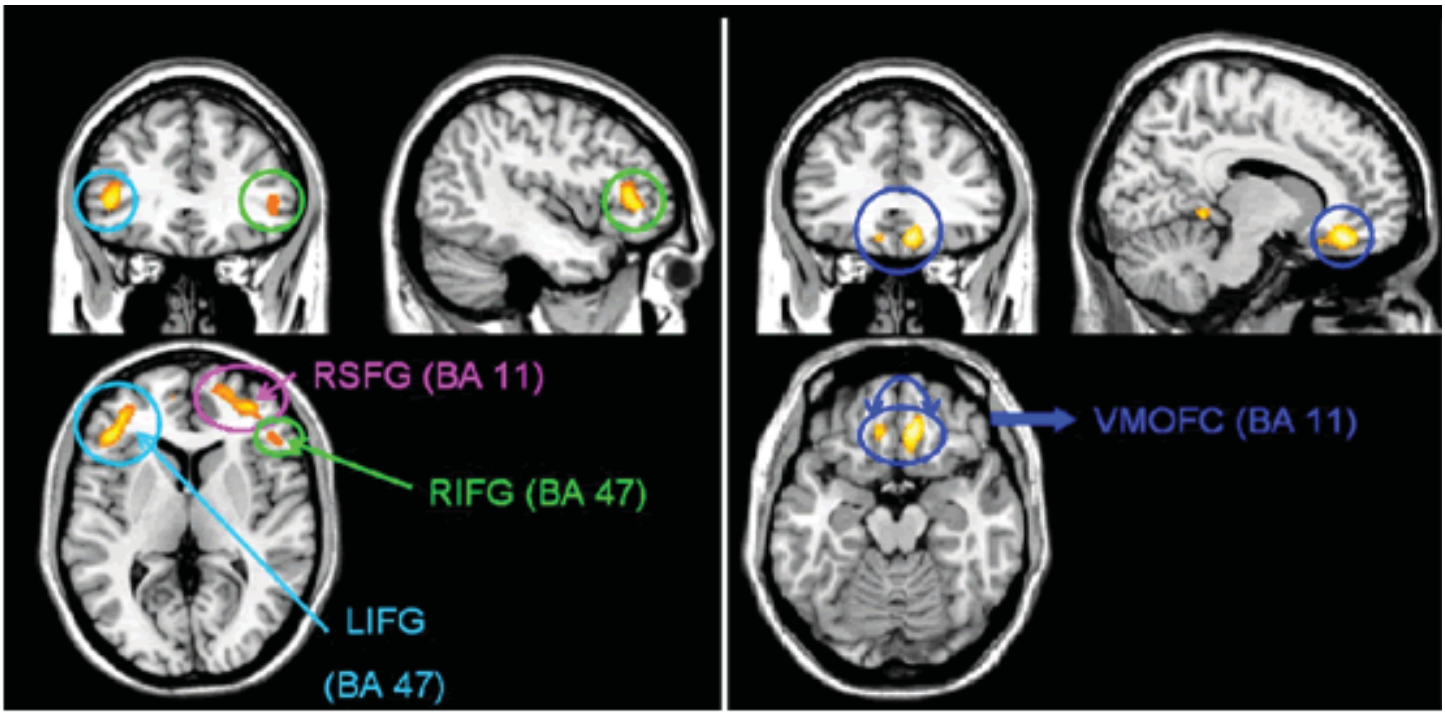

LIFG=Left Inferior Frontal Gyrus
RIFG=Right Inferior Frontal Gyrus
RSFG=Right Superior Frontal Gyrus

VMOFC=Ventromedial Orbitofrontal Cortex (Left/Right)

Figure 3. Uncorrected threshold of .001 and k=20. Left and Right Inferior Frontal Gyrii (L & RIFG; Brodmann's Area 47; L: Z=4.51, p=.026 R: Z=4.09, p=.019) & the Right Superior Frontal Gyrus (RSFG; Brodmann's Area 11; Z=4.36, p=.019). Ventromedial Orbitofrontal Cortex (VMOFC; Brodmann's Area 11; Z=3.99, p(svc)=.002).

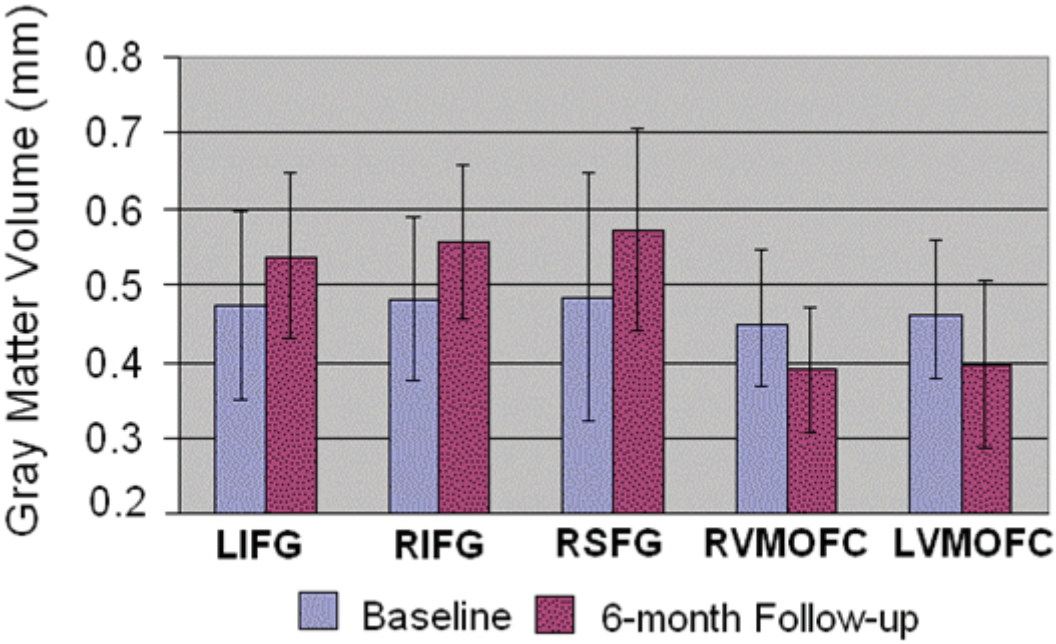

Figure 4. Gray matter volumes at baseline & 6-months. (From left) LIFG (BA 47)=Left inferior frontal gyrus, RIFG (BA 47)=Right inferior frontal gyrus, RSFG (BA 11)= Right superior frontal gyrus, RVMOFC (BA 11)=Right ventromedial orbitofrontal cortex, LVMOFC (BA 11)=Left ventromedial orbito frontal cortex.

Mechanistic investigation of novel Ruthenium π-Arene water oxidation catalysts

Long Dinh Phan
Stony Brook University, Stony Brook, NY 11794
Jonathan F. Hull
Brookhaven National Laboratory, Upton NY 11973

ABSTRACT

Our long term goal for this project was to convert solar energy into fuels. Using energy from the sun, it is possible to catalytically split water into protons, electrons, and oxygen. The protons and electrons can be stored chemically as hydrogen or hydrogenated liquids, conveniently making fuels easier to store and transport. This summer, I focused on the oxidative half reaction of water splitting to create oxygen from water; the next step was to reduce the resulting protons to H2 fuels. We investigated the properties of ruthenium complexes as a transition metal catalyst to discover whether or not they are good water oxidation catalysts. We measured the UV-Vis spectra of the cerium, an oxidant, in the presence and absence of ruthenium complexes in order to evaluate the mechanism of the reaction. The results from this investigation showed that the reaction rate was proportional to the cerium concentration, and had a rate constant of approximately 0.240 $M^{-1}s^{-1}$. The production of oxygen was observed during the reaction as a measure of the efficiency of the catalyst. With these studies, we were able to show that the ruthenium complexes with hexamethylbenzene as ligand was the best water oxidation catalyst. This investigation is a preliminary study of clean energy storage and production from renewable energy sources.

I. Introduction

Artificial photosynthesis is a process of storing solar energy in chemical bonds such as hydrogen or hydrogenated liquids. The main point of this research seeks to split water catalytically into protons, electrons, and oxygen so hydrogen can be produced for fuel (Eq. 1 and 2). Out of the two half-water reactions, we are interested in the oxidative one (Eq. 3) which has a high activation barrier and requires a good catalyst.

$$2H^+ + 2e^- + S\,SH_2 \quad (1)$$

$$2H^+ + 2e^-\ H_2 \quad (2)$$

$$2H_2O \rightarrow O_2 + 4H^+ + 4e^-,\ \Delta G^0 = 1.23\ V \quad (3)$$

Cerium was used as a terminal oxidant to investigate the kinetics of oxidation in the presence of three ruthenium complexes. These ruthenium catalysts had different donor ligands, such as hexamethylbenzene (HMB), trimethylbenzene (TMB), and benzene (BZ) in order to discover which one of them was the best water oxidation catalyst (Figure 1).

II. Method

A. UV-Vis kinetics

In a typical experiment, a 5 mM cerium stock solution was made by dissolving 5.48 mg of ceric ammonium nitrate (CAN) in 2 mL of 1M HNO_3. A 0.6756 mM **1a** stock solution was made by dissolving 1.08 mg of $RuHMB(OH_2)(SO_4)$ into 3 mL milliQ water. The solutions were made following Table 1, and their spectra were recorded using Agilent UV-Vis spectrometer.

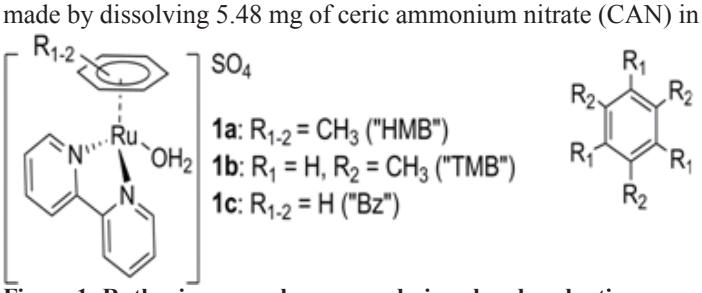

Figure 1: Ruthenium complexes were designed and evaluating.

[Ce]/[Ru]	1M HNO_3 (µL)	0.6756 mM RuHMB (µL)	5 mM CAN (µL)
200	3720	10	270
300	3585	10	405
400	3450	10	540
500	3315	10	675
700	3045	10	945

Table 1: Experimental data for UV-Vis measurement.

Using the Origin v7 program, the plots of cerium concentration vs. time and initial rate vs. cerium concentration were sketched to help showing the relationship between cerium and the reaction rate as well as how the catalytic effect of **1a** on cerium decomposition.

B. Spectroelectrochemistry

A 100 µL of 2.55 mM 1b (in H_2O) added in to a thin layer quartz glass cuvette containing 400 µL H_2O. Potentials were inserted through a platinum gauze working electrode to oxidize Ru^{II} to Ru^{III} and to Ru^{IV}, while the spectra were being recorded.

C. Electrochemistry

Cyclic voltammograms were run as the pH was titrated from 1 to 12 using 15 µl aliquots of 1 M NaOH. The purpose for this experiment was to find out the oxidation and reduction potential of the catalysts, which were then analyzed using spectroelectrochemistry. The plots of the catalyst spectra and pH-potential were plotted in Origin v7.

III. Results and Discussion

A. UV-Vis Kinetic

The UV-Vis spectra in kinetics mode of cerium with concentration of 8.44×10^{-4} M in presence of **1a** with concentration of 0.0169×10^{-4} M were taken in 1 M HNO3 over 8 hours (Figure 2).

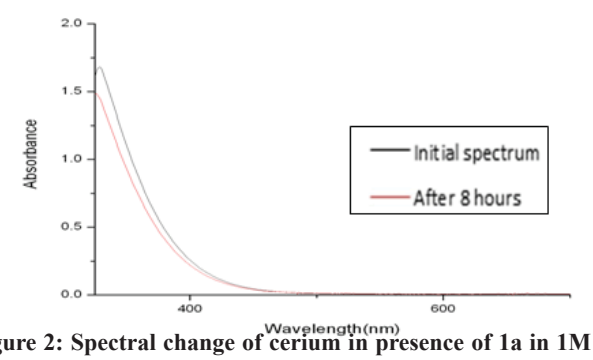

Figure 2: Spectral change of cerium in presence of 1a in 1M HNO3 over 8 hours.

The spectrum decreased as time increased, which indicated the cerium decomposed when reacting with ruthenium.

Single wavelength data at 335 nm were plotted to determine the catalytic cerium decomposition rate over 8 hours (Figure 3). The absorbance decreased rapidly in the first 2 hours and, as expected, slowed toward the end. However, an excess of cerium was left at the end of the reaction, indicating that the catalyst may decompose over time.

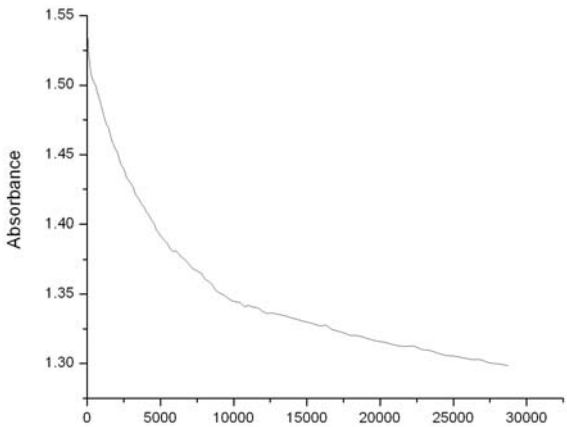

Figure 3: Single wavelength data at 335 nm of cerium in the presence of 1a.

The plot of concentration of cerium versus time (Figure 4) was extracted from the first 65 seconds of Figure 3 after converting absorbance to concentration using Beer's Law (with the absorptivity ϵ=1964.8cm^{-1}M^{-1} at λ=335nm) . Since the concentration of the reactants was known, the initial rate was easily determined by taking a slope of the linear line, which was 0.42796 µM/s in this case.

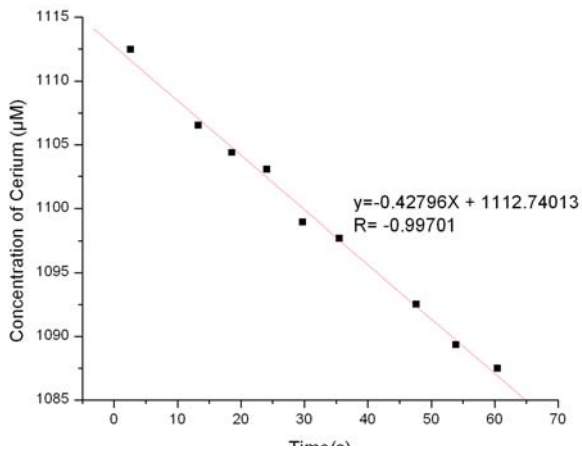

Figure 4: Plot of concentration of cerium versus time over 65 seconds.

The experiment was repeated with varied concentrations of cerium and a fixed concentration of ruthenium **1a** (0.0169×10-4 M); the data are summarized in Table 2. The plot of the initial rate versus the cerium concentration (Figure 5) was approximately linear, showing that the reaction rate was proportional to the cerium concentration and has a rate constant k = 0.240 M^{-1}s^{-1}.

[Ce],M (µM/s)	Initial rate
0.00118	-0.427959796
8.44E-04	-0.410804071
6.75E-04	-0.374724173
5.06E-04	-0.323053944
3.38E-04	-0.300281934

Table 2: Cerium concentration vs. initial reaction rate.

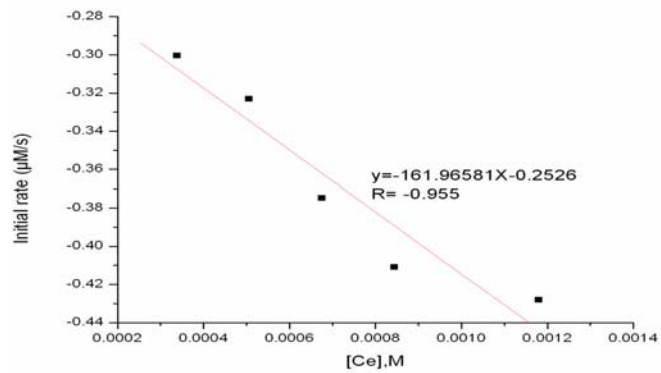

The spectra of three ruthenium catalysts (Figure 6) were taken at pH 5.5 by adding 0.4mL of catalyst stock solution (made by dissolving 4.21 mg of the catalyst in 8.33 mL mili-Q H_2O) in a 1 cm length cuvette containing a 3.6 mL 0.4 M Britton Robinson buffer. While **1b** solution had lightest color, **1c** solution was darkest.

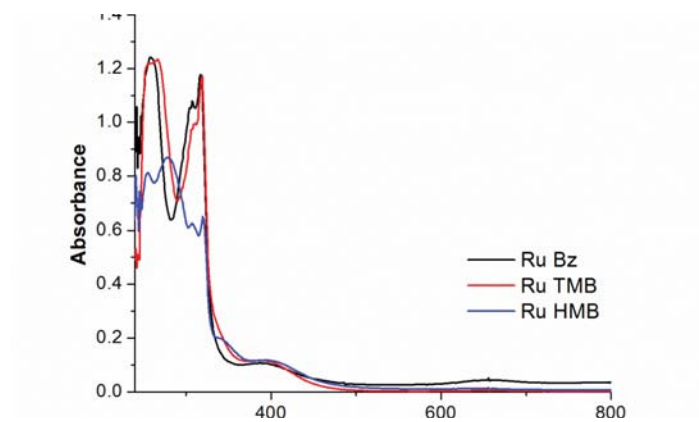

Figure 6: Spectra of three ruthenium complexes at pH 1.81.

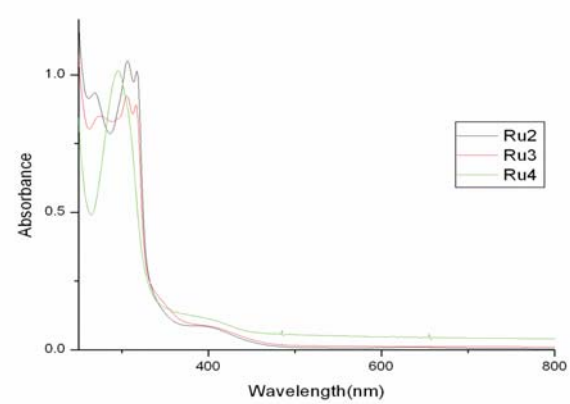

Figure 7: Oxidation state of 1b under acidic condition.

B. Spectroelectrochemistry

Spectroelectrochemistry was used to show how the spectrum of **1a** changed when Ru was in the II, III, and IV oxidation states. The fixed potential used to obtain these oxidation states Ru^{III} and Ru^{IV} were 105 mV and 1400 mV, respectively (Figure 7). At 350 nm, the absorbance decreased from II to IV state while the actual color of the solution lightened as well.

C. Electrochemistry

Cyclic voltammograms of **1b** was used to determine the oxidation and reduction potentials in the pH range 1-12. This also showed that the oxidation potentials are pH-dependent, which indicates that a proton was lost during oxidation as shown in equation 4. Notably, there is no slope for $Ru^{IV|V}$ oxidation state because there is no proton lost between Ru^{IV} and Ru^{V} (Eq. 6; Figure 9, a and b).

$$Ru^{II}\text{-}OH_2 \xrightarrow{e^-} Ru^{II}\text{-}OH_2 + H^+ \quad (4)$$

$$Ru^{III}\text{-}OH \xrightarrow{e^-} Ru^{IV}\text{-}O + H^+ \quad (5)$$

$$Ru^{IV}{=}O \xrightarrow{e^-} Ru^{IV}{=}O \quad (6)$$

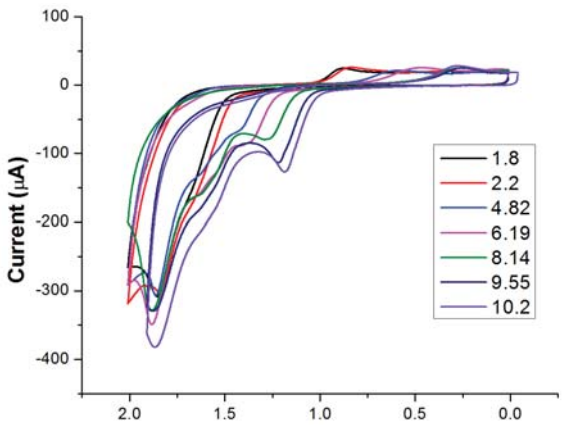

Figure 8: Cyclic voltammogram of 1b at various pH.

The Pourbaix diagrams were simply a plot of pH versus potential (Figure 9, a and b), which determined the potential needed to oxidize the ruthenium at given pH. For instance, at pH 1.8 for **1a**, the required potentials were approximate 0.6, 1.2, and 1.5 V to oxidize Ru^{II} to Ru^{III}, $Ru^{IV,}$ and Ru^{V} respectively.

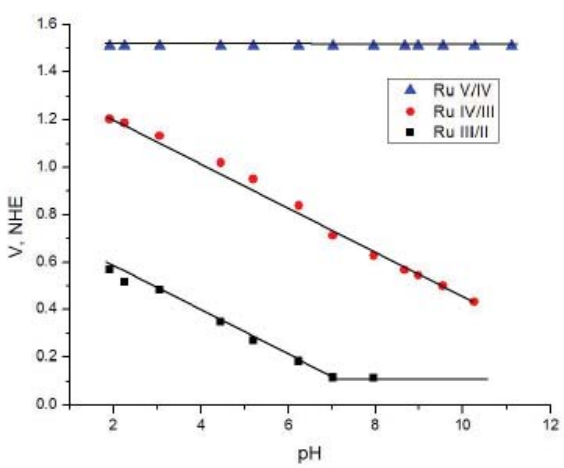

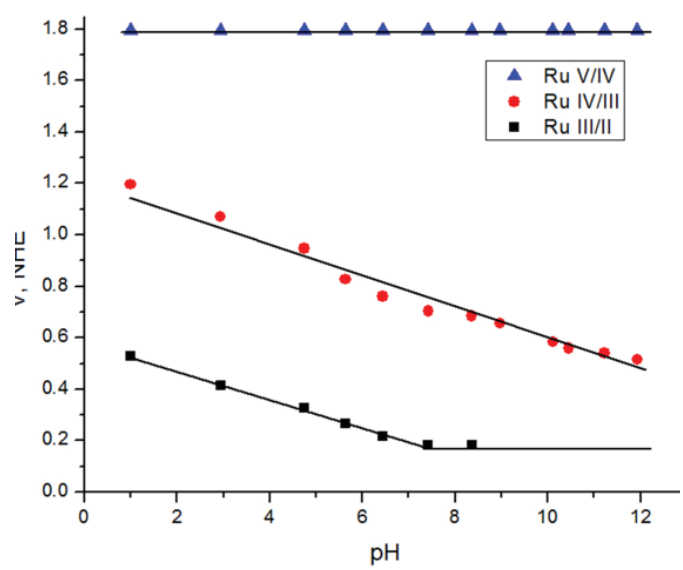

Figure 9: Pourbaix diagrams of (left) 1a and (right) 1b.

IV. Conclusion

A kinetic investigation of the cerium consumption was performed in the presence of **1a**. The rate of the reaction was proportional to the cerium concentration, and appeared to be first order in cerium. Electrochemistry experiments were used to determine the redox potentials of the intermediates $Ru^{IV|V}$ had potential of 1.6V (**1a**) and 1.8V (**1c**), showing hexamethylbenzene is a stronger donor ligand benzene. The observation that oxygen was produced and the cerium consumption was faster with 1a indicates that donor ligands are better for water oxidation in this system. Investigations using 1b as a catalyst are in progress.

V. Acknowledgments

This work was supported by Brookhaven National Laboratory at Upton, New York, Department of Energy, Science Undergraduate Laboratory Internship Program through Stony Brook University, National Science of Foundation, and Office of Education Program at BNL. I would like to specially thank my mentor Jonathan Hull and Etsuko Fujita. I would also like to thank Dmitry Polyansky, Yosra Badiei, Suzanne Golisz, and Nicholas Patterson for their assistance.

Post-growth thermal annealing and characterization of Cadmium Zinc Telluride radiation detector material

Asja Radja
University of Texas at Dallas, Richardson, TX 75063
Rodney Pinder and Aaron Adams
Alabama A&M University, Normal, AL 35762)
Ge Yang and Ralph James
Brookhaven National Laboratory, Upton, NY 11973

ABSTRACT

Cadmium Zinc Telluride (CZT) is considered the principle candidate material for radiation detection due to its ability to operate at room temperature, its high average atomic number (i. e., high photopeak efficiency), large band gap resulting in low leakage currents, good electron transport properties, and high availability. CZT detectors are thus imperative to ensuring national security since they are to be used as radiation detectors around the world. The quality of CZT crystals has not yet been fully optimized as there remain several types of structural defects. Tellurium (Te) inclusions, micrometer-size pockets of Te-rich which have phase separated from the CZT matrix, are of primary concern for this study since these inclusions decrease the resolution and efficiency of CZT detectors. We employ multiple characterization methods such as infrared (IR) transmission microscopy and X-ray diffraction topography (available at the National Synchrotron Light Source) to investigate these defects. Furthermore, we use post-growth thermal annealing to reduce the sizes of inclusions based on the diffusion and thermo-migration mechanisms of Te inclusions. We found a clear decrease in Te inclusion size after annealing thereby potentially improving the properties of CZT crystals. It is also evident that annealing temperature, time, and original inclusion size influence the amount of Te inclusion size reduction. Comparisons of samples show that a higher annealing temperature results in a larger percent decrease in inclusion sizes and that although annealing temperature is an important factor, time of annealing is also imperative.

I. INTRODUCTION

Cadmium Zinc Telluride (CZT) is considered the principle candidate material for radiation detection because of several of its material properties. It has replaced HPGe (high purity Germanium) as the most prominent radiation detector material primarily because of its independence from use of cryogens and low-temperature conditions.[1] Other significant properties which lend to its popular and effective use as a radiation detector include a high average atomic number resulting in high photopeak efficiency, large band gap resulting in low leakage currents, good electron transport properties, and high availability. Since their development, CZT detectors have been applied in a multitude of fields including use in nonproliferation efforts by federal agencies such as the Department of Homeland Security (DHS) and the Department of Defense (DOD), medical imaging, industrial monitoring, and astronomical observation. Because of their potential and diverse uses creation of efficient, large CZT crystals is imperative to national security, industry, and other scientific fields of study.

Production of CZT crystals for use as radiation detectors has not yet been optimized. There are several defects which limit their resolution and efficiency such as voids, pipes, impurities from source materials, Tellurium inclusions, Tellurium precipitates, vacancies, and vacancy-impurities. Other extended defects include grain boundaries, micro twins and walls of dislocations (sub-grain boundaries).[2,3]

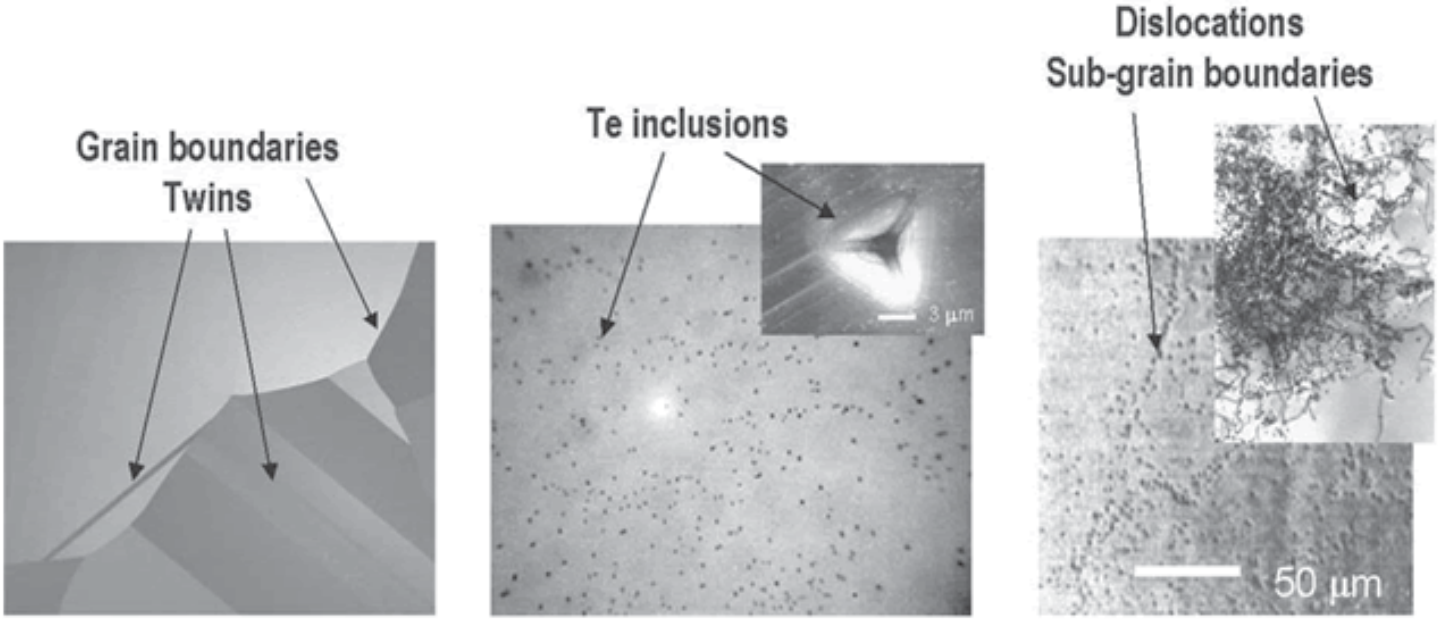

Figure 1: Images of most common defects found in CZT crystals[4]

Each of these defects originates from material properties of CZT and they all cause charge trapping which decreases the yield and resolution of the crystals. Identification, control and elimination of these defects and other charge compensators in the bulk material are currently important tasks that will potentially improve detector yield and resolution. These defects can be removed by improving crystal growth methods and/or through post-growth thermal annealing. This study focuses on post-growth thermal annealing to remove the Tellurium (Te) inclusions which are considered the most detrimental type of defect to CZT crystals.

A. Tellurium Inclusions

Te inclusions are pockets of liquid Te separated from the CZT matrix created both during and after the growth process at the interphase of the solid and melt regions. It is postulated that larger inclusions are created during growth and smaller inclusions during post-growth. Te inclusions decrease the crystal efficiency by charge trapping.[5] This is detrimental to the radiation detector as it no longer accurately determines the energy of the incident radiation proportional to the amount of charge collected at the electrodes. Additionally, because Te has a lower band gap than that of CZT, an abundance of Te inclusions lowers the resistivity of the crystal which additionally decreases the device's performance because of a high signal-to-noise ratio. It is clear then that the removal of Te inclusions is imperative to the improvement of the efficiency of CZT crystals.

Currently there are two techniques commonly employed to remove Te inclusions: 1) the migration of tellurium inclusions using a temperature gradient and 2) the reduction of tellurium inclusion sizes using constant temperature annealing in Cd vapor. In this study we focus on the later method and study the effects of constant temperature post-growth annealing on CZT properties. Our goal is to determine the optimal annealing conditions (temperature and time) which allow for the maximum size reduction of Te inclusions.

B. Post-Growth Constant Temperature Thermal Annealing

There are two proposed mechanisms for size reduction of Te inclusions during post-growth constant temperature thermal annealing. The first is called the diffusion mechanism. Here Cd atoms diffuse into the CZT crystals and react with excess tellurium to form CdTe which ultimately removes or at least reduces the size of the inclusion. The other mechanism is the migration mechanism in which liquid-phase tellurium droplets migrate to the crystal's surface in a thermal gradient field and react with Cd vapor. It is unknown and unclear which mechanism is the dominant one.

C. Annealing Parameters

In order to ensure effective results, the following conditions during annealing must be maintained. First, the Cd vapor in the ampoule is saturated and the vapor pressure of Cd annealing source is always higher than the Cd partial pressure of a crystal of the same temperature. Since tellurium's melting point is around 450°C annealing experiments are required to be performed above 450°C to take advantage of diffusion behaviors of liquid-phase tellurium atoms. According to the high temperature phase diagram of CdTe, there is a phase transformation from α phase of the zinc-blend structure to β phase of the wurtzite structure at temperatures near 877°C (1150 K). The presence of the β phase seriously deteriorates the electrical properties and results in high stress of crystals.10 Therefore, the upper limit of annealing temperature will be below 877°C. Recently, it has been shown that small tellurium inclusions are eliminated from CZT crystals after annealing at 650°C for 24 hours, whereas the larger inclusion persisted.11 Also, it was also observed that inclusions lying on grain boundaries are removed faster during annealing at this condition.

II. METHODS

In order to measure the effect of constant temperature post-growth annealing we must quantify the Te inclusion size both before and after annealing. Several methods are employed to characterize the crystals including Infrared (IR) Transmission Microscopy (using a Nikon Eclipse LV100D-U microscope) and White Beam X-Ray Diffraction Topography. First, all as-grown crystals are polished prior to characterization. Next, infrared transmission images of the crystal are taken. The samples are then annealed under specific conditions. The crystal must then be characterized again so that comparisons of before and after annealing may be performed to determine the effects of temperature-gradient post-growth annealing.

1. Mechanical Polishing: CZT crystals are first mechanically polished using 800 grit paper to remove rough scratches and uneven surfaces. This is followed by a series of Al2O3 polishing powders, which decrease in size from 5.0 to 0.1 microns as

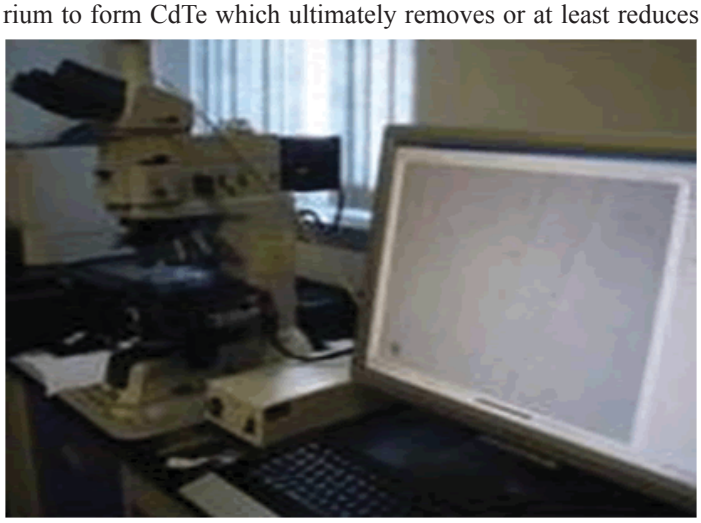

Figure 5: Infrared Transmission Microscope and Computer Setup used for imaging of Te inclusions

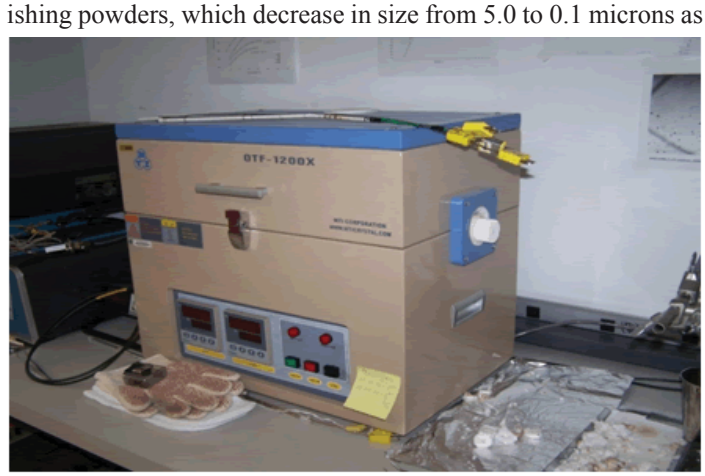

Figure 4: High Temperature dual-zone annealing furnace used for annealing CZT crystals

necessary. This step is imperative as polishing creates a smooth, reflective surface which is needed for proper imaging.

2. Infrared transmission microscopy: IR images of areas highly populated with inclusions are taken next. Under IR light, the CZT matrix is transparent while the Te inclusions are opaque due to the different band gaps of the materials. Consequently, we can see inclusions as dark spots on a lighter CZT background. We employed IR transmission microscopy to assess the number, distribution, and sizes of the Te inclusions within the CZT bulk crystals.

3. White Beam X-Ray Diffraction Topography: We next imaged samples using x-ray diffraction topography at the Brookhaven National Laboratory's National Synchrotron Light Source (NSLS). This technique is used to image sub-grain boundaries within the crystal bulk as the x-ray directly reflects the small lattice distortion causes by them.

4. Current-Voltage Measurements: Prior to annealing we also measure the resistivity of the crystals to quantify the change of the crystal's resistivity before and after annealing. First, a 5% gold chloride solution is applied to the top and bottom surfaces of the crystal creating a contact. The sample is then put into a Detector Test Probe Station and placed between two copper contacts. A voltage is then applied across the sample and the current generated is measured. From this, the resistivity of the crystal can be measured. The contacts are then removed by polishing with Al2O3 polishing powders.

5. Post-growth Thermal Annealing: The CZT crystals have now been completely characterized and are ready for annealing. They are sealed in a quartz ampoule and placed into a computer controlled high temperature furnace (model OTF-1200X2-A split dual zone tube furnace). Samples are annealed at various temperatures between 450-877ºC for a certain amount of time depending on the temperature and desired results.

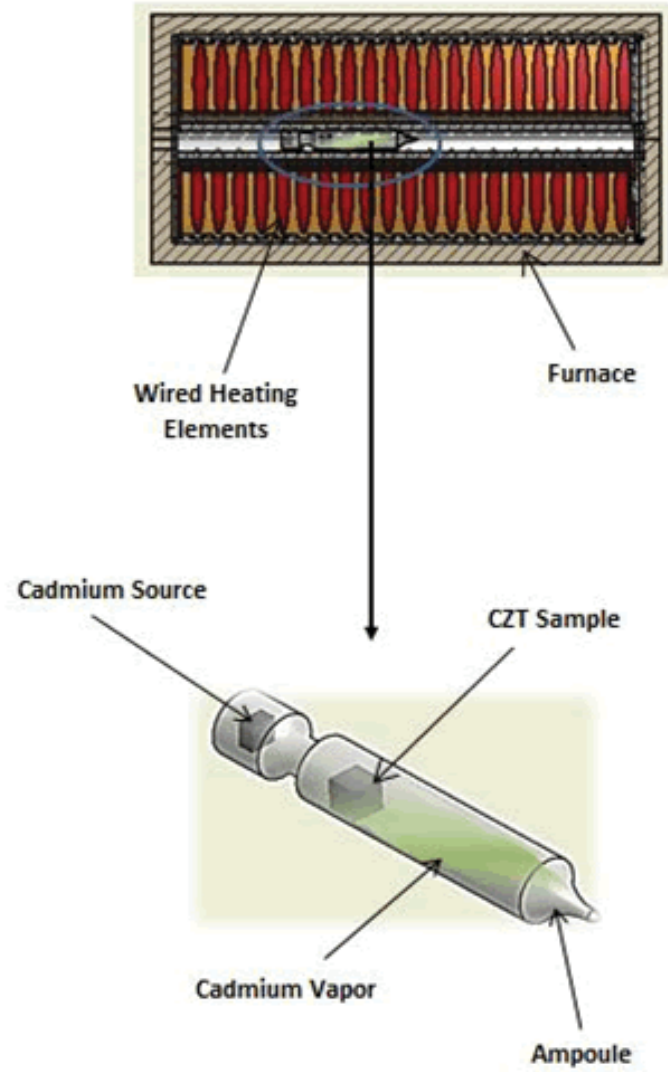

Figure 6: Furnace and Quartz ampoule schematic. CZT crystals are sealed in quartz ampoules with gas overpressure before being put in the furnace for annealing.

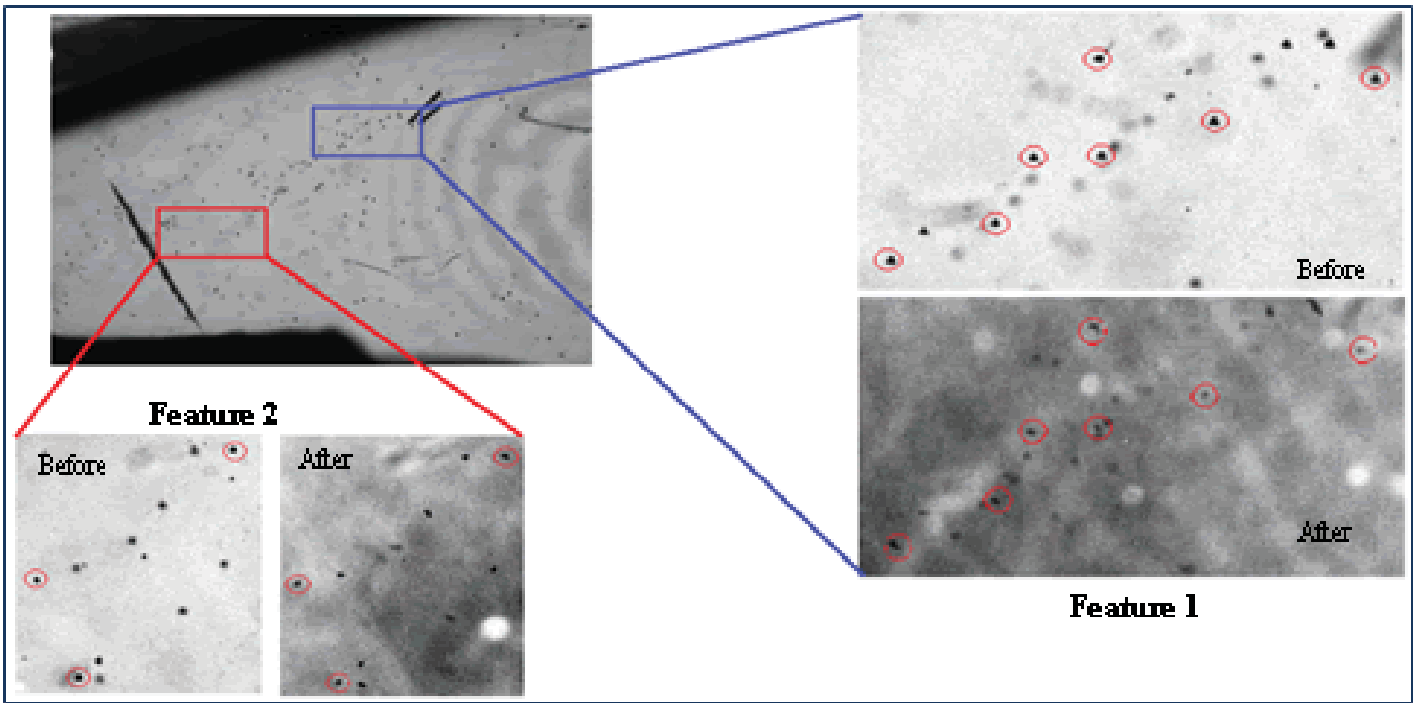

Figure 8: IR Transmission Microscope Images of CZT crystal sample A#4. Shown is the surface of sample with insets of two features both before and after annealing.

Sample	A#3	A#4	G#2
Temperature (ºC)	560	510	480
Time (hours)	20	60	20
Size Decrease	53.5% ± 9.5%	68.3% ± 9.5%	17.6% ± 8.1%

Table 1: Size Reduction of Te inclusions in three differently annealed samples

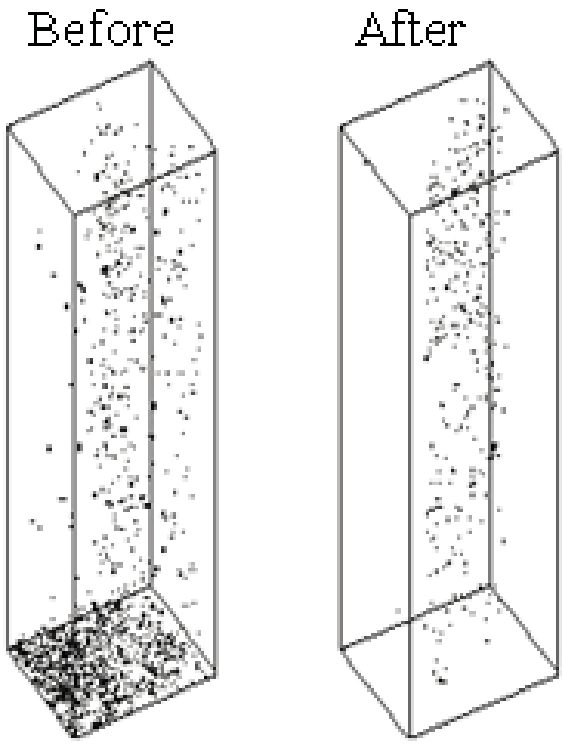

Figure 9: 3D Infrared Transmission Microscopy Images of CZT crystal A#4 before and after annealing

6. Characterization after annealing: The surface of the annealed CZT is now re-polished and all characterization processes are repeated for analysis.

III. RESULTS

All images shown are of CZT crystal sample A#4, a CZT crystal which was annealed at 560oC for 60 hours. We show three sets of data: IR transmission images, 3D IR images, and White-beam X-Ray Diffraction Topography images. Although only results for sample A#4 are shown for concision, all samples were analyzed in the same way and provided consistent results unless otherwise noted.

1. IR Transmission Microscopy Images: First presented are IR transmission microscopy images of the sample. We show a large scale view of the surface of the whole crystal. The two insets shown are portions of the crystal with the Te inclusions isolated from any other types of crystal defects, such as sub-grain boundaries. The purpose of this project is to study Te size reduction and as Te inclusions decorating sub-grain boundaries behave differently from those isolated from them, we only analyzed those isolated from other crystal defects. Additionally, the crystals are imaged in all three coordinate directions. As they are roughly 2000µm deep, we were able to analyze Te inclusions at different depths of the crystal. In the analysis, large Te inclusions of around 20µm (before annealing) were measured and compared to those in the after annealing images. Care was taken that the same inclusions were compared before and after annealing. The insets of figure 7 show examples of two features of the Te inclusions from which data was collected. Circled Te inclusions represent data points used to calculate the average size percent decrease of Te inclusions following annealing at specific conditions.

2. 3D IR Transmission Microscopy Images: 3D IR images were taken in order to visually display the decrease in inclusion sizes throughout the samples. Although quantitative measurements weren't taken from these images, a comprehensive picture of overall behavior of the inclusions due to annealing can be attained.

3. White-Beam X-Ray Diffraction Topography: X-Ray Topography images were taken at the NSLS. X-ray images were collected and developed both before and after annealing of CZT crystal samples. As mentioned in the methods section, X-ray diffraction topography is used to image features such as sub-grain boundaries and other dislocation features.

IV. DISCUSSION AND CONCLUSIONS

As has been proposed, there is a clear decrease in the large Te inclusion size after annealing. We can clearly see that post-growth thermal annealing does indeed reduce the size of inclusions thereby potentially improving the properties of CZT crystals. It is evi-

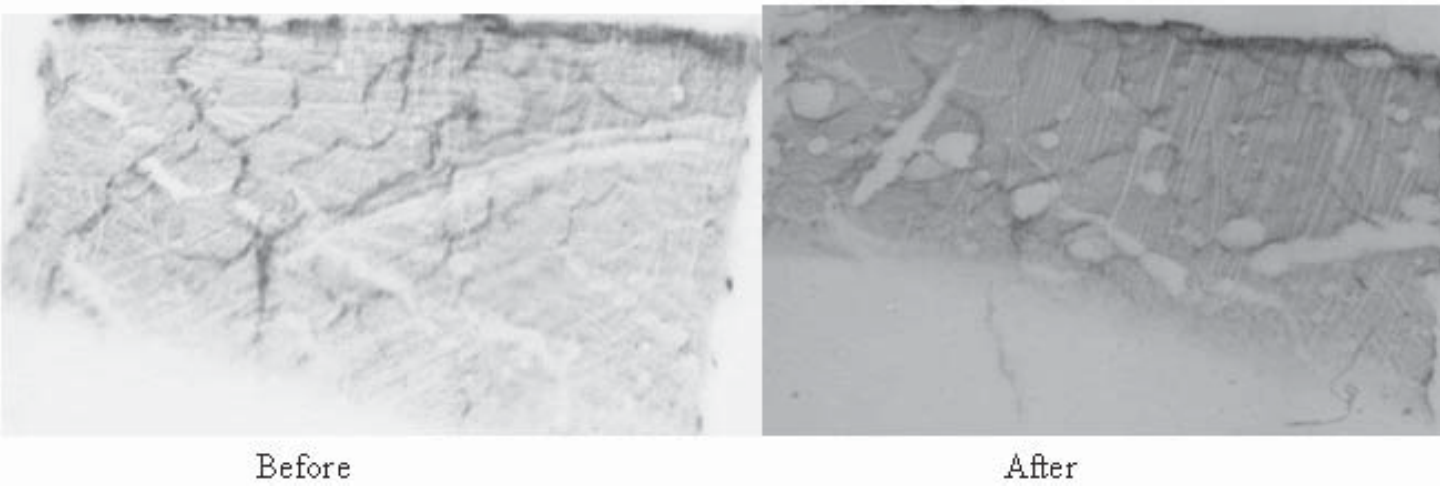

dent also that annealing temperature, time, and original inclusion size influence the amount of Te inclusion size reduction. Comparisons of samples A#3 and G#2 of table 1 show that a higher annealing temperature results in a larger percent decrease in inclusion sizes. Additionally, comparisons of A#3 and A#4 indicate that although the annealing temperature is an important factor, the time of annealing is also imperative. Further experiments should be conducted to determine an accurate correlation between all parameters and the reduction of inclusion sizes.

It was also observed that during annealing, the radially outermost Te inclusions decrease the most as can be seen in figure 9. This is logical as heat from the surrounding furnace can more easily penetrate the surface layers of the crystal in comparison to the center of the bulk. From this we can suggest that constant temperature annealing creates regions of crystals free of Te inclusions which are close to the surface and can be cut away from the rest of the sample and used as detectors.

Finally, we also observed 'star-like' defects after Cd over-pressure annealing, which were possibly caused by dislocation loop punching. Although we propose that these are correlated to Te inclusion locations, further experiments and analysis must be done to confirm this assumption. Although we cannot confirm the origin of these defects, we can confirm their presence in our samples.

V. REFERENCES

[1]T. E. Schlesinger and R. B. James, Semiconductors and Semimetals," in Semiconductors for Room Temperature Nuclear Detector Applications, San Diego, CA: Academic, 1995.

[2]A. E. Bolotnikov, S. O. Babalola, G. S. Camarda, H. Chen, S. Awadalla, Yonggang Cui, S. U. Egarievwe, P. M. Fochuk, R. Hawrami, A. Hossain, J. R. James, I. J.Nakonechnyj, J. Mackenzie, Ge Yang, Xu Chao, R. B. James, "Extended Defects in CdZnTe Radiation Detectors", IEEE Transactions on Nuclear Science 56(4), 2005, pp. 1775.

[3]A. Bolotnikov, S. Babalola, G. Camarda, Y. Cui, S. Egarievwe, R. Hawrami, A. Hossain, G. Yang, R. B. James, "Te Inclusions in CZT Detectors: New Methods for Correcting Their Adverse Effects", IEEE Transactions on Nuclear Science 57(2), 2010, pp. 910.

[4]Csaba Szeles, "Advances in the Crystal Growth and Device Fabrication Technology of CdZnTe Room Temperature Radiation Detectors", IEEE transactions on nuclear science, vol. 51, no. 3, June 2004

[5]G.S. Camarda, A.E. Bolotnikov, Cui Yonggang, A. Hossain, S.A. Awadalla, J. Mackenzie, H. Chen, R.B. James. "Polarization Studies of CdZnTe Detectors Using Synchrotron X-Ray Radiation." IEEE Trans. Nucl. Sci,.Vol. 55 Issue 6, pages 3725 – 3730, Dec. 2008

VI. ACKNOWLEDGMENTS

This work was supported by the U.S. Department of Energy's Office of Nonproliferation R&D and Treaty Verification (NA-22). We would like to thank the scientists, faculty, staff, and students at Brookhaven National Laboratory. We would especially like to thank Dr. Ralph B. James and his team for allowing us the opportunity to learn from them. Finally, we extend a special thanks to the OEP members for all their guidance and support.

Large grain electron gun testing

Denzel Pressey
Southern Polytechnic State University, Marietta, GA 30060
Lee Hammons
Brookhaven National Laboratory, Upton, NY 11973

Abstract

The large grain electron gun test will be conducted upon a unique, large-grain niobium superconducting radio frequency (SRF) cavity that has been designed to allow for a high current to be run through it. An RF cavity is a key component in particle accelerators, such as the new energy recovery linear accelerator (LINAC) facility being developed at Brookhaven National Laboratory, because it imparts energy to the charged particles. Construction of a LED light tube for a camera with visual access inside the cavity can be utilized to test the functionality of the camera under cryogenic conditions. The camera, in turn, will be used to understand an issue with cavities called multipacting. Multipacting occurs when electrons spontaneously appear and begin to crash on the walls of the cavity, depleting the cavity of energy and degrading its performance. A prototype and early model circuit board for the light tube was developed as a start to test the camera. This testing also requires assembly of components for the SRF cavity was needed for the test to be efficient. The development of the prototype circuit board is an important preliminary step in preparing the LED light tube will work to begin with. Assembly of the cavity required work in a clean room to ensure that particles weren't deposited on the inside surface of the cavity, potentially compromising its performance. I learned clean room etiquette as well as the appropriate procedure for component assembly during the course of my work on the project. This was necessary to complete my assigned activities and to ensure optimal results.

I. Introduction

Traditionally in accelerator physics, the use of copper as a conducting cavity to achieve proposed results in physics experiments was extensive. Copper is known to be the best conductor next to silver, based on several parameters such as resistivity and temperature. Also, copper has been the preferred material to use in accelerators compared to silver, because of its cost efficiency. Historically, copper has fluctuated between $1.00 and $3.00 per pound in the precious metals market. Therefore, physicists would tend to gravitate toward copper for cavity development instead of silver, despite a loss in conductivity, which is a measure of a material to conduct an electric current.

As physics experiments become more sophisticated and demanding in their energy requirements, the use of normal conducting materials such as copper and lead will decrease and research of other materials will occur more frequently to meet these demands. Physicists have discovered that certain materials, when placed under stringent temperatures, tend to achieve large increases in conductivity and large reductions in resistivity. This is where the material, niobium, comes into play. Niobium achieves superconductivity, a state in which there is a substantial increase in normal conductivity, when exposed to extremely low temperatures. Niobium begins to exhibit this superconductivity at as low as 9 Kelvin, which is equivalent to -264°C. Therefore, we see that the study of chemistry and/or materials science in relation to accelerator physics has given physicists the ability to engage in more complex experiments.

To usher in the next wave of accelerator physics experiments, this project's overview was to focus on understanding the properties of a superconducting niobium cavity. In particular, my involvement focused on the development of an LED light tube, which is used in testing of a camera to be mounted on the cavity. The component, a circuit board harboring the LED light source, was successfully designed, but can be refined, possibly building a more complex circuit to harbor more LED's and achieve better results from the camera.

II. Progress

The preliminary step for the assembly of components of the cavity consisted of cleaning the overall cavity and components by wiping them down with ethanol until a low particle count, i.e. dust and debris, was achieved. "The surface must be dried before the cavity is evacuated and cooled down for re tests. There are several different approaches to this last step. At Cornell, the surface is dried by blowing warmed, filtered nitrogen gas through the cavity."1 Afterwards, the components, which consisted of a power coupler and outer camera chamber, were placed inside a clean room for a few weeks to ensure that the chances of contamination were mitigated. "The laboratory workers in the vicinity need to wear special particulate-free clothing and follow strict protocols to reduce particulate generation."2

The power coupler had to be constructed, such that the orientation of it did not interfere with the other parts of the cavity, while the construction of the outer camera chamber did not interfere with the perpendicular orientation of its "arm" relative to the cavity's vertical axis.

An analysis of the design of the circuit board followed to ensure that the circuit would work correctly. Next, a prototype built to ensure that initial analysis on paper made was correct. Fabrication started by measuring the dimensions of the circuit board that would suffice relative to the camera chamber. A soldering iron with aluminum solder was used to attach the components, capacitors, resistors, LED light, and logic chip, to a component holder. A wire wrapping gun and wire was then utilized to establish the connections to the electrical components and the logic chip. The process of making the connections was a tedious one, in that there were several instances where I'd have to refer to the circuit design to make sure the wiring was on the correct component. Nonetheless, after the connections were secured, the following step was to use the battery to test if the circuit functioned properly. Fortunately, the first attempt at fabrication was completed.

III. Future Work

An upcoming test will see if frosting on the camera lens occurs which can degrade the image displayed on the camera. If the image on the camera is degraded, observing the multipacting effect would not occur. Provided that the illumination system, which is the circuit with LED light and camera, functions

adequately under the cryogenic conditions, then a string of tests will follow, possibly including the fabrication of the LED light tube and development of a new circuit configuration that acquires power from the camera and controlled by it to allow for illumination. The use of additional LED lights can possibly be tested as well.

IV. Impact on Laboratory or National Missions

The project that I have worked on during my stay at the laboratory will affect the future development of particle accelerators. Since an RF cavity is one of, if not the most important, component of a particle accelerator, research and development in RF cavities can aid in achieving energy and cost efficiency relative to the development of particle accelerators. The energy recovery LINAC that is currently being developed within the Collider-Accelerator Department, will utilize the type of RF cavity that I assembled for its future experiments. As the name implies with this new linear accelerator, one of its goals is to reduce the use of energy by ensuring that a previous beam of particles used in an experiment can be utilized again for a following one.

V. Conclusions

My internship at Brookhaven National Laboratory has provided me with access to not only world class scientists and engineers and the cutting edge research they are working on, but also has provided an opportunity to grow in my work ethic and ability to understand the minute details and broad scope of the various assignments and projects I've worked on. I believe that being able to understand both of these perceptions of research is a useful skill for future graduate students in the STEM disciplines. This internship has been a rewarding experience in terms of professional development, and even social development in relation to my peers at the laboratory. Lastly, I appreciate being able to have the mentor, Lee Hammons, that I had during this internship. The mentoring I received was not just for the advancement of the projects bestowed upon me, but also mentoring for important life and career decisions.

VI. References

[1]Padamsee Hasan. Jens Knobloch. Tom Hays. RF Superconductivity for Accelerators. Wiley-VCH. 2008. Print.

[2]Padamsee Hasan. Jens Knobloch. Tom Hays. RF Superconductivity for Accelerators. Wiley-VCH. 2008. Print.

Figure 1: A photo of myself and the cavity in a class 1000 area.

VII. Appendix

Participants -

Names	Institutions	Roles
Denzel Pressey	Southern Polytechnic State Univ.	Intern
Lee Hammons	SRF Group, CAD Dept.	Co-Contributor, provided assembly of components in the clean room.
Tom Seda	ERL Group, CAD Dept.	Aided in analysis in the prototype and fabrication of circuit board.
Dave Pate	ERL Group, CAD Dept.	Provide support with sufficient work space, and advice on the project.
Steven Bellavia	C-AD Dept.	Aided in dimensional analysis of circuit board transfer into camera chamber.
John Carlson	C-AD Dept.	Aided in optical testing of the camera-circuit board system.

Scientific Facilities – Bldg. 966 (ERL R& D) and Bldg. 905 (Machinery & Clean Room).

Hot-pressing and physical properties characterizations of polycrystalline specimens of boron carbide (B4C) for elasticity studies at extreme conditions

Brandon Rhymer
University of the Virgin Islands, Charlotte Amalie, VI 00802
Gabriel D. Gwanmesia
Delaware State University, Dover, DE 19901
Lars Ehm
Brookhaven National Laboratory, Upton, NY 11973

ABSTRACT

Hot-pressing of polycrystalline specimens of boron carbide (B4C) have been carried out in the pressure range of 7.5 to 10 GPa, and temperatures of 1375 K and 1675 K, using a 2000-ton uniaxial split-sphere apparatus (USSA 2000) and the 1000-ton Walker-type uniaxial split-cylinder apparatus (USCA 1000) installed at the Stony Brook High Pressure Laboratory. The starting material for the synthesis experiments was fine-grained commercial B4C loaded into platinum (Pt) or rhenium (Re) capsule. The hot-pressing experiments were conducted using the 14/8 cell assembly having a graphite resistance heater and a WRe25%--WRe5% thermocouple for temperature measurements. Recovered samples have been examined by x-ray diffraction techniques and bulk density measurements by Archimedes' technique. A high acoustic-quality specimen was obtained at a pressure of 7.5 GPa and 1675 K for a one hour duration. X-ray diffraction analysis of the specimen reveals the specimen to be single-phased B4C with a bulk density of sample (2.519 g/cm^3) that is well within 1% of B4C x-ray density.

I. INTRODUCTION

Boron carbide, also known as black diamond, is ranked behind boron nitride and diamond as the third hardest material. It can be used for abrasive, refractory, and ballistic applications due to its light weight, elastic modulus, chemical inertia, extreme hardness (2300vickers), high melting point (2450°C), flexural strength (300MPa), fracture toughness (3-3.5 MPam$^{1/2}$), and semiconductor properties. It is applied mechanically to ceramics as a coating to improve resistivity and strength or processed into ballistic armour for protection against high-impulse impacts from bullets or explosions. Industrially, it can be utilized as an antioxidant for refractory compositions or developed into nozzles for slurry, grit, ultrasonic, or aquatic blasting.[1] For nuclear relevance, it serves as an excellent thermal neutron absorber within nuclear control rods and its very low radioactive waste production is recyclable.[2] It is also essential for other advanced procedures because of its thermal conductivity (30-40 W/mK), electrical resistivity (10^6 μΩ-cm), thermal expansion coefficient ($5x10^6$ K^{-1}), and Young's modulus (450-470 GPa).

Boron carbide is made commercially by reacting carbon with boron oxide (B_2O_3) through gas phase reactions or carbothermic reduction in an electric arc furnace or graphite resistance heater.[3] This carbothermal process is an endothermic reaction which produces B4C aggregates that have to be grounded into a fine powder and yields the chemical reaction $2B_2O_3 + 7C \longrightarrow B_4C + 6CO$.[4] It is mainly fabricated this way at pressureless conditions with temperatures above 1750°C, even when sintered after purification by chemical and thermal oxidation means because of contamination.[5] It can also be synthesized using a magnesiothermic reduction of boric oxide in the presence of amorphous carbon, which gives way to the following reaction $2B_2O_3 + 6Mg + C \rightarrow B_4C + 6MgO$.[4] The magnesiothermal process is an exothermal reaction that produces fine grain size powder with an average size about 1 micron.[2-5] These two powders can then be used for nuclear applications and measured for micro-cracks, swelling, absorption rate, and porosity after being sintered to make pellets between 5 to 15 microns once chemical removal of magnesia and carbon oxide is completed.[2]

Three main problems with the study of fabricating polycrystalline boron carbide pellets via hot-pressing is the fact that B_4C contains free carbon, is extremely brittle, and has poor sintering, which is due to its strong covalent bonds.[6] For this reason, sintering aids like binders are particularly used to hold B_4C aggregates together. These additives like Ti, Al, and Fe help to reduce brittleness and improve sinterability,[1] but do not enhance the nuclear applications of boron carbide. In regards to nuclear relevance, property characteristics and elasticity studies aid in better understanding the heterogeneous swelling and cracking of B_4C pellets that occurs within nuclear reactors and helps in the study of expanding the lifetime limit and reducing the porosity of the pellets. Measurements of the elastic properties of B_4C as a function of pressure and temperature are also important for engineering design applications. However, to date only limited studies have been carried out, with most attention being focused on the room temperature technological elasticity such as the Young's and shear moduli and Poisson's ratio. The purpose of this study is to utilize hot-pressing techniques that have been developed for the USSA 2000 to synthesize dense polycrystalline B_4C specimens of high-acoustic quality free of any sintering aids such as binders, to completely characterize the physical properties of the samples by x-ray diffraction, optical, and electron microscopy and by density measurements, and to investigate the elasticity of the material at high pressure and high temperature by acoustic interferometry techniques.

II. EXPERIMENTAL PROCEDURES AND RESULTS

Six hot-pressing experiments were carried out in two Kawai-type multi-anvil high pressure devices, the USSA 2000 also known as the Sumitomo Press and a Walker-type press (called Kennedy) installed in the High Pressure Laboratory at Stony Brook University. Each press consists of a two-stage anvil system driven by a ram force and can generate pressures up to 30 GPa (300 000 atmospheres for Sumitomo) and 16 GPa (for Kennedy) and sustain temperatures to 2500oC (4532°F). Specimen sizes can range from 3 mm^3 at 30 GPa to 30mm^3 at 10GPa. The first stage of these high-pressure systems consist of six pieces of tool steel cut from a sphere (for Sumitomo) and cylinder (for Kennedy) that are well situated into lower and upper guide blocks with each press. The second pressure stage consists of 8 tungsten carbide (WC) cubes of high strength whose corners are truncated to triangular faces to form an octahedral cavity to host an octahedral MgO pressure medium that houses the sample under investigation. Six phenolic sheets are used to insulate the second stage from the first and hold the eight WC cubes with the octahedral semi-sintered ceramic pressure medium containing the sample located within the octahedral space created by the cubes. The eight cubes are insulated from one another by pyrophyllite gaskets and balsa wood spaces that also provide structural support for pressurizing. Two of the phenolic sheets each carry a piece of copper through which current is transmitted from the external circuit to a graphite resistance furnace to heat the sample.

The MgO octahedron pressure medium has an edge length of 14 mm and is used in combination with WC carbide cubes whose corners are truncated to an 8-mm triangular face, generally called the 14-8 cell assembly. The MgO contains a cylindrical graphite resistance furnace that makes contact with two opposing cubes faces via molybdenum (TZM) rings. The furnace is surrounded by a zirconia sleeve that serves to minimize heat loose from the sample environment. The B_4C powder was loaded into a platinum (or rhenium) capsule and insulated from the graphite furnace by an MgO (or NaCl) sleeve. A WRe25%-WRe5% thermocouple wire, threaded into a 4-hole ceramic (alumina) with its junction located at the top of one end of the sample was used to monitor the sample temperature during heating.

For this cell assembly, two 2.5 to 3 mm long specimens were fabricated at a high pressure range of 7.5 to 10 GPa and at temperature conditions of 1375 to 1675 K. These pellets were examined under a microscope and appeared to be well-sintered and without any noticeable macro-cracks. Both samples were further examined by x-ray diffraction techniques, using the Ultima IV X-Ray Diffractometer and by bulk density measurements using Archimedes' method. The x-ray diffraction patterns for the first specimen revealed extra coesite (SiO_2) peaks from quartz introduced into the starting powder through grinding of the B4C powder in an agate mortar. The quartz (SiO_2) from the starting powder transformed to coesite at high temperature and pressure. This specimen yielded a bulk density of 2.63g/cm^3. The second specimen that was hot-pressed from Alfa Aesar industrial powder was a single-phased, approximately fully dense (2.519 g/cm^3) specimen, and was without any extraneous diffraction peaks.[7]

III. SUMMARY

Although much work has been carried out on boron carbide more research is required in order to improve its general applications and usage. We have succeeded in hot-pressing pure B4C polycrystalline specimen having a density within less 1% of x-ray density. To be utilized for acoustic velocity measurements, further characterization of the hot-pressed sample is underway to ensure that the polycrystal is fine-grained, homogeneous, and free of any preferred orientation.

IV. ACKNOWLEDGEMENTS

We thank the SULI program for the summer internship privilege, the Stony Brook Geosciences department for use of their High Pressure facilities and X-ray equipment, the National Synchrotron Light Source (NSLS) and office of Education Programs at Brookhaven National Laboratory (BNL) and the U.S. Department of Energy, Office of Science, Office of Basic Energy Sciences under Contract No. DE-AC02-98CH10886. We are grateful to William Woerner for assisting with the x-ray diffraction analysis and for useful discussions.

V. REFERENCES

[1]K. Silver. "Processing of Nano-Sized Boron Carbide Powder," Georgia Institute of Tech. 1-37 (2007).

[2]B. Kryger and P. Herter. "Behaviour of PWR Type B4C Irradiated at High Capture Rate," Proceedings of a Technical Committee meeting (IAEA, Vienna, Austria, 1993), pp. 37-48.

[3]A. K. Suri, N. Krishnamurthy and C. Subramanian. "Issues in the Synthesis and Fabrication of Refractory Carbides, Borides, Silicides and Their Mixtures," Am. Ceram. Soc. 30 (8), 69 (2009).

[4]C. Jung, M. Lee and C. Kim. "Preparation of carbon-free B4C powder from B2O3 oxide by carbothermal reduction process," Material Lett. 58, 609-614 (2004).

[5]J.A. Bigdeloo and A. M. Hadian, "Synthesis of High Purity Micron Size Boron Carbide Powder from B2O3/C Precursor," Int. J. of Recent Trends in Eng. 1 (5), 176-180 (2009).

[6]I. T. Ostapenko et al., "Densification of Boron Carbide During Hot-Pressing," Powder Metallurgy and Metal Ceram. 18 (5), 312-316 (1979).

[7]G. D. Gwanmesia and R. C. Liebermann. High-pressure Research: Application to Earth and Planetary Sciences, edited by Y. Syono and M. Manghnani, American Geophysical Union, Washington, D.C., (1992) 117-135.

The science spectrum: Reporting on different disciplines at Brookhaven National Laboratory

Aviva Rutkin
Union College, Schenectady, NY 12308
Karen McNulty Walsh\
Brookhave Naitonal Laboratory, Upton, NY 11973

Photon Sciences | eNews | NSLS Helps Fine-Tune Vision of New NASA ...
... Small Explorers program. Aviva Rutkin. 2012-3227 INT/EXT | Media &
Communications Office. Issue Contents: Wednesday, July 18, 2012. ...
www.bnl.gov/ps/enews/news.php?a=23227 - 22k
BNL Newsroom | EEG Provides Insight into Drug-Related Choice in ...
... icon Print. EEG Provides Insight into Drug-Related Choice in Addiction. November
13, 2012. By Aviva Hope Rutkin. Scott Moeller Click ...
www.bnl.gov/newsroom/news.php?a=11470 - 26k
BNL Newsroom | Electronics Play By a New Set of Rules at the ...
... Print. Electronics Play By a New Set of Rules at the Molecular Scale. September
2, 2012. By Aviva Hope Rutkin. atomic-scale model Click ...
www.bnl.gov/newsroom/news.php?a=11449 - 28k
BNL Newsroom | Scientists Create Low-Lignin Plants with Improved ...
... Contacts: Peter Genzer, (631) 344-3174 | Written by Aviva Hope Rutkin printer
icon Print. Scientists Create Low-Lignin Plants with ...
www.bnl.gov/newsroom/news.php?a=11439 - 29k
BNL Newsroom | Titan Supercomputer Hours Awarded to Collaborative ...
... By Aviva Hope Rutkin | July 16, 2012 printer icon Print. Titan Supercomputer
Hours Awarded to Collaborative Protein Project. Scientists ...
www.bnl.gov/newsroom/news.php?a=23199 - 38k
BNL Newsroom | Sarah Ackerman Explores How Cells Fare in Space
... By Aviva Hope Rutkin | July 30, 2012 printer icon Print. Sarah Ackerman Explores
How Cells Fare in Space. Sarah Ackerman. SUNY Geneseo ...
www.bnl.gov/newsroom/news.php?a=23205 - 36k
BNL Newsroom | Brookhaven Lab Chemists Win R&D 100 Award for Fuel ...
... Contacts: Peter Genzer, (631) 344-3174 | Written by Aviva Hope Rutkin printer icon
Print. Brookhaven Lab Chemists Win R&D 100 Award for Fuel Cell Research. ...
www.bnl.gov/newsroom/news.php?a=11428 - 27k
BNL | Global and Regional Solutions | Physicist James Dickerson ...
... By Aviva Hope Rutkin | August 9, 2012 printer icon Print. Physicist James
Dickerson Joins CFN. James Dickerson. James Dickerson will ...
www.bnl.gov/gars/news/news.php?a=23251 - 25k
BNL Newsroom | NIH Grants $1 Million Dollars for New Detectors at ...
... perspective. August 8, 2012. By Aviva Hope Rutkin. Lin Yang and Marc Allaire
Click on the image to download a high-resolution version. ...
www.bnl.gov/newsroom/news.php?a=11443 - 26k
BNL Employees Keep On Learning
... By Aviva Hope Rutkin | Tuesday, July 03, 2012. BNL Employees Keep On Learning. Karim
Hamdi. Karim Hamdi always knew he wanted to go back to school. ...
www.bnl.gov/rhic/news2/news.asp?a=3187&t=today - 16k
BNL Newsroom | Athena Marneris Studies What Makes Glass Tubes ...
... By Aviva Hope Rutkin | August 6, 2012 printer icon Print. Athena Marneris
Studies What Makes Glass Tubes Implode. Athena Marneris. ...
www.bnl.gov/newsroom/news.php?a=23242 - 38k
BNL Newsroom | Former Brookhaven Intern to Race in Olympic Games
... By Aviva Hope Rutkin | July 25, 2012 printer icon Print. Former Brookhaven
Intern to Race in Olympic Games. Maria Michta. This summer ...
www.bnl.gov/newsroom/news.php?a=23208 - 37k

BNL Newsroom | Veljko Radeka Wins IEEE Award for Outstanding ...
... The Head of Brookhaven's Instrumentation Division will be honored for his work on radiation detectors. August 1, 2012. By Aviva Hope Rutkin. Veljko Radeka ...
www.bnl.gov/newsroom/news.php?a=11440 - 26k
BNL Newsroom | Paul Kline Codes Carbon's Journey Through a Plant
... By Aviva Hope Rutkin | July 16, 2012 printer icon Print. Paul Kline Codes Carbon's Journey Through a Plant. ...
www.bnl.gov/newsroom/news.php?a=23204 - 37k
BNL Newsroom | BNL, SUNY's Zimpher and Killeen Say Goodbye to ...
... By Aviva Hope Rutkin | August 17, 2012 printer icon Print. BNL, SUNY's Zimpher and Killeen Say Goodbye to the 2012 Summer Students. ...
www.bnl.gov/newsroom/news.php?a=23291 - 39k
BNL Newsroom | BNL Employees Keep On Learning
... By Aviva Hope Rutkin | July 3, 2012 printer icon Print. BNL Employees Keep On Learning. Karim Hamdi. Karim Hamdi always knew he wanted to go back to school. ...
www.bnl.gov/newsroom/news.php?a=23187 - 36k
Technology Commercialization and Partnerships | Physicist James ...
... By Aviva Hope Rutkin | Thursday, August 09, 2012. Physicist James Dickerson Joins CFN. James Dickerson. James Dickerson will serve ...
www.bnl.gov/techtransfer/news/news.asp?a=3251&t=today - 29k
BNL Newsroom | Physicist James Dickerson Joins CFN
... By Aviva Hope Rutkin | August 9, 2012 printer icon Print. Physicist James Dickerson Joins CFN. James Dickerson. James Dickerson will ...
www.bnl.gov/newsroom/news.php?a=23251 - 36k
BNL Newsroom | Amanda Pflumm Analyzes Gray Matter
... By Aviva Hope Rutkin | July 23, 2012 printer icon Print. Amanda Pflumm Analyzes Gray Matter. Amanda Pflumm. Amanda Pflumm can't decide ...
www.bnl.gov/newsroom/news.php?a=23206 - 36k
BNL Newsroom | ESOL Program Reaches Ten Years and Counting
... By Aviva Hope Rutkin | July 9, 2012 printer icon Print. ESOL Program Reaches Ten Years and Counting. Brookhaven's English for Speakers ...
www.bnl.gov/newsroom/news.php?a=23188 - 36k
BNL | TCP News | Physicist James Dickerson Joins CFN
... Staff Specialist. By Aviva Hope Rutkin | August 9, 2012 printer icon Print. Physicist James Dickerson Joins CFN. James Dickerson. James ...
www.bnl.gov/techtransfer/news/news.php?a=23251 - 28k
BNL | Global and Regional Solutions | Brookhaven Lab Chemists Win ...
... Contacts: Peter Genzer, (631) 344-3174 | Written by Aviva Hope Rutkin printer icon Print. Brookhaven Lab Chemists Win R&D 100 Award for Fuel Cell Research. ...
www.bnl.gov/gars/news/news.php?a=11428 - 27k
BNL | TCP News | Brookhaven Lab Chemists Win R&D 100 Award for ...
... Contacts: Peter Genzer, (631) 344-3174 | Written by Aviva Hope Rutkin printer icon Print. Brookhaven Lab Chemists Win R&D 100 Award for Fuel Cell Research. ...
www.bnl.gov/techtransfer/news/news.php?a=11428 - 30k
Education News | Amanda Pflumm Analyzes Gray Matter
... By Aviva Hope Rutkin | Monday, July 23, 2012. Amanda Pflumm Analyzes Gray Matter. Amanda Pflumm. Amanda Pflumm can't decide what ...
www.bnl.gov/education/news/news.asp?a=3206&t=today - 21k
Education News | Paul Kline Codes Carbon's Journey Through a ...
... By Aviva Hope Rutkin | Monday, July 16, 2012. Paul Kline Codes Carbon's Journey Through a Plant. ...
www.bnl.gov/education/news/news.asp?a=3204&t=today - 21k
Education News | BNL Employees Keep On Learning
... By Aviva Hope Rutkin | Tuesday, July 03, 2012. BNL Employees Keep On Learning. Karim Hamdi. Karim Hamdi always knew he wanted to go back to school. ...
www.bnl.gov/education/news/news.asp?a=3187&t=today - 20k
Education News | BNL, SUNY's Zimpher and Killeen Say Goodbye to ...
... By Aviva Hope Rutkin | Friday, August 17, 2012. BNL, SUNY's Zimpher and Killeen Say Goodbye to the 2012 Summer Students. Interns ...
www.bnl.gov/education/news/news.asp?a=3291&t=today - 23k

Photon Sciences News | NIH Grants $1 Million Dollars for New ...
... perspective. August 8, 2012. By Aviva Hope Rutkin. Lin Yang and Marc Allaire
Click on the image to download a high-resolution version. ...
www.bnl.gov/ps/news/news.php?a=11443 - 34k
Photon Sciences News | Former Brookhaven Intern to Race in Olympic ...
... By Aviva Hope Rutkin | July 25, 2012 printer icon Print. Former Brookhaven
Intern to Race in Olympic Games. Maria Michta. This summer ...
www.bnl.gov/ps/news/news.asp?a=3208&t=today - 33k
BNL Employees Keep On Learning
... By Aviva Hope Rutkin | Tuesday, July 03, 2012. BNL Employees Keep On Learning. Karim
Hamdi. Karim Hamdi always knew he wanted to go back to school. ...
www.bnl.gov/physics/news/news.asp?a=3187&t=today - 17k
Former Brookhaven Intern to Race in Olympic Games | Newsroom ...
... By Aviva Hope Rutkin | Wednesday, July 25, 2012. Former Brookhaven Intern to
Race in Olympic Games. Maria Michta. This summer, Brookhaven ...
www.bnl.gov/HR/careers/news/news.asp?a=3208&t=today - 25k
Physicist James Dickerson Joins CFN | Newsroom | Careers
... By Aviva Hope Rutkin | Thursday, August 09, 2012. Physicist James Dickerson
Joins CFN. James Dickerson. James Dickerson will serve ...
www.bnl.gov/HR/careers/news/news.asp?a=3251&t=today - 24k
Paul Kline Codes Carbon's Journey Through a Plant | Newsroom ...
... By Aviva Hope Rutkin | Monday, July 16, 2012. Paul Kline
Codes Carbon's Journey Through a Plant. ...
www.bnl.gov/HR/careers/news/news.asp?a=3204&t=today - 25k
Amanda Pflumm Analyzes Gray Matter | Newsroom | Careers
... By Aviva Hope Rutkin | Monday, July 23, 2012. Amanda Pflumm Analyzes Gray
Matter. Amanda Pflumm. Amanda Pflumm can't decide what ...
www.bnl.gov/HR/careers/news/news.asp?a=3206&t=today - 24k
Sarah Ackerman Explores How Cells Fare in Space | Newsroom ...
... By Aviva Hope Rutkin | Monday, July 30, 2012. Sarah Ackerman Explores How
Cells Fare in Space. Sarah Ackerman. SUNY Geneseo junior ...
www.bnl.gov/HR/careers/news/news.asp?a=3205&t=today - 24k
BNL Employees Keep On Learning | Newsroom | Careers
... By Aviva Hope Rutkin | Tuesday, July 03, 2012. BNL Employees Keep On Learning. Karim
Hamdi. Karim Hamdi always knew he wanted to go back to school. ...
www.bnl.gov/HR/careers/news/news.asp?a=3187&t=today - 24k
Titan Supercomputer Hours Awarded to Collaborative Protein Project
... By Aviva Hope Rutkin | Monday, July 16, 2012. Titan Supercomputer Hours
Awarded to Collaborative Protein Project. Scientists at the ...
www.bnl.gov/physics/news/news.asp?a=3199&t=today - 19k
Athena Marneris Studies What Makes Glass Tubes Implode
... By Aviva Hope Rutkin | Monday, August 06, 2012. Athena Marneris Studies What
Makes Glass Tubes Implode. Athena Marneris. For the last ...
www.bnl.gov/physics/news/news.asp?a=3242&t=today - 19k
BNL | Center for Functional Nanomaterials (CFN) | Physicist James ...
... By Aviva Hope Rutkin | August 9, 2012 printer icon Print. Physicist James
Dickerson Joins CFN. James Dickerson. James Dickerson will ...
www.bnl.gov/cfn/news/news.php?a=23251 - 27k
BNL | Center for Functional Nanomaterials (CFN) | Electronics Play ...
... Print. Electronics Play By a New Set of Rules at the Molecular Scale. September
2, 2012. By Aviva Hope Rutkin. atomic-scale model Click ...
www.bnl.gov/cfn/news/news.php?a=11449 - 30k
Photon Sciences News | NIH Grants $1 Million Dollars for New ...
... perspective. August 8, 2012. By Aviva Hope Rutkin. Lin Yang and Marc Allaire
Click on the image to download a high-resolution version. ...
www.bnl.gov/ps/news/news.asp?a=1443&t=pr - 34k
Photon Sciences News | Scientists Create Low-Lignin Plants with ...
... Contacts: Peter Genzer, (631) 344-3174 | Written by Aviva Hope Rutkin printer
icon Print. Scientists Create Low-Lignin Plants with ...
www.bnl.gov/ps/news/news.asp?a=1439&t=pr - 37k

Education News | Paul Kline Codes Carbon's Journey Through a ...
... By Aviva Hope Rutkin | Monday, July 16, 2012. Paul Kline
Codes Carbon's Journey Through a Plant. ...
www.bnl.gov/education/news/news.asp?a=3204&t=today - 21k
Education News | Amanda Pflumm Analyzes Gray Matter
... By Aviva Hope Rutkin | Monday, July 23, 2012. Amanda Pflumm Analyzes Gray
Matter. Amanda Pflumm. Amanda Pflumm can't decide what ...
www.bnl.gov/education/news/news.asp?a=3206&t=today - 21k
Education News | BNL, SUNY's Zimpher and Killeen Say Goodbye to ...
... By Aviva Hope Rutkin | Friday, August 17, 2012. BNL, SUNY's Zimpher and
Killeen Say Goodbye to the 2012 Summer Students. Interns ...
www.bnl.gov/education/news/news.asp?a=3291&t=today - 23k
Education News | BNL Employees Keep On Learning
... By Aviva Hope Rutkin | Tuesday, July 03, 2012. BNL Employees Keep On Learning. Karim
Hamdi. Karim Hamdi always knew he wanted to go back to school. ...
www.bnl.gov/education/news/news.asp?a=3187&t=today - 20k
Photon Sciences News | Former Brookhaven Intern to Race in Olympic ...
... By Aviva Hope Rutkin | July 25, 2012 printer icon Print. Former Brookhaven
Intern to Race in Olympic Games. Maria Michta. This summer ...
www.bnl.gov/ps/news/news.php?a=23208 - 33k
Photon Sciences News | Scientists Create Low-Lignin Plants with ...
... Contacts: Peter Genzer, (631) 344-3174 | Written by Aviva Hope Rutkin printer
icon Print. Scientists Create Low-Lignin Plants with ...
www.bnl.gov/ps/news/news.php?a=11439 - 37k
[pdf] The Bulletin Vol. 66 - No. 29 August 24, 2012
... Radeka will receive the Marie Sklodows- ka-Curie Award in a ceremony later this
year. Aviva Hope Rutkin ... Aviva Hope Rutkin BNL Blood Drive, 9/13 ...
www.bnl.gov/bnlweb/pubaf/bulletin/2012/bb082412.pdf - 2012-08-24
BNL | TCP News | Physicist James Dickerson Joins CFN
... Staff Specialist. By Aviva Hope Rutkin | August 9, 2012 printer icon Print.
Physicist James Dickerson Joins CFN. James Dickerson. James ...
www.bnl.gov/techtransfer/news/news.php?a=23251 - 28k
Technology Commercialization and Partnerships | Physicist James ...
... By Aviva Hope Rutkin | Thursday, August 09, 2012. Physicist James Dickerson
Joins CFN. James Dickerson. James Dickerson will serve ...
www.bnl.gov/techtransfer/news/news.asp?a=3251&t=today - 29k
GARS | Physicist James Dickerson Joins CFN
... By Aviva Hope Rutkin | Thursday, August 09, 2012. Physicist James Dickerson
Joins CFN. James Dickerson. James Dickerson will serve ...
www.bnl.gov/GARS/news/news.asp?a=3251&t=today - 29k
BNL Employees Keep On Learning
... By Aviva Hope Rutkin | Tuesday, July 03, 2012. BNL Employees Keep On Learning. Karim
Hamdi. Karim Hamdi always knew he wanted to go back to school. ...
www.bnl.gov/rhic/news2/news.asp?a=3187&t=today - 16k
BNL | TCP News | Brookhaven Lab Chemists Win R&D 100 Award for ...
... Contacts: Peter Genzer, (631) 344-3174 | Written by Aviva Hope Rutkin printer icon
Print. Brookhaven Lab Chemists Win R&D 100 Award for Fuel Cell Research. ...
www.bnl.gov/techtransfer/news/news.php?a=11428 - 30k
Single Molecule Spectroscopy | Physicist James Dickerson Joins CFN
... By Aviva Hope Rutkin | Thursday, August 09, 2012. Physicist James Dickerson
Joins CFN. James Dickerson. James Dickerson will serve ...
www.bnl.gov/sms/news/news.asp?a=3251&t=today - 16k
Single Molecule Spectroscopy | Electronics Play By a New Set of ...
... Electronics Play By a New Set of Rules at the Molecular Scale. Sunday,
September 02, 2012. By Aviva Hope Rutkin. atomic-scale model ...
www.bnl.gov/sms/news/news.asp?a=1449&t=pr - 19k
GARS | Physicist James Dickerson Joins CFN
... By Aviva Hope Rutkin | Thursday, August 09, 2012. Physicist James Dickerson
Joins CFN. James Dickerson. James Dickerson will serve ...
www.bnl.gov/gars/news/news.asp?a=3251&t=today - 29k

BNL | Global and Regional Solutions | Physicist James Dickerson ...
... By Aviva Hope Rutkin | August 9, 2012 printer icon Print. Physicist James
Dickerson Joins CFN. James Dickerson. James Dickerson will ...
www.bnl.gov/gars/news/news.php?a=23251 - 25k
GARS | Physicist James Dickerson Joins CFN
... By Aviva Hope Rutkin | Thursday, August 09, 2012. Physicist James Dickerson
Joins CFN. James Dickerson. James Dickerson will serve ...
www.bnl.gov/gars/news/news.asp?a=3251&t=today - 29k
BNL | Global and Regional Solutions | Brookhaven Lab Chemists Win ...
... Contacts: Peter Genzer, (631) 344-3174 | Written by Aviva Hope Rutkin printer icon
Print. Brookhaven Lab Chemists Win R&D 100 Award for Fuel Cell Research. ...
www.bnl.gov/gars/news/news.php?a=11428 - 27k
[pdf] The Bulletin Vol. 66 - No. 25 July 27, 2012
... Aviva Hope Rutkin ... You can read more about her journey to the Olympics at
www.mariamichta.com. Aviva Hope Rutkin The Bulletin July 27, 2012 C alendar ...
www.bnl.gov/bnlweb/pubaf/bulletin/2012/bb072712.pdf - 2012-07-27
Sarah Ackerman Explores How Cells Fare in Space | Newsroom ...
... By Aviva Hope Rutkin | Monday, July 30, 2012. Sarah Ackerman Explores How
Cells Fare in Space. Sarah Ackerman. SUNY Geneseo junior ...
www.bnl.gov/HR/careers/news/news.asp?a=3205&t=today - 24k
Amanda Pflumm Analyzes Gray Matter | Newsroom | Careers
... By Aviva Hope Rutkin | Monday, July 23, 2012. Amanda Pflumm Analyzes Gray
Matter. Amanda Pflumm. Amanda Pflumm can't decide what ...
www.bnl.gov/HR/careers/news/news.asp?a=3206&t=today - 24k
BNL Employees Keep On Learning | Newsroom | Careers
... By Aviva Hope Rutkin | Tuesday, July 03, 2012. BNL Employees Keep On Learning. Karim
Hamdi. Karim Hamdi always knew he wanted to go back to school. ...
www.bnl.gov/HR/careers/news/news.asp?a=3187&t=today - 24k
Physicist James Dickerson Joins CFN | Newsroom | Careers
... By Aviva Hope Rutkin | Thursday, August 09, 2012. Physicist James Dickerson
Joins CFN. James Dickerson. James Dickerson will serve ...
www.bnl.gov/HR/careers/news/news.asp?a=3251&t=today - 24k
Paul Kline Codes Carbon's Journey Through a Plant | Newsroom ...
... By Aviva Hope Rutkin | Monday, July 16, 2012. Paul Kline
Codes Carbon's Journey Through a Plant. ...
www.bnl.gov/HR/careers/news/news.asp?a=3204&t=today - 25k
Former Brookhaven Intern to Race in Olympic Games | Newsroom ...
... By Aviva Hope Rutkin | Wednesday, July 25, 2012. Former Brookhaven Intern to
Race in Olympic Games. Maria Michta. This summer, Brookhaven ...
www.bnl.gov/HR/careers/news/news.asp?a=3208&t=today - 25k
Photon Sciences | eNews | NSLS Helps Fine-Tune Vision of New NASA ...
... Small Explorers program. Aviva Rutkin. 2012-3227 INT/EXT | Media &
Communications Office. Issue Contents: Wednesday, July 18, 2012. ...
www.bnl.gov/ps/enews/news.php?a=23227 - 22k
[pdf] The Bulletin Vol. 66 - No. 23 July 13, 2012
... For more information about the Lab's continuing education pro- grams, contact
Munson at munson@ bnl.gov, Ext. 7631. Aviva Rutkin ...
www.bnl.gov/bnlweb/pubaf/bulletin/2012/bb071312.pdf - 2012-07-12
GARS | Physicist James Dickerson Joins CFN
... By Aviva Hope Rutkin | Thursday, August 09, 2012. Physicist James Dickerson
Joins CFN. James Dickerson. James Dickerson will serve ...
www.bnl.gov/GARS/news/news.asp?a=3251&t=today - 29k
[pdf] The Bulletin Vol. 66 - No. 24 July 20, 2012
... "It feels cool to be able to say, 'I've been there.'" Aviva Hope Rutkin The Bulletin
July 20, 2012 C alendar Joseph Rubino D7340612 Joseph Rubino ...
www.bnl.gov/bnlweb/pubaf/bulletin/2012/bb072012.pdf - 2012-07-19
[pdf] The Bulletin Vol. 66 - No. 26 August 3, 2012
... gov/esol. Aviva Hope Rutkin The Bulletin August 3, 2012 C alendar Silke Baron
Roger Stoutenburgh D7130612 Caterpillar's Armor from p.1 its lifespan. ...
www.bnl.gov/bnlweb/pubaf/bulletin/2012/bb080312.pdf - 2012-08-02

[pdf] The Bulletin Vol. 66 - No. 27 August 10, 2012
Page 1. the B ulletin Vol. 66 - No. 27 August 10, 2012 Michael Herbert D0800812 Michael Herbert D10200512 BNL Director Aronson Gives Update on Lab ...
www.bnl.gov/bnlweb/pubaf/bulletin/2012/bb081012.pdf - 2012-08-09
[pdf] The Bulletin Vol. 66 - No. 28 August 17, 2012
Page 1. the B ulletin On August 2 and 3, BNL hosted the Graduate Fellowship Annual Meeting for the DOE Office of Science (SC). Every ...
www.bnl.gov/bnlweb/pubaf/bulletin/2012/bb081712.pdf - 2012-08-16
Photon Sciences News | NIH Grants $1 Million Dollars for New ...
... perspective. August 8, 2012. By Aviva Hope Rutkin. Lin Yang and Marc Allaire Click on the image to download a high-resolution version. ...
www.bnl.gov/ps/news/news.php?a=11443 - 34k
Photon Sciences News | Scientists Create Low-Lignin Plants with ...
... Contacts: Peter Genzer, (631) 344-3174 | Written by Aviva Hope Rutkin printer icon Print. Scientists Create Low-Lignin Plants with ...
www.bnl.gov/ps/news/news.php?a=11439 - 37k
Photon Sciences News | Former Brookhaven Intern to Race in Olympic ...
... By Aviva Hope Rutkin | July 25, 2012 printer icon Print. Former Brookhaven Intern to Race in Olympic Games. Maria Michta. This summer ...
www.bnl.gov/ps/news/news.php?a=23208 - 33k
BNL | Center for Functional Nanomaterials (CFN) | Electronics Play ...
... Print. Electronics Play By a New Set of Rules at the Molecular Scale. September 2, 2012. By Aviva Hope Rutkin. atomic-scale model Click ...
www.bnl.gov/cfn/news/news.php?a=11449 - 30k
BNL | Center for Functional Nanomaterials (CFN) | Physicist James ...
... By Aviva Hope Rutkin | August 9, 2012 printer icon Print. Physicist James Dickerson Joins CFN. James Dickerson. James Dickerson will ...
www.bnl.gov/cfn/news/news.php?a=23251 - 27k

Fabrication of a sample holder for air-sensitive samples to be used on X-18B and X-19A beam lines at the National Synchrotron Light Source

Wahaj Saleem
Department of Mechanical Engineering, City College of New York, New York NY 10031
Syed Khalid
Department of Photon Sciences, Brookhaven National Laboratory, Upton NY 11973

Abstract

A sample holder has been fabricated for the collection of x-ray absorption fine structure (XAFS) data from air-sensitive materials. A four-way commercial cross from MDC Vacuum Products was taken to be used as the sample chamber for this experiment. The top and the bottom of the cross were closed with blank flanges, O-rings, and hinged clamps. A tray was attached to the top flange to hold the sample. The other two sides of the cross had flanges with Kapton windows pasted at the center for x-rays to pass through. The chamber was placed in the glove box along with the reduced sample and then the sample was placed into the chamber. The experiment was conducted on an oxidized sample of Pt-supported nanoparticles and then compared with the same reduced sample in the fabricated chamber. The change in data shows that this sample holder can be used for handling air-sensitive materials for XAFS data collection.

I. Introduction

Analysis of air-sensitive materials by x-ray absorption spectroscopy (XAS) has always been challenging. Therefore, for quantitative x-ray absorption fine structure (XAFS) analysis, a sample holder has been fabricated using different parts from MDC Vacuum Products. All products are made for ultra-high vacuum systems able to bear 10-9 torr pressure.[1] Since these parts are already made for use with ultra-high vacuum systems, they are suitable to be used as the sample holder for our XAFS analysis. The sample used to test the holder is the mixture of Boron Nitride and Pt supported nanoparticles. Pt nanoparticles are present at different ionic state in open air and become neutral when treated with hydrogen bubbles.[2] Using XANES analysis, we can find out difference between oxidized and reduced Pt particles to see if the sample was oxidized in our sample holder.

II. Literature Review

X-ray absorption fine structure (XAFS) is a technique that is widely used for the determination of the local geometric and/or electronic structures of the matter. The experiment is performed using synchrotron radiation as an energy source which is emitted by the grating electrons in a storage ring which provide ultra-bright, ultra-violet light and soft x-rays. The XAFS spectrum is dependent on the formal oxidation state, coordination chemistry, the distances, the coordination number, and the species of the atoms surrounding the selected elements. This provides a practical and simple way to determine the chemical state and local atomic structure for a selected atomic species. Therefore, XAFS is used in wide range of scientific studies including biology, environmental science, catalyst research, and material science.[3]

X-ray absorption fine structure data includes both x-ray absorption near edge structure (XANES) and extended x-ray absorption fine structure (EXAFS). The difference between these two is the energy range; XANES data are mainly focused near the edge while the rest of extended data, starting somewhat past an absorption edge and extending typically 1000 eV further, is called EXAFS.[4] XANES is strongly sensitive to the formal oxidation state and coordination chemistry like tetrahedral/octahedral coordination of absorbing atom, but the EXAFS is used to determine the distances, coordination number, and the species of the neighbors of the absorbing atom.

A. Properties of EXAFS

1. Sing long-range order is not required for the EXAFS analysis, any state of the substance (crystalline or non-crystalline) can be used for EXAFS experiment.
2. The local atomic arrangement can be determined about each type of atom separately and EXAFS is usually able to provide the atomic arrangement with greater resolution.
3. Structural information is obtained from EXAFS by simple and direct analysis and the measurement is relatively easy and rapid.

B. Design of an EXAFS experiment:

EXAFS is typically used to determine the local structure and the coordination number in the sample. It is much easier to manipulate EXAFS in any state of matter which is the reason of it is being widely used in the scientific studies. For an EXAFS experiment, the monitoring of absorption technique is used which leads to the following equation,

$$\mu x = \ln\left(\frac{I_o}{I_t}\right),$$

where x is the thickness of the sample and μ is the absorption coefficient I_0 is incident intensity and I_t is transmitted intensity.[5]

C. Mode of XAFS experiments:

There are two typical modes of XAFS experiments as dis-

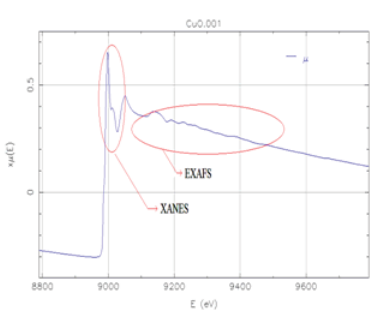

Figure 1. XAFS graph indicating the difference between XANES spectra and EXAFS spectra.

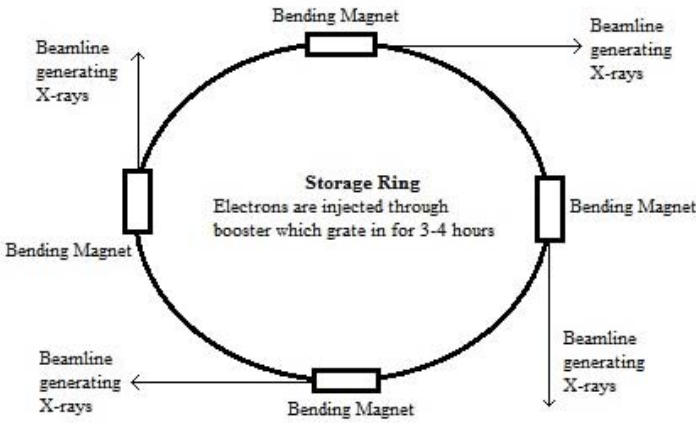

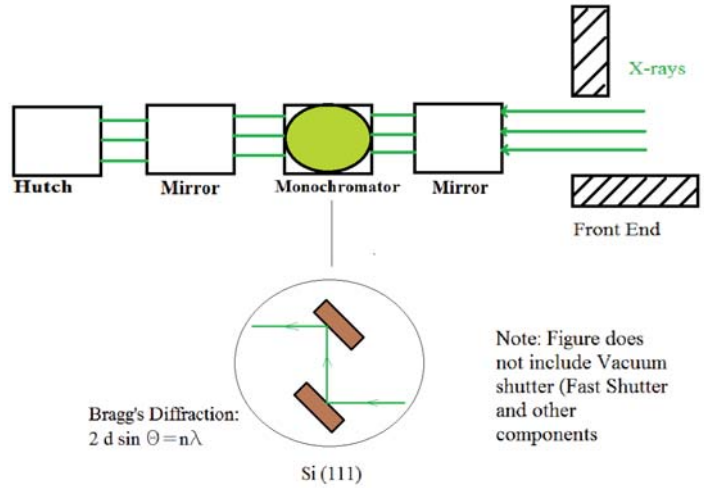

Figure 3. Picture indication the design of beamline between the front end and hutch (Safety Personnel).

cussed below:

1. Transmission: This uses the phenomenon of Auger electron emission and the electrons are detected using different types of detectors such as ion chamber, a silicon drift detector, etc.
2. Fluorescence: every element gives specific type of fluorescence when enacted by x-ray. This mode uses the same phenomenon using different fluorescence detectors such as a PIPS detector.

In some cases, fluorescence detection is better, depending upon the usage; e. g., to study light elements, transmission is suitable while for the heavy elements, fluorescence detection is suitable. Similarly, fluorescence detection produces better data when the absorption of the element of our interest is less the percent of the total absorption in the whole sample. Also, for the K-edge (binding energy of K-shell orbit) below 2000 eV, transmission detection is advantageous because the fluorescence at this point becomes small. The other factor that may determine the choice between these two modes depends on the type of sample to be studied.[6]

D. XAFS using synchrotron radiation:

The use of synchrotron radiation is useful in XAFS experiment. The typical disadvantage of XAFS experiment is that the experimenter has less understanding of the whole apparatus since it is mostly operated through computers. Therefore, it is also advantageous to understand the working principle of it.

Storage rings are developed for the stable source of synchrotron radiation. Since XAFS requires more energy of several KeV, more powerful machines were needed to complete this task. Storage rings have sufficiently ultra-high vacuum (10-9 -10-10 torr) the electrons are accelerated and can be maintained for few hours.[7] Synchrotron radiations are produced at the bending magnets that are attached to the experiment through a beam port tangential to the ring. The beam port makes available 10-100 mrad of radiation to be divided among different beamlines and associated optics. The advantage of storage ring is its extensive pumping capability for 10-9-10-10 torr vacuum in the presence of heat and radiation load of synchrotrons. The equipment that makes synchrotron radiation available to users is called an x-ray beam line. It has three major sections: the machine interface, beam line optics and the experimental apparatus with personnel safety interlocks (also known as hutches). In the machine interface, it is important to protect the ring and the beam line from accidental loss of vacuum, so it has a fast closing shutter (time<10 ms) that

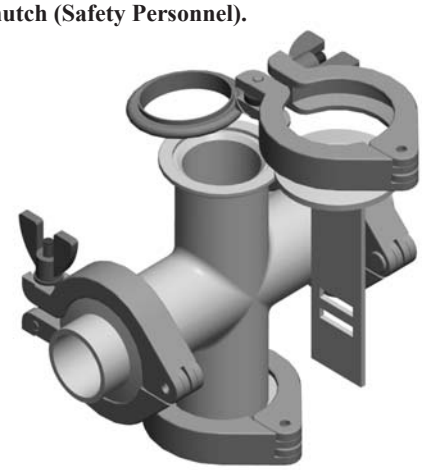

Figure 4. Model of the sample holder.

provides sufficient flow impendence to protect the ring while the UHV valve closes. In some devices, an acoustic delay line can be employed optionally to slow the arrival time of the pressure wave front. There is also shielding provided to stop electron dump through 20-30 cm lead and some low atomic number materials (such as concrete, wax, etc.) to stop any photo induced neutrons.[8]

The mirror to be used for beam lines must be resistant to radiation, have good thermal properties, be highly polishable and be available in large sizes. The mirrors are used to collimate the radiation to pass through the monochromator (made with Si 111) which uses the Bragg's Diffraction to give the desired energy for our experiments. There are different slit sizes to limit the size of beam for improving the energy resolution and data in our experiments.[9]

III. Methods and Materials

A. Design and Fabrication

The design of the sample holder included two main processes: selection and assembly. Figure shows the model of the sample holder. A four way commercial cross from MDC Vacuum Products was used as the sample chamber for this experiment. Other components selected for the assembling were four centering rings to which robust O-rings were attached, two blank KB flanges, two other KB flanges with a hole in the center, and four hinged clamps. The bottom of the cross was closed with blank KB flange, centering ring including the O-ring and hinged clamps. A tray for holding specimen was then attached to the other blank KB flange

Figure 5. (left) HEPA filtered nano-hood used during the preparation of sample pellet. (right) Glove box used during the experiment.

Figure 6. (left) Nashner-Adler reaction cell used for the reduction of platinum nano particles treating with 5% hydrogen gas at 200°C temperature. (right) Sample in fabricated chamber after XAFS data collection.

Figure 7. Comparing data of the sample in oxidized and reduced form. By XANES analysis, the peak of the reduced sample is lowered and the rest of the data remains similar. Also, the data remains same in the chamber meaning that it was not oxidized in fabricated sample holder.

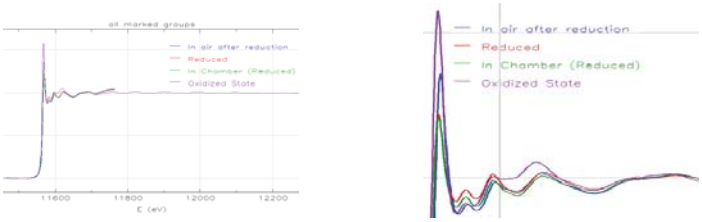

Figure 8. . Comparing all the data together. The Reduced and In chamber data remains same while the sample exposed to air at the end (after 12 hrs) shows that the sample is oxidizing slowly.

which was held to the top of the cross. The remaining two sides of the cross were closed KB flanges with holes where Kapton windows were pasted at the center for the x-rays to pass through. Kapton is a polyimide with chemical formula (C22H10O4N2) that can remain stable in a wide range of temperature from -273°C to 400°C. Because of its high thermal stability and high transmittance to x-rays, it is the preferred material to be used in the sample holder. It is also relatively insensitive to radiation damage.10 Hinged clamps were then used to lock the remaining sides making it air tight.

B. Sample Preparation

The compound used to test the sample holder was a mixture of Pt-supported nanoparticles. The aim was to use mixers of very light non-reactive elements to make pellets that would not crack. For this reason 200 mg of boron nitride was mixed with 20 mg of Pt nanoparticles inside the nano-hood. The mixture was then compressed to form the sample pellet.

C. XAFS Data Collection

After preparation, the sample was then transferred into the Nashner-Adler reaction cell on which XAFS data were collected in an oxidized state in transmission mode. The sample was then treated with 5% hydrogen gas at 200°C which causes the reduction of the Pt-nanoparticles. A gas flowing pipe stops near the sample's surface to allow in situ studies in temperature and gas flow controlled reduction or oxidation of the sample. The XAFS data were collected again on the reduced sample. The cell was then brought to the glove box where the reduced sample was transferred into the designed sample holder. The XAFS data were then collected again on the reduced sample in the sample holder for about 1 hour.

IV. Results

A comparison of the data of the reduced sample in the designed sample holder with the reduced sample in the cell revealed no significant change in the data which demonstrates that the sample was not oxidized in the sample holder. The sample was not oxidized in the chamber showing that the chamber is suitable for handling air sensitive compounds.

V. Discussion

The successful attempt of the experiment shows that this type of chamber can be used to deal with the air sensitive compounds. Within the glovebox (nitrogen atmosphere), the oxygen and water level is < 0.5 ppm which provides an inert atmosphere for the sample to be dealt with. This chamber makes it easy to remove the sample while maintaining the same conditions those as in the glove box; and so, the sample does not interact with the air. Most catalysts used in industries are air-sensitive and change their properties after interacting with the open air and moisture. Due to the change in data, it is hard to study their specific properties and conducting experiments on them becomes a waste of time. This chamber serves as a user-friendly, easily operated holder to deal with these types of elements or compounds. This also eliminates the inconvenience of using large and expensive vacuum chambers for this purpose.

VI. Conclusion

A four way sample holder has been designed and fabricated for the use with air-sensitive materials that require sample preparation within a glove box. The sample holder has a robust seal and the design is easily adjustable to the beamline inside the hutch. XAFS scans collected with this holder are suitable for data analysis and interpretation.

VII. Acknowledgements

This project was done under the instruction and supervision of Dr. Syed Khalid leading to the successful completion of the project. I also acknowledge Dr. Nebojsa Marinkovic for his useful discussion during experiment. The experiment was conducted on X-19A beamline at National Synchrotron Light Source. Therefore, I acknowledge the hospitality and kindness of Brookhaven National Laboratory under the U.S. Department of Energy which has supported the SULI program.

VIII. References

1. MDC Vacuum Products LLC., http://www.mdcvacuum.com/DisplayContentPage.aspx?cc=77c1cf92-e798-4ed2-880e-a2f5a3af0194
2. Temer S. Ahmadi et al. http://www.sciencemag.org/content/272/5270/1924.full.pdf
3. Matt Newville, Consortium for Advanced Radiation Sources (University of Chicago, IL), http://xafs.org/Tutorials?action=AttachFile&do=get&target=Newville_xas_fundamentals.pdf
4. Edward A. Stern, in X-ray Absorption: Principles, Applications, Techniques of EXAFS, SEXAFS, and XANES, edited by D. C Koningsberger and R. Prins (John Wiley & Sons, 1988), pp. 3.
5. Steve M. Heald, in X-ray Absorption: Principles, Applications, Techniques of EXAFS, SEXAFS, and XANES, edited by D. C Koningsberger and R. Prins (John Wiley & Sons, 1988), pp. 89.
6. Steve M. Heald, in X-ray Absorption: Principles, Applications, Techniques of EXAFS, SEXAFS, and XANES, edited by D. C Koningsberger and R. Prins (John Wiley & Sons, 1988), pp. 90-91.
7. Steve M. Heald, in X-ray Absorption: Principles, Applications, Techniques of EXAFS, SEXAFS, and XANES, edited by D. C Koningsberger and R. Prins (John Wiley & Sons, 1988), pp. 125-127.
8. Steve M. Heald, in X-ray Absorption: Principles, Applications, Techniques of EXAFS, SEXAFS, and XANES, edited by D. C Koningsberger and R. Prins (John Wiley & Sons, 1988), pp. 132-134.
9. Steve M. Heald, in X-ray Absorption: Principles, Applications, Techniques of EXAFS, SEXAFS, and XANES, edited by D. C Koningsberger and R. Prins (John Wiley & Sons, 1988), pp. 154-157.
10. DuPont Kapton polyimide film, http://www2.dupont.com/Kapton/en_US/assets/downloads/pdf/summaryofprop.pdf

A dislocation study of CZT crystals

Valissa Sams
Alabama Agricultural and Mechanical University, Huntsville, AL 35811
Ki Hyun Kim and Wing Chan
Brookhaven National Laboratory, Upton, NY 11973

Abstract

Cadmium Zinc Telluride (CZT) is known to be one of the best room-temperature, x-ray and gamma-ray radiation detector materials. A CZT detector's performance can be improved more if we remove or minimize intrinsic and extrinsic defects such as dislocations, Te secondary phase defects, and grain boundaries. Dislocations are generated due to the stress/strain in the crystal growth process. In this research, we tried to characterize dislocation densities in CZT crystals grown using different methods--e. g., varying the carbon thicknesses and ampoule designs--in order to suggest better growth techniques. Dislocation densities were revealed using a Saucedo solution and analyzed by an infrared transmission microscope. The thick graphite-coated ampoules generated fewer dislocations than the thin graphite-coated ampoule. Also, we concluded that a proper crystal growth rate and cooling down rate is one important factor in minimizing dislocations in CZT crystals. The effects of dislocations on the detector's performance were evaluated from the 241-Am gamma-response of CZT detectors which were fabricated from the high and low etch pitch density regions in the same wafer.

I. Introduction

A CZT detector's performance is limited by the intrinsic and extrinsic defects in CZT materials. Two extreme types of dislocation distributions, mainly generated during the growth phase of the CZT materials are known: a fully polygonized cell-like structure and a randomly distributed arrangement of dislocations. As a result of these dislocations, deformation occurs during the cooling process of the post-growth, grain boundary structures become manifested throughout the material, and clusters are produced.1 We tried to minimize such dislocations by controlling the carbon coating thickness and the ampoule design.

II. Experiment

Three CZT(Zn=10%) ingots were grown by the Bridgman method, doped with indium of 2.0 x 10^{17} cm^{-3} for the compensation. The same stoichiometry, growth rate, and cooling rate were used for the crystal growth procedure except the carbon coating thickness and ampoule shape. Wafer 1 and 2 were prepared from ingots which were grown using normal shape quartz tubing with 0.1- and 2-µm carbon thickness, respectively. Wafer 3 was prepared from an ingot grown with unique tapered ampoule design (Figure 1) with a 2 µm carbon coating. The growth rate and temperature gradient in the solid-liquid interface were 9 mm/day and a 13°C/cm.

The three ingots were sliced into wafers with a high precision wire, polished mechanically with alumina powder, and polished chemically with Bromine and ethylene glycol solution. The etch pit density (EPD) of three CZT wafers were revealed with Saucedo's solution (H_2O:HNO_3:HF:$AgNO_3$) by dipping them in the solution for 25 seconds. EPD densities are directly correlated with dislocation in CZT samples. Using an optical microscope at a magnification of 5 to 20, the EPD distribution in each wafer

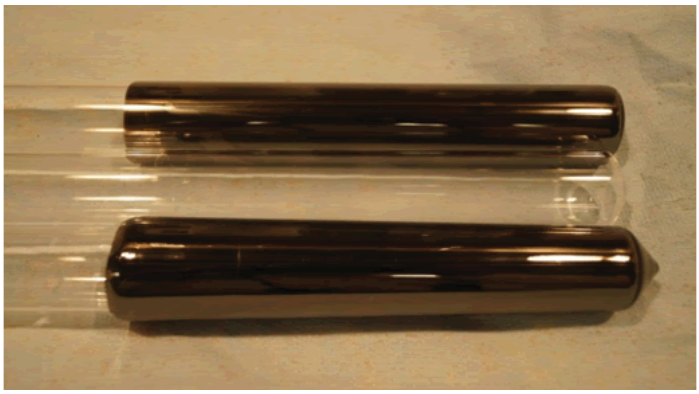

Figure 1. Photograph of ampoule with normal shape (top), normal shape without carbon coating (middle), and tapered ampoule with carbon coating.

was taken and their concentrations were counted using the built-in software. Two CZT detectors from the edge and central region of wafer 1 were fabricated for the detector's performance measurement. The detector's size was 5 x 5 x 3 mm^3 and Au electrode was prepared by an electroless plating method.

III. Results and Discussion

The shape of the etch pit and distribution for each wafer is shown in Figures 2, 3, and 4. The shape of the etch pits are triangular and their distribution is not uniform throughout the entire wafer. All three CZT wafers exhibited higher EPD near the edge versus the central region. This might be due to the thermal stress delivered to the ingots from the quartz tubing during cool-down process. Also, the grain-boundaries and twin-boundaries regions showed more EPD than a normal CZT matrix, which indicate high dislocations around them. Figure 5 shows the radial distribution of EPD in three CZT wafers. It follows a U-shape. The average EPD value grown with thick carbon coating gives 0.9 -1 x 10^4 cm2 and its distribution is also uniform throughout the whole wafer.

However, wafer 3 which was grown with a thin carbon coating produced 3 to 5 times more dislocations than a wafer grown with a thick carbon coating. Also, its values are varible in a radial direction. As shown in Figure 5, the ampoule design does not affect the EPD as much than carbon-coating thickness. Surprisingly, the overall EPD in three wafers are lower than that of other reported values (0.5- 3 x 10^5 cm-2) in CdTe and CdZnTe.[3] This differnce might be caused by the slow cool-down rate used here when compared with other Bridgman grown CZT ingots.

The effects of dislocation on the detector's performance were evaluated from the 241-Am gamma-response of CZT detectors which were fabricated from the high and low EPD regions in the same wafer. Electrical resistivity of CZT detector fabricated from a high EPD region is 6 x 10^9 cm and 6 to 7 times lower than that of a low EPD one.

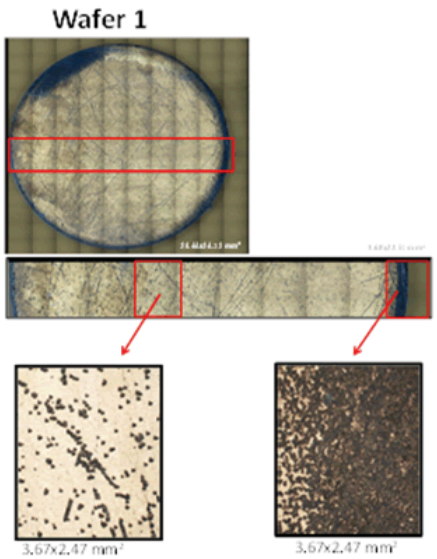

Fig. 2. EPD distribution in wafer 1 prepared from ingot which grown with a normal ampoule with thin (0.2µm) caborn coating. Photos were taken with a magnification 5 and 20.

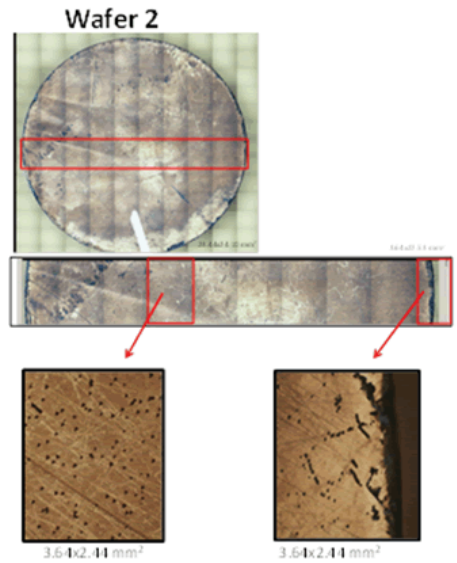

Fig. 3. EPD distribution in wafer 2 prepared from ingot which grown with a normal ampoule with thick (2µm) caborn coating. Photos were taken with a magnification 5 and 20.

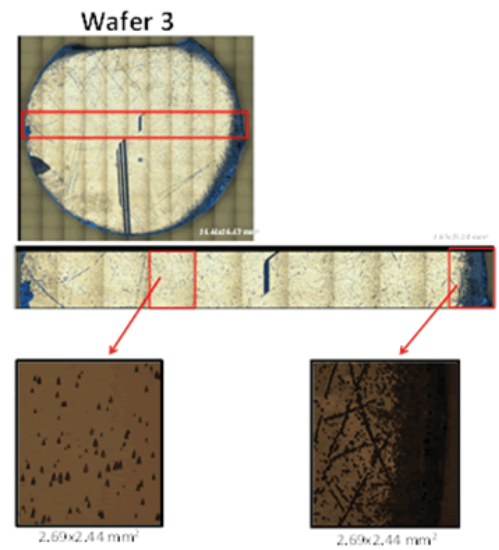

Fig. 4. EPD distribution in wafer 3 prepared from ingot which grown with a tapered ampoule with thick (2µm) carbon coating. Photos were taken with a magnification 5 and 20.

Figure 6 shows CZT gamma spectra taken with a high and low EPD. The mobility-lifetime extracted from Hecht equation fitting of high EPD CZT detector is 5.38 x 10^{-4} cm^2/V. The mobility-lifetime product of the low EPD CZT detector is 7.54 x10^{-4} cm^2/V, but it is 10 times lower than the other detectors fabricated from wafers 2 and 3.

IV. Conclusion

We compared dislocation densities of CZT ingots which were grown using different carbon coating thicknesses and the ampoule designs. The edge regions, which contact with crucible wall, exhibit higher EPD (dislocation densities) than the central region. Also, the thicker carbon coating helps reduce dislocation densities in a CZT wafer more than the thinner carbon coating. Our CZT wafers shows to 10 times less EPD when compared to other reported CdTe and CZT wafers (0.5-3 x 10^5 cm^{-2}). This difference may originate from slow growth rate (9 mm/day) and slow

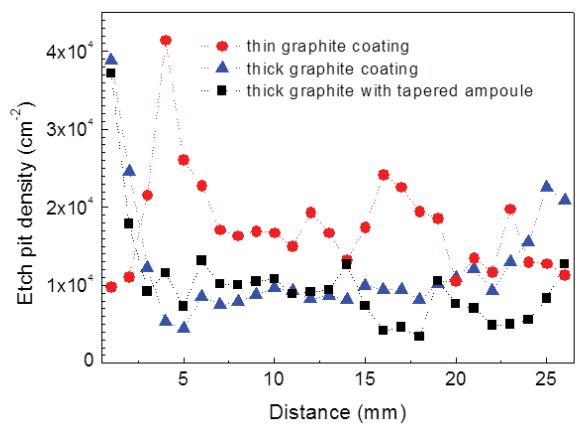

Fig. 5. Radial distribution of EPD in three different CZT wafers. Thick graphite coating is more useful method to minimize dislocation densities in CZT crystals.

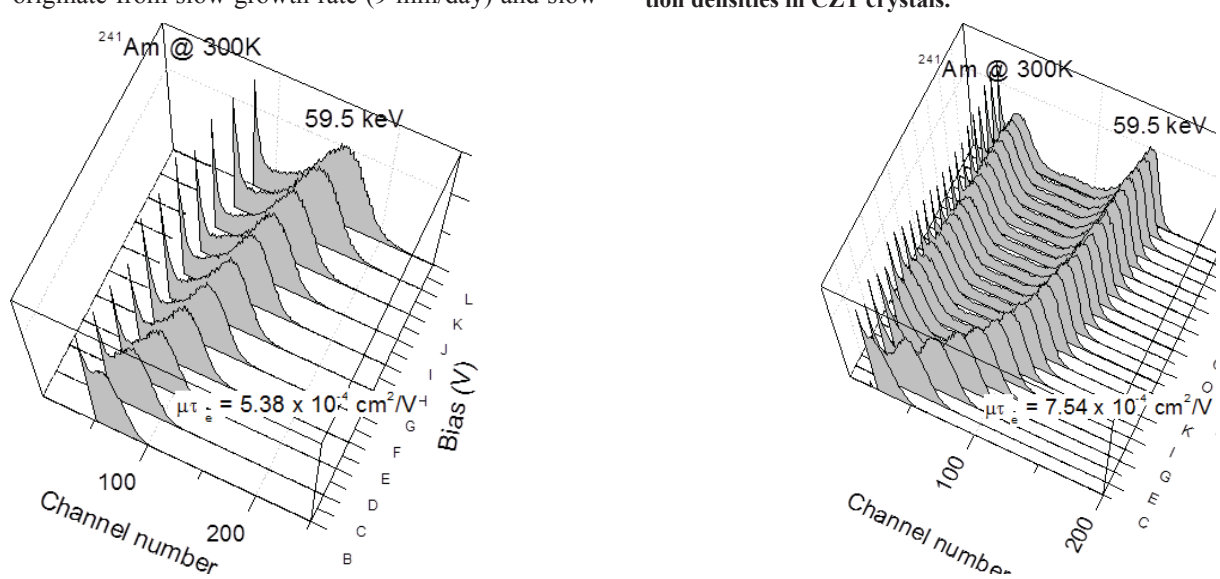

Fig. 6. 241Am gamma-spectra of CZT detector fabricated from (left) high EPD area and (right) low EPD area in same wafer shown in Fig. 2. The detector size is 5 x 5x 3 mm^3.The mobility lifetime product of detector (a) and (b) is 5.38 x 10-4 and 7.54 x10-4.cm^2/V, respectively.

cooling rate (10°C/h) of CZT ingot. The gamma-spectra measurements with CZT detectors which contain high and low EPD validate the importance of low dislocation densities for high quality CZT detectors with better mobility-lifetime product.

V. Acknowledgements

I would like to acknowledge all the support given to me through the Nonproliferation and National Security Department of Brookhaven National Laboratory, especially Ralph B. James and Ki Hyun Kim. I would also like to thank Alabama A&M University Physical Science and Technology Department, especially Dr. Wing Chan. Most importantly, I would like to thank Jesus Christ for making all things possible in my life, for letting me know that all things are possible through Him.

VI. References

[1] Fisher, J.C., W.G. Johnston, R. Thomson, and T. Vreeland, Jr. Dislocations in CdTe, CdZnTe and CdTeSe. New York and London: John Wiley & Sons, Inc. Chapman & Hall, Limited, 1957.

[2] Rose, D., K. Durose, W. Palosz, A. Szczerbakow, and K. Grasza. "Methods of dislocation distribution analysis and inclusion identification with application to CdTe and (Cd,Zn) Te." (August 26, 1997): n.

[3] Inoue, Morio, Iwao Teramoto, and Shigetoshi Takayanagi. "Cd and Te Dislocations in CdTe." 34.2 (1963): 404 - 405.

[4] D. J. William, "Dislocation in CdTe, CdZnTe and CdTeSe." Trans. Peter Capper Properties of Narrow Cap Cadmium-based Compounds. London, United Kingdom: INSPEC, the Institution of Electrical Engineer, 1994. 505-510.

Radiosynthesis of [^{18}F] fluorosucrose and purification of sucrose synthase

Alexandra Scavelli
Department of Chemistry, SUNY Albany, Albany NY, 12222
Caitlin Bennett
Department of Chemistry, Fordham University, Bronx NY, 10458
Andrew N Gifford
Medical Department, Brookhaven National Laboratory, Upton NY, 11973

Abstract

Sucrose synthase (Sus; EC2.4.1.13) is an enzyme that catalyzes the production of sucrose and UDP from UDP-glucose and fructose, and vice versa. Fluorinated sucrose analogues and sucrose synthase can be used in combination to study sucrose production and cleavage throughout a plant vascular system from source tissues to sink tissues. For this study, I prepared and purified sucrose synthase from wheat germ. Since both invertase (EC3.2.1.26) and Sus can be present in the purified enzyme solution, it was necessary to run multiple tests to determine specific enzyme activity. Currently, test results confirm the presence of fructose, indicating the presence of invertase in the reverse direction of the reaction. Sucrose synthase has been found to work successfully in the forward direction, catalyzing the production of sucrose. Future work will focus on purifying a high yield of sucrose synthase with minimal invertase through various purification and synthesis techniques.

I. Introduction

Sucrose, an essential transported disaccharide sugar in plants, is carried throughout the plant by the vascular system in order to provide nutrition to sink tissues. Radiolabeled fluorosucrose analogues allow efficient sugar transport studies, providing a greater understanding of plant biochemistry and the potential for biofuel crops engineered through synthetic biology. Sucrose synthase can work in both the forward and the reverse direction, either cleaving or producing sucrose ($C_{12}H_{22}O_{11}$). In the reverse direction, sucrose synthase catalyzes the production of UDP-glucose and fructose. Invertase, an enzyme often found in solutions with sucrose synthase, works in the reverse direction producing glucose and fructose.

An understanding of sucrose synthase and invertase activity in plants, with the use of synthetic analogues, will provide valuable information on nutritional biosystems. For example, Card and Hitz used fluorinated sucrose analogues to study the root sink strength for sucrose.[1] Successful sucrose synthase production and bioassays are necessary for analyzing the effectiveness of a [18F] Fluorosucrose analogue and its similarity to natural sugar found in biosystems. Some of the advantages of using [^{18}F]fluorine for the radio-label are that it has a long half-life compared with some other PET isotopes and is easily accessible. The half-life is 109 minutes, and this time span of almost 2 hours allows for the reaction of transforming sucrose to fluorosucrose to successfully take place. The fluorosucrose analogues can then be used to conclusively study the nature of the plant vascular system from source tissues to sink tissues.

II. Methods and Materials

In order to purify sucrose synthase, hexane in 100 mL aliquots was added to wheat germ (20 g) to remove excess oil. The solution was then homogenized in an assay medium (50 mM Tris, 10 mM $MgCl_2$, 2 mM DTT, 0.5 mM EDTA, protease inhibitor cocktail) and centrifuged at 4000 rpm for 10 minutes. Ammonium sulphate, at 30% saturation, was added to the supernatant (60 ml) and then spun at 14 000 rpm for 20 minutes. Ammonium sulphate, at 50% saturation, was then added to the supernatant and spun at 14000 rpm for 10 minutes. The pellets were then dissolved in a minimal quantity of buffer and filtered (22 um filter). The solution was then applied to a pre-equilibrated sephadex column in conjunction with High Performance Liquid Chromatography (HPLC). The purified enzyme, with 1 mL of polyethylene glycol, was then frozen on dry ice in aliquots.

We then tested the enzyme activity of our purified sucrose synthase solution by using radio-HPLC and LC-MS to determine the presence of either UDP-glucose and fructose or sucrose, depending on the direction of the reaction. This was necessary due to the possibility of the presence of invertase in the enzyme mixture, which can inhibit sucrose cleavage in the reverse direction. An aliquot of the purified sucrose synthase enzyme was added to a solution containing fructose (10 mg), 14C UDP-glucose (40 000 CPM/ml) in buffer (50 mM Tris, 2 mM DTT, 2 mM $MgCl_2$, 1 mM EDTA). The solution was then incubated at 30°C in a water bath. Acetonitrile was added to aliquots of the reaction mixture at different time points ranging from 5 to 80 minutes. Spin columns (10000 rpm, 5 min) were used to separate enzyme from product and the filtrate (2 000 CPM/ml) was added to acetonitrile. The formation of [14C] sucrose was measured using radio-HPLC (200 ul injection volume, NH2 column, gradient of 85% to 60% ACN over 25 minutes, 1 ml/min flow rate, 1 min fractions). The amount of radioactivity was measured using a liquid scintillation counter. Cold sucrose was also added to the radio-HPLC with the resulting fractions heated in a carbon dioxide environment, charring the tubes where sucrose was present. An identical procedure was followed using 2 mg of fructose and 2 mg of UDP-glucose in place of 10 mg of fructose and 14C UDP-glucose (40 000 CPM/ml) with sucrose measurements recorded on the Liquid Chromatography Mass Spectrophotometer (LCMS, 40 ul injection volume, NH2 column, 85% to 60% ACN gradient).

Sucrose synthase was found to be successfully purified, producing 14C-sucrose from [14C] UDP-glucose and fructose. We could not get the reaction to work in the reverse direction, and suspect the presence of invertase or errors with the current protocol. To make sure our enzyme was sufficiently present in the enzyme mixture, we calculated the enzyme concentration using Pierce BCA Protein Assay Kit. The enzyme concentration was found to be 11.6 units/mg. This value was high compared to the enzyme concentrations found in literature. For example, Su and Preiss[1] had a sucrose synthase enzyme concentration of 0.46 units/

mg, which is significantly lower than our enzyme concentration. In this reasoning, we think that there is an error in the protocol in the reverse direction and are currently working on producing a sufficient one.

We also synthesized [18F] Fluorosucrose from 4' sucrose heptaacetate triflate. In order to optimize the amount of sucrose heptaacetate as a product of the reaction, the best reaction conditions were investigated through a series of test reactions. Various enzymes were tested in different solvent systems. Liquid Chromatography-Mass Spectrum analysis was taken at two time points. The results from the traces showed the amount of sucrose octaacetate and sucrose heptaacetate, as well as any side products. Overall, there were 16 different esterase enzymes that were tried in 5 different solvent systems, and 42 overall test reactions. To do this, we took a protected form of sucrose that was commercially available and reacted it with an esterase enzyme. The enzyme activity targets one specific position on the molecule and allows regioselective deacetylation to take place. The product that results from this reaction is sucrose heptaacetate, which has 7 acetates and one hydroxyl group. This hydroxyl group is reacted with triflic anhydride. This structure allows the 18Flourine to react quickly by SN2, because the triflate is a very good leaving group. Specifically, the [18F] Fluoride was dried together with K2CO3 (1 mg) and K.2.2.2 (10mg) at 100°C under argon, followed by three azetropic drying steps using acetonitrile. Sucrose heptaacetate triflate (5-10 mg) in DMSO (0.5ml) was added to the dried residue and reacted for 15 minutes at 90°C. Water (2 ml) containing acetic acid (5 ul) was added to the solution after cooling. The [^{18}F] fluoroheptaacetate sucrose product was eluted through a preconditioned C-18 sep pack. After neutralizing the mixture with acetic acid (10 ul), the solutions was diluted with acetonitrile and injected into the HPLC system (200 ul injection volume, NH2 column, gradient of 85% to 60% ACN over 25 minutes, 1 ml/min flow rate, 1 min fractions). This fluorosucrose compound can then be tested with the purified sucrose synthase enzyme working in the reverse direction and compared to the activity of standard sucrose. The radiolabeled [^{18}F]fluorosucrose can also be injected into plants to trace the movement of sucrose through the plant through either planar scintographic imaging or Positron Emission Tomography (PET).

III. Conclusion

This experiment took the commercially available sucrose octaacetate and converted it to [^{18}F]fluorosucrose in three steps. These steps were (1) the translation of sucrose octaacetate to sucrose heptaacetate, with one exposed hydroxyl group and 7 acetate groups, (2) the conversion of sucrose heptaacetate to sucrose heptaacetate triflate, and (3) the reaction with fluorine to create [^{18}F]fluorosucrose. The information discovered in this experiment about the reaction involving the esterase enzyme Candida rugosa and the transformation of sucrose octaacetate to 18Fluorosucrose is new. To our knowledge, the 4' position of sucrose has not been radio-fluorinated before.

Also, out of the 42 test reactions, 4 showed good results. This shows that there was an impressive conversion of starting material to the desired sucrose heptaacetate product with one sharp peak from the LC-MS with minimal side products. Out of all the enzymes tested, the best reaction was from Candida rugosa in diisopropyl ether.

Successful synthesis of sucrose synthase was demonstrated by the production of 14C-sucrose. Currently, studies are being conducted to determine the ability of the enzyme to work in the reverse direction (sucrose cleavage). Future directions include work on successful bioassays for both the forward and the reverse direction of the sucrose synthase reaction. Sucrose synthase is essential in testing sucrose analogues, and operates as a standard for radiotracer comparison to standard sucrose. Radiotracers in plants will allow us to follow sucrose throughout the plant vascular system, and consequently allow us to create highly efficient biofuels.

IV. Acknowledgements

We would like to thank the Department of Energy for funding the research and the facilities at Brookhaven National Laboratory, and in particular the Medical Department, that had everything that we needed for my research to run smoothly. We would also like to thank our mentor, Dr. Andrew Gifford, for helping us understand all of the background information and for his willingness to answer all of our questions.

V. References

1. Card PJ, Hitz W D. Synthesis of 1'-Deoxy-1'-Fluorosucrose Via Sucrose Synthetase Mediated Coupling of 1-Deoxy-1-Fluorofructose with Uridine-Diphosphate Glucose. J Am Chem Soc 1984; 106: 5348-5350.
2. Su, Jong-Ching and Jack Preiss. Purification and Properties of Sucrose Synthase from Maize Kernels. Plant Physiol 1978; 61: 389-393.

Exploration of the epigenetic state of the Monoamine oxidase A gene

Alice Shanklin
Juniata College, Huntingdon, PA 16652
Taylor Stiegler
Boston College, Chestnut Hill, MA 02467
Elena Shumay
Brookhaven National Laboratory, Upton, NY 11973

ABSTRACT

The monoamine oxidase A (MAO-A) gene is located on the X-chromosome and codes for monoamine oxidase A, an enzyme that degrades brain neurotransmitters, such as serotonin and dopamine. Because of the critical role MAOA enzyme plays in behavioral control, polymorphisms in the MAOA gene have been heavily investigated in relationship with depression and aggressive behavior as well as several other neuropsychological disorders, including drug addiction. The importance of the environment in modulating the effect of the MAOA genotype suggests that epigenetic mechanisms are likely to be involved in MAOA regulation. In this study, we aimed to investigate the methylation status of the promoter region of the MAOA gene using genomic DNA obtained from blood cells. We analyzed in four sub-regions. To reduce the inherent variability between the individuals that can confound the results, we included in our analysis only males (males have only one copy of the gene) of African-American descent (because patterns across ethnic groups differ), N=124 to explore history of cocaine abuse, (CA, N=XXX) with healthy controls (HC, N=XXX). We found that while in the vicinity of the MAOA transcription start site (TSS) DNA methylation varied across individuals, regions further upstream of the MAOA core promoter are uniformly unmethlayed. No correlation was observed between methylation status of tested loci and age or drug addiction.

I. INTRODUCTION

DNA methylation is an epigenetic control mechanism and is thought to exhibit partial control over gene expression. While the DNA nucleotide sequence remains static throughout an individual's lifetime, factors of epigenetic control change with respect to both age and environment. Methylation greatly varies across the different cell types, but in those of the same tissue methylation patterns are largely conserved.2 DNA methylation occurs on a cytosine nucleotide which follows a guanine nucleotide (CpG site) where methylated cytosine possesses a methyl group at the 5' carbon. Areas of the genome larger than 300 bp with CG content greater than 50% are termed "CpG islands," and usually found near a gene's transcription start site.3 While the majority of cytosines in the genome are methylated, cytosines residing within the CpG islands remain methylation-free.3 Aberrant methylation of CpG islands has been linked to gene silencing.4 DNA methylation is an epigenetic mark directly imposed on the DNA sequence and can be analyzed by different assays that are based on bisulfate conversion (BS conversion) of genomic DNA in combination with various downstream applications, including enzymatic digestion (COBRA assay).

The MAOA gene encodes the MAO A enzyme which breaks down monoamines including serotonin and dopamine. Variations in the MAOA sequence have been linked to aggressive behavior in males.1 Because this association is dependent on environmental exposure, it is possible that MAOA regulation includes epigenetic mechanisms. The MAOA promoter region has two CpG islands. Here, we analyzed several loci of its promoter, aiming to obtain most complete information on the MAOA methylation state. We wanted to reveal differences in the methylation state of the MAOA promoter between individuals addicted to cocaine and healthy controls, as well as well as whether methylation status is affected by age. We hypothesized that the different brain environments of the individuals, varying in cocaine addiction status and age will be reflected in their methylation states.

II. MATERIALS AND METHODS DNA

A. Sample Description

DNA samples of 100 males of African-American descent, half of which are addicted to cocaine were obtained from the DNA extraction 124 blood samples by Elena Shumay. DNA was extracted from white blood cells using the Quiagen DNA purification kit.

B. Bisulfite conversion of DNA

Bisulfite conversion was completed with the Qiagen Bisulfite-Conversion Kit using approximately 600 ng of DNA. Samples were stored at -20°C until PCR amplification.

Amplicon #	Chromosome Location (Hg18)	Sequence
1	ChX: 43398925-43399181	F:TTAAAGAATGAAAGTATTAGGTTGAGAGTT R:ATACCCACTCTTAAAAACCAACCCC
2	ChX: 43399430-43399858	F:GGGTGTTGAATTTTGAGGAGAAG R:AAAACACAACTACCCAAATCCC
3	ChX: 43400453-43400805	F:GGGGAGTTGATAGAAGGGTTTTTTTTAT R:TATATCTACCTCCCCCAATCACACC
4	ChX: 43400525-43515800	F:GTTAAAGTATGGAGAATTAAGAGAAGG R:CAAAATATAAAACCAAACCATAACTACA

Table 1. Location and BP Sequence of Amplicons 1-4

C. Amplification of bisulfite converted DNA

PCR was conducted using hot star taq dha polymerase (guiagen, UK) and cycling conditions of 45 cycles with an annealing temperature of 56°C for all amplicons. Successful amplification was determined by running the PCR product and loading dye on a 1.25% agarose gel for one hour at 95 volts.

D. Determination of methylation status through restriction enzyme digests

Four different restriction enzymes: HPYCH4IV, HHAI, BSTUI and RSAI were used to digest amplified regions of the samples. Because the enzymes all cleaved DNA at sequences conserved in the BS conversion by methylated DNA, if PCR product was not digested by a given enzyme it was observed to be unmethylated.

Gel electrophoresis was used to determine the relative percentages of "cut" and "uncut" DNA using a 1.25% agarose gel at 95 volts and visualized the DNA bands under ultraviolet light. A 100 base-pair DNA ladder was used to determine fragment size. Controls consisted of genomic PCR product containing restriction enzyme "cut" sites for at least one of the restriction enzymes used.

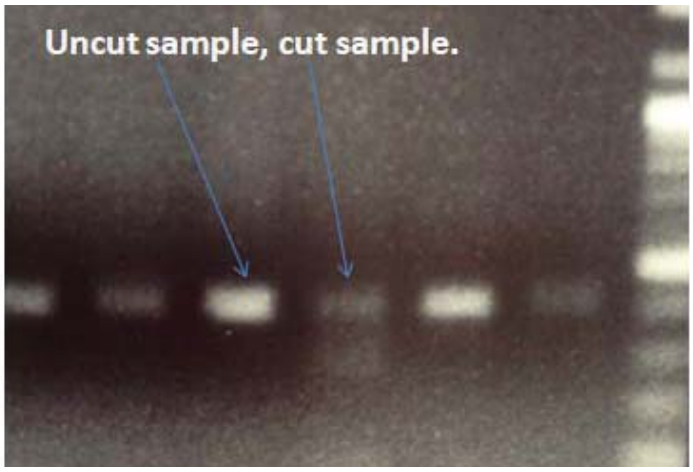

Figure 1. Gel electrophoresis of both a digested and an undigested amplified region. "Cut sample" exhibits 50% methylation.

E. Data analysis

Methylation percentages were inferred based on our observations of band brightness.

III. RESULTS

Methylation status of amplicons 1-4 at specified CpG units are described in Figure 5. Significant methylation variation was observed in nested regions 3 and 4 (cut site 3, Figure 5) at a locus close to the transcription start site (Figure 2). A slight positive correlation was observed between this region and subject age (Figure 4). The loci located in amplicons 1 and 2 generally exhibited low levels of methylation as expected (cut sites 1-3, Figure 5). Although the methylation status of the TSS-proximal locus (cut site 3, Figure 5) varied widely across individuals, no correlation was observed between methylation percentage and +/- cocaine addiction status.

IV. DISCUSSION/CONCLUSION

The DNA methylation of CpG islands near a gene transcription start site is a mechanism of epigenetic control hypothesized to inhibit gene expression.3 In this study, we obtained the methylation status at 4 different loci on the MAOA promoter region using 5 different amplicons. Of the 4 individual loci, two were in CpG island 28 and two of which were in CpG island 52 (Figure 5, cut sites 1 and 2, 3 and 4 respectively). Results were verified using by using multiple restriction enzymes to cult the same site (Figure 5, cut site 2) and by using nested PCR and cutting at the same restriction enzyme sites in two different amplicons (Figure 5, cut sites 3 and 4). The methylation percentage as observed by eye on gel electrophoresis of our restriction digests, was determined, averaged among controls, and plotted with respect to 'cut site' (Figure 5). Supplementary methylation data was averaged with original methylation data in data analysis.

The results for cut sites 1, 2, and 4 were expected because of the general tendency for CpG islands to be unmethylated. However, the variable methylation status of cut site 3 was significant because of its proximity to the transcription start site. These results point to a possible link between the regulation of expression of the MAOA gene and cytosine-methylation at the transcription start site. This type of methylation variation was originally hypothesized to be related to cocaine addiction status, as an individual

Amplicon #	RsaI	HhaI	BSTUI	HpYCH4IV
1	----------	ChX: 43399076	----------	----------
2	ChX: 43399557	----------	----------	Chx: 43399557
3	----------	----------	ChX: 43400562	Chx: 43400578
4	----------	----------	ChX: 43400562	Chx: 43400578

Table 2. Enzyme and Restriction Site Location for Amplicons 1-4

Enzyme	RsaI	HhaI	BSTUI	HpYCH4IV
Reaction Setup	2 ul PCR product, 2 ul NEB buffer 4, 0.25 ul RsaI enzyme, 15.75 ul ddH2O	2 ul PCR product, 2 ul NEB buffer 4, 0.25 HhaI enzyme, .2 ul BSA, 15.6 ul ddH2O	2 ul PCR product, 2 ul NEB buffer 2, 0.25 ul BSTUI enzyme, 15.75 ul ddH20	2 ul PCR product, 2 ul NEB buffer 1, 0.25 ul HPYCH4IV enzyme, 0.2 ul BSA, 15.75 ul ddH2O
Incubation	37°C for 16 hours.	37°C for 16 hours.	60°C for 16 hours.	37°C for 16 hours.

Table 3. Restriction Enzyme Reaction Conditions

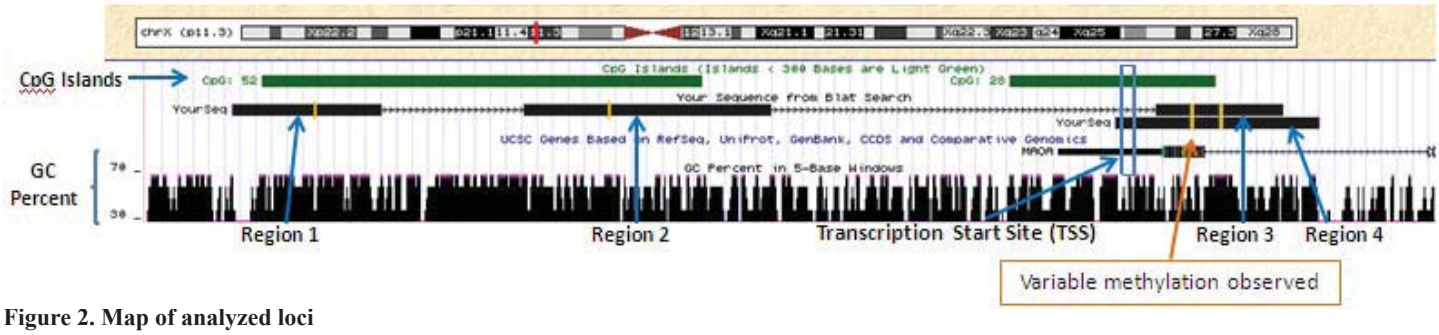

Figure 2. Map of analyzed loci

Figure 2 displays the analyzed region in the context of the UCSC genome browser. Green bars represent CpG islands. Black bars represent analyzed regions, shown as custom tracks. Blue arrows indicate relative locations of regions 1-4. Yellow arrow indicates the restriction site at which variable methylation was found. Green bars represent CpG islands. Blue box indicates the TSS region.
Yellow dashes indicate restriction enzyme sites.
Yellow arrow indicates the restriction site at which variable methylation was observed.

TSS-Proximal Methylation Percentages (fig. 5, cut site 3)				
	Lowest % Methylation	**Highest % Methylation**	**Average % Methylation**	**Standard Deviation**
Cocaine Addicts	0%	60%	14%	+/- 18%
Normal Controls	0%	80%	13%	+/- 19%

Figure 3. TSS Methylation and Addiction Status

addicted to cocaine may have altered his environment and, therefore, his MAOA gene expression would be regulated. Because results indicated no correlation between TSS-proximal methylation status and cocaine addiction, this hypothesis was proven to be false. However, there was a slight positive correlation between the methylation status of the variable region and age, suggesting an alternate gene-environment interaction.

V. ACKNOWELEDGEMENTS

This project is dedicated in loving memory to Dr. John J. Dunn, and was funded by Dr. Elena Shumay and the Department of Energy's "Science undergraduate laboratory internship" (SULI) program. Laboratory space was provided by the Dunn Lab Group.

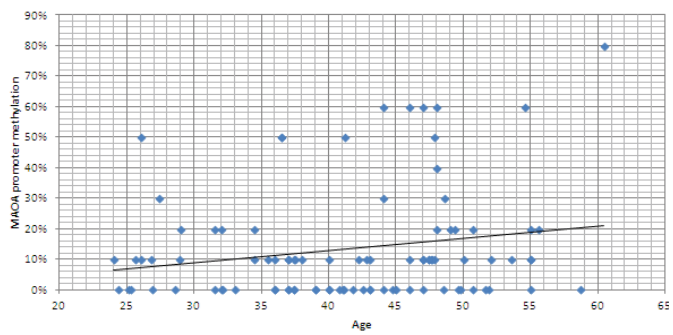

Figure 4. TSS-Proximal (Cut Site 3) Methylation vs. Subject Age

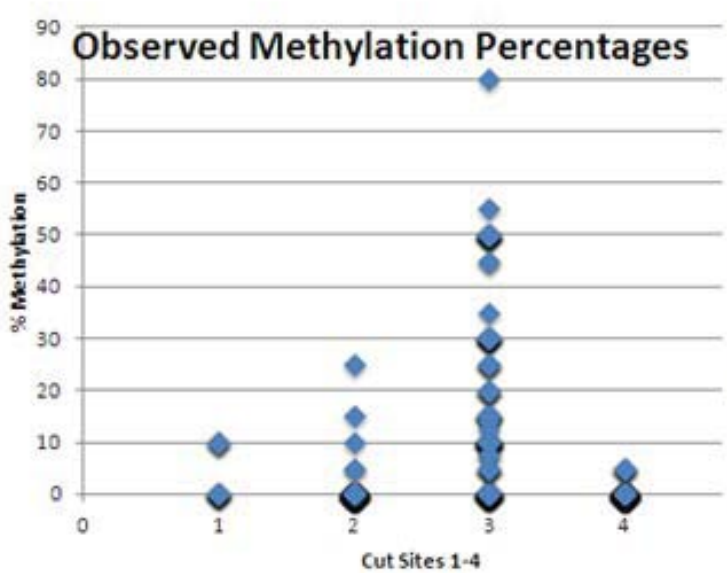

Cut Site	Description
1	Observed methylation percentages at HHAI site in region 1.
2	Average observed methylation percentages for region 2 HPYCH4IV and BSTUI cut sites, which recognize the same sequence.
3	Average observed methylation percentages for HPYCH4IV in nested regions 3 and 4. Nearest to TSS.
4	Average observed methylation percentages for BSTUI in nested regions 3 and 4.

Figure 5. Overall Methylation Percentages in Cut Sites 1-4.

Cut Site #3 Methylation: Cocaine Addicts and Normal Controls

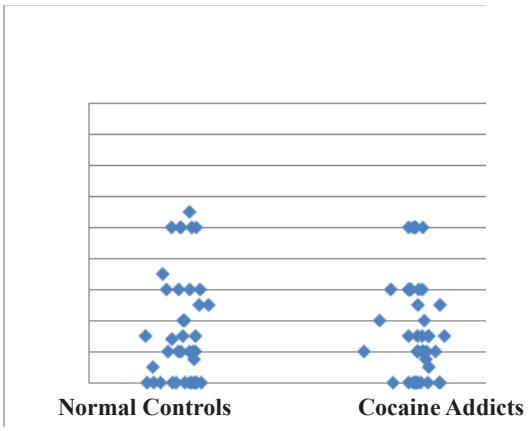

Figure 6. Methylation Percentages at Cut site #3 for Cocaine Addicts and Normal Controls.

Figure 6 shows the methylation percentages at restriction site 3 for cocaine addicts and normal controls. Normal controls (left) and cocaine addicts (right) were individually plotted with respect to increasing age on the x-axis. No significant difference in methylation was noted between normal controls and cocaine addicted individuals.

VI. REFERENCES

[1]McDermott, R, Tingley, D, Crowden, J, Frazzetto, G, & Johnson, D. D. P. (2008). Monoamine oxidase a gene (maoa) predicts behavioral aggression following provocation. PNAS.

[2]Jaenisch R, Bird A. Epigenetic regulation of gene expression: how the genome integrates intrinsic and environmental signals. Nat Genet. 2003;33:245-254.

[3]Donoly, Dana C., Jennifer R. Weildman, and Randy R. Jirtle. "Epigenetic Gene Regulation: Linking Early Developmental Environment to Adult Disease." Reproductive Toxicology 23.3 (2007): 209-307. Web.

[4]Phillips, T. (2008) The role of methylation in gene expression. Nature Education 1(1).

Engineering in the Superconducting Magnet Division

Ryan E. Sheedy
Department of Mechanical and Aerospace Engineering, University of Florida, Gainesville, Florida 32611
Michael D. Anerella, Paul E. Kovach, and Jesse Schmalzle
Department of Engineering/Environmental, Brookhaven National Laboratory, Upton, New York 11973

The Superconducting Magnet Division at Brookhaven National Laboratory (BNL) is responsible for designing and fabricating various superconducting magnets for particle accelerators like the Relativistic Heavy Ion Collider (RHIC), the Large Hadron Collider, and others. The magnets built at BNL are an example of the work that needs to be done to provide scientists with the tools and technology needed to conduct research in the fields of nuclear and particle physics. As a mechanical engineering intern, most of my work has involved using Pro-Engineer modeling software and ANSYS finite element analysis software to create and analyze 3-D parts and assemblies of a magnet's components and associated tooling and then make the drawings used for production. I worked on various projects including shipping fixtures, cooling fans, and an epoxy impregnation system. I believe the practical experience has benefited me the most in regard to my professional development as a mechanical engineer.

I. INTRODUCTION

As an engineering intern in the Superconducting Magnet Division (SMD) at Brookhaven National Laboratory (BNL), I have had the opportunity to learn and practice a variety of engineering skills as well as learn about the superconducting magnets and the manufacturing methods by which they are produced. Superconducting magnets are electromagnets which utilize superconducting wire capable of very high current density and very low resistance, requiring cooling to cryogenic temperatures.1 I worked on various projects related to current programs being worked on by the magnet division. Working under the engineers has been a fantastic opportunity for me to gain real-world experience. This report will detail some of the work I have done thus far, what I have learned as a result, and how this work has impacted my professional development as an engineer.

II. OVERVIEW OF ACTIVITIES

The projects I have worked on have all revolved around the central theme of engineering parts and related tooling for the magnets. The majority of my work was done using engineering software including Pro/Engineer and ANSYS. Pro/Engineer is a 3-D modeling program used to create 3-D models of parts and assemblies of parts. Then from the models, 2-D drawings can be made complete with all dimensions and details for manufacturing the part or assembly. ANSYS is an engineering analysis program which I primarily used for performing static structural analyses. Working in the magnet division has also allowed me to have access to the magnet division shop where the magnets are fabricated, assembled and tested.

III. PROJECTS

Although I have done work related to several programs currently being worked on in the magnet division, there are a few that stand out. The first project involved modifying a magnet shipping fixture to support just the magnet's cold mass (the inner core of the magnet which is kept at cryogenic temperatures during operation) rather than the complete magnet section. The magnet's cold mass is a long cylinder approximately a foot in diameter, 40 feet in length and weighing about 8 000 pounds. The shipping fixture is a frame-like structure that fits inside a shipping container and ensures the magnet is not damaged. I was responsible for completing all modeling and drawings of the modifications to the shipping fixture as well as performing the structural analysis for it. I designed three steel support columns that would mount to the frame of the shipping fixture and interface with the cold mass. The design consisted of a large diameter steel pipe with flanges on both ends. The two end posts were different from the center post in that the center post did not have a bolt hole pattern on the top flange. With both ends bolted, the cold mass would be securely held in place during shipping. The structural analysis confirmed that the design could support the weight of the cold mass and the possible lateral loads incurred during shipping. The support columns are currently in production and will soon be ready for shipping to The European Organization for Nuclear Research (CERN).

The second project was developed as a solution for cooling the magnet form block after it has been heat-cured in the curing press. The magnet coils are created by winding superconducting cable around a centerpost onto a cylinder in a length-wise cylindrical path. Once the coils are wound and wrapped with a Teflon release film, they are moved into the curing press and heated under pressure to create one solid block, ensuring they remain in place during the magnet assembly process. The problem we encountered was that once heated, the form block would take almost twenty hours to cool back to room temperature. The idea was proposed to set up a series of fans to blow along the sides of the form block and thus reduce the time for the block to cool though the added effect of convective cooling. The fans chosen were twelve inch diameter blowers and I was tasked with designing a way to mount the fans in place alongside the form block, which is five feet off the floor when in the press. Using Pro/Engineer I designed and modeled a small frame made from Unistrut Metal Framing System that would mount the fans to the sides of the curing press. The frame was made up of three sections of Unistrut and a vertical section of steel pipe. The Unistrut was assembled in an "H" shape to bolt to the four holes in the legs of the fan. This design, thanks to the Unistrut sliding nuts and threaded pipe, allowed the frame to be adjustable in the forward and sideways directions in the horizontal plane as well as allow the fan to rotate. The four frames were created and assembled and are now ready for use. I also performed heat transfer calculations using the dimensions of the press and form block as well as the output of the fans. The fans are estimated to reduce the cooling time from twenty hours to only eight hours.

The third project involves redesigning the system for impregnating magnet coils with epoxy or other resins under vacuum for The U.S. LHC Accelerator Research Program (LARP). The current system uses a mixing bowl under vacuum connected by

plastic tubing to the impregnation fixture. However, the magnet division wants to begin using a new epoxy which also needs to be heated to and maintained at 120°C throughout the process. To accomplish this, the mixing bowl will be redesigned to include a heating plate and all piping between the mixing bowl and the impregnation fixture must also be heated. The method of heating the piping will be to wrap it in an electric heating element in the form of tape. The vacuum chamber itself will be ordered through a supplier and will include all of the necessary features including the heating plate, electric motor with attached mixing blade, and feed-throughs for all wiring (heating plate and thermocouples), vacuum inlet and outlet, and the piping for the epoxy. I helped develop the concept design for the vacuum chamber and have been researching parts resources and communicating with the vendor we selected for the chamber. As of now we are continuing communications with the vendor on the specifications of the chamber before the order is placed.

IV. LESSONS LEARNED

More than anything working in the magnet division has been a learning experience. I learned about superconducting magnets, the engineering behind them and the manufacturing methods and processes used to create them. I also learned how to use a few new software programs which are generally applicable to any mechanical engineering work. However, I also learned a lot of not so obvious things from working with the engineers working in the magnet division. For me it is the practical experience and learning all of the little things you can't get from a textbook that has been the most important. Through the projects I have worked on I have become much more knowledgeable of the level of detail and accuracy that real-world engineering projects require. I've learned how to design parts to be easier to manufacture and cheaper to produce, as well the importance of these factors related to the larger project or goal.

V. CONCLUSION

Working in the Superconducting Magnet Division at Brookhaven National Laboratory has been an immensely important step in my engineering career. I have worked on a variety of projects related to the manufacturing process for the superconducting magnets. This variety has allowed me to learn a little about many steps of the process. The technical knowledge of modeling software and general engineering practices can be applied to any engineering job and will be utilized and expanded upon throughout my career. Learning about the magnets and the manufacturing process for them was a unique experience to learn about something engineering related that is on the cutting edge of scientific research. Most important to me are the experiences of working on real engineering applications and following along with the production process to see the result of my work. As a result of my internship I am much more confident in my abilities as a mechanical engineer and I look forward to applying what I have learned in the future.

VI. REFERENCES

1. "Characteristics of Superconducting Magnets." American Magnetics. n.d. Web. 30 Jul. 2012. <http://www.americanmagnetics.com/charactr.php>.

Analyzing perfluorocarbon tracer compound stock solutions and gaseous mixtures with a thermal conductivity detector using gas chromatography

Mackenzie Shipley
Department of Chemistry, Hartwick College, Oneonta, NY 13820
Richard Wilke and Thomas Watson
Environmental Science, Brookhaven National Laboratory, Upton, NY 11973

Abstract

This research project sought to create a primary calibration standard for quantifying the concentration of Perfluorocarbon Tracer Compounds (PFTs) in samples. PFTs are used as tracers to help hunt for underground leaks in utility company cable systems, evaluate air exchange in homes and commercial buildings, as well as provide input for modeling atmospheric transport. The objective of this research project was to determine the composition of the PFT compounds using gas chromatography. By using a thermal conductivity detector to analyze which PFT peaks are present in each PFT sample, the composition of each sample was calculated. This research supports the Department of Energy's mission by increasing understanding of global climate by quantifying atmospheric transport and dispersion, measuring building energy efficiency, and developing tools that can be used to support emergency response planning and operations. The data gathered in this research project will be used to prepare standard mixtures used to quantify PFT concentrations in samples. I have learned how to develop analytical methods for analyzing PFTs, calculate the composition of the measured samples and solve mechanical and operational problems of gas chromatography. The opportunity to work at a government laboratory with professional scientists and equipment has given me and helped me develop many laboratory skills that will be useful in my scientific career.

I. Introduction

Perfluorocarbon Tracer Compounds (PFTs) are hydrocarbons in which the hydrogen atoms have been replaced with fluorine atoms. Due to the strength of the fluorine-carbon bond, these compounds are very stable and inert. PFTs will persist in the atmosphere for thousands of years due to their stability and resistance to oxidation in the atmosphere. The only way in which these compounds can be destroyed is by photolysis in the mesosphere. The quantities of PFTs used in tracer programs are so small that their environmental effect has been found to be minimal (Watson, et al. 2007).

PFTs have been used to measure rates of building infiltration, detect gas leaks, and track mass movement in geological formations. PFTs are used to study transport in the atmosphere on local, regional and continental scales (Watson, et al. 2007). These compounds are present in the atmosphere at extremely low concentrations and background levels can be measured at parts per quadrillion (10-15) levels.

A. Current Research Project

The purpose of this research is to develop analytical methods that will be used to measure the composition of the six major PFTs. The physical properties of the six PFTs are given in Table 1 (Watson, et al. 2007). The purity of the PFTs must be determined so that the exact composition of the standard will be known.

II. Materials and Methods

The instrument used for analysis of the PFT compounds was a Hewlett-Packard (HP) 6890 gas chromatograph with a thermal conductivity detector (TCD) and a 30 m carbograph capillary column with 0.25 mm diameter. Samples of each PFT at several hundred to several thousand parts per million were injected directly into the inlet of the gas chromatograph. The results were a chromatogram that displays the signal (mV) vs. time (min). Depending upon the level of interaction that occurs between each component of the sample and the stationary phase, there will be different retention times for each individual component of the sample. The most important factor when attempting to improve chromatograms and data is the retention time of the peak(s). If the retention time of one peak is identical to the retention time of another, then it will be virtually impossible to determine which peaks belong to which component of the sample. Therefore, the methods developed for analyzing each PFT sample must have unique retention times for each component of the sample. The order of elution of each PFT is determined by the molecular weight of each compound; the lightest PFTs elute the fastest while the heavier PFTs elute later.

Acronym	Chemical Name	Formula	Molecular Weight (g mol^{-1})	Boiling Point (°C)
PDCB	perfluorodimethylcyclobutane	C_6F_{12}	300	45.0
PMCP	perfluoromethylcyclopentane	C_6F_{12}	300	48.1
PMCH	perfluoromethylcyclohexane	C_7F_{14}	350	76.0
o-PDCH	perfluoro-1,3-dimethylcyclohexane	C_8F_{16}	400	102.0
i-PPCH	perfluoroisopropylcyclohexane	C_9F_{18}	450	130.0
PTCH	perfluorotrimethylcyclohexane	C_9F_{18}	450	125.0

Table 1. PFTs used as tracers by BNL Tracer Technology Group; acronyms, IUPAC names, chemical formulas, molecular weights, and boiling points.

A. Developing an Analytical Method

A chromatogram that has good separation of all of the sample's components will have narrow peaks that are sharp and symmetrical. Separation of components is a function of column diameter, column length, type of stationary phase, type of carrier gas, and column temperature (Hyver and Sandra, 1989). Retention times can be changed by changing the conditions in the column. The most significant adjustable parameters are the flow rate of the carrier gas and oven temperature. Higher temperatures cause less interaction between the PFT sample and the stationary phase and shorter retention times for the components within the sample. The faster the carrier gas flows through the column, the less interaction that the sample has with the stationary phase. While a slower flow results in more interaction between the sample and the stationary phase and improved separation of component peaks.

B. Oven Temperature Program

The necessary separation was achieved by developing an analytical method based on changing the temperature of the column oven. A unique oven program was created that separated all six PFTs within twenty minutes. For the first five minutes, the oven held at a low temperature of 35°C. The lighter PFTs—PDCB 1, PDCB 2, and PMCP were separated from each other at this temperature. PDCB and PMCP typically co-elute and it is difficult to integrate the two peaks separately. Next, the oven increased at a rate of 15°C/min for one minute to reach 50°C where the temperature was held for two minutes. Increasing the temperature quickly helps eliminate dead time in the chromatogram, in which no peaks are eluting. Finally, the oven was ramped up at a rate of 50°C/min for one minute to reach a final temperature of 100°C that was held constant for the final eleven minutes of the run. This oven temperature caused the heavier PFT compounds—o-PDCH, iPPCH and PTCH—to move through the column faster and elute sooner. Initially, PTCH's six isomers were taking longer than twenty minutes to elute. Also, there was a large gap in the chromatogram between the o-PDCH isomers, the iPPCH peak and the six PTCH isomers. Increasing the temperature of the oven caused all of these PFTs and their isomers to elute much sooner.

C. Intermediate Standards

There were eight total samples containing the six major PFT compounds that were analyzed. To analyze these samples, a 250 µL aliquot from each bag was directly injected into the inlet on the gas chromatograph. Five injections of each sample bag were made. Then the data for each set of samples was combined and averaged. All of the minor peaks present in each chromatogram were also combined and averaged. The composition of each PFT was determined using the calculated averages from the data.

D. Calculations

- Percent Composition (%) = ((major peak area average)/(major peak area average+first minor peak area average))*100
- Relative Standard Deviation = ((standard deviation of peak area)/(mean peak area))
- Percent Composition Error

$$\sqrt{\left(\frac{\delta}{\delta A_m}\right)^2(\delta\overline{A_m})^2+\left(\frac{\delta}{\delta A_1}\right)^2(\delta\overline{A_1})^2}$$

Where A_m is the average value of the peak areas of the major PFT in the sample, A_1 is the average value of the first minor peak present in the PFT sample. Depending on the number of minor peaks present in each sample, there will be more partial derivatives to be calculated.

- Standard Deviation of Mean $(\delta\overline{A_m}) = \frac{\sigma A_m}{\sqrt{n}}$

Where σA_m is the standard deviation of the peak areas of the major PFT in the sample and *n* is the number of trials performed for that specific PFT.

III. Results and Discussion

Most of the intermediate PFT samples had other PFTs present (Appendix 1, Tables 3-17). The relative standard deviation calculations for each PFT demonstrate that the five trials performed yielded consistent results. Table 2 presents a summary of the calculated composition for each PFT intermediate sample.

The calculated compositions of each of the eight measured intermediate standards were not as pure as expected. For instance, iPPCH (Tables 15-16 and Figure 7) yielded a composition of approximately 89%. These PFTs cannot be used as a primary standard.

Another interesting result was the data collected for both samples of PMCH (Tables 9-12 and Figures 4-5). One problem with the data was that the compositions of both samples were not consistent within the five trials performed and they were also inconsistent with one another. Although the two sample bags have different concentrations of PMCH, their composition should have been identical. Another concern with the PMCH data was that the impurities found in the PMCH 1 sample were not the same impurities found in the PMCH 2 sample. PDCB 2 was found in both samples, but PMCP was only present in the PMCH 1 sample. These problems could be due to contamination of the syringe used to inject the samples into the gas chromatograph or another issue such as a dirty sample bag or poor peak integration. In future work of this type, more sample injections should be performed to acquire more consistent data.

Now that the purity of the individual PFTs has been determined, the next step of this research project is to measure the response of the analytical instrument to the tracers as well as quantify the detection limits of each PFT. The goal of this project is to develop a gas phase, primary calibration standard using the analyzed compounds. The primary calibration standard will be used to quantify the PFT levels in air samples.

IV. Acknowledgements

I would like to acknowledge the Department of Energy for their funding and support of the SULI Program at BNL as well as the funding of my internship. I would like to thank Brookhaven National Laboratory and the Office of Educational Programs for hosting me and providing an exceptional research atmosphere. I also thank the Tracer Technology Group at BNL for their knowledgeable insight and help they provided me during my internship. I would especially like to thank my mentors Dr. Tom Watson and Rick Wilke for their continuous support and constructive criticism throughout the entire research project.

Major PFT		Minor Component								
		PDCB 1	PDCB 2	PMCP	PMCH 1	PMCH 2	oc-PDCH	mt-PDCH	ot-PDCH	mc-PDCH
PDCB 1	100±2.36%	-	-	-	-	-	-	-	-	-
PDCB 2	100 ± 1.83%	-	-	-	-	-	-	-	-	-
PMCP	98.92 ± 0.05%	-	-	-	-	0.11 ± 0.05%	0.47 ± 0.05%	0.04 ± 0.05%	0.39 ± 0.05%	0.07 ± 0.05
PMCH 1	91.42 ± 0.34%	-	8.16 ± 0.34%	0.42 ± 0.34%	-	-	-	-	-	-
PMCH 2	82.66 ± 1.90%	-	17.34 ± 1.90%	-	-	-	-	-	-	-
oc-PDCH	42.00 ± 0.27%	-	-	-	-	6.49 ± 0.27%	-	-	-	-
mt-PDCH	5.55 ± 0.27%	-	-	-	-	6.49 ± 0.27%	-	-	-	-
ot-PDCH	38.88 ± 0.27%	-	-	-	-	6.49 ± 0.27%	-	-	-	-
mc-PDCH	7.08 ± 0.27%	-	-	-	-	6.49 ± 0.27%	-	-	-	-
iPPCH	89.14 ± 0.45%	-	-	-	-	-	-	3.02 ± 0.45%	1.78 ± 0.45%	1.14 ± 0.45%
PTCH-1	55.64 ± 0.34%	-	-	-	-	-	-	3.59 ± 0.34%	-	4.06 ± 0.34%
PTCH-2	18.35 ± 0.34%	-	-	-	-	-	-	3.59 ± 0.34%	-	4.06 ± 0.34%
PTCH-3	4.11 ± 0.34%	-	-	-	-	-	-	3.59 ± 0.34%	-	4.06 ± 0.34%
PTCH-4	5.36 ± 0.34%	-	-	-	-	-	-	3.59 ± 0.34%	-	4.06 ± 0.34%
PTCH-5	5.11 ± 0.34%	-	-	-	-	-	-	3.59 ± 0.34%	-	4.06 ± 0.34%
PTCH-6	3.77 ± 0.34%	-	-	-	-	-	-	3.59 ± 0.34%	-	4.06 ± 0.34%

Table 2. Summary of composition results for each PFT intermediate standard.

V. References

Atkins, P.W. Physical Chemistry. P.W. Atkins 1978. 141. Hewlett-Packard. HP 6890 Series IV Plus Operating Manuals. Agilent Technologies 2000. Hyver, K. J., Sandra, P. High Resolution Gas Chromatography. Third Edition. Hewlett-Packard Co. 1989, 1-15, 4-7.

McNair, H.M.; Bonelli, E.J. Basic Gas Chromatography. Varian Aerograph 1968. 1, 9, 29, 91-94, 236, 239.

Watson, T. B., Heiser, J.; Kalb, P.; Wilke, R. The atmospheric background of Perfluorocarbon compounds used as tracers. Environ. Sci. and Technol. 2007, 41, 6909.

Watson, T. B., Sullivan, T. Feasibility of a Perfluorocarbon tracer based network to support Monitoring, Verification, and Accounting of Sequestered CO2. Environ. Sci. Technol. 2012, 46, 1692-1699.

VI. Appendix 1

Injection #	Percent Composition PDCB 1	Percent Composition Impurities
1	100%	0%
2	100%	0%
3	100%	0%
4	100%	0%
5	100%	0%

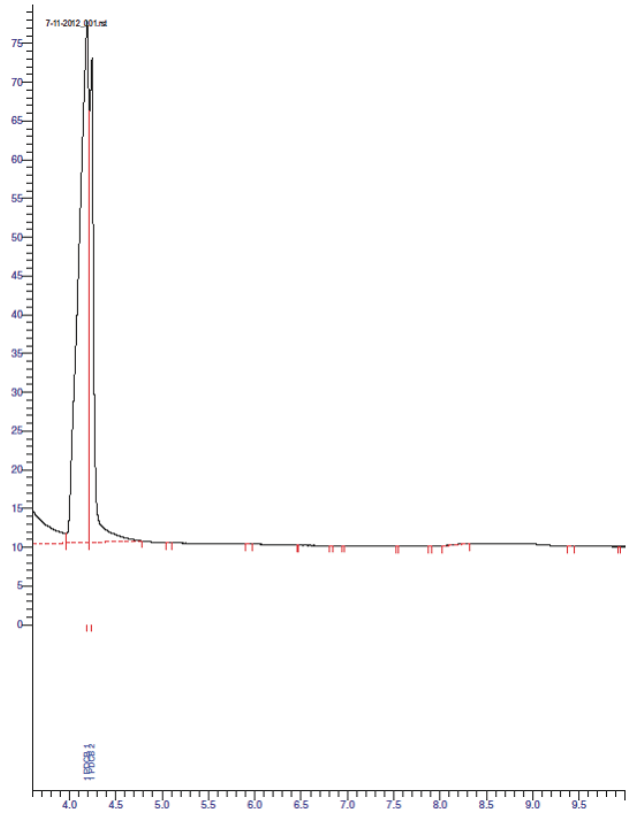

Figure 1. Chromatogram of intermediate standard PDCB 1 isomers using developed analytical method.

Table 3. Percent composition of PFT intermediate standard PDCB 1.

Mean Peak Area	Standard Deviation (Major Peak Area)	Relative Std Dev (Peak Area)	Standard Deviation of Mean	Error of % Comp
7.3×10^5	0.4×10^5	5%	0.2×10^5	0

Table 4. Mean and standard deviation data for PDCB 1 intermediate standard.

	iPPCH	PTCH-1	PTCH-2	PTCH-3	PTCH-4	PTCH-5	PTCH-6
	-	-	-	-	-	-	-
	-	-	-	-	-	-	-
%	-	-	-	-	-	-	-
	-	-	-	-	-	-	-
	-	-	-	-	-	-	-
	-	-	-	-	-	-	-
	-	-	-	-	-	-	-
	-	-	-	-	-	-	-
	-	-	-	-	-	-	-
%	-	0.41 ± 0.45%	-	-	-	-	4.51 ± 0.45%
%	-	-	-	-	-	-	-
%	-	-	-	-	-	-	-
%	-	-	-	-	-	-	-
%	-	-	-	-	-	-	-
%	-	-	-	-	-	-	-
%	-	-	-	-	-	-	-

Injection #	Percent Composition PDCB 2	Percent Composition Impurities
1	100%	0%
2	100%	0%
3	100%	0%
4	100%	0%
5	100%	0%

Table 5. Percent composition of PFT intermediate standard PDCB 2.

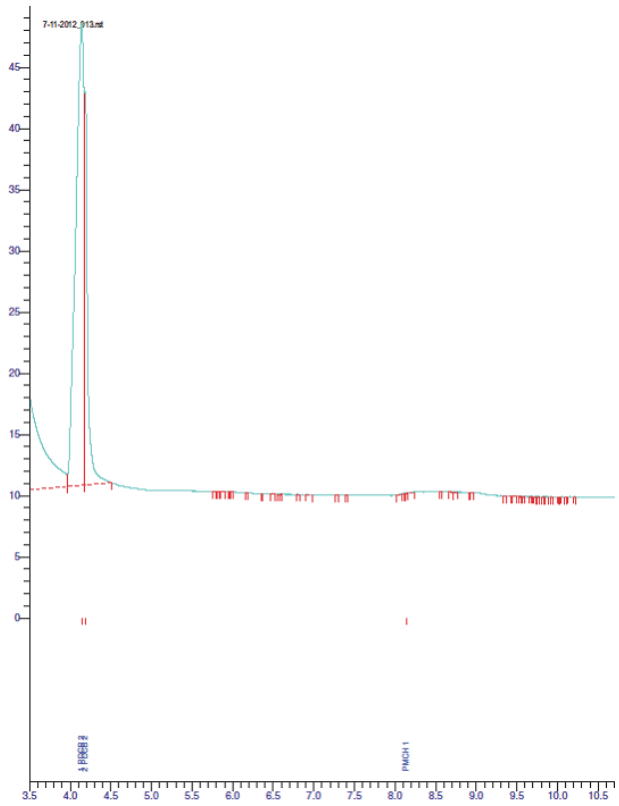

Figure 2. Chromatogram of intermediate standard PDCB 2 isomers using developed analytical method.

Mean Peak Area	Standard Deviation (Major Peak Area)	Relative Std Dev (Peak Area)	Standard Deviation of Mean	Error of % Comp
$3.5x10^5$	$0.1x10^5$	4%	$0.06x10^5$	0

Table 6. Mean and standard deviation data for PDCB 2 intermediate standard.

Injection #	% Comp PMCP	% Comp PMCH 2*	% Comp oc-PDCH	% Comp mc-PDCH	% Comp ot-PDCH	% Comp mt-PDCH
1	98.98%	0.08%	0.48%	0.03%	0.39%	0.06%
2	98.96%	0.10%	0.47%	0.03%	0.39%	0.05%
3	99.10%	0%	0.45%	0%	0.37%	0.08%
4	98.96%	0%	0.46%	0.06%	0.44%	0.07%
5	98.89%	0.13%	0.48%	0.04%	0.38%	0.09%

Table 7. Percent composition of PFT intermediate standard PMCP.

Mean (Major Peak Area)	Standard Deviation (Major Peak Area)	Standard Deviation Mean (Major Peak)	Relative Std Dev (Peak Area)	Error
$7.1x10^5$	$0.7x10^5$	$0.3x10^5$	10%	$3.4x10^2$

Table 8. Mean and standard deviation data for PMCP intermediate standard.

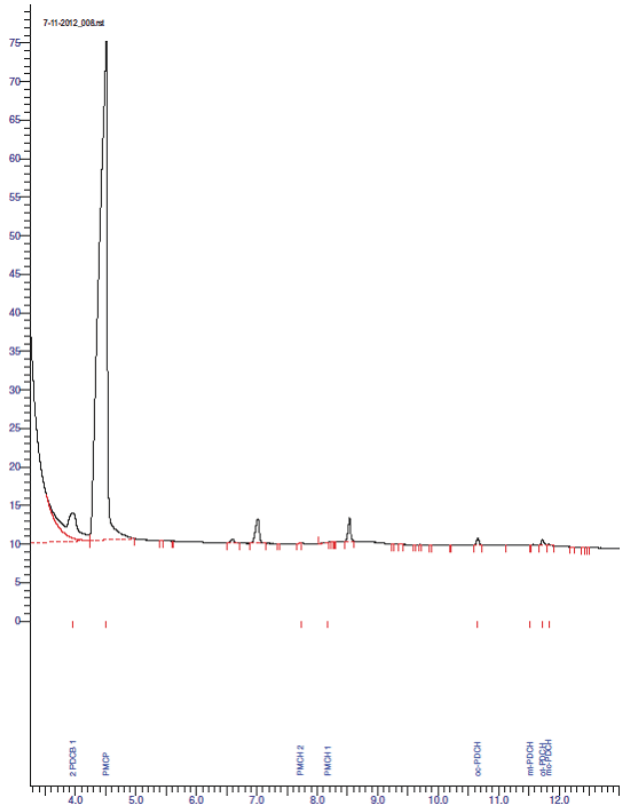

Figure 3. Chromatogram of intermediate standard PMCP using developed analytical method.

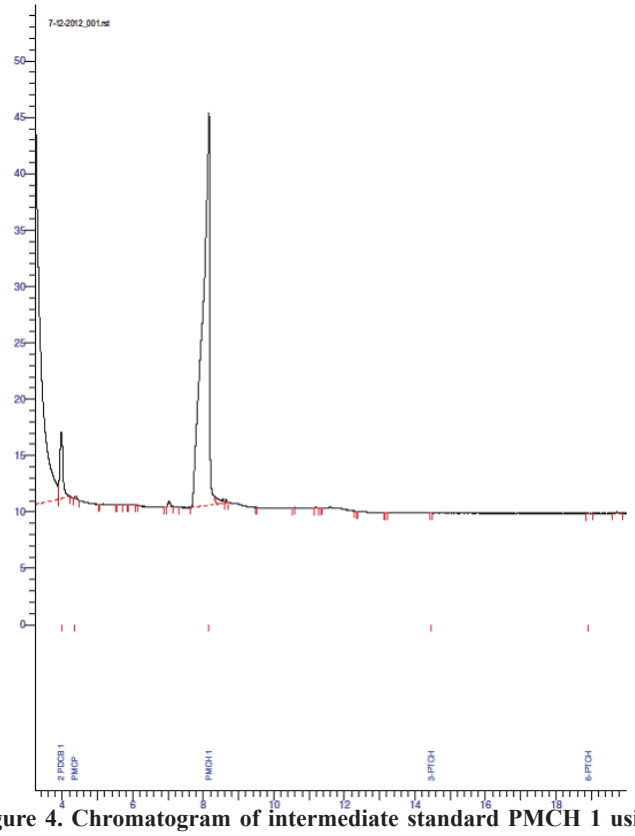

Figure 4. Chromatogram of intermediate standard PMCH 1 using developed analytical method.

Injection #	% Comp PMCH 1	% Comp PDCB 2	% Comp PMCP
1	92.34%	7.66%	0%
2	89.97%	9.41%	0.62%
3	90.29%	9.14%	0.57%
4	92.47%	7.28%	0.24%
5	92.43%	7.37%	0.20%

Table 9. Percent composition of PFT intermediate standard PMCH 1.

Mean (Major Peak Area)	Standard Deviation (Major Peak Area)	Relative Std Dev (Peak Area)	Standard Deviation of Mean	Error
$5.6x10^5$	$0.6x10^5$	10%	$0.3x10^5$	$0.03x10^5$

Table 10. Mean and standard deviation data for PMCH 1 intermediate standard.

Injection #	% Comp PMCH 2	% Comp PDCB 2
1	81.66%	18.34%
2	80.70%	19.30%
3	86.58%	13.42%
4	86.61%	13.39%
5	78.21%	21.79%

Table 11. Percent composition of PFT intermediate standard PMCH 2.

Mean (Major Peak Area)	Standard Deviation (Major Peak Area)	Relative Std Dev (Major Peak Area)	Standard Deviation of Mean	Error
0.98x105	$0.03x10^5$	3%	$0.01x10^5$	$0.02x10^5$

Table 12. Mean and standard deviation data for PMCH 2 intermediate standard.

Injection #	% Comp oc-PDCH	% Comp mt-PDCH	% Comp ot-PDCH	% Comp mc-PDCH	% Comp PMCH 2
1	41.90%	5.55%	38.88%	7.21%	6.46%
2	41.94%	5.70%	39.04%	6.91%	6.41%
3	41.95%	5.47%	38.85%	7.15%	6.58%
4	42.44%	5.41%	38.90%	6.89%	6.36%
5	41.75%	5.62%	38.76%	7.22%	6.65%

Table 13. Percent composition of PFT intermediate standard o-PDCH.

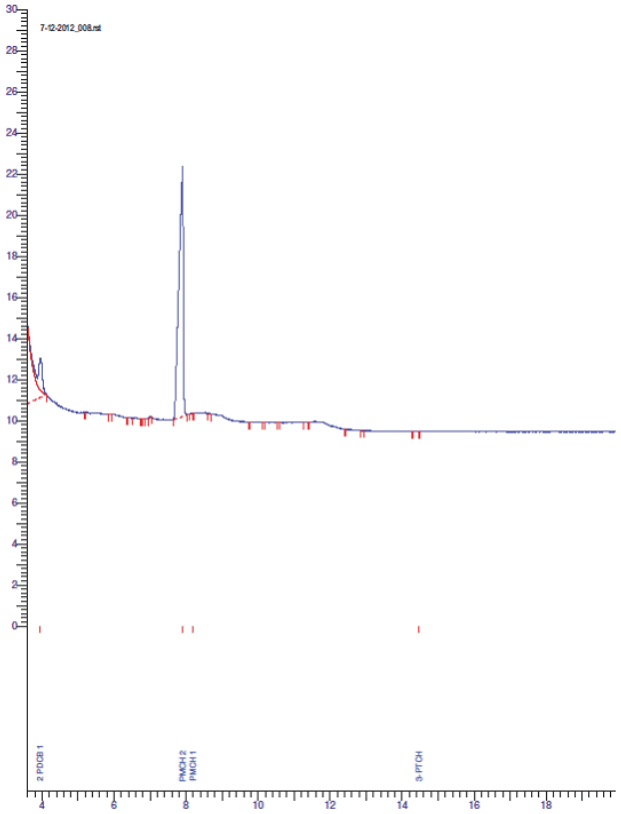

Figure 5. Chromatogram of intermediate standard PMCH 2 using developed analytical method.

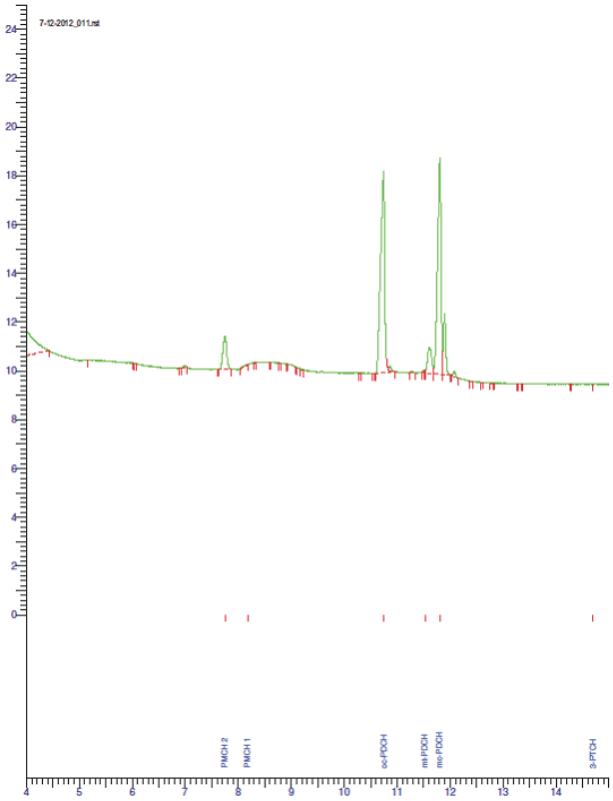

Figure 6. Chromatogram of intermediate standard o-PDCH using developed analytical method.

o-PDCH Isomer	Mean (Major Peak Area)	Standard Deviation (Major Peak Area)	Relative Std Dev (Major Peak Area)	Standard Deviation of Mean	Error
oc-PDCH	$0.4x10^5$	$0.02x10^5$	4.7%	$0.009x10^5$	$0.003x10^5$
mt-PDCH	$0.06x10^5$	$0.001x10^5$	2.3%	$6.0x10^1$	$0.003x10^5$
ot-PDCH	$0.4x10^5$	$0.02x10^5$	4.1%	$0.008x10^5$	$0.003x10^5$
mc-PDCH	$0.08x10^5$	$0.003x10^5$	4.1%	$0.001x10^5$	$0.003x10^5$

Table 14. Mean and standard deviation data for o-PDCH intermediate standard.

Injection #	% Comp iPPCH	% Comp mc-PDCH	% Comp ot-PDCH	% Comp mt-PDCH	% Comp PTCH 1	% Comp PTCH 6
1	89.25%	3.03%	1.77%	1.11%	0.37%	4.46%
2	89.41%	3.10%	1.80%	1.12%	0%	4.58%
3	89.52%	3.00%	1.79%	1.20%	0%	4.49%
4	89.66%	3.02%	1.79%	0.97%	0%	4.38%
5	89.36%	3.00%	1.77%	1.15%	0%	4.73%

Table 15. Percent composition of PFT intermediate standard iPPCH.

Mean (Major Peak Area)	Standard Deviation (Major Peak Area)	Relative Std Dev (Peak Area)	Standard Deviation of Mean	Error
$1.5x10^5$	$0.2x10^5$	12%	$0.8x10^5$	$0.008x10^5$

Table 16. Mean and standard deviation data for iPPCH intermediate standard.

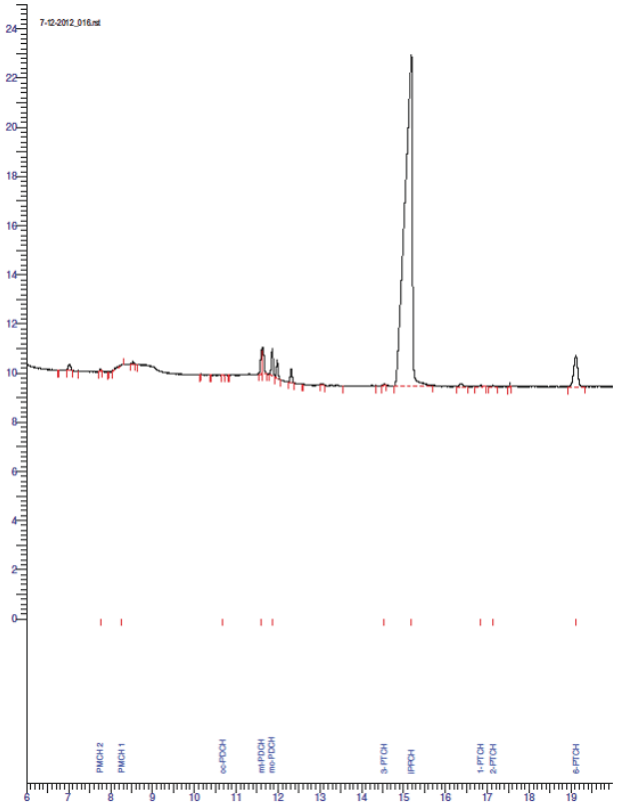

Figure 7. Chromatogram of intermediate standard iPPCH using developed analytical method.

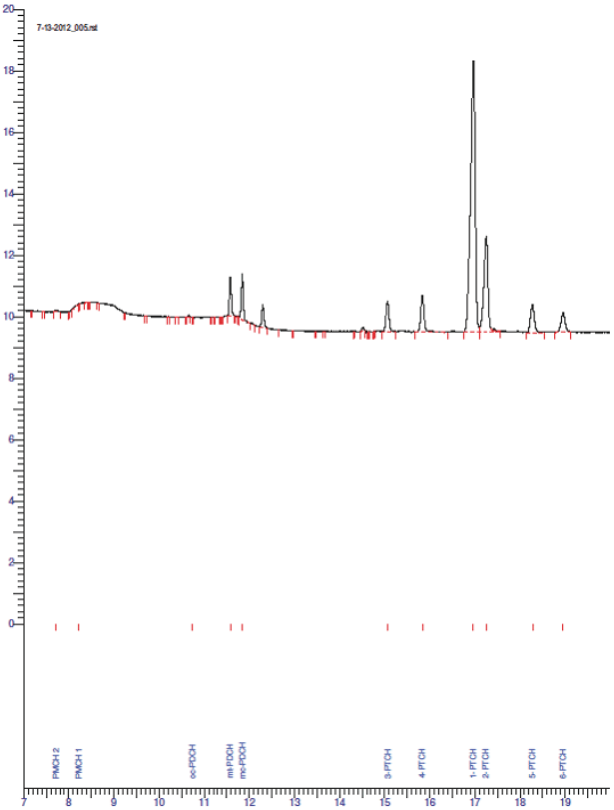

Figure 8. Chromatogram of intermediate standard PTCH using developed analytical method.

Injection #	Total Peak Area PTCH (µVs)	% Comp PTCH-1	% Comp PTCH-2	% Comp PTCH-3	% Comp PTCH-4	% Comp PTCH-5	% Comp PTCH-6	% Comp mt-PDCH	% Comp mc-PDCH
1	1.1x105	55.1%	18.6%	4.0%	5.0%	6.0%	3.7%	3.5%	4.0%
2	1.0x105	56.0%	17.6%	4.1%	5.9%	4.9%	3.6%	3.6%	4.2%
3	0.95x105	56.6%	17.2%	4.2%	5.3%	4.9%	3.9%	3.7%	4.3%
4	0.98x105	55.4%	19.1%	4.2%	5.1%	5.0%	3.8%	3.5%	4.0%
5	1.1x105	55.2%	19.2%	4.0%	5.5%	4.7%	3.9%	3.6%	3.9%

Table 17. Percent composition of PFT intermediate standard PTCH.

PTCH Isomer	Mean (Major Peak Area)	Standard Deviation (Major Peak Area)	Relative Std Dev (Major Peak Area)	Standard Deviation of Mean	Error
PTCH 1	$0.6x10^5$	$0.03x10^5$	5.2%	$0.01x10^5$	$0.004x10^5$
PTCH 2	$0.2x10^5$	$0.02x10^5$	9.5%	$0.009x10^5$	$0.004x10^5$
PTCH 3	$0.05x10^5$	$0.002x10^5$	3.8%	$0.0008x10^5$	$0.004x10^5$
PTCH 4	$0.06x10^5$	$0.006x10^5$	9.5%	$0.003x10^5$	$0.004x10^5$
PTCH 5	$0.06x10^5$	$0.007x10^5$	13.1%	$0.003x10^5$	$0.004x10^5$
PTCH 6	$0.04x10^5$	$0.003x10^5$	6.5%	$0.001x10^5$	$0.004x10^5$

Table 18. Mean and standard deviation data for PTCH intermediate standard.

Software development for integrated spectroscopy and X-ray diffraction experiments at the PXRR NSLS beamlines

Michael Skinner
School of Computer Science, Marist College, Poughkeepsie, NY 12601
Allen Orville
Biology Department, Brookhaven National Laboratory, Upton, NY 11973

ABSTRACT

Solving the structure of certain proteins is essential to understanding how biological systems work. Techniques such as x-ray crystallography and spectroscopy are often used to determine protein structure. These techniques are highly software-intensive involving advanced experimental equipment control and synchronization, while at the same time requiring user-friendly program interfaces. This paper describes three developments aimed at facilitating protein structure determination experiments at beamlines run by the Protein Crystallography Research Resource (PXRR) at Brookhaven National Laboratory's National Synchrotron Light Source (NSLS). First, at NSLS beamline X26C, Horiba JY's Raman Spectroscopy control program, LabSpec, has been integrated with the beamline control program CBASS. Second, an interface to the radiation damage assessment program RADDOSE has been integrated into the CBASS Graphical User Interface. Finally, the PXRR Crystal Centering software has been modified to employ Websockets instead of Ajax for monitoring EPICS database parameters.

I. INTRODUCTION

Scientists can often learn how something works by understanding its structure. At the molecular level, this means how atoms are arranged and how they are held together. Solving the structure of certain proteins is essential to understanding how biological systems work. Scientists accomplish this by performing experiments on protein crystals.

The Protein Crystallography Research Resource (PXRR) operates five beam lines at Brookhaven National Laboratory's (BNL) National Synchrotron Light Source (NSLS). These beam lines are dedicated to solving protein structures with X-ray Crystallography. In addition, Beam line X26C of the PXRR combines spectroscopy and x-ray crystallography to further understand protein structure.

Beam line control and data acquisition at these beam lines are challenged by the need to integrate and synchronize complex experimental equipment. The purpose of my internship was to aid in the software development efforts for the PXRR beam lines.

II. Background and Objectives

A. X-ray Crystallography and Raman Spectroscopy Control Integration

X-ray crystallography is a method of determining the arrangement of atoms within a crystal by hitting the crystal with an x-ray beam and then analyzing the diffracted beam. From the angles and intensities of these diffracted beams, software that implements a Fourier Transform can produce a three-dimensional picture of the electron density within the crystal. From this electron density, the positions of the atoms in the crystal can be determined, and the nature of the bonds that hold the atoms together can be understood.

The software that handles data collection and beam line control for the PXRR, called CBASS, is a Python-based system that synchronizes the control of all components of the beam line and experiment. CBASS is integrated with PXDB, which is an experiment tracking and user group management relational database system.[1]

Raman spectroscopy is a spectroscopic technique used to study vibrational, rotational, and other low-frequency modes in a system. It relies on the inelastic scattering, or Raman scattering, of monochromatic light, usually from a laser in the visible, near infrared, or near ultraviolet range. The laser light interacts with molecular vibrations, phonons, or other excitations in the system, resulting in the energy of the laser photons being shifted up or down. The shift in energy gives information about the bonds between atoms. Infrared spectroscopy yields similar, but complementary, information.[2]

The software that controls beam line X26C's Raman experimental setup including lasers and spectrometer is called LabSpec. It is supplied by Horiba JY, the vendor of the Raman control apparatus. One of my goals was to integrate Raman control into CBASS in order to synchronize operation of CBASS-controlled hardware with equipment under LabSpec's control.

B. RADDOSE and CBASS Integration

RADDOSE is a program that calculates the total and terminal radiation dosage applied to a crystal by an x-ray beam over the course of an experiment, as well as the degradation of a crystal relative to those figures.4 This information allows scientists to tailor their experimentation to what the crystal can handle, and reduce time wasted gathering data from crystals which have been taxed past their limits. RADDOSE takes in a list of crystal and experimentation parameters to perform its calculations, and then outputs relevant data to an output file. During my 2011 BNL High School Research Program (HSRP) Internship, I wrote a Graphical User Interface (GUI) to RADDOSE for the specific purpose of facilitating RADDOSE usage in correlated X-ray Diffraction and Absorption Spectroscopy experiments at beamline X26C. This GUI was written in Java in a Netbeans IDE and GUI builder. This interface was able to pass and receive data to and from RADDOSE using CGI scripts. Understanding radiation damage is important to all Protein Crystallography experiments, so it would be advantageous to add a RADDOSE GUI to the CBASS GUI. This was another objective of my internship.

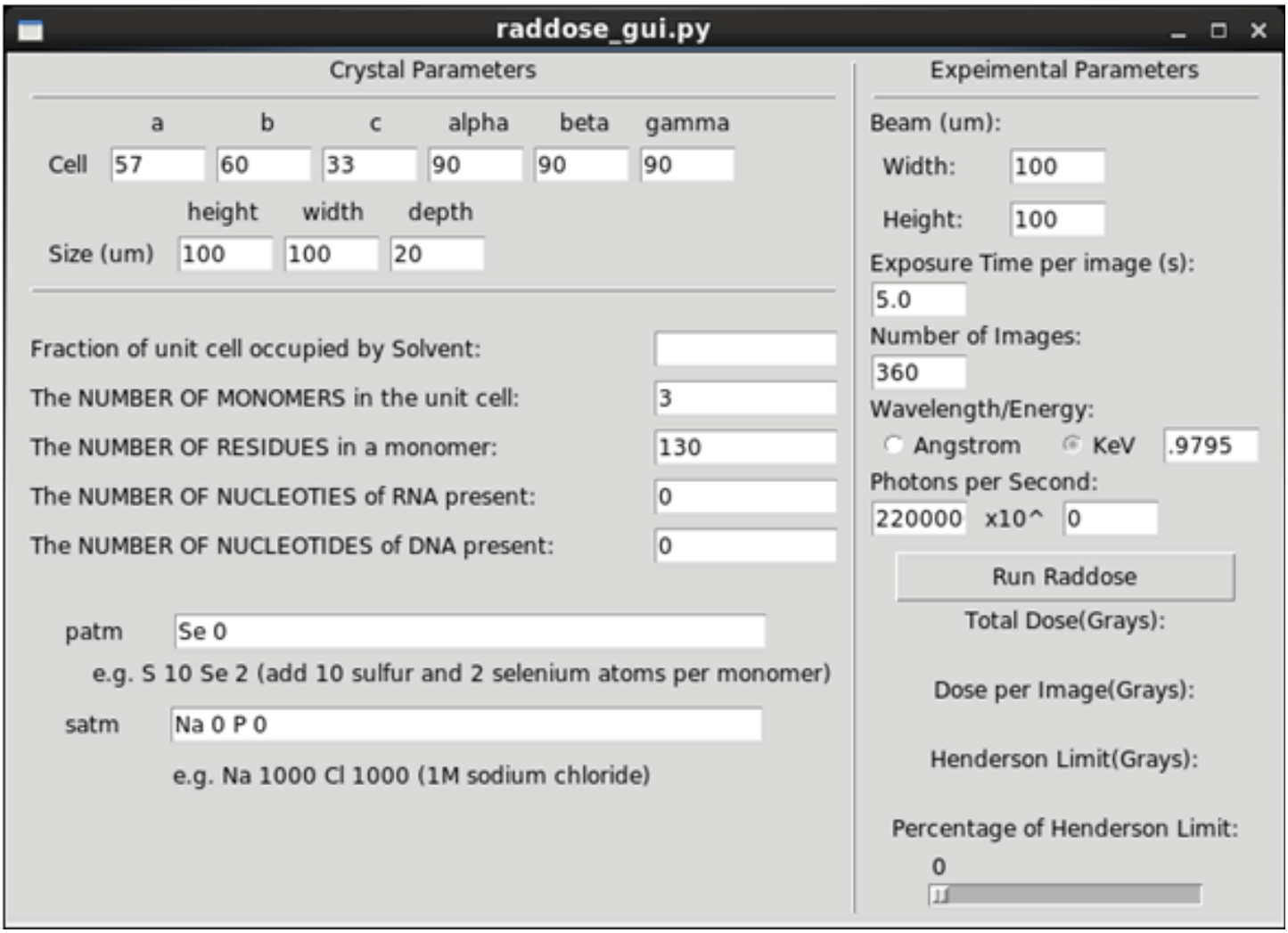

Figure 1. GUI for RADDOSE with several default values filled in. [3]

C. Click-to-Center Websocket Conversion

The PXRR crystal centering web page features a live video stream display of the crystal and provides users with the ability to control the location and orientation of their crystal relative to the beam. My third objective was to reconstruct the method it used to retrieve the beam size and region of interest parameters from an EPICS database and display them to the user. The central square (red) illustrates the dimensions of the beam and the outer square (green) illustrates the region of interest. Prior to my engagement with the program, these values were gathered using AJAX, a client-side system (meaning that its operation originates from the web browser) which must constantly and periodically poll the EPICS server through a CGI program to see if any changes have occurred in the size of the beam or its encompassing region of interest. This constant battery of queries heavily taxes both the client and the server. My goal was to replace AJAX with a new protocol called Websockets which allows the client to establish a persistent 2-way communication channel with a websocket server. This new paradigm of web-communication systems would place less strain on both the client and the server and provide a persistent, stable method of communication between them.

III. METHODS

A. CBASS/LabSpec Integration

LabSpec controls Raman Spectroscopy and provides the interface for both its inputs and outputs. The only way to interact with LabSpec at beam line X26C has been through the LabSpec GUI. However, LabSpec provides additional methods of interfacing, one of which is a command file input system. LabSpec monitors a predetermined folder, awaiting a Visual Basic script file of a specific name to be placed in it. Upon reception, the file is read, processed, and deleted. The instructions encoded in that file can call the majority of LabSpec's functions and was the method of choice for remotely controlling LabSpec's Raman-based operations.

The majority of the PXRR beam line control is built into CBASS. In order to integrate LabSpec's Raman Spectroscopy control into CBASS, the CBASS program must be able to call LabSpec functions. While it was impossible for CBASS to directly affect LabSpec through its GUI, CBASS could write and read files for use with LabSpec's command-file based input system. Though, perhaps outdated, it is far from uncommon for one program to interface with another through input and output files; however, a slight barrier between these two is that while LabSpec runs on a Windows computer, CBASS operates on a Linux based system. This could be overcome by using Samba and Network File System (NFS).

As this was the first attempt of interacting with the beam line X26C LabSpec installation with an external program, bugs and unexpected behavior needed to be worked through. This troubleshooting and debugging required weeks of collaboration with LabSpec's creators to fully solve.

It was important that CBASS wait for the completion of the LabSpec functions it called. This was solved by creating a flag file in the Visual Basic script, and then polling for that file in CBASS. Once the Visual Basic script composed by CBASS is executed, LabSpec writes files with the results of its data acquisition in accordance with the parameters defined in the Visual Basic script. From the time CBASS sends its command file to the time LabSpec produces its output file, CBASS must wait until the final operation of LabSpec's command file is performed, which produces the flag file signifying LabSpec's completion. The existence of the flag file proves to CBASS that it is free to continue its operation in handling LabSpec's output or that it is safe to give LabSpec further commands.

B. CBASS/RADDOSE Integration

The integration of RADDOSE's functionality into the CBASS program required that the interfacing methods be constructed in the same language as CBASS, Python. The previous GUI for the RADDOSE program was written in the Java programming language using the GUI builder feature of the Netbeans IDE. This made creating the interface simple and effective, and allowed it to be re-customized equally so, assuming that was also done using the Netbeans IDE. In the absence of a simple visual builder, the most effective way to construct a graphical system using Python relies on a series of stacked frames which function within the Tkinter library. These frames define the sizes and arrangements of the user interface components inside of them, and placement control can be further refined by placing frames within other frames. The boundaries of frames can morph their positions and dimensions with the frames they are placed in, and the frames that are placed in them, making them extremely flexible building units. Framing, coupled with Tkinter's other modular interface components, makes controlling the functionality and layout of the interface simple and flexible.

C. Crystal Centering Websocket Conversion

The AJAX system previously responsible for the handling of the click-to-center visual display of the beam and region of interest information worked primarily by a constant and persistent polling of the EPICS database. It queried every second to see if something was new, and most seconds it found nothing. This resulted in a large amount of unnecessary messaging by the client to the server. The new websocket system of updating client information is entirely event-driven, meaning that the program would function only when it is necessary. This entailed rewriting the server code to handle websocket connections and event occurrences rather than constantly responding to a polling query. The client code, the HTML and Javascript that implements the web page, needed to create and maintain websocket connections and be prepared to react to the event occurrences.

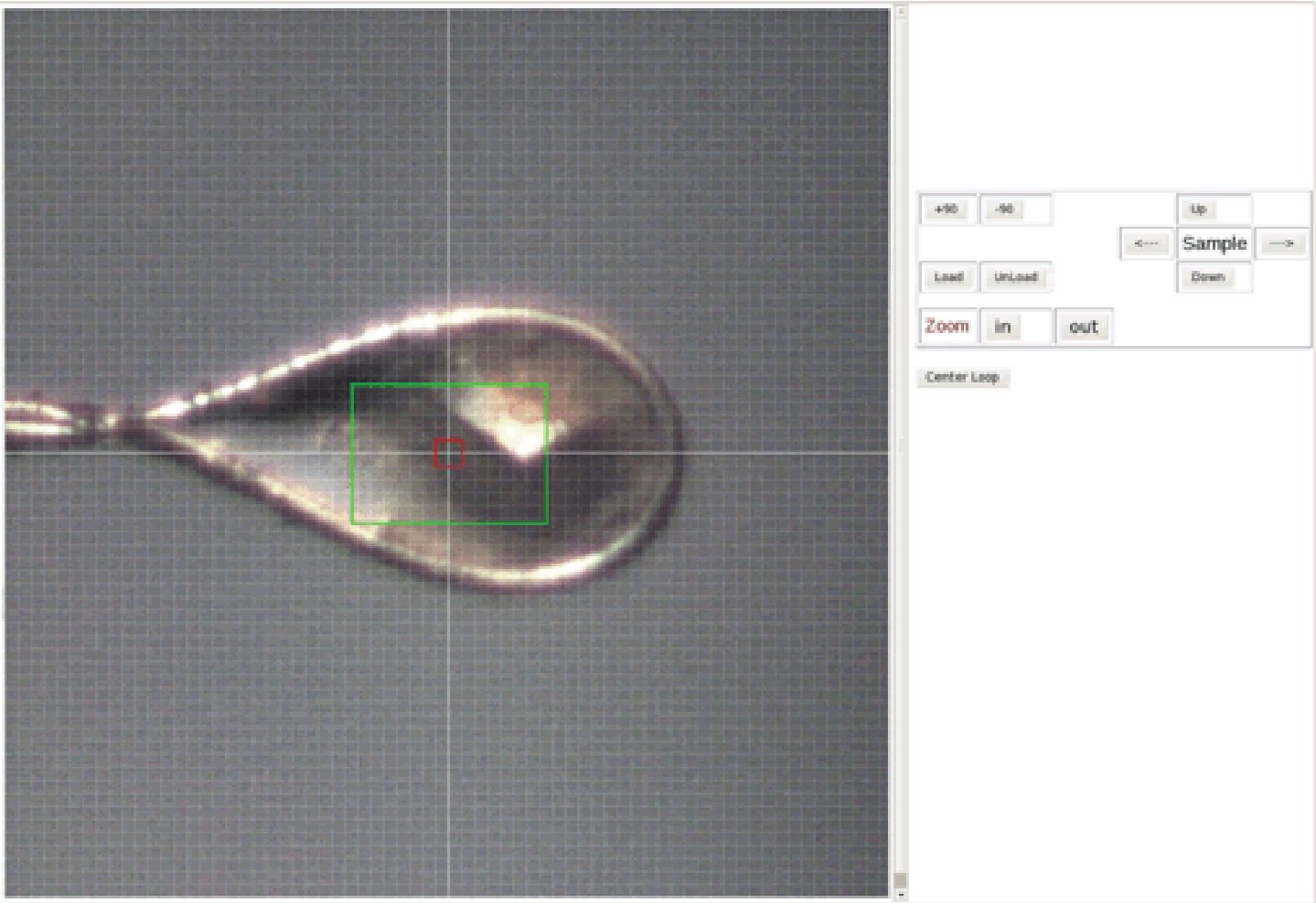

Figure 2. Remote control system for crystal positioning. 3

IV. RESULTS

A. CBASS/LabSpec Integration

The necessary functionality of Horiba JY's LabSpec program is now a built-in feature of the CBASS program and lends its operation to making the performance of Raman-based spectroscopy experiments a more elegant process within the new system. This will provide the ability to control experiments in a way not possible before the integration. One example is the possibility of doing "vector" scans of crystals with Raman spectroscopy. This will integrate and synchronize the control of the sample positioning motors under CBASS control with the RAMAN experimental equipment under LabSpec control.

B. CBASS/RADDOSE Integration

This new RADDOSE interface will have access to CBASS data collection parameters and allow users to enter information about their samples so that they may quickly calculate radiation dose to their samples caused by proposed experiments. The end result of running RADDOSE before data collection will result in data collection strategies that allow users to obtain their desired data before the crystal is destroyed by radiation damage.

C. Crystal Centering Websocket Conversion

The new display system for the click-to-center program significantly reduces the strain its operation places on the webserver, which previously flooded log files with messages regarding the AJAX polling. This server now monitors, rather than polls, the size of the beam via EPICS and sends updated beam size dimensions to the web browser only when those dimensions change.

V. CONCLUSION

In many programming environments, the designers of software are detached from its users. However, the unique environment of the PXRR allows the software designers to work closely with their end-users to ensure that the software produced is able to effectively meet the wants and needs of beam line scientists and users.

VI. ACKNOWLEDGEMENTS

I'd like to thank Brookhaven National Laboratory's Student Undergraduate Research Program (SURP) and the Protein Crystallography Research Resource (PXRR) for hosting me. I'd especially like to thank my mentor, Dr. Allen Orville.

VII. REFERENCES

[1]J. Skinner, M. Cowan, R. Buono, W. Nolan, H. Bosshard, H. Robinson, A. Heroux, A. Soares, D. Schneider, R. Sweet, Acta Cryst D26, 1340 (2006).

[2]Wikipedia, http://en.wikipedia.org/wiki/Raman_spectroscopy

[3]Figures 1, 2 – Michael Skinner

[4]K. Paithankar, R. Owen. E. Garman, Journal of Synchrotron Radiation. 16, 152 (2009).

In silico knockout analysis of developing *Brassica napus* embryos for the overproduction of α-tocopherol

Griffin St. Clair
Biomedical Engineering Department, State University of New York at Stony Brook, Stony Brook, New York 11794
Jordan O. Hay and Jörg Schwender
Biology Department, Brookhaven National Laboratory, Upton, NY 11973

Abstract

Metabolic engineering is useful across a variety of applications, including agriculture, pharmacy, and basic science. The development of metabolic network modeling software has been of great use in making predictions and analyses with regard to metabolic engineering. We sought to model ways to increase the vitamin E (α-tocopherol) content in the oil of the developing *Brassica napus* seed. B. napus, otherwise known as oilseed rape or rapeseed, was a viable target for our purposes because its developing seeds are rich in oil and a network for the core metabolism in a developing *B. napus* embryo has already been established. α-tocopherol is vital to human health and is also an energy-rich lipid, serving as an ideal model compound for the alternative fuels industry as well as agriculture and pharmacy. We used computational methods to obtain an optimal set of metabolic reactions, such that when these were knocked out, α-tocopherol production in the developing embryo was maximized.

I. Introduction

Much of biotechnology today relies upon the ability to accurately predict how changes in a biological system's workings will impact the function of that system. In metabolic engineering, this is especially important since understanding the structure and dynamics of a metabolic network is key to understanding how to manipulate that network. Metabolic network modeling software has proven extremely useful in understanding and analyzing metabolic networks on a quantitative level. One such software package is called the Constraint-Based Reconstruction and Analysis Toolbox (COBRA).[1] Using COBRA in conjunction with MATLAB, we can simulate the fluxes through different reactions in a metabolic network under given input or output conditions, such as nutrient uptake into the system, or the outflux of biomass or a desired compound. The OptKnock[2] function of the COBRA Toolbox can be used to determine which set of reactions can be constrained to zero flux, simulating inhibition of the metabolic pathway though genetic means or otherwise in order to maximize the production of a target metabolite. This can provide metabolic engineers with valuable information about where to begin searching for possible genes to knock out or inhibit.

We sought to predict how vitamin E (α-tocopherol) production could be maximized in developing seeds of *Brassica napus*, commonly known as oilseed rape or rapeseed. Developing *B. napus* seeds are rich in oil (Figure 1) and *B. napus* is closely related to the extensively studied model plant *Arabidopsis thaliana*.[3,4] Furthermore, a compartmented metabolic network model for the core metabolism of developing *B. napus* embryos (bna572) was already in existence.[5] These features made B. napus an ideal candidate for our studies. α-tocopherol plays an important role in human health[6] and is an energy-rich lipid, the likes of which also have potential biofuels applications.[7] We used OptKnock to determine the set of reactions that, when knocked-out, would produce the greatest yield of α-tocopherol, while setting reasonable lower bounds on the growth rate so as to make the model realistic in physiologic terms. We predicted that we would be able to find a numerical solution for the reaction rates in the network that would display increased α-tocopherol production.

II. Materials and Methods

A computer with 32-bit Windows 7 was installed with Microsoft Excel 2010 and MATLAB 7.1.1.0 (R2010b). COBRA 2.0.4 and TOMLAB 7.8 were also installed. An existing model of B. napus, bna572,[5] was modified to a COBRA-compliant format and stored and made freely available in both .xls and SBML formats. The pathways required for vitamin E synthesis, documented in the *A. thaliana* literature,[3,4] were added to bna572, to produce bna572+ve. bna572 contained 572 reactions and 579 metabolites, which increased to 604 reactions and 606 metabolites in bna572+ve. In becoming a COBRA-compliant model, bna572+ve was converted to a linear programming problem of the form elucidated in Equation 1. In MATLAB, the COBRA solver was set to tomlab_cplex. The growth rate was constrained to the documented rate5 of 0.0725 mg h-1. The biomass synthesis (growth) reaction was modified to include α-tocopherol as a biomass component, replacing a fraction of the biomass-bound oil according to the average mass fraction for three *B. napus* cultivars.[8]

Equation 1.

$$\text{maximize } c^T x$$
$$\text{subject to } A x = b$$
$$lb \leq x \leq ub$$

Linear program formulation.This is the form taken by bna572+ve. In our case, cTx was the biomass exchange flux, A was a stoichiometric matrix representing the stoichimetric coefficients of each metabolite in each reaction. x was the optimal flux solution, b is a zero vector for mass balance constraints, and lb and ub were lower and upper bounds imposed on the model, so that the input and output fluxes could be fixed to desired values and unidirectional.

OptKnock problems were formulated according to the following scheme: maximize the α-tocopherol exchange rate in the aforementioned linear programs through a specified number of reaction knockouts, subject to fixed light and nutrient uptakes and to flux bounds based on the thermodynamic directionality associated with the reactions in the model. Using this formulation, twenty-four separate OptKnock problems were formulated according to the following distinctions: the number of reactions to

Source: www.floralimages.co.uk/images2/brassica_napus_1fc5.jpg

Source: http://www.bridgat.com/files/rapeseed_Oil_refined_rapeseed_oil.jpg

Source: http://www.sciencephoto.com/image/6963/530wm/A6140005-Vitamin_E_molecule-SPL.jpg

Figure 1. *Brassica napus* and its derivatives. A stalk of *Brassica napus* (a) is shown, displaying yellow flowers, each of which will eventually bear a silique (b). Developing seeds from this fruit contain oil, which can be processed and refined for a variety of applications (c). This oil naturally contains the compound α-tocopherol (d), more commonly known as vitamin E.

simultaneously knock out using OptKnock (1-6), a light condition (photoheterotrophic or heterotrophic), and a minimum growth rate (0.05 or 0.02 mg h-1). Input fluxes such as light and nutrients were constrained according to light condition and values obtained from flux balance analysis of the wild type bna572+ve model.

To save computational time, only reactions that were not knockout-lethal and those that weren't already blocked due to the input flux constraints were considered as possible knockout candidates (Figures 2 and 3).

This process, in addition to the non-consideration of reactions whose knockout would not have made physiological or practical sense, such as maintenance ATP drain or transmembrane carbon dioxide flux, significantly reduced the number of reactions to consider in OptKnock to 152, 25.2% of the 604 total reactions in bna572+ve. To obtain a list of knockout-lethal reactions, a single knockout of every reaction was made in succession, by setting its lower and upper bounds to 0 μmol h-1. Next, the COBRA function OptimizeCbModel was called to perform flux balance analysis on each of these modified models. Those reactions whose knockout caused the flux balance analysis algorithm to have no solution were noted as knockout-lethal. This lethality analysis assigned a lethality score to each reaction in the model, calculated as the percent deviation in biomass synthesis after the single knockout of that reaction. To obtain a list of blocked reactions, the COBRA function fluxVariability was called to perform flux variability analysis on the model after setting the input constraints. Those reactions whose minimum and maximum fluxes were both 0 μmol h-1 were considered blocked.

Each of the 24 problems formulated was solved using OptKnock, and the optimal knockout target reactions and flux distributions were recorded.

III. Results

Flux balance analysis and flux variability analysis confirmed that the new pathways for α-tocopherol synthesis in bna572+ve (Figure 4) were functional and capable of carrying flux under a variety of constraints in terms of nutrient influxes, light conditions, and growth rate lower bounds. The MEP isoprenoid precursor pathway was found to be essential for α- tocopherol synthesis and growth.

The OptKnock function returned valid solutions for all 24 problems formulated. Growth rate generally dropped in order to approach its lower bound. The maximum α-tocopherol synthesis rate, 0.0167 mg h-1, occurred under photoheterotrophic conditions with a growth rate lower bound of 0.02 mg h-1 (Table 1). The growth rate in this case was surprisingly higher than its lower bound, arriving at a value of 0.0386 mg h-1. The reactions that were knocked out in this case were cytosolic adenylate phosphorylation (adenlyate kinase), pyruvate transport from cytosol to mitochondria, and plastidial acetyl-transferring pyruvate dehydrogenase. The dry weight fraction of α-tocopherol in the embryo increased from to 9.70x10-3% to 30.2%. The carbon conversion efficiency of the embryo decreased from 85.2% in the wild type to 78.3%.

IV. Discussion and Conclusion

The results shown in Table 1 indicate that by knocking out particular reactions in bna572+ve, production of excess α-tocopherol was achieved while keeping the biomass exchange rate, or growth rate, above zero. OptKnock provided a list of reactions to knock out of the bna572+ve model in order to achieve these α-tocopherol synthesis rates, confirming our hypothesis. We obtained valid solutions for all twenty-four problems formulated under both photoheterotrophic and heterotrophic simulation constraints, giving credence to the efficacy of computational metabolic engi-

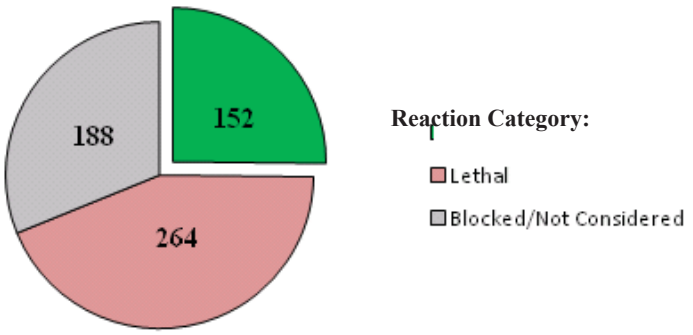

Figure 2. Reaction categories. Shown are the numbers of reactions that were either considered in OptKnock, knockout- lethal, or blocked or otherwise not considered because their removal would not have made sense physiologically.

neering methods. The fact that α-tocopherol production was able to be simulated under a variety of conditions provides support for similar studies in the future that relate to the production of compounds for use in pharmacy, agriculture, and the biofuels industry. However, there may be difficulties in knocking out some of the reactions nominated by OptKnock: some reactions may be governed by multiple genes, and some genes may govern multiple reactions. Additionally, the mesopolyploidy of *B. napus* may present further difficulties, as reactions may need to be knocked out in all three genomes in order to have the desired effect. Nevertheless, these results provide a useful starting point in attempting to optimize *B. napus* for α-tocopherol production and can save considerable time in the planning and testing phases of the genetic engineering process. These in silico knockout analysis methods can be applied to a wide variety of metabolic engineering problems and appear to have vast potential.

V. Acknowledgements

I thank my mentor Dr. Jordan O. Hay for his patience, generosity, and guidance, and for working together with me on this project. I thank Dr. Jörg Schwender for his gracious oversight and guidance. I thank Dr. Shinjae Yoo for his gracious assistance with the computational aspects of this project. I thank Dr. Inga Hebbelmann for her gracious assistance with photography. I thank Dr. Creighton Wirick for his motivation and support. I thank Dr. Wei Lin, Mr. Ruofeng Wen, and Dr. Mikhail Mazin for their support during the SULI program application process. I thank the Office of Educational Programs for its efforts and for allowing me to research this project.

VI. References

[1]Schellenberger J, Que R, Fleming RM, Thiele I, Orth JD, Feist AM, Zielinski DC, Bordbar A, Lewis NE, Rahmanian S, Kang J, Hyduke DR, Palsson BO (2011) Quantitative prediction of cellular metabolism with constraint-based models: the COBRA Toolbox v2.0. Nat Protoc 6: 1290-1307

[2]Burgard AP, Pharkya P, Maranas CD (2003) OptKnock: a bilevel programming framework for identifying gene knockout strategies for microbial strain optimization. Biotechnol Bioeng 84: 647-657

[3]Mueller LA, Zhang P, Rhee SY (2003) AraCyc: a biochemical pathway database for *Arabidopsis*. Plant Physiology 132: 453-460

[4]Mintz-Oron S, Meir S, Malitsky S, Ruppin E, Aharoni A, Shlomi T (2012) Reconstruction of Arabidopsis metabolic network models accounting for subcellular compartmentalization and tissue- specificity. Proc Natl Acad Sci U S A 109: 339-344

[5]Hay J, Schwender J (2011) Metabolic network reconstruction and flux variability analysis of storage synthesis in developing oilseed rape (*Brassica napus L.*) embryos. Plant J 67: 526-541

[6]Hunter SC, Cahoon EB (2007) Enhancing vitamin E in oilseeds: unraveling tocopherol and tocotrienol biosynthesis. Lipids 42: 97-108

[7]Metzger P, Largeau C (2005) *Botryococcus braunii*: a rich source for hydrocarbons and related ether lipids. Appl Microbiol Biotechnol 66: 486-496

[8]Goffman FD, Möllers C (2000) Changes in tocopherol and plastochromanol-8 contents in seeds and oil of oilseed rape (Brassica napusL.) during storage as influenced by temperature and air oxygen. J Agric Food Chem 48: 1605-1609

Developing an inventory web application for network switches

Isaac Stein
Computer Technology, Tallahassee Community College, Tallahassee, FL 32304
Nicholas Franco
C-ADCES Group, Brookhaven National Laboratory, Upton NY 11973

I. Introduction

Previously, the inventory of the network switches was monitored with Excel spreadsheets that were very difficult and time consuming to keep up to date and accurate. Bill Eisele has successfully created other web applications with PERL in a UNIX environment to help monitor other network systems. Because of their effectiveness, it was clear that there should be similar applications to monitor other systems on the Web. Nicholas Franco and Bill Eisele decided that the inventory of the network switches would be the next project to work on.

II. Impact on BNL

Network Switches cost thousands of dollars; and so, if any of them goes unaccounted for that could be a loss of a substantial amount of money. A Web application designed for inventory control of these network switches is a cost-effective and efficient way to solve the potentially expensive problem of keeping track of inventory with spreadsheets. With the man hours saved on maintaining the inventory, employees can work on other projects.

III. What I did

I first designed Web forms according to the specifications given to me by Bill Eisele. I then researched PERL code and wrote the web forms in CGI. I then researched UNIX commands and compiled the CGI forms in UNIX until there were no errors. Bill Eisele then debugged the CGI forms in UNIX until they worked with the database. I gained more understanding of debugging in UNIX by watching Bill Eisele.(See Appendix 2.)

IV. DOE Mission

The Web application for inventory control of the network switches is aligned with the Department of Energy's mission by providing operational excellence and helps to ensure America's security and prosperity by addressing technological solutions that help make a more efficient system to manage energy and operational challenges through a Web application that can monitor and maintain the Network Switch inventory.

V. Outcome

The Web application for inventory control of the network switches is finished and working well. After two months of research, testing, and trial and error, we finally ended up with a Web application that can do the important job of monitoring hundreds of network switches in the Collider Accelerator Department. (See Appendix 1.)

VI. Future Work

As with most programs with databases, continued maintenance and updates will be needed. All of the current inventory will need to be entered into the database. And any changes like the state and location of a switch will need to be updated. Validation of the input could also be very important. (See Appendix 3.)

VII. Acknowledgements

I would like to acknowledge the entire C-ADCES Group for everyone's support.

I would like to especially thank Nicholas Franco for leading this project, choosing me to assist and instructing me on the various network systems; and Bill Eisele for providing the design specifications, building the MySQL database, debugging, and technical instruction.

VIII. Appendices

Appendix 1:

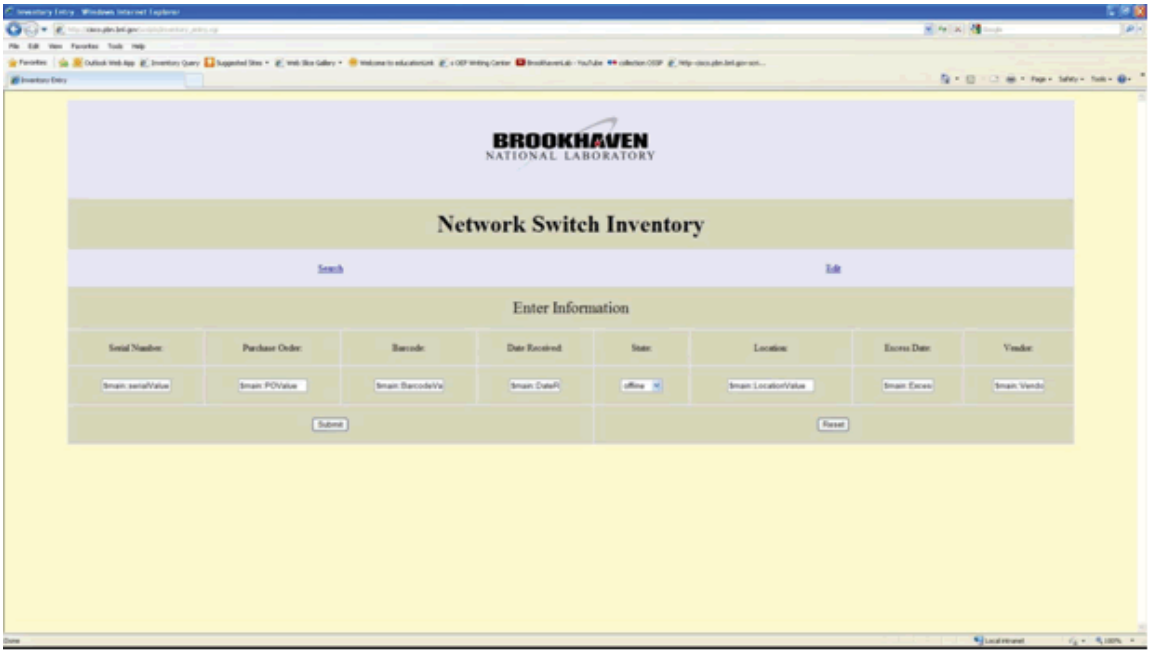

Appendix2:

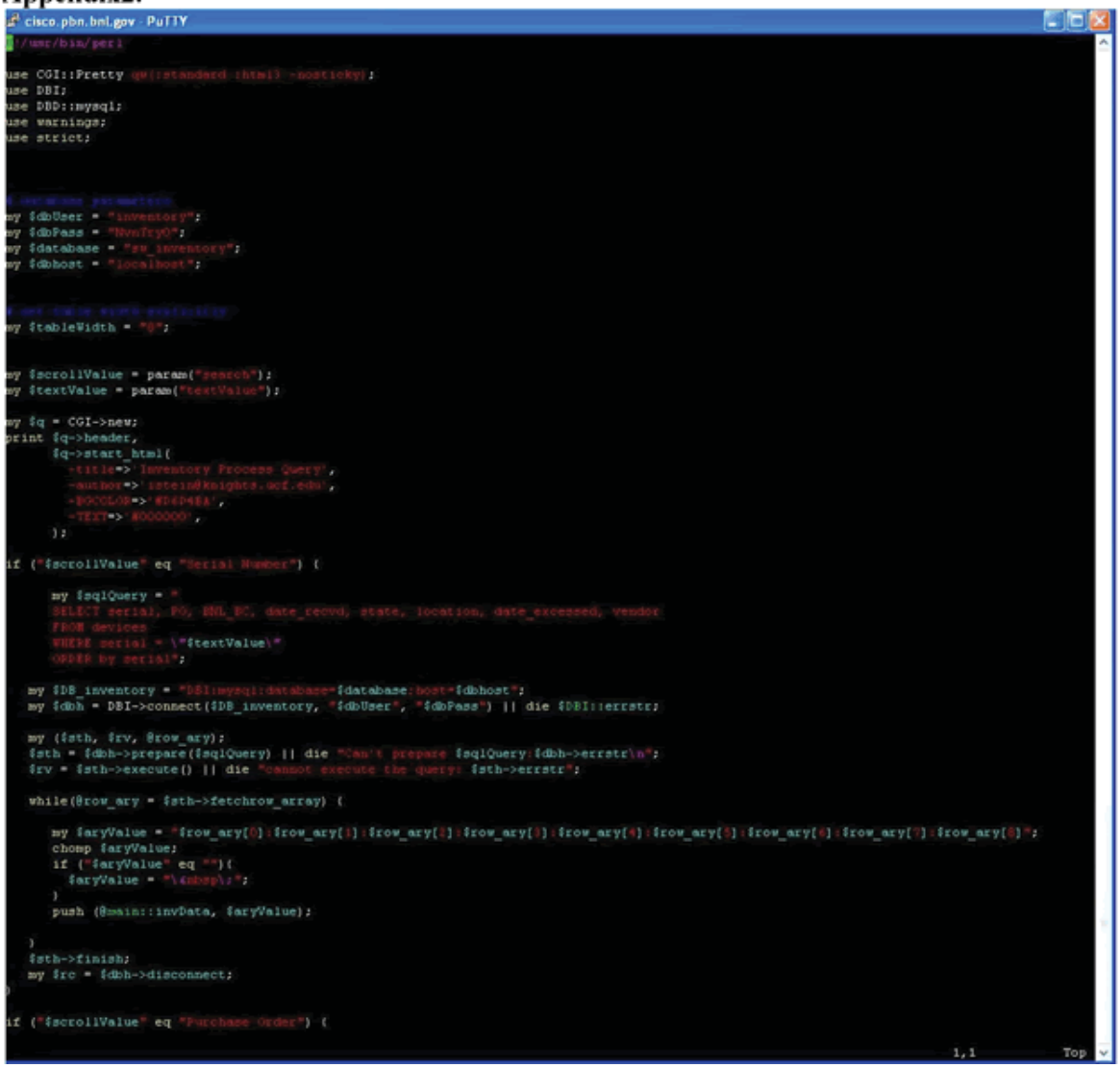

Appendix 3:

Crimson Editor - [C:\Documents and Settings\istein\My Documents\Books\inventory_query.cgi]

File Edit Search View Document Project Tools Macros Window Help

inventory_query.cgi

```
#!/usr/bin/perl

use CGI::Pretty qw(:standard :html3);
use warnings;
use strict;
use DBI;
use DBD::mysql;

# database parameters
my $dbUser = "harmless";
my $dbPass = "caduceus";
my $database = "sw_inventory";
my $dbhost = "localhost";

my $page;

$page = new CGI();

my $q = CGI->new;
print $q->header,
      $q->start_html(
        -title=>'Inventory Query',
        -author=>'istein@knights.ucf.edu',
        -BGCOLOR=>'#FFFFCC',
        -TEXT=>'#000000',
);

      print $q->start_table((-cellpadding=>'20',-style=>'background-color: #E6E6FA',
      -border=>'0',-align=>'center',-width=>'90%')),"\n";

    print Tr(
          $q->td(((-colspan=>'3',-align=>'center')),[$q->img((-src=>'http://cisco.pbn.bnl.gov/images/BNLsmaller.png',-alt=>'BNL Logo'))]),
);

    print Tr(
          th((-style =>'font-size: 30pt',-align=>'center', style =>'background-color: #D6D4BA',-colspan=>'2'),'Network Switch Inventory'),
);

          print Tr((-align=>'center'),
            $q->td(a((-href=>'http://cisco.pbn.bnl.gov/scripts/inventory_entry.cgi'),'Entry')),
            $q->td(a((-href=>'http://cisco.pbn.bnl.gov/scripts/inventory_edit.cgi'),'Edit')),
);

    print Tr(
      $q->td((-style =>'font-size: 20pt',-colspan=>'2',-align=>'center', style =>'background-color: #D6D4BA'), 'Search by Field'),
);

print $q->start_form(
      -action    =>"/scripts/inventory_process_query.cgi",
      -method    =>"GET",
      -encoding  =>"multipart/form-data",
);

   print Tr(
      $q->td((-colspan=>'3',-align=>'center', style =>'background-color: #D6D4BA'), ($q->scrolling_list(
      -name=>"search",
      -values=>['Serial Number','Purchase Order','Barcode','Date Received','State','Location','Excess Date','Vendor'],
      -size=>"1",
```

Ready Ln 1, Ch 1 68 ASCII, DOS READ REC COL V

Does cocaine use affect the epigenetic state of DNA? A study of brain candidate genes

Taylor Stiegler
Boston College, Chestnut Hill, MA 02467
Elena Shumay
Brookhaven National Laboratory, Upton, NY 11973

Abstract

The methylation status of a gene promoter is biologically important because it modulates an expression of the respective gene. In this study we analyzed promoter-associated CpG islands of the dopamine receptor D4 (DRD4), the serotonin transporter (SERT), and the monoamine oxidase A (MAOA). The proteins encoded by these genes, which underlie critical brain functions, regulate behavior and emotions. Aiming to reveal potential difference in methylation between healthy controls (HC) and cocaine abusers (CA), we analyzed primary genomic samples obtained from 124 individuals (African-American males). We hypothesized that the methylation of these three genes may be affected by individual environments (i. e., exposure to the drug of abuse), resulting in the differences in degree of methylation and the methylation pattern between HC and CA. We found that methylation in the promoter region of two genes, DRD4 and MAOA, increased with age. We also found that the DRD4 methylation was significantly greater in CA than in HC. In contrast, we detected no difference in methylation of the MAOA promoter between those groups, suggesting that cocaine exposure affects epigenetic marks in a locus- and site-specific manner.

I. Introduction

Cocaine dependence is a devastating disorder with no FDA approved pharmacological treatments available. Genetic studies estimate that 65-78% of the vulnerability for cocaine dependence is heritable;[11] however, the identification of genetic risk factors remains difficult due to the complex mode of inheritance, as well as clinical and genetic heterogeneity. It is likely that multiple genes confer risk for addiction disorder, where the contribution of each gene to the overall risk is rather small.

DNA methylation is an important regulator of gene expression. It entails the addition of a methyl group to the 5 carbon of cytosine in a context of guanine (CpG dinucleotides). CpG islands are typically defined as regions of DNA that are 300 base pairs or longer with over 50% of the base pairs being CpG units. CpG islands occurring near the gene promoter are typically methylation free; hence, methylation found in a CpG island of the promoter region of the gene is thought to act as transcriptional repressors.6 Methylation of DNA is a reversible process and does not change the actual sequence of the DNA; however, it can modulate gene expression, thereby affecting phenotype. It is commonly accepted that DNA methylation is influenced by environmental factors, but the mechanisms by which environment affects DNA methylation state remain largely unknown.[6]

Here, we wanted to explore the contribution of epigenetic mechanisms to drug addiction by investigating the link between the methylation status of the three brain candidate genes (DRD4, SERT, and MAOA) and drug addiction.

Genetic variations in those 3 genes have been linked to different behavior traits and diseases: a DRD4 polymorphism (chr11:639989-640194) has previously been linked to ADHD,[1] Alzheimer's disease,[2] drug addiction,[3] schizophrenia,[4] and cigarette smoking.[5] Variations in the human SERT gene (chr17:28,523,378-28,562,954) have previously been linked to depression,[7] low inhibitory control,[8] and alcoholism.[9] The MAOA gene (chrX:43,515,409-43,606,068) has most commonly been linked to inhibitory control, anti-social behavior, and aggression.[10]

We hypothesized that promoter methylation of the DRD4, the MAOA, and the SERT gene may be affected by cocaine exposure and also change with age.

The results of this study suggest that the methylation of the DRD4 promoter region in CA individuals was greater than that in HC. We also found evidence on increase of methylation of DRD4 and MAOA with age.

II. Materials and Methods

The DNA used in this experiment was purified from white blood cells using the Qiagen DNA purification kit.

The DNA samples were treated with the Qiagen Epitect bisulfite kit using approximately 600 ng of DNA. The bisulfite modification changes the sequence of the DNA such that if a CpG dinucleotide is methylated it will be unchanged, but if a CpG is unmethylated the cytosine will be converted to a uracil. The sequence differences between the template and BS-converted DNA can be revealed by restrictive digestion.

A. Polymerase Chain Reaction (PCR) Amplification

The bisulfite (BS) modified DNA was amplified with PCR. We used primers and protocol previously reported by Wong et al6. The primers for the three regions are shown in Table 1.

Bisulfite-PCR amplification was conducted using Hot Star Taq DNA polymerase (Qiagen, UK) and cycling conditions of 45 cycles with an annealing temperature of 56°C for all amplicons.

Gene	Genomic Region	PCR primers
DRD4	chr11:636508-636904	F: GGGATTTTTTGTTTAGGGTTAGAGG R:CACCCTAATCCACCTAATATCTAACA
SERT	chr17:28562435-28562812	F: GGTTAGTTTTAGTTTTGGTTTTTGTT R: CAAAAATTCTTCAAAAACTCTTTAAC
MAOA	chrX: 43515581-43515800	F:GTTAAAGTATGGAGAATTAAGAGAAGG R:CAAAATATAAAACCAAACCATAACTACA

Table 1: Summary of Primer Sequences for PCR Amplification

B. Restriction Enzymatic Digestion

The DRD4 amplicons were digested with the restriction enzymes HhaI and RsaI: 2.5 units of enzyme were used to digest 2 µg of PCR product in a final volume of 20 µl at 37ºC for 16 hours for both enzymes.

The SERT amplicons were digested with the restriction enzyme HpyCH4IV: 2.5 units of enzyme were used to digest 2 µg of PCR product in a final volume of 20 µl at 37ºC for 16 hours.

The MAOA amplicons were also digested with HpyCH4IV in the same set up at the SERT PCR products. The MAOA amplicons were also digested with BstUI: 2.5 units of enzyme were used to digest 2µg of PCR product in a final volume of 20 µl at 60ºC for 16 hours.

Table 2 displays the summary of the regions and restriction sites analyzed in this study.

C. Gel electrophoresis

The digested products were resolved on 1.25% agarose gel at 95V. The bands were visualized under ultraviolet light.

III. Results

We used the following criteria to quantify the methylation state of the analyzed CpG sites: if the product had been cut completely, it was assigned the status of "methylated;" if it was partially cut, it was assigned a percentage based on the thickness of the bands, and if it was completely uncut, it was assigned the status of "unmethylated."

The percent methylation status assigned was based on the following formula:

% methylation = 100 x (digested fragments/(undigested fragments + digested fragments))

Examples of the gel electrophoresis images are shown in Figures 1 and 2.

Next, we analyzed changes of the DRD4 promoter (chr. 11:636750) related to age by plotting the methylation values against individual's age (Fig. 3).

Analysis of the age-related changes in the MAOA methylation revealed increase in methylation with age. A similar analysis was performed on the MAOA promoter region and it was also found that methylation status increases with age (Fig. 4).

Next, we wanted to explore whether there are differences in DRD4 methylation status in CA compared with HC. We found that the average percent methylation at HhaI restriction site in CA was greater than that in HC (Table 3). This is a very significant finding. It should also be noticed that the lowest percent methylation in cocaine addicted individuals was 40%; whereas, in healthy controls, it was 0%.

	Average % Methylation	Lowest % Methylation	Highest % Methylation	Standard Deviation
Cocaine Addicts	62%	40%	80%	13.62%
Healthy Controls	52%	0%	80%	20.25%

Table 3: Methylation Status of DRD4 in CA and HC

In contrast, methylation of the MAOA promoter was similar in CA and HC groups (Table 4).

	Average % Methylation	Lowest % Methylation	Highest % Methylation	Standard Deviation
Cocaine Addicts	14%	0%	60%	18%
Healthy Controls	13%	0%	80%	19%

Table 4: Methylation Status of the MAOA promoter in CA and HC

The specific region of the SERT gene that was studied was upstream of the promoter region at chr17:28562435-28562812. Unfortunately, there was failed amplification for most samples in the SERT region and we were unable to collect significant data for that gene.

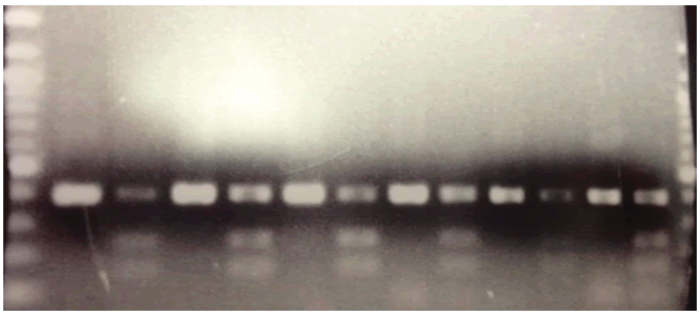

Figure 1. DRD4 restriction with HhaI (chr.11:636750)
The gel is loaded such that the uncut samples are always to the left of the cut samples. The percent methylation of the samples in this gel are as follows, from left to right: 60%, 50%, 75%, 50%, 40%, 60%

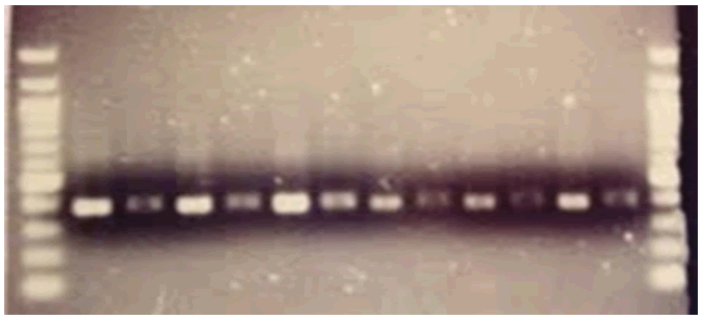

Figure 2. DRD4 restriction with RsaI (chr.11:636789)
The percent methylation of the samples in the gel in Fig. 2 are all 0% (unmethylated)

	HhaI restriction site	RsaI restriction site	HpyCH4IV restriction site	BstUI restriction site
DRD4	chr11:636750	chr11:636789	-	-
SERT	-	-	chr17:2856404	-
MAOA	-	-	chrX:43515634	chrX:4351618

Table 2: Positions of the Restriction Sites Within the Analyzed Genomic Regions

IV. Discussion

This study aimed to explore the methylation status of the DRD4, MAOA, and SERT promoter regions and to reveal potential differences between cocaine addicted individuals and healthy controls, as well as to detect changes in methylation associated with age. The analysis was completed using bisulfite modification of DNA, PCR, and restriction enzyme digests. The method by which the methylation status was determined was chosen for its originality and the fact that it was a fun and interesting assay to perform.

This project can help us to advance our understanding of the biological mechanisms underlying drug addiction and point out to potential new therapeutic targets. This project is relevant to the Department of Energy Mission Statement because its analytical approach makes use of the technologies earlier developed at Brookhaven National Laboratory (BNL) and its results can have important social implication aiming to ensure America's prosperity by addressing the need of America's people to be helped in the war against drugs.

One very interesting finding was the difference in methylation between two sites in the DRD4 promoter region. Methylation at chr. 11:636750 was significantly greater than methylation at chr. 11:636789, despite the fact that they exist within the same CpG island. Previous studies have suggested that within a CpG island all CpG residues will be either methylated or unmethylated. The finding that these two CpG residues, which exist within the same CpG island, are very dissimilar in methylation status contradicts this previous theory.

We found that in the DRD4 promoter region methylation status was 10% greater in cocaine addicted individuals than in healthy controls. This finding is very interesting. It is possible that the interaction between cocaine and the dopamine transporter caused an increase in methylation of the dopamine receptor genes in cocaine addicted individuals. Further study of this region would be very interesting and would lead to more definitive and conclusive results.

It was also found in the DRD4 region, as well as the MAOA region, that methylation status increased with age. No significant results were found for the SERT region due to failed amplification in the PCR assay.

The results of this study both agreed and disagreed with previous results found by Chloe Chung Ye Wong, et al.6 While Wong explored the exact regions that were explored in this study, Wong found that for the DRD4 region, methylation decreased with age. However, our findings contradict this, as we found that methylation increases with age. Wong also found that methylation in the MAOA region increases with age, findings our study agrees with. Wong found that average methylation in the DRD4 promoter was greater than that in the MAOA promoter, which our study found also.

Wong's study provides very good data for us to compare our data with; however it is not a perfect match. Wong's study explored methylation across specific individual's DNA at two different ages, whereas our study explored methylation across specific individual's DNA at only one age. We then compared our methylation data with individuals who were of different ages, whereas Wong compared methylation data for one individual at different ages.

V. Conclusions

We found that methylation state of the single CpG island is not uniform. Two CpG sites within the DRD4 promoter have dissimilar methylation state: most samples were methylation free at Chr. 11:636789 (RsaI cleavage site) while heavily methylated at Chr. 11:636750 (HhaI cleavage site). This finding challenges the originally proposed postulate that all CpG sites within a CpG island have the same methylation state. We also found that methylation at Chr. 11:636750 of the DRD4 promoter, as well as methylation at chr. X:43515634 of the MAOA promoter, increased with age. Our data indicated that average methylation of the DRD4 promoter in cocaine addicted individuals (CA) is greater than that in healthy controls (HC). In contrast, there is no significant difference in methylation of the MAOA promoter between HC and CA, suggesting that effect of the illicit drugs on epigenetic marks might be locus- and site-specific.

VI. Sources and Acknowledgements

This project is dedicated in loving memory to Dr. John J. Dunn.

Special Thanks Dr. Elena Shumay, Dr. John Dunn, Dr. Carl Anderson, BNL Medical Department Neuropsychoimaging group, Brookhaven National Laboratory, The United States Department of Energy, the Office of Educational Programs, and the SULI program.

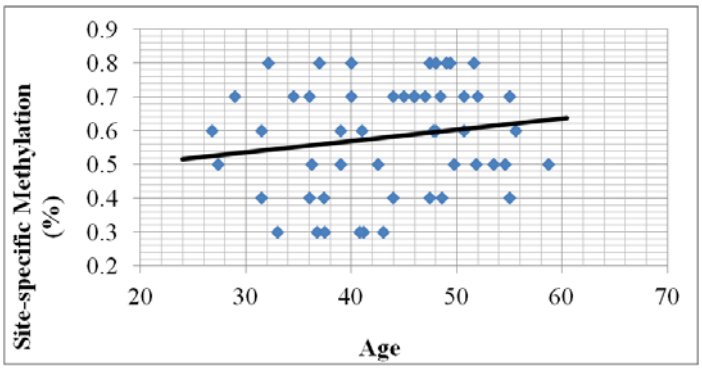

Figure 3: Correlation between DRD4 methylation and age
Axis X represents individual's age; corresponding methylation values in percentile are shown on Y-axis. Regression line is shown in black.

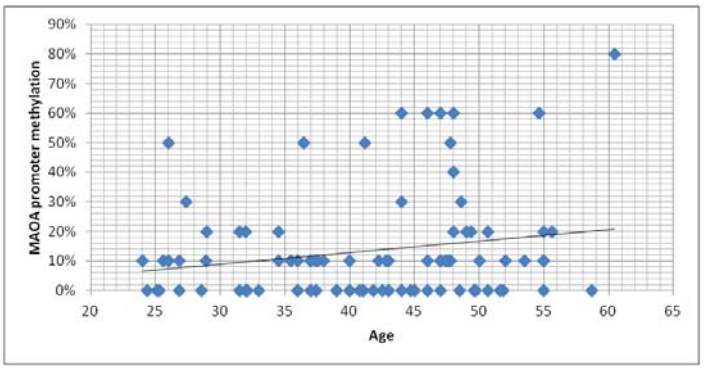

Figure 4: A regression slop of methylation value plotted against the individual age in the MAOA promoter.

[1]Li D, Sham PC, Owen MJ, He L. Meta-analysis shows significant association between dopamine system genes and attention deficit hyperactivity disorder (ADHD) Hum Mol Genet. 2006;15:2276-2284

[2]Pritchard, A. L., Ratcliffe, L., Sorour, E., Haque, S., Holder, R., Bentham, P. and Lendon, C. L. (2009), Investigation of dopamine receptors in susceptibility to behavioural and psychological symptoms in Alzheimer's disease. Int. J. Geriat. Psychiatry, 24: 1020–1025. doi: 10.1002/gps.2214

[3]McGeary J. The DRD4 exon 3 VNTR polymorphism and addiction-related phenotypes: a review.

[4]Kaufman J, Birmaher B, Brent D, Rao U, Flynn C, Moreci P, Williamson D, Ryan N. Schedule for affective disorders and schizophrenia for school-age children- present version and lifetime version (K-SADS-PL): initial reliability and validity data. Journal of the American Academy of Child and Adolescent Psychiatry. 1997;36:980-988.

[5]Hutchingson KE, LaChance H, Niaura R, Bryan A, Smolen A. The DRD4 VNTR polymorphism influences reactivity to smoking cues. J abnorm Psychol. 2002 Feb; 111(1):134-43. [PubMed]

[6]Wong CC, Caspi A, Williams B, Craig IW, Houts R, et al. A longitudinal study of epigenetic variation in twins. Epigenetics. 2010;5:516–26.

[7]Caspi A, Sugden K, Moffitt TE, Taylor A, Craig IW Harrington H, et al. Influence of life stress on depression: Moderation by a polymorphism in the f-HTT gene. Science. 2003;301:386-389; PubMed]

[8]Zalsman G, Patya M, Frisch A, Ofek H, Schapir L, Blum I, et al. Association of polymorphisms of the serotonergic pathways with clinical traits of impulsive-aggression and suicidality in adolescents: a multi-center study. World J Biol Psychiatry. 2011;12:33–41. [PubMed]

[9]Heinz A., Ragan P., Jones D.W., Hommer D., Williams W., Knable M.B., Gorey J.G., Doty L., Geyer C., Lee K.S., Coppola R., Weinberger D. R., Linnoila M. (1998). Reduced central serotonin transporters in alcoholism. Am. J. Psychiatry 155, 1544-1549. [PubMed].

[10]McDermott R, Tingley D, Cowden J, Frazzetto G, Johnson DD. Monoamine oxidase A gene (MAOA) predicts behavioral aggression following provocation. Proc Natl Acad Sci USA.2009;106:2118–2123.

[11]Kendler KS, Prescott CA. Cannabis use, abuse, and dependence in a population-based sample of female twins. Am J Psychiatry. 1998;155:1016–1022.

Simulating a Training, Research, Isotopes, General Atomics Reactor core through modeling with the Purdue Advanced Reactor Core Simulator

Jared Stier
Nuclear Engineering, North Carolina State University, Raleigh, North Carolina 27695
Peter Kohut
Nuclear Science and Technology Department, Brookhaven National Laboratory, Upton, New York 11973

ABSTRACT

Over the past two summers, other Brookhaven National Laboratory (BNL) interns have attempted to simulate a model for the Training, Research, Isotopes, General Atomics (TRIGA) Reactor at Texas A&M. While the Purdue Advanced Reactor Core Simulator (PARCS), a software designed to model reactor physics, is generally used to simulate large, high-power reactors, a TRIGA reactor is small and asymmetrically designed. While the past two summers' efforts have produced inconclusive results, it was determined that the PARCS software had errors that did not account for the geometry of a TRIGA reactor. Exploring this further, we wanted to determine if there were other errors in addition to the PARCS code that could contribute to the results. In the past, it was assumed that one could dissect the reactor into smaller pieces to determine cross sections and then compile them together in PARCS and achieve an accurate result, as opposed to modeling the entire reactor at once and homogenizing over the smaller regions. The benefit of this method is that it would shorten the time (more than 24 hours) it takes to develop the cross sections through the program NEWT3. This year we decided to see how accurate these cross sections actually were by taking the longer route. We have found that there was a difference in some of the cross sections by as much a factor of 10. This is beneficial to BNL and the Department of Energy as this project has shown that the standard assumption of dissecting the reactor into smaller pieces does not always provide accurate results, and it would be safe to check and make sure before moving on with a project. Through this project I have learned a lot about reactor physics that will help in my studies as I dive deeper into my major at school.

The Texas A&M NSC TRIGA_LEU 30/20 is a one megawatt reactor cooled by convection. It is also a non-critical nuclear research reactor used for many diverse applications and found at universities, government, and industrial laboratories, and medical centers in 24 countries. The fuel is composed of lightly enriched uranium and zirconium hydride. The arrangement of the fuel pins and control rods can be found in the middle of the poster.

The original goal set out for each of the past two summers was to create a computer model to simulate a transient rod ejection. Each of the past two years, errors have appeared during the PARCS stage of the process which returned a completely unrealistic output. The Purdue Advancement Reactor Core Simulator (PARCS) is software designed to model real-time reactor physics based on a provided input of composition and core geometry. PARCS was designed for large circular reactors that generally have high powers, such as a civilian reactor; whereas, a TRIGA reactor is very small and generally has unique core geometries. In addition to these differences, TRIGA reactors have also only been simulated in the steady state. It was assumed PARCS was at fault since the program is generally used to model large, circular reactors as opposed to the smaller rectangular shaped one at Texas A&M. This year, we set out to see if PARCS was truly at fault or if it was caused by other reason throughout the project.

Here is a brief description of the programs used in this project (See Figure 1):

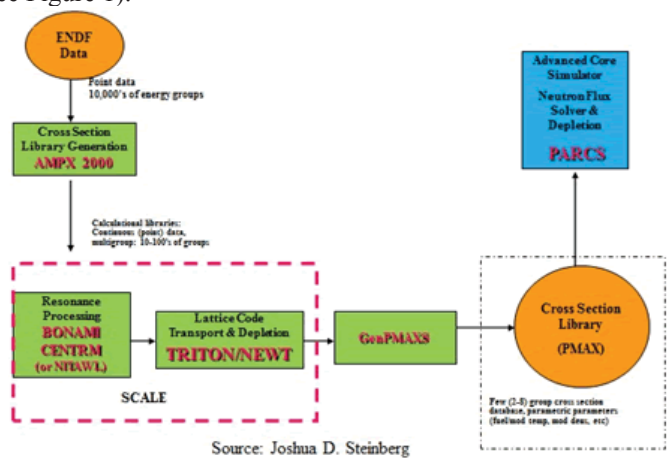

Source: Joshua D. Steinberg

Figure 1. Flow chart of the different programs used in this experiment

SCALE, developed by Oak Ridge National Laboratory, is suited to performing calculations for criticality safety, reactor physics, and radiation shielding. SCALE calls upon "sequences" to execute computation modules that determine particle fluxes and nuclear cross- sections. Benchmark problems are included in the SCALE program package. One of these problems, entitled NEWT3, was the basis for the fuel assembly input deck as well as for the control assembly input deck.

GenPMAXS is only used briefly and its purpose is to put the cross sections determined by SCALE in a format readable by the next program, PARCS.

The Purdue Advanced Reactor Core Simulator (PARCS) predicts the power distribution in nuclear reactor cores when they are subject to changes such as the movement of control rods or changes in coolant conditions. PARCS uses the cross-sections obtained in SCALE as well as other reactor specifications, to create the power distribution.

In summer 2011, it was assumed that one could split the reactor up into multiple sections to determine the cross sections, and then compile them in PARCS to accurately model the reactor (See Figure 2). It was determined to dissect the reactor into 11 different parts that can be used to model the entire reactors. They are: water, graphite, fuel near fuel, fuel near water, fuel near graphite, fuel near control rod, fuel near transient rod, fuel near regulating rod, control rod, transient rod, and the regulating rod.

The best way to determine how many different regions to homogenize over would be to look at the two group flux charts that show the concentration of neutrons throughout the reactor. If pins

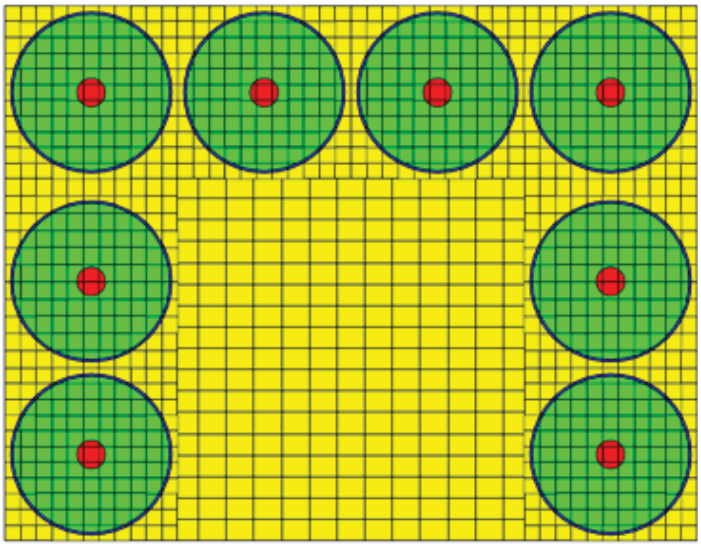

Figure 2. 2011 style of modeling the TRIGA reactor

have differing fluxes, it would be better to add more homogenized regions to make sure you receive accurate results.

To test this theory, I constructed a model of the entire reactor. In designing the input deck for the TRIGA reactor, we took the core geometry and number densities of all the materials. A global unit was made filling in "holes" of the different assemblies found in the reactor. To get cross sections for a specific fuel pin, we had to specify the fuel as a different material and homogenize over it (See Figure 3).

Merely for comparison purposes, only three cross sections were determined from the 2012 model: fuel near fuel, fuel near water, and fuel near graphite. The results were staggering, differing by about an order of magnitude. The fast to thermal flux ratios also varied by 10-15% (See Table 1).

To conclude, last year's cross sections were thrown out due to the large deviation from the newly determined data. While there may still be a problem with PARCS, it is clear that a large error was caused by the previous input deck for SCALE.

In order to receive closure on this project, I see three more experiments that need to be tested. The first is taking the full reactor model and creating cross sections for the same 11 regions used in 2011 and determine if PARCS can give an accurate power distribution of the reactor. Compare the k-infinity value found to that from SCALE. If the results are not accurate, I would recommend

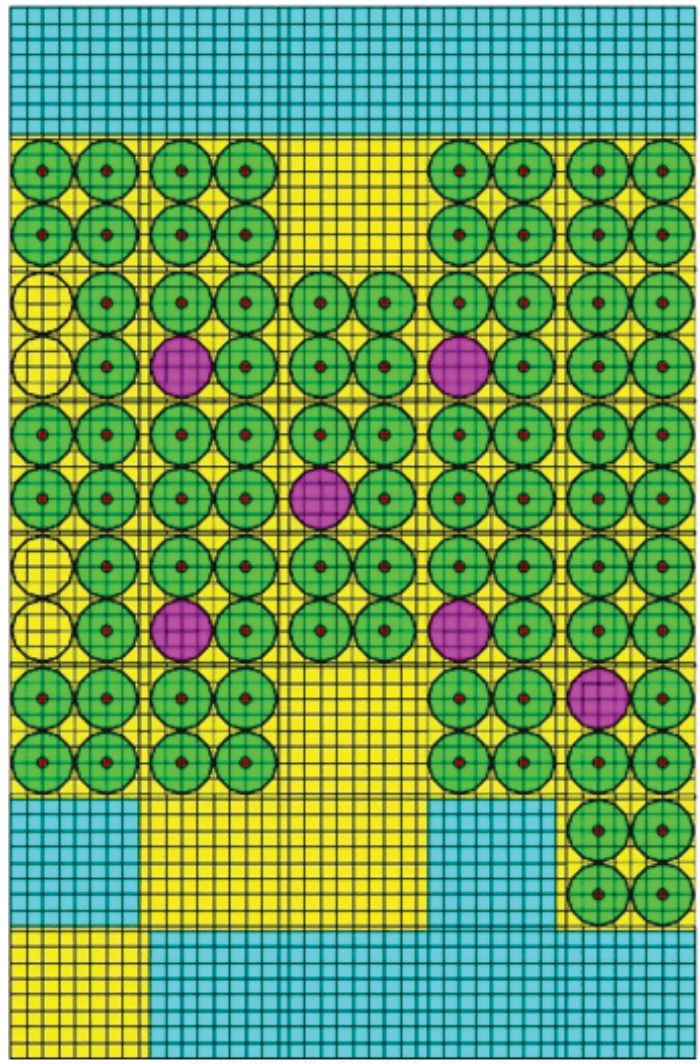

Figure 3. Current SCALE model of TRIGA

trying to homogenize of each individual fuel pin. This would be the most accurate possible model of the Texas A&M reactor. If this does not give proper results, it can safely be concluded that there is a software error in the PARCS coding.

If accurate results are found, then experiment number two would be comparing these results to the Safety Analysis Report of the Texas A&M TRIGA reactor. If the numbers are not close, the

Table 1. Cross section comparison

		Energy Group	Total	Total-transfer	Transport	Nu*fission	Kappa*fission	Fast/Thermal flux
Jared	Fuel near fuel	1	8.25E-01	1.50E-02	2.94E-01	1.45E-02	1.83E-13	9.55E+00
Jared	Fuel near fuel	2	2.53E+00	2.82E-01	1.69E+00	4.58E-01	5.84E-12	
2011	Fuel near fuel	1		3.18E-01	1.37E-02	1.20E-02	1.51E-13	8.03E+00
2011	Fuel near fuel	2		1.07E+00	1.87E-01	2.96E-01	3.78E-12	
Jared	Fuel near water	1	8.14E-01	1.52E-02	3.10E-01	1.47E-02	1.85E-13	7.21E+00
Jared	Fuel near water	2	2.63E+00	2.85E-01	1.78E+00	4.75E-01	6.06E-12	
2011	Fuel near water	1		3.17E-01	1.31E-02	1.16E-02	1.46E-13	6.07E+00
2011	Fuel near water	2		1.24E+00	2.01E-01	3.25E-01	4.15E-12	
Jared	Fuel near graphite	1	8.02E-01	1.42E-02	2.86E-01	1.39E-02	1.74E-13	7.21E+00
Jared	Fuel near graphite	2	2.66E+00	2.85E-01	1.81E+00	4.73E-01	6.03E-12	
2011	Fuel near graphite	1		2.59E-01	1.42E-02	1.24E-02	1.56E-13	8.58E+00
2011	Fuel near graphite	2		1.04E+00	1.94E-01	3.08E-01	3.93E-12	

next step would be to go back to the input deck for SCALE and see if any errors could exist in that. If they are similar, we would finally be ready model the transient rod ejection, which was the original goal of this project. Getting the power distribution from PARCS of the transient rod ejection would inform us where the highest fuel temperature would be located within the reactor. That data would help prevent any possible nuclear meltdown.

Finally, I would go back to the 2011 model of dissecting the reactor and test one last time if that method could give accurate results. There are other problems that could have been fixed in the input decks, including homogenization regions and grid lines. Fixing those would definitely make the results slightly more precise, but not necessarily perfect. If it is possible to find the proper results, it would save others plenty of time in the future to confirm that the dissection method actually works.

In summation, it was determined that it would be possible to come to more conclusive conclusions, yet unfortunately the summer only lasts so long. Maybe next year's summer student can come to a more conclusive decision on what caused all of the error.

I would like to thank the following people for their help and guidance along the way: Peter Kohut, Nicholas Brown, and Arantxa Cuadra.

Search for critical behavior in relativistic heavy ion collisions

Mingxiu Sun
Mechanical Engineering Department, University of Illinois, Urbana, IL
Jeffery Mitchell
Physics Department, Brookhaven National Laboratory, Upton, NY 11973

ABSTRACT

The Pioneering High Energy Nuclear Interaction eXperiment (PHENIX) detector consists of four spectrometers and three global detectors. Before being applied, the data collected from those detectors requires calibration after every run in order to compensate for alignment and timing errors. Physicists are expecting that there is a critical point in the phase diagram of Quantum Chromodynamics (QCD). Changes in the behavior of charged particle and transverse energy production are expected near the critical point. In order to measure these quantities, we have estimated the geometry of the collision by running Glauber model simulations. The data has also been corrected for the coverage of the detectors and the particle identification efficiency. We are measuring this for 27 GeV Au+Au, 19.6 GeV Au+Au, 200 GeV Cu+Au, and 193 GeV U+U collisions. To identify particles, the square of the mass versus transverse momentum shows six clusters. They are the pion, kaon, proton, and their respective antiparticles. Dividing the clusters by transverse momentum, the resulting one-dimensional plots have three peaks. We fit all of those three peaks to Gaussian functions for all the transverse momentum divisions and then use 2 standard deviation cuts to select our pion, kaon, and proton data from all the background. Once we purify the data selection for each of the particle groups and correct for the detector configuration, we plot the antiproton versus proton and transverse momentum for each of the hadrons. A large increase in the ratio at high transverse momentum is expected near the critical point. Discovery of the QCD critical point will further our understanding of the basic dynamics of matter and the early universe.

I. Introduction/ Problem Description

Quark–gluon plasma (QGP) is expected to be produced under extremely high temperature and density, under which situation there only exist free quarks and gluons. More specifically, only quarks and gluons might be what were present in the universe a few nanoseconds after the big bang. While the temperature dropped precipitously, those quarks and gluons started forming protons and neutrons, and gradually the universe was formed by that matter and anti-matter. Studying QGP can give physicists a better understanding of the formation and structure of the universe.

As it is one of the only two operating relativistic particle colliders in the world, the Relativistic Heavy Ion Collider (RHIC), is designed and built to reproduce the big bang on a small scale. RHIC accelerates gold particles in a 2.4-mile circular tunnel until they reach a speed of 99.9995% of light speed. There are two acceleration beams running in the opposite direction. Once the designated speed is reached, the two beams are made to collide into each other at detector stations. Because of the high temperature (2*10^12 degree kelvin) and high pressure, gold particles will breakdown into hadrons, and even quarks. As the QGP "fireball" expands and cools hadrons are again formed from quarks and gluons, the fundamental constituent of hadronic matter. By measuring the production of hadrons produced after the collision, the properties of the media within the collision zone are explored.

The data analyzed in this paper are collected by the PHENIX detector station. The project is to search for critical behaviors of hadron formation at different energy levels and compare particle behaviors at similar energy levels using different types of particles. For the first time, RHIC will operate using uranium on uranium collisions and an asymmetric collision using copper on gold. In order for us to study the physics aspect of the collision, data need to be calibrated and graphs need to be plotted first. C-based programming together with the data analysis framework ROOT were used to help us analyze the data and generate plots and histograms.

II. Data used

Data from Run2012 200 GeV Cu+Au and 193 GeV U+U, Run 2011 27 GeV Au+Au and

19.6 GeV Au+Au, and Run 2005 200 GeV Cu+Cu and 62.4 GeV Cu+Cu have been analyzed by our group this year. dN/dη and dET /dη have been plotted. Multiplicity fluctuations at the lower energies have been calculated.

Here are the cuts we applied for the time of flight data:

1. |z-vertex|<30 cm
2. Dch quality: 19 || 23 || 31 || 51 || 63
3. West: tofwsdphi<2.0 && tofwsdz<2.0
   East: tofsdphi<2.0 && tofsdz<2.0

III. Procedure/ Methods

A. Calibration

1. Trigger Efficiency

The detectors are not managed to be triggered by every collision, due to the instability of the energy levels of all the projectile particles and the certainty of each individual detector's property. Each detector slides have a different efficiency coefficient, and they typically have a value around 80% to 95%. Before analyzing the experimental data, the trigger efficiency for each detector slide needed to be determined. Then, we divided the detected data with this number to estimate the real data happenings in the collision. In order to get the efficiency values, an established macro was used to fit a "number hit" graph with negative binomial equation. Alpha, k, and mua are subjected to change, in order for us to search for the combination along with efficiency value to achieve the minimum chi square value for the fitting curve. The efficiency value determined here is the optimum estimation for the efficiency of the detecting device. With the efficiency, the centrality of the collisions can be estimated.

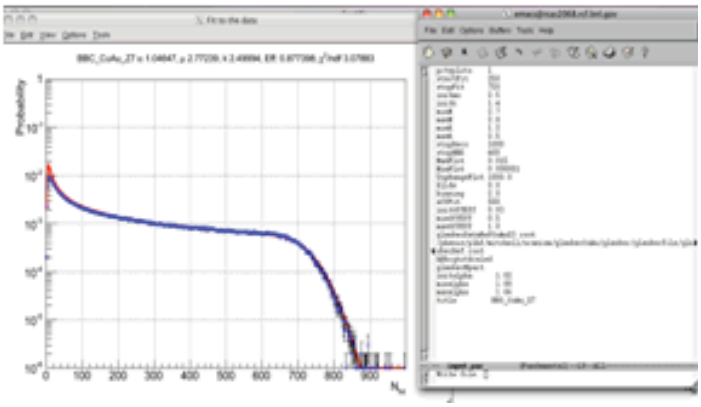

Figure 1

2. Particle Identification (PID)

On the mass square versus momentum graph, there are clearly six clusters existing. According to its mass square scales and charge values, those clusters indicate the hadron groups of pion, kaon, proton, and their anti-particles respectively. However, in the areas between those peaks, particles are detected all over the place. It's not so clear whether those points belong to pion or kaon when they are sitting in between. In order to improve the data used for analysis, refining the plots is necessary. Therefore, cutting off this noise and only reserving the parts that are purified is the next step to do.

Values for mean and standard deviation for each of the hadron are determined, and 2 standard deviation cuts are applied. In order to deal with the overlapping of pion and kaon after the 2 standard deviation plots, an algorithm was written in the macro code that helped to identify those overlapped areas and eliminate points there. In the end, a graph that has three clear clusters without any overlapping area is resulted. (Figures 2, 3, 4, 5, and 6)

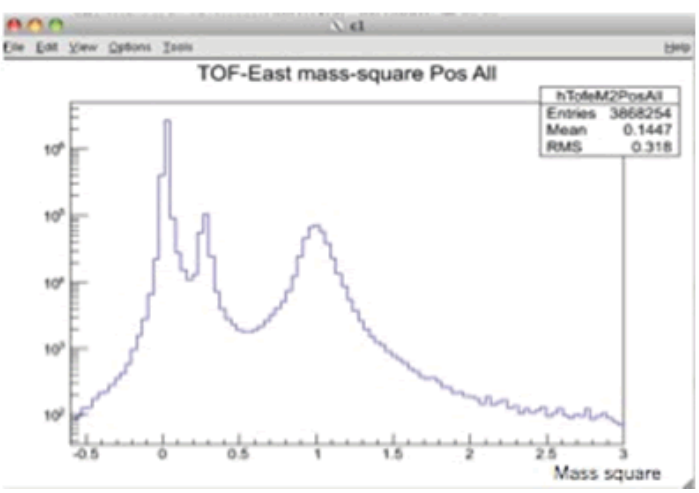

Figure 2

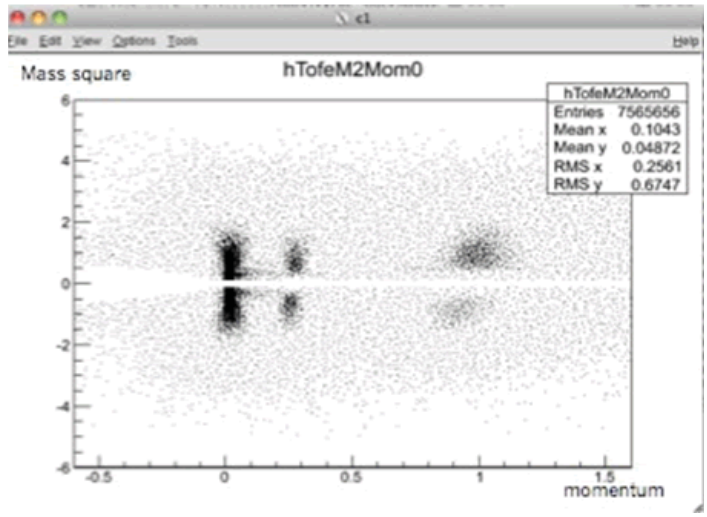

Figure 3

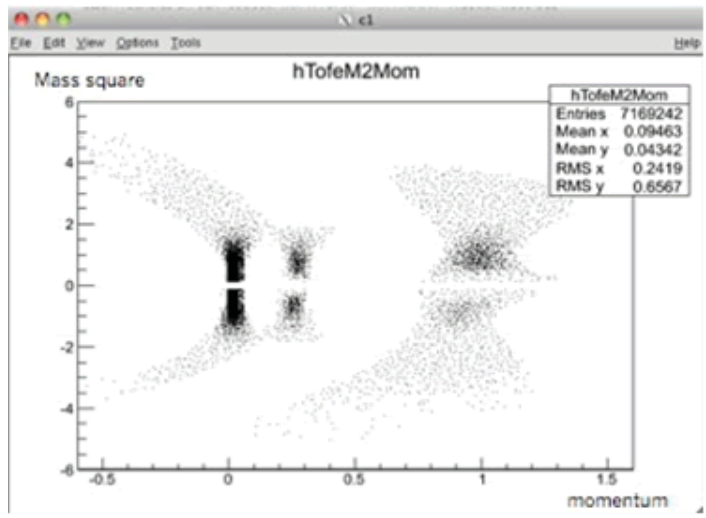

Figure 4

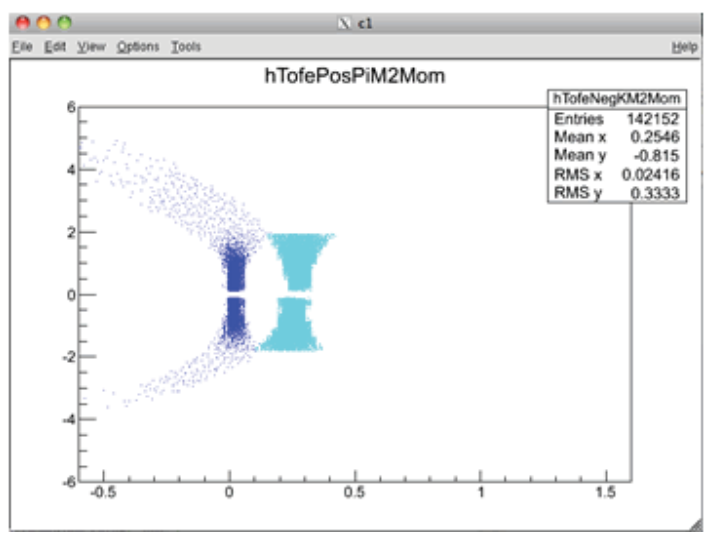

Figure 5

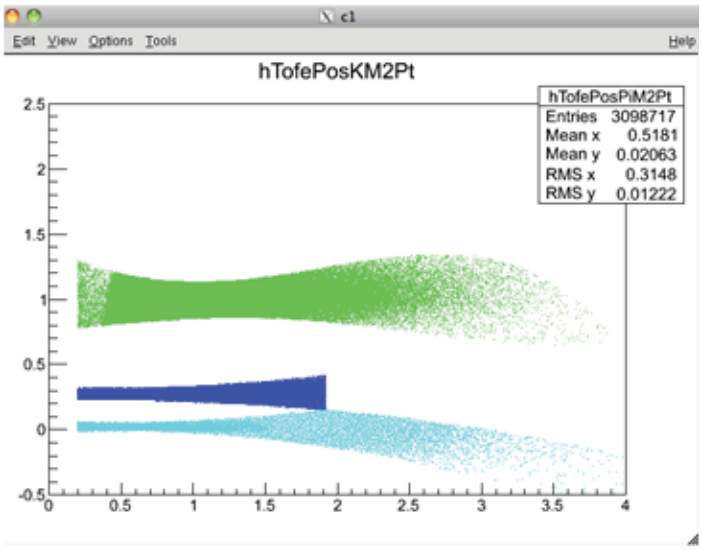

Figure 6

3. Dead/ Warm Map for Calorimeter

A detector board consists by hundreds of detecting probes sitting in rows and columns. Due to electrical overheating or circuit failure, the detector may not work properly. Those detecting probes will report obviously unrealistic data values compared to the normal. The ones having huge values are called warm map, and the ones with small values are called dead map. Using fitting plots and two-standard-deviation cut, the data collected from the warm and dead mass can be removed.

4. Momentum Scale Calibration

It is commonly accepted and proved that the mass square of pi is 125. However, due to shift or systematic error, the detector will give us some values other than 125 on some of the graphs. That is obviously inaccurate; and so, momentum scale calibration is needed. The measured values divide by the real value will give us a correction factor. Then, the measured value will be shifted with this correction factor to make the measured data more accurate and valuable.

B. Physics Results

1. Multiplicity for low energy

The multiplicity plots are categorized into 16 groups with 5% centrality bins for each. It is proven that the lower the centrality, the lower the energy level. That's shown on the summary plot of all first 13 of them. The last 3 of them are excluded because their centralities are too small to have a clear view on this plot. As the graph shows, when it goes out on the X-axis of centrality, the peak on Y-axis gets lower proportionally.

It's worth noticing that this is the first time the PHINEX group has used the drift chamber to measure the charged particle multiplicity. PC1 and PC3 are usually used to do the same job. However, at low energy, PC1 and PC3 will bring in noticeable amount of background to the multiplicity measurement. Each of those 13 plots is fitted, and their mean and standard deviation values are extracted.

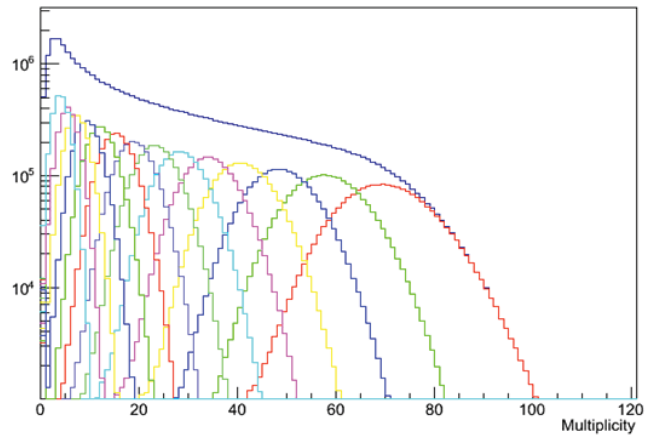

Figure 7

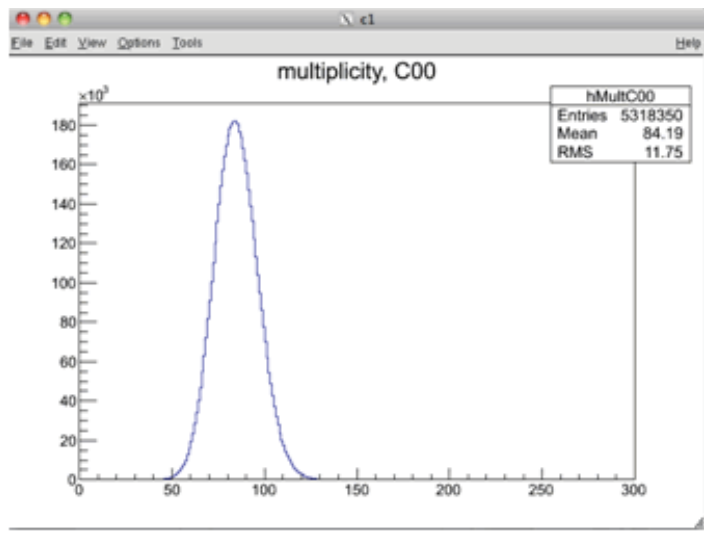

Figure 8

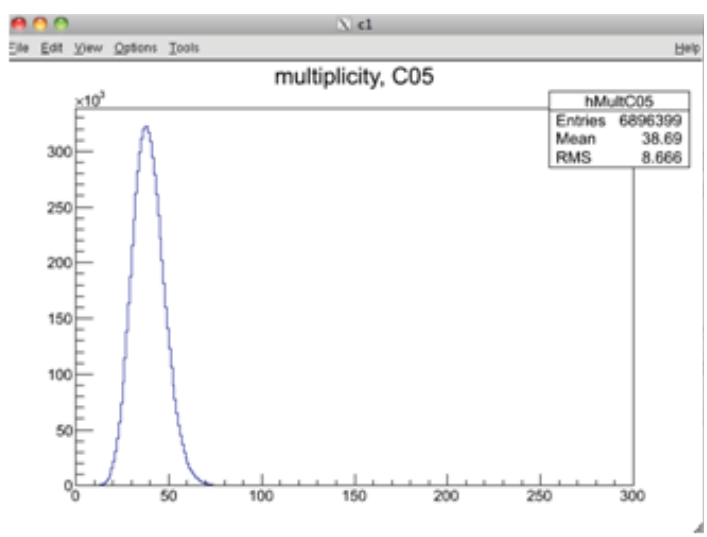

Figure 9

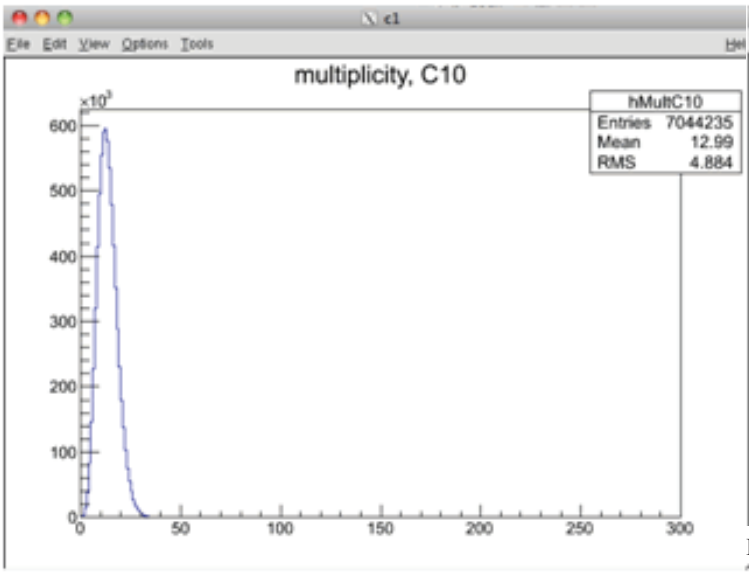

Figure 10

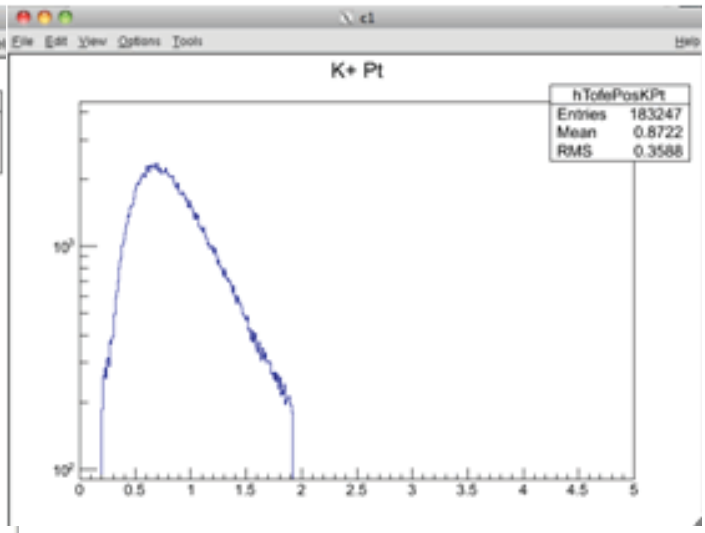

Figure 12

2. Pt Spectra

Pi, kaon, proton, and their anti-particles are extracted from the combined mass square plots as shown in the particle identification section. Then, the transverse momentum plots are plotted, which are also called the Pt spectra. They are in an exponential function as expected. The higher the temperature, the faster the particles travel and the flatter the slop should be. The simultaneous temperature can be estimated by observing the slope of the Pt spectra, which can help the scientists to estimate the temperature achieved in each collision in the RHIC.

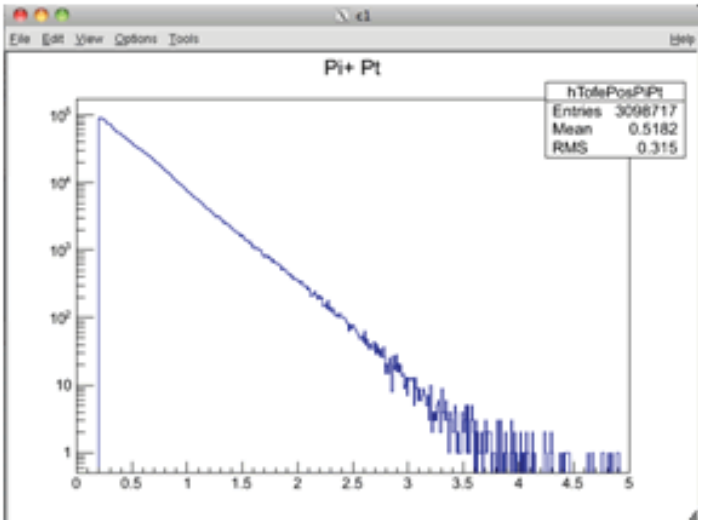

Figure 11 (Y- axis Number of particles, X- Transverse momentum)

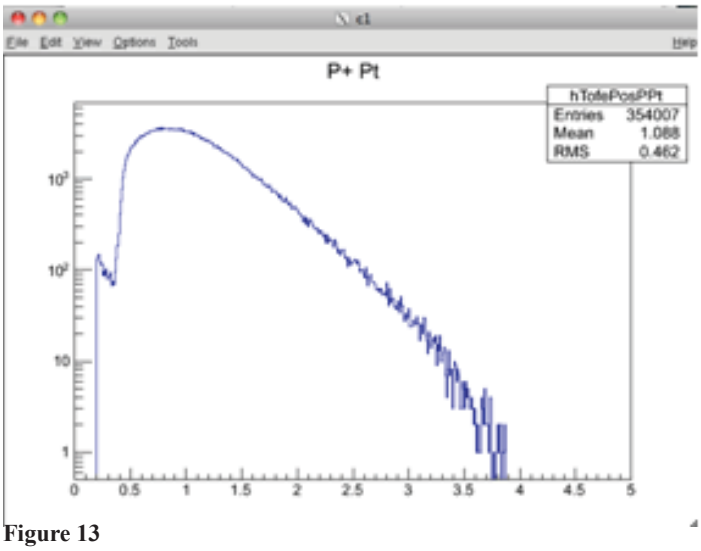

Figure 13

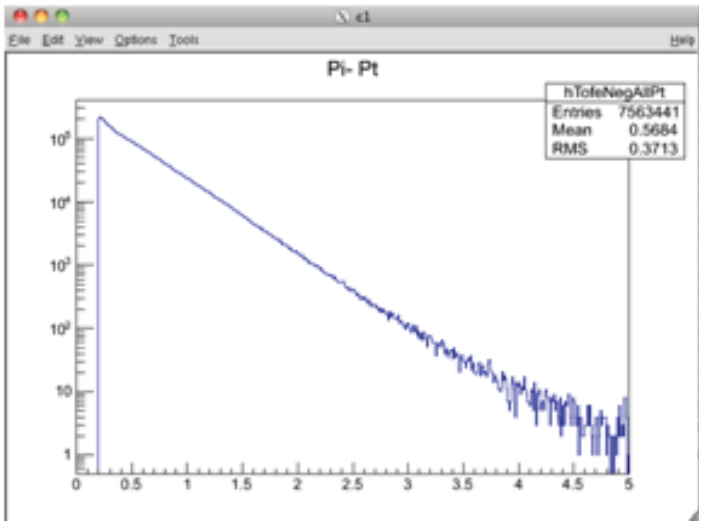

Figure 14

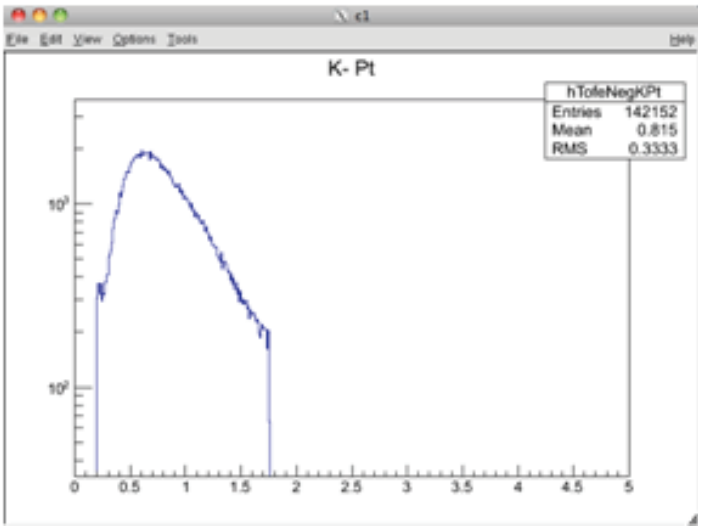

Figure 15

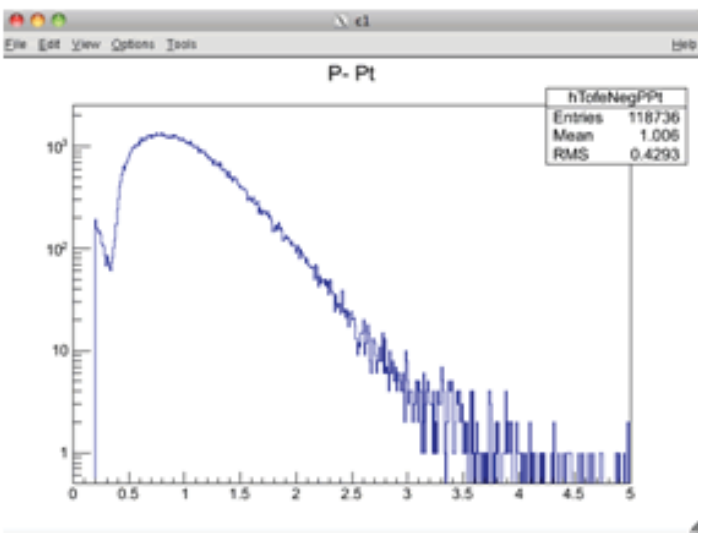

Figure 16

3. Uranium and Uranium Collision

Since uranium particles are heavier than gold particles, the number of particles produced during a RHIC collision is higher than those for gold particles at the same collision energy. In addition, gold particles are spherical, while uranium particles are shaped like an American football. When tip-to-tip collisions happen, the higher energy density is produced, because energy is focus on a relatively small area. As showed in the plot, multiplicity density is the same for both particles, but the transverse momentum goes up for uranium collisions. The higher energy density and higher particle density will produce a more favorable situation for the experiment. There will be a higher probability to form QGP.

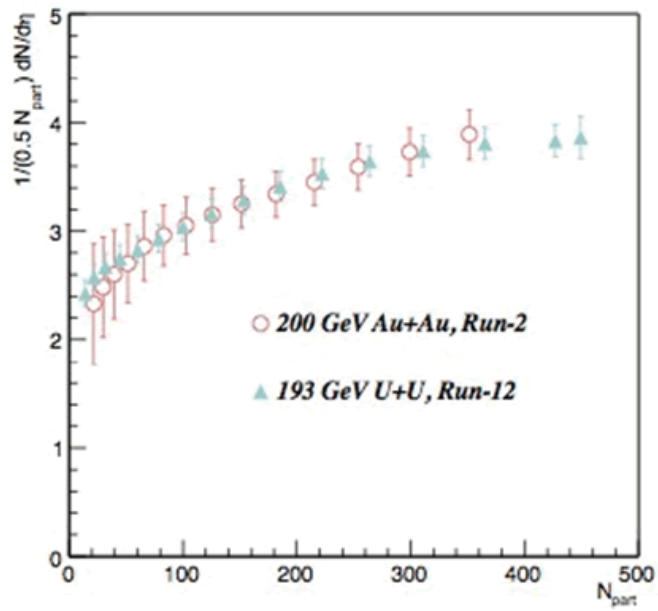

Figure 17

4. Anti proton vs proton plot

An anti-proton versus proton plot is one of the most significant plots in terms of searching for a critical point. According to the quantum chromodynamics theory, with higher energy, higher rates of antiprotons will be produced. In theory, the universe is formed by matter, but not anti-matter. In another words, when the universe was just formed after the big bang, the ratio of various anti-matters versus various matters is one. Then, when the temperature and pressure cool down gradually, the anti-matters become matters until the ratio becomes 0. Previous experiments using RHIC show us that when the collision is running at low energy levels, the ratio of anti-protons versus protons is 0. It indicates that when everything is cooled down, no anti matters exist. On the other hand, it's also tested when the energy is at 200GeV the ratio of anti-protons versus protons is slightly below one. At 39 GeV, the fitting slope for the ratio of the plot is -0.1, and the error range is ±0.4. The value zero is sits well in this range. Therefore, the slope of the fitting for anti-protons versus protons is normal when compared to other collision energy levels. It's not likely for a critical point to exist at 39 GeV. As can be observed on the plot, the ratio has a value of 0.29 at 39GeV. (Figure 18)

The anti-proton versus proton ratio plot in our experiment is produced simply using all the anti-protons divided by protons. Fitting the graph after plotting is needed. A significant change in the fitting slope is expected at where the critical point exists. For all the energy levels that have been tested in RHIC, 7GeV, 19GeV, 27Gev, 39GeV, 63GeV and 200GeV, the lope of the fitting of anti proton vs proton are always very close to zero.

This tells the scientists that the expected Quark- Gluon Plasma is not occurring at those energy levels. They may be ruled out runs from the following years, and some other energy levels will be tested.

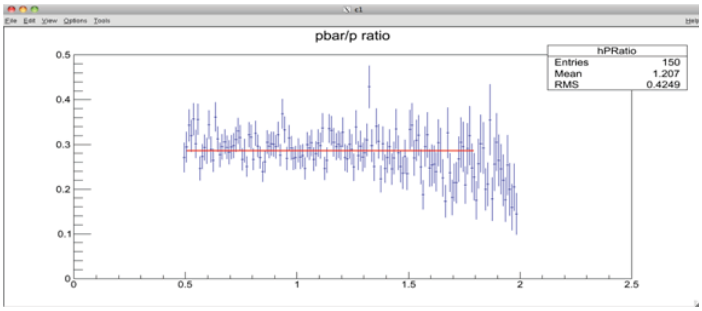

Figure 18

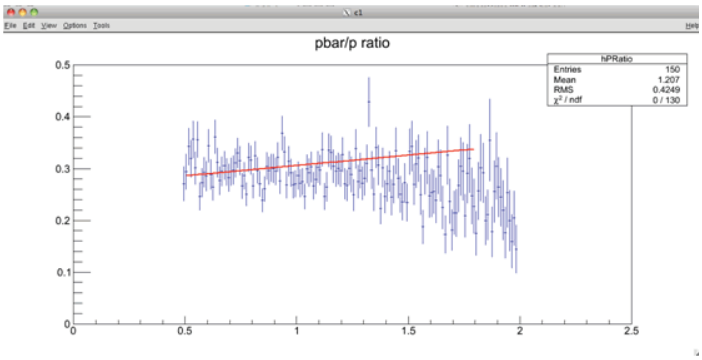

Figure 19

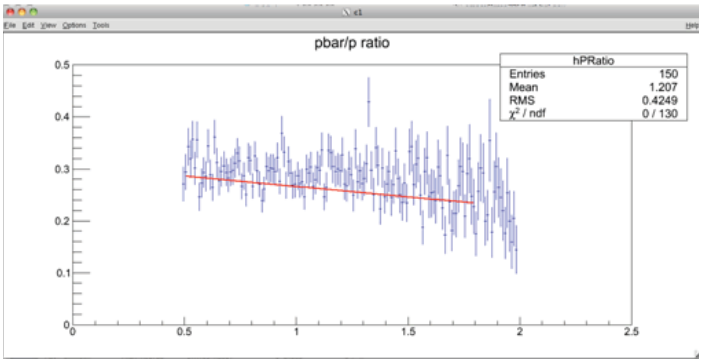

Figure 20

5. dn/dy Plots

The plot of 27 GeV is landing right on the fitting line for other gold-gold collision, which indicates little possibility that anything critical happens at this collision energy. (Figure 21)

IV. Result

As it shows on the dE/dy plot, the newly plotted point of 27 GeV is sitting right on the fitting line. In addition, the anti proton versus proton plot gives a ratio of slope close to zero. Therefore, there is no evidence for critical point existing at 27 GeV.

It is a success to see that the plots of the uranium collisions agree with the ones of the gold the first time we ran it. Our graphs prove that uranium collisions will achieve higher energy density compared to gold collision at the same collision energy when uranium particles' tip-to-tip collisions happen. That will produce a more favorable condition for us to search for the QGP.

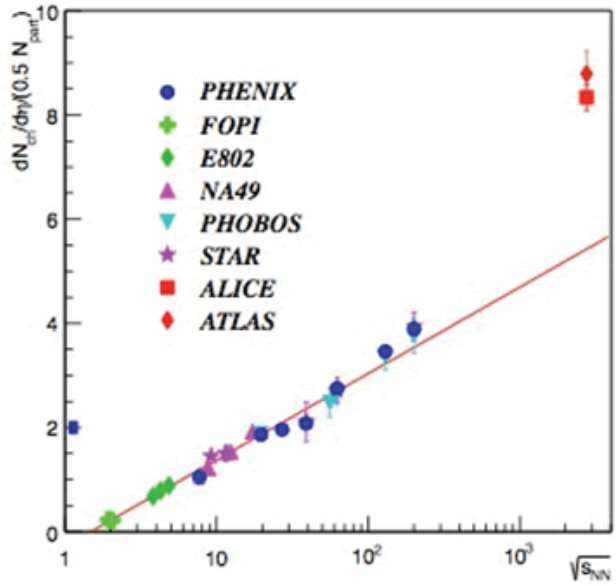

Figure 21

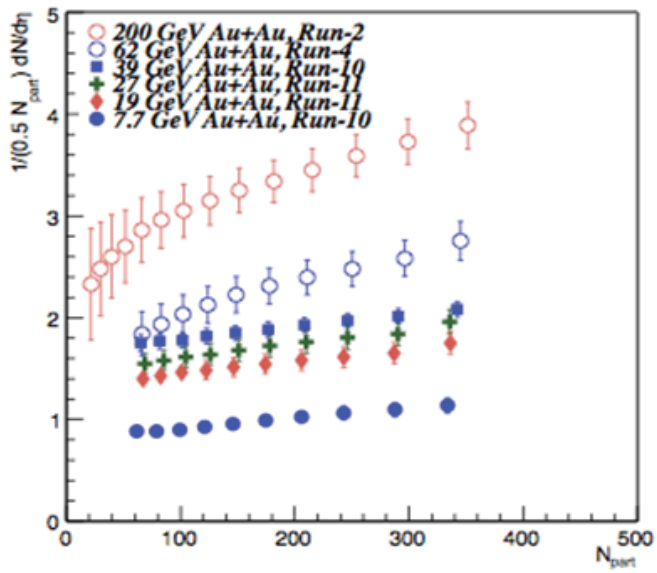

Figure 22. dn/dy plots for AuAu at all collision energy levels

V. Acknowledgements

I would thank the following. Dr. Jeffery Mitchell for his generous effort and patience to our team, helping us with our data analysis and calibration. The Department of Energy, and the Office of Educational Programs at Brookhaven National Laboratory. Dr. Raul Armendariz and Dr. Tak Cheung for giving me the precious opportunity to work in Brookhaven National Laboratory.

VI. Literature Cited

PHENIX Analysis Note 1054 Global Measurements for Au + Au, Cu+Au, Cu+Cu, and U+U Collisions. J.T. Mitchell, Mike Dai, Mingxiu Sun. July 30, 2012.

PHENIX Analysis Note 994 Charged Particle Multiplicity Analysis for the Run-10 7.7 and 39 GeV Au + Au Datasets. J.T. Mitchell. June 21, 2012.

Manipulating geo-spatial data for managing air quality control

Greg Swirson
Stony Brook University, Stony Brook, NY 11794
Terry Sullivan
Brookhaven National Laboratory, Upton, NY 11973

ABSTRACT

The issue of air quality control within subway systems is a large concern in the New York City area. If a chemical pollutant were to leak into a station, actions would be necessary to be taken in order to monitor and understand the flow of the contaminant. The Environmental Science Department at Brookhaven National Laboratory (BNL) is building equipment that can trace contaminations in the air in order to conduct studies in New York's subway systems that will determine air flow and air pollution concentrations. This project, the Subway Surface Air Flow Exchange (S-SAFE), helps ensure that health risks and damages due to a potential leak can be completed prevented or reduced. Using Python, a programming language, and ArcGIS, a geo-spatial analyst tool, I designed a template that can be used to create a support tool. The support tool would be a user interface where the user can plug in a station, the time a pollutant was measured, and the measured value of the pollutant. The script will then take the entered data and evaluate it based on an equation that I included in the interface code. Once the values are calculated over a period of time they can be exported into a format that will be read by ArcGIS. ArcGIS will provide a map of the stations organized by concentration at certain times.

I. INTRODUCTION

Geo-spatial data can be used to analyze crucial information in vital situations. One situation may be when New York City subway officials encounter a gaseous chemical leak in one of their stations that may be hazardous to subway users. The ultimate goal of my project was to create a program that can be used as a template for a decision support tool that could be used to control the damage from that specific situation, using data collected by the S-SAFE project. The tracer technology used in S-SAFE will tell the rate that air is exchanged from station to station. The main platform we decided to choose is ArcGIS, a geographical information system (GIS) based computer program which can analyze and display geo-spatial data. This program was the best option because its capability of analysis is far better than any other program available, and also provides access to a versatile programming language, Python. Python is an open source (free to share) language where all of the program coding could be written. The Python language allows you to compute complex calculations, create user interfaces, and execute commands within the ArcGIS window. These are the three main criteria needed to complete the goal. Since ArcGIS has Python built in, this would allow us to stay within one programming platform and cut the cost of any additional programs that are designed to do one of those specific functions. Another important feature needed is provided by the built-in extension, the tracking analyst which displays temporal data in a geo-spatial environment. This means time becomes a function of the map.

II. LIMITATIONS/RESTRICTIONS

In this project I had to use a lot of techniques that were completely new to me. I have never worked with differential equations, programming in any language, or even some of the more advanced features in ArcGIS, which was the bulk of my project. Another major limitation was time, especially because I would be learning these techniques from scratch.

III. THE CODE/OUTCOMES

A. The Equation

The equation uses Euler's Method for solving differential equations calculate the change in concentrations at specific locations over a period of time. The flow matrix will be populated by the actual data measured in New York City using the tracer technology. Currently, the flow matrix that is being used was made up by estimated flows that could represent a reasonable comparison to the actual data. Each station is represented by an index that represents the actual name from the NYC subway stations. Euler's Method uses small time step intervals. Written within the equation is a converter that takes a unit of time in hours, over a 24 hour period, and converts it into a time step so it can be plugged into the solving part of the equation. Concentration in the equation uses an arbitrary unit of measurement and can be entered. When the user enters these three values into the interface, the equation solves the concentration and how it flows for the 24-hour period. When the results need to be more accurate in the future, the Euler's Method will be replaced by the Runge Kutta Method which can provide different solving methods to create the accuracy.

B. The User Interface

The user interface allows a user to quickly enter a station identifier, a time of day, and a concentration. The original code written called for individual pop-up windows for each. When all the values are entered, a new window pops up with four buttons. Print, which showed the user what the populated matrices consist of, Plot, which shows the user a graph for each station, Export, which exports the data to a table in a format that ArcGIS can use, and Make Layer, which quits the window and creates a map in ArcGIS of all the stations including the data for concentration and time. The pop-up windows evolved into one user-friendly window that allows the user to enter multiple source concentrations at any time while having access to the button controls. The first new button is Update, which plugs the entered data into the solver. The buttons that did not change were Plot, Export, and Make Layer. The other two new buttons are Make Time Layer, which creates a layer in ArcGIS that uses the time data to display the changes, and Quit, which exits the window. These buttons need to be clicked in this order and they will not work if a previous button was not clicked.

C. The Map and Results

Already set up in this program there is a base map of imagery for the NYC area. This map has the actual MTA subway lines separated by line and displayed by color. Also included is every subway station as well as all of the entrances and exits to each station. When the user selects to make a layer, the program puts on the map image the points from every station, including tables that hold the data for the concentrations and times that were solved by the equation. When the user selects to makes a temporal layer, or time layer, it can display on the map an animation of how the concentration will flow over the time period of the simulation. The user can pause the animation at any time and check the data. It displays the station as a point and the point a certain color to represent concentration. The map also already provides population density information and MTA subway user traffic numbers for all times of the day. This would allow the user to see where they would need to act first in order to maximize the amount of people they could help. There is also a layer provided for bus stops and routes so that people could be rerouted if needed for a potential subway station closing.

D. Future work needed

The template in the end needs to be a working extension within ArcGIS so that the user does not even has to look at the code and just be provided the simple interface. When the flow data is gathered by S-SAFE it needs to be plugged into the flow matrix to be used by the equation. Currently the data entry uses a station index for the entry because that is what the code uses. There will need to be a database where the user selects the subway line and specific station by name and it will call that database and relate the selected name to the index so that it could then be plugged into the equation. This will make it easier for the user to select a station quickly and consolidate by line. A quick easy fix for the code to make the interface simple and neat it to combine all the steps that the user does while clicking buttons into one step. This way the user does not need to use the interface in a specific order and they can just see results in one step.

IV. CONCLUSION

The template can be used to provide a way to create an interface that could potentially save many lives. The results seen by just the template provide so much information already. If a contamination posed harmful health risks, this tool could be used to reroute trains, close off stations, and evacuate people to prevent spreading the pollutant and stop the exposure to subway users.

V. ACKNOWLEDGEMENTS

I would like to thank the following people:

My mentor Terry Sullivan for his guidance and the help he provided for me throughout my internship. Dr. Robert J. Frey for helping teach me method's in solving differential equations and with programming advice. Nathan Gubser for assisting me with programming advice.

A graphical user interface for cloud data discovery

Josh Tiffany
Southwest Baptist University

The Department of Energy's Atmospheric Radiation Measurement (ARM) Program measures cloud properties at a number of climatically important sites around the world. Long-term measurements are collected and made available to scientists who use the information in their research to better understand the impact of clouds on climate change and to improve global climate models. A graphical user interface (GUI) application, called SpectraView, exists to aid in data discovery and visualization. SpectraView was written in the proprietary IDL scripting language, which has drawbacks such as the cost of development licenses, the requirement for users to install the IDL virtual machine, and barriers to ongoing community development. In an effort to solve these issues and others, the decision was made to translate the program from IDL to the open source Python language during this summer internship.

To start out the summer, I was presented with a few different options for a summer project. The choices were to extend and quality test the current IDL SpectraView application, translate the IDL into some other language, or work on a simulator that would run alongside SpectraView. To figure out what I wanted to do, I had to spend about a week and a half playing around with the SpectraView. Karen also had a little learning time to teach what the entire program could do. She told me in more or less words, the user selects an ARM site, type of radar, and starting date. The day's time-height radar reflectivity data is displayed in the left-most panel. Right-clicking on the day image selects an hour. A set of buttons representing the available radar operating modes is enabled. Once a mode button is pushed, a close-up of the hour appears in the top middle pane. The user then selects a point of interest on the hour graph. The user can then 'Plot Spectrograms' to display time and height spectrograms as well as the Doppler spectrum at the selected time-height point (bottom right panel). Alternatively, the user can load the hour's 'Full Spectral Analysis' and examine additional related hourly images. Changes in the spectrum shape in time can be explored by clicking on the 'Next Time' or 'Prev Time' buttons under the time spectrogram, which redraws the spectrum in the bottom right pane. Similarly, changes with height can be viewed with the 'Height Below', 'Height Above' buttons under the upper right height spectrogram. Along with how the program works, she gave me an idea of what the data is. SpectraView is intended to assist users in visualizing cloud radar Doppler spectra in order to discover cloud features of interest. Each ARM vertically pointing cloud radar typically collects up to 15 gigabytes of cloud radar spectral data per day--hence the need for data discovery tools. The cloud radar Doppler spectrum is the distribution of the radar echo (returned by a pulse volume of cloud and/or drizzle droplets) over the range of velocities observed by the radar. Spectrum velocities can be related to droplet sizes, if vertical air velocity can be estimated. These Doppler spectra potentially contain a wealth of high resolution information on cloud and drizzle microphysical and dynamical properties. Such information is critical to improvements in the cloud parameterizations used in global climate models.

After studying the code, discovering what was created by what code, I had to change it in a way that displayed my knowledge of IDL and convince Karen that I could handle this project. I added two functional abilities to the application. The first was adding a simple menu item that actually did not really do anything. The second was much more practical, because it could possibly speed up the user's experience of the program. I noticed that the GEcopol button was the most used of the six at the bottom. The short sight could have been that I just used this button the most, but either way the user had to click one of these six buttons after selecting an hour to view. So to speed up this process, I changed the code to automatically show the GEcopol hour view when an hour is selected, without having to click the GEcopol button.

Having shown my knowledge of IDL, I was able to move on to the next step, selecting the project. We talked about which of the three might have the best return to the lab and to me. Extending and bug fixing the application would be easy to do, but it would not be much of project that I could display well saying, "Look what I have done." We could not yet work with the simulator because the designer in Canada had not sent it to us. So the best option was to translate the IDL application to some other language. But what language should I use? After the decision was made to translate the program, we needed to decide how and into what the program would be translated. One of the goals was that the program should look and feel the same as the original. We also needed to decide which programming language to use for the new program. Multiple problems existed with the current program like the cost of licenses, time and effort to download and install the IDL virtual machine, and such a restricted proprietary environment. To move away from these problems, we wanted a language that was open source. Although Python is the best known open source language available, I only had about two weeks of experience with it. Most of my coding experience was in Java, so the decision was between those two languages, Java and Python. Within the language, I needed to easily work, but the language also needed to have the right tools to expand the program from just the GUI. Expansion was the largest part of Karen's argument. Once I leave the internship, Karen will need to expand the program to include the underlying libraries. There is also a Python class and symposium this fall where she will use my work to show off the capabilities of working with Python in meteorology. So to have a good knowledge of the both sides of the argument, I did a little research of the GUI toolkits in Java as well as in Python. Java had some, but I think their size and complexity made them a little intimidating. Another argument against Java was that Oracle was often sending out updates which could easily break the program once it was deployed. Open source Python does not have that same problem. While looking at the toolkits for Python, the decision was sort of between TkInter and wxPython. In gen-

eral, wxPython was the hip new toolkit with a growing support base and better portability. TkInter was old news with bad looks and portability. The early code of TkInter with which I worked, seemed easier to pick up than wxPython, but that was because it was much more primitive, lacking functionality shine. So the decision was made to go with wxPython.

Starting out in this new toolkit in a language in which I had only had two weeks of experience, was not that bad. I had remembered a lot of the syntax differences from Java, which made working very smooth. But I had never done GUI work before, so I had to do a lot of combing through the web to find whatever I needed. I started the journey from a tutorial which compared TkInter to wxPython. I then found another tutorial to guide me in adding menu items, which I did. Following the menu, added the first text and buttons which are displayed in the first section, at the top of the program. I tried to add an image to the next part, and this is where problems arose. To get everything arranged nicely in the window, a sizer was used, the GridBagSizer. This sizer is the most complicated of the sizers, but that is because it allows the most functionality. In the end, many sizers were used to get everything lined up. Anyway, I struggled for about a week with getting the sizers correct to place everything in its proper place. The next big problem was putting images into the program. I wanted to just use a bitmap, but I was not able to switch those out. After another week of struggling and looking for an answer, the solution was found in the form of a StaticBitmap, allowing for switching of images. The rest of the layout of buttons, text, and images was placed and drawing was the next challenge. The user needed to see a box drawn when she clicked on the image. After a week of hunting for a solution to that, I found the fix in the form of a MemoryDC and I that I had to deselect the image after the box was drawn on it.

The future for this program includes adding full functionality to it. It must be able to contour the graphs itself by interpreting the raw data fed to it. I will be doing a few hours a week from my school while keeping up a phone and email relationship with Karen.

This internship has been an amazing opportunity. I am so thankful to have the opportunity of working with these brilliant people and doing a project that will for sure make a difference.

Comparison and optimization of mechanical designs for enhanced performance of the Long-Baseline Neutrino Experiment

Nikita Timofeev
Department of Mechanical Engineering, SUNY at Stony Brook, Stony Brook, NY, 11790
Craig Thorn
Department of Physics, Brookhaven National Laboratory, Upton, NY, 11973-5000

ABSTRACT

The Long-Baseline Neutrino Experiment (LBNE) will allow scientists to observe the interactions of neutrinos with matter and study the properties of the neutrinos. At the heart of the experiment is a 10 kiloton Liquid Argon Time Projection Chamber (LAr TPC) which makes neutrino interactions visible. Anode Plane Assembly (APA), a rectangular structure 2.5 m x 7.0 m x 5 cm thick, is the essential element of the detector. It is wrapped with three wire planes that collect the ionization charge of particle tracks to produce three dimensional images of interactions. Unfortunately, the wire tension deforms the frame, distorting the coordinate system, which is established by the nominal wire positions. Structural analyses of the mechanical components for the LAr TPC APA were conducted to compare and optimize two designs for enhanced performance of the LBNE project, while gaining engineering experience and learning new software. Using Finite Element Analysis (FEA) in Autodesk Inventor Professional 3D CAD software, functional behavior and physical performance of rectangular hollow frame members was evaluated. Design components were analyzed for deformations, tensile and compressive stress, strain, bending, and buckling. The structural analysis illustrates the weaker portions of the stainless steel APA frame and helps to better understand how to support the structure during transportation and installation. While my primary challenge was to learn how to use FEA in Autodesk Inventor and simulate the model, my goal was to improve the mechanical performance of the project.

I. INTRODUCTION

A. What are the Neutrinos?

Neutrinos are electrically neutral and weakly interacting elementary particles, leptons. Neutrinos have three flavors: electron neutrino, muon neutrino, and tau neutrino. Although the mass differences are known, the exact mass of the particles has never been measured. Since neutrinos are not affected by electromagnetic force, they can travel for a long distances through matter. Approximately 65 billion solar neutrinos per second pass through every cm2 of the Earth (420 billion every in2).[16]

B. Why are Neutrinos Important?

Standard model is a great basis for understanding the particle world, but it does not explain everything. [Figure 1] Scientists are hoping that neutrinos will give more knowledge about CP violation, matter and anti-matter asymmetry, and role of neutrinos in the universe.[12]

II. LONG-BASELINE NEUTRINO EXPERIMENT

Methods of Detecting Neutrinos. Detector Scales.

Since the original Cowan-Reines neutrino experiment, in the last 50 years, there has been a rapid development in particular of very large water Cerenkov neutrino detectors and large LAr TPCs. The first LAr neutrino detector that produced physics data in United States was ArgoNeuT.8 Its TPC was approximately 0.4m x 0.47m x 0.9 m, used 3 sense wire planes, and contained in 175L of LAr.5 The ionization charge from neutrino interaction products was measured on induction and collection wire planes to produce a three dimensional stereo image of the charged particle tracks.4 ArgoNeuT was the first step to building larger detectors with LAr.

A. Time Projection Chamber

As Figure 2 shows, LBNE is a successor of ArgoNeuT. It is the future generation of LAr detectors. The experiment will stretch from Fermilab to the Homestake Mine in South Dakota (~1300km). The LBNE beamline is intended to transport protons from the Fermilab Main Injector to a local target area, where the collisions generate a secondary beam of pions. This secondary beam, aimed toward the far detector, is followed by a decay-pipe in which the pions and muons decay into neutrinos to generate a neutrino beam that travels at almost the speed of light to the Homestake Mine.[10]

Once the beam reaches the Time Projection Chamber (TPC), and a neutrino strikes an argon atom, a collection of reaction particles is produced. The charged particles ionize the argon as they pass through it. Due to high applied electric field between Cathode Plane Assemblies (CPA) and Anode Plane Assemblies (APA) the ionization electrons drift to the APAs, which collect them and send the signals to amplifier boards. Neutrinos striking argon will produce the same flavor charged lepton; i. e., a muon neutrino

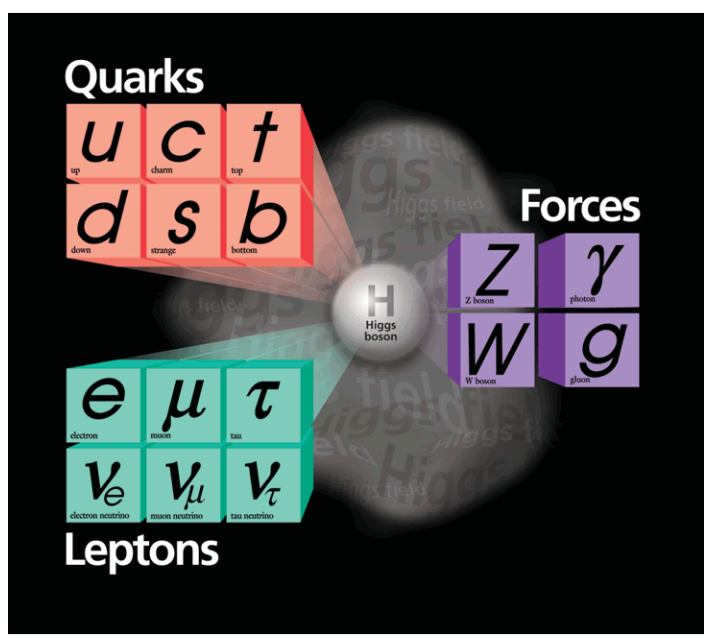

Figure 1. Standard Model as it is known today.

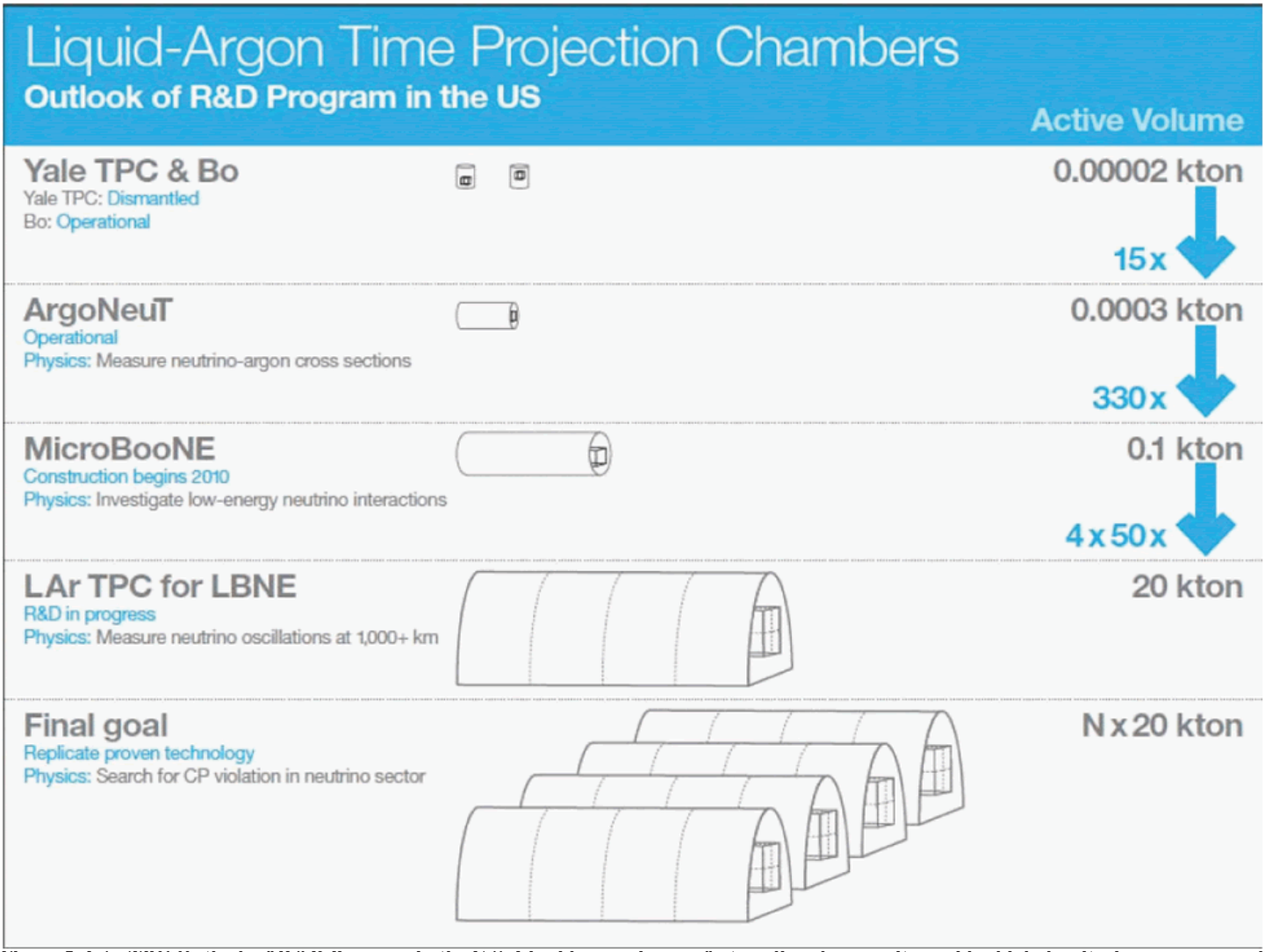

Figure 2. LAr TPC Outlook of R&D Program in the U.S. Liquid argon is a perfect medium because it provides high density, is very pure, and allows charge and light to propagate long distances.[1]

will turn into muon--its charge flavor partner--where an electron neutrino will turn into an electron.

The volume of the TPC contains the interactions of the neutrinos. It consists of APAs and CPAs fully immersed into LAr at a temperature of 87 K. Figure 3 illustrates one pair of APAs mounted between two pairs of CPAs. The size of a single TPC module is 14.0 m x 2.5 m x 2.5 m, and encloses 61 tons of LAr. Each 5kt cryostat contains 60 TPC modules.[9]

B. Anode Plane Assembly

The frame is 7m long by 2.5m wide (5mm thick) and consists of 4”x2” and 2”x2” (1/8” thick) rectangular hollow tubing. There are 4 supporting members inside the frame. The material used is stainless steel grade 304 (SS304). Wires spread in three directions: diagonal at 45.7^0 (U), diagonal at -44.3^0 (V), and vertical (X). The wire pitch is 5 mm. Each wire is stretched at a tension of 0.5 kg (5N).

C. Experiment Set-Up

Figure 4 illustrates a single lower APA, which was used in analyses. The simulations attempt to predict the behavior of the lower APA, since it will be subjected to the most stress in the assembly. The lower APA is attached to the one above by bolts through the openings in the 4x2 members and hangs downwards. This analysis does not take into consideration density and temperature effects of liquid argon on the strength of the frame or the wires, and the buoyancy effect of the LAr. In cryogenic environment the yield strength will increase.2 Wire tension is assumed to be uniform throughout. The frame is analyzed after the entire unit is wrapped around wires. Although this analysis is supposed to look at two existing designs of APA frame, since the structural appearance is nearly identical, all calculations were done for the design with higher loads (D2). Table 1 provides information about the applied loads on the frame. (See Figure 4 to understand how the loads are applied.)

The longer edge of the frame remains under the same loading conditions because only U and V planes are attached to that member. However, the loading conditions vary for the shorter edge. Oleg Prokofiev’s design includes an extra wire plane to provide the ground, where Bo Yu’s design simply uses wire mesh with no tension. This creates almost 34% less force on the member. Therefore, it is fair to test both frames for the same conditions.

III. RESULTS and METHODS

A. Finite Element Analysis

Finite Element Analysis was done in Autodesk Inventor Professional software. Some issues were encountered with the frame generator tools. Unfortunately Autodesk part library does not

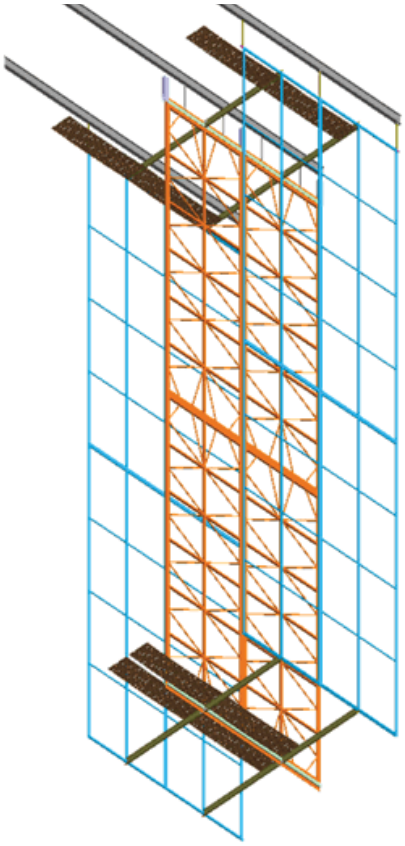

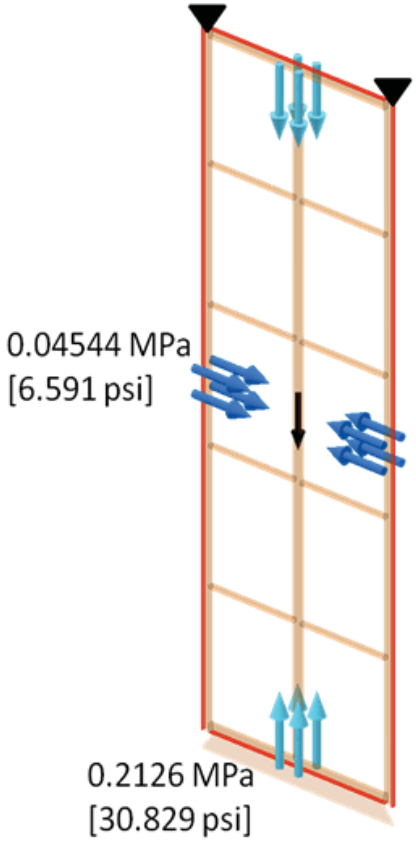

Figure 3 (left). Time Projection Chamber.
The bracing of the APA shown here has been replaced to a simpler one with four equally-spaced 2"x2" tubing. It is 1/30th of the 5 kt cryostat. [CPA in blue, APA in orange]

Figure 4 (right). Orientation of a single lower Anode Plane Assembly in a simulation environment showing compressive loadings from the wire tension. [See Table 1]

have every beam cross section, and specifically for this study a 4x2x1/8" hollow rectangular cross section was required but not available in the library. It was decided to create a new type of tubing with the missing cross section. Once the part was added to the library, it did not work properly in the frame analysis environment and was discarded. That is the main reason why stress analysis environment was used for this simulation.

Stress analysis added more options and flexibility to the model. It was possible to create custom beam cross sections as well as to model welding joints. Although it required more time to create a model, it was possible to generate a more realistic structure. Also stress analysis created a mesh (a mosaic of pieces connected with nodes), which allowed for a more detailed analysis.

CALCULATION OF LOADS APPLIED TO THE MEMBER – BO YU's DESIGN (D1) [17]										
	Short Edge					**Long Edge**				
	G	X	U	V	Mesh	G	X	U	V	Mesh
# of wires per plane	560	560	360	360	0	0	0	1000	1000	0
Tension along wire axis [N]	2800	2800	1800	1800	0	0	0	5000	5000	0
Total load on the member [N]	**16290**					**14139**				
Stress/ Pressure [MPa]	0.15818					0.045442				
Distributed Load [N/mm]	7.0313					2.01989				

CALCULATION OF LOADS APPLIED TO THE MEMBER – OLEG PROKOFIEV's DESIGN (D2) [15]										
	Short Edge					Long Edge				
	G	X	U	V	Mesh	G	X	U	V	Mesh
# of wires per plane	560	560	360	360	560	0	0	1000	1000	0
Tension along wire axis [N]	2800	2800	1800	1800	2800	0	0	5000	5000	0
Total load on the member [N]	**21890**					**14139**				
Stress/ Pressure [MPa]	0.21256					0.045442				
Distributed Load [N/mm]	9.44843					2.019888				

Table 1. Calculations of applied loads on the member.

B. Comparing APA Designs

	Bo Yu Design	Oleg Prokofiev Design
Wire Winding Technique	Conventional wire-winding machine	Transfer frames, Wire module contains 64 wires
	~Wires are wrapped around the APA frame. Wrapping boards are preassembled to the frame. Winding machine determines the tension and the placing of the wire.	~Wires are wrapped onto transfer frames first. Then soldered to the modulus board. Epoxy strip is applied to secure the wire. A single 64-wire module could be stored or positioned on the frame. Winding machine determines the tension and the placing of the wire.
Number of Wire Planes	X, U, V, Grid (4)	X, U, V, Grid, Ground (5)
Mounting Method	Steel pin through the frame	Steel pin through the frame
Wire Attachment	Epoxy and solder	Epoxy and solder
Wire Cleaning/ Flux Removal	Must be done on entire wire frame	Done on a single 64-wire module
Repair of a Broken Wire	Must restring entire plane	If the wire broke on the outer plane, replace the module. If the breakage is internal, must restring entire plane.
Structural Appearance	2 - 4”x2”x7000mm 1 - 4”x2”x6796.8mm 2 - 4”x2”x2316.8mm 4 - 2”x2”x1107.6mm	2 - 4”x2”x7000mm 1 - 4”x2”x6796.8mm 2 - 4”x2”x2316.8mm 4 - 2”x2”x1107.6mm
Dead Space	Wire Support ~ 1mm Long Edge - 8mm Short Edge - 14 mm	All Edges (except for amplifier side) ~ 33mm Solution: mount additional boards along the edges.

Table 2. APA Features Compared.[14]

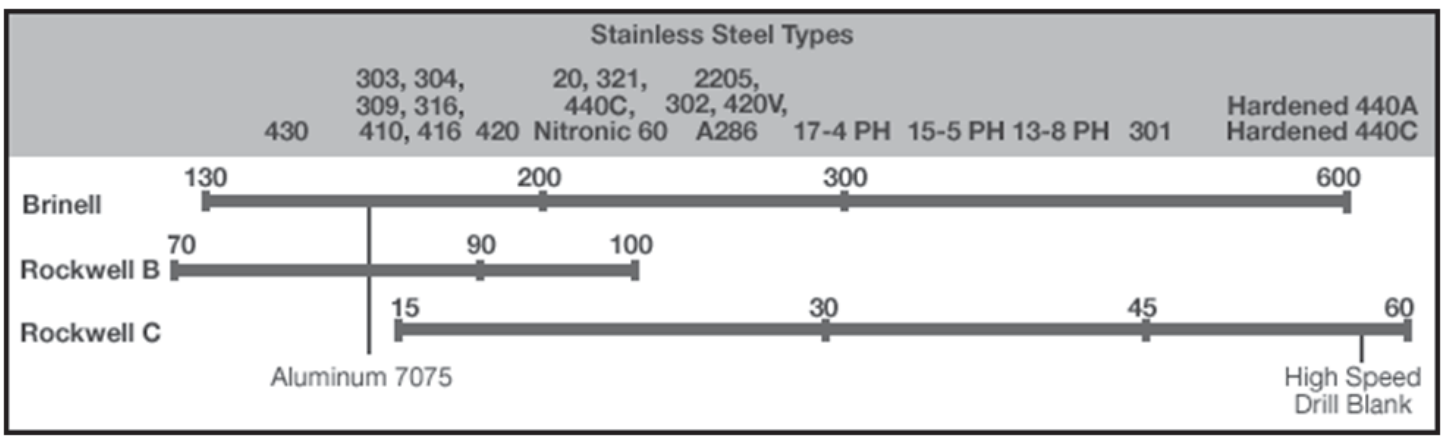

Figure 5. Hardness for Stainless Steel.
The hardness of a material is its resistance to another material penetrating its surface. Harder metals have more wear resistance, but they are also more brittle. [1]

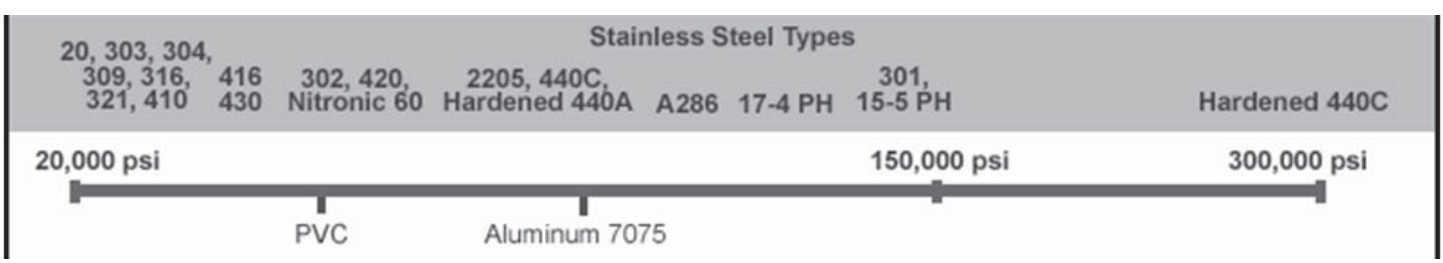

Figure 6. Yield Strength for Stainless Steel.
Yield strength is the point at which metal bends and will not return to its original shape. At this point the metal has changed shape permanently but does not break. [1]

C. What is the Importance of Tension?

It is crucial for LBNE to have constant uniform tension in the wires. The wires are the coordinate system and provide exact location of the particle, collected on the wire. Low and high tensions can be caused by deflections and bending of the frame. To minimize the effects of the coordinate system distortion, the deflection have been specified to be less than 0.5 mm. There are three causes for the propagation of wire sag in the planes:

- Gravitational wire sag – causes distorted measurements from the shift in the coordinate system.
- Electrostatic wire sag – since wires have charge, having them closer to each other will lead to electrostatic displacement, also distorting the coordinate system.
- Microphonic effect – the wires will move with motion of the liquid argon, either from acoustic waves or liquid flow, making the coordinate system time dependent. [13]

Vertically oriented X and ground wires won't be affected by the gravitation since they are parallel to it in the hanging position.

Additionally to deflection, maximum von Mises and principal stresses are important in identifying factor of safety of the structure. The yield strength of SS304 is approximately 205 MPa (30 ksi).6 Once the material starts to deform plastically that means it has reached its yield strength. The minimum factor of safety can be calculated if the yield strength and design stress are known.

	Alternative Frame Model 1 [2x2x1/8]	**Current Frame Model [2x2x1/8 + 4x2x1/8]**	**Alternative Frame Model 2 [2x2x3/16 + 4x2x3/16]**
Deflection	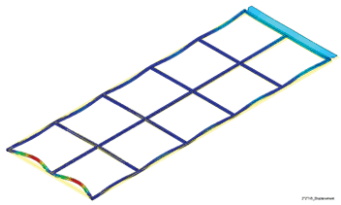 Maximum Displacement: 1.532 mm (0.0603 in)	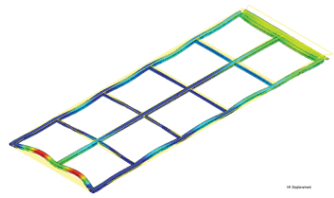 Maximum Displacement: 0.3475 mm (0.0137 in)	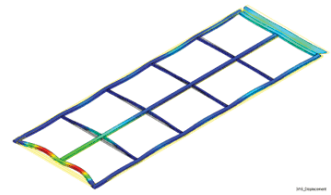 Maximum Displacement: 0.2402 mm (0.00945 in)
Von Mises	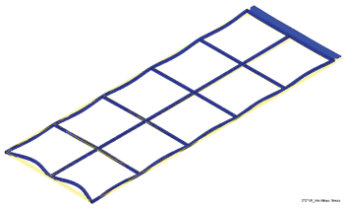 Maximum Von Mises Stress: 575.8 MPa (83512.7 psi)	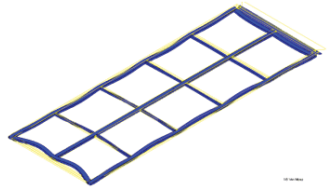 Maximum Von Mises Stress: 304.6 MPa (44178.4 psi)	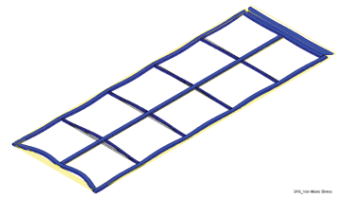 Maximum Von Mises Stress: 68.88 Mpa (9990.2 psi)
Factor of Safety	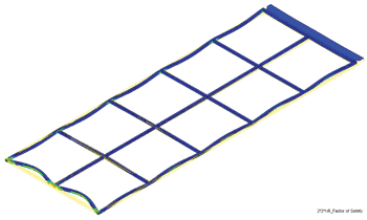 Minimum Factor of Safety: 0.49	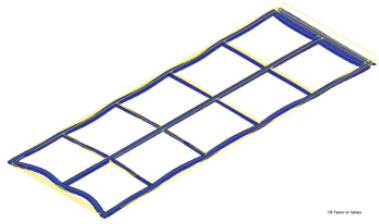 Minimum Factor of Safety: 0.74	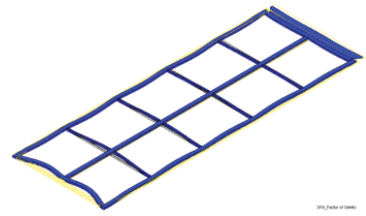 Minimum Factor of Safety: 3.12
Welding Joint Safety Factor	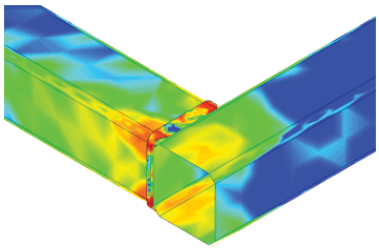	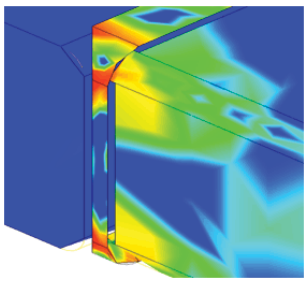	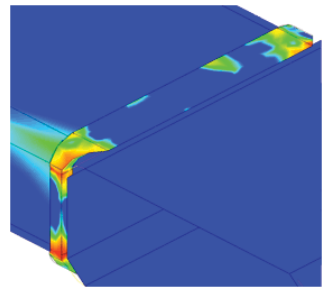

Table 3. Simulation Results.

While running simulations, I looked at the various types of stainless steel trying to substitute for the currently used SS304, and found that there is no major difference among 300 series in the material strength. However, only SS304 and SS316 are available in rectangular/square shape on the market. SS304 on average is 20-25% cheaper than SS316.1

IV. Simulation Discussion

In order to better understand the behavior of the APA frame, similar frames were modeled and subjected to identical loads. The entire alternative frame model 1 consists of 2x2x1/8" SS304 tubing. The benefits that this frame has over the other two are: lower material costs, lighter weight, and manufacturability. However, the frame proved to be weak and unstable, with the deflection three times larger than the allowed. Another structural disadvantage of 2x2" is higher buckling chance and available inner space. 2x2" members will have only 1x1" opening vacant for the cables and wiring, which is insufficient.

Current frame model proved that it will not deflect more than 0.5mm. It consists of 4x2x1/8" and 2x2x1/8" tubing. Since I didn't model the welding joints specifically, the simulation points out those regions with the factor of safety less than 1. Welds won't fail if they are properly done. Also it can be observed that the stress at the joints decreases as the structure becomes stronger. That is why alternative frame model 2 was model using 4x2x3/16" and 2x2x3/16" tubing, which provides much stronger construction. The displacement is half of the maximum limit and the factor of safety is more than 3. This also means that the welds are not failing. Since 3/16 is a thicker material it provides enough area for a proper welding joint in alternative frame model 2.

A. What could be Done Differently

However, with very small additional costs current design can be improved by inserting gussets in the location of most stress concentration. A triangular piece 1/8" thick was placed in four corners of the frame. The gusset is 500mm by 500mm and has a small cut out to not interfere with the weld. Material is identical to the frame, which is stainless steel grade 304. The simulation showed that the deflection decreased from 0.3475mm to 0.2838mm, von Mises stress decreased almost by 45%, allowing for an increase in minimum factor of safety to 1.34. This means that with small additional material and labor costs it is possible to create a much stronger frame.

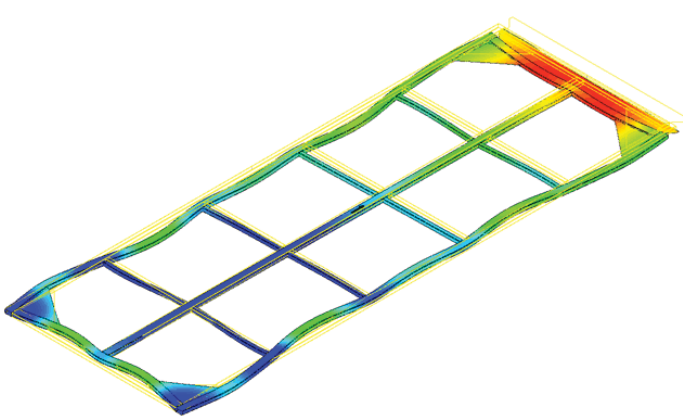

Table 5. Simulation Results. Frame with Gussets.
Max Displacement: 0.2838mm

B. Deformation in Frame Handling

It is important to look how the frame behaves without any wires as well. The longest beam is 7m and at such long spreads one can expect the beam to sag. The deflection of a simply supported beam can be calculated by the formula:

$$\Delta = \frac{PL^3}{48EI} \qquad I = \frac{\left(w_o * h_o^3\right) - \left(w_i * h_i^3\right)}{12}$$

Depending on the orientation of the beam the deflection will be different. [See Figure 7] For 7 m long 4"x2" (1/8" thick) beam the deflection in orientation 1 is 5.3 mm, where in orientation 2 it is 1.95 mm.

Therefore, there could be two ways of orienting the frame in space – orientation 1 (or horizontal) and orientation 2 (or vertical). The moment of inertia for each orientation will be different, leading to a different deflection. [3]

Table 4 demonstrates that under its own weight the frame will sag in gravity. However, frame in orientation 1 deflected more than a single beam, where frame in orientation 2 deflected less than a single beam. This suggests the frame is stronger in vertical position than in horizontal.

V. CONCLUSION

Three distinct cases were selected to optimize the design. Using Autodesk Inventor Professional, I was able to better understand the structural behavior of the APA frame. Analysis suggests that the alternative model 2 (beam thickness 3/16"), with a factor of safety greater than 3, is an optimal solution. Another proposition is to add gussets to the current frame design to reinforce

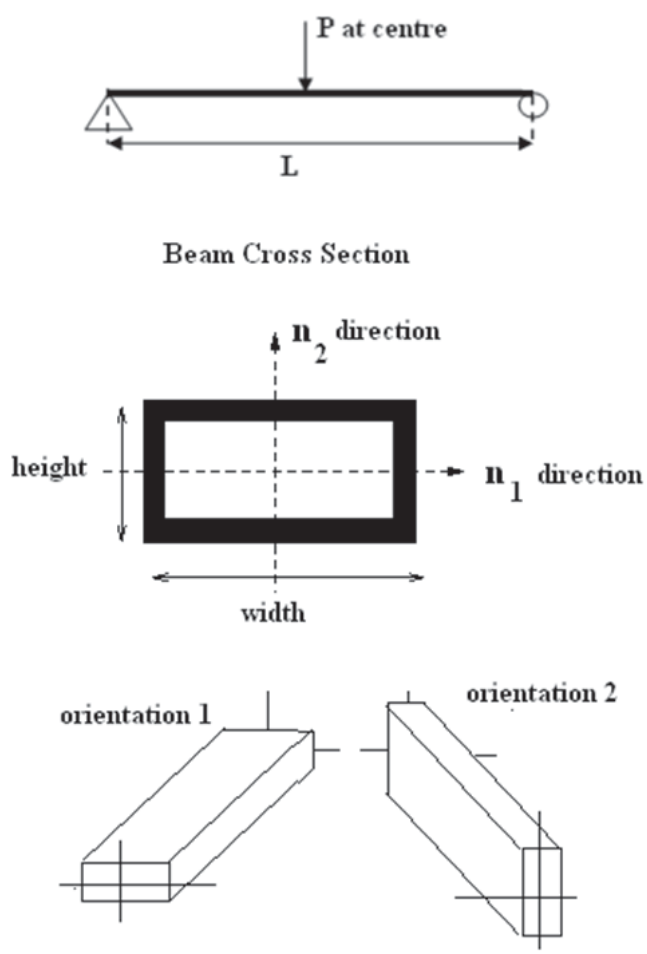

Figure 7. Beam Deflection and Two Possible Orientations

the strength of the beams and distribute stress on the joints more evenly. Handling methods still need to be developed to minimize stress the frame and wires during transportation. However, it is suggested to orient the frame vertically (orientation 2) to decrease any possible chance of wire breakage while moving.

VI. APPENDIX

A. Acknowledgements

I wish to thank my mentor, Dr. Craig Thorn, for giving me an opportunity to be a part of LBNE project this summer, for his guidance, and generosity. Additionally, I would like to express my gratitude to Rahul Sharma, George Mahler, Bo Yu, and Oleg Prokofiev for their help in this project, as well as Jason Farrell and Richard Ruggiero for helpful discussions. Finally, I wish to thank the Office of Science Education, Brookhaven National Laboratory, and the Department of Energy for this incredible experience.

VII. Works Cited

"About Stainless Steel." McMaster-Carr. Web. 15 Aug. 2012. <http://www.mcmaster.com/>.

"Stainless Steels for Cryogenic Applications." KEY to METALS. Web. 16 Aug. 2012. <http://www.keytometals.com/page.aspx?ID=CheckArticle>.

"Strength of Materials - Mechanics of Materials - Engineers Edge." Strength of Materials - Mechanics of Materials. Engineers Edge, LLC, Web. 31 July 2012.

"First Measurements of Inclusive Muon Neutrino Charged Current Differential Cross Sections on Argon", C. Anderson et al. (ArgoNeuT), Phys. Rev. Lett. 108 (2012) 161802, arXiv:1111.0103

Anderson, C., et. al. "The ArgoNeuT Detector in the NuMI Low-Energy Beam Line at Fermilab." ArXiv:1205.6747v2 [physics.ins-det]. N.p., 5 June 2012. Web. 20 Aug. 2012. <http://arxiv.org/abs/1205.6747v2>.

Frame in Orientation 1 (Horizontal) **Max Displacement: 7.113mm** **Max von Mises: 358.5 MPa** **Min Factor of Safety: 0.84**	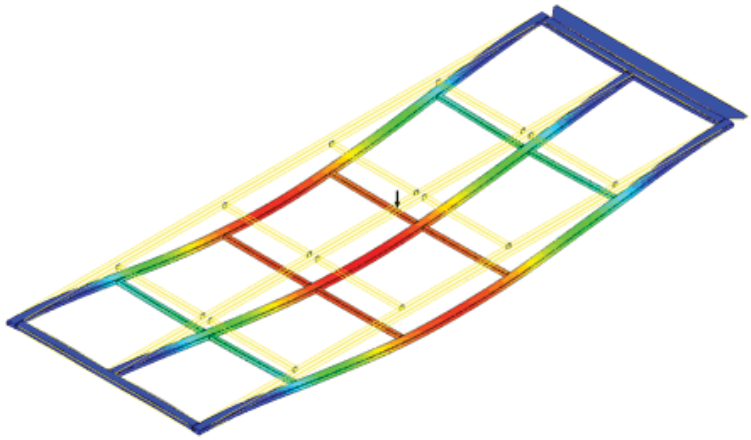
Single beam **Max Displacement:5.251mm**	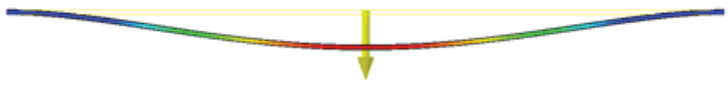
Frame in Orientation 2 (Vertical) **Max Displacement: 1.484 mm** **Max von Mises: 340 MPa** **Min Factor of Safety: 0.67**	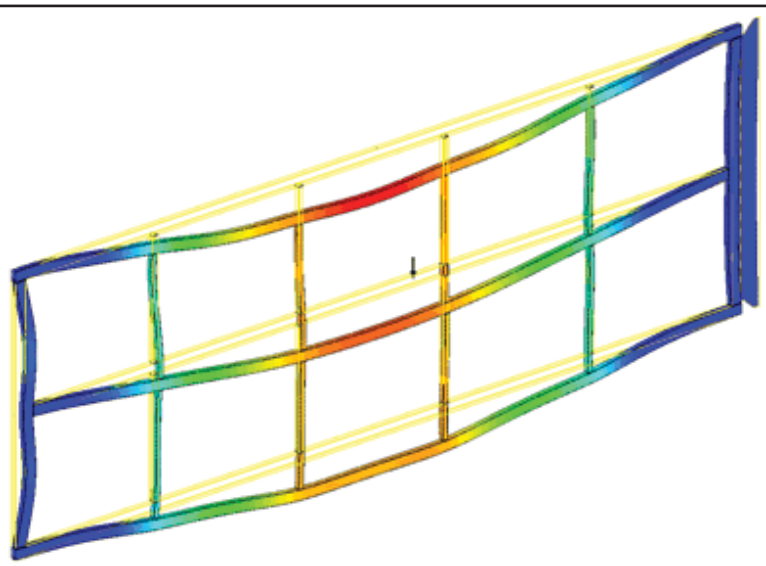
Single beam **Max Displacement:1.95mm**	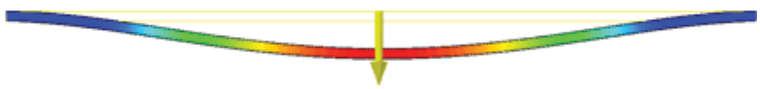

Table 4. Deformation in Frame Handling. Two Orientations.

Baddoo, N. R., and B. A. Burgan. “Structural Design of Stainless Steel (SCI-P291).” Online Information Center for Stainless Steel in Construction - Design. The Steel Construction Institute, n.d. Web. 06 Aug. 2012. <http://www.stainlessconstruction.com/design>.

Diwan, Milind. “Physics and Feasibility of a Very Large Detector“. http://lbne.fnal.gov/. Fermi National Accelerator Laboratory, 24 Nov. 2009. Web. 30 July 2012

Fermilab. “ArgoNeuT: Mini LArTPC Exposure to Fermilab’s NuMI Beam.” ArgoNeuT. N.p., n.d. Web. 06 Aug. 2012. <http://t962.fnal.gov/>.

Fermilab. “CDR Volume 4: The Liquid Argon Detector at the Far Site. Document 4892-v8.”, 15 Mar. 2012. Web. 20 Aug. 2012.

Fermilab. “How Does LBNE Work?” Fermilab. Web. 06 Aug. 2012. <http://lbne.fnal.gov/how-work.shtml>.

Fermilab. “Liquid Argon R&D at Fermilab.” About LArTPC R&D at Fermilab. N.p., n.d. Web. 06 Aug. 2012. <http://www-microboone.fnal.gov/public/about_r_and_d.html>.

Fermilab. “Why Neutrinos?” Web. <http://lbne.fnal.gov/why-neutrinos.shtml>.

Hagiwara, K., et. al. “Review of Particle Properties.” Phys. Rev. D 66, 010001 (2002). 1 July 2002. Web. 20 Aug. 2012. <http://prd.aps.org/abstract/PRD/v66/i1/e010001>.

Johnson, Marvin. “Compare of Design Alternatives for LBNE Anode Plane Arrays.” Fermi National Accelerator Laboratory, Web. 06 Aug. 2012. <http://lbne.fnal.gov/>.

Prokofiev, Oleg, E. Borissov, and S. Cheban. “Updated TPC Design for Mass Production.” http://lbne.fnal.gov/. Fermi National Accelerator Laboratory, 16 May 2011. Web. 27 June 2012.

University of Massachusetts at Amherst. “Measuring elusive solar neutrinos flowing through the Earth, physicists learn more about the sun.” ScienceDaily, 11 Oct. 2011. Web. 6 Aug. 2012. <http://www.sciencedaily.com/releases/2011/10/111007113949.htm>.

Yu, Bo. “FD Time Projection Chamber Mechanical WBS 130.05.04.” http://lbne.fnal.gov/. Brookhaven National Laboratory, 26 Mar. 2012. Web. 20 June 2012.

Examining the hydrogen purification performance of an electrochemical separation system

Daniel Weinman and Hazem Tawfik
Department of Mechanical Engineering Technology, Farmingdale State College, Farmingdale, NY 11735
James Wegrzyn
Department of Sustainable Energy Technologies, Brookhaven National Laboratory, Upton, NY 11973

Abstract

An electrochemical separation system was experimentally tested using a membrane electrode assembly to purify hydrogen from gas mixtures containing carbon monoxide and methane with hydrogen. Current was applied to the electrochemical cell ranging from 0.25-2.25 amps to pump protons across the membrane. A gas chromatograph was used to determine that the electrochemical cell was able to purify hydrogen to <10 ppm of CO and methane. The exiting hydrogen was compressed to pressures exceeding 50 psi in a closed system arrangement. The applied current in an open system showed a linear relationship with the purified hydrogen flow rate which resulted in an optimal product flow rate of 16 cubic centimeters per minute occurring at the greatest current of 2.25 amps. This system has proven its ability to produce pure hydrogen at flow rates required by fuel cells in addition to its ability to compress hydrogen for storage.

I. Introduction

Today's society is dependent on the use of fossil fuels as the main source of energy. Fossil fuels are not only expensive but they are also severely pollutant to the earth's environment and this has increased demand for a cleaner alternative energy source. Hydrogen (H2) is known for its unique properties and is a leading candidate to produce clean and renewable energy. Currently, there is a considerable focus on the research and development on new systems for producing pure hydrogen from biomass. Biomass is a renewable organic/plant material such as wood chips, agricultural crops farm waste, etc. with excellent potential to be converted into hydrogen fuel for a Proton Exchange Membrane (PEM) fuel cells (Figure 1). This process starts with a source of biomass which is fed to a gasifier to be heated to a temperature of about 700°C. Air, steam, and a controlled amount of oxygen (O2) are combined with biomass inside the gasifier. This O2 level is controlled at approximately one-third the amount needed for combustion. When heated in an oxygen deficient environment, the gasifier produces synthetic gas (syngas) composed of 10% carbon dioxide (CO2), 20% carbon monoxide (CO), 19% hydrogen (H2), and 51% nitrogen (N2). The main objective of the present work is to extract the hydrogen from the syngas and minimize or eliminate CO from the hydrogen before feeding and powering the PEM fuel cell. It should be noted that a small amount (>10 ppm) of CO can severely damage the catalyst in a PEM hydrogen fuel cell. Many studies have proven that negative impacts occur in the presence of CO, as Cheng, et al. states.1 Therefore, hydrogen gas must be cleaned by extracting CO from the syngas and purified to 99.99% before it can be admitted in a PEM fuel cell to produce combined heat and power (CHP). For this reason, an electrochemical separation system is integrated into the system to separate and purify hydrogen. However, syngas must be first treated using the water-gas-shift (WGS) reaction to reduce the CO concentration in the syngas before being admitted to the electrochemical separator since the active platinum catalyst, similar to the proton exchange membrane, can be contaminated from a presence of high CO concentrations.

The water-gas shift (WGS) reaction is an ideal system to reduce the CO concentration while increasing the hydrogen concentration in the syngas. The WGS lowers the concentration of CO in the syngas by converting it to CO2 which is less harmful to the electrochemical separator. The WGS reaction using copper zinc oxide catalyst oriented in a packed bed arrangement is currently under analysis by another research group.

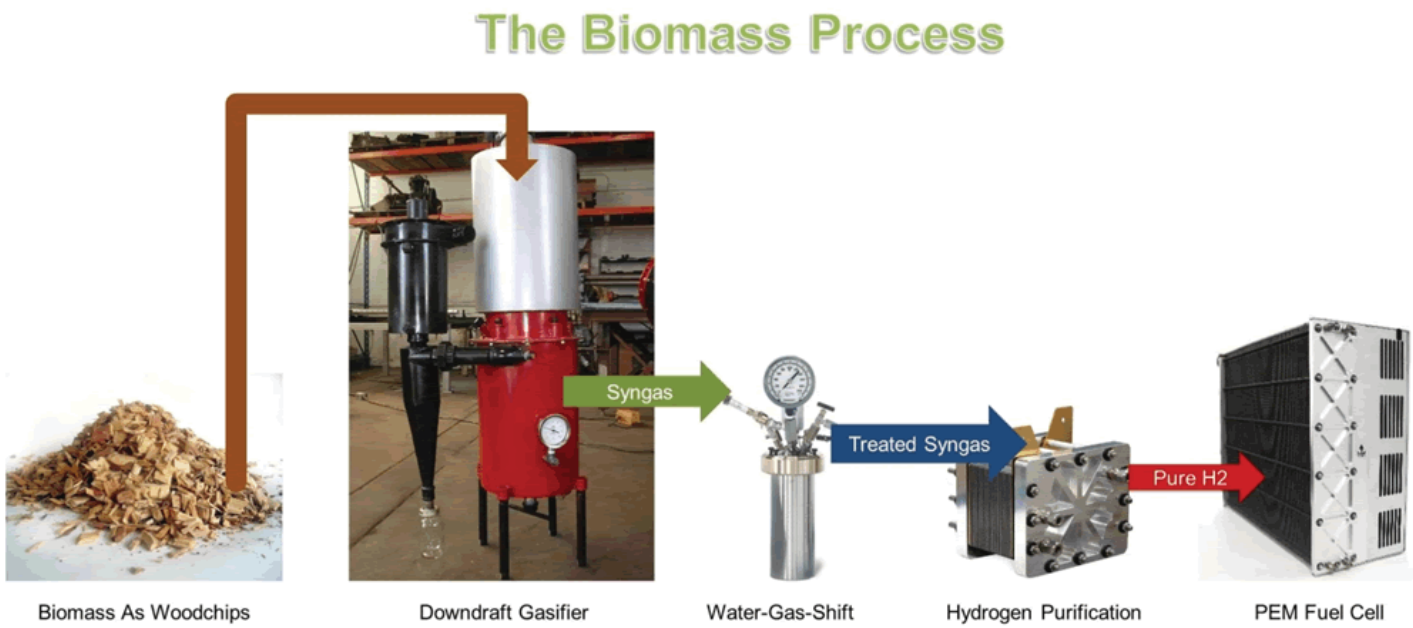

Figure 1: The biomass process that is under development at Farmingdale State College.

The electrochemical separator, also known as a hydrogen pump, is very similar to a PEM fuel cell in that it uses the same membrane electrode assembly (MEA). Figure 2 shows a schematic of a standard PEM fuel cell producing an electric load, which is comparable to the hydrogen pump shown in Figure 3. This MEA composed of a polymer electrolyte is only permeable to hydrogen protons, which gives the hydrogen pump its ability to separate hydrogen from mixed streams of gases. As stated by Onda, et al., an external source of power must be applied to the hydrogen pump in order to dissociate the hydrogen gas molecules and propel the proton across the membrane while the electron travels through the electrical circuit.2 The positive terminal is placed on the input chamber which is also called the anode chamber. The negative terminal is attached to the output side which is called the cathode chamber.

Aside from purifying hydrogen in a biomass process, electrochemical separation systems have been developed in the past to study its efficiency when used in a steam reformation process.3 Additionally, the hydrogen pump can also be used to compress hydrogen for storage purposes.4 When the fuel cell is not consuming hydrogen, the hydrogen pump can continue to compress and store hydrogen surplus. The versatility and efficiency of the hydrogen pump is what makes it an ideal candidate for use in a biomass process.

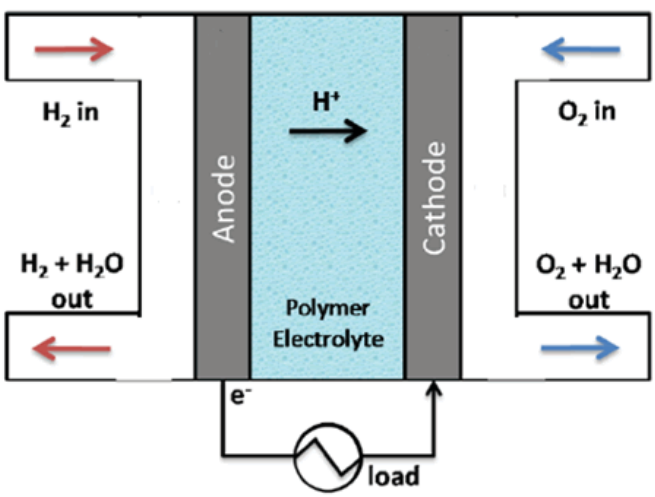

Figure 2: Standard PEM fuel cell producing electrical power.

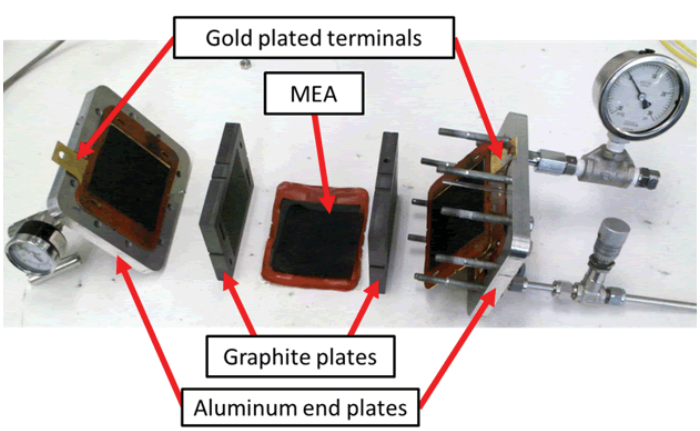

Figure 4: Exploded view of the electrochemical cell.

II. Materials and Methods

A. Apparatus

The electrochemical separation module that was used in this study had originally been manufactured and assembled at Farmingdale State College in the Institute for Research and Technology Transfer (IRTT) with the intention of being operated as a single cell PEM fuel cell. The module consists of two aluminum end plates, two gold plated terminals, two graphite plates that have a designed and machined serpentine as well as a membrane electrode assembly MEA as shown in Figure 4. The MEA consisted of a 5 layer design that includes a nafion membrane that allows for proton permeation only and is located in the center of this assembly. Two layers, one on the cathode side and one on the anode side of the membrane, consisted of a platinum catalyst loading of 4.0 mg Pt/cm²/side. The two outside layers of this assembly were gas diffusion layers. The module has 50 cm2 of active membrane area and the MEA thickness is 0.035 inches. When assembled as shown in Figure 5, the body of the module is approximately 2.25 inches thick, 5.5 inches in width, and 4.5 inches in height. The input, vent and output plumbing have all been labeled in Figure 5.

B. Experiment Setup and Materials

A schematic displaying the entire experimental setup is shown in Figure 6. Stainless steel fittings and valves were installed onto the module to incorporate a pressure gage on both the anode and cathode side of the electrochemical cell. The pressure gage on the input side was able to measure a range of -30 in Hg to 30 psig which was necessary to record negative pressures occurring in the anode chamber. A pressure regulator was used to control the feed pressure that was delivered from the high pressure gas tank. A flow meter was also inserted into the system to record the

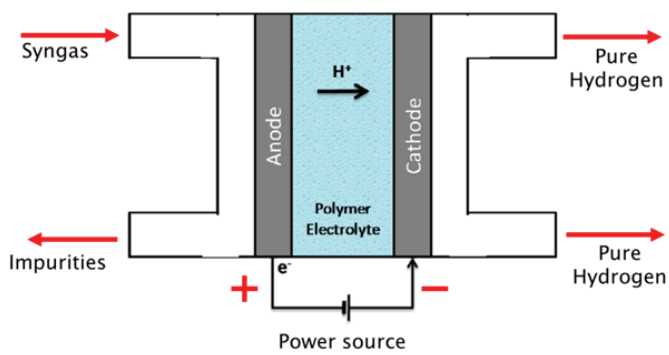

Figure 3: Hydrogen pump with power being applied to purify syngas to pure hydrogen.

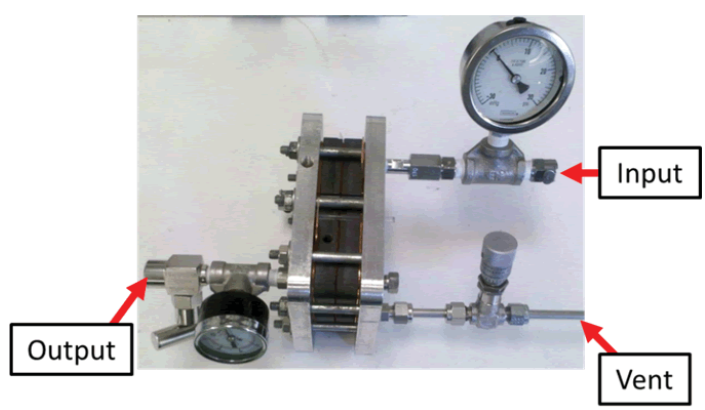

Figure 5: The assembled electrochemical cell.

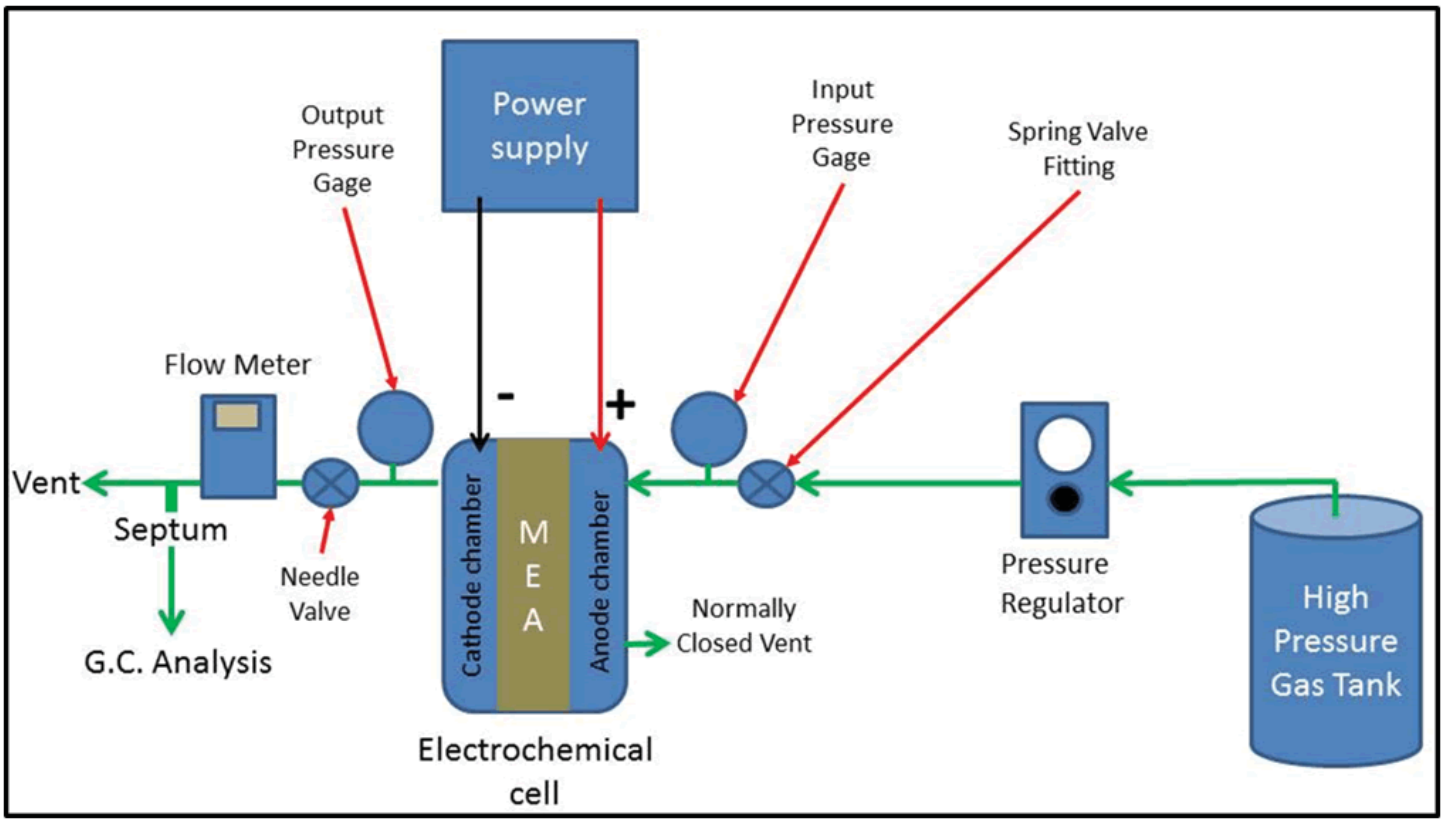

Figure 6: The experimental setup schematic.

volumetric flow rate that was being produced by the hydrogen pump. One of the most important components of the system was the DC power source used to apply an adjustable range of electrical current.

In order to simulate the product gases resulting from the WGS reaction and be able to test for the hydrogen pumps separation ability, two 500 cubic centimeter tanks were used for generating sample gas mixtures of desired composition. The first tank was filled with 80 psi of pure hydrogen gas and 20 psi of pure methane gas with the intentions of creating a mixture containing 20% methane and 80% hydrogen. The actual tank composition was tested using a Gow-Mac Series 580 Gas Chromatograph (GC), which is shown in Figure 7. The results showed that the tank consisted of 11.66% methane and 88.34% hydrogen, this discrepancy in the gas content is attributed to the slight lack of accuracy in the pressure gauges used in this study. The second tank was intended to contain 10% CO and 90% hydrogen, but the GC results showed that the actual concentrations were 8.3% CO and 91.7% hydrogen. The GC was also used to determine if the output gases, downstream from the MEA contained any impurities.

C. Experimental Methods

The first test aimed towards determining of the optimal output volumetric flow rate. This test was conducted as an open system arrangement, with the cathode chamber open to atmospheric pressure. The DC power source was increased at steady current intervals and at each interval the output flow rate was measured using the digital flow meter. This test was repeated several times to ensure repeatability. A closed system with a pure hydrogen feed was also examined to study the hydrogen pump's ability to compress the product gases. During this test, the input and output pressure and the applied power were all measured throughout a 15 minute pumping cycle with data being recorded every minute.

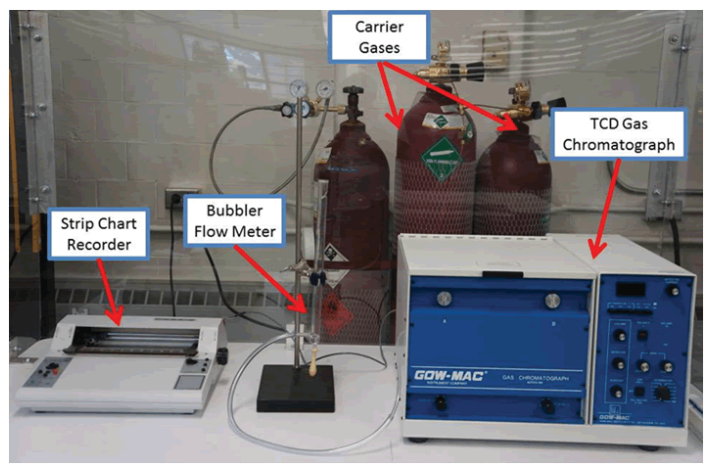

Figure 7: The gas chromatograph machine

The next experiment tested the separation efficiency of the hydrogen pump by running a closed system arrangement using the mixed tank of methane and hydrogen that was mentioned earlier. After a 15 minute pumping cycle, the gases in the cathode chamber were sampled using the GC. The anode and cathode chambers were then purged with pure hydrogen to prevent any residual gases from interfering with the next test. The last test conducted in this work was similar to the previous test except for the feed gas was a mixture of the CO and hydrogen. The GC was again used to sample the produced gases and examine the purity.

III. Results

The graph shown in Figure 8 clearly displays the direct linear relationship between the applied current and the output flow rate. The value of applied current results in a fairly repeatable output flow rate. The feed pressure was held constant at 5 psig during these trials meanwhile the cathode (output) chamber was open to

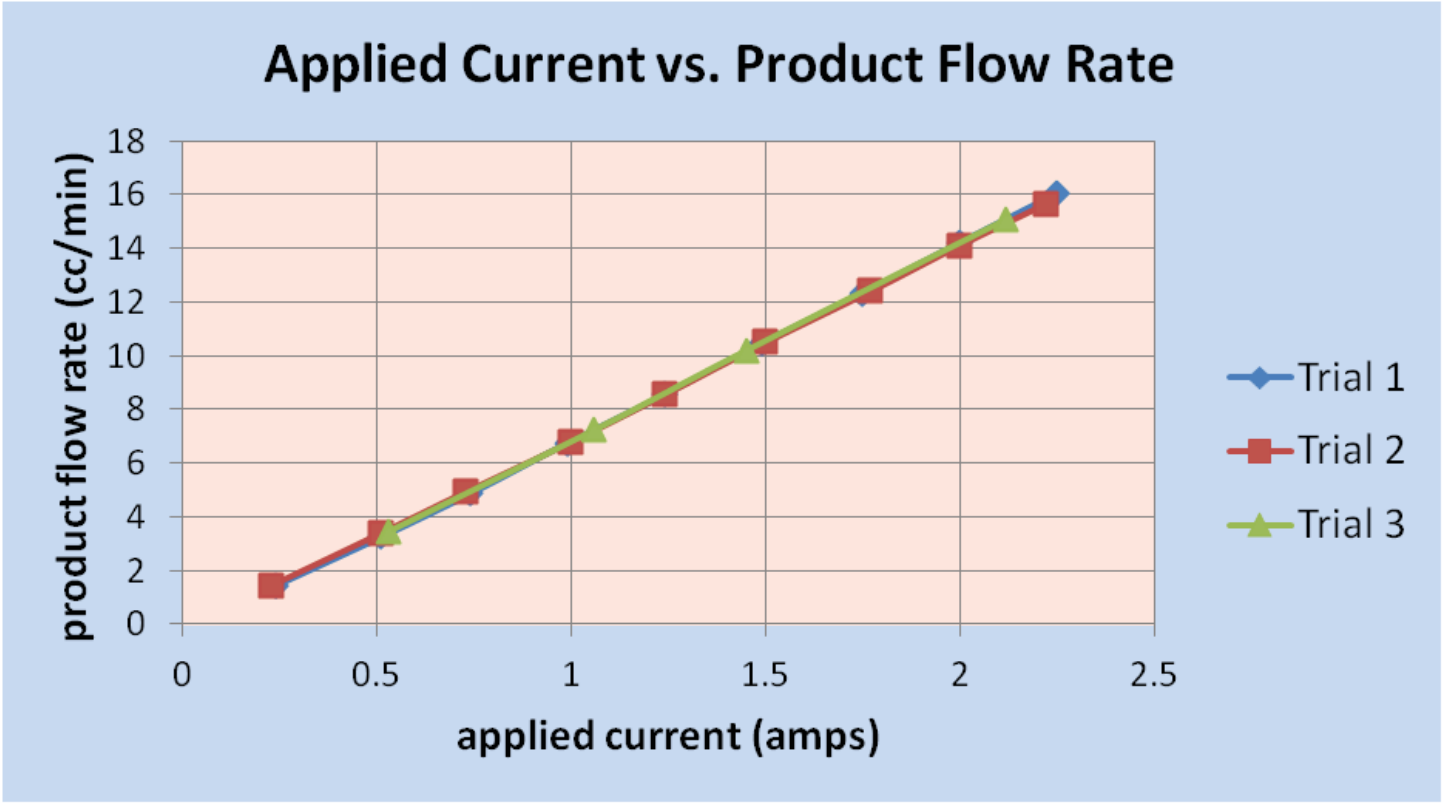

Figure 8: Product flow rate measured in relation to the applied current

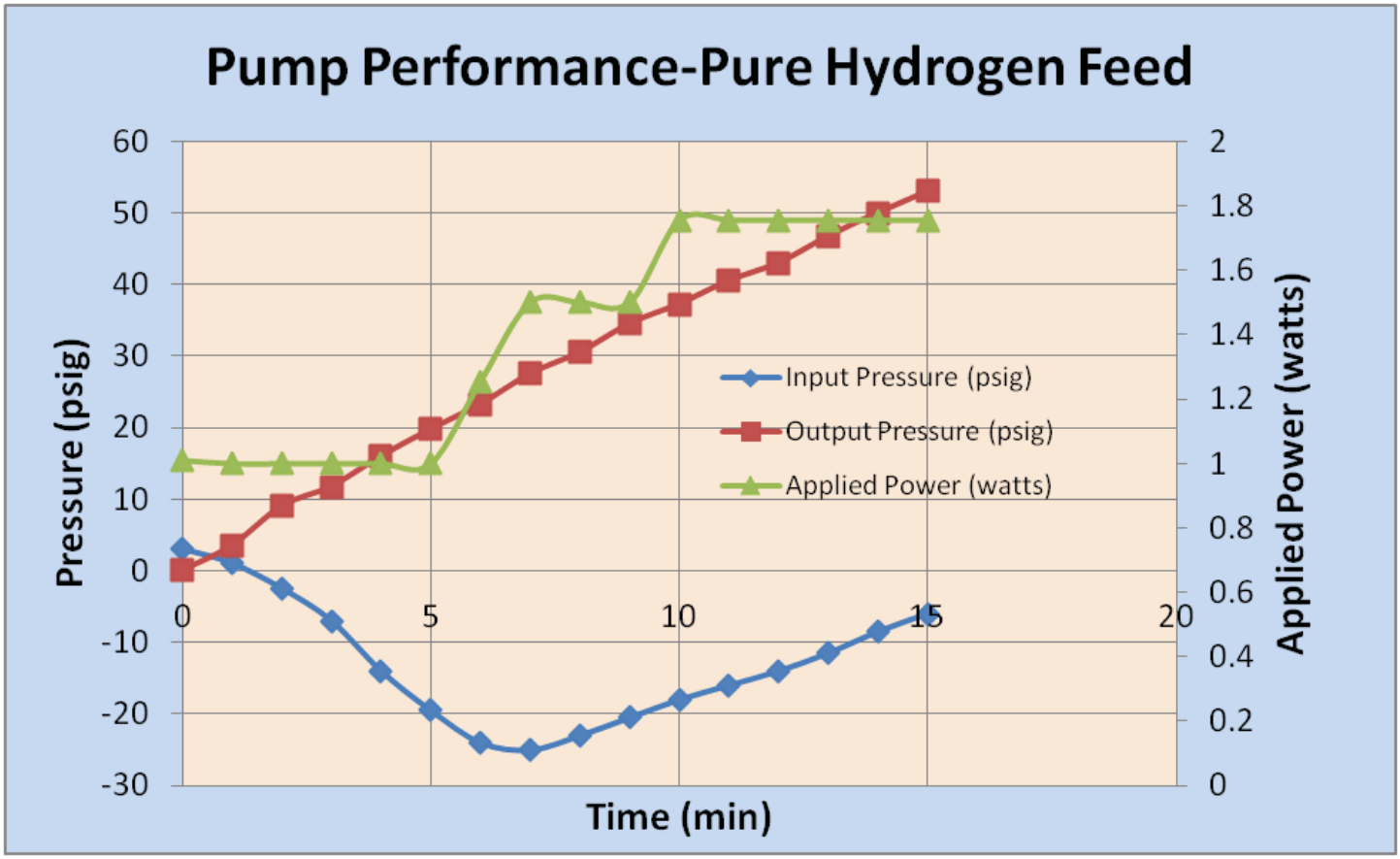

Figure 9: Pump performance over 15 minute pumping cycle

atmospheric pressure. The temperatures of the anode and cathode chambers were approximately 20°C throughout these tests. Trial 1 and 2 were conducted using pure hydrogen (grade 5.0) and trial 3 was conducted using industrial grade pure hydrogen.

The pressure of the compressed hydrogen in the closed cathode chamber was plotted along with the pressure in the anode chamber and the applied current. This data is plotted in the graph displayed in Figure 9. Three psig of pure hydrogen was initially applied to the anode chamber; meanwhile the cathode chamber was initially at 0 psig. Throughout the 15 minute trial, the applied current was kept at a constant 0.5 amps while the initial cell temperature was about 20°C.

The mixture of methane and hydrogen was fed to the hydrogen pump and then all input and output valves were closed. The power source applied a constant current of 0.5 amps to compress the output gas at the cathode. To observe the separation efficiency of the hydrogen pump, a closed system trial was conducted using the mixing tank of hydrogen and methane, and then the gases in the cathode chamber were sampled twice using the gas chromatograph. There was no methane detected in either of the samples, which means that there was less than 10 ppm methane in each of the samples according to the detection limit of the GC.

The gas mixture containing 8.3% CO and 91.7% hydrogen was inserted into the anode chamber at 3 psig and the power source was set to apply 0.5 amps of current. After 15 minutes the pump cycle ended and again two samples downstream from the membrane were analyzed using the G.C. There were no CO peaks detected within the GC detector limit of 10 ppm.

IV. Conclusions

In an open system the results show that as the applied current increases, the hydrogen flux through the membrane increases linearly. The optimal product flow rate of 16 cubic centimeters per minute was achieved with 2.25 amps of applied current, which was at the upper limit of the used flow meters range. The electrochemical separation system is able to compress the produced hydrogen to greater than 50 psig inside the cathode chamber within a 15 minute pumping cycle. This compression rate could be increased knowing that the applied current is the ultimate driving force in the electrochemical separation system. This system can be used to compress pure hydrogen in a tank for storage when hydrogen is not being directly consumed by fuel cells. The hydrogen pump was able to effectively separate and purify the hydrogen to contain < 10 ppm of Methane or CO. This hydrogen product purity successfully meets the requirements needed for optimal operation of PEM fuel cells.

Additional testing will include analysis of parameters such as internal cell temperature and internal cell humidity. Observing how the increase in power causes the input chamber to return to a positive pressure indicates that temperature increase could be playing an active role in these closed system tests. An increase in temperature could react with the impurities that are trapped in the input chamber causing the pressure to rise. Further studies on this will help determine if temperature is indeed an effective parameter. The optimal operating conditions of the electrochemical separator will be determined with energy efficiency being a priority.

V. Acknowledgements

I would like to thank the National Science Foundation, Brookhaven National Laboratory, Stony Brook University, Farmingdale State College, and the U.S. Department of Energy for the opportunity to conduct this research in their state-of-the-art laboratories. I would like to express my gratitude towards the Office of Educational Programs for conducting the Student Undergraduate Laboratory Internship (SULI) program that took place during the summer of 2012. Special thanks to my mentor, Dr. James Wegrzyn and Professor, Dr. Hazem Tawfik for their guidance throughout the program. I would also like to thank my fellow SULI participants, Alex Pereira and Andrew Hubert for their support during this program.

VI. References

[1]X. Cheng, et al. Journal of Power Sources 165 (2007) 739–756
[2]K. Onda, et al. Journal of Power Sources 188 (2009) 1–7
[3]A. Abdulla, et al. AlChE Journal 57 (2011) 1767–1779
[4]R. Ströbel, et al. Journal of Power Sources 105 (2002) 208-215

South Complex worker efficiency

Tarletta Williams
Facilities Management, Tallahassee Community College, Tallahassee FL 32304
Thomas Roza
Facilities Management, Brookhaven National Laboratory, Upton NY 11973

During my stay at Brookhaven National Laboratory (BNL), I was under the guidance of Thomas Roza, the Facilities Complex Manager of the BNL South Complex. Working with him--along with the participation of the BNL South Complex Facility Project Managers (FPMs): Patrick Browne, Christopher Harris, Arthur Piper, and Chuck Schuster--I was able to accomplish, or set into motion, numerous objectives to help the BNL South Complex run safely and more efficiently. Such activities include alarm response systems and the affixation of Ground Fault Circuit Interrupter (GFCI) labels throughout the BNL South Complex. My final project was to create a system that would allow the FPMs to better approximate the amount of time a worker should need to complete a job safely and in a timely manner. By doing this, the BNL South Complex would be able to better approximate the burden of man hour resources when constructing their budget.

Within the South Complex there are certain critical alarms that report to the Central Chilled Water Facility, Building 600. Most, but not all of them are connected to pieces of scientific equipment and are monitored by site shift supervisors after-hours when the lab is closed. Critical alarms are alarms that correspond to scientific work being done such as a freezer that must stay below or at -80°C or a growth chamber that needs to be kept around 74°F. The initial problem was that, although there were steps taken in case an alarm were to go off, there was no set procedure. Beginning with the alarm response system for building 463 (Biology), I understood there would be a great deal of work ahead of me because the procedure had not been updated since 1999. My goal was to stop the reoccurrence of an incident we had a few years ago, in Building 490, the Animal Research Facility and Health Clinic, when a -80°C freezer was improperly alarmed and 10 plus years of scientific study that included the use of brain culture tissues was lost and had to be restarted. In Building 463 there are two alarms panels that list the 48 alarms that are monitored in the Central Chilled Water Facility. Within those panels I discovered that some of the naming was wrong: some equipment had been removed or replaced, and some alarms now belonged to new pieces of equipment that were improperly named or the alarm itself was simply no longer in use. The problem with the misrepresentative labeling was that the current label is used to tell site shift where to go if the alarm went off. If the label is wrong, they go to the wrong piece of equipment, or even the wrong room, which is exactly what happened with the culture tissue freezer. Working with the Research Space Manager, Rich Sautkulis, I was able to verify an emergency contact list and a chain of command that would take place after hours, which all helped to finalize an alarm response instruction sheet for site shift to follow. A similar approach was taken in Building 490 with the help of Environmental Safety and Health Coordinator Robert Colichio and Research Space Manager Sal Sclafani.

Another project I was tasked with completing was the placement of GFCI outlet labels. These labels needed to be placed near outlets that were close to wet areas, such as in restrooms and kitchens. They look similar to the plug of a blow dryer in that they have a test and a reset button. It was my job to survey all of the buildings in the South Complex to create a condition assessment that would identify how many labels we would need to complete the task. Ranging from 1 to 200 plus missing labels, it took a tremendous amount of work to ensure that all of the labels were taken care of before the end of the Community College Internship program on August 10. With the condition assessment, I was able to create an outline that would help keep track of what was going on in terms of having the labels placed. I also created several spreadsheets that would be used to track the progress of the maintenance crew as the labels were being placed as well as separate spreadsheets to be used by the FPMs and Tom for their own records. In the process of conducting the assessments, as well as monitoring the development, I was exposed to certain skills, such as learning to properly write and address an e-mail, how to conduct a meeting, how to conduct myself in a meeting, and how to contribute ideas in a constructive atmosphere.

The South Complex encompasses every building located south of Brookhaven Avenue. Divided amongst the four FPMs of the South Complex, we are allowed the resources of approximately 16-20 union workers to do our best to ensure that every piece of equipment, restroom, lab room, and office, is operating at its best for the scientists that secure our services. The workers are divided into specialized trades and assigned maintenance orders from the area that best suit. There are some weeks where the demand for what needs to be done far exceeds the man hour resources that are afforded to us. Recurring examples would be the spike in A/C work that happens to come up every summer, the excessive work that needs to be done with the steam pipes during the winter, and the more frequent cleaning of the air filters during the fall. For these, along with many other maintenance issues that occur throughout the year, we generate a work order which is given to the mechanic who can best fill the order.

One of the problems we are having in, but not exclusive to, the South Complex, is the amount of time we are willing to designate for a job to be completed. Most of the managers have never done the type of work they are subscribing to have done so it can be difficult to set an appropriate space of time. Each work order requires an estimate of the number of hours a job should take; however, the workers understand that it is simply a guideline. In most cases this works fine, but after doing some research, I found that some workers do take advantage of the self-directed freedom. One example would be the placement of the GFCI labels. In a building that had about 230 missing labels, which took me no more than an hour and a half to assess, we had a worker charge 17.5 working man hours across approximately 7 work days. One day, he charged an entire 7.5 hours and because he still managed to miss a few, two more workers were sent to finish the job which added another 8 working man hours. That's 23.5 hours that we

had to pay for to put stickers in one building. That is unacceptable.

My final project was to take a few jobs that come up routinely and try to find a way to approximate how many hours a worker, or a pair of workers, can spend on a job before it becomes outrageous. It was understood that not all variables can be eliminated, such as the workers being called to another job hat has a higher priority, having to come back to the shop for a piece of equipment, or safety precautions that might prevent them from starting or continuing; however, there should be a ceiling where management and/or supervisors should step in and talk to the individual to see what's going on.

Unfortunately, I wasn't able finish that project to my satisfaction. After several discussions with the workers, how long a specific job should take is subject to many variables. The most important of which is safety. Some of the workers felt that by being given a deadline, it increased their level of stress and it would distract them from their work putting them in an unsafe situation. Overall, we came to the conclusion that it is up to the multi-craft supervisor (MCS) to make the call as to when a job is taking too long, and to step in and question the mechanic if necessary. In the South Complex we have two MCSs: Brian Conroy and Bruce Laakmann. Laakmann recently transferred to the South Complex and has very limited knowledge of how things work and what our workers actually do, while Brian is largely more informed about the trades that we house and what is expected of them.

While I was unable to satisfy my initial goal, I was able to pull some data to compare the South Complex, as far as how much it spends on labor, to BNL as a whole. The BNL fiscal year begins on October 1 and ends September 30 so my data came from the 2010-2011 fiscal year. BNL used 27.09% of its labor cost on preventative maintenance and the other 72.91% repairing things that were already broken. Similarly, the South Complex used 29.89% of its labor resources on preventative maintenance and the remaining 70.11% on reactive maintenance. Throughout most of the quarterly data, an approximate 30:70 split comes into play.

I didn't have enough data to come up with an accurate statistical analysis, but of the work done in the South Complex, one could construct a bell curve for the amount of preventative maintenance with a mean of 29.75 and a standard deviation of 6, meaning that the percentage of preventative maintenance that will be done in a given quarter will most likely range from 23.75 and 35.75 percent. Statistically speaking, this is a large deviation which means there is a large margin of error.

Among the four complexes, the South Complex makes up 27.97% of all costs for maintenance, 30.86% of that being used for preventative maintenance. BNL as a whole averages 27.085% of preventative maintenance that is done each quarter with a standard deviation of 7.49. This margin is even larger than the average for the South Complex. From this we can see that although the South Complex uses slightly more than a quarter of the labor resources, we do make an effort to prevent things from happening which is still in equal balance with the rest of the site.

For both the South Complex and BNL, during the third quarter there is a larger portion of labor costs that go towards preventative maintenance in comparison to other times of the year. In the South Complex it rises to 37.88% and for BNL it goes up to 37.07%, which is most likely what contributes to the large deviations in earlier mentioned statistics. This leads me to believe that during the months of April, May and June, we either have more time, or less new work that needs to be done.

From the data I was able to pull, I have come to the conclusion that the South Complex uses its labor resources efficiently. Had I been able to review how many work orders were done in each quarter, I may have been able to use that information to lend a hand in understanding just how much work we are able to get done. Although there are instances where this efficiency is stretched, as stated in the example above, I feel that the South Complex team does its best to ensure that we provide the best services we can.

This summer I gained a greater perspective of what it means to play a role in management. I was able to participate in meetings, meet with the workers, talk with them, as well as watch the entire maintenance process from start to finish. The work that I completed at BNL this summer plays a crucial role in the mission of the Department of Energy by providing new and creative ideas to the management and operational excellence team. By providing a fresh set of eyes and a new perception, we have made minor changes that will continue to the effect the South Complex for years to come.

Saving energy in the Brookhaven National Laboratory Computing Center: Cold aisle containment implementation and computational fluid dynamics modeling

Rebecca Winter
Earth and Environmental Engineering, Columbia University, New York, NY 10027
Conor McNamara
Chemical Engineering, University of Rochester, Rochester, NY 14627
Mark Toscano
Energy Utilities Department, Brookhaven National Lab, Upton, NY 11973
Tom Butcher
Sustainable Energy Technologies Department, Brookhaven National Lab, Upton, NY 11973

Abstract

This research project in the Energy Utilities Department is a study of energy efficiency improvement in the Data Center building at Brookhaven National Laboratory. The Data Center houses rows of large computer servers. These servers, like all computers, give off a substantial amount of heat and must always be kept cool to run efficiently. The total electricity usage of data centers, primarily computer power and A/C units, accounted for 1.6% of all US electricity usage in 2006, and is projected to increase by 12% annually. Due to the growing importance of data centers in an increasingly computer-dependent world and the large amount of cooling necessary to keep them running, the DOE has recently committed to a new energy efficiency standard for data centers that requires a 30% reduction in energy usage from their expected energy requirements, based on size.This study focuses on the modeling and implementation of curtains and baffles to save cooling energy by containing the cold air entering the server rooms. These curtains ensure that none of the cold air is cycled back into the A/C units without first passing through and cooling the servers. A 3D model was made of the airflow and temperature distribution in the data center using Ansys CFX, a Computational Flow Dynamics software. A temporary trial of the containment was performed using plastic sheets to verify the computer model and identify major benefits and problems with containment. The trial showed that containing two of three aisles with incoming cold air led to an 8.9°F decrease in the hottest inlet temperature to the computers. The model supported this excellent result and can now be used to model other curtain placements and configurations to find the most efficient and inexpensive solution.

I. Background

A. Data Centers and Energy Usage

Data centers are extremely important, large users of energy. In 2006, they accounted for about 1.6% of all US electricity usage,[1,2] and this figure is projected to grow by 12% annually.[1] Data centers use this energy not only to run the extremely powerful computers housed there, but also to power air conditioning units throughout the facility to prevent the computers from overheating. Of the 23.8 million kilowatt-hours of energy that the Brookhaven Data Center consumes each year, about 60% powers the computer servers and 40% goes to cooling.[4] While it is nearly impossible to reduce the amount of energy used by the computers without reducing the Center's computing capabilities, there are a number of techniques that can be employed to cool the servers more efficiently. Lowering the amount of energy required to cool a data center would yield large energy savings.

B. Air Flow in a Data Center and Cold Aisle Containment

In many data centers, including the Data Center at Brookhaven National Laboratory, the air conditioning units pump cold air into an area below the floor called the plenum, as shown in Figure 1. This cold air comes up through porous floor tiles into an aisle with computer racks facing inward, called the cold aisle. This air in the cold aisle goes through the small fans in the computers and into the neighboring outflow aisle, called the hot aisle, where all the server racks are back-to-back. The air then rises up from the hot aisle and eventually reenters the air conditioners.

There are two main inefficiencies that result from this. The first and most significant source of inefficiency is the fact that the recirculated cold air wastes fan energy because this air does nothing to cool the actual servers, but it leaves the cold aisle and enters to the air conditioner unit simply to be blown back to the cold aisle it came from. The second source of inefficiency is the fact that the entire room is being cooled. Any cooling leakage that the room experiences, for example from an open door to an adjacent room or the sun's radiation on a hot day, will require that the air conditioners work harder to counteract those effects and chill the entire volume of the room.

Both of these sources of inefficiency can be corrected with containment. In the containment model, shown in Figure 2, the top of the cold aisle is blocked off. In a three-dimensional view of the aisles, the two sides of the cold aisles would also be shown as blocked off. This containment does not allow any cold air to escape the cold aisle without first passing through the servers. This solves the first problem because it makes the system such that the air must first pass through and cool a server to return to the air conditioner and be pumped into the plenum. The second issue is significantly improved, as well, because the volume of space that is cooled has been reduced to simply the cold aisles, instead of the entire room. The cold aisles will therefore become colder, while the ceiling above the cold aisles, where the air returns to the air conditioner, will be hotter. Using cold aisle containment is one of the most energy efficient options and often the least expensive

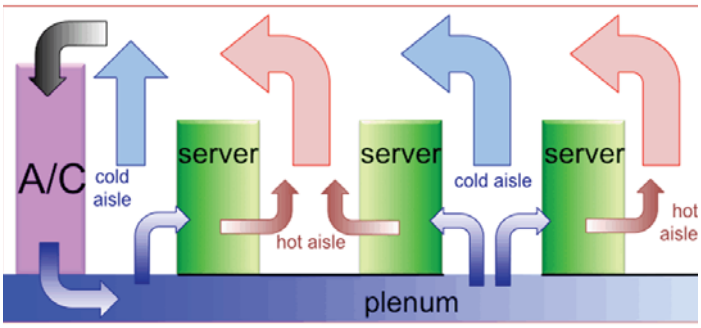

Figure 1. Diagram of typical airflow inside a data center

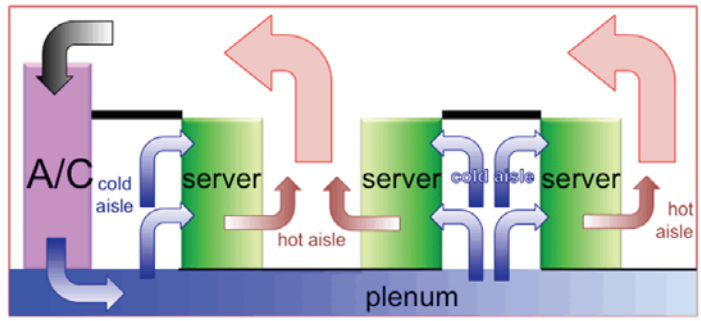

Figure 2. Diagram of airflow inside a data center with cold aisle containment

method of reducing cooling energy because it does not require the purchase of a new, more efficient air conditioner and its purpose is simply to make sure the cold air is channeled only to where it can best be used.

C. Proven Benefits of Cold Aisle Containment

Cold aisle containment, as well as containment in the plenum and within individual server racks, can significantly reduce the cooling load of a server room. The national laboratory at Savannah River reduced their data center's cooling load by 43% and had a payback of just two and a half months from their containment initiative.[5] Lawrence Berkley National Laboratory also implemented a large-scale containment project throughout their data center with a payback of two to four years.6 Due to the large reduction in cooling requirements of their existing servers, Lawrence Berkley added new servers to rooms that were previously at maximum capacity instead of turning off all the air conditioners that were no longer needed for their previous capacity. They estimate the total increase in cooling capacity at 21%.6 The alternative to adding this quantity of new servers would have likely been a large construction project to add an additional server room extension to the data center.

II. Methods

A. Overview of the Study

This study is comprised of both a real-world experimental component and a computer modeling component. As a real-world experiment, temporary cold aisle containment baffles were put in the RCF room. Temperature, pressure, and other useful data were taken at strategic points along the hot and cold aisles and at the air conditioners before and after the containment experiment. The data taken before the containment experiment were used to build a three-dimensional computer model of airflow and temperature distribution through the room without and with the inclusion of containment structures, modeled like those used in the real-world experiment. The results of the "after containment" computer model were then compared to the results found in the actual experiment in order to validate the model.

B. Overview of the Room

The entirety of this study is focused on Brookhaven National Laboratory's RHIC Computing Facility (RCF) room, which is a room in the Computing Center dedicated to the analysis of data from Brookhaven's Relativistic Heavy Ion Collider (RHIC). The RCF room contains three cold aisles, three hot aisles, and two primary air conditioning units (AC1 and AC7). Additionally, some of the computer racks have small "top-hat" air conditioning units, which sit directly on top of the rack. These units take hot air in from the top of the hot aisle, cool the air, and pump it directly into the top of the cold aisle.

C. Real-world Experiment

The temporary cold aisle containment curtains, consisting of thin plastic sheets, were placed on the top and sides of two of the three cold aisles of the RCF room. Pictures of the RCF room before and after the containment was implemented can be seen in Figures 5-6 and Figures 7-8 respectively. The containment was implemented under careful observation for approximately 12 hours before removal.

D. Computer Model

A three-dimensional k-epsilon turbulent airflow computer model of the RCF server room was built using a Computational Fluid Dynamics modeling (CFD) software called Ansys CFX. The model was built in two configurations, one without containment, shown in Figure 9, and one with containment, shown in

Figures 5 and 6. Pictures of a cold aisle before containment

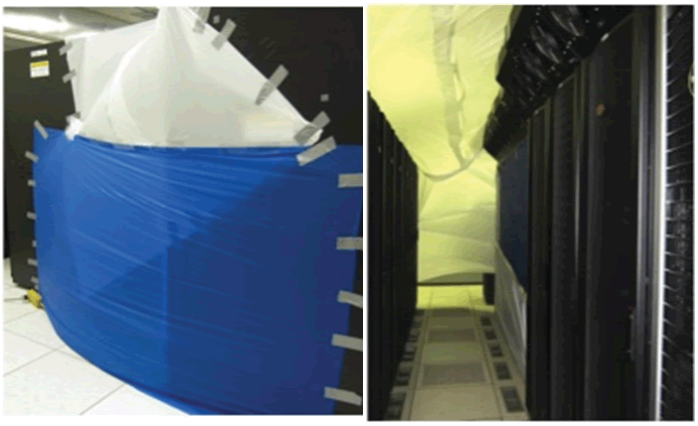

Figures 7 and 8. Pictures of a cold aisle after containment

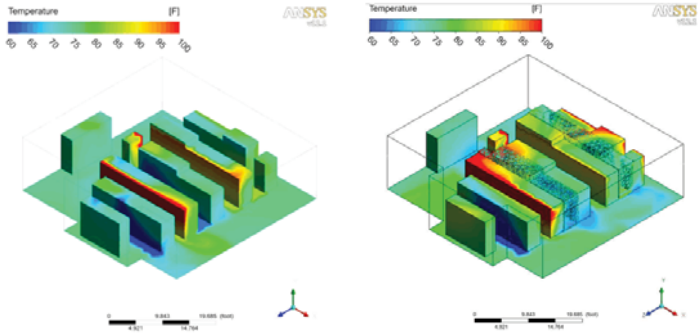

Figure 9 and 10. (left) Model of RCF room without containment. (right) Model of RCF room with containment

Figure 10. The before containment model was built based on temperature and pressure data in the server room. Adiabatic wall boundaries were added to the room model where the actual containment sheets were hung in the real-world experiment to create the after containment model. No other inputs of boundary conditions, temperatures, or pressures were changed in creating the after containment model. These computer models were built in order to compare airflow and heat distribution in the before and after containment scenarios.

III. Data and Results

A. Real-World Experiment Data and Analysis

The real-world experiment yielded excellent results and showed significantly colder cold aisles, which will result in energy savings if permanently implemented. Figures 12 and 13 show floor plan views of the data center near the top of the computer server racks with a color contour of temperatures before and after containment, respectively. Each small black box represents a location where temperature is monitored. As shown in these contour maps, the cold aisles are significantly colder after containment. In fact, the experimental data shows that the containment resulted in an 8.9°F decrease in the hottest cold aisle temperature. Since the air conditioning units are ideally set so that the hottest temperature in a cold aisle is the maximum allowable operating temperature of the servers, a reduction in hottest cold aisle temperature directly leads to a decrease in chilling requirements. It is also important to note that AC7, one of the two air conditioner units in the room, significantly reduced its chilled water intake during the experiment and was cooling at approximately 65% capacity. This and the very low cold isle temperatures both suggest that if containment was implemented, this air conditioner unit could be turned off permanently or both units' cooling could be significantly reduced, greatly decreasing energy usage.

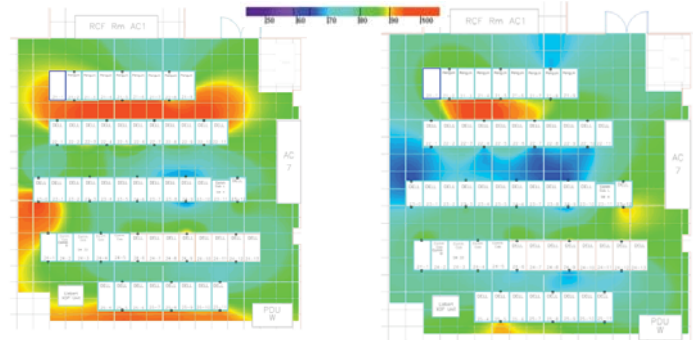

Figures 12 and 13. Temperature floor plan views of RCF server room before and after containment

B. Computer Model Validation

In validating the computer model, two main regions were compared for temperature. The first is the server inlet air temperatures at the top of the servers in the cold aisles that were contained. This is an important temperature comparison because if this model were used to predict results of containments that were not experimentally tested, an approximation of the decrease in top of cold aisle temperature would indicate how much less cooling would be required after containment implementation. Figures 14 and 15 show the experimental temperature data uncontained and contained respectively, while Figures 16 and 17 show the model prediction uncontained and contained respectively. The black boxes highlight the two cold aisles that had containment in the contained model for comparison. Comparing the uncontained scenario in Figures 14 and 16, the temperature profiles match very well because the experimental data in Figure 14 was used to build the model shown in Figure 16. The true test of the model's validity is therefore the comparison of the model's prediction of containment in Figure 17 with the actual experimental data taken in the containment scenario, shown in Figure 15. These temperature gradients also match very well and support the model's accuracy.

The second focus of comparison was the temperature of the air returning to each of the two air conditioner units. Table 1 shows the uncontained and contained temperatures of return air to the air conditioners in both the experimental data and the model predictions. The model's return air predictions are consistently colder than the experimentally measured temperatures. This could likely be fixed by adjusting boundary conditions of the model slightly. Despite overall colder temperatures predicted by the model, the changes in temperature from uncontained to contained are quite close to the experimentally measured values. In both the experiment and the model, AC1 return air became significantly warmer while AC7 return air became slightly colder. Since the change in

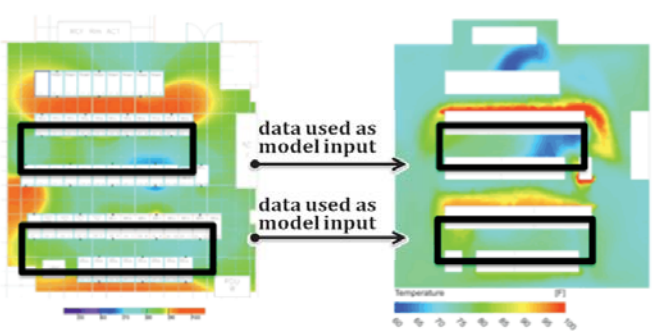

Figures 14 and 16. Uncontained scenario of experimental data and computer model, respectively

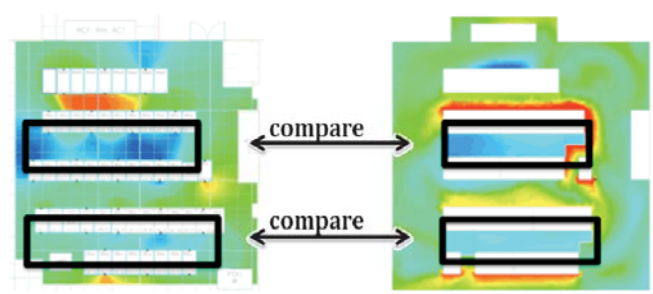

Figures 15 and 17. Contained scenario of experimental data and computer model, respectively

temperature was predicted well by the model, the overall colder predicted temperatures are not a significant issue. It is assumed that if this model is implemented for a containment that was not experimentally tested, there will still be uncontained temperature data from the room. This experimental uncontained value of return air temperature, if warmer than the model's predicted uncontained value, can be used to adjust the contained model prediction and determine a more accurate temperature value as long as the change in temperature predicted by the model is accurate.

		Real-world	Model
AC1	Uncontained	81.9°F	71.7°F
	Contained	88.7°F	80.9°F
	Change	**+6.8°F**	**+9.2°F**
AC7	Uncontained	81.9°F	76.4°F
	Contained	77.1°F	74.7°F
	Change	**-4.8°F**	**-1.7°F**

Table 1. Air conditioner return temperatures

C. Computer Model Data and Analysis

Figures 17 and 18 show the temperature cross-sections of the room in the uncontained and contained computer models. The cold aisles in the uncontained model have a large temperature gradient from bottom to top, signifying that the bottom servers must be overcooled in order to reach the desired temperature in the upper servers. In the containment model, the temperature remains consistent and colder throughout the aisle, so the air conditioners can cool all the servers to the desired temperature without needing to overcool the bottom half of the room. Another important observation in Figures 17 and 18 is the difference in temperature of the ceiling above the racks. The ceiling has become warmer because less air from the cold aisles is escaping the cold aisles and returning to the air conditioning units.

This warmer ceiling temperature led to a higher return air temperature to AC1, as shown in Table 1. This can be seen when comparing the uncontained AC1 in Figure 19 with the contained AC1 in Figure 20, and means that less cold air is recycling back into AC1. AC7 return air actually became colder in the contained model. Figure 21 from before containment and Figure 22 after containment show that when the cold aisle is contained, there is too much cold air being pumped into the cold aisle, implying that an air conditioning unit should be turned down or off completely if the aisle is contained. The excess of cold air in the aisle causes some of the cold air to leak out of the 2-foot opening left in containment for emergency access to the aisle. As shown in Figure 24 of the containment model, this cold air leakage travels along the floor and directly into AC7. This colder temperature entering AC7 caused the air conditioner to greatly reduce its chilled water intake during the experiment. As shown in the experimental data, this reduction in chilled water usage by AC7 did not negatively affect the ability to chill the cold aisles, as the cold aisles were colder than they had been previously. The slight drop in temperature of the AC7 return air can be seen by comparing Figures 23 and 24.

IV. Conclusions and Recommendations

When compared with experimental data, the computer model successfully showed the trends and locations of temperature in-

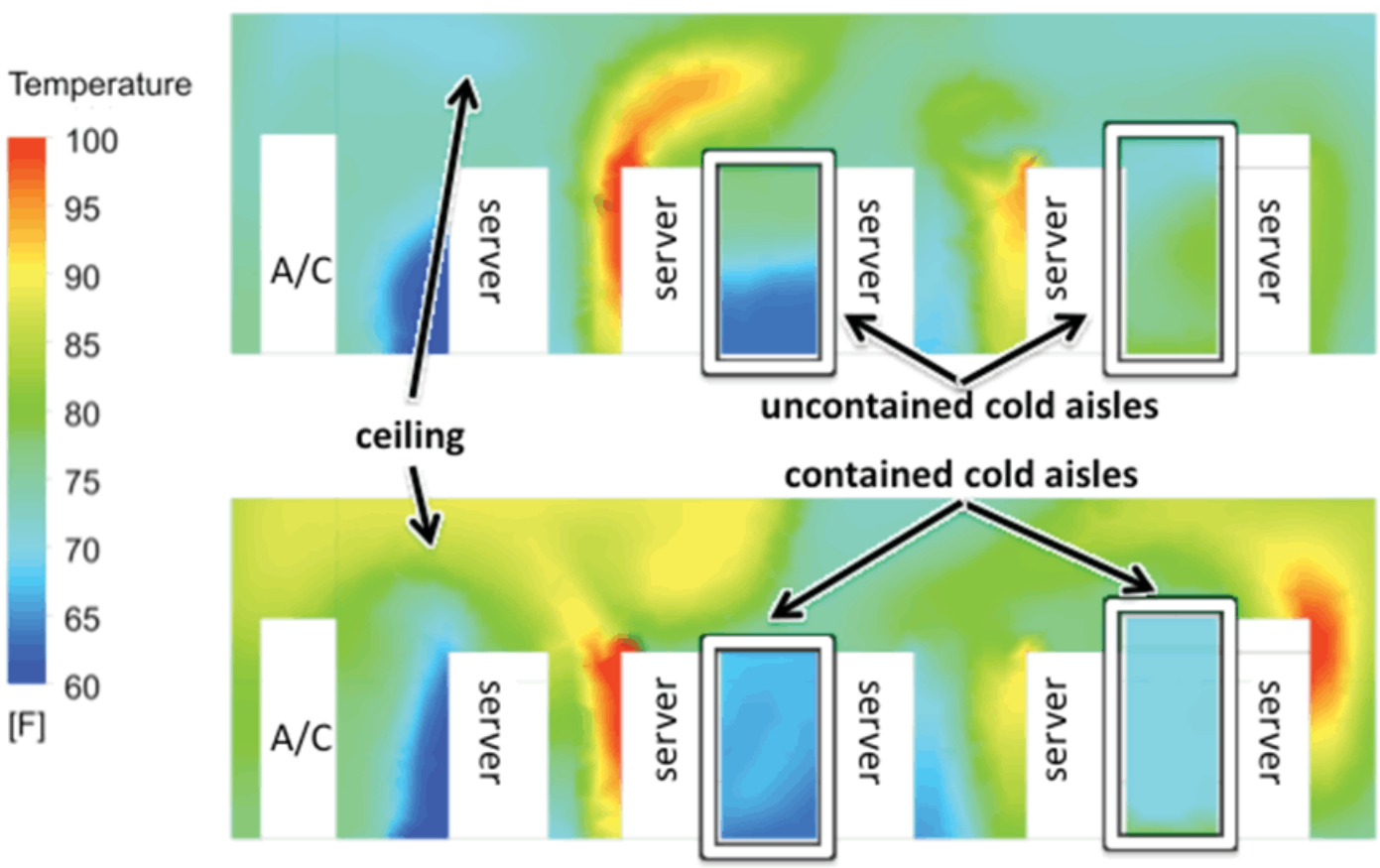

Figures 17 (top) and 18 (bottom). Temperature cross-sections before and after containment, respectively

creases and decreases throughout the server room. This computer model can now be used to model the room with only one air conditioner unit turned on, to model other geometries of containment, or to model other server rooms in the data center. This will give a general idea of what containment is needed and how the room can be best contained to optimize energy savings and reduce installation costs.

Both the computer model and the experimental data show that cold aisle containment should be implemented in the RCF server room to save cooling energy. Recommissioning is an important step after implementing cold aisle containment in the data center. As shown in the analysis of AC7, there will likely be overcooling once containment is implemented, so the room must be analyzed and each air conditioner should be considered separately for a reduction in chilled water usage, an increase in set point temperature, or a decrease in fan speed with the addition of a Variable Frequency Drive unit. Some air conditioning units may even be turned off with no negative impact on server inlet temperatures. This reanalysis step after implementation will allow for the maximum energy savings from containment.

Cold aisle containment, when implemented correctly, can lead to significant energy savings, both in other national labora-

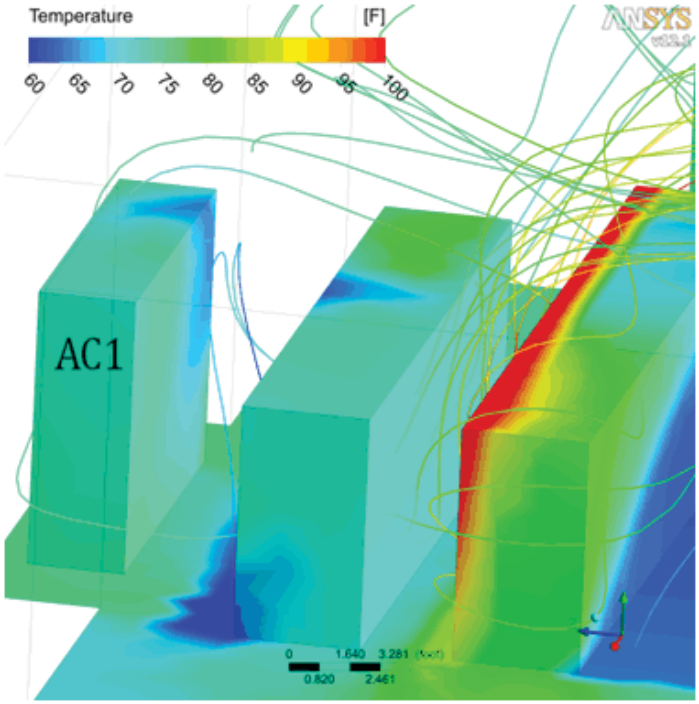

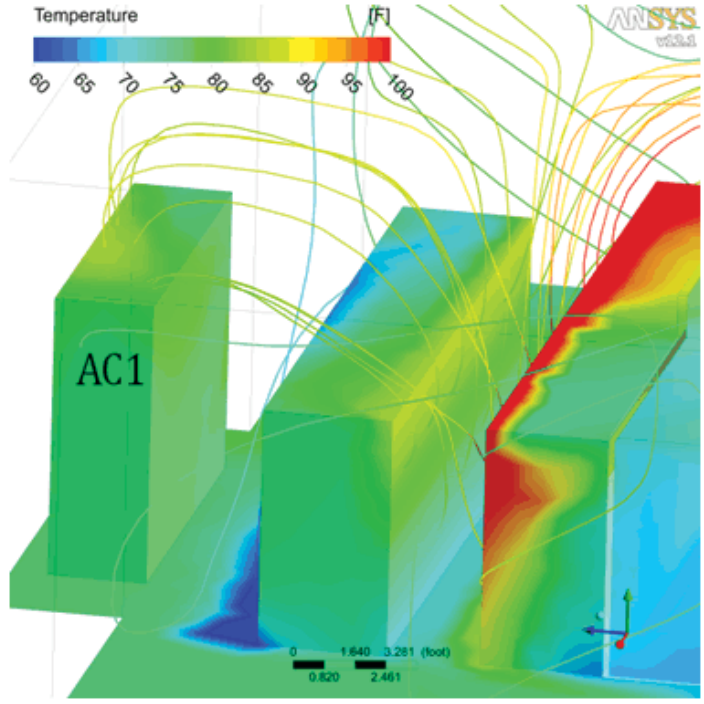

Figures 19 and 20. Temperature contours near AC1 before and after containment

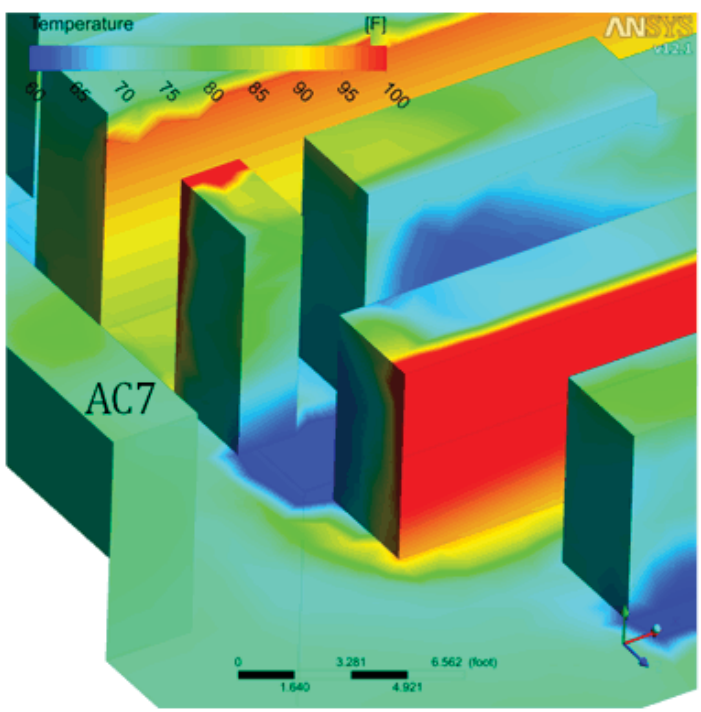

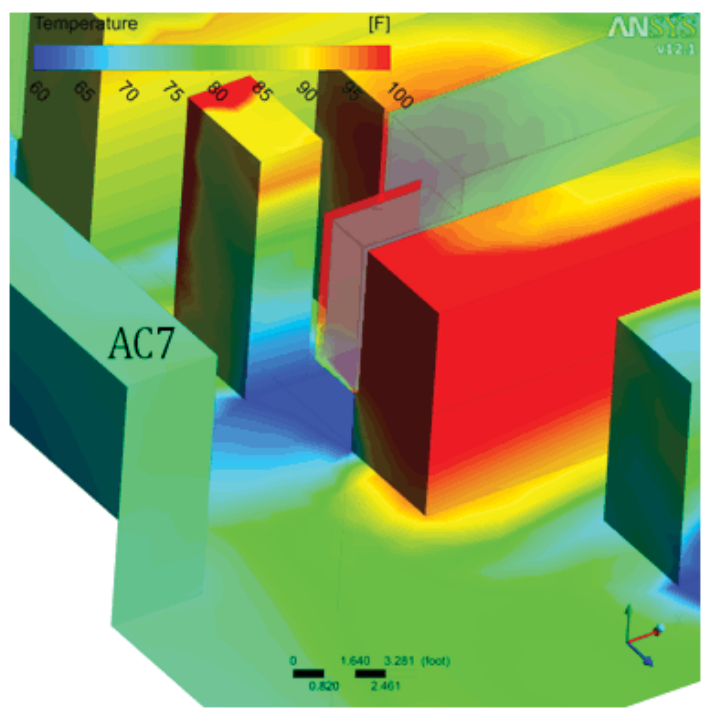

Figures 21 and 22. View of temperature contours near AC7 before and after containment

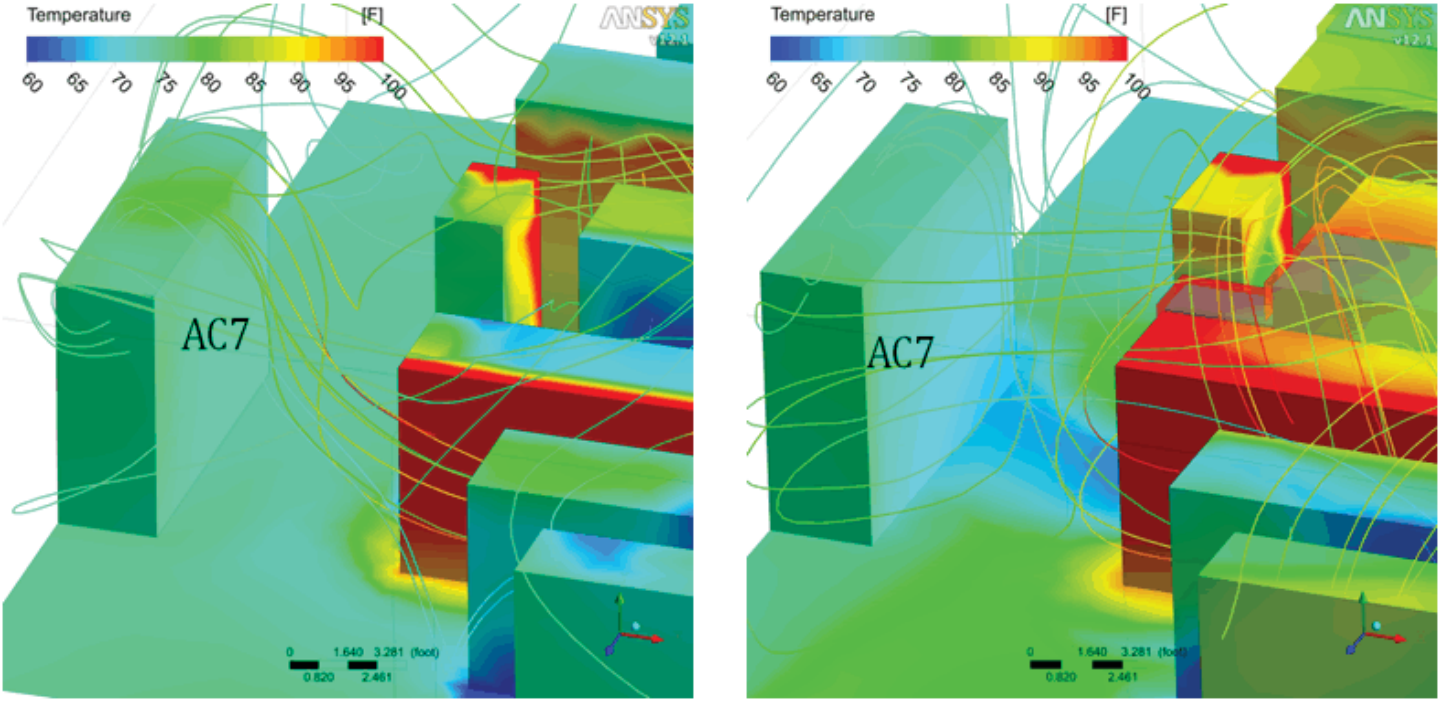

Figures 23 and 24. Opposite view of temperature contours near AC7 before and after containment

tories and in the RCF room at Brookhaven National Laboratory. With a fluid flow model that is capable of predicting temperature distributions and cooling loads associated with different configurations, Brookhaven National Laboratory would benefit greatly from a containment project in their data center.

V. References

[1]ENERGY STAR Program, US Environmental Protection Agency. "Report to Congress on Server and Data Center Energy Efficiency Public Law 109-431." Aug 2007.

[2]US Energy Information Administration. <http://www.eia.gov/totalenergy/data/ annual/showtext.cfm?t=ptb0801>

[3]ASHRAE. "Recommendations for Meeting Energy Efficiency Requirements for New Federal Data Centers." Aug 2011.

[4]Lizardos, Brookhaven National Lab. "Computer Facilities Energy Efficiency Study: Building No.s 459 and 515." Dec 2011.

[5]Federal Energy Management Program, US Dept of Energy. "Retro-Commissioning Increases Data Center Efficiency at Low- Cost: Success at Savannah River Site (SRS) at Low-Cost." Dec 2010.

[6]Federal Energy Management Program, US Dept of Energy. "Data Center Airflow Management Retrofit: Technology Case Study Bulletin." Sept 2010.

Appendix

This appendix lists those reports which were completed, but not included in the preceding compendium. They were withheld because their contents were not available for one or more of the following reasons: in prepartion for publication in a peer-reviewed journal, incomplete data, preliminary data for a longitidunal study, or other reasons.

Intern	Mentor	Title
Beverly Agtuca	Richard Ferrieri	Carbon-11 used to study the effects of plant hormones on root development in maize as a model grass for bioenergy
Lawrence Barrett	Javier Pulecio	Unavailable
Courtney Buckley	Jennifer Higbie	Radio telemetry analysis of nighttime movement and home range of Southern Flying Squirrels at Brookhaven National Laboratory
Cherise Burton	Peter Johnson	Unavailable
Nikita Butakov	Jun Wang	Unavailable
Staci Cambria	Tim Green	Statistical analysis of point count bird surveys and measuring biodiversity
Morgan Campbell	Chang-Jun Liu	Unavailable
Juan Casillas-Plazola	Vincent Castillo	Unavailable
Anshu Chawla	Joseph Brennan	Unavailable
Kristi Confortin	Jennifer Higbie	Distribution of small mammals within a large solar insulation at Brookhaven National Laboratory
Jewel Cumberbatch	Kevin Yager	Growth and characterization of CVD graphene via Raman spectroscopy
Richard Darienzo	Elke Aschenauer	Superconducting magnet design for the eRHIC Detector.
Kyle Davis	Jinsuo Nie	Unavailable
Alyssa DiScipio	James Wishart	Examining electron transfer kinetics in ionic liquids
Kaitlyn Eng	James Mills	Site Drainage Modification for CFN, Building 735
Joseph Garlow	Javier Pulecio	Modulation of graphene's binding energy via sublimation of a solid carbon source
Ben Garth	Daniel Bacescu	Engineering a Pinhole selection device for soft X-ray beam lines/ Pinhole Selection Device for the CSX Beamline of NSLS II/ Pinhole selection device for the CSX beamline of NSLS II
Yigit Gol	Benjamin Babst	A comparison of sugar concentrations and composition in sweet and grain sorghum
Nora Goscinski	Suzanne Smith	Radiochemistry of Yttrium-86: designing Yttrium-86 positron emission tomography imaging agents for personalized medicine
JaQueeta Hall	Anwar Hossain	Unavailable
Pelle Hall	Jorg Schwender	Unavailable
Chad Hannibal	Joanna Fowler	Acyl halides preparation from Friedel-Crafts carbonylation of alkyl amines with carbon monoxide and aluminium chloride
Sumar Hayan	Chang-Jun Liu	Unavailable
Harold Hickey	Swami Swaminathan	Unavailable
Anthony Hoang	Paul Wilson	Unavailable
Nichelle Jackson	Kathy Schwager	Unavailable
Andrew Javidfar	Wing Louie	Unavailable
Jasmine Jenkins	Tim Green	Solar farm effects on Eastern Box Turtle (*Terrapene carolina carolina*) home range
Beatris Jimenez	Dario Stacchiola	Unavailable

Nicholas Karker	James Wishart	Study of radiation effects on wet ionic liquids for use in reprocessing spent nuclear fuel
Ryan Katz	Paul Freimuth	Unavailable
Douglas Kenny	Benjamin Babst	Auxin signaling in bioenergy crops: Development of [F18] and [C11] benzoic acid labeling chemistry for novel auxin transport imaging technique
Charlotte Kirk	Oleg Gang	Exploration of engineering control of the structures formed by DNA-functionalized gold nanoparticles
Paul Kline	Jean Logan	Unavailable
Brandon Krouppa	William Morse	Unavailable
Luke Latario	Tim Green	Isolation and identification of radiation resistant microorganisms from Pine Barrens soil
Qudus Lawal	Matthew Sfeir	Unavailable
Lucas Loffredo	Tim Green	Attempting to isolate microorganisms from Pine Barrens soil treated with high-frequency gamma irradiation
Joseph Maggio	Vasilis Fthenakis	Unavailable
Allison Matus	Kin Yip	Soil activation evaluation in the current Beam Dump (B6) and Septum (D6) of Booster
Timothy McDonnell	Jessie Wilke	The Achitectural Planning of room 1-31 in building 815, to create two admissions spaces
Lucas Mladek	Keith Lally	Unavailable
Amanda Muraca	Lynne Ecker	Polymer modified foamed cement for mitigating steel-corrosion
Maja Oblepias	Kevin Yager	Growth and characterization of CVD graphene via Raman spectroscopy
Amita Patel	Vincent Castillo	Unavailable
Simon Peggs	Dejan Trbojevic	Misalignment tolerances in the iRCMS
Vanessa Petion	Alicia Reid	Unavailable
Paul Phillipsberg	Biays Bowerman	Graphite sampling tool: sampling assistance software upgrade
Thomas Quartararo	Jun Wang	Design of an environmental cell for in situ transmission X-ray microscopy
Asja Radja	Ge Yang	Post-growth thermal annealing and characterization of Cadmium Zinc Telluride radiation detector material
Sharon Ramati	James Wishart	Effect of side chain branching on the structure and properties of ionic liquids
Shelby Rice	Eswar Eswaramoorthy	Unavailable
Evgeniya Rubin	Vivian Stojanoff	Unavailable
Katherine Sanidad	Benjamin Babst	A comparison of photosynthate allocation and transport speeds in sweet and grain sorghum using $_{11}CO_2$
Heather Savage	Carl Schultheiss	Embedded communications for the Relativistic Heavy Ion Collider power supplies
Janki Shah	David Schlyer	Unavailable
Paul Sieradzki	James Wishart	Model metal derivatized peptides to study electron transfer kinetics in neutral solvents and ionic liquids
Michael Skinner	Allen Orville	Unavailable
Phil Smith	Kevin Yager	Measurement of the elastic properties and intrinsic strength of few-layer graphene
Amanda Stasiewicz	Tim Green	Revegetation success of a solar facility: an analysis of the first year post construction

Jordan Stubleski	Suzanne Smith	Radiochemistry of Copper-67 - Designing Cu-67 Radiopharmaceuticals for Radiotherapy
Nouze Takougang	Nicholas Franco	Unavailable
Yunli Tang	Michael McGuigan	2+1-Dimensional black hole method as an alternative perspective on materials
Alanna Tieman	Alex Soares	Unavailable
Adam Vorwald	Steve Bellavia	Unavailable
Alyssa Watt	Jennifer Higbie	Geographic Information System (GIS) analysis of the ecological effects of the solar farm
Ryan Wong	Oleg Gang	pH-triggered nanoparticle crystallization through the application of a chemical oscillator
Christopher J. Wright	Sanjit Ghose	Unavailable
Katarzyna Zabrocka	Walter Mangel	Determining the mechanism of action of a new inhibitor of adenovirus protease en route to an antiviral drug
Nicole Zmich	James Wishart	Ionic liquids for super capacitor applications

List of interns, their colleges or univerisities, and location in this compendium

Intern	College / University	Page
Paige Abrunzo	Rensselaer Polytechnic Institute	9
Sarah Ackerman	SUNY Geneseco	14
Beverly Agtuca	SUNY College of Environmental Science and Forestry	301
Stephen Albright	Brown University	18
Christine Anerella	New York University	24
Helen Bagnato	University of North Carolina at Chapel Hill	26
Lawrence Barrett	Brigham Young University	301
Kimberly Basil	SUNY ESF	32
Adam Batley	Tallahassee Community College	184
Caitlin Bennett	Fordham University	37, 238
Brian Bergh	University of Buffalo	41
Kiersten Blauer	Southern Utah University	44
Taryn Boucher	Bucknell University	48
Courtney Buckley	SUNY College of Environmental Science and Forestry	301
Cherise Burton	University of the Virgin Islands	301
Nikita Butakov	University of Buffalo	301
Jamie Butcher	SUNY at Geneseo	165
Adeel Butt	Stony Brook University	51
Staci Cambria	St. Joseph's College	301
Morgan Campbell	SUNY New Paltz	301
Juan Casillas-Plazola	San Joaquin Delta College	301
Trevor Chan	University of Alabama in Huntsville	55
Anshu Chawla	Juniata College	301
Richie Chen	Stony Brook University	60
Shushanna Cherian	Stony Brook University	64
Thomas Chiesa	Stony Brook University	71
William Christie	SUNY Binghamton	75
Daniel Comas	SUNY Stony Brook	77
Kristi Confortin	SUNY Cobleskill	301
Jessica Cruz	Graduating Senior	79
Clara Cuervo	Suffolk Community College	84
Jewel Cumberbatch	University of the Virgin Islands	301
Eric Cushing	The Pennsylvania State University	86
Mike Dai	Stony Brook University	89
Lezou Dali	Stony Brook University	184
Richard Darienzo	Stony Brook University	301
Bianca Datta	University of Pennsylvania	106
Kyle Davis	University of Delaware	301
Remy Devoe	University of Tennessee	112
Alyssa DiScipio	Fordham University	301

Kaitlyn Eng	SUNY University at Buffalo	301
Daniel Ferguson	St. Joseph	115
Joseph Garlow	Stony Brook University	301
Ben Garth	Penn State	301
Yigit Gol	Stony Brook University	301
Nora Goscinski	California Polytechnic State U. San Luis Obispo	301
Nathan Gubser	University of the Virgin Islands	117
Skyler Hagen	Ripon College	119
Jonathan Haimoff	Nassau Community College	123
JaQueeta Hall	Alabama A&M University	301
Pelle Hall	Grinnell College	301
Chad Hannibal	Medgar Evers College	301
Terance Harper	Alabama A&M University	126
Sumar Hayan	Stony Brook University	301
Lauren Herrera	Suffolk Community College	131
Harold Hickey	United States Naval Academy	301
Anthony Hoang	Contra Costa College	301
Andrew Hubert	Farmingdale State College	134
Nichelle Jackson	Vassar College	301
Peter Jandovitz	Cornell University	137
Andrew Javidfar	Stony Brook University	301
Jasmine Jenkins	Southern University of New Orleans	301
Beatris Jimenez	Suffolk County Community College	301
Trevor Johnson	West Virginia University	140
Nicholas Karker	SUNY Buffalo	302
Ryan Katz	Graduating Senior	302
Douglas Kenny	University of Delaware	302
Jacob Kiefer	Cornell University	142
Charlotte Kirk	Massachusetts Institute of Technology	302
Paul Kline	Blackburn College	302
Christopher Kolz	SUNY Binghamton	148
Benjamin Kramer	Villanova University	152
Brandon Krouppa	Jacksonville University	302
Luke Latario	Grove City College	302
Qudus Lawal	Stanford University	302
Benjamin Le	Georgia Institute of Technology	157
Emily Leonard	Stony Brook University	161
Lucas Loffredo	Vanderbilt University	302
Joseph Maggio	SUNY ESF	302
Matthew Marshall	University of New Mexico	165
Allison Matus	Suffolk County Community College	302
April McCray	Tallahassee Community College	184
Timothy McDonnell	Suffolk County Community College	302
Jesse Miller	California State	168
Louie-John Mistretta	Worcester Polytechnic Institute	173
Lucas Mladek	Stony Brook University	302

Ahmad Mohammad	Oregon State University	179
Juan Mojica	Tallahassee Community College	184
Alyssa Montalbano	Rensselaer Polytechnic Institute	186
Patrick Montalto	Stony Brook University	192
Ammar Morgan	Stony Brook University	194
Amanda Muraca	William Paterson University	302
John Mwathi	Alabama A&M University	197
Maja Oblepias	Contra Costa College	302
Max Osmulski	Vanderbilt University	200
Amita Patel	Somerset Community College	302
Nicholas Patterson	Stony Brook University	202
Simon Peggs	University at Buffalo	302
Alexandre Pereira	Farmingdale State College	205
Vanessa Petion	Medgar Evers College	302
Amanda Pflumm	Washington & Jefferson College	210
Long Phan	Stony Brook University	213
Paul Phillipsberg	Stony Brook University	302
Rodney Pinder	Alabama A&M University	216
Denzel Pressey	Southern Polytechnic State University	221
Thomas Quartararo	Stony Brook University	302
Asja Radja	University of Texas at Dallas	302
Sharon Ramati	Queensborough Community College	302
Brandon Rhymer	University of the Virgin Islands	223
Shelby Rice	Oklahoma State University	302
Evgeniya Rubin	City College of New York	302
Aviva Rutkin	Union College	225
Wahaj Saleem	City College of New York	231
Valissa Sams	Alabama A&M University	235
Katherine Sanidad	Stony Brook University	302
Heather Savage	Stony Brook University	302
Alexandra Scavelli	University at Albany	238
Janki Shah	Stony Brook University	302
Alice Shanklin	Juniata College	240
Ryan Sheedy	University of Florida	244
Mackenzie Shipley	Hartwick College	246
Paul Sieradzki	Fordham University	302
Michael Skinner	Marist College	253
Katherine Skinner	Princeton University	302
Phil Smith	University of the Virgin Islands	302
Griffin St. Clair	Stony Brook University	257
Amanda Stasiewicz	Siena College	302
Isaac Stein	Tallahassee Community College	260
Taylor Stiegler	Boston College	240, 263
Jared Stier	North Caolina State University	267
Jordan Stubleski	Michigan State University	303
Mingxiu Sun	University of Illonios	270

Greg Swirson	Stony Brook University	276
Nouze Takougang	Montgomery College	303
Yunli Tang	Binghamton University	303
Alanna Tieman	University of Delaware	303
Joshua Tiffany	Southwest Baptist University	278
Nikita Timofeev	Stony Brook University	280
Steven Trabocchi	Stony Brook University	288
Adam Vorwald	Roger Williams University	303
Alyssa Watt	Villanova University	303
Daniel Weinman	Farmingdale State College	288
Tarletta Williams	Tallahassee Community College	293
Rebecca Winter	Columbia University School of Engineering	295
Ryan Wong	Northeastern University	303
Christopher J. Wright	Brown University	303
Katarzyna Zabrocka	Stanford University	303
Nicole Zmich	Queensborough Community College	303